

NASA Contractor Report 4645

NASA-UVa Light Aerospace Alloy and Structures Technology Program Supplement: Aluminum-Based Materials for High Speed Aircraft

Semi-Annual Report July 1, 1992–December 31, 1992

*Edited by
E. A. Starke, Jr.
University of Virginia • Charlottesville, Virginia*

This publication is available from the following sources:

NASA Center for AeroSpace Information
800 Elkrige Landing Road
Linthicum Heights, MD 21090-2934
(301) 621-0390

National Technical Information Service (NTIS)
5285 Port Royal Road
Springfield, VA 22161-2171
(703) 487-4650

TABLE OF CONTENTS

	Page
Introduction	1
TASK 1. I/M 2XXX and 6XXX Alloy Development (Alcoa Lead; Boeing & Douglas Participation)	3
Subtask 1A. I/M 2XXX Alloy Development (Alcoa)	5
Subtask 1B. I/M 6XXX Alloy Development (Alcoa)	32
TASK 2. I/M Al-Cu-Li-Mg-Ag Alloy Development (Reynolds Lead; UVa, Boeing & Douglas Participation)	52
Subtask 2A. Evaluate RX818 Variation Alloys as Model Materials to Understand the Role of Various Strengthening Phases During Thermal Exposure (Reynolds Metals Company)	55
Subtask 2B. A Study of the Microstructure/Property Evolution Characteristics of the Al-Li-Cu-Mg-Ag Systems with RX818 (University of Virginia)	92
TASK 3. P/M 2XXX Alloy Development (Alcoa Lead; Boeing & Douglas Participation)	103
TASK 4. Al-Si-Ge Alloy Development (University of Virginia)	119
TASK 5. Toughness Study of P/M Al-Fe-X System (Alcoa)	135
TASK 6. Processing-Based Improvements in the Mechanical Isotropy and Intermediate Temperature Damage Tolerance of Al-Fe-V-Si Alloy 8009 (Allied Signal/UVa)	151
Subtask 6A. HTA 8009 Processing (Allied-Signal)	152
Subtask 6B. Fracture Toughness Evaluations (UVa)	262

TASK 7.	Strength/Toughness Combination in DMMCs (Alcoa Lead; Boeing & Douglas Participation)	312
TASK 8.	Investigation of the Formation of the Ω Phase in Modified 2009 and Characterization of the Modified Alloys' Thermomechanical Properties (UVa)	320
TASK 9.	Accelerated Exposure Study (Alcoa)	349
TASK 10A.	Materials Technology Trade-Off Studies for the Airframe (Boeing)	357
TASK 10B.	Materials Technology Trade-Off Studies for the Airframe (Douglas)	365
	BOEING REPORT ON MATERIALS CHARACTERIZATION	366
	MCDONNELL DOUGLAS REPORT ON MATERIALS CHARACTERIZATION	376

Introduction

Market projections indicate that a substantial potential demand exists for a high-speed civil transport (HSCT) to operate in the long-range international market. Preliminary design and technology development efforts are underway to better understand all requirements including the technical and economic feasibility of the HSCT. Ongoing studies show airplanes designed to fly between Mach 2.0 and 2.5, with a capacity of 250 to 300 passengers and a range of at least 5000 nmi, have the best opportunity of meeting the economic objectives. The key critical development issue for an economically viable HSCT airframe will be the development of materials and processes which allow a complex, highly-stressed, extremely weight-efficient airframe to be fabricated and assembled for a dollar-per-pound not greatly different than today's mature airframes. Considering challenges in environmental control, propulsion, and materials technologies, it is believed that an acceptable aircraft could be certified for airline service in 2005.

The present study titled "Aluminum-Based Materials for High Speed Aircraft" was initiated to identify the technology needs associated with advanced, low-cost aluminum base materials for use as primary structural materials. Using a reference baseline aircraft, these materials concepts will be further developed and evaluated both technically and economically to determine the most attractive combinations of designs, materials, and manufacturing techniques for major structural sections of an HSCT. Once this has been accomplished, the baseline aircraft will be resized, if applicable, and performance objectives and economic evaluations made to determine aircraft operating costs.

The two primary objectives of this study are: (1) to identify the most promising aluminum-based materials with respect to major structural use on the HSCT and to further develop those materials, and (2) to assess these materials through detailed

trade and evaluation studies with respect to their structural efficiency on the HSCT.

TASK 1. I/M 2XXX and 6XXX ALLOY DEVELOPMENT

Principal Investigator, Alcoa:	Dr. L.M. Angers
Principal Investigator, Boeing:	Dr. W.E. Quist
Principal Investigator, Douglas:	Mr. R. Kahandal
UVa Contact:	Dr. E.A. Starke, Jr.

Abstract

Four classes of aluminum alloys have been investigated as candidates for the lower wing and fuselage of a high speed aircraft. Three of these classes, e.g., I/M 2XXX, I/M 6XXX and P/M 2XXX alloys, were targeted at a Mach 2.0 aircraft while the fourth type, e.g., P/M Al-Fe-Ce-Mg, was targeted at a Mach 2.4 aircraft. All were produced as 0.125" thick sheet. Of the Mach 2.0 candidates, the best strength/plane stress toughness combination was achieved in a P/M alloy having the composition Al-5.72 Cu-0.54 Mg-0.31 Mn-0.51 Ag-0.57 Zr-0.1V. That alloy achieved a tensile yield strength of 74 ksi at a K_{IC} of 126 ksi $\sqrt{\text{in}}$. The best I/M 2XXX alloy, Al-5.75 Cu-0.52 Mg-0.30 Mn-0.49 Ag-0.16 Zr-0.09V achieved a tensile yield strength of 70 ksi at a K_{IC} of 110 ksi $\sqrt{\text{in}}$. Since the alloys are similar in composition except for the higher Zr content of the P/M alloy, the difference in strength/plane stress fracture toughness combination may be due to grain structure differences, i.e., the P/M sheet was predominantly unrecrystallized while the I/M sheet was recrystallized. The hardnesses and strengths of all the I/M 6XXX alloys were too low to warrant further study. The best I/M 2XXX alloys have been chosen for further investigation.

Although Mg additions to the P/M Al-8 Fe-4 Ce alloy resulted in greater work hardenability, the plane stress fracture toughness was reduced. For the Al-8 Fe-4 Ce-0.5 Mg alloy, the best strength/plane stress fracture toughness combination was achieved in product forms receiving the highest degree of thermomechanical processing. Furthermore, the greatest crack growth resistance and

the most stable crack growth was measured in specimens that were tested at low crosshead speeds.

Some characterization of 0.125" thick sheet of discontinuously reinforced metal matrix composites was also carried out in the current program since these materials are considered as candidates for the upper wing of a high speed aircraft. Variations in rolling practice did not produce significant differences in strength/plane stress fracture toughness combinations. In the composites having a 2XXX-T6 matrix and 20% SiC, tensile yield strengths varied from 70 to 76 ksi, while all K_{Ic} values were less than 30 ksi $\sqrt{\text{in}}$. Higher toughnesses and lower strengths were obtained for composites having a 6113-T6 matrix.

Preliminary studies of the effects of stressed and unstressed elevated temperature exposure on residual strengths were also conducted for three materials: 2519-T87, 2080/SiC/20p and 6013-T6. All materials were degraded as a result of exposures at 300°F, however, stresses of 18 ksi did not enhance degradation in any of the materials.

Subtask 1A. I/M 2XXX Alloy Development (Alcoa)

Principal Investigator: Dr. L.M. Angers
Senior Engineer: Dr. G. Dixon

Objective

The primary objective of this task is to develop a damage tolerant aluminum based material for the lower wing and fuselage of a Mach 2.0 aircraft. This material must first meet preliminary strength and toughness targets at room temperature and then several criteria associated with elevated temperature service (e.g., retention of room temperature properties after exposure, performance at the operating temperature and resistance to creep deformation).

The ingot metallurgy (I/M) 2XXX alloys are under consideration here because existing Al-Cu-Mg alloys combine relatively high strengths with good thermal stability.

Background

A series of four alloys were selected to explore the effects of trace element additions in 2519. Specifically, the effects of Mg, Si and Ag on precipitation were of interest. During the first reporting period (1), these alloys were cast as 6" thick x 16" wide x 60" long ingots, stress relieved in an 850°F furnace and preheated. Their actual compositions in weight percent were:

689245: Al-5.71 Cu-0.18 Mg-0.29 Mn-0.15 Zr-0.09 V-0.05 Fe-0.06 Si
689246: Al-5.78 Cu-0.22 Mg-0.29 Mn-0.14 Zr-0.09 V-0.06 Fe-0.25 Si
689247: Al-5.83 Cu-0.52 Mg-0.30 Mn-0.14 Zr-0.10 V-0.05 Fe-0.05 Si
689248: Al-5.75 Cu-0.52 Mg-0.49 Ag-0.30 Mn-0.16 Zr-0.09 V-0.06
Fe-0.05 Si.

Alloys 689245 through 689248 were designed to study the effects of Mg, Si and Ag on precipitation in 2519-type alloys.

Note that alloy 689245 is the 2519 control, alloy 689246 contains excess Si, alloy 689247 contains excess Mg and alloy 689248 contains combined additions of Mg and Ag. Alloy 2519 was chosen as a baseline since recent data suggest that it has a promising strength/plane stress toughness combination when compared to 2024-T3 and 6013-T6. Furthermore, 2519-T87 has a significantly higher tensile yield strength than either of the other two alloys. Si, Mg and Ag were all expected to provide further improvements in strength.

Two additional alloys were selected by Professor E.A. Starke for evaluation by University of Virginia researchers. The alloys, whose nominal compositions are Al-4.2 Cu-1.2 Li-0.08 In-0.15 Zr and Al-4.2 Cu-1.2 Li-0.15 Zr were designed to examine the role of In as a nucleation aid for the relatively stable T_1 plates.

Procedure

(a) 2519 Variants

The four I/M 2519 variants were rolled to sheet, using a combination of cross rolling and straight rolling. Preheated rolling sections were initially heated to 825°F and reheated whenever surface temperatures reached about 750°F. Twelve passes and two reheats were used to produce sheet having a width of 17" and a thickness of 0.125".

A set of sheet samples were heat treated, stretched 8% and artificially aged at 350°F to produce T8-type tempers. Aging times of 1, 3, 8 and 24 hr were selected for all alloys. In addition, a set of sheet samples were heat treated, stretched less than 1% in order to straighten the sheet, and artificially aged at 350°F to produce T6-type tempers. Aging times of 2, 8, 16 and 48 hr were selected for all alloys.

The solution heat treatment temperatures varied for the four alloys. These temperatures were chosen based on differential scanning calorimetry on preheated ingot samples.

S. No.	Alloy Description	Solution Heat Temperature (°F)
689245	2519 control	995
689246	High Si 2519	990
689247	High Mg 2519	985
689248	High Mg 2519 + Ag	985

Rockwell B hardness and electrical conductivity measurements were taken for each of the four aging times. Optical metallography and Guinier X-ray diffraction were done on samples aged to peak hardness. Additional preheating studies using optical metallography and thermal analysis were carried out on S. Nos. 689247 and 689248, in order to determine whether maximum solid solubilities for Cu and Mg had been exceeded in these alloys.

Two longitudinal tensile samples were prepared for each alloy and aging condition. One tensile sample was used to generate complete stress-strain curves, the other to obtain precise values for tensile yield strength and ultimate tensile strength. A single L-T 6.3" x 20" center crack panel and two L-T Kahn tear samples were prepared for each alloy and condition.

Once the aging time required to reach peak strength was determined, peak aged T8-type samples were subjected to a Mach 2.0 simulation of 600 hr at 300°F. Two longitudinal tensile samples and a single L-T 6.3" x 20" center crack fracture toughness panel were tested from these samples.

(b) Li-bearing Alloys

Four 2" x 10" x 14" Al-Cu-Li-Zr-(In) ingots were cast for University of Virginia researchers. These alloys are 2020 variants which utilize Zr for grain structure control. Two ingots

contain In additions as nucleation aids and two do not. Their actual compositions are given below.

<u>S. No.</u>	<u>Cu</u>	<u>Li</u>	<u>In</u>	<u>Zr</u>	<u>Fe</u>	<u>Si</u>
725036-A	4.04	1.2	0.09	0.15	0.05	0.04
725036-B	4.06	1.21	0.09	0.16	0.04	0.05
725037-A	4.08	1.26	<0.005	0.15	0.04	0.06
725037-B	4.01	1.24	<0.005	0.16	0.04	0.05

Differential scanning calorimetry on one of the ingots, S. No. 725036-A, indicated that the onset temperature for the eutectic melting reaction was at 969°F. Therefore, ingots were preheated for 24 hr at 960°F prior to rolling in order to dissolve soluble constituent.

All four ingots were heated to 800°F. One ingot of each composition was rolled to 1.0" thick plate using three passes. The other ingot of each composition was rolled to 0.125" thick sheet using seven passes and two reheats.

All plate and sheet were provided to University of Virginia researchers.

Results And Discussion

(a) 2519 Variants

Rockwell B hardness and electrical conductivity measurements as a function of T8 aging time are presented in Table I. Hardness and electrical conductivity values represent averages from 5 and 2 readings, respectively.

Figure 1 shows how Rockwell B hardness values varied for the four alloys. The highest hardnesses were achieved in the Ag-bearing variant of 2519 (S. No. 689248); however, a significant hardness advantage over the 2519 control (S. No. 689245) was also

achieved in the high Mg variant (S. No. 689247).

Differential scanning calorimetry (DSC) data, e.g., onset temperatures, maximum temperatures and areas of reactions, from preheated ingot and T8-type sheet are presented in Table II. A single eutectic melting reaction occurs in all of the preheated ingot and T8 sheet samples. The reaction of interest, $L \rightarrow Al (ss) + Al_2Cu$, begins at temperatures of 989°F or higher in the preheated samples. Since the maximum temperature seen during preheating by all four variants was 985°F, there should have been no eutectic melting in any of the samples and this was confirmed by optical metallography. However, there was undissolved θ phase in all, suggesting that the actual compositions are beyond maximum solubility or that the preheating temperatures used were not high enough. Similarly, the eutectic melting reaction persists in DSC data from the solution heat treated and aged samples and undissolved θ phase was seen in optical metallography.

Additional DSC data from further investigation of solution heat treatment practices for S. Nos. 689247 and 689248 are presented in Table III. By increasing solution heat treatment temperature in increments of 5°F, eutectic melting reactions and solvi were approximated. For S. No. 689247, the eutectic melting reaction could not be eliminated entirely, indicating that maximum solid solubility for Cu and Mg has been exceeded. Solution heat treatments for this alloy must be limited to 990°F in order to avoid the melting reaction. For S. No. 689248, the reaction $L \rightarrow Al (ss) + Al_2Cu$ was eliminated if a solution heat treatment temperature of 995°F or higher was used, suggesting that the solvus is between 990°F and 995°F and that solid solubilities have not been exceeded for this composition. The second melting

reaction which appears in S. No. 689248 probably involves the $\text{Al}_{20}\text{Cu}_2\text{Mn}_3$ phase and is not a concern since it is not necessary to eliminate that reaction. Furthermore, it is at a high enough temperature that we can avoid it during solution heat treatment.

The grain structures of sheet from the 2519 variants were fully recrystallized throughout the entire thicknesses of the sheets. The optical micrographs in Fig.2 show this for two representative samples: S. Nos. 689247 and 689248 in the T8 temper. This is not surprising since the 2XXX alloys are frequently recrystallized, especially in thin plate and sheet.

Guinier X-ray diffraction and transmission electron microscopy results provided information on the dispersoids and precipitates in the 2519 variants. The results of Guinier X-ray diffraction on the T8 sheet samples are presented in Table IV. All of the 2519 variants contain $\text{Al}_{20}\text{Cu}_2\text{Mn}_3$ dispersoids and $\text{Al}_7\text{Cu}_2\text{Fe}$ constituent. The only sample for which any Zr-bearing phase was detected by this method was the high Si variant. In that sample, reflections consistent with a tetragonal Al-Si-Zr phase (2) were observed. That phase is probably related to Al_3Zr . The L_{12} or DO_{23} forms of Al_3Zr were not detected in any of the other samples; however, this does not necessarily mean neither are present. Both forms are difficult to detect by this method unless present in relatively large quantities.

Transmission electron microscopy revealed Al-Cu-Mn and Al-Cu-Zr dispersoids in all of the variants. A representative bright field micrograph from the T8 temper of S. No. 689248 is shown in Fig. 3. The Al-Cu-Mn particles tend to be rod-like or equiaxed; the Al-Cu-Zr phase is frequently cuboidal. The composition of the Al-Cu-Mn phase is described by $\text{Al}_{20}\text{Cu}_2\text{Mn}_3$ as suggested by X-ray

diffraction but the composition of the Al-Cu-Zr phase is unknown. No structural characterization by TEM was done, although it could be hypothesized that it is a Cu- modified form of Al_3Zr , e.g., $(\text{Al,Cu})_3\text{Zr}$, since there is a precedence for the substitution of Cu onto the Al sublattice to stabilize the Ll_2 phase. This is probably the same phase that has been called Al_3CuZr_2 by Pearson. It has the Ll_2 structure and a lattice parameter of 0.404 nm (3).

Guinier X-ray diffraction data reveals the θ' and θ phases in the T8 tempers of all four variants, but the technique does not distinguish between θ phase and Ω phase. In the Ag-bearing alloy, S. No. 689248, diffuse background intensity is present at the θ phase reflections, suggesting that these reflections are due to fine Ω precipitates. Since the X-ray diffraction technique provides no size information, it is impossible to say whether the θ phase is present as undissolved constituent, grain boundary precipitate, etc.

Transmission electron microscopy confirmed the presence of Ω in the T8 temper of the Ag-bearing alloy, S. No. 689248. The selected area diffraction patterns for S. Nos. 689247 and 689248 are compared in Fig. 4. The reflections are characteristic of θ' and Ω precipitates in S. Nos. 689247 and 689248, respectively.

The results of tensile and toughness testing of sheet of 2519 variants in the T8 and T6 type tempers are presented in Tables V and VI, respectively. None of the plane stress toughness tests produced valid K_{IC} numbers. All failed the criterion requiring that the net section stress/tensile yield strength is < 0.8 .

Representative true stress-true strain curves are presented in Fig. 5 for the T6 tempers of sheet from the Ag-bearing alloy, S. No. 689248. Note that the general shape of the curve does not

change as the sheet proceeds from an underaged condition to an overaged condition.

Representative plots of crack growth resistance vs. effective crack extension (R-curves) are presented in Fig. 6 for peak aged T8 conditions of sheet from the 2519 variants. Although all K_{IC} values are invalid, they occur before any inflection points in the R-curves, suggesting that the K_{IC} values are conservative.

In T8 type tempers, additions of Mg and combined additions of Mg and Ag are equally effective in increasing the strength of alloy 2519. Tensile yield strength is plotted as a function of aging time at 350°F in Fig. 7 for the sheet which had been solution heat treated, quenched and stretched 8%. The high Si variant developed a tensile yield strength equivalent to the 2519 control, while the other two variants developed 10% higher tensile yield strengths. The rate of overaging in all of the variants was similar.

In T6 type tempers, combined additions of Mg and Ag are most effective in increasing the strength of alloy 2519, but additions of Mg or Si alone also have a strengthening effect. Tensile yield strength is plotted as a function of aging time at 350°F in Fig. 8 for the sheet which had been solution heat treated and quenched. The high Si and high Mg variants developed 10% higher tensile yield strengths and the alloy with both Ag and Mg developed 20% higher yield strengths than the 2519 control. As in the T8 tempers, the rate of overaging in all of the variants was similar.

The most promising strength/toughness combinations were obtained in the T8 tempers of the high Mg variant and the high Mg variant with Ag (Fig. 9). Both alloys exhibited a significant performance improvement over the 2519 control. When combined with

the optical metallography results which suggest that constituent volume fraction can be further reduced to improve toughness, these strength/toughness combinations are particularly promising.

The T8 and T6 strength/toughness combinations are very similar for the Ag-bearing alloy, while the T8 strength/toughness combinations are superior to the T6 combinations for all of the other variants (Fig. 10).

Losses in strength and toughness occur in the 2519 variants after a Mach 2.0 simulation of 600 hr at 300°F. Tensile and toughness data from T8 sheet tested before and after simulation of Mach 2.0 service are presented in Table VII and Fig. 11. The greatest losses in strength (about 8%) and toughness (about 15%) occur in the highest strength alloys, e.g., the high Mg variant and the high Mg variant with Ag; however, both still have a strength/toughness advantage over the 2519 control and the high Si variant. The possibility that reductions in K_c and K_{app} after exposure may be due solely to strength loss cannot be ruled out since all toughness tests were invalidated because of net section yielding.

Values for unit propagation energies (UPE) from the Kahn tear test are not a good indication of the plane stress fracture toughness (see Table V). For a given variant, the highest values for UPE were measured in samples given a different aging time than the samples which produced the highest values for K_c . In some instances, very different values for UPE were measured in two samples in which similar values for K_c were measured. Finally, the alloy that had the highest values for K_c (S. No. 689248) had some of the lowest values for UPE.

Summary

- When using the conservative practices suggested by DSC results, soluble phases were still present in heat treated and aged sheet. Further heat treating studies indicate that reduced levels of constituent can be achieved without causing eutectic melting.
- The grain structures of all sheet samples were recrystallized, which is not unexpected considering the gage and the amount of dispersoid forming elements present.
- Two types of dispersoid forming elements were present in all four 2519 variants: $\text{Al}_{20}\text{Cu}_2\text{Mn}_3$ and an Al-Cu-Zr phase. Both types were several tenths of a micron in size. No Ll_2 Al_3Zr particles were observed.
- Transmission electron microscopy and X-ray diffraction indicate that the 2519 control, the high Si variant and the high Mg variant are strengthened by θ' . The high Mg variant with Ag is strengthened by Ω phase.
- The best strength/toughness combinations were achieved in T8-type tempers of the high Mg variant and the high Mg variant with Ag. The T6 temper of the high Mg variant with Ag had nearly the same strength/toughness combination as the T8 temper.
- Losses in strength and toughness of the T8 tempers occurred as a result of Mach 2.0 simulation of 600 hr at 300°F. The greatest losses occurred in the alloys with the best strength-toughness combinations, e.g., the high Mg variant and the high Mg variant with Ag; however, these alloys maintained an advantage over the 2519 control and the high Si variant.

References

1. E.A. Starke, Jr., "NASA UVa Light Aerospace Alloy and Structure Technology Program Supplement: Aluminum-Based Materials for High Speed Aircraft," NASA Contractor Report 4517, June 1993.
2. JCPDS - International Center for Diffraction Data, "Powder Diffraction File, Inorganic Phases," Swarthmore, PA, 1992.
3. P. Villars and L.D. Calvert, Pearson's Handbook of Crystallographic Data for Intermetallic Phases, Vol. 2, ASM, Metals Park, OH, 1985.

Table I. Rockwell B hardness and electrical conductivity (EC) as a function of T8 aging time for the 2519 variants. Sheet samples were heat treated, quenched, stretched 8% and artificially aged at 350°F for the times indicated. Hardness and EC values represent averages from 5 and 2 readings, respectively.

S. No.	Alloy Description	Aging Time (hr)	Hardness	EC (% IACS)
689245	2519 Control	1	77.8	32.3
		3	80.0	32.7
		8	79.4	34.1
		24	78.0	35.1
689246	High Si 2519	1	77.3	32.4
		3	78.3	33.6
		8	81.0	34.2
		24	78.9	35.6
689247	High Mg 2519	1	78.4	31.2
		3	81.7	32.6
		8	82.3	34.2
		24	81.0	35.1
689248	High Mg 2519 + Ag	1	82.3	32.0
		3	84.9	32.4
		8	84.4	33.8
		24	82.0	34.4

Table II. Onset temperatures, maximum temperatures and areas for the eutectic melting reactions observed in preheated samples and solution heat treated and aged samples of the 2519 variants^a

S No.	Alloy Description	Preheated Ingot Samples				Solution Heat Treated & Aged Sheet ^b			
		Maximum Temperature of Preheat (°F)	Onset Temperature (°F)	Maximum Temperature (°F)	Reaction Area (J/g)	Temperature of Solution Heat Treatment	Onset Temperature (°F)	Maximum Temperature (°F)	Reaction Area (J/g)
689245	2519 Control	985	1000	1007	2.7	995	1004	1012	0.8
689246	High Si 2519	985	995	1004	2.0	990	997	1008	2.5
689247	High Mg 2519	985	989	997	1.2	985	991	1000	2.0
689248	High Mg 2519 + Ag	985	992	1001	2.1	985	995	1007	2.3

^a All differential scanning calorimetry data were collected using a heat-up rate of 36°F/min.

^b Sheet samples were heat-treated, quenched, stretched 8% and artificially aged to peak strength at 350°F.

Table III. Onset temperatures, maximum temperatures and areas for the eutectic melting reactions observed in sheet samples solution heat treated and quenched from various temperatures^a. All samples were held 1 hr prior to quenching.

S No.	Alloy Description	Temperature of Solution Heat Treatment	First Reaction			Second Reaction		
			Onset Temperature (°F)	Maximum Temperature (°F)	Reaction Area (J/g)	Onset Temperature (°F)	Maximum Temperature (°F)	Reaction Area (J/g)
689247	High Mg 2519	985	991.7	1004.6	1.69	-	-	-
		990	997.4	1005.6	0.322	-	-	-
		995	991.3	1038.8	15.80	-	-	-
		1000	985.9	1051.4	8.62	-	-	-
689248	High Mg 2519 + Ag	985	997.4	1007.2	1.21	1035.2	1059.7	11.11
		990	995.9	1006.8	1.29	1038.1	1059.9	8.85
		995	-	-	-	1034.2	1058.8	8.49
		1000	-	-	-	1030.7	1061.3	20.1

^a All differential scanning calorimetry data were collected using a heat-up rate of 36°F/min.

Table IV. Relative quantities of phases identified using Guinier X-ray diffraction on sheet of the 2519 variants. Sheet samples were heat-treated, quenched, stretched 8% and artificially aged at 350°F.

S. No. ^a	Alloy Description	S'	θ'	θ(CuAl ₂)	Al ₂₀ Cu ₂ Mn ₃	Al ₇ Cu ₂ Fe	Al ₁₂ (Mn,Fe) ₃ Si	(Al,Si,Zr) ^c
689245-3A	2519 Control	-	v. small +	small +	medium -	medium -	-	-
689246-8A	High Si 2519	-	medium -	medium +	small	small -	medium -	medium
689247-8A	High Mg 2519	poss. trace	small +	medium +	medium	medium	-	-
689248-3A	High Mg 2519 + Ag	poss. trace	small -	medium + ^b	medium	medium	-	-

^a The number preceding "A" in the S. number indicates the number of hours of artificial aging.

^b Guinier X-ray diffraction cannot distinguish between θ and Ω phase. Diffuse background at strong θ phase reflections suggest the presence of Ω phase.

^c Card 14-G25 from Reference 2. Crystal structure is tetragonal with a = 0.5519 nm and c = 0.9008 nm; composition is Al_{0.45} Zr_{0.333} Si_{0.217}, e.g., Al₃Ti type.

TABLE V. Results of tensile^a and fracture toughness^b testing of sheet of 2519 variants in T8 type tempers. All sheet was solution heat-treated, cold water quenched, stretched 8% and aged at 350°F.

S. Number	Alloy Description	Aging Time, hr	Tensile Yield Strength, ksi	Ultimate Tensile Strength, ksi	% Elongation ^c	Uniform Strain	Strain Hardening Exponent	K _C ksi√in.	K _{app} ksi√in.	Validity Status ^d	Average Unit Propagation Energy in-lb/in ²
689245	2519 Control	1	59.7	69.1	16	0.1276	0.097	99.7	73.1	No	1025
		3	62.8	70.2	14	0.1038	0.079	105.2	74.7	No	804
		8	62.9	69.5	12	0.0826	0.074	100.9	70.0	No	518
		24	60.8	68.8	12	0.0734	0.082	97.5	70.4	No	588
689246	High Si 2519	1	57.1	67.5	17	0.1451	0.109	98.7	71.5	No	812
		3	62.4	69.3	13	0.0873	0.069	98.3	70.4	No	437
		24	62.8	69.8	11	0.0735	0.073	78.7	58.9	No	293
689247	High Mg 2519	1	62.1	70.6	17	0.1218	0.086	105.6	74.6	No	1094
		3	69.1	73.1	13	0.0865	0.059	107.0	75.8	No	885
		8	70.3	74.0	13	0.0736	0.057	94.5	69.2	No	648
		24	67.1	72.2	11	0.0651	0.059	100.4	70.6	No	330
689248	High Mg 2519 + Ag	1	67.6	73.2	14	0.0883	0.054	108.9	76.8	No	724
		3	70.4	74.4	11	0.0780	0.053	110.4	73.5	No	526
		8	69.5	74.5	11	0.0713	0.055	101.6	73.7	No	588
		24	65.4	71.9	10	0.0721	0.063	100.1	71.1	No	385

a All tensile data are from longitudinal specimens. A single specimen was used to measure tensile yield strength, ultimate tensile strength and % elongation; another specimen was used to measure uniform elongation and hardening exponent.

b All toughness data are from L-T specimens. A single 6.3 in. wide x 20 in. long panel was used to determine K_C and K_{app}. Values for unit propagation energy are averages from 2 Kahn tear tests.

c 2.0 in. gage length.

d Validity Criterion: Is net section stress/tensile yield strength <0.8?

TABLE VI. Results of tensile^a and fracture toughness^b testing of sheet of 2519 variants in T6 type tempers. All sheet was solution heat-treated, cold water quenched, and aged at 350°F.

S. Number	Alloy Description	Aging Time, hr	Tensile Yield Strength, ksi	Ultimate Tensile Strength, ksi	Elongation ^c , %	Uniform Strain	Strain Hardening Exponent	K _C ksi√in.	K _{app} ksi√in.	Validity Status ^d
689245	2519 Control	2	47.4	67.7	21.5	0.1848	0.170	123.6	62.2	No
		8	53.3	67.5	16.0	0.1267 ^f	0.121	101.3	67.0	No
		16	54.7	66.7	13.0	0.0926	0.106	99.9	67.1	No
		48	52.9	65.2	11.0 ^e	0.0734	0.109	97.3	65.8	No
689246	High Si 2519	2	46.8	64.3	23.0	0.1722	0.154	94.3	61.1	No
		8	55.9	67.4	14.0	0.1062 ^f	0.099	93.0	66.0	No
		16	60.5	69.2	10.5	0.0758	0.082	91.9	65.9	No
		48	57.0	67.2	10.0	0.0671 ^f	0.092	83.2	60.8	No
689247	High Mg 2519	2	49.6	69.2	16.0 ^e	0.1777	0.152	111.3	63.6	No
		8	58.2	69.1	13.0	0.1083	0.105	100.0	69.9	No
		16	60.5	69.3	10.5	0.0728	0.074	104.0	71.0	No
		48	60.0	68.4	10.0 ^e	0.0635 ^f	0.080	95.6	67.3	No
689248	High Mg 2519 + Ag	2	63.6	71.9	12.5 ^e	0.1044	0.078	107.6	74.9	No
		8	68.3	74.0	10.0 ^e	0.0637 ^f	0.053	108.3	75.2	No
		16	67.7	73.6	10.0 ^e	0.0620	0.051	97.0	67.5	No
		48	63.3	71.0	10.5	0.0618	0.069	84.4	63.3	No

- ^a All tensile data are from longitudinal specimens. A single specimen was used to measure tensile yield strength, ultimate tensile strength and % elongation; another specimen was used to measure uniform elongation and hardening exponent.
- ^b All toughness data are from L-T specimens. A single 6.3 in. wide x 20 in. long panel was used to determine K_C and K_{app}.
- ^c 2.0 in. gage length.
- ^d Validity Criterion: Is net section stress/tensile yield strength <0.8?
- ^e Sample failed outside middle half of gage length.
- ^f Sample failed at extensometer gage length.

TABLE VII. Results of tensile^a and fracture toughness^b testing of sheet of 2519 variants before and after simulation of Mach 2.0 service. All sheet was solution heat-treated, cold water quenched, stretched 8% and aged at 350°F.

S. Number	Alloy Description	Aging Conditions ^c	Tensile Yield Strength, ksi	Ultimate Tensile Strength, ksi	% Elongation ^d	K _c ksi√in.	K _{app} ksi√in.	Validity Status ^e
689245	2519 Control	T8 T8 + 600 hr/300°F	62.8 60.4	70.2 68.2	14 11	105.2 104.6	74.7 71.4	No No
689246	High Si 2519	T8 T8 + 600 hr/300°F	62.4 61.8	69.3 69.4	13 11 ^f	98.3 95.0	70.4 66.0	No No
689247	High Mg 2519	T8 T8 + 600 hr/300°F	69.1 66.0	73.1 71.9	13 10 ^f	107.0 91.3	75.8 65.2	No No
689248	High Mg 2519 + Ag	T8 T8 + 600 hr/300°F	70.4 65.1	74.4 71.7	11 10 ^f	110.4 97.2	73.5 67.5	No No

a All tensile data are from longitudinal specimens. Data for "T8" samples were from a single specimen. Data for "T8 + 600 hr/300°F" samples were averages from 2 specimens.

b All toughness data are from L-T specimens. A single 6.3 in. wide x 20 in. long panel was used to determine K_c and K_{app}.

c All "T8" samples were aged 3 hr at 350°F.

d 2.0 in. gage length.

e Validity Criterion: Is net section stress/tensile yield strength <0.8?

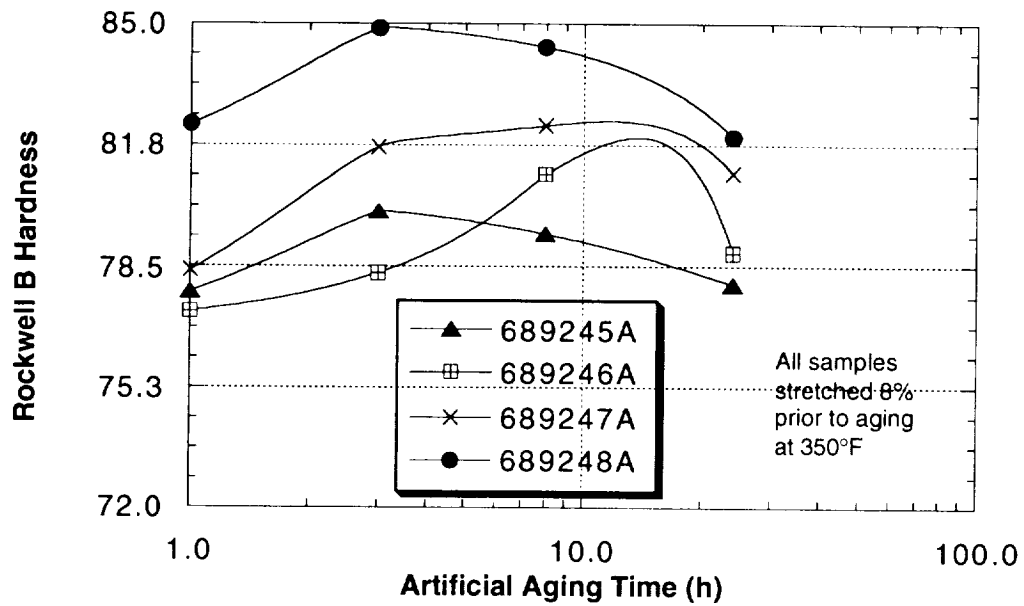


Figure 1. Rockwell B hardness as a function of artificial aging time for the 2519 variants solution heat treated, quenched and stretched 8%.



(a)

(b)

Figure 2. Optical micrographs of the L-LT plane of 0.125" thick sheet from: (a) S. No. 689247-T8 and (b) S. No. 689248-T8, revealing recrystallized grain structures. Samples were etched in a modified Barker's etch and viewed under cross-polarized light.

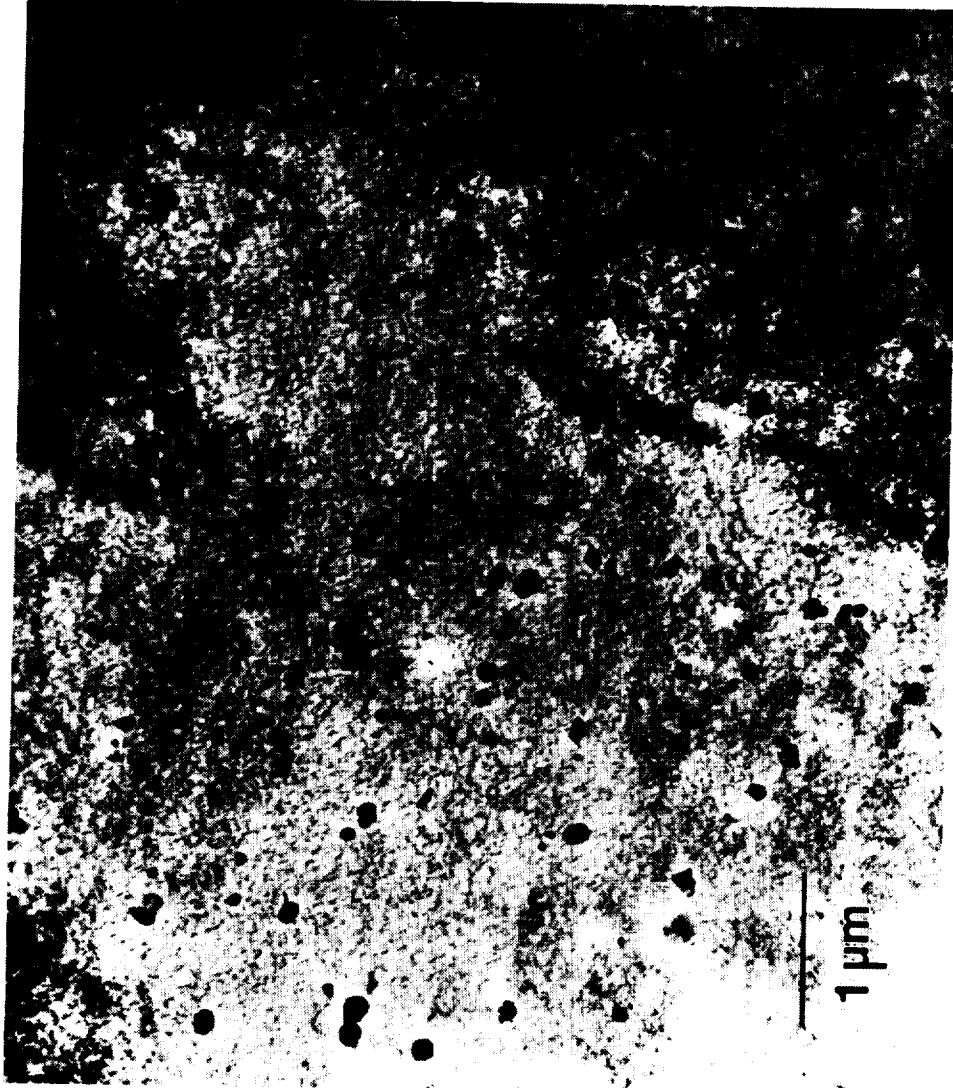
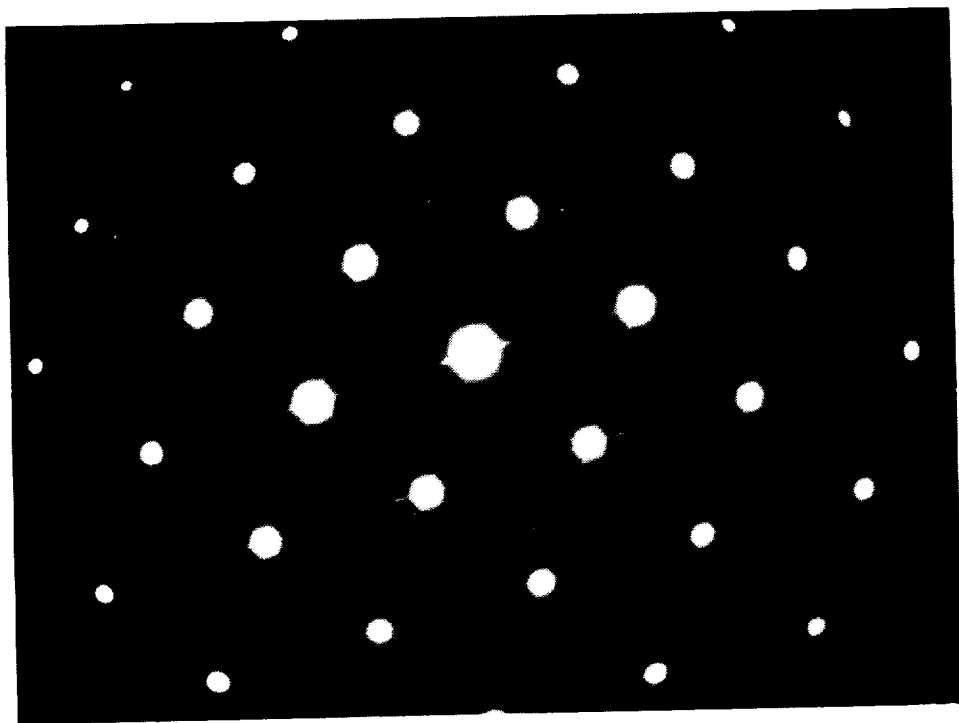
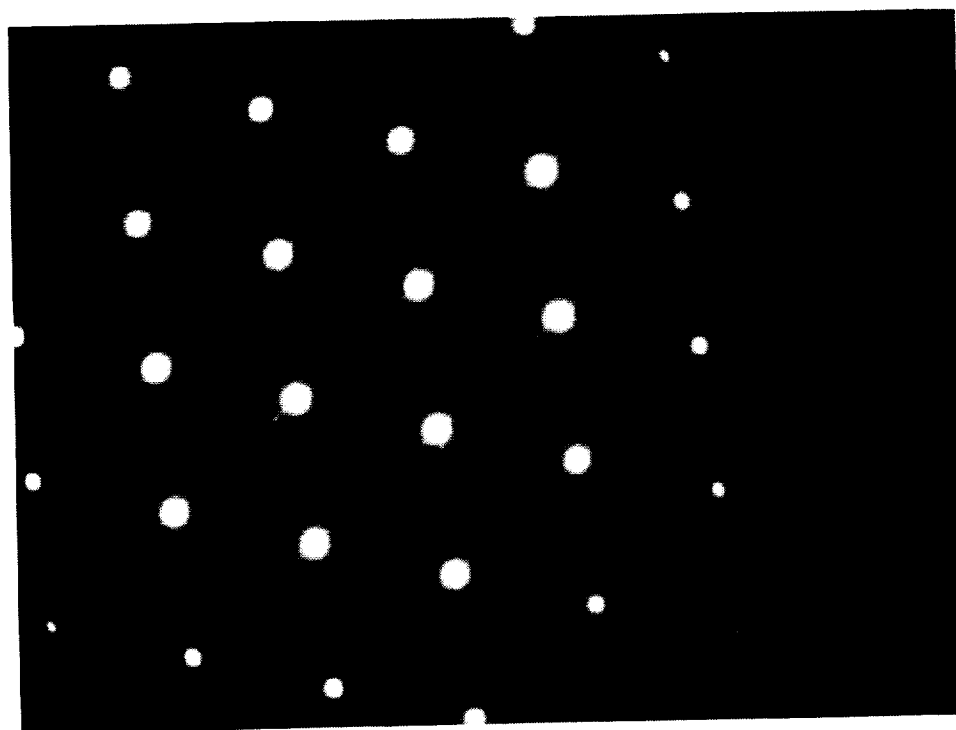


Figure 3. Transmission electron micrograph from 0.125" thick sheet of S. No. 689248-T8, revealing Al-Cu-Mn and Al-Cu-Zr dispersoids.



(a)



(b)

Figure 4. Selected area electron diffraction patterns from 0.125" thick sheet showing characteristic θ' reflections in:
(a) S. No. 689246-T8 and characteristic Ω reflections in (b) S. No. 689248-T8.

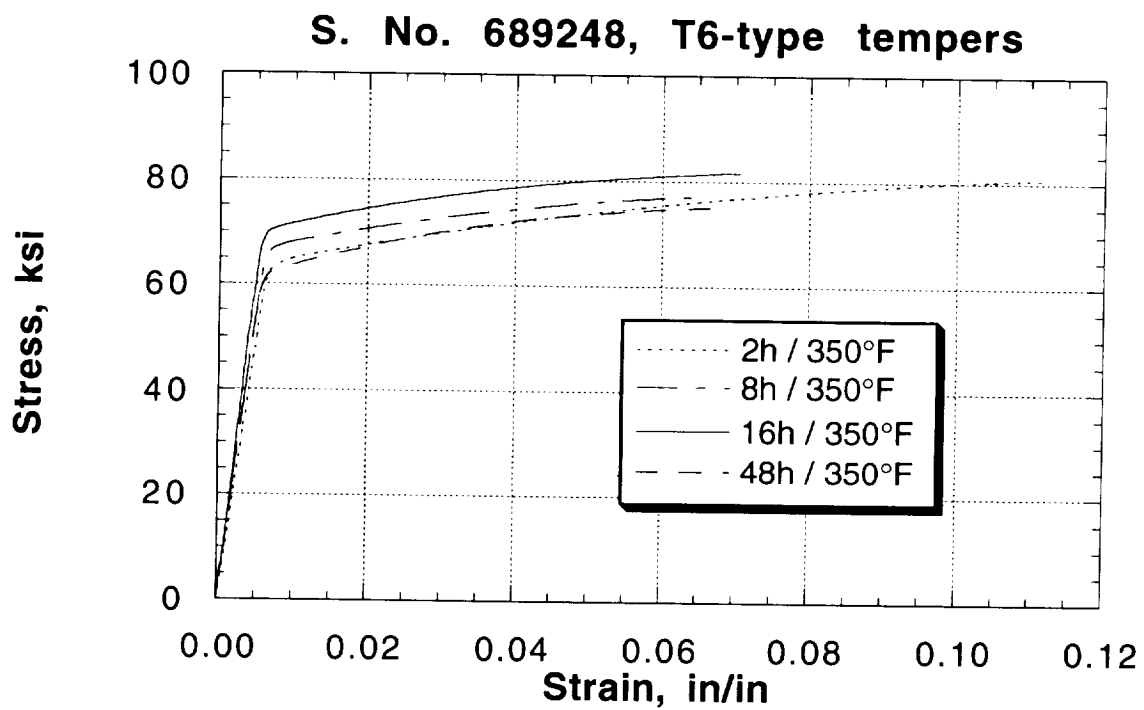


Figure 5. True stress vs. true strain for T6 tempers of sheet from the Ag-bearing alloy, S. No. 689248.

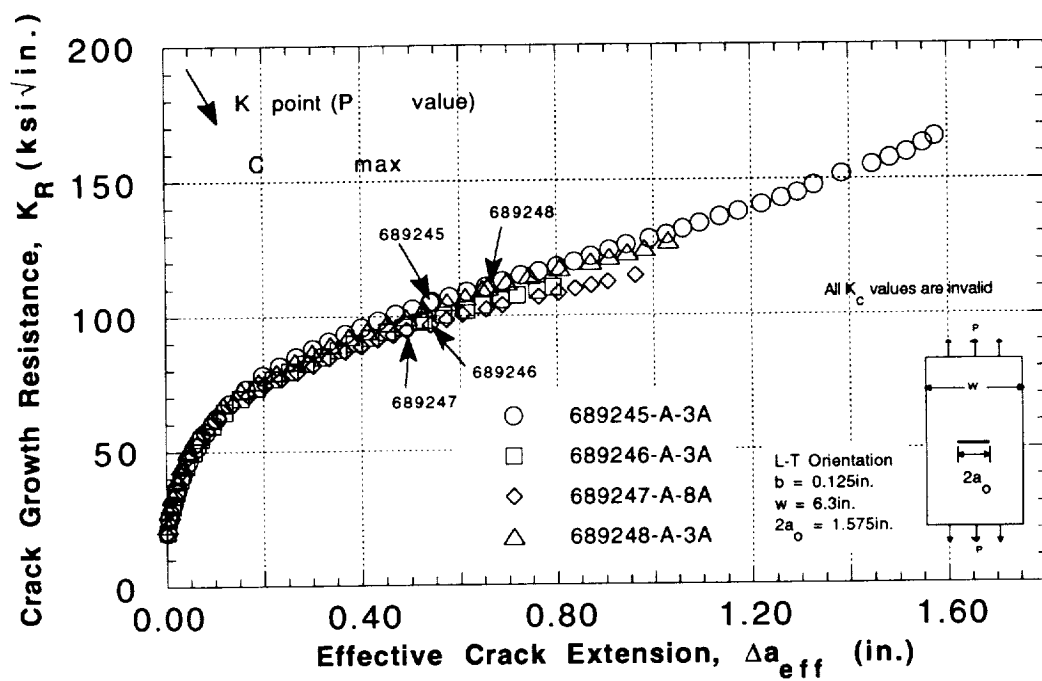


Figure 6. Crack growth resistance, K_R , vs. effective crack extension, Δa_{eff} , for peak aged T8 tempers of sheet from the 2519 variants.

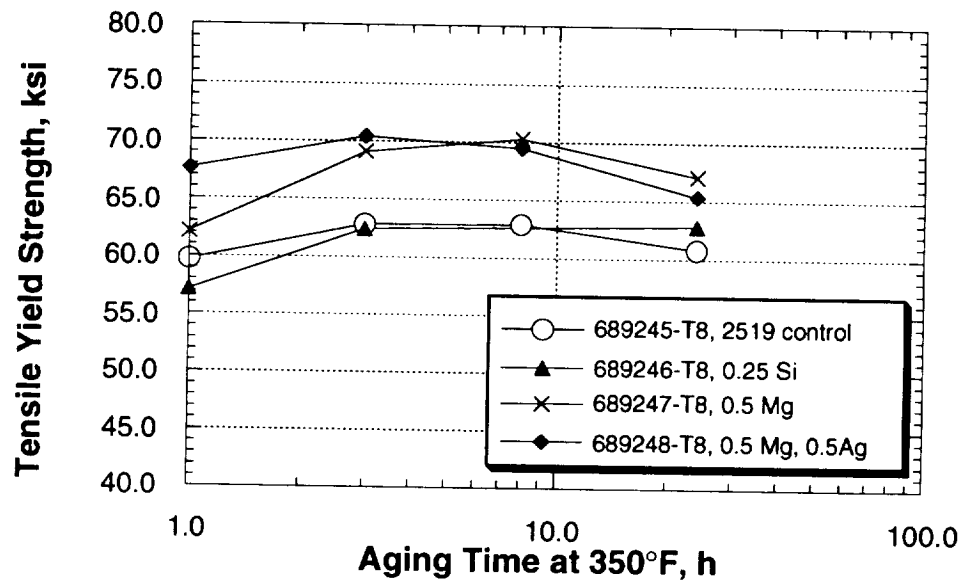


Figure 7. Tensile yield strength as a function of aging time at 350°F for the 2519 variants aged to T8-type tempers.

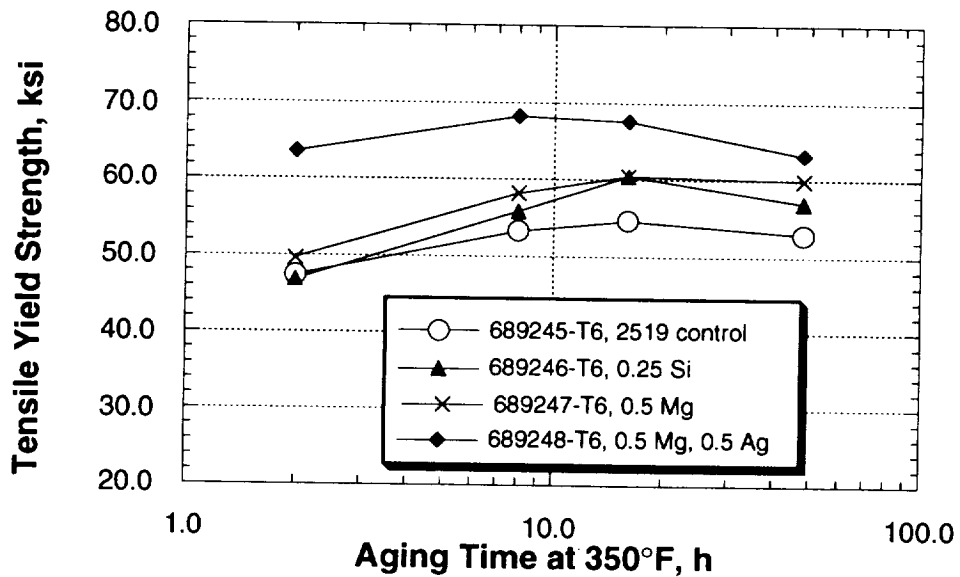


Figure 8. Tensile yield strength as a function of aging time at 350°F for the 2519 variants aged to T6-type tempers.

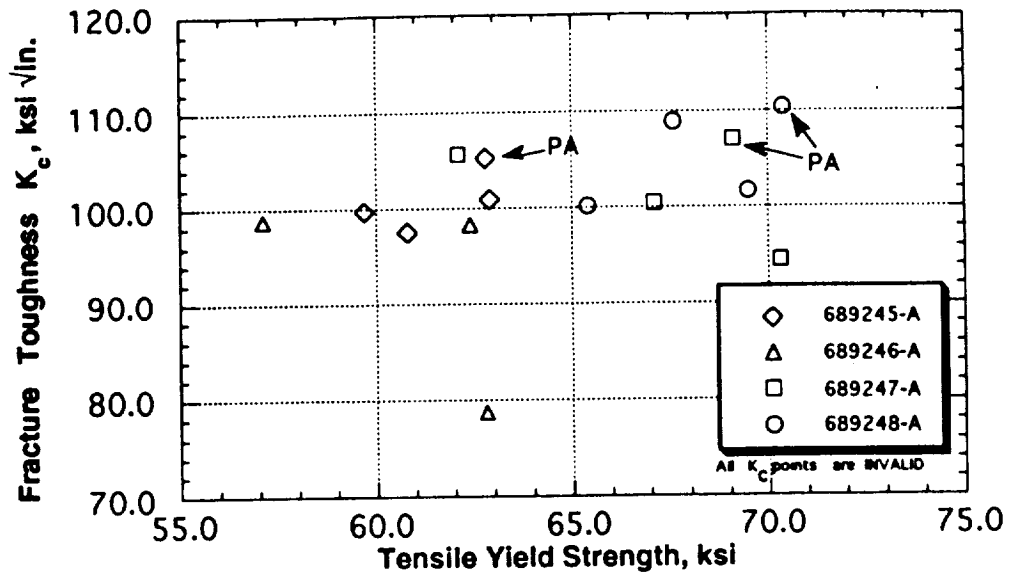


Figure 9. K_c fracture toughness as a function of tensile yield strength for the 2519 variants aged T8-type tempers.

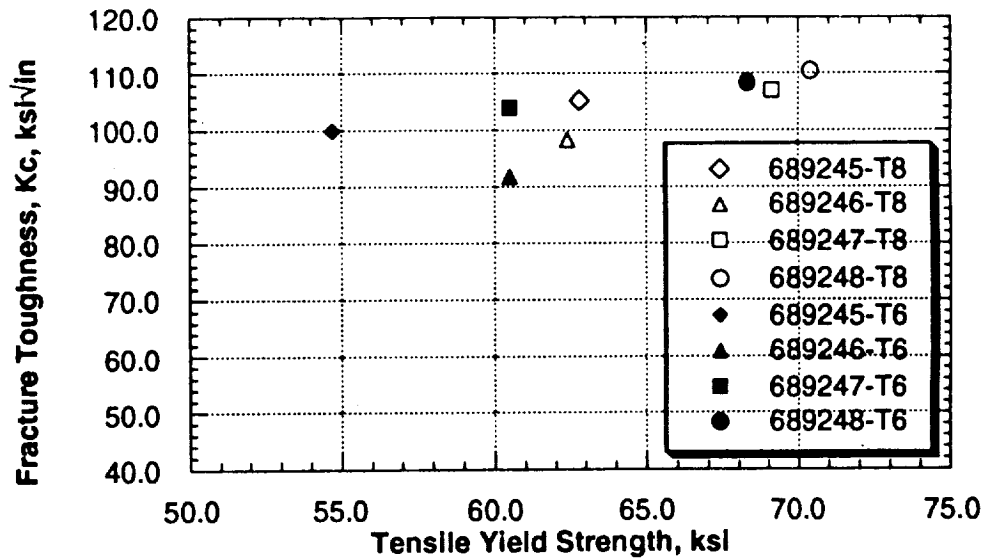


Figure 10. K_c fracture toughness as a function of tensile yield strength for the 2519 variants aged to peak strengths in T6- and T8-type tempers.

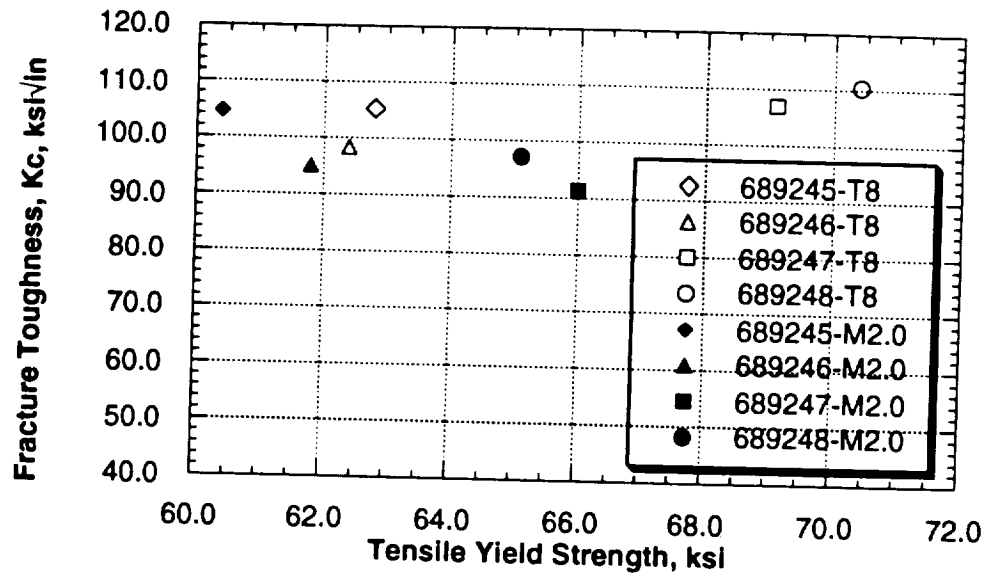


Figure 11. K_c fracture toughness as a function of tensile yield strength for 2519 variants aged to peak strength using a T8-type temper and then exposed to a Mach 2.0 simulation of 600 h at 300°F.

Subtask 1B. I/M 6XXX Alloy Development (Alcoa)

Principal Investigator: Dr. L.M. Angers
Senior Engineer: Dr. G. Dixon

Objective

The primary objective of this task is to develop a damage tolerant aluminum based material for the lower wing and fuselage of a Mach 2.0 aircraft. This material must first meet preliminary strength and toughness targets at room temperature and then several criteria associated with elevated temperature service (e.g., retention of room temperature properties after exposure, performance at the operating temperature and resistance to creep deformation).

The I/M 6XXX alloys, or Al-Mg-Si-Cu alloys, are under consideration here because alloy 6013-T6 exhibits a strength/toughness combination equivalent to 2024-T3, but with significantly greater thermal stability.

Background

A set of alloys representing modifications to 6013 was selected. Thermodynamic modeling by Joanne L. Murray (1) was used to select compositions which would utilize the maximum amount of Mg, Si and Cu which can be put into solution during heat treatment. The actual compositions are shown below. S. Nos. 715670 through 715674 represent total weight percents of solute of 2.7, 3.5, 4.4, 5.1 and 5.8, respectively. With respect to Cu, Mg and Si levels, S. Nos. 715670 and 715674 may be thought of as approximate 6013 and 2519 controls, respectively while the other compositions explore the Cu, Mg and Si levels of compositions

intermediate to 2519 and 6013 (e.g., if these commercial compositions are corrected for their losses of Cu, Mg and Si to form constituent and dispersoid). During aging, these compositions were expected to produce Mg_2Si , Q and θ' phases in various proportions. Zr was chosen as the dispersoid forming element in all of the alloys.

715670: Al-0.8 Cu-1.01 Mg-0.84 Si-0.14 Zr
715671: Al-1.81 Cu-0.86 Mg-0.69 Si-0.15 Zr
715672: Al-3.16 Cu-0.75 Mg-0.60 Si-0.15 Zr
715673: Al-3.93 Cu-0.66 Mg-0.55 Si-0.15 Zr
715674: Al-5.17 Cu-0.21 Mg-0.25 Si-0.16 Zr

Several compositions exploring the effects of certain elevated temperature dispersoid-forming elements and Ag effects on the θ' precipitates were also selected. Actual compositions of those ingots are shown below.

715675: Al-1.18 Cu-1.02 Mg-0.83 Si-0.18 Zr-0.50 Mn-0.09 V
715676: Al-0.81 Cu-1.03 Mg-0.85 Si-0.14 Zr-0.51 Ag
715677: Al-3.13 Cu-0.78 Mg-0.60 Si-0.17 Zr-0.55 Ag

S. No. 715675 was designed to contain the same strengthening phases as S. No. 715670 but with additional high temperature dispersoids. In this alloy, Cu levels were increased from 0.85 wt% in alloy 715670 to 1.2 wt% to account for the loss of Cu expected as a result of formation of $Al_{20}Cu_2Mn_3$ in S. No. 715675. S. Nos. 715676 and 715677 were selected to determine whether there is any advantage to having Ω phase, rather than θ' , in these

alloys. By analogy to the work done on Ag additions to 2519, it was expected that any θ' would be replaced by Ω in these alloys. During aging, these compositions were expected to produce Mg_2Si , Q and Ω .

During the first reporting period, book mold ingots approximately 6" x 2.75" x 1.25" in size were cast. Slices were taken from each ingot for optical metallography and thermal analysis on preheated samples. Optical metallography revealed relatively clean microstructures and thermal analyses showed less than 0.5 J/g of melting reaction in any sample, suggesting that solubilities were not substantially exceeded in any of the alloys.

Procedure

Differential scanning calorimetry was done on as-cast samples and preheated samples in order to first establish the practices and then determine their effectiveness.

Book mold ingots were then preheated, rolled to 0.125" thick sheet and heat treated. Severe blistering occurred on the surfaces of all of the alloys. This is most likely due to hydrogen and, therefore, is not expected to be a problem in larger lab scale ingots where hydrogen levels can be controlled.

After solution heat treatment, samples of each alloy were cold water quenched. Unlike the 7XXX Al-Zn-Mg-Cu alloys which typically require a particular natural aging interval prior to artificial aging in order to achieve the highest peak strengths, the Al-Cu-Mg-Si alloys behave less predictably. Some Al-Cu-Mg-Si alloys achieve the highest peak strengths if the natural aging interval is eliminated while others require a finite natural aging time. Since a wide range of Al-Cu-Mg-Si compositions are under

investigation here, two natural aging intervals were studied, e.g., half of the samples were artificially aged immediately at 350°F, the other samples were naturally aged 10 days before artificial aging. Rockwell B hardness measurements were taken as a function of artificial aging time for both sets of samples. Average values from five measurements were recorded; generally, values vary by no more than one or two points, although there was greater scatter in some of the samples of the current study.

Optical metallography and transmission electron microscopy were carried out on selected samples. Tensile testing was carried out on peak aged conditions, i.e., the samples which developed the highest hardnesses.

Results and Discussion

Results of the differential scanning calorimetry studies on as-cast and preheated samples are summarized in Table I. All of the as-cast samples exhibited a eutectic melting reaction with an onset at a relatively low temperature, e.g., 952°F to 961°F. This reaction was the reason to give each alloy an initial preheat at 950°F before attempting to preheat above the highest solvus. The data in Table I shows that the 950°F preheat was effective in eliminating this reaction completely in all alloys.

Five of the alloys, S. Nos. 715670 through 715674, were also given a stepped preheat involving a hold at 950°F, followed by a hold at a higher temperature (990°F to 1080°F, depending on composition). In S. Nos. 715672, 715673 and 715674, samples given the stepped preheat were free of eutectic melting reactions. Samples from S. Nos. 715670 and 715671, on the other hand, experienced minor amounts of melting during the stepped preheat.

This can be seen in the data of Table I, where low temperature melting reactions re-appear in the analyses from samples given the stepped preheats. The extents of melting, however, were small.

Rockwell B hardness and electrical conductivity data are summarized in Table II. Hardness data are also presented in graphical form in Figs. 1 through 5. A great deal of scatter was present in all hardness data, some of which was likely due to the blistering problem described earlier.

Three of the exploratory compositions, S. No. 715672, 715673 and 715677, achieved Rockwell B hardnesses higher than achieved by the approximate 6013 control composition (Figs. 1 and 3) but none achieved higher hardnesses than the approximate 2519 control.

Ag had very little effect on the hardnesses of the Al-Cu-Mg-Si alloys (Figs. 2 and 3). Any small hardness advantage Ag may have in the approximate 6013 control is far outweighed by the still higher hardnesses of the approximate 2519 (Fig. 2). Similarly, there is no effect of Ag on the hardness which can be achieved in the alloy with intermediate Cu, Mg, and Si levels, e.g., compare hardness of S. Nos. 715672 and 715677 in Fig. 3. The data in Fig. 3; however, does indicate that there may be a stability advantage in the Ag-bearing alloy.

Finally, Mn had little or no effect on the peak hardness of the approximate 6013 control (Fig. 4). This is not unexpected, though, since it was added for its effect on grain structure, ductility and toughness, not strength.

The 10-day natural aging interval had no beneficial effect on peak hardness for any of the compositions examined here. The peak hardnesses of the samples that had the natural aging interval were equal or less than the peak hardnesses of the samples aged

immediately after quenching. Figure 5 illustrates this effect for the approximate 6013 control.

Optical metallography revealed clean structures, with fully recrystallized coarse grains. Micrographs from S. Nos. 715672 and 715677 are shown in Fig. 6. The microstructures of S. Nos. 715670, 715671, and 715673 through 715676 were similar.

Preliminary transmission electron microscopy studies suggest that a rod-like phase along $\langle 100 \rangle$ directions is the dominant strengthening phase in both 715672 and 715677. No crystal structure determination was made; however, it is expected that this phase is related to either Mg_2Si or Q. The Ag did not appear to have a significant impact on precipitation (Fig. 7). No Al_3Zr precipitation was observed.

Tensile data, like the hardness data, were not encouraging for the I/M 6XXX alloys, Table III. Tensile yield strengths and ultimate tensile strengths for three of these Al-Cu-Mg-Si alloys, e.g., S. Nos. 715672, 715674, and 715677 and two of the 2519 variants, S. Nos. 689246 and 689248 are compared in Fig. 8. Several points are worth noting. Firstly, both yield and ultimate strengths are similar for S. No. 715674 and S. No. 689246, the high Si 2519 variant. This is expected since both are similar in composition. Secondly, the alloys having intermediate Cu, Mg and Si levels, e.g., S. Nos. 715672 and 715677, have lower strengths than the other alloys.

Summary

- Minimal undissolved soluble constituents were present in sheet produced from these Al-Cu-Mg-Si alloys, suggesting that the appropriate compositions were selected.

- The highest peak hardnesses were achieved in the approximate 2519 control and lowest peak hardnesses were achieved in the approximate 6013 control. Alloys having intermediate Cu, Mg and Si levels developed intermediate peak hardnesses.
- Ag had little or no effect on hardnesses which developed during T6 aging, although there was some indication that it may confer a stability advantage.
- A 10-day natural aging period preceding artificial aging provided no hardening benefit.
- While thermodynamic modeling would have predicted that the alloys with intermediate Cu, Mg and Si levels would be strengthened by Mg_2Si , Q and θ' , transmission electron microscopy indicated that a single rod-like precipitate along $\langle 100 \rangle$ was dominant. Ag did not appear to alter the structure or morphology of the precipitate.

Reference

1. J.L. Murray, unpublished research, Alcoa Technical Center, 1992.

TABLE I . Onset temperatures, maximum temperatures and areas for the eutectic melting reactions observed in as-cast and preheated Al-Cu-Mg-Si samples.

S. No.	Preheat Max. Temp. (°F) ^a	Onset Temp. (°F)	Max. Temp. (°F)	Reaction Area (J/g)	Onset Temp. (°F)	Max. Temp. (°F)	Reaction Area (J/g)	Onset Temp. (°F)	Max. Temp. (°F)	Reaction Area (J/g)
715670	AC 950 1080	952 - 921	956 - 930	0.47 - 0.31	1009 - 1005	1016 - 1010	0.23 - 0.105	1033 - 1028	1042 - 1037	1.48 - 0.17
715671	AC 950 1040	959 - 920	964 - 930	4.22 - 0.35	986 - -	997 - -	0.27 - -	1039 1055 1011	1053 1075 1019	0.60 1.94 0.04
715672	AC 950 1015	959 - -	969 - -	17.1 - -	- -	- -	- -	- -	- -	- -
715673	AC 950 990	961 - -	972 - -	20.2 - -	- -	- -	- -	- -	- -	- -
715674	AC 950 990	960 - -	963 - -	0.34 - -	1004 - -	1021 - -	21.1 - -	- -	- -	- -
715675	AC 950	952 -	957 -	1.45 -	997 -	1009 -	0.43 -	1060 1066	1079 1086	4.80 2.97
715676	AC 950	951 -	955 -	0.38 -	1007 -	1015 -	0.28 -	1031 -	1041 -	0.63 -
715677	AC 950	955 -	964 -	15.4 -	- -	- -	- -	1062 1058	1081 1082	6.15 4.65

^a AC refers to the as-cast condition. Samples were held at 950°F as an initial preheat. Additional samples were held at 950°F, ramped to the higher temperature indicated and held.

TABLE II. Rockwell B hardness and electrical conductivity (EC) as a function of T6 aging time for the Al-Cu-Mg-Si alloys. Samples were heat-treated, quenched, and artificially aged at 350°F. Hardness and EC values represent averages from 5 and 2 readings, respectively.

S. Number	Alloy Description	Solution Heat Treatment Temperature (°F)	No Natural Aging				10 days Natural Aging			
			Aging Time, hr	Hardness	EC (%IACS)		Aging Time, hr	Hardness	EC (%IACS)	
715670	Al-0.8 Cu-1.0 Mg-0.84 Si-0.14 Zr	1080	0.5	50.0	40.0		0.5	49.2	39.4	
			2	60.1	40.6		2	56.3	40.0	
			4	68.2	37.5		4	64.9	37.5	
			8	73.2	43.3		8	73.1	44.2	
			16	73.4	44.2		16	75.1	45.8	
			24	75.2	46.3		24	73.3	45.2	
			48	74.0	45.6		48	69.1	46.0	
715671	Al-1.81 Cu-0.86 Mg-0.69 Si-0.15 Zr	1040	0.5	61.5	39.2		0.5	58.5	38.7	
			2	71.1	40.5		2	67.9	40.0	
			4	75.5	41.5		4	74.2	41.3	
			8	78.4	42.1		8	77.3	42.1	
			16	78.5	43.3		16	77.2	44.3	
			24	77.8	43.8		24	77.3	44.3	
			48	77.2	43.8		48	76.8	44.4	
715672	Al-3.16 Cu-0.75 Mg-0.6 Si-0.15 Zr	1015	0.5	60.2	37.5		0.5	59.4	37.9	
			2	71.5	38.7		2	64.2	33.6	
			4	75.3	40.1		4	76.3	40.7	
			8	77.9	41.4		8	76.5	41.5	
			16	76.9	42.2		16	76.4	41.3	
			24	77.3	39.8		24	78.8	39.4	
			48	80.0	40.4		48	78.0	40.3	
			76	76.4	42.2		76			

TABLE II (cont'd). Rockwell B hardness and electrical conductivity (EC) as a function of T6 aging time for the Al-Cu-Mg-Si alloys. Samples were heat-treated, quenched, and artificially aged at 350°F. Hardness and EC values represent averages from 5 and 2 readings, respectively.

S. Number	Alloy Description	Solution Heat Treatment Temperature (°F)	No Natural Aging				10 days Natural Aging			
			Aging Time, hr	Hardness	EC (%IACS)	Aging Time, hr	Hardness	EC (%IACS)	Aging Time, hr	Hardness
715673	Al-3.93 Cu-0.66 Mg-0.55 Si-0.15 Zr	990	0.5	52.6	33.3	0.5	51.2	35.1		
			2	76.6	39.8	2	66.5	37.8		
			4	75.4	39.0	4	75.2	37.3		
			8	80.4	38.5	8	71.8	38.8		
			16	79.0	39.3	16	78.7	39.7		
			24	78.2	37.7	24	78.6	39.9		
			48	74.8	41.6	48	77.7	40.9		
715674	Al-5.17 Cu-0.21 Mg-0.25 Si-0.16 Zr	990	0.5	60.7	37.1	0.5	59.4	36.7		
			2	69.5	36.5	2	65.3	37.2		
			4	77.8	37.1	4	76.2	38.6		
			8	79.7	37.9	8	75.0	38.7		
			16	81.3	38.1	16	81.4	39.4		
			24	81.3	39.6	24	78.6	39.9		
			48	79.7	33.8	48	79.6	40.5		
715675	Al-1.18 Cu-1.02 Mg-0.83 Si-0.18 Zr-0.5 Mn-0.09 V	1080	0.5	54.8	33.2	0.5	55.5	32.5		
			2	68.3	33.7	2	62.6	30.2		
			4	61.8	34.7	4	68.9	33.0		
			8	76.0	34.6	8	72.7	34.8		
			16	76.3	35.7	16	75.7	35.5		
			24	75.9	35.3	24	76.5	36.1		
			48	75.3	34.4	48	75.7	35.6		

TABLE II (cont'd). Rockwell B hardness and electrical conductivity (EC) as a function of T6 aging time for the Al-Cu-Mg-Si alloys. Samples were heat-treated, quenched, and artificially aged at 350°F. Hardness and EC values represent averages from 5 and 2 readings, respectively.

S. Number	Alloy Description	Solution Heat Treatment Temperature (°F)	No Natural Aging			10 days Natural Aging		
			Aging Time, hr	Hardness	EC (%IACS)	Aging Time, hr	Hardness	EC (%IACS)
715676	Al-0.81 Cu-1.03 Mg-0.85 Si-0.14 Zr-0.51 Ag	1080	0.5	59.6	39.6	0.5	55.7	39.5
			2	67.6	40.9	2	62.3	40.3
			4	72.2	36.8	4	68.3	41.5
			8	74.8	43.8	8	74.6	43.6
			16	75.9	44.4	16	72.5	44.1
			24	75.5	40.7	24	76.0	45.1
			48	74.6	44.9	48	72.9	45.1
715677	Al-3.13 Cu-0.78 Mg-0.60 Si-0.17 Zr-0.55 Ag	1015	0.5	65.2	35.8	0.5	65.7	37.2
			2	76.6	38.3	2	76.2	36.0
			4	75.7	40.2	4	77.8	39.2
			8	78.1	40.7	8	78.5	40.3
			16	79.2	39.9	16	77.8	40.8
			24	79.7	40.7	24	79.3	41.0
			48	79.6	41.2	48	79.9	39.6
			76	79.9	40.1	76		

TABLE III Tensile yield strength, ultimate tensile strength and % elongation in exploratory Al-Cu-Mg-Si alloys and 2519 variants. All samples were solution heat-treated, cold water quenched and aged to peak strength at 350°F.

S. Number	Alloy Description	Tensile Yield Strength (ksi)	Ultimate Tensile Strength (ksi)	% Elongation
715672 ^a	Al-3.16 Cu-0.75 Mg-0.60 Si-0.15 Zr	57.0	63.0	4.0 ^{d,e}
715674 ^b	Al-5.17 Cu-0.21 Mg-0.25 Si-0.16 Zr	61.2	70.0	8.2
715677 ^a	Al-3.13 Cu-0.78 Mg-0.60 Si-0.17 Zr-0.55 Ag	58.8	63.4	4.0 ^{d,e}
689246 ^c	High Si 2519	60.5	69.2	10.5
689248 ^c	High Mg 2519 + Ag	68.3	74.0	10.0 ^f

^a Results are averages from 2 longitudinal samples.

^b Results are averages from 4 longitudinal samples.

^c Results are from a single longitudinal sample.

^d Both samples failed outside middle half of gage length.

^e Internal discontinuity observed in one of the samples used to calculate the average.

^f Sample failed outside middle half of gage length.

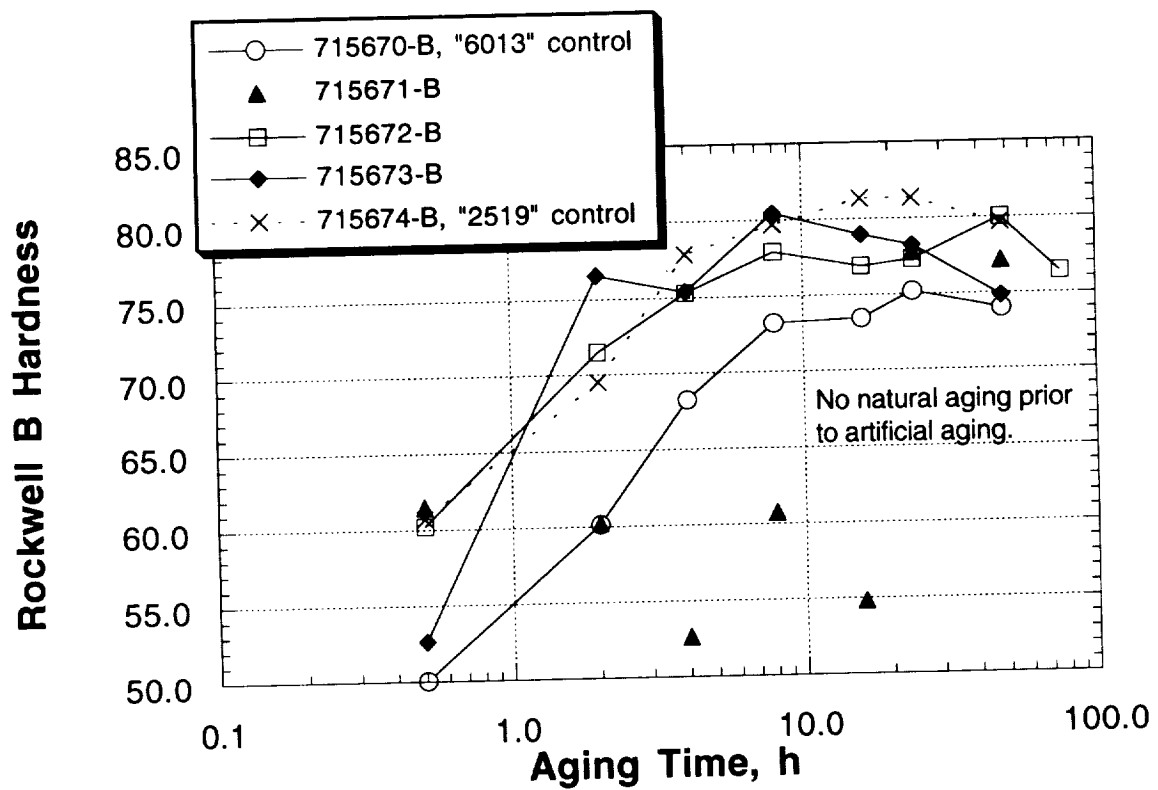


Figure 1. Rockwell B hardness as a function of aging time for the exploratory Al-Cu-Mg-Si alloys S. Nos. 715670 through 715674. No natural aging occurred prior to artificial aging.

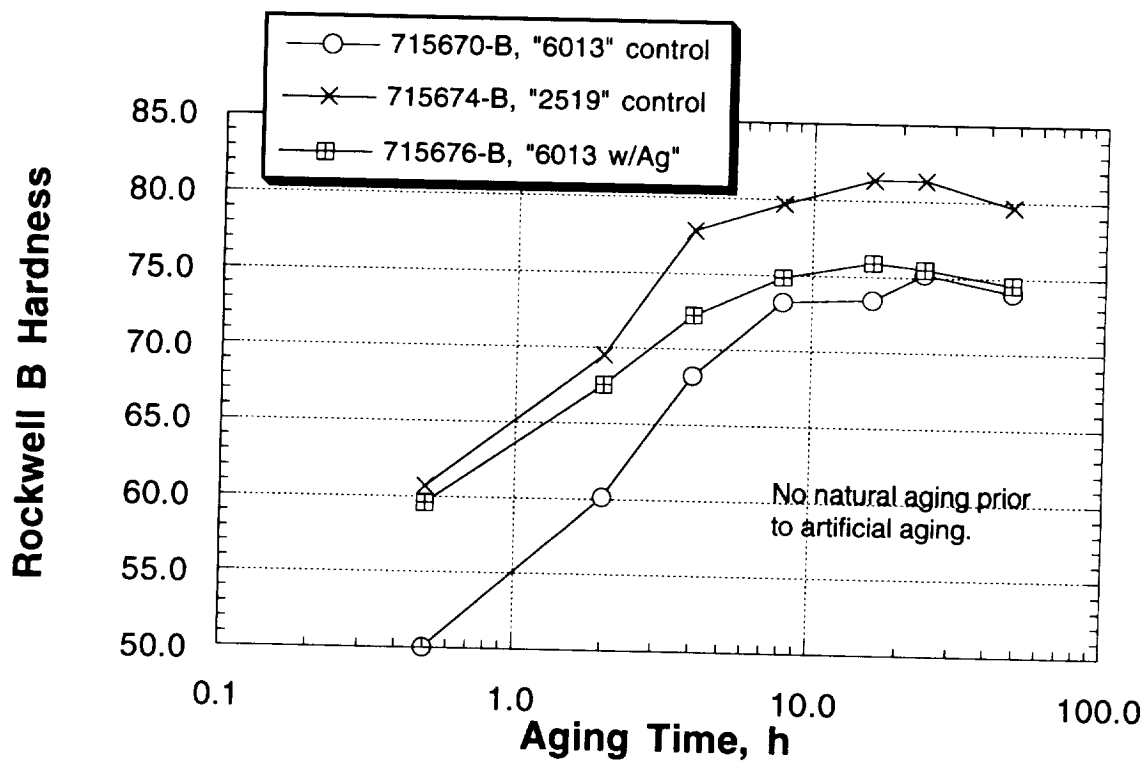


Figure 2. Rockwell B hardness as a function of aging time for exploratory Al-Cu-Mg-Si alloys, comparing a Ag-bearing near-6013 composition (S. Nos. 715676) to a near-6013 control (S. No. 715670) and a near-2519 control (S. No. 715674). No natural aging occurred prior to artificial aging.

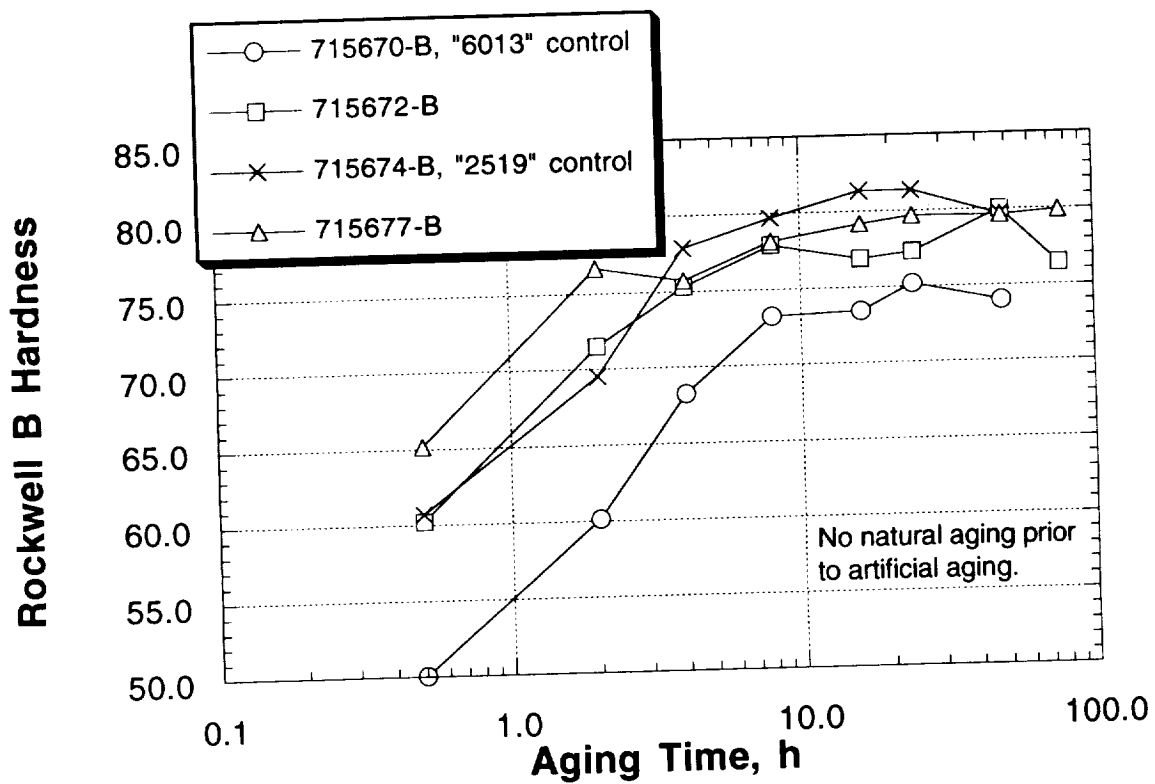


Figure 3. Rockwell B hardness as a function of aging time for the exploratory Al-Cu-Mg-Si alloys, comparing an Al-Cu-Mg-Si alloy (S. No. 715672), a Ag-bearing Al-Cu-Mg-Si alloy (S. No. 715677), and a near-2519 control (S. No. 715674). No natural aging occurred prior to artificial aging.

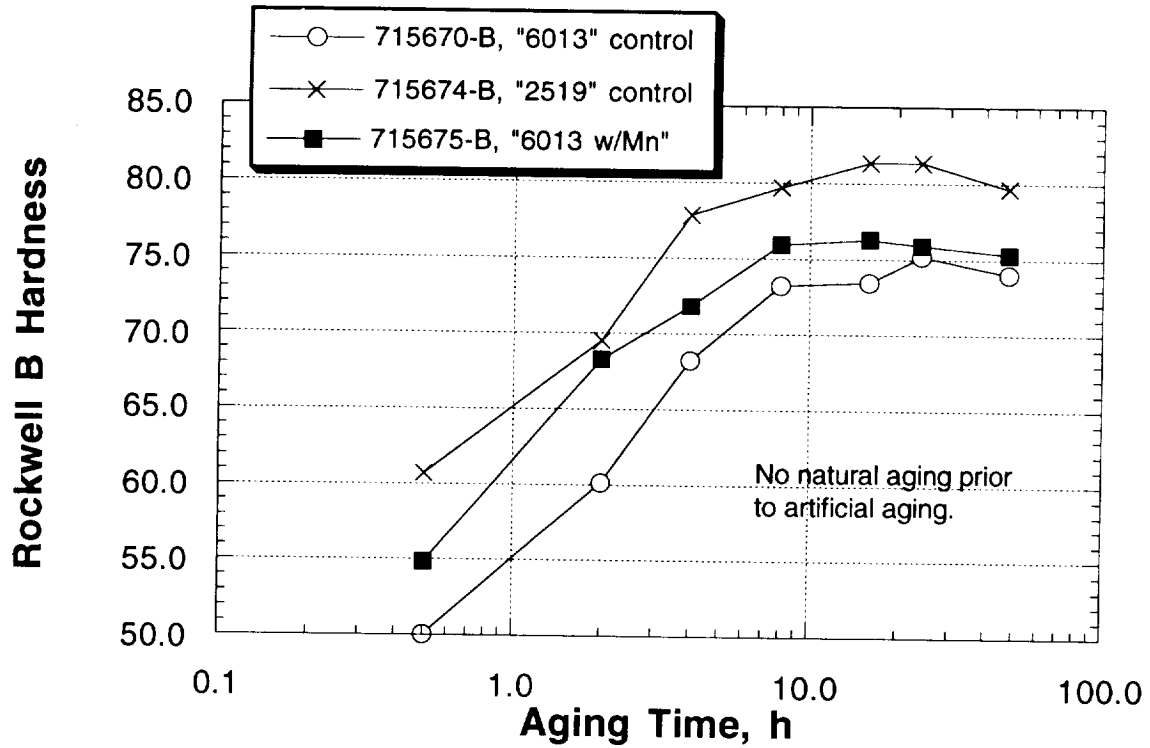


Figure 4. Rockwell B hardness as a function of aging time for the exploratory Al-Cu-Mg-Si alloys, comparing a near-6013 control (S. No. 715670), a Mn-bearing near-6013 control (S. No. 715675), and a near-2519 control (S. No. 715674). No natural aging occurred prior to artificial aging.

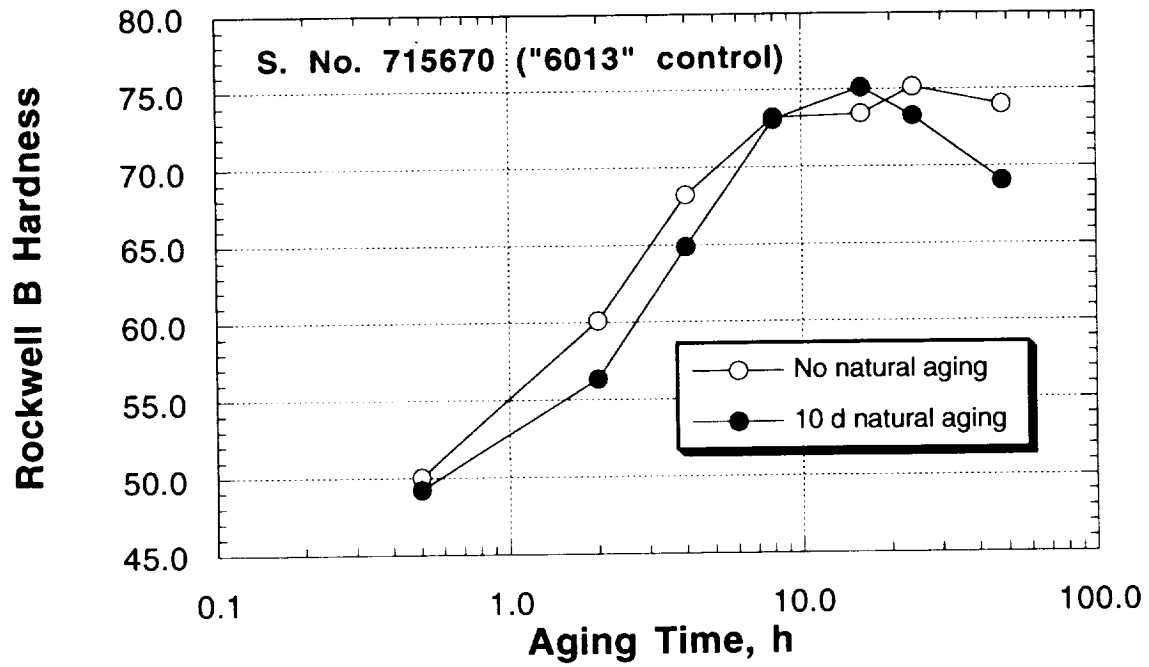
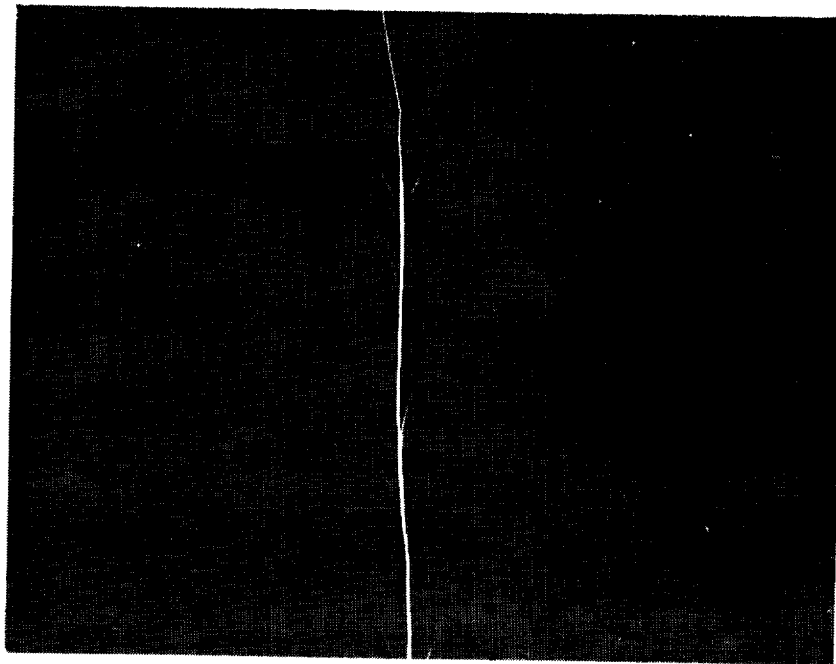
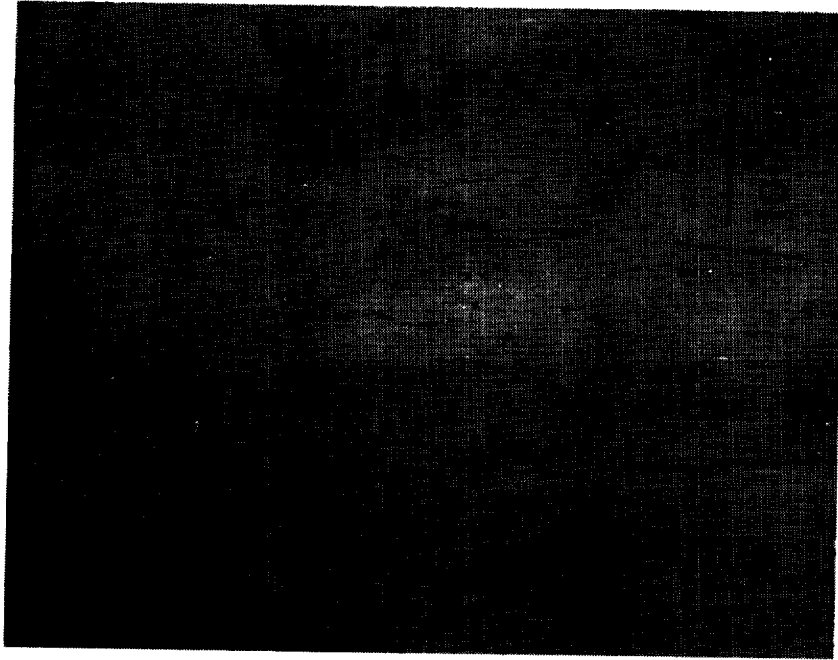


Figure 5. Rockwell B hardness as a function of aging time at 350°F for a near-6013 control given either no natural aging or 10 days of natural aging prior to artificial aging.

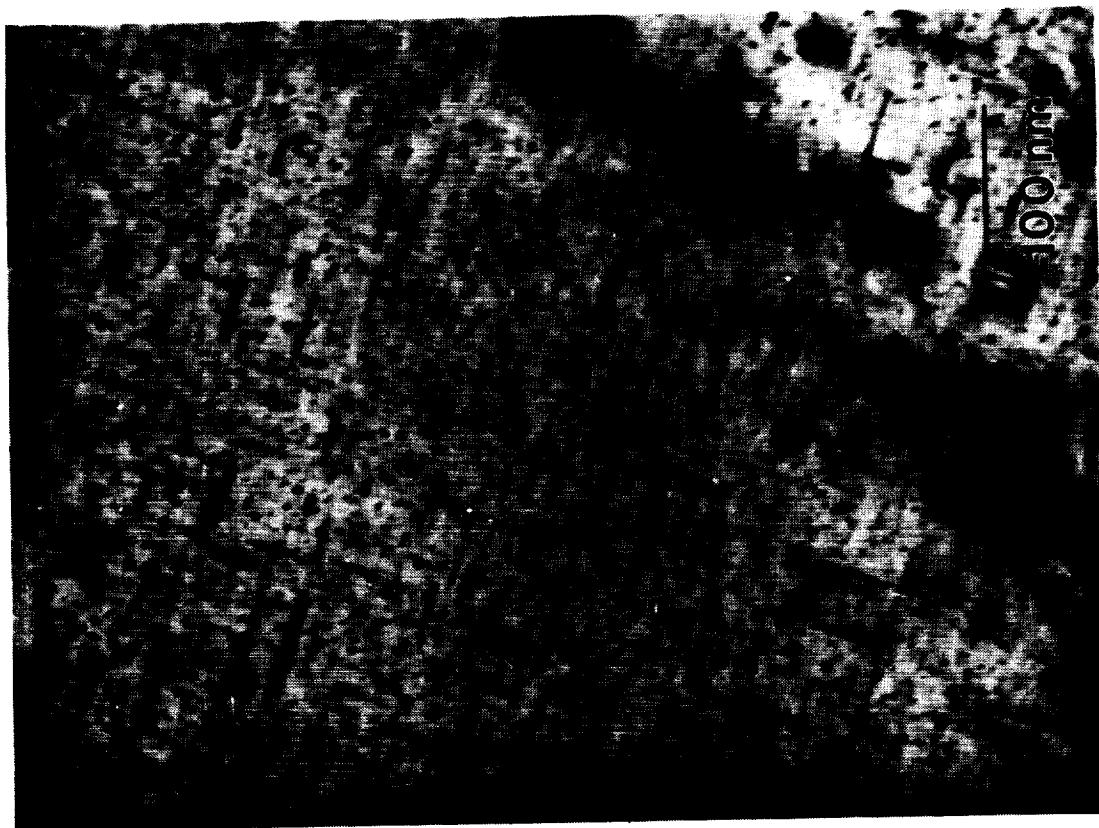


(a)

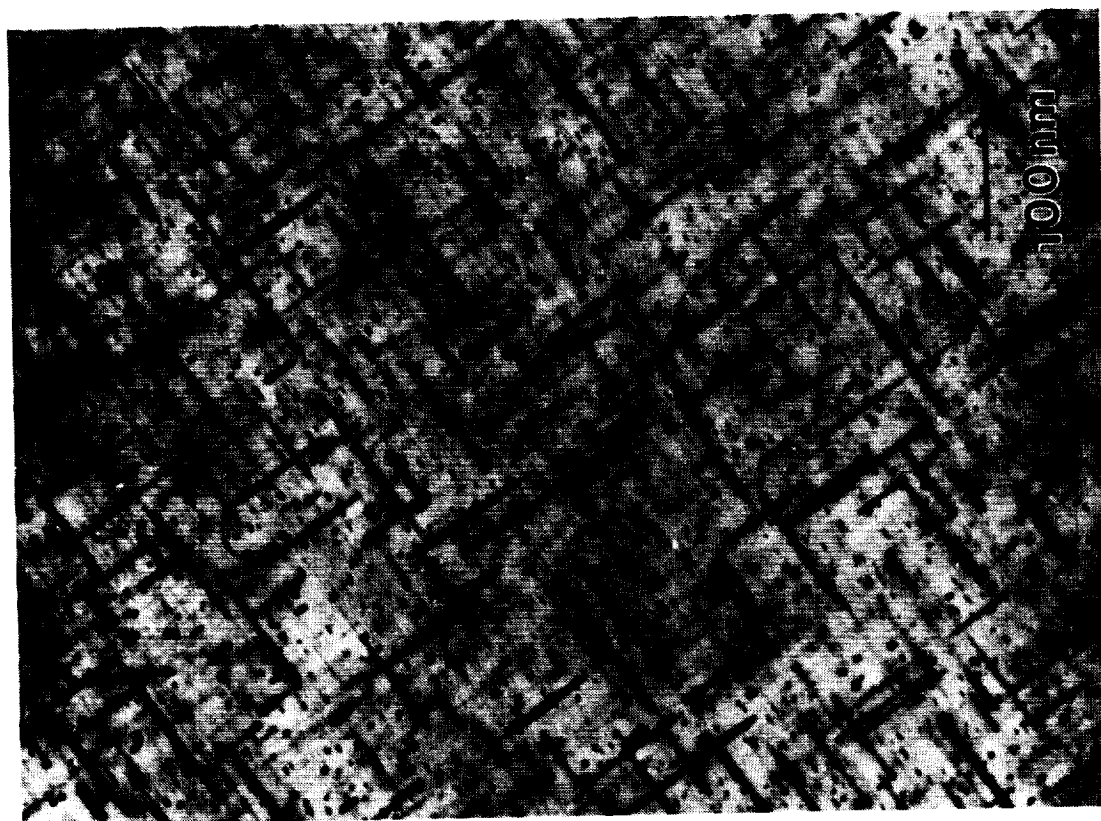


(b)

Figure 6. Optical micrographs of 0.125" thick sheet from: (a) S. No. 715672-T6 and (b) 715677-T6, revealing coarse recrystallized grains.



(b)



(a)

Figure 7. Transmission electron micrographs of: (a) S. No. 715672-T6 and (b) S. No. 715677-T6, revealing rod-like precipitates along $\langle 100 \rangle$ directions.

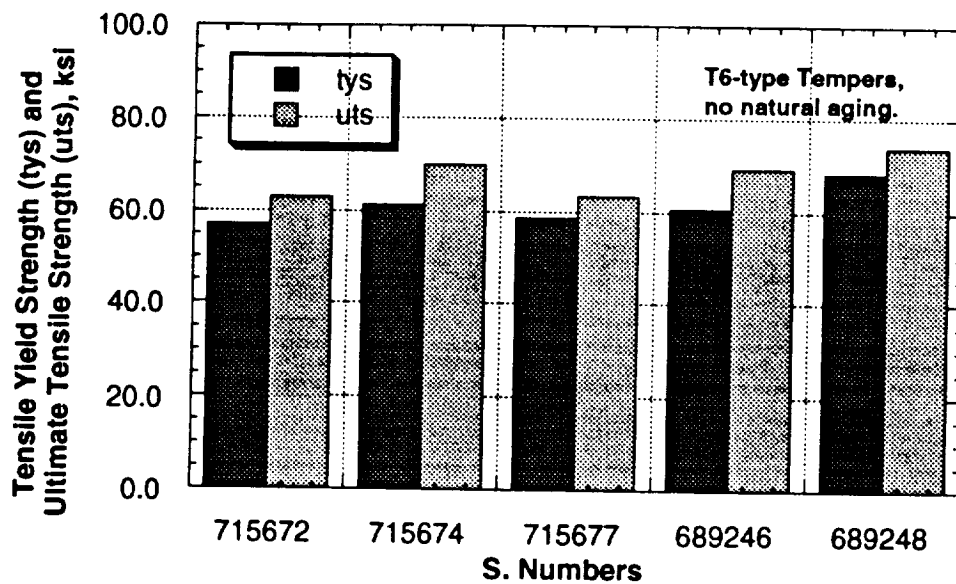


Figure 8. Tensile yield strength and ultimate tensile strength for three Al-Cu-Mg-Si alloys of this Task, e.g. S. Nos. 715672, 715674 and 715677 and two of the 2519 variants from Task 1, e.g. S. Nos. 689246 and 689248.

TASK 2. I/M Al-Cu-Li-Mg-Ag ALLOY DEVELOPMENT

Principal Investigator, Reynolds:	Dr. A. Cho
Principal Investigator, UVa:	Dr. J.M. Howe
Principal Investigator, Boeing:	Dr. W.E. Quist
Principal Investigator, Douglas:	Mr. R. Kahandal

Objectives

The objective of Task 2 is to optimize a precipitate strengthened ingot metallurgy alloy, based on the Al-Cu-Li-Mg-Ag system, to meet the property and thermal stability requirements of the High Speed Civil Transport Research Program. A concurrent goal is to understand the effects of thermal exposure on the microstructural/property evolution of the alloy as a function of time and temperature in order to help composition optimization and to develop techniques for predicting the evolution of the alloy during long term service environments.

Property Goals

Boeing Aircraft Company proposed several ambitious property goals for ingot metallurgy aluminum alloys for damage tolerant HSCT applications. It is desired that the combination of tensile yield strength and K_{app} fracture toughness fall within the range between 70/140/ ksi/ksi-inch^{1/2} to 80/100 ksi/ksi-inch^{1/2} after exposure to an anticipated elevated temperature service environment of about 275°F (135°C).

Background

Successful development of the high speed civil transport system (HSCT) depends on the availability of high performance elevated temperature materials. Among the conventional aluminum alloy systems, 2XXX series alloys are commonly used for elevated temperature applications because Cu-bearing particles exhibit greater thermal stability. For example, alloys 2618 and 2519

contain a large volume fraction of coarse intermetallic particles, which not only enhance thermal stability, but also contribute to alloy strength. Unfortunately, coarse intermetallic particles are only marginally effective as strengthening agents while being deleterious on fracture toughness. Therefore, conventional 2XXX alloys offer limited strength and fracture toughness capability.

Among conventional aluminum alloy systems, only 7XXX series alloys could potentially meet the proposed property goals, but only prior to any thermal exposure. 7XXX series alloys are strengthened by a combination of metastable GP zones and $MgZn_2$ precipitates which provide a good combination of high strength and fracture toughness; however, these precipitate phases are not stable above 100°C. Therefore, 7XXX series alloys are not suitable for elevated temperature applications.

Recent work at Reynolds Metals Company has demonstrated that a new proprietary Al-Cu-Li-Mg-Ag alloy (RX818) could potentially meet Boeing's requirements for high combinations of strength and fracture toughness. RX818 is mainly strengthened by thermodynamically stable phases which form extremely fine distributions of precipitates (i.e., T_1 and S'-like phases). These are effective in providing high combination of strength and fracture toughness because the formation of large intermetallic particles is avoided. A high level of property stability in RX818 has been established in thermal exposure studies at Reynolds. Further improvement of thermal stability of the alloy could be achieved by adding optimum amounts of dispersoids in addition to the precipitate distribution. In Task 2, the optimum amounts of precipitates and dispersoids will be established to improve the mechanical properties and thermal stability of RX818 alloy.

Approach

To accomplish the above objectives, this task consists of the following subtasks:

Subtask 2A: Evaluate RX818 Variation Alloys as Model Materials to Understand the Role of Various Strengthening Phases During Thermal Exposure.
(Reynolds Metals Company)

Subtask 2A1:
Evaluate the three variants of RX818 alloy with modified Mg and Ag content to examine the effect of T_1 and S' -like phases on thermal stability of RX818 alloy.

Subtask 2A2:
Examine the effect of dispersoids on thermal stability and mechanical properties of RX818 alloy - moderate level of dispersoids for conventional casting.

Subtask 2A3:
Examine the effect of dispersoids on thermal stability and mechanical properties of RX818 alloy - high level of dispersoids by Spray Deposition Technique.

Subtask 2B: A study of the microstructural evolution of the Al-Li-Cu-Mg-Ag System with RX818 alloy
(UVa)

Subtask 2C: Al-Cu-Li-Mg-Ag Alloy Development
(Boeing)

Subtask 2D: Al-Cu-Li-Mg-Ag Alloy Development
(Douglas)

Subtask 2A: Evaluate RX818 Variation Alloys as Model Materials to Understand the Role of Various Strengthening Phases During Thermal Exposure.

Subtask 2A1: Evaluate the three variants of RX818 alloy with modified Mg and Ag content to examine the effect of T_1 and S'-like phases on thermal stability and mechanical properties during long term thermal exposure.

Composition selection and casting

RX818 alloy is mainly strengthened by thermodynamically stable phases which form extremely fine distributions of plate-shaped precipitates (T_1 phases) and lath-shaped precipitates (S'-like phases). Depending on the alloy compositions, different volume fractions of T_1 (Al_2CuLi) and S'-like (Al_2CuMg) phases would precipitate according to thermodynamic requirements. As a result, the over-aging characteristics of RX818 alloy would be determined by not only diffusion controlled coarsening kinetics of the two strengthening phases but also the solute partitioning between the two phases according to their solvus temperatures. Therefore, this work will examine the effect of different volume fractions of T_1 phase and S'-like phase by varying the amount of Mg and Ag content. Within the composition range of RX818, the volume fraction of S'-like phase will increase with higher Mg content. The effect of Ag content in this alloy is more complicated. However, it appears that higher Ag content increases the volume fraction of T_1 phase particles.

For this work, three levels of Mg and Ag contents are selected with fixed Cu and Li contents as three RX818 variant alloys. To meet the material requirement, four ingots were cast.

Compositions:

	<u>Cu</u>	<u>Mg</u>	<u>Li</u>	<u>Zr</u>	<u>Ag</u>	<u>Si</u>	<u>Fe</u>
(target)	3.6	.8	1.0	.14	.4	<.08	<.08
64627(actual)	3.8	.8	.9	.13	.4	.06	.06
(target)	3.6	.8	1.0	.14	.8	<.08	<.08
64641(actual)	3.6	.76	.8	.14	.8	.06	.07
(target)	3.6	.4	1.0	.14	.4	<.08	<.08
64653(actual)	3.6	.4	.8	.14	.4	.05	.07
64667(actual)	3.4	.4	.8	.14	.5	.04	.07

Fabrication

The ingots were homogenized, scalped and hot rolled to 0.125" gauge sheet. Sheet products were solution heat treated at 990°F for 1 hour followed by cold water quench and 5% stretch. The sheet products were aged at 320°F for 16 hours as a standard age practice for all of the RX818 variant alloys.

Microstructural examination

Grain structure - Optical metallographic examination revealed that all the sheet gauge products are unrecrystallized in T8 temper condition. Fig. 1, Fig.2, Fig.3 and Fig. 4 are the optical micrographs showing near surface and T/2 location (i.e. middle thickness) grain structures. Grain structures in both areas are mostly unrecrystallized. However, near surface areas show more visible subgrain structures which are the results of extensive polygonization process by subgrain coalescence and growth. It also appears that there are a few very small recrystallized grains present at near surface areas.

Precipitate structure - A quantitative transmission electron microscopic study was carried out by Prof. J. Howe at UVA with S-64667. Alloy S-64667 is strengthened by T₁ and S'-like phases. As a first step, Prof. Howe quantified the size and density of T₁ precipitates during coarsening at 325°F. The results are reported in Task 2B. Since most of the work evaluating the effect of

thermal exposure on mechanical properties was conducted at 275°F, Prof. Howe's work will be extended to the precipitation and coarsening behavior of T_1 phase at 275°F in the future.

Mechanical properties and thermal exposure effects

Tensile tests and plane stress fracture toughness test results by 16" wide center notched panel tests in longitudinal direction are listed in Table 1. Also included are the tensile and fracture toughness properties in longitudinal direction after a thermal exposure of 1,000 hours at 275°F. After the thermal exposure, tensile strengths increased by 2-3 ksi and the ductility (tensile elongation) by 3-4% at the same time. However, fracture toughness (K_{Ic}) decreased by 20-30 ksi-inch^{1/2}. Tensile yield stress vs. fracture toughness values by K_{Ic} are plotted in Fig. 5 to compare the results to the typical properties of 7075-T6, 2024-T3 and 2090-T8. The T8 temper fracture toughness values of the three alloys, S-64641, S-64667 and S-64627 are significantly higher than both 2090-T8 and 7075-T6 properties. Even after the thermal exposure, the K_{Ic} fracture toughness values of S-64667, S-64627 and S-64653 are still higher than that of 7075-T6. Based on K_{Ic} fracture toughness values, S-64627 (high Mg with low Ag variant) shows the best strength-fracture toughness combination in T8 temper condition. However, after thermal exposure, S-64627 shows more degradation of fracture toughness than others and its K_{Ic} values decrease to slightly below that of S-64653. Microstructural investigation would be warranted in the future to identify if higher Mg content in S-64627 is responsible for such fracture toughness degradation during thermal exposure. In order to compare the fracture toughness values to the property targets proposed by Boeing Aircraft Company, the K_{app} values of RX818 type alloys are plotted in Fig. 6. Prior to the thermal exposure, the K_{app} fracture toughness values of the RX818 type alloys in T8 temper are higher than the proposed fracture toughness goal.

However, after the thermal exposure, the fracture toughness values of these alloys are lower than the proposed goal, even though the strengths are still higher than the mechanical strength goal. This suggests that alloy composition modifications and/or microstructural modifications by thermomechanical processing would be necessary to reduce the thermal degradation of fracture toughness of these alloys. To compare these fracture toughness test results to the other type of tests such as small compact tension type specimen tests, K(R)-curves are provided in Fig.7 and Fig.8 which represent the material before and after the thermal exposures, respectively.

Conclusions

- All the alloys tested show excellent combination of strength and fracture toughness in the T8 temper.
- The thermal exposure at 275°F for 1,000 hours increases the tensile strengths and elongation of the alloys.
- The thermal exposure at 275°F for 1,000 hours decreases the fracture toughness of all four alloys.
- All four alloys show strengths higher than the target tensile yield strength after the thermal exposures at 275°F for 1,000 hours.
- The best property combination in T8 temper condition was achieved by S-64627 which contains high Mg(.8%) with low Ag (0.4%).
- The highest K_{app} . fracture toughness value after thermal exposure was achieved by S-64653 which shows the lower strength than others. This alloy has essentially the same chemistry as S-64667. The lower strength of S-64653 could be a reason for the higher K_{app} . value of S-64653 than that of S-64667.

TABLE 1

Longitudinal Tensile Test and L-T Plane Stress Fracture Toughness Test Results from hot rolled 0.125" gauge sheet of four RX818 type alloys in T8 temper and in T8 after 1,000 h at 275°F.

<u>S.No.</u>	<u>UTS(ksi)</u>	<u>TYS(ksi)</u>	<u>El.(%)</u>	<u>K_c</u>	<u>K_{app.}</u>
64627-T8	84.7	82.3	6.3	148.3	119.9
T8+1,000h	87.2	84.6	10.5	101.6	76.2
64641-T8	87.8	85.4	6.3	116.9	98.2
T8+1,000h	89.7	87.1	9.5	67.9	62.1
64653-T8	82.1	78.9	8.0	--	--
T8+1,000h	85.1	81.7	12.0	102.0	89.4
64667-T8	85.4	82.1	8.0	131.0	102.8
T8+1,000h	87.3	84.1	11.5	92.9	78.9

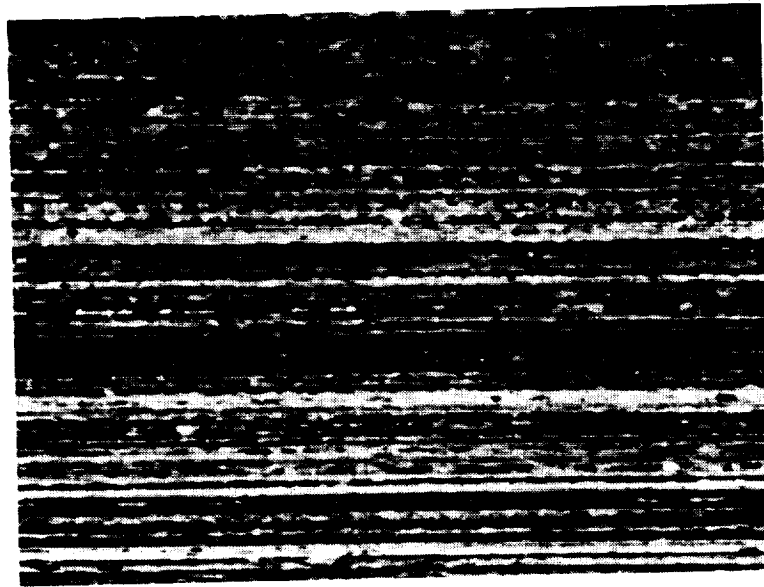
Note:

All the tensile properties are averaged from duplicate test results.

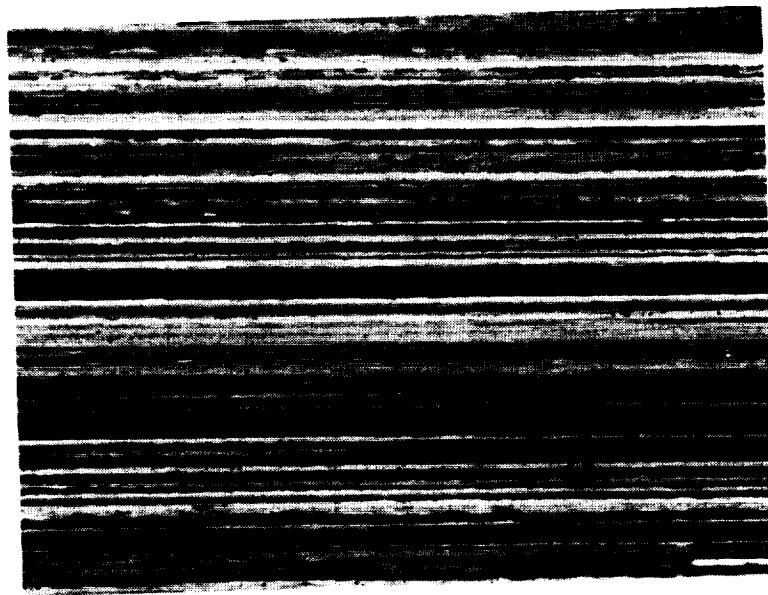
K_c and K_{app.} values were tested by 16" wide center notched and fatigue precracked specimens

K_c and K_{app.} values are from single test.

K_c and K_{app.} values are in Ksi-(inch)^{1/2}



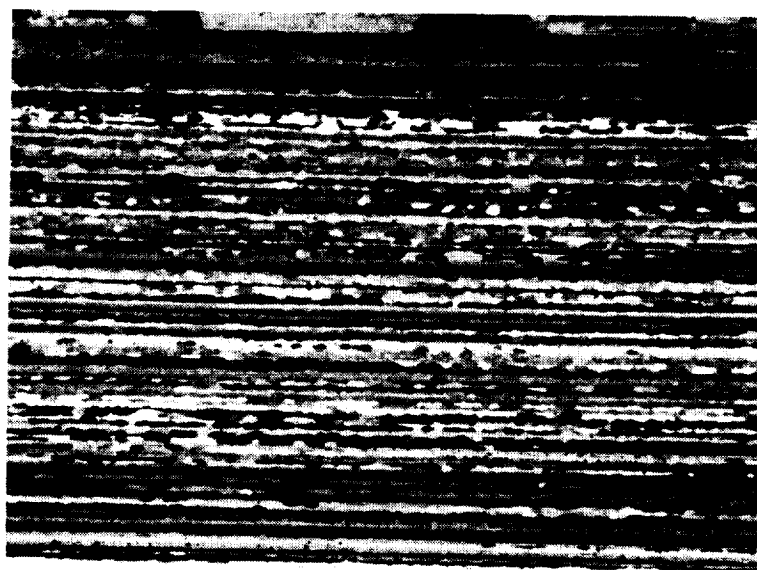
(a)



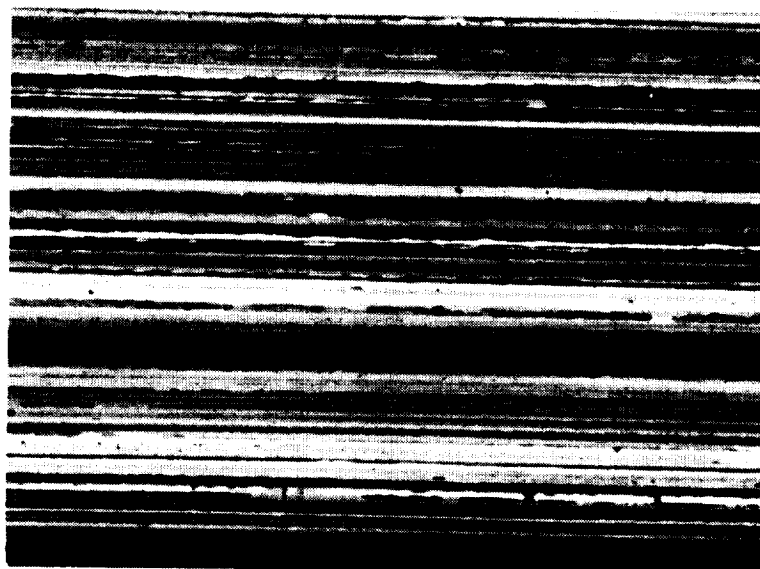
(b)

Photomicrographs of metallographically prepared longitudinal cross-sections of RX818 type alloy (S#64627-T8) showing near surface (a) and at T/2 location (b) in the sheet. Magnification is 100X.

Fig. 1



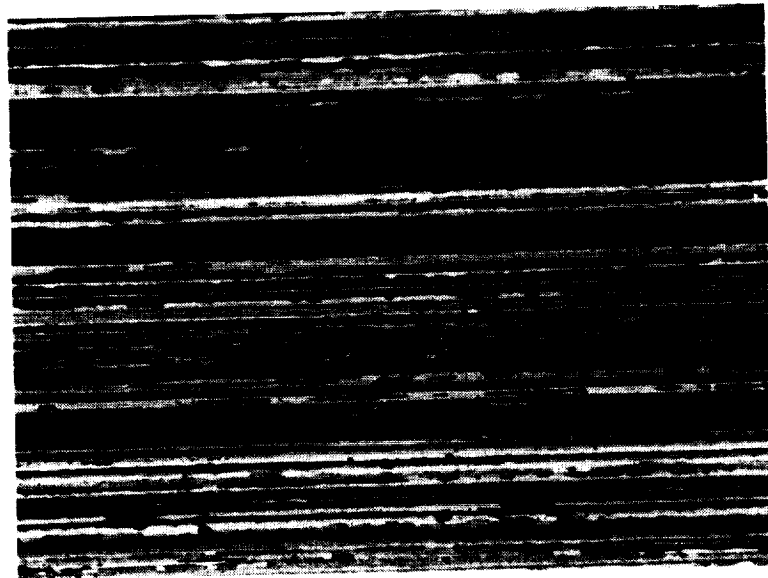
(a)



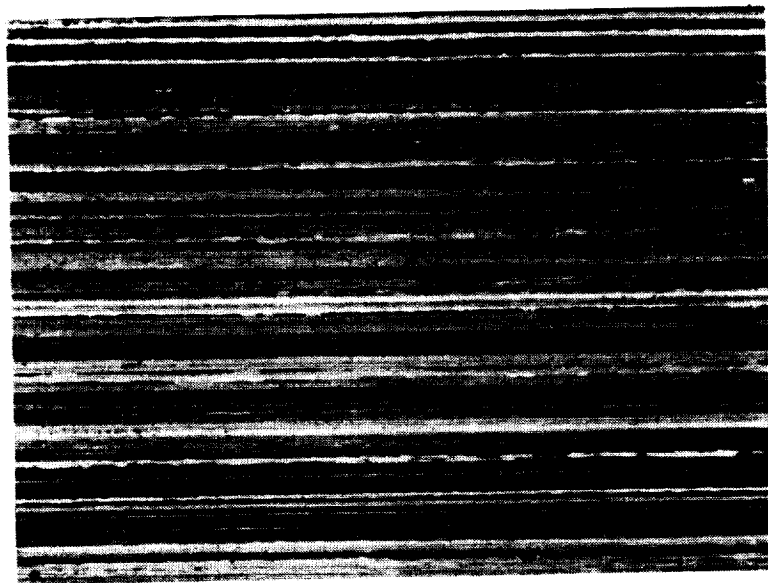
(b)

Photomicrographs of metallographically prepared longitudinal cross-sections of RX818 type alloy (S#64641-T8) showing near surface (a) and at T/2 location (b) in the sheet. Magnification is 100X.

Fig.2



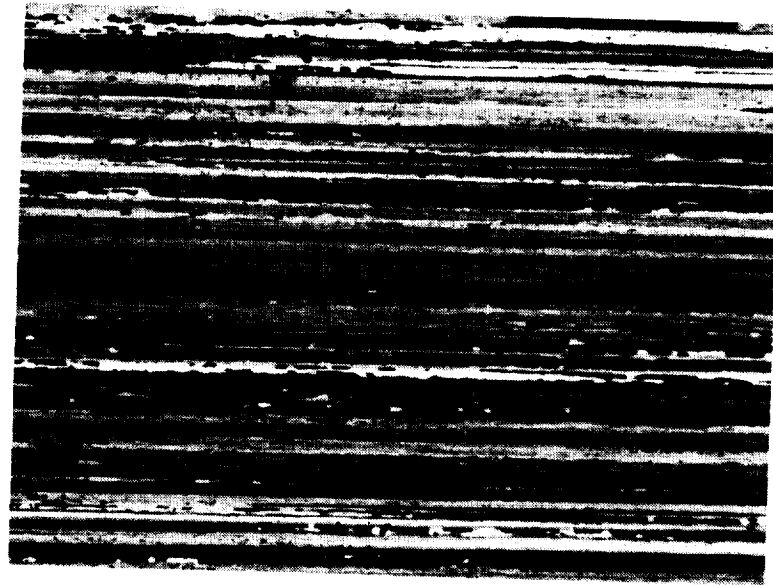
(a)



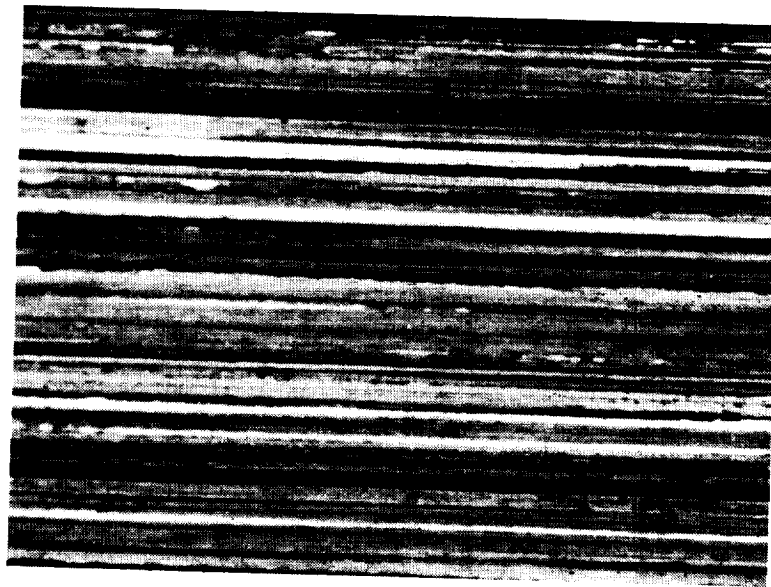
(b)

Photomicrographs of metallographically prepared longitudinal cross-sections of RX818 type alloy (S#64653-T8) showing near surface (a) and at T/2 location (b) in the sheet. Magnification is 100X.

Fig.3



(a)



(b)

Photomicrographs of metallographically prepared longitudinal cross-sections of RX818 type alloy (S#64667-T8) showing near surface (a) and at T/2 location (b) in the sheet. Magnification is 100X.

Fig.4

FRACTURE TOUGHNESS OF RX818-T8 TYPE ALLOYS **Center Notched 16" Wide Panel(Fatigue Precrack)**

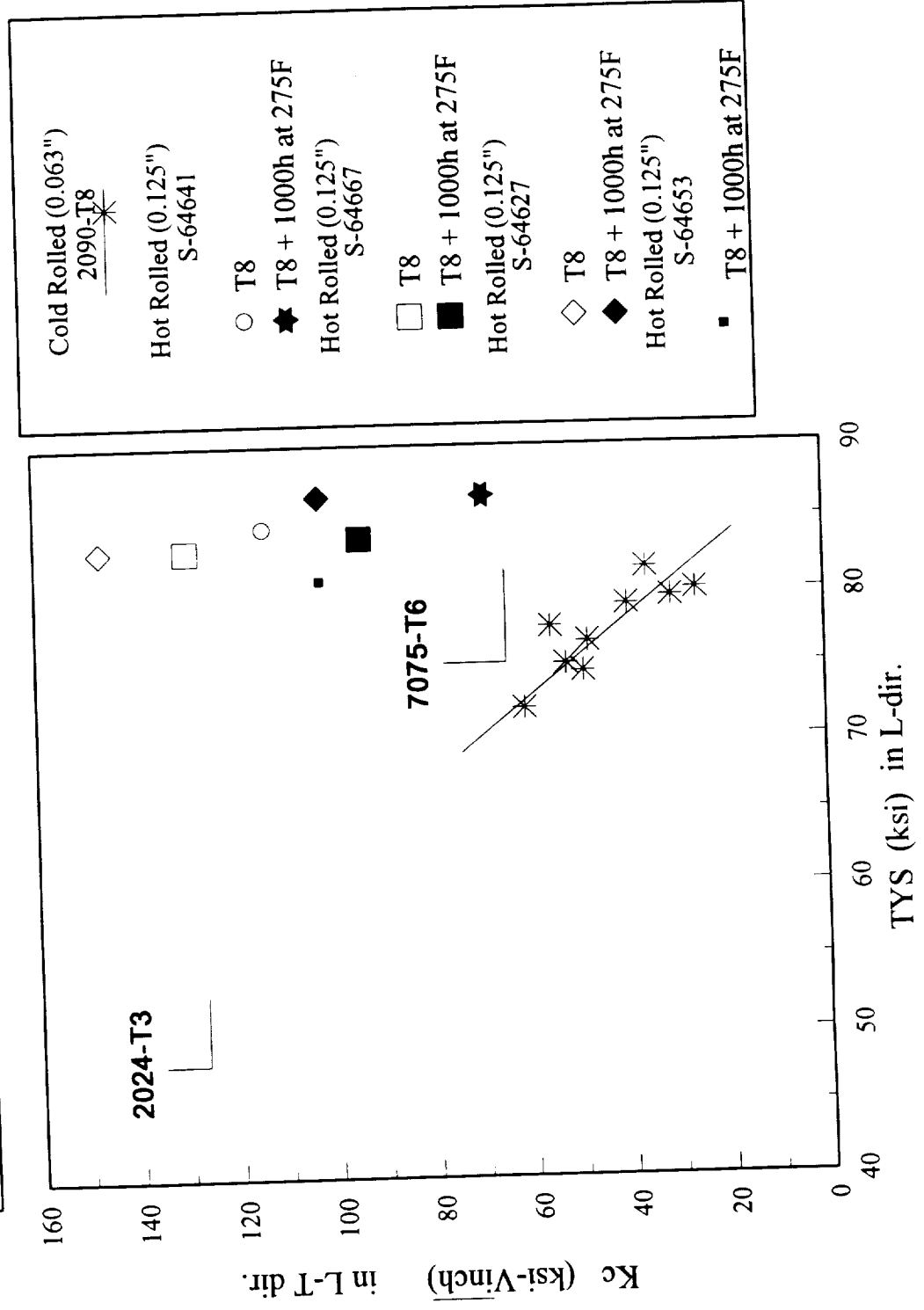


Fig.5

FRACTURE TOUGHNESS OF RX818-T8 TYPE ALLOYS **Center Notched 16" Wide Panel(Fatigue Precrack)**

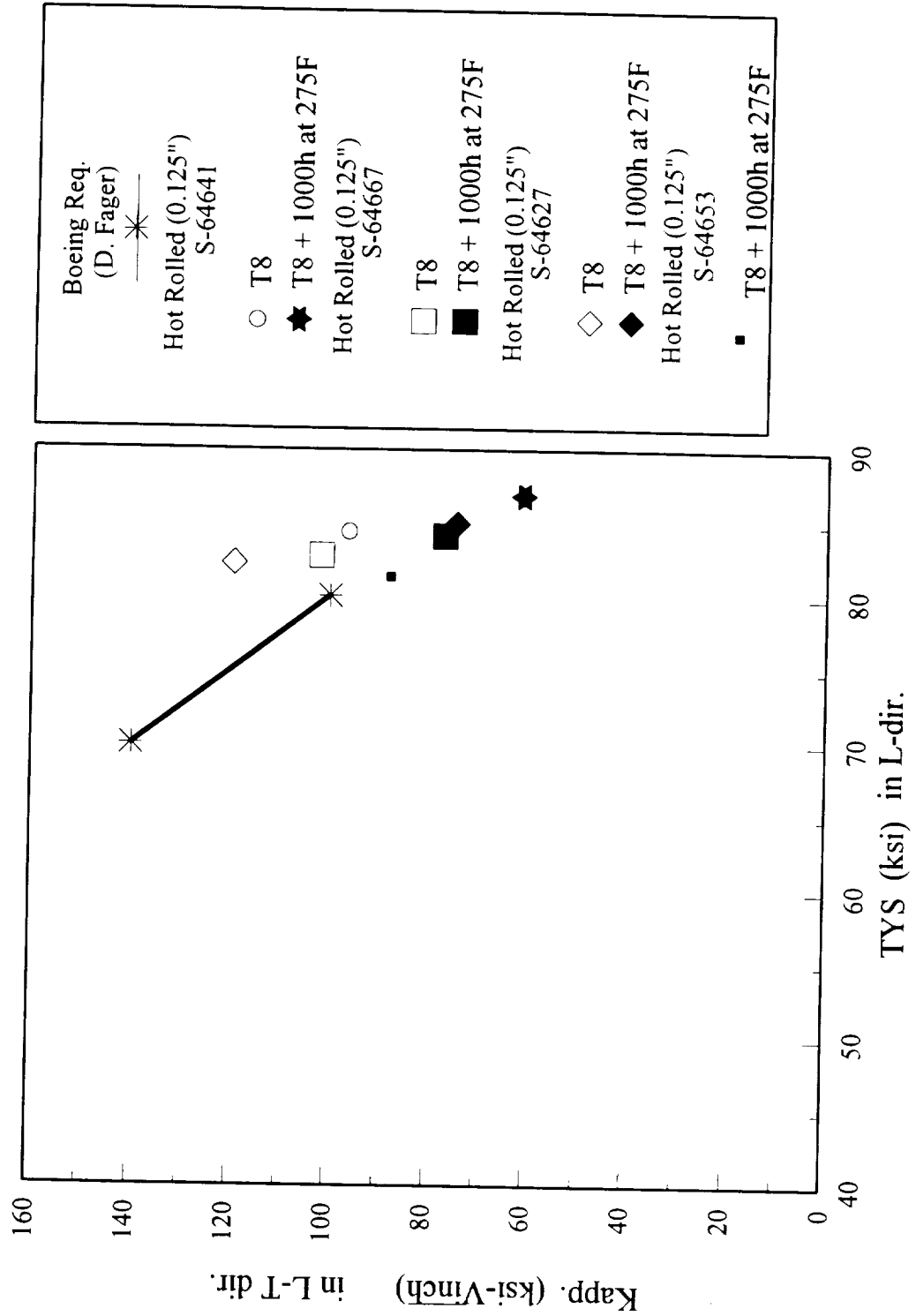


Fig.6

**R - CURVES OF RX818 TYPE 0.125" ga.
Center notched 16" Wide Panel (Fatigue Precrack)
in T8 Temper.**

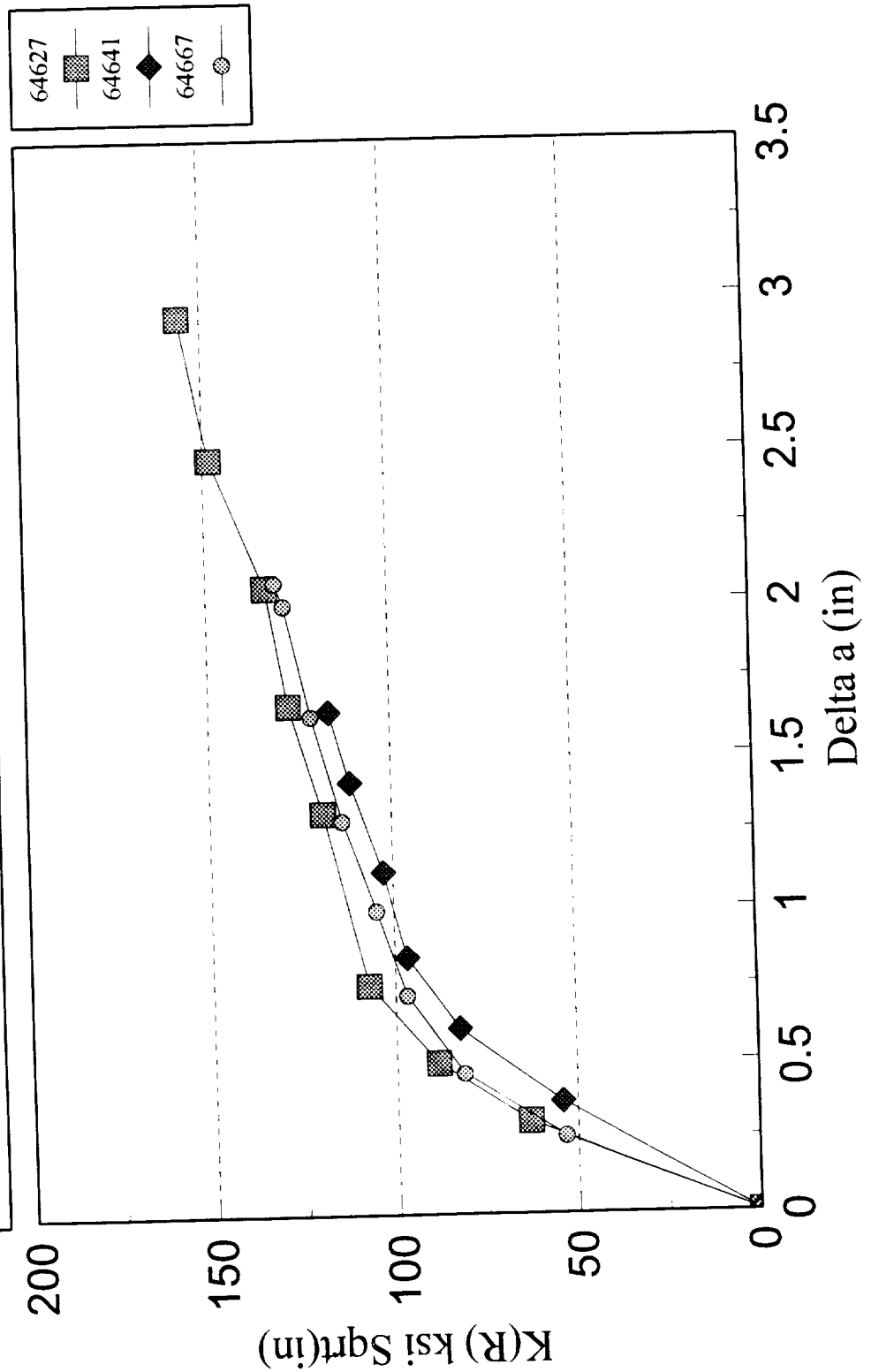


Fig.7

**R - CURVES OF RX818 TYPE 0.125" ga.
Center notched 16" Wide Panel (Fatigue Precrack)
in T8 Temper + 275 deg. F for 1000 hrs.**

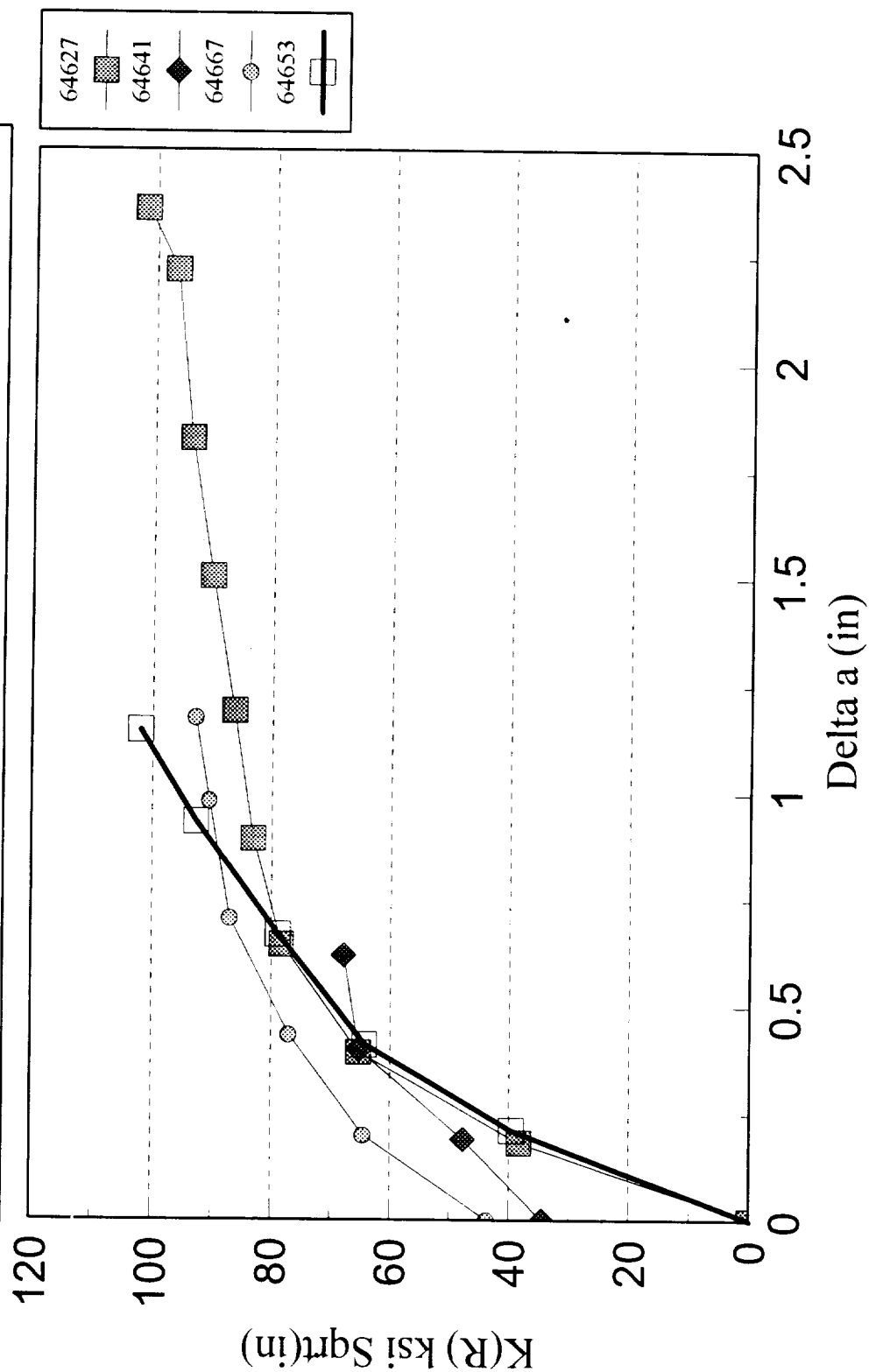


Fig. 8

Subtask 2A2

Examine the effect of dispersoids on thermal stability and mechanical properties of RX818 alloy - moderate level of dispersoids for conventional casting.

Composition selection and casting

The strength of RX818 alloy is based on precipitate strengthening. Further improvement of thermal stability of the alloy could be achieved by introducing the optimum amount of dispersoids in addition to the precipitate distribution. The addition of dispersoids will improve thermal stability but could be deleterious to fracture toughness if too much of the dispersoids are added. The key to further improvement, therefore, could be identifying the optimum combination of precipitation strengthening and dispersoid strengthening. Two considerations were given in selecting alloying elements to form dispersoids: the first, its ability to form a thermally stable coherent phase to maximize strengthening effect, and the second, its cost to be economical enough for commercial scale production.

In this work, Zirconium, Vanadium and Manganese additions are being examined among the peritectic elements. Zirconium, Vanadium or Manganese containing dispersoids in aluminum alloys, such as Al_3Zr , Al_3V and Al_6Mn , could help thermal stability and creep resistance by pinning down grain boundaries and subgrain boundaries during the long term thermal exposure. It would be interesting to know the actual volume fraction of these dispersoid particles. The maximum volume fraction of these dispersoids could be calculated assuming that no elements are left in solid solution and that only one phase is formed per element such as Al_3Zr , Al_3V and Al_6Mn . However, without knowing the amount of these elements in solid solution, the amount of non-equilibrium phases and other intermetallics present such as $\text{Al}_{12}\text{Cu}_2\text{Mn}_3$ or $\text{Al}_{12}\text{CuMn}_2$, the validity of such calculations is very questionable. Actual measurements of the volume fraction of those dispersoids are beyond the scope of this study at present. For the initial five compositions of 30

lbs. permanent mold ingots were selected and cast. The target and actual compositions are as follows:

Compositions:

	<u>Cu</u>	<u>Li</u>	<u>Mg</u>	<u>Ag</u>	<u>Zr</u>	<u>V</u>	<u>Mn</u>
65836(target)	3.5	1.0	.4	.4	.17	.1	.3
(actual)	3.4	.99	.52	.34	.15	.12	.3
65837(target)	3.5	0.8	.4	.4	.17	.1	.3
(actual)	3.5	.86	.39	.22	.18	.12	.3
65838(target)	3.0	1.2	.4	.4	.17	.1	.3
(actual)	3.1	1.21	.4	.36	.15	.12	.29
65839(target)	3.5	1.0	.4	.4	.17	.1	--
(actual)	3.35	1.04	.4	.34	.17	.12	--
65840(target)	3.5	1.0	.4	.4	.17	--	--
(actual)	3.5	1.0	.39	.36	.16	.01	--

Fabrication

The ingots were homogenized, scalped and hot rolled to 0.125" gauge sheet. The hot rolled sheets were then, cold rolled to .090" gauge sheet. The final gauge sheet products were solution heat treated at 990°F for 1 hour followed by cold water quench. T8 temper sheets were stretched by 5% and aged at 320°F for 16 hours as a standard T8 temper practice. T6 temper sheets were straightened by stretching nominally 1% then aged at 350°F for 12 hours.

Microstructural examination

Both T6 and T8 temper sheet were hot rolled and solution heat treated as a one piece. Since these alloys recrystallize during solution heat treatment step, the degree of recrystallization between the T6 and T8 temper sheet are expected to be identical. Therefore, to simplify the task, optical metallographic examination was conducted only in the T8 temper sheet and the micrographs were included in the previous 6 month report. The results revealed that S. Nos. 65836, 65837 and 65838 are completely recrystallized. S.No. 65839 is partially

recrystallized, and S.No. 65840 is not recrystallized. The degree of recrystallization was reflected in the strength of the material.

Mechanical properties

Tensile test results for the T8 and T6 temper samples of the five alloys were reported in the previous report (First Semi-Annual Report (January 1992 to June 1992) for NASA-UVA Subcontract 5-28411, NAG-1-745). In addition, the tensile properties after thermal exposures of 100 hours, 500 hours and 1,000 hours at 275°F were also reported earlier. In this report, the tensile properties of T8 and T6 temper materials after a thermal exposure of 2,500 hours at 275°F are listed in Table 2 and Table 3, respectively. The effect of long term thermal exposures on the tensile yield stresses are plotted in Figures 9, 10, 11 and 12. As stated earlier, four out of five variant alloys were recrystallized at varying degrees, which would affect the mechanical properties of the material. Therefore, comparing the mechanical properties of these variants are not as straightforward as originally intended, for example, S.N. 65840 shows the highest strength because of its completely unrecrystallized grain structure. Nevertheless, we can learn valuable information regarding property evolution during the thermal exposure at 275°F. In Fig.9, the longitudinal tensile yield stresses of T8 temper materials show that the strengths increase from T8 temper within 100 hours of thermal exposure. However, the strengths decrease as the thermal exposure continues to 500 hours (S.N. 65836, 65837, 65839 and 65840) or to 1,000 hours (S.N. 65830). S.No.65838 shows the continuous strength increase until 1,000 hours of thermal exposure. However, the strength increases at a considerably slower rate between 100 hours and 1,000 hours of thermal exposure. Such complex age strengthening behavior during the thermal exposure at 275°F is believed to be a manifestation of age strengthening by two different phases, T_1 and δ' particles, which

precipitate and coarsen at different rates at different temperatures. This also can explain why S.N. 65838 which contains lower Cu and higher Li than the rest, behaves differently from the rest of the material. In S.N. 65838, higher Li content would provide additional strengthening effect at 275°F by precipitating more δ' particles during the thermal exposure than the other alloys with higher Cu and lower Li contents. Prof. Howe from UVA reported that little δ' particles were observed in T8 temper material which were aged at 320°F but a considerable increase of δ' particles in the material after thermal exposure at 275°F and 225°F. After 1,000 hours at 275°F, the strength changes are not significant within the tested range. The long transverse tensile yield stresses of T8 temper material in Fig. 10 shows a similar response of softening after 100 hours than followed by strength increase until 1,000 hours of thermal exposure. All five alloys show softening between 1,000 hours and 2,500 hours. This could be a result mainly from coarsening of δ' particles. To better understand the evolution of these tensile properties of these alloys, a TEM study would be conducted in the future. Figures 11 and 12 show the evolution of tensile properties from T6 temper material. T6 temper materials do not show the softening behavior between 100 hours and 1,000 hours of thermal exposures. This observation lead us to believe that the observed softening of T8 temper material during the early stage of the thermal exposure could be related to the recovery of cold worked structure. The comparison of T6 and T8 temper materials are shown in Figs. 13 and 14. An interesting observation is that the significant initial strength differences between the T6 and T8 temper material become rather small after the 2,500 hour thermal exposure. This result indicates that one of the main reasons for the strength differences between T6 and T8 temper materials is due to the significant difference in precipitation kinetics of T_1 phase between the two tempers.

Fracture toughness tests by 10" wide, center-notched, fatigue pre-cracked panel tests were conducted on the materials after the thermal exposure. Due to the limitation of the amount of material available (30 lbs. ingots), only two test specimens per composition variant were available. Without the information regarding the property evolution as discussed above, a decision was made that the two specimens would be used to evaluate the fracture toughness values after 1,000 hours and 2,500 hours of thermal exposures at 275°F. The test results for the tensile and fracture toughness tests (K_c and $K_{app.}$) after 1,000 hours and 2,500 hours exposure at 275°F are listed in Table 4. Fracture toughness values by K_c are plotted in Fig. 15. Comparing the properties after 1,000 hours and 2,500 hours of exposure at 275°F, both strength and fracture toughness values are not much different showing only a small drop in K_c values after 2,500 hours. S-65837 shows the highest K_c values and maintained K_c value over 120 ksi-inch^{1/2} even after the 2,500 hours exposure at 275°F. However, the tensile yield stress is slightly short of 70 ksi. Figure 16 shows $K_{app.}$ values from the same tests in Fig. 15. Again, there are very little differences between the $K_{app.}$ values from the materials exposed for 1,000 hours compared to those for 2,500 hours. S-65837 shows the highest $K_{app.}$ values after both 1,000 hours and 2,500 hours of exposure at 275°F.

As demonstrated by the tensile test results after various thermal exposure conditions, it is now clear that complex microstructural changes take place in the early stage of the thermal exposures. Therefore, it should be stated that strength-fracture toughness evaluations only after 1,000 hours and 2,500 hours are not adequate to address the thermal stability of the material. The evolution of strength and fracture toughness during the earlier stage of the thermal exposure should be examined more closely in a later date which could provide a valuable information to optimize the temper practice for better thermal stability.

Conclusions

- Four variant alloys containing Mn and V were partially recrystallized at various degrees after solution heat treatment. One variant (S.N. 65840) which contains only Zr, retained unrecrystallized grain structure after solution heat treatment.
- Tensile strengths of T6 temper material continue to increase during the thermal exposure at 275°F indicative of underaged condition in T6 temper.
- The tensile properties of all five variants in T8 temper material undergo complex property changes during the initial stage of the thermal exposure at 275°F.
- The lowest solute alloy with high dispersoid elements (Zr, V & Mn), S-65837, showed the lowest strength with the highest fracture toughness.
- The unrecrystallized alloy, S-65840, exhibited the highest strength with the fracture toughness similar to the other high strength variants.
- No significant changes occurred in strength or fracture toughness after an exposure for 1,000 hours at 275°F., up to an exposure for 2,500 hours.

TABLE 2

Tensile test results from T8 temper material aged at 320°F/16 hours, then exposed to 2,500 hours at 275°F.

<u>S. No.</u>	<u>Dir.</u>	<u>UTS(ksi)</u>	<u>TYS(ksi)</u>	<u>El.(%)</u>
65836-1D	L	76.6	74.0	8.5
	45	75.3	70.0	8.0
	LT	75.3	70.3	5.5
65837-1D	L	72.3	68.5	8.5
	45	68.8	63.1	9.0
	LT	70.9	65.6	6.0
65838-1D	L	73.6	70.7	5.5
	45	67.9	62.5	10.5
	LT	72.9	66.8	6.3
65839-1D	L	78.2	74.6	7.0
	45	73.9	68.2	10.0
	LT	76.3	71.4	7.5
65840-1D	L	82.8	78.4	8.5
	45	72.3	67.7	13.5
	LT	77.4	71.3	10.5

Note:

1. All the property values are averaged from duplicate test results.
2. Tensile tests were conducted with subsize 0.25" wide x 1.00" long gauge length sheet specimens.

TABLE 3

Tensile test results from T6 temper material aged at 320°F/16 hours, then exposed to 2,500 hours at 275°F.

<u>S. No.</u>	<u>Dir.</u>	<u>UTS(ksi)</u>	<u>TYS(ksi)</u>	<u>El.(%)</u>
65836-4D	L	77.5	72.5	8.5
	45	72.1	65.2	11.0
	LT	75.6	69.5	7.5
65837-4D	L	72.3	68.0	10.0
	45	68.8	62.3	11.0
	LT	70.7	63.4	9.0
65838-4D	L	73.2	68.7	8.5
	45	67.6	60.7	11.5
	LT	71.6	66.3	7.0
65839-4D	L	74.6	69.6	7.0
	45	71.3	64.4	9.5
	LT	75.3	69.5	7.0
65840-4D	L	80.7	75.2	10.0
	45	72.3	66.5	12.5
	LT	76.3	70.8	10.5

Note:

1. All the property values are averaged from duplicate test results.
2. Tensile tests were conducted with subsize 0.25" wide x 1.00" long gauge length sheet specimens.

TABLE 4

Tensile Test and Plane Stress Fracture Toughness Test Results by 10" wide Center Notched Panel from cold rolled 0.090" gauge sheet of five RX818-T8 type alloys after thermal exposures at 275°F for 1,000 hours (-2's) and 2,500 hours (-3's)

<u>S.No.</u>	<u>UTS(ksi)</u>	<u>TYS(ksi)</u>	<u>El(%)</u>	<u>K_c</u>	<u>K_{app.}</u>
65836-2	77.3	74.0	9.0	105.7	81.1
-3	76.6	74.0	8.5	93.3	77.4
65837-2	72.3	67.6	9.0	139.7	93.3
-3	72.3	68.5	8.5	126.0	88.1
65838-2	73.7	70.6	8.0	92.5	75.8
-3	73.6	70.7	5.5	91.2	72.9
65839-2	78.0	75.0	7.0	87.2	73.3
-3	78.2	75.1	7.0	82.4	67.7
65840-2	83.6	79.8	6.5	80.4	71.6
-3	82.8	78.4	8.5	88.7	73.2

Note:

All the tensile properties are averaged from duplicate test results.

K_c and K_{app.} values were tested with 16" wide center-notched and fatigue precracked specimens

K_c and K_{app.} values are from single test.

K_c and K_{app.} values are in Ksi-(inch)^{1/2}

THERMAL STABILITY OF RX818 TYPE ALLOYS (T8) **L-dir. Tensile Yield Stress of 0.09 inch ga. sheet**

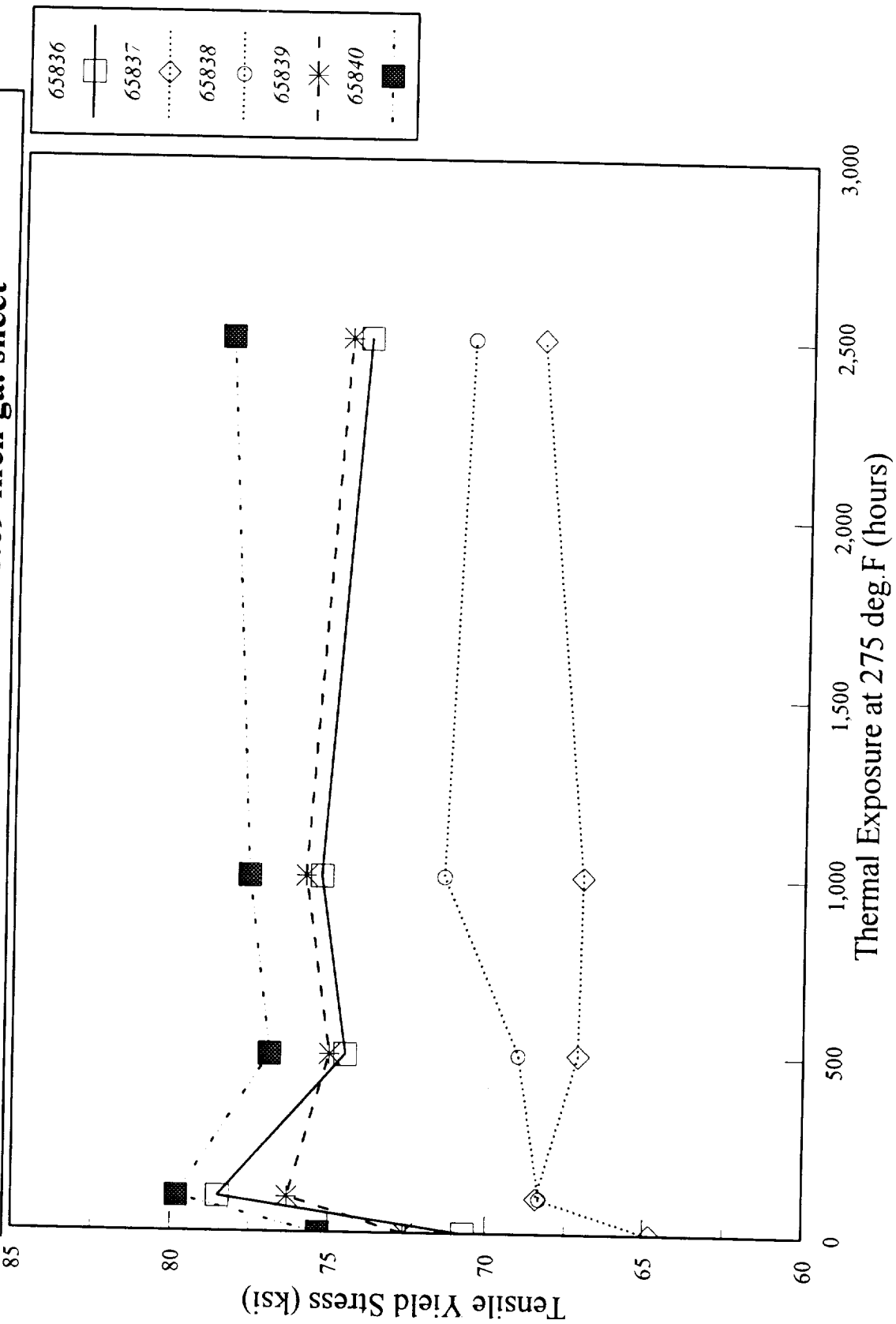


Fig. 9

THERMAL STABILITY OF RX818 TYPE ALLOYS (T8) **LT dir Tensile Yield Stress of 0.09 inch ga. sheet**

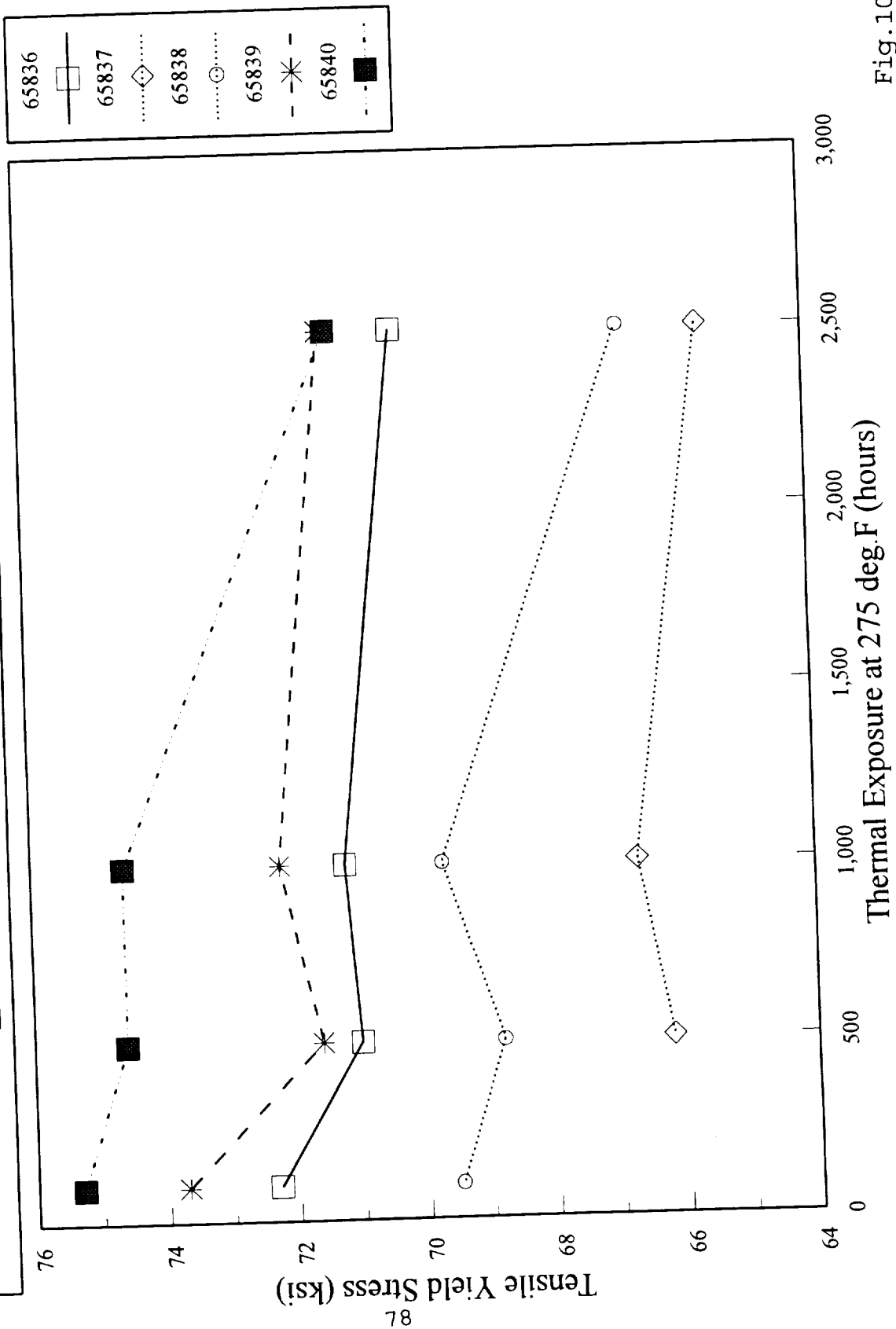


Fig.10

THERMAL STABILITY OF RX818-TYPE ALLOYS (T6) **L-dir. Tensile Yield Stress of 0.09 inch ga. sheet**

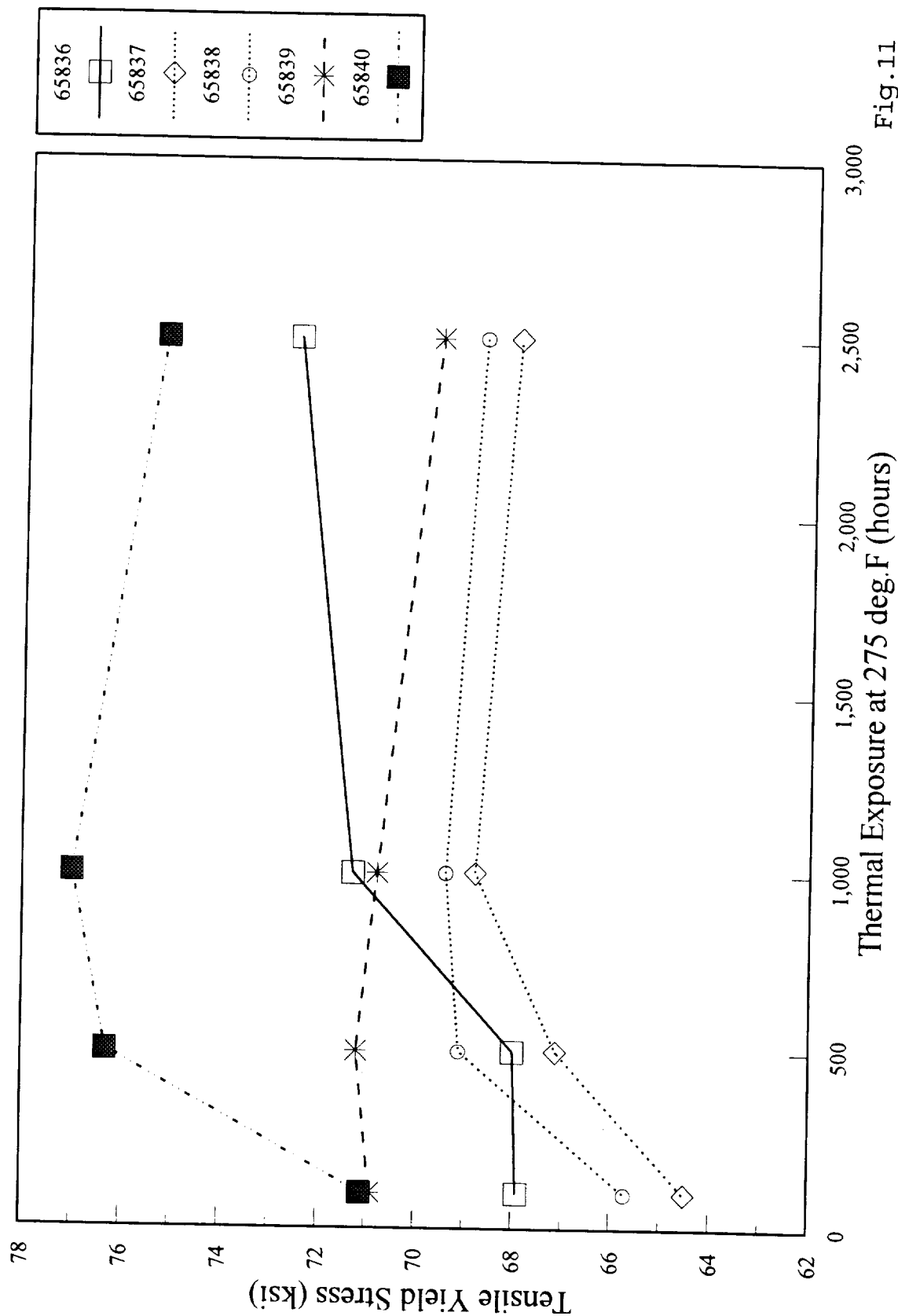


Fig.11

THERMAL STABILITY OF RX818-TYPE ALLOYS (T6) **LT - dir. Tensile Yield Stress of 0.09 inch ga. sheet**

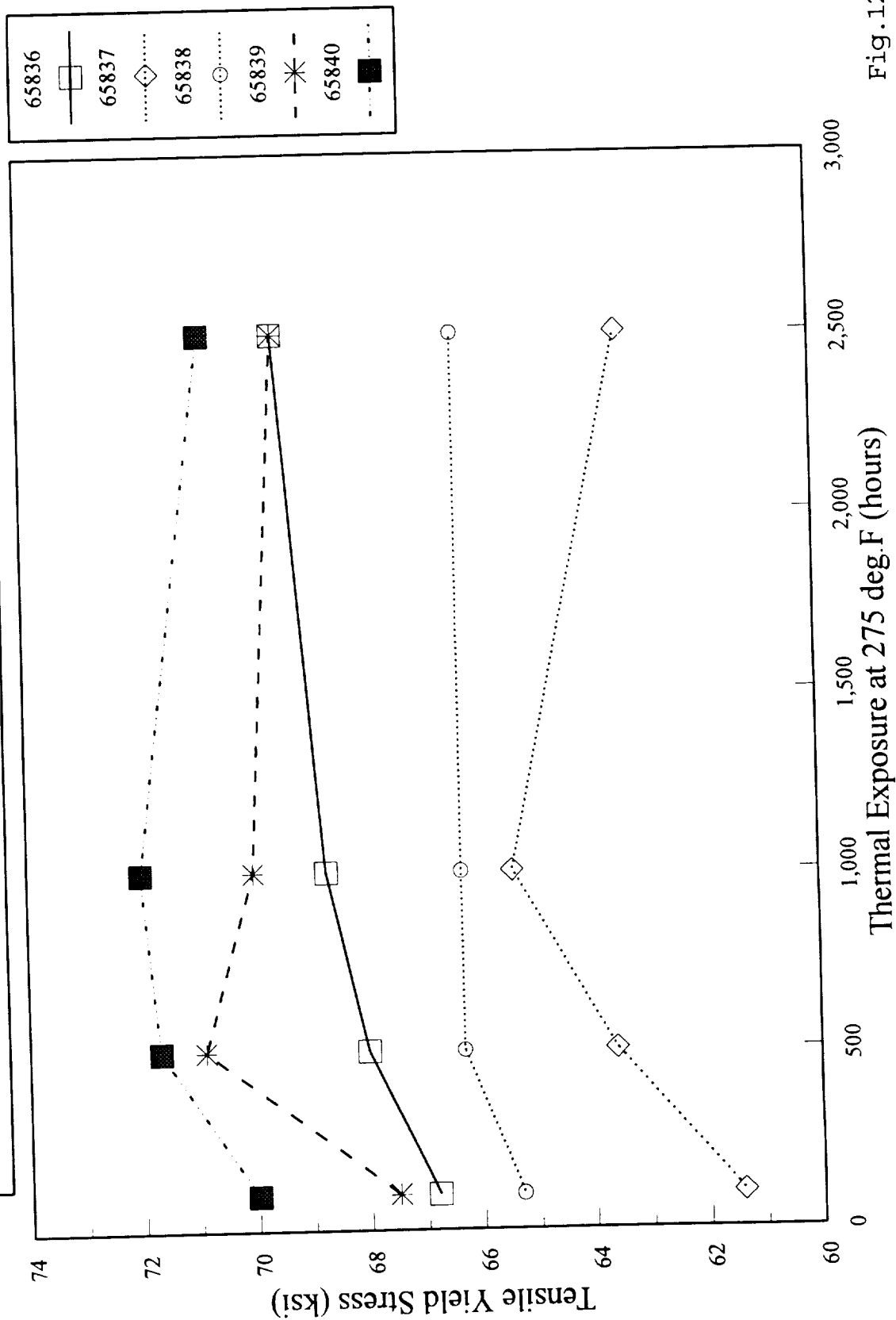


Fig.12

THERMAL STABILITY OF RX818 - TYPE ALLOYS **L-dir. Tensile Yield Stress of 0.09 inch ga. sheet**

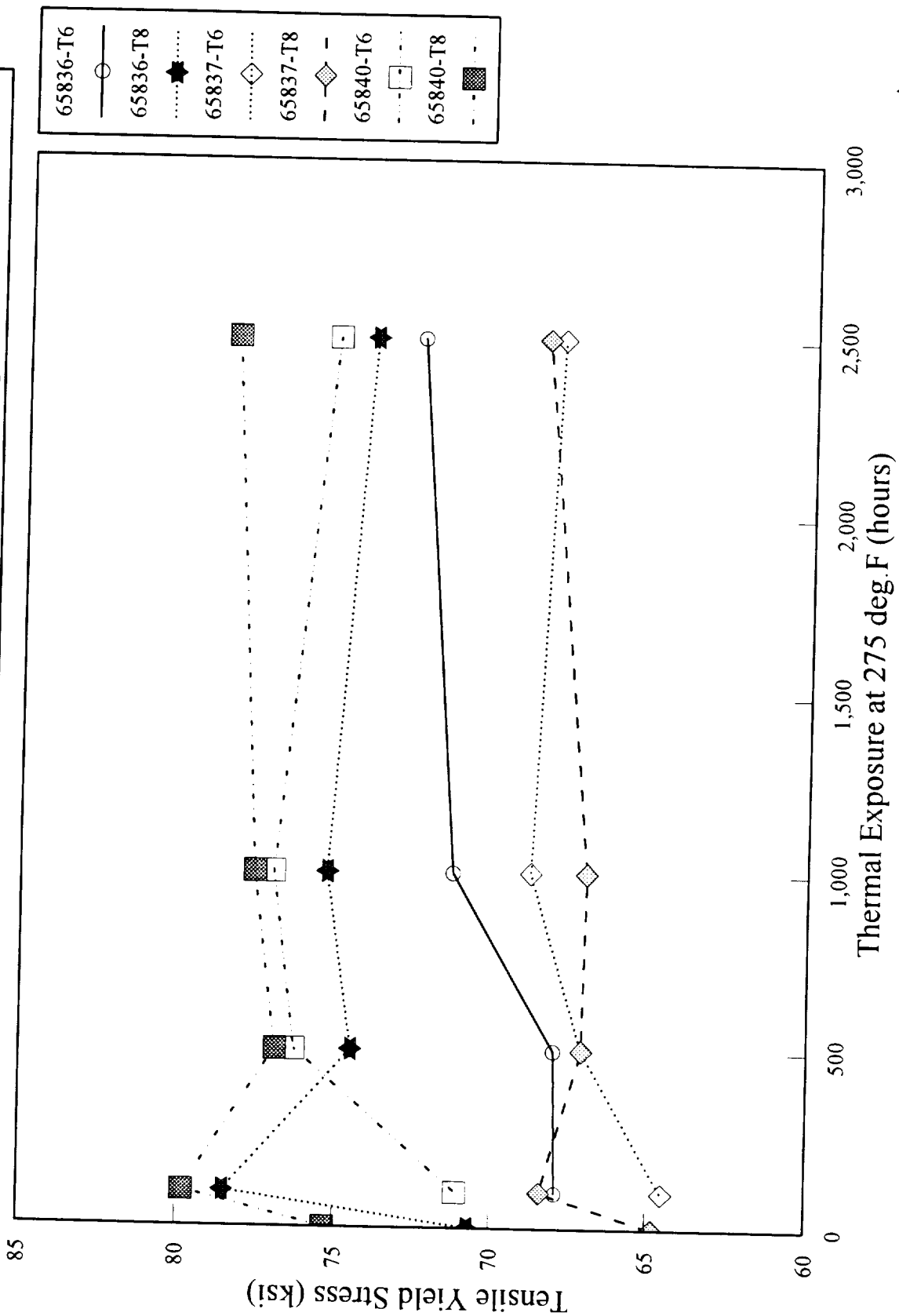


Fig.13

THERMAL STABILITY OF RX818 TYPE ALLOYS **LT-dir. Tensile Yield Stress of 0.09 inch ga. sheet**

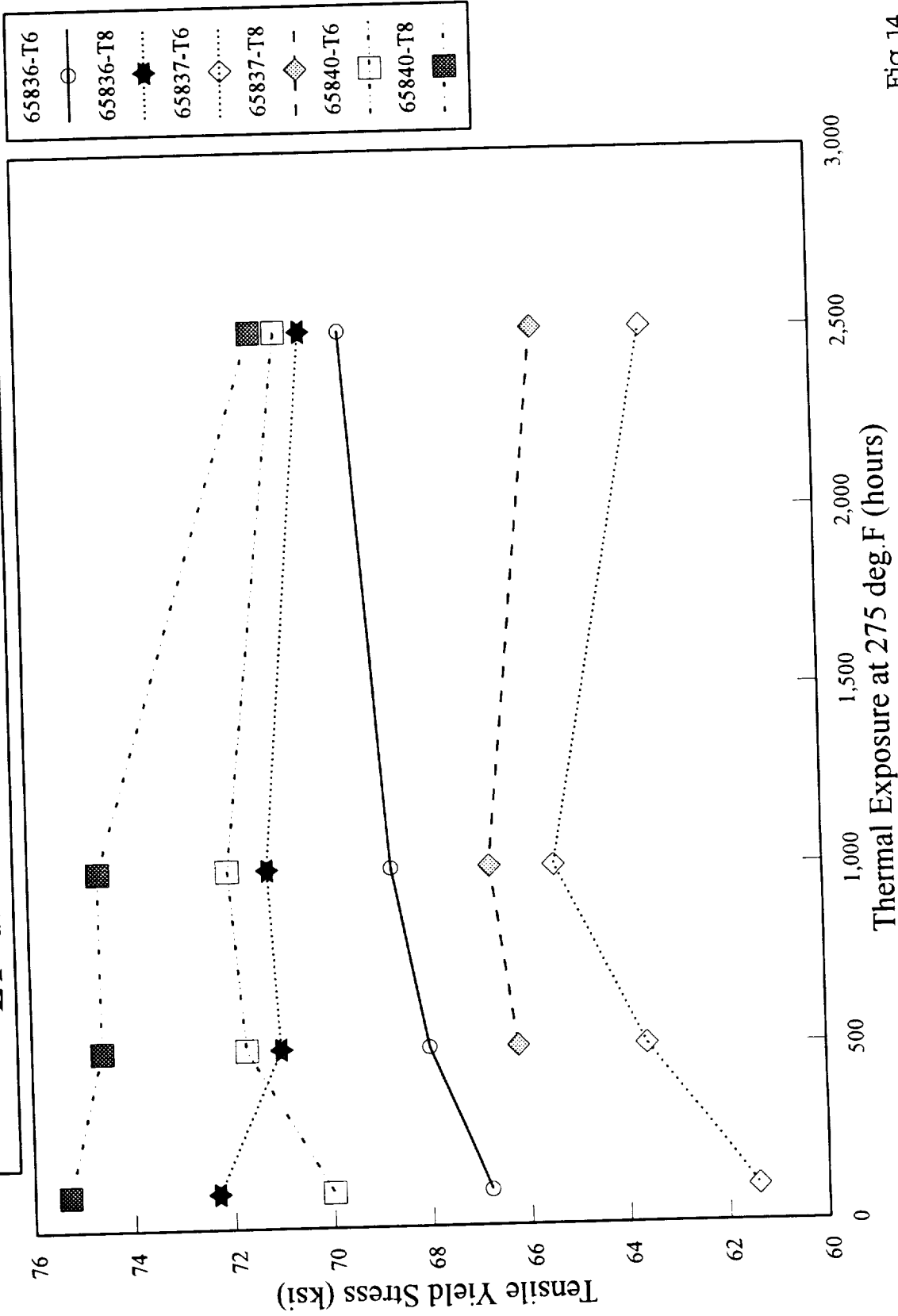


Fig.14

FRACTURE TOUGHNESS OF .09" ga. RX818-T8 VARIANTS
Center Notched 10" Wide Panel (Fatigue Precrack)
After Exposure at 275 deg.F

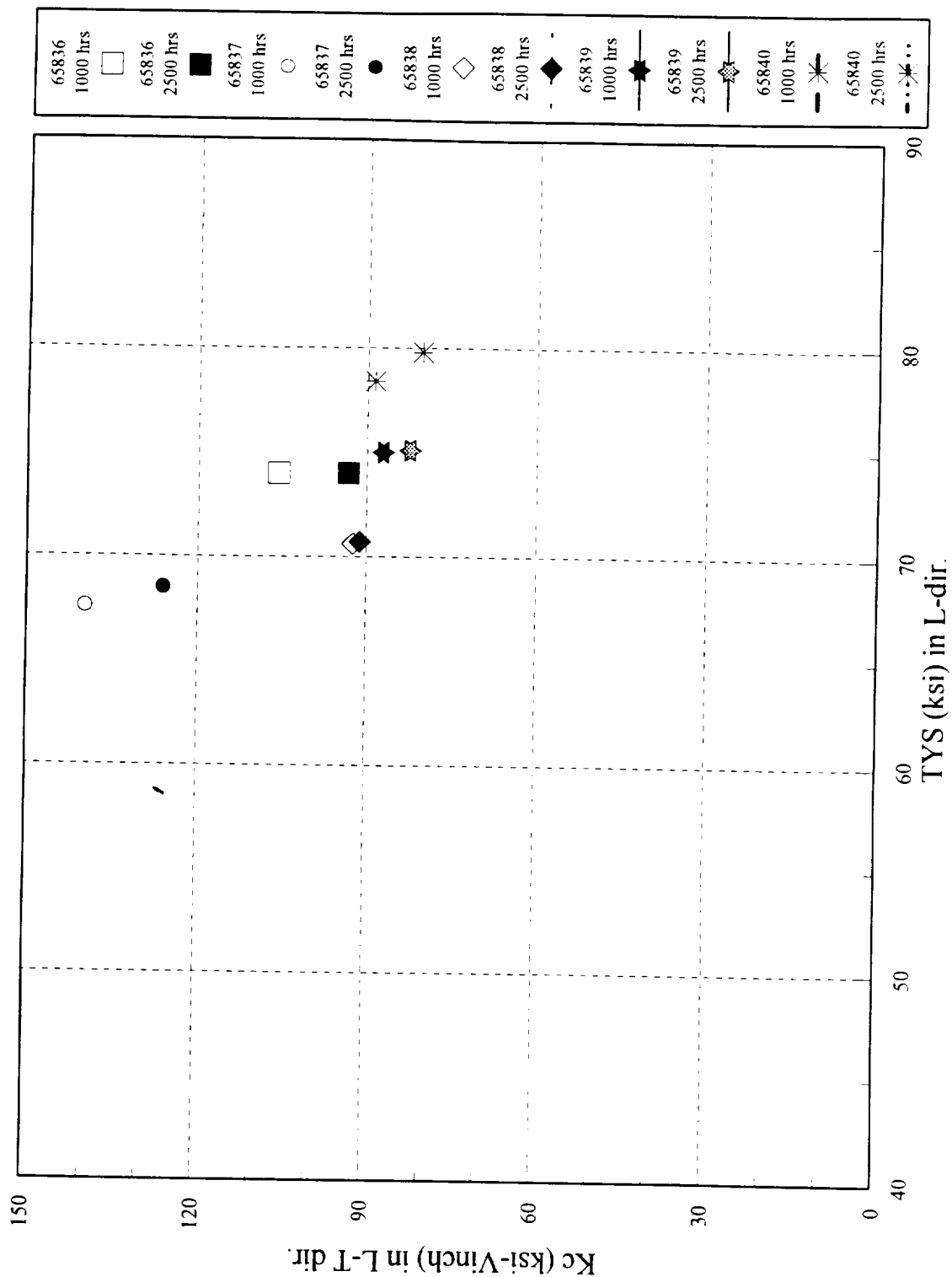


Fig.15

FRACTURE TOUGHNESS OF .09" ga. RX818-T8 VARIANTS
Center Notched 10" Wide Panel (Fatigue Precrack)
After Exposure at 275 deg.F

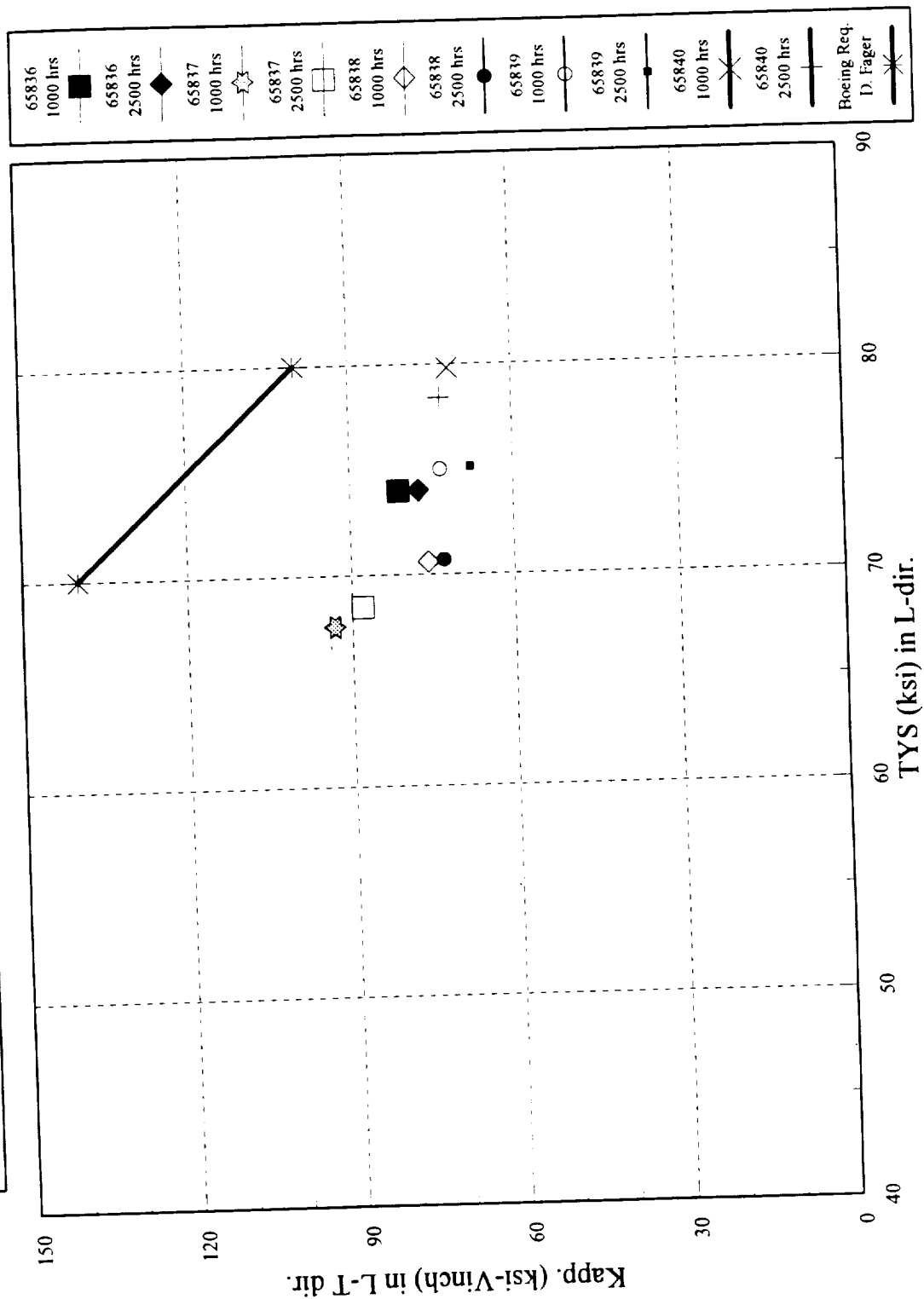


Fig.16

Subtask 2A3:

Examine the effect of dispersoids on thermal stability and mechanical properties of RX818 alloy - high level of dispersoids by Spray Deposition Technique.

Composition selection and casting by Spray Deposition

The dispersoid particles containing Zr, V, and Mn such as Al_3Zr , Al_3V and Al_6Mn , could help thermal stability and creep resistance. However, these dispersoid particles are most effective when these particles remain as coherent phases. In order to maintain the coherency of these particles, these dispersoids should be formed by solid state reaction instead of forming during solidification. Therefore, addition of too much of these elements in the melt would result in high volume fraction of coarse incoherent particles in the ingot. Such coarse incoherent particles are extremely deleterious to fracture toughness.

Therefore, the total amount of fine coherent dispersoid particles in conventionally cast material is very limited. One way to increase the amount of these coherent dispersoid particles is to employ a casting technique with a faster solidification rate. Such a casting practice would provide a high level of supersaturated solid solution so that a large volume fraction of coherent intermetallic particles could form by solid state reaction.

In this work, therefore, Spray Deposition technique was selected to produce material with high volume fraction of coherent dispersoids. The main reason for selecting the Spray Deposition technique among other rapid solidification techniques was for its economic feasibility for commercial scale production. Five compositions of 30 lbs permanent mold ingots were cast as starting stock material for Spray Deposition casting. The compositions are as follows:

Compositions:

<u>S.No.</u>	<u>Cu</u>	<u>Li</u>	<u>Mg</u>	<u>Ag</u>	<u>Zr</u>	<u>V</u>	<u>Mn</u>
65831 (target)	3.5	1.0	.4	.4	.3	.2	--
(actual)	3.45	1.0	.43	.29	.29	.18	.01
65632 (target)	3.5	1.0	.4	.4	.3	.2	.5
(actual)	3.6	1.04	.43	.38	.28	.18	.44
65833 (target)	3.5	1.0	.4	.4	.25	.2	.3
(actual)	3.6	1.1	.43	.44	.26	.17	.32
65834 (target)	3.5	1.0	.4	.4	.25	.1	.3
(actual)	3.39	1.02	.41	.43	.22	.09	.3
65835 (target)	3.0	1.2	.4	.4	.3	.2	--
(actual)	3.58	1.21	.42	.46	.27	.17	--

Spray Deposition and fabrication

Prof. E. Lavernia's group at the University of California at Irvine completed casting of five spray deposited billets. The billets were machined to 3" diameter billets and extruded to .25" x 1.5" cross section bars. To compare the properties to the sheet gauge product fabricated from the conventionally cast ingots, these extrusions were hot rolled to 0.125" gauge and then cold rolled to 0.090" gauge sheet. The final gauge sheet products were solution heat treated at 990°F for 1 hour followed by cold water quench. T8 temper sheet were stretched by 5% and aged at 320°F for 16 hours as a standard T8 temper practice.

Microstructure

Optical micrographs of the five alloys in the final temper condition are shown in Fig.17. The drastic difference in grain structures between the alloys with and without Mn are very interesting. The alloys containing Zr and no Mn, S.N. 65831 and S.N. 65835, are completely unrecrystallized and the alloys containing both Zr and Mn, S.N. 65832, S.N. 65833 and S.N. 65834 are fully recrystallized with coarse recrystallized grains. This observation proves that the presence of Mn interferes strongly

with Zr and prevents formation of coherent Al_3Zr dispersoid particles which is known as the most effective recrystallization preventing phase. It was not expected that a small amount of Mn addition to Zr containing alloys would drastically alter the grain structures.

Apparently the formation of intermetallics from these peritectic elements are quite complex. A TEM study will be conducted in the next report period to clarify the effect of Mn and Zr particles in controlling grain structures. It appears that V content does not show a strong effect on the recrystallization behavior.

Mechanical properties

The tensile test results of T8 temper sheet from the Spray Deposition technique are listed in Table 5. For comparison purposes, the tensile properties of conventionally produced material is listed in Table 6. Fig. 18 compares the tensile properties of the materials processed from the two different processing techniques. Based on the comparison of tensile properties, there is no significant difference in properties between the materials from the conventional processing and the Spray Deposition technique. Obviously, it is difficult to draw conclusions without fracture toughness comparisons. It should be noted that the strengths of these alloys are strongly influenced by the degree of recrystallization. The higher strengths achieved among the Spray Deposition alloys are from the two unrecrystallized alloys, S.N. 65831 and 65835, both of which do not contain Mn. S.N. 65835 shows the highest strength because of higher Cu and Li content than S.N. 65831. Due to the narrow sheet material from the Spray Deposited billets, Kahn tear tests will be conducted as a fracture toughness indicator test in the next report period.

TABLE 5

Longitudinal Tensile Test results of 0.090" gauge sheet in T8 temper which are extruded and rolled from Spray Deposited billets (Aged at 320°F for 16 hours)

<u>S. No.</u>	<u>UTS(ksi)</u>	<u>TYS(ksi)</u>	<u>El.(%)</u>
65831	78.8	74.8	9.5
65832	72.6	69.7	10.5
65833	69.8	67.2	12.5
65834	68.9	67.1	10.5
65835	83.9	80.6	9.5

Note:

1. All the property values are averaged from duplicate test results.
2. Tensile tests were conducted with subsize 0.25" wide x 1.00" long gauge length sheet specimens.

TABLE 6

Longitudinal Tensile Test results of 0.090" gauge sheet in T8 temper which are rolled from 30 pound permanent mold ingot (Aged at 320°F for 16 hours)

<u>S. No.</u>	<u>UTS(ksi)</u>	<u>TYS(ksi)</u>	<u>El. (%)</u>
65836	73.5	70.7	10.0
65837	68.3	64.8	10.5
65839	75.7	72.7	7.0
65840	79.4	74.9	10.0

Note:

1. All the property values are averaged from duplicate test results.
2. Tensile tests were conducted with subsize 0.25" wide x 1.00" long gauge length sheet specimens.
3. The actual compositions of these alloys are listed in the Subtask 2A2.

100X Barkers Etch Micrographs of Spray Deposition Cast 0.090" RX818
 Sheet in T8 Temper after Thermal Exposure at 275°F for 2500 hours



65831

65832

65833



65834

65835

Fig.17

TENSILE PROPERTIES FOR RX818 TYPE ALLOYS
L- dir. Elongation v. TYS of 0.09 inch ga. sheet
Conventional (Open Markers) Spray deposition (Solid Markers)

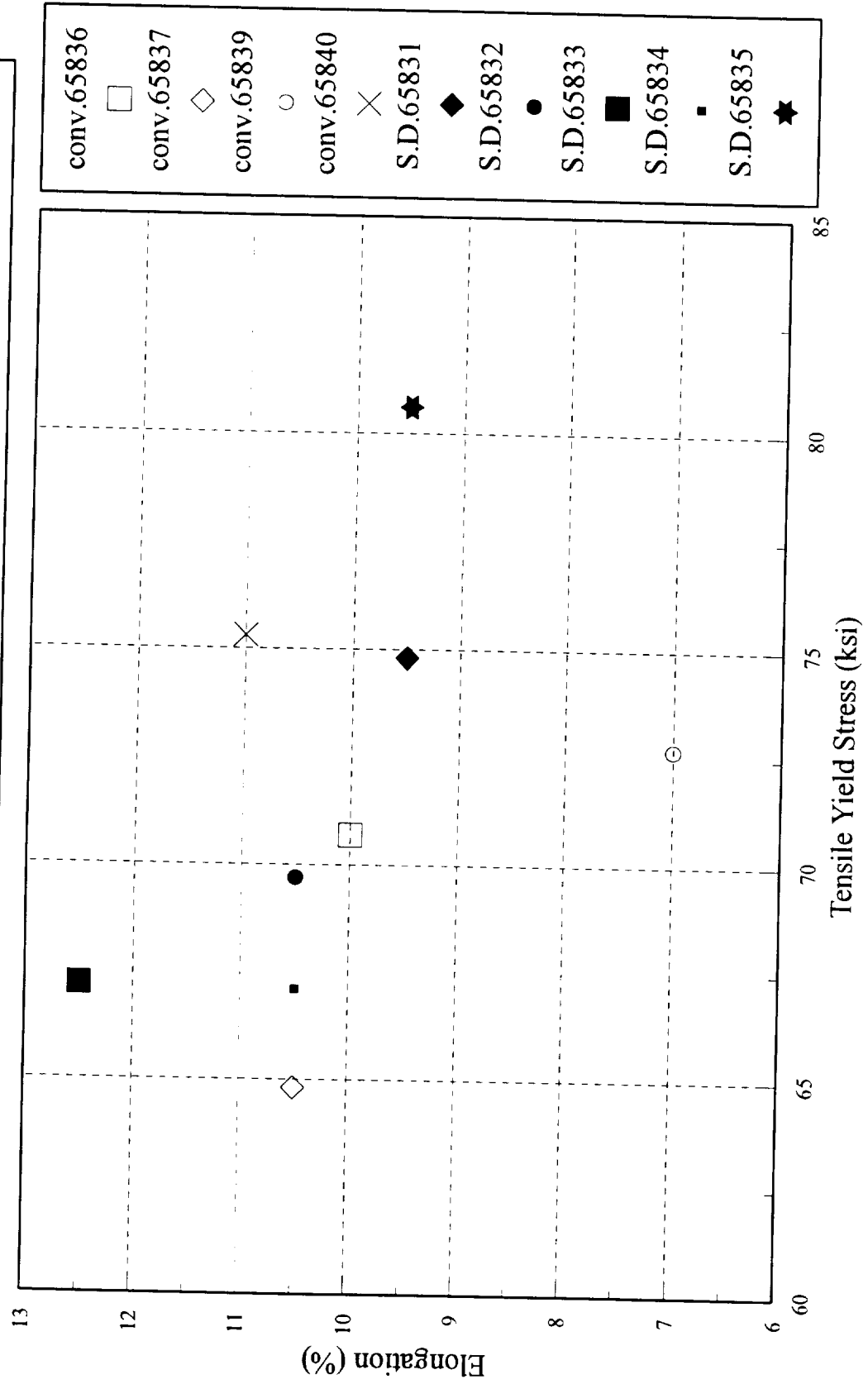


Fig.18

Subtask 2B. A Study of the Microstructure/Property Evolution Characteristics of the Al-Li-Cu-Mg-Ag System with RX818 (Uva)

Principal Investigator: Dr. J.M. Howe
Research Associate: Dr. Y. Mou

Objectives

The main objectives for the second six months of this subtask were: i) to develop a method of quantifying the size and number density of matrix T_1 plates, and ii) to begin quantifying the coarsening behavior of matrix T_1 plates in the RX818 base alloy.

Approach

i) Method of quantifying precipitate size and number density

In order to investigate the coarsening kinetics of T_1 precipitates in RX818 alloy, it is necessary to determine the size distribution and number density of T_1 plates in specimens aged for various times at different temperatures. In the present work, the geometry and distribution of T_1 particles are recorded as two-dimensional projections on TEM micrographs. There are some well-established techniques in the literature for obtaining actual three-dimensional information about the T_1 distribution from the TEM micrographs, as described further below.

All of the TEM micrographs, two of which are shown in Figs. 1(a) and (b), were taken along a $\langle 112 \rangle$ zone axis at about 60,000X magnification. Since T_1 plates form on the $\{111\}$ Al matrix planes, and only one $\{111\}$ plane is parallel to the $\langle 112 \rangle$ zone axis, only one of the four T_1 variants appears edge-on with the face parallel to the electron beam in this orientation. This situation requires that a measured number density of T_1 precipitates be multiplied by four in order to obtain the actual number density in a specimen. If stretching or some other factor results in precipitation on one

variant of {111} plane to be favored over others, then this method of totaling the precipitates may not be accurate. At this time, there is no data which show that this occurs.

Figure 2 shows the size relationship between actual T_1 plates and their TEM images. If the hexagonal shape of a T_1 plate is approximated as a circular disk with the faces parallel to the electron beam for simpler mathematical treatment, then the T_1 precipitates have the same thickness in the foil as in the TEM micrograph, provided the measured value is corrected for the magnification. However, a complex situation arises for the particle diameters. When a particle is centered within the foil, such as particles O_1 and O_3 in Fig. 2, the measured diameter is equal to the actual diameter after correction for the magnification. When a precipitate is centered outside the foil (but within a certain vicinity of the foil), such as for the other particles in the figure, the measured diameter is less than the actual diameter. Since it is not possible to distinguish whether a particle is centered inside or outside the foil from the projection in a TEM micrograph, the precipitate number density obtained from a micrograph is higher than the actual value, and histograms of particle diameter are biased towards the smaller sizes. The following method was used to correct for these effects.

The observed precipitate diameters in a group of micrographs were divided into a few size classes. At a magnification of 60,000X, for example, if the size increment ΔD is taken as 1 μ m, the observed diameters can be divided into some ten classes with diameter ranges $(D_i - \Delta D, D_i)$, e.g., (0,1), (1,2) If N_i and M_i are the number densities per unit micrograph area and per unit specimen volume, respectively, for the particles in the diameter range $(D_i - \Delta D, D_i)$, then as shown in Fig. 2, N_i can be expressed as a summation of contributions from M_i (inside particles) and all M_j ($j \geq i$, outside particles) as:

$$\begin{aligned}
N_1 &= M_1 t + M_1 \Delta p_{11} + M_2 \Delta p_{12} + \dots + M_r \Delta p_{1r} \\
N_2 &= M_2 t + M_2 \Delta p_{22} + M_3 \Delta p_{23} + \dots + M_r \Delta p_{2r} \\
&\dots \\
N_r &= M_r t + M_r \Delta p_{rr}
\end{aligned} \tag{1}$$

where t is the foil thickness (determined by convergent-beam electron diffraction (CBED) (1), as illustrated in Fig. 1(c)) and p_{ij} is the probability that an outside particle of diameter D_j gives a truncated image in the diameter range $(D_i - \Delta D, D_i)$. An expression for p_{ij} has been derived as (2):

$$p_{ij} = (j^2 - (i-1)^2)^{1/2} - (j^2 - i^2)^{1/2} \quad (j \geq i). \tag{2}$$

With $p_{ij} = 0$ for $i > j$, Eqn. [1] may be written in matrix form and solved for the actual diameter distribution as:

$$\mathbf{m} = (t\mathbf{I} + \Delta\mathbf{P})^{-1}\mathbf{n} \tag{3}$$

where \mathbf{I} is the identity matrix, $\mathbf{P} = (p_{ij})$, $\mathbf{n} = (N_i)^T$ and $\mathbf{m} = (M_i)^T$. A measured diameter distribution (histogram), \mathbf{n} , can be readily converted to the actual specimen distribution \mathbf{m} through Eqn. [3], and the sum of all the components of \mathbf{m} is the actual number density.

ii) Coarsening behavior of matrix T_1 plates

Figures 3 and 4 show the diameter and thickness distributions of RX818 alloy (Lot. No. 64667) in the initial -T8 condition (20 hrs at 163°C (325°F)) and after additional aging to total times of 1006 and 2518 hrs at 163°C (325°F). The distributions were obtained using the procedure described above and at least 500 precipitates were measured in each sample. Note that the particle diameters and thicknesses are normalized by the average thickness and diameter

in each of the graphs.

The average diameter, thickness, number density and volume fraction of the matrix T_1 plates versus aging time at 163°C (325°F) are shown in Figs. 5(a) through (d), respectively. From these data, it is apparent that the average diameter and thickness of the T_1 plates increases with aging time at 163°C (325°F), with the average diameter increasing from about 45 nm after 20 hrs of aging to 91 nm after 2518 hrs, and the average thickness increasing from about 1.5 nm (about two unit cells of the T_1 phase) to about 5.8 nm thickness. A decrease in average aspect ratio (diameter/thickness) from about 30:1 to 16:1 accompanied this process and such a decrease is also indicative of coarsening of the precipitate plates.

In contrast to the behavior of the average precipitate diameter and thickness, both the number density and volume fraction of the matrix T_1 plates initially increased during aging from 20 to 1006 hrs at 163°C (325°F), followed by a substantial decrease in the number density and only a slight decrease in the volume fraction with further aging time. The increase in number density and volume fraction of precipitates upon aging for 1006 hrs indicates that the matrix was probably still partially supersaturated with solute after the initial 20 hrs of aging and that further precipitation occurred during further aging of the alloy. The subsequent decrease in the number density of precipitates for a relatively constant volume fraction after aging for 2518 hrs is characteristic of particle coarsening. The maximum volume fraction of T_1 phase obtained from these three samples was about 0.03 (or 3%) after 1006 hrs aging, but the volume fraction could have been slightly higher at earlier aging times where no data were available. At this time, no interpretation is offered regarding the changes in distribution of the diameters (Fig. 3) and thickness (Fig. 4) with exposure, since the coarsening behavior has not been compared with any theoretical models.

Summary

A TEM procedure was developed to quantify the diameter, thickness, number density and volume fraction of matrix T_1 plates in RX818 base alloys. Quantification of T_1 plates in RX818-T8 alloy (Lot. No. 64667) exposed for additional total times of 1006 and 2518 hrs aging at 163°C (325°F) shows that there is an increase in the average diameter and thickness of the plates with a corresponding decrease in the number density for nearly constant volume fraction of precipitates, indicative of a coarsening process.

References

1. P.M. Kelly, A. Jostons, R.G. Blake and J.G. Napier, "The Determination of Foil Thickness by Scanning Transmission Electron Microscopy", Phys. Stat. Sol. (a), vol. 31, 771 (1975).
2. J.M.G. Crompton, R.M. Waghorne and G.B. Brook, "The Estimation of Size Distribution and Density of Precipitates from Electron Micrographs of Thin Foils", Brit. J. Appl. Phys., vol. 17, 1301 (1966).

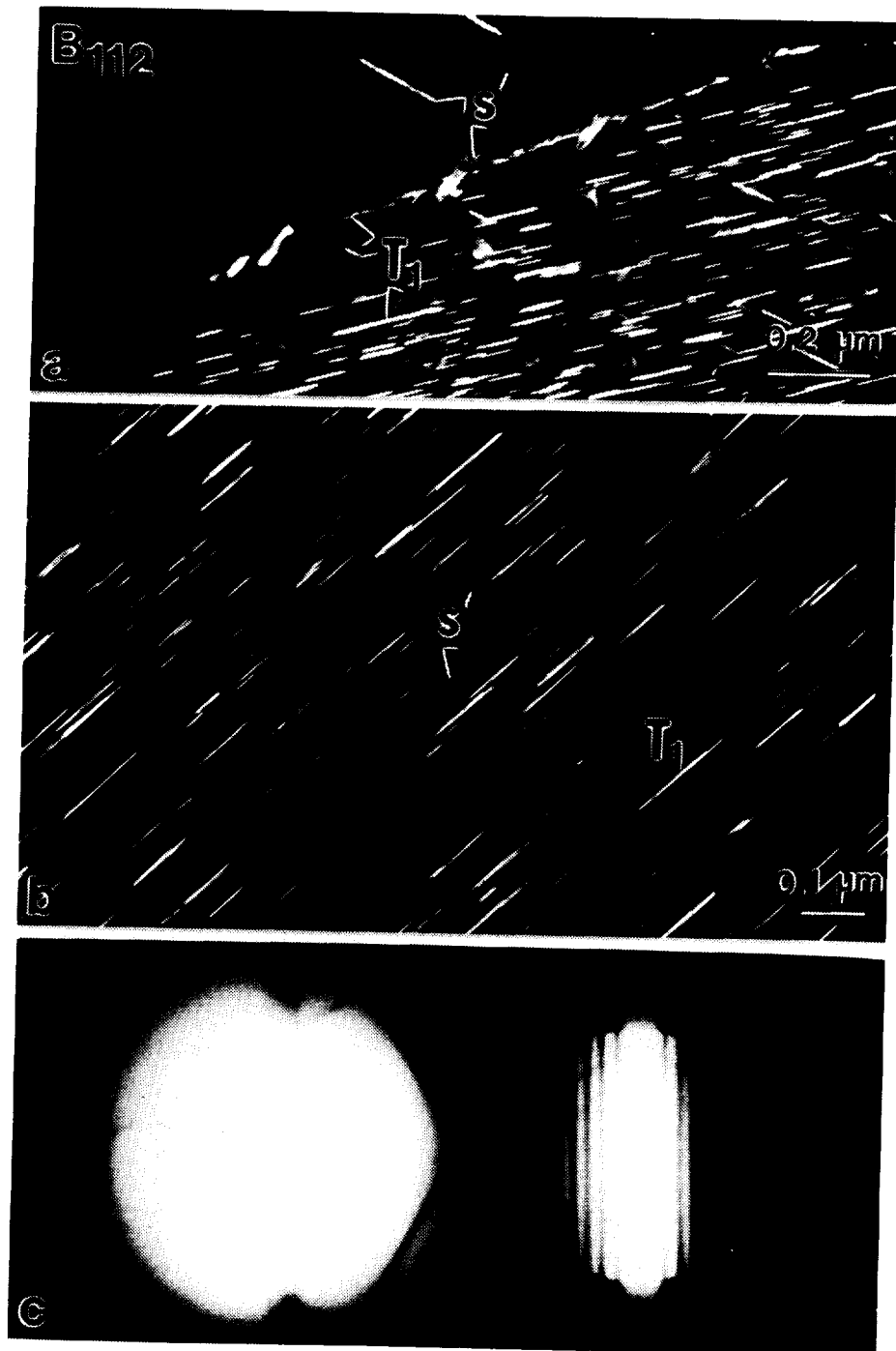


Figure 1. (a) $\langle 112 \rangle$ dark-field TEM image of a low-angle grain boundary in RX818 alloy aged for 1006 hrs at 163°C (325°F), (b) $\langle 112 \rangle$ dark-field TEM image showing one variant of T_1 plates and a few S' laths in a grain interior in the same sample, and (c) a CBED pattern from the area shown in (b) used to determine the sample thickness. The dark-field TEM images in (a) and (b) were formed by including both T_1 and S' precipitate reflections in the objective aperture.

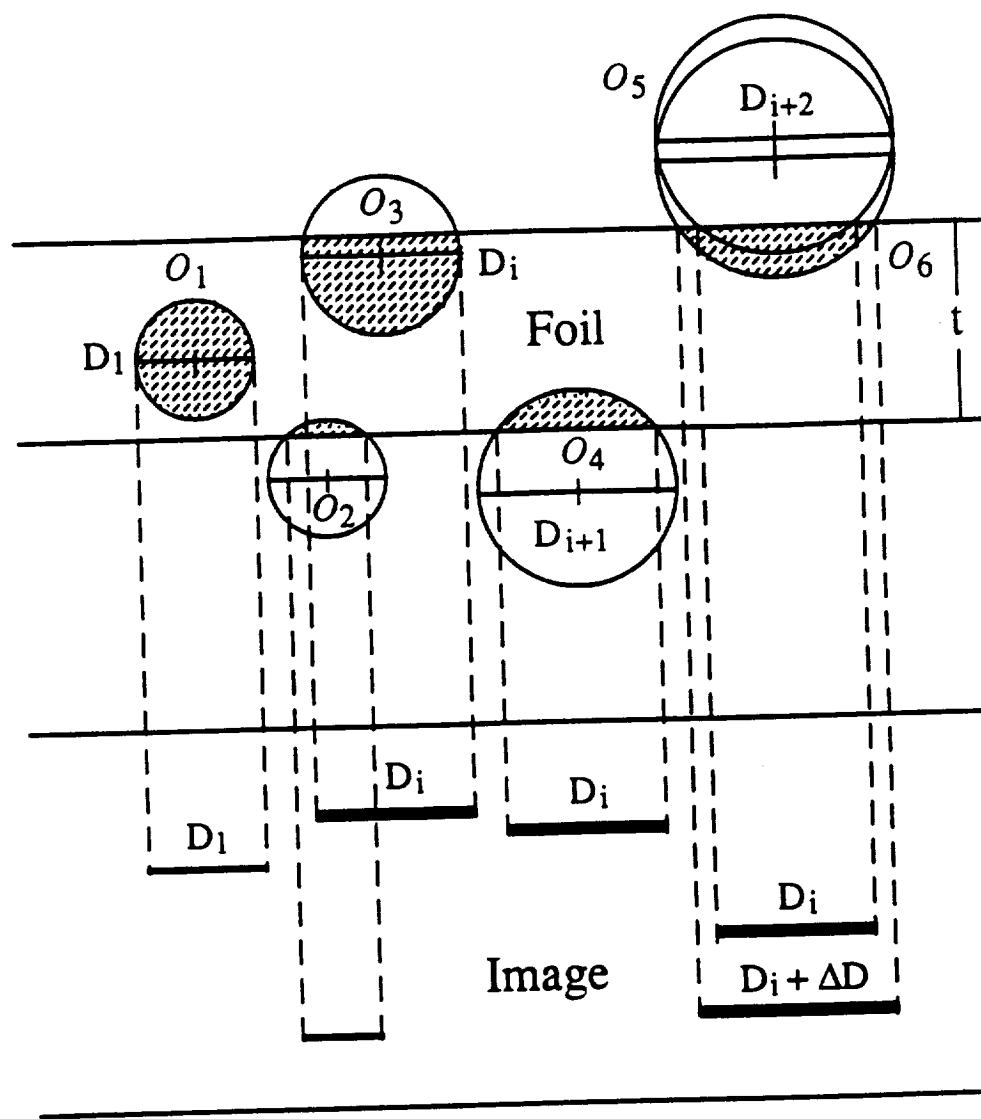


Figure 2. Schematic size relationships between T₁ plates and their TEM images with unit magnification.

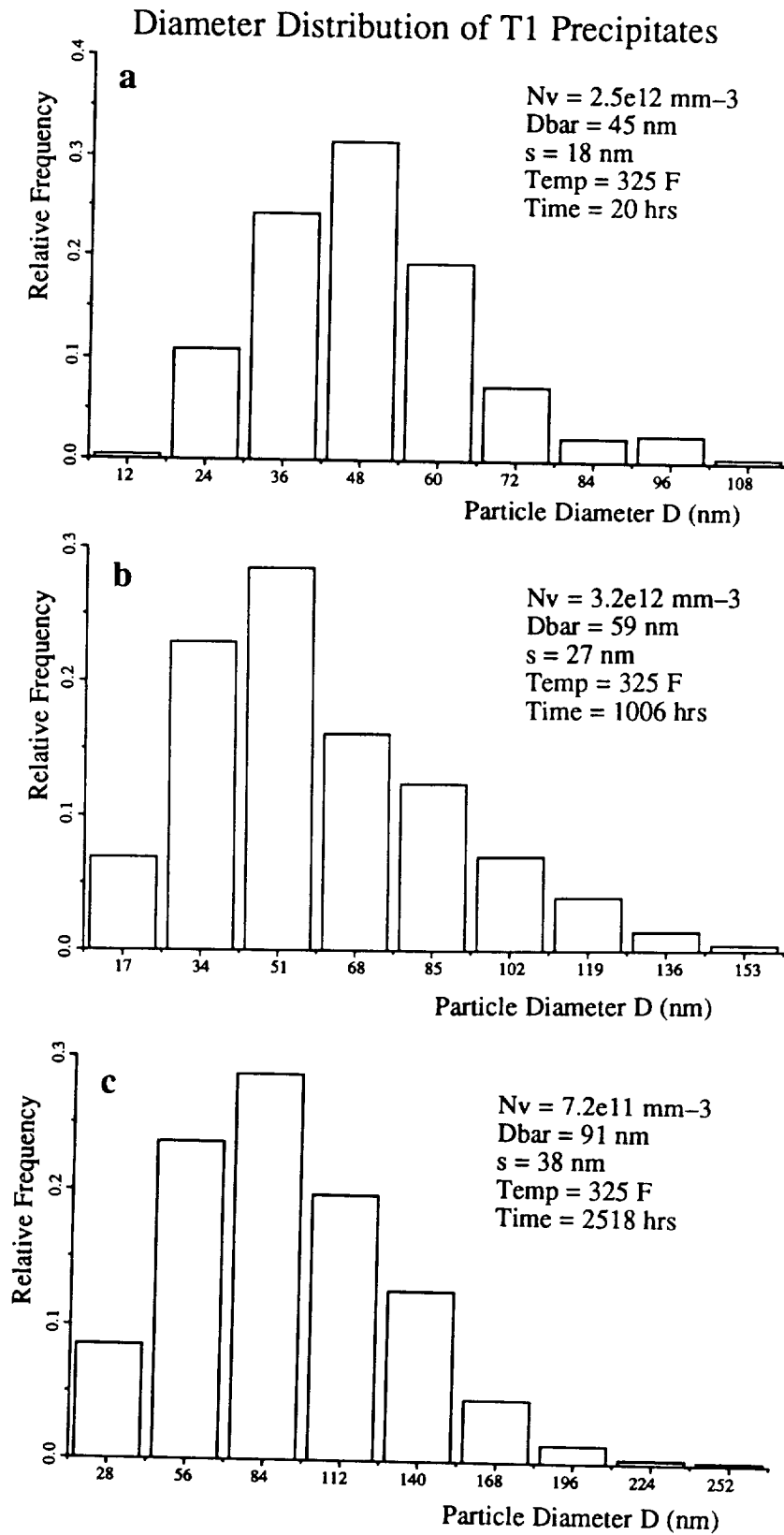


Figure 3. Diameter distributions of matrix T₁ plates in RX818 alloy aged for: (a) 20, (b) 1006 and (c) 2518 hrs at 163°C (325°F).

Thickness Distribution of T1 Precipitates

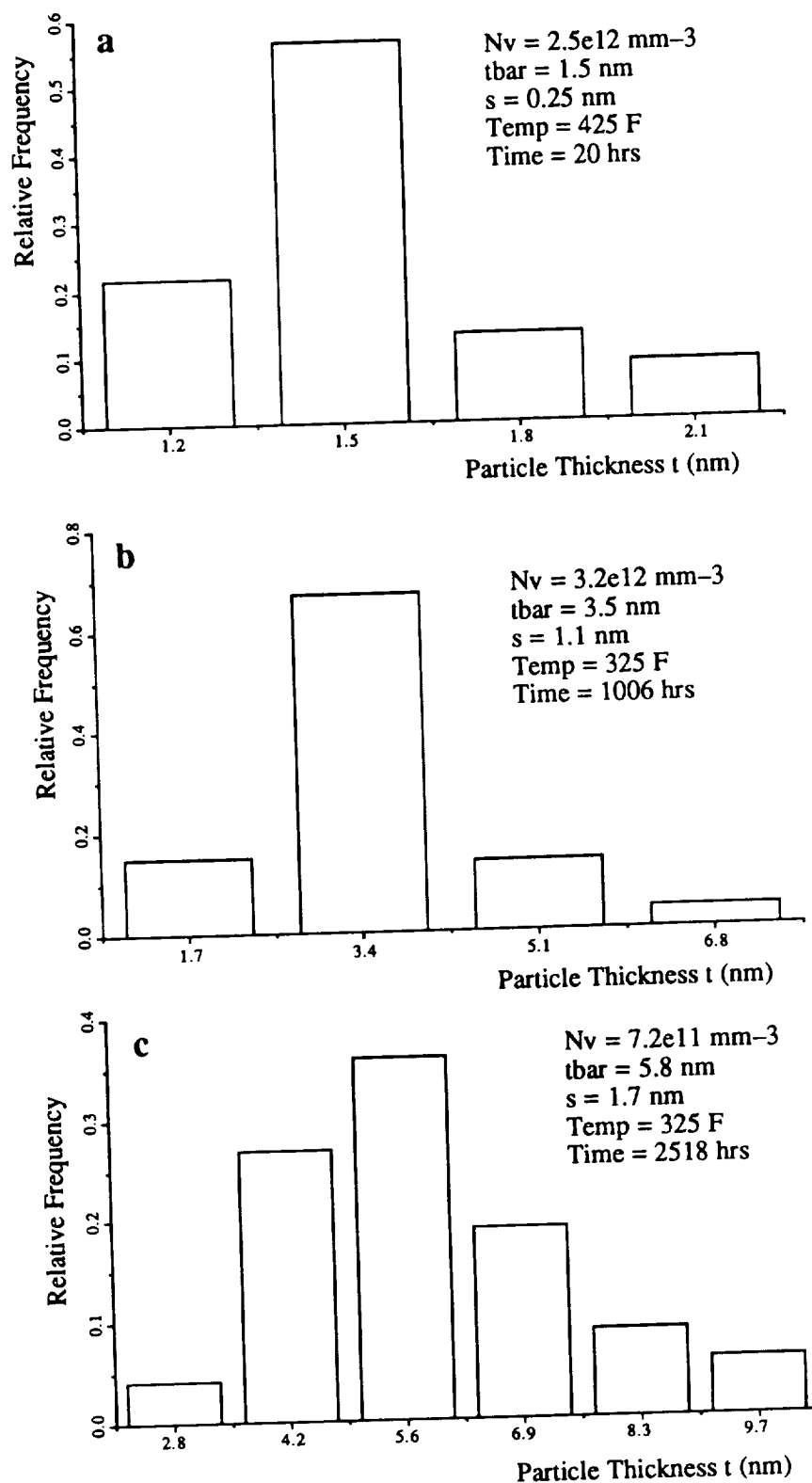


Figure 4. Thickness distributions of matrix T₁ plates in RX818 alloy aged for: (a) 20, (b) 1006 and (c) 2518 hrs at 163°C (325°F).

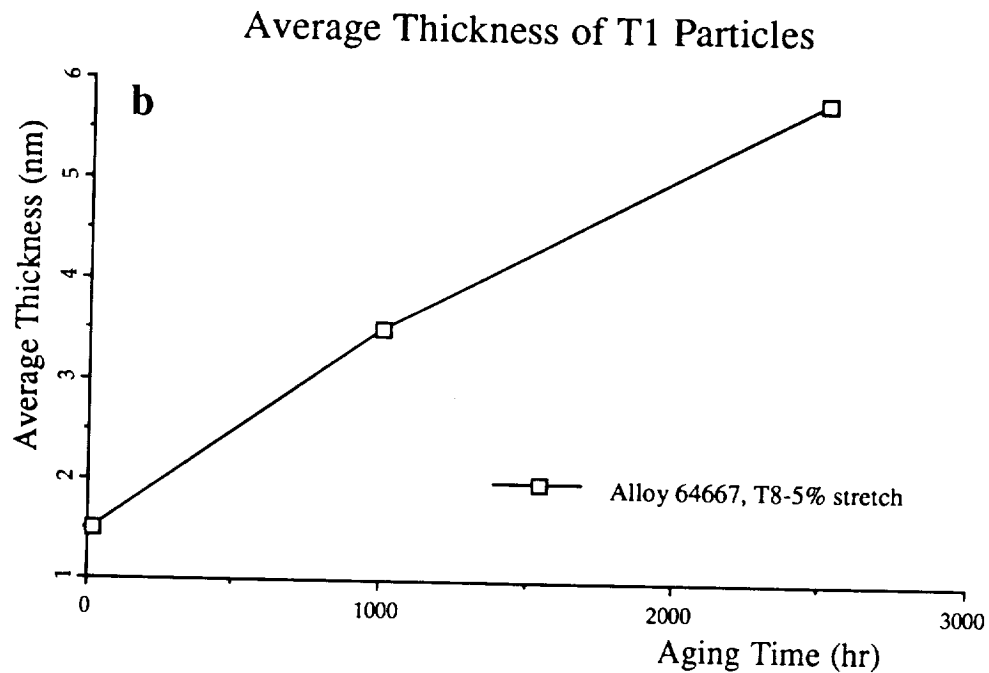
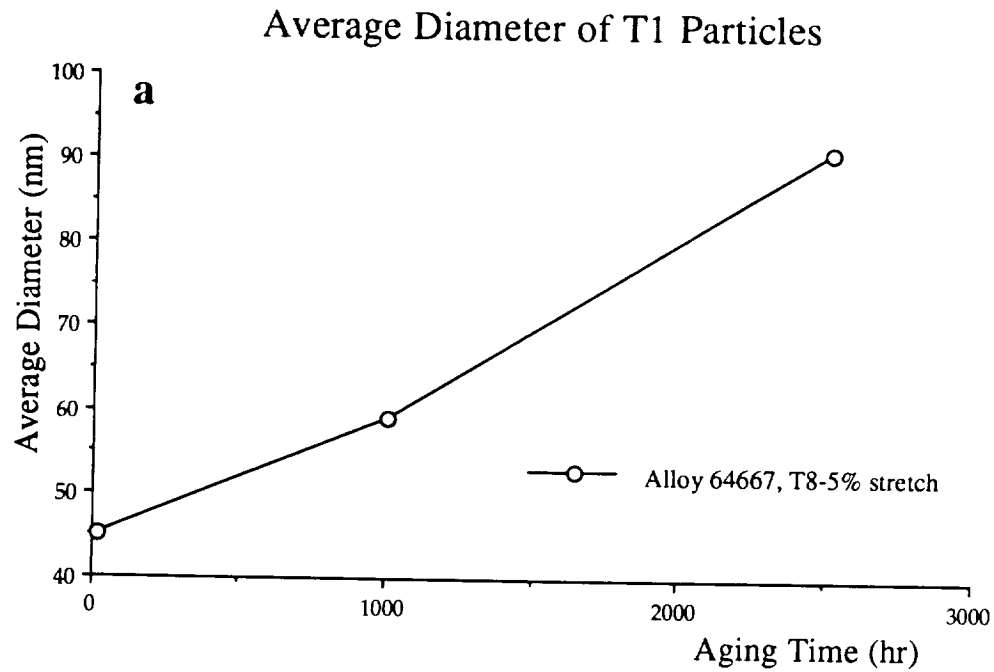
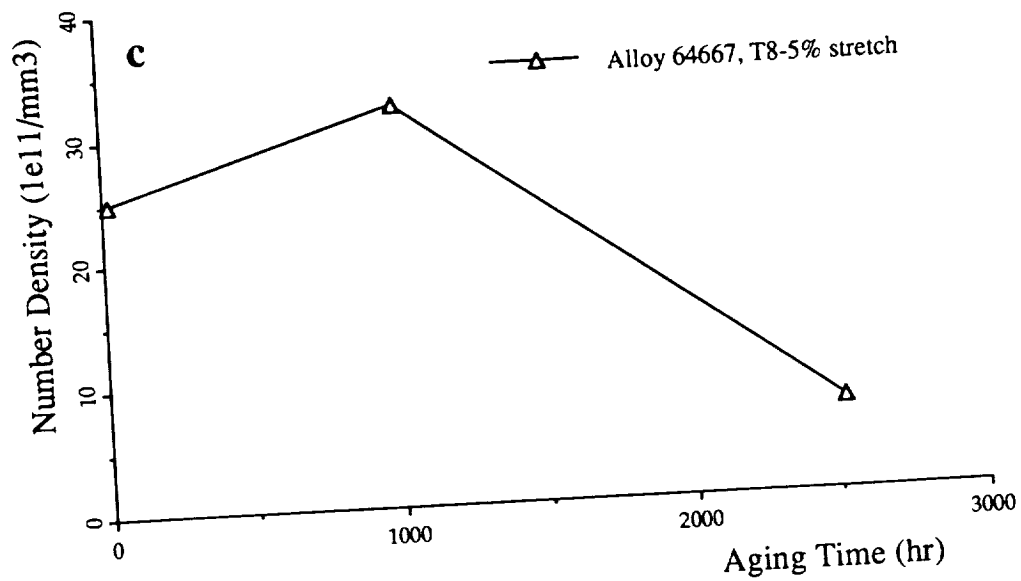
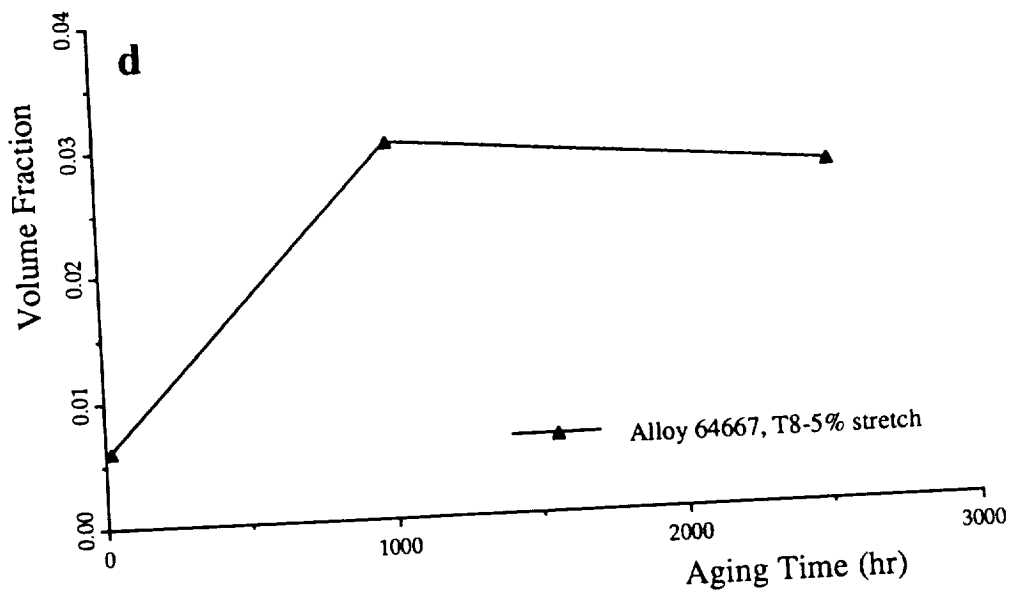


Figure 5. (a) Average diameter, (b) thickness, (c) number density and (d) volume fraction of matrix T₁ plates as a function of aging time in RX818 alloy aged for 20, 1006 and 2518 hrs at 163°C (325°F).

Number Density of T1 Particles



Volume Fraction of T1 Particles



TASK 3. P/M 2XXX ALLOY DEVELOPMENT

Principal Investigator:	Dr. L.M. Angers, Alcoa
Senior Engineer:	Dr. G. Dixon, Alcoa
Boeing Contact:	Dr. W.E. Quist
Douglas Contact:	Mr. R. Kahandal
UVA Contact:	Dr. E.A. Starke, Jr.

Objective

The primary objective of this task is to develop a damage tolerant aluminum based material for the lower wing and fuselage of a Mach 2.0 aircraft. This material must first meet preliminary strength and toughness targets at room temperature and then several criteria associated with elevated temperature service (e.g., retention of room temperature properties after exposure, performance at the operating temperature and resistance to creep deformation).

The P/M 2XXX alloys are under consideration here for several reasons. Firstly, P/M processing provides rapid solidification rates, enabling one to introduce greater amounts of dispersoid forming elements into the aluminum solid solution than can be introduced using conventional ingot metallurgy methods. As a result, the wrought P/M products may be more resistant to recrystallization than I/M alloys with lower levels of these additions. Generally, unrecrystallized structures possess better strength/toughness combinations than recrystallized structures. Furthermore, if these additions are added in great enough amounts, modest dispersion strengthening may result. Finally, the refinement of constituent which is expected to accompany the rapid solidification will also have beneficial effects on toughness.

Background

Because of the anticipated promising strength/toughness relationships, the P/M 2XXX alloys were pursued in the present

investigation. Three alloys having high levels of dispersoid forming elements were selected and atomized:

S. No. 710820: Al-4.34 Cu-1.46 Mg-0.57 Mn-0.55 Zr-0.1 V
S. No. 710821: Al-5.72 Cu-0.54 Mg-0.31 Mn-0.51 Ag-0.57 Zr-0.1 V
S. No. 710822: Al-6.68 Cu-0.52 Mg-1.70 Mn-0.52 Ag-0.20 Zr-0.1 V

S. No. 710820 is essentially a high Zr version of 2124. Its composition is nearly identical to the alloy studied in the NASA program where excellent strength/toughness relationships were achieved (1-4).

S. Nos. 710821 and 710822 represent high Zr and Mn versions of the Ω phase alloy being considered in the ingot metallurgy portion of this program. Since the Ω phase alloy is expected to be our highest strength 2519 variant, it was chosen as a baseline into which excess Zr and Mn could be added. The Cu level in S. No. 710822 was increased to account for the loss of Cu to formation of the $\text{Al}_{20}\text{Cu}_2\text{Mn}_3$ phase.

The addition of 0.1% V to all three alloys was made since all contain some Mn and Alcoa internal research has shown that V additions may refine the $\text{Al}_{20}\text{Cu}_2\text{Mn}_3$ phase which forms.

Procedure

The three lots of atomized powder were cold isostatically pressed, hot pressed and extruded to produce extrusions having a 2" by 4" cross-section. Extrusions were heated to 800°F prior to rolling. They were then rolled by a combination of cross rolling and straight rolling to produce sheet 8" wide by 0.125" thick. A total of seven passes and two reheats were used.

Differential scanning calorimetry was used to select solution heat treat temperatures:

<u>S. No.</u>	<u>Solution Heat Treatment Temperature (°F)</u>
710820	930
710821	980
710822	980

Sheet was solution heat treated for 1 hr, cold water quenched, stretched 8% and aged at 350°F for times between 1 and 16 hr.

Optical metallography, microprobe, Guinier X-ray diffraction and TEM were used to characterize microstructures. Duplicate longitudinal tensile samples and single L-T center crack fracture toughness samples 6.3" wide by 20" were tested.

Results and Discussion

Optical metallography revealed unrecrystallized structures in sheet from all three alloys (Fig. 1). Coarse clusters of particles, which were identified by microprobe analyses to be rich in Fe, Cu and Ce and depleted in Mg and Zr, were present as defects in all (Fig. 2). Such defects are probably related to prior lot contamination at the atomization facility.

Information regarding dispersoids and strengthening precipitates was derived from Guinier X-ray diffraction and TEM. The results of Guinier X-ray diffraction are presented in Table I. All three P/M 2XXX alloys contain the $\text{Al}_{20}\text{Cu}_2\text{Mn}_3$ and $\text{Al}_7\text{Cu}_2\text{Fe}$ phases and the two with high Zr levels, e.g., S. Nos. 710820 and 710821, also contain the DO_{23} tetragonal form of Al_3Zr . No Ll_2 Al_3Zr was detected in any of the alloys. Transmission electron microscopy of the T8 temper of the high Zr 2024 type alloy, S. No. 710820, revealed at least two type of dispersoids and S' precipitation. Figure 3 presents low and high magnification bright field images and a selected area electron diffraction pattern. The low magnification micrograph includes one grain boundary and a high number density of dispersoids. Diffracting conditions reveal substructure in one of the grains, confirming at least a partially

unrecrystallized structure. The higher magnification micrograph shows dispersoid morphology. Microanalysis identified the rod-like particles as an Al-Cu-Mn phase and the cuboid as an Al-Cu-Zr particle. The Al-Cu-Mn phase is likely $\text{Al}_{20}\text{Cu}_2\text{Mn}_3$. The finer particles in the background are also Al-Cu-Zr. The characteristic reflections for S' are observed in the $\langle 100 \rangle$ diffraction pattern but none of the characteristic reflections for the Ll_2 Al_3Zr phase are present.

Figure 4 presents a bright field image and selected area diffraction pattern from the T8 temper of the high Zr Ω phase alloy, S. No. 710821. The bright field image reveals coarse Al-Cu-Mn dispersoids and finer Al-Cu-Zr cuboids. The $\langle 100 \rangle$ electron diffraction pattern contains characteristic Ω phase reflections, but no Ll_2 Al_3Zr reflections.

Figure 5 presents a bright field image and selected area diffraction pattern from the T8 temper of the high Mn Ω phase alloy, S. No. 710822. The bright field image reveals coarse Al-Cu-Mn dispersoids although some of the Al-Cu-Zr cuboids have been observed in other images. As in S. No. 710821, the $\langle 100 \rangle$ electron diffraction pattern from S. No. 710822 contains characteristic Ω phase reflections, but no Ll_2 Al_3Zr reflections.

Tensile and toughness data for the three P/M 2XXX alloys are summarized in Table II and Figs. 6 through 8. The highest tensile yield strength, 79 ksi, was obtained in the high Mn Ω phase alloy, S. No. 710822, although overaging of this alloy was rapid at 350°F. The high Zr 2024 type alloy and the high Zr Ω phase alloy achieved peak tensile yield strengths of 75.9 and 74.5 ksi, respectively.

Representative true stress-true strain curves are presented in Fig. 7 for the peak aged T8 tempers of sheet from the P/M 2XXX alloys, S. Nos. 710820, 710821 and 710822. Included for comparison is the curve for the peak aged T8 temper of sheet from the Ag-bearing I/M 2XXX alloy, S. No. 689248. Although the P/M

alloys achieve higher strengths than the I/M alloys, the stress-strain curves have the same shape.

The best strength/toughness combination was achieved in the high Zr Ω phase alloy, S. No. 710821. Figure 7 shows that a K_{IC} value of 125.5 ksi $\sqrt{\text{in}}$ was achieved at a tensile yield strength of 74.5 ksi. The lowest strength/toughness combination was measured for the high Mn Ω phase alloy, S. No. 710822.

Summary

Unrecrystallized grain structures were present in 0.125" thick sheet produced from the P/M 2XXX alloys. Defects, likely due to prior lot contamination, were present in the three products.

S' precipitates are the dominant strengthening phase in S. No. 710820; Ω phase is the dominant strengthening phase in S. Nos. 710821 and 710822.

At least two types of dispersoids were present in these alloys. The Mn was present in large rod-like or globular particles which probably have a composition close to $\text{Al}_{20}\text{Cu}_2\text{Mn}_3$. The Zr was present in Al-Cu-Zr cuboids which are finer than the $\text{Al}_{20}\text{Cu}_2\text{Mn}_3$ particles but coarser than expected for the coherent L_{12} phase. These particles may have the DO_{23} crystal structure since that structure was detected by Guinier X-ray diffraction.

The highest yield strengths, 79 ksi, were achieved in the high Mn Ω phase alloy. The best strength/toughness combinations were achieved in the high Zr Ω phase alloy.

References

1. D.J. Chellman, "Development of Powder Metallurgy Al Alloys for High Temperature Aircraft Structural Applications - Phase II," NASA Contractor Report 165965, 1982 November.
2. D.J. Chellman, "Development of Powder Metallurgy 2XXX Series Al Alloys for High Temperature Aircraft Structural

- Applications," NASA Contractor Report 172408, 1984 November.
3. D.J. Chellman, "Development of Powder Metallurgy 2XXX Series Al Alloy Plate and Sheet Materials for High Temperature Aircraft Structural Applications," NASA Contractor Report 172521, 1985 April.
 4. D.J. Chellman, T.B. Gurganus and J.A. Walker, "Development and Characterization of Powder Metallurgy (PM) 2XXX Series Al Alloy Products and Metal Matrix Composite (MMC) 2XXX Al/SiC Materials for High Temperature Aircraft Structural Application," NASA Contractor Report 187631, 1992 February.

TABLE I. Relative quantities of phases identified in the T8 tempers of the P/M 2XXX alloys by Guinier X-ray diffraction. All sheet was solution heat-treated, cold water quenched, stretched 8% and aged at 350°F.

S. Number ^a	Alloy Description	Al ₂₀ Cu ₂ Mn ₃	Al ₃ Zr ^c (Tetragonal, DO ₂₃)	Al ₇ Cu ₂ Fe	Al ₁₁ V	θ"	θ'	θ
710820-A8	High Zr 2124-type	medium	small +	small +	v. small	v. small -	small	v. small +
710821-B4	High Zr Omega Phase Alloy	small	small	v. small -	-	v. small	small -	medium ^b
710822-B4	High Mn Omega Phase Alloy	medium +	-	v. small	-	-	v. small -	medium + ^b

- ^a The number following "A" or "B" in the S. Number indicates the number of hours of aging at 350°F.
^b Guinier X-ray diffraction cannot distinguish between θ and Ω phase. Diffuse background at strong θ phase reflections suggest the presence of Ω phase.
^c No L1₂ Al₃Zr detected in any sample.

TABLE II. Results of tensile^a and fracture toughness^b testing of sheet from P/M 2XXX alloys in T8 type tempers. All sheet was solution heat-treated, cold water quenched, stretched 8% and aged at 350°F.

S. Number	Alloy Description	Aging Time, hr	Tensile Yield Strength, ksi	Ultimate Tensile Strength, ksi	% Elongation, 2.0 in. gage	Uniform Elongation	Strain Hardening Exponent	K _c ksi√in.	K _{app} ksi√in.	Validity Status ^c
710820	High Zr 2124-type	2	62.7	71.9	18.5	0.1082	0.086	103.0	67.5	No
		4	67.7	73.2	14.0	0.1003	0.076	94.6	67.1	No
		8	75.9	77.5	8.0	0.0412	0.030	85.0	60.5	No
		16	74.4	76.6	6.0	0.0349 ^d	0.029	74.5	55.7	Yes
710821	High Zr Omega Phase Alloy	1	68.9	76.0	14.0	0.0954	0.081	114.8	75.1	No
		2	70.0	74.2	13.0	0.0865	0.071	121.6	76.6	No
		4	74.5	78.0	10.0	0.0670	0.060	125.5	72.1	No
		8	72.1	75.7	10.5	0.0677	0.061	116.7	81.3	No
710822	High Mn Omega Phase Alloy	1	78.9	83.1	8.0	0.0655 ^e	0.049	54.9	43.2	Yes
		2	76.5	80.6	8.5	0.0648	0.040	51.0	44.2	Yes
		4	74.8	79.6	8.5	0.0615 ^e	0.046	47.0	38.3	Yes
		8	74.9	79.4	7.5	0.0487 ^d	0.038	51.4	40.8	Yes

^a All tensile data are from longitudinal specimens. A single specimen was used to measure tensile yield strength, ultimate tensile strength and % elongation; another specimen was used to measure uniform elongation and strain hardening exponent.

^b All toughness data are from L-T specimens. A single 6.3 in. wide x 20 in. long panel was used to determine K_c and K_{app}.

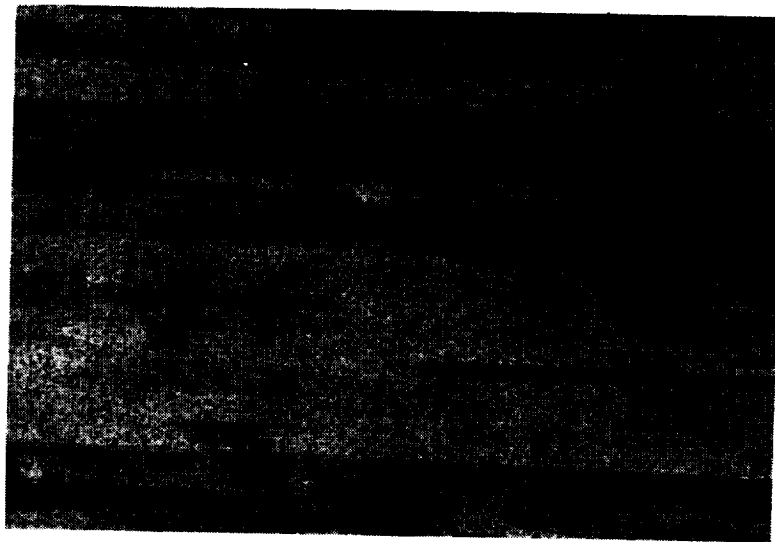
^c Validity Criterion: Is net section stress/tensile yield strength <0.8?

^d Failed outside extensometer gage length.

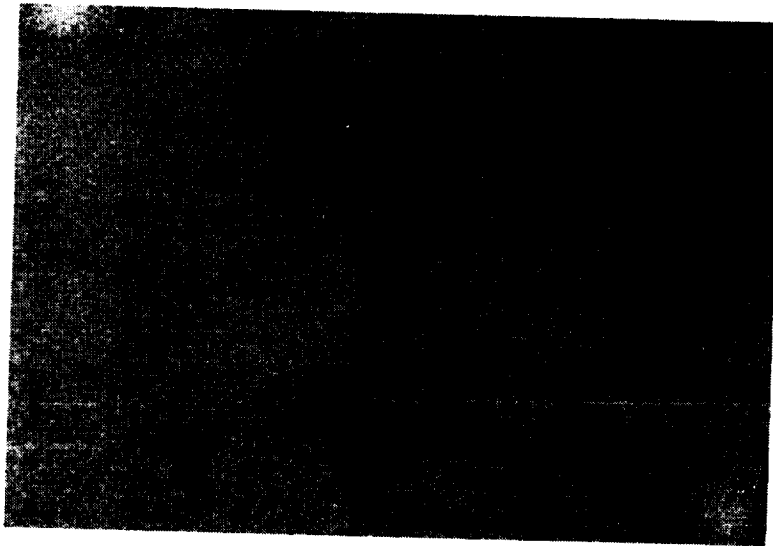
^e Failed at extensometer gage length.



(a)



(b)



(c)

Figure 1 . Optical micrographs of 0.125" thick sheet from the P/M 2XXX alloys in T8 tempers, revealing unrecrystallized grain structures: (a) S. No. 710820-A8, (b) S. No. 710821-B4 and (c) S. No. 710822-A4.

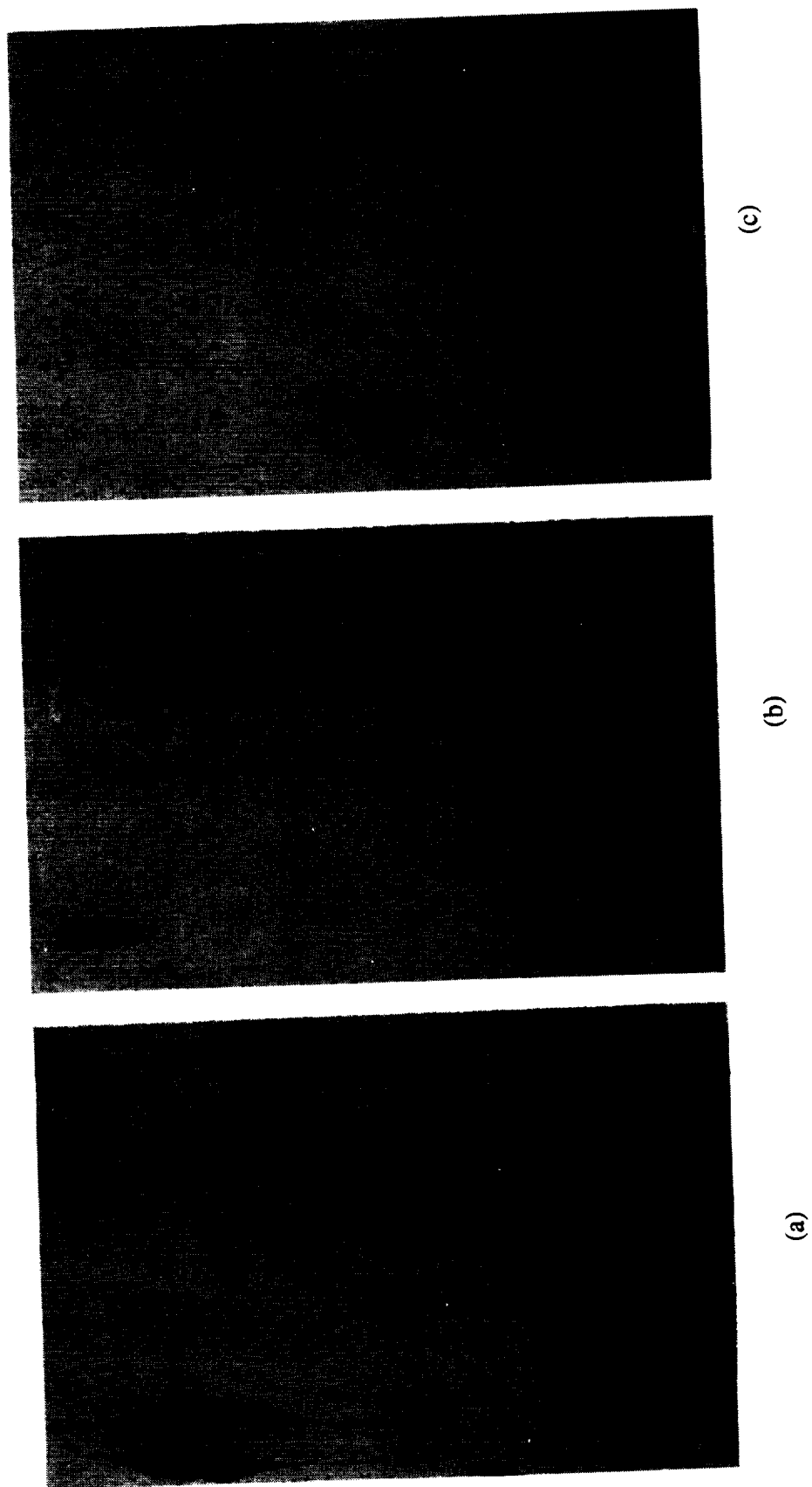


Figure 2. Optical micrographs of 0.125" thick sheet from the P/M 2XXX alloys in T8 tempers, revealing defects comprised of coarse clusters of particles: (a) S. No. 710820-A8, (b) S. No. 710821-B4 and (c) S. No. 710822-A4.

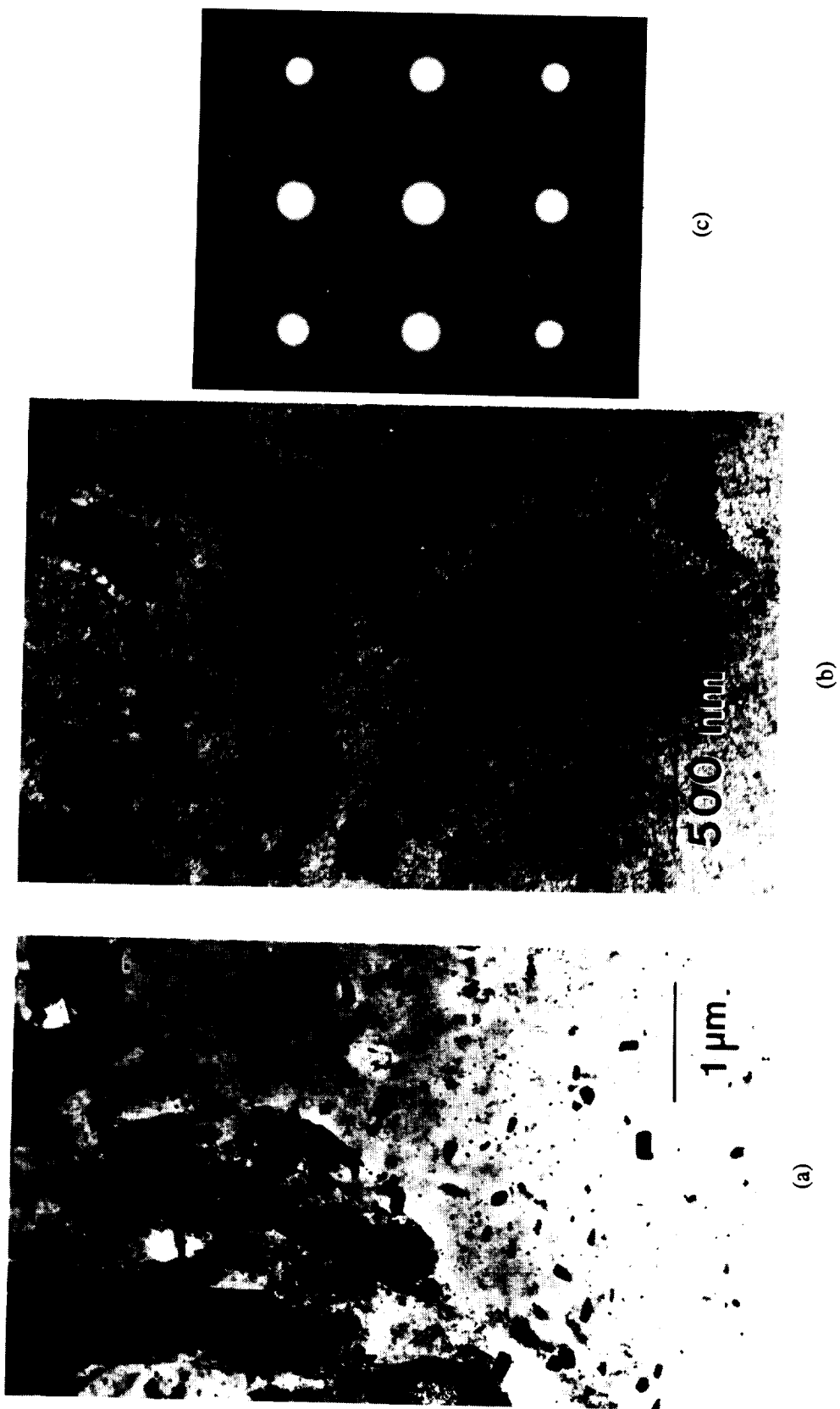


Figure 3. Transmission electron micrograph (a,b) showing dispersoids and selected area electron diffraction pattern, (c) revealing characteristic S' precipitates in S. No. 710820-A8.

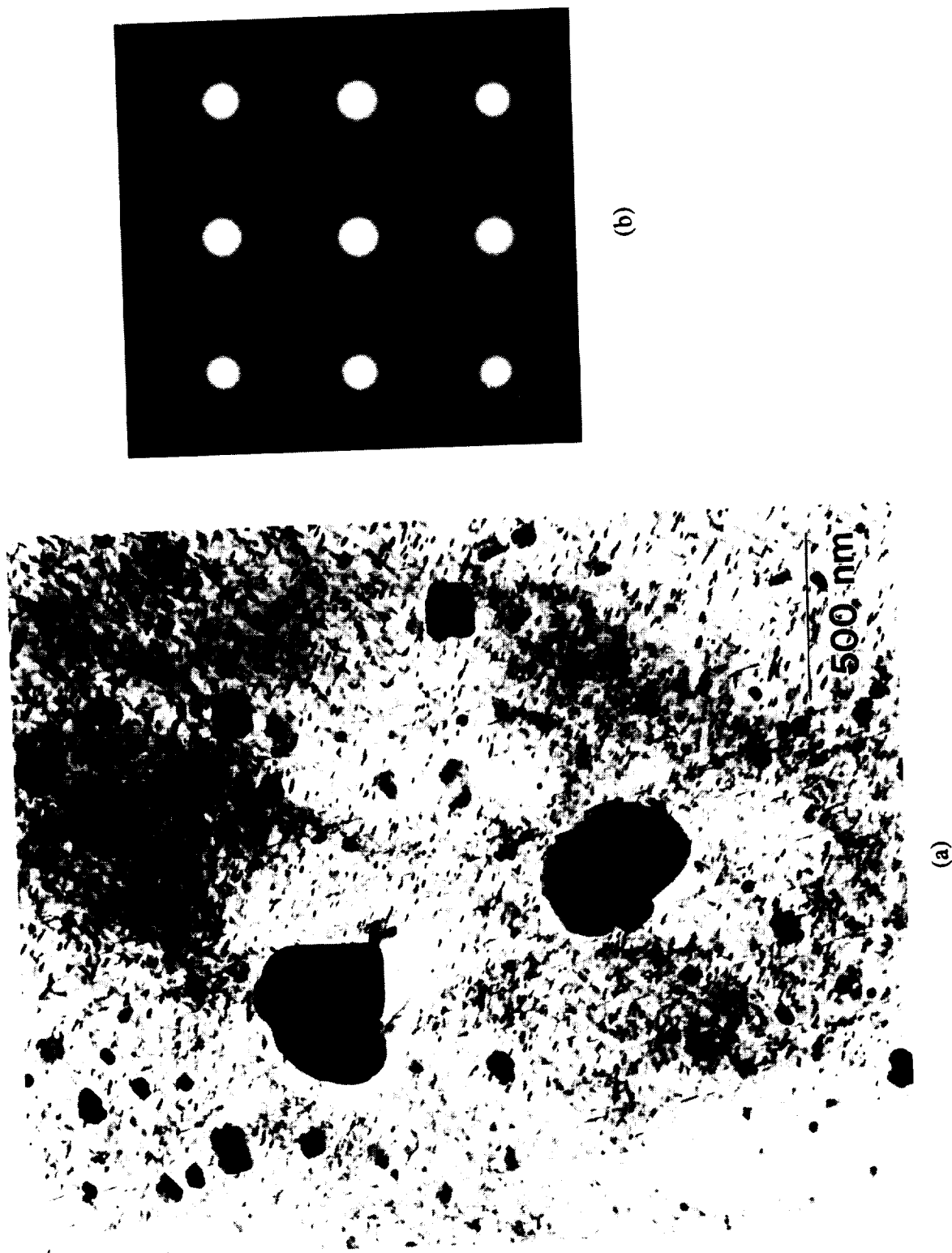
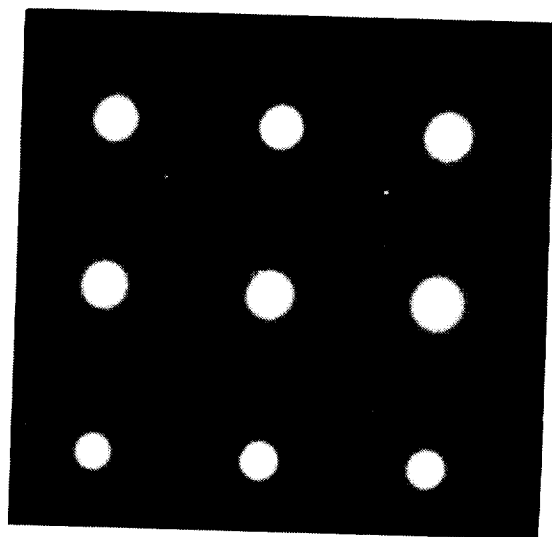
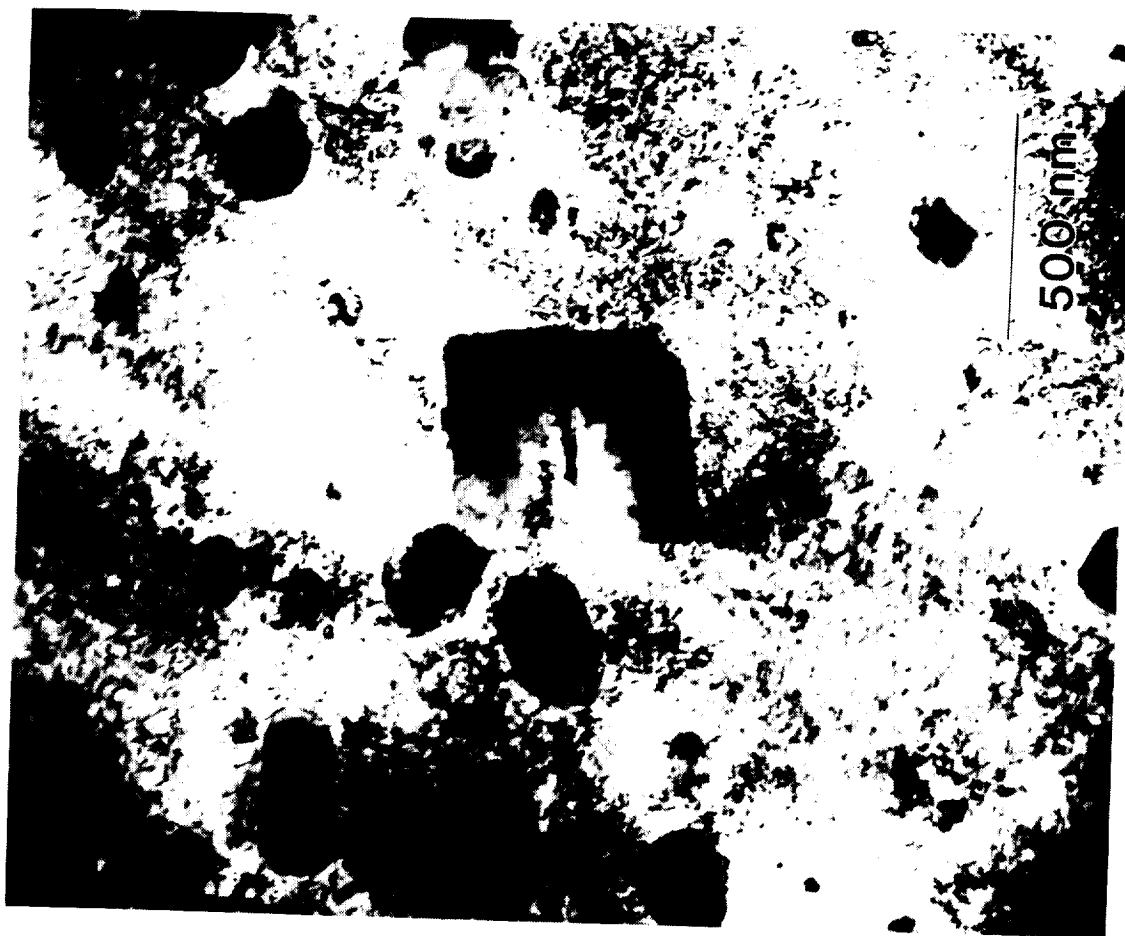


Figure 4. Transmission electron micrograph: (a) showing dispersoids and selected area electron diffraction pattern, (b) revealing characteristic Ω precipitates in S. No. 710821-B4.



(b)

Figure 5. Transmission electron micrograph: (a) showing dispersoids and selected area electron diffraction pattern, (b) revealing characteristic Ω precipitates in the S. No. 710822-A4.

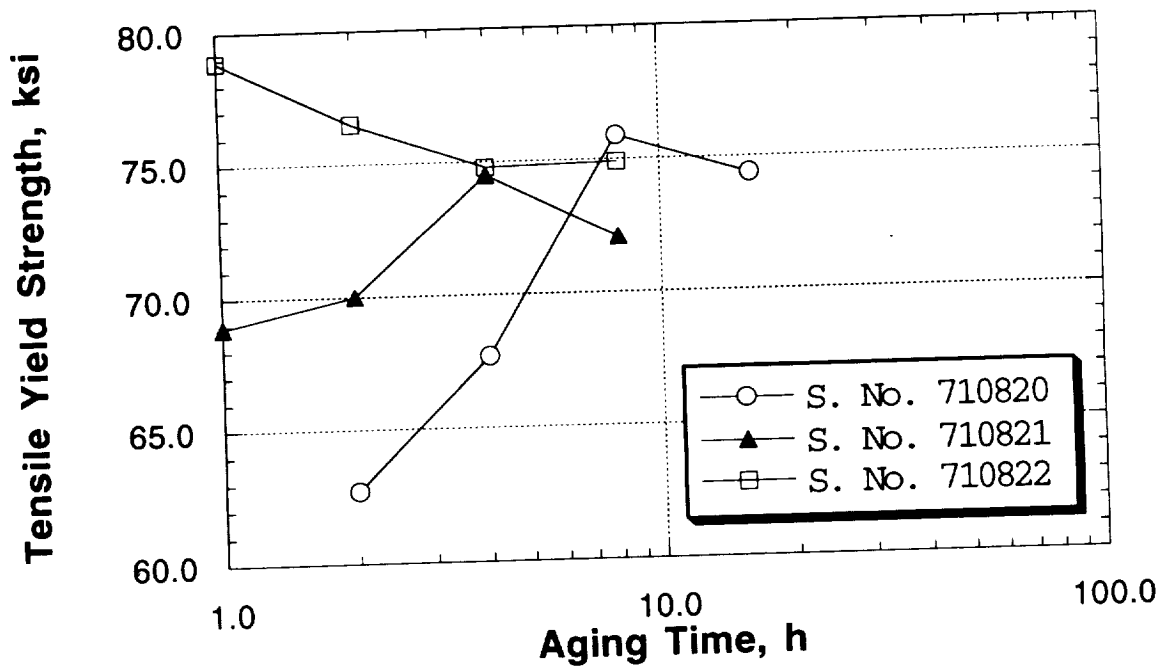


Figure 6. Tensile yield strength as a function of aging time at 350°F for three P/M 2XXX alloys aged to T8-type tempers, e.g., S. No. 710820: high Zr, 2024-type, S. No. 710821: high Zr, Ω phase alloy and S. No. 710822: high Mn, Ω phase alloy.

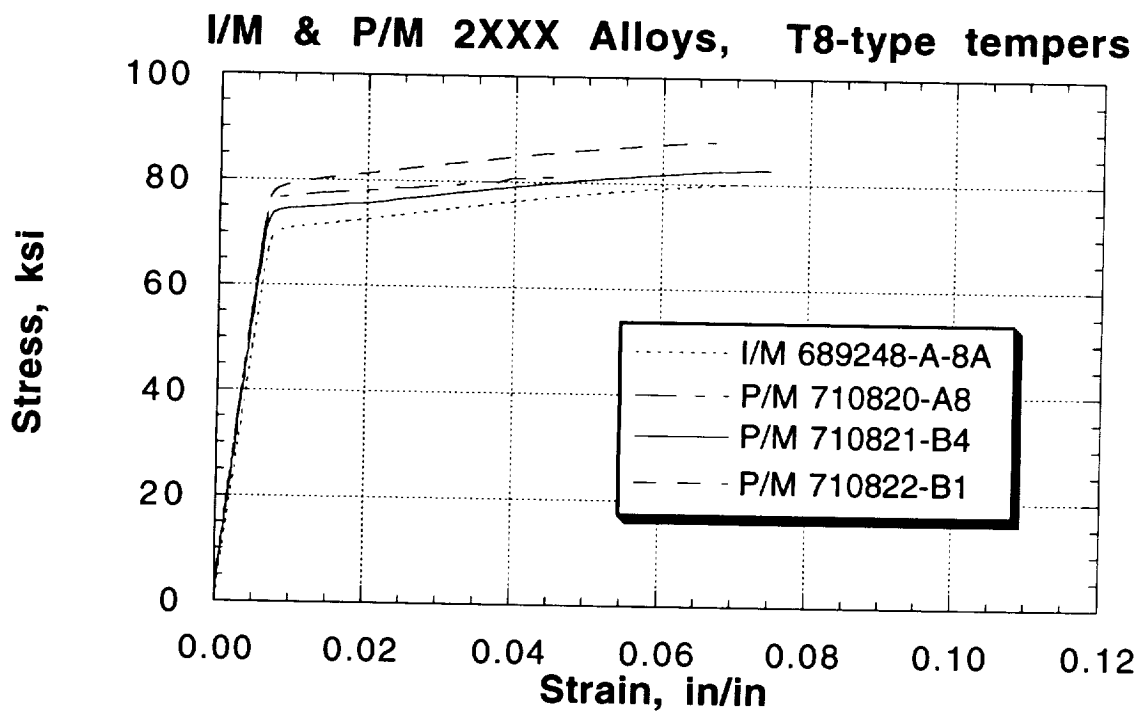


Figure 7. Representative true stress-true strain curves for the peak aged T8 tempers of sheet from the P/M 2XXX alloys, S. Nos. 710820, 710821 and 710822, and the I/M 2XXX alloy, S. No. 689248.

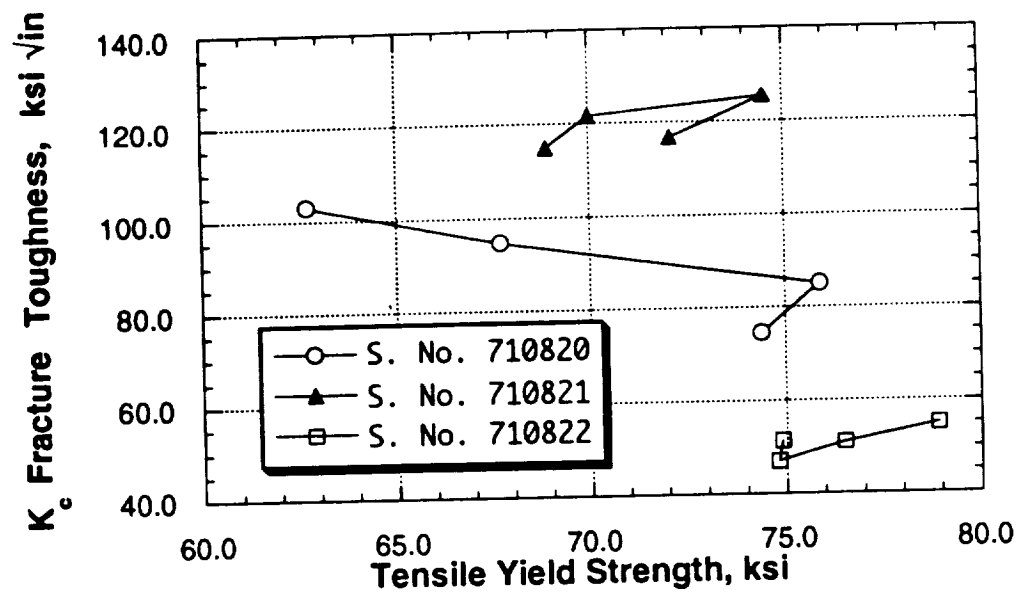


Figure 8. K_c as a function of tensile yield strength for the three P/M 2XXX alloys aged to T8-type tempers, e.g., S. No. 710820: high Zr, 2024-type, S. No. 710821: high Zr, Ω phase alloy and S. No. 710822: high Mn, Ω phase alloy.

TASK 4. Al-Si-Ge ALLOY DEVELOPMENT (UVa)

Principal Investigator: Dr. E.A. Starke, Jr.
Graduate Student: Mr. Holger Koenigsmann
Alcoa Support: Dr. R.W. Hyland

Objective

The objectives of this research are to determine the microstructural evolution and the concomitant property variations in a new class of experimental aluminum-based alloys that contain Si, Ge and Cu as the major alloying elements. The stability of the microstructures at moderate temperatures, and the critical dependence of hardness and strength on alloy composition and types of phases present are being investigated. This program uses theoretical concepts for selecting solute additions for an I/M age hardenable aluminum alloy that may have the strength and thermal stability necessary to meet the requirements for the proposed high speed civil transport (1).

Introduction

The age-hardenable Al-Si-Ge alloy utilizes a fine and uniform distribution of incoherent Si-Ge particles that have a very small critical size for the transition from shearing to looping by dislocations at the yield stress. These features result in a high degree of hardening for a small volume fraction of particles. As compared to other age-hardenable aluminum alloys, the Si-Ge precipitates can be expected to be more thermally stable because of the low solubility of Si and Ge in Al and the incoherent nature of the precipitate interface. However, the strengths of the Al-Si-Ge alloys are not competitive with other age-hardenable aluminum alloys. Work reported in the first semi-annual report (UVa report under Grant No. NAG-1-745, for the period 1/1/92-6/30/92) showed that the addition of Cu has the effect of increasing the number of precursory clusters during quenching which act as nucleation centers for the diamond Si-Ge precipitates

during aging. This increases the hardness level by about 60%. Copper contents equal to or greater than about 2.6 wt.% to the baseline Al-1at.%Si-1at.%Ge alloy result in the nucleation of θ' (Al_2Cu) precipitates in addition to the diamond Si-Ge precipitates. θ' nucleation occurs on matrix dislocations as well as at the (Ge-Si)/ α -Al interfaces. θ' coarsens during aging at 160°C and there is an associated drop in hardness.

The present report presents results obtained during the period 7/1/92-12/31/92. The focus of the research during that period was to characterize the microstructural and hardness evolution of a ternary Al-Si-Ge alloy and a quaternary Al-Si-Ge-Cu alloy at both 120°C and 160°C. The room temperature strength of a high-Cu Al-Si-Ge-Cu alloy was compared to that of 2014 after various aging times at 157°C (315°F). In addition, we examined the effect of additions of Mg and Ag on the hardness evolution of an Al-0.5Si-1.31Ge-3.25Cu alloy (composition in wt.%).

Experimental Procedure

A ternary Al-0.7wt.%Si-2.6wt.%Ge alloy and a quaternary Al-1.1wt.%Si-1.55wt.%Ge-2.7wt.%Cu alloy were cast, homogenized, and solution heat treated for 1 hr. at 487°C (ternary alloy) and 479°C (quaternary alloy). Samples of both alloys were aged at 120°C for up to 800 hrs. and at 160°C for up to 400 hrs. Microhardness values were taken at room temperature using a Kentron Microhardness Tester AK. Samples for transmission electron microscopy were prepared using standard techniques and examined in a Philips EM 400T. The average radii of the diamond precipitates were determined by quantitative stereological methods (2) and corrected for truncation and overlap (3). Foil thicknesses were determined under two-beam conditions from the oscillations in intensity of convergent beam diffraction patterns (CBED) (4).

Peak-aged samples of both alloys were held in oil baths at 200°F (93°C), 250°F (121°C) and 300°F (149°C), and the

microhardness values were determined over a period of 10 days both at room temperature and at the temperature of the corresponding oil bath using a Nikon High-Temperature Microhardness Tester QM. The yield strength of the quaternary alloy was measured as a function of time at 160°C. The yield strength of a higher Cu variant (Al-1.0Si-1.0Ge-4.5Cu) was measured at room temperature after aging for various times at 325°F and compared with 2014 (Al-0.65Si-0.4Fe-4.1Cu-0.79Mn-0.35Mg).

An alloy containing Mg and Ag was prepared to examine the possibility of improving the thermal stability of the Al-Si-Ge-Cu alloy by transforming the θ' phase to the more stable Ω phase (see Task 8 results by Li and Wawner, this report). Aging experiments were conducted at both 120°C and 160°C.

Results and Discussion

Al-Si-Ge and Al-Si-Ge-Cu Alloys:

The hardness curves for the ternary and the quaternary alloys aged at 120°C and 160°C are shown in Figs. 1 and 3, respectively, and the relationship between the cube of the average radii of the Si-Ge diamond precipitates and the aging time at 120°C and 160°C is shown in Figs. 2 and 4, respectively (note that the full time scale is 800 hrs. for 120°C and 400 hrs. for 160°C). The magnitude of the values is in correspondence with the estimated particle size for the transition from shearing to bypassing (1) which is related to the size at which the particles form from a cluster. The relationship between the cube of the average radii and the aging time is in all cases linear within the errors of measurement. This is in agreement with the prediction of the coarsening theory by Lifshitz (5) and Wagner (6). The coarsening rate for both the ternary and the quaternary alloys is significantly higher at 160°C than at 120°C as expected from the exponential temperature dependence of the diffusion coefficient.

The average radii of the diamond precipitates are higher for the quaternary alloy than for the ternary alloy. This can be

explained by the fact that the composition of the quaternary alloy is not optimum for minimizing the strain energy associated with the Si and Ge additions compared with the ternary alloy. This, in turn, results in a higher critical energy for the formation of stable nuclei and therefore in a larger critical size of the nuclei for the quaternary alloy. Unfortunately, the different relation between the Si and Ge contents in both alloys did not allow for the investigation of the influence of Cu on the coarsening behavior independent of other factors.

The coarsening theory by Lifshitz and Wagner predicts that the variation of the mean radius, r , with time, t , is given by:

$$r^3 - r_0^3 = 8\gamma D c_0 V_m^2 (t - t_0) / 9RT \quad [1]$$

where r_0 is the mean particle radius when coarsening commences at the time t_0 , γ is the specific precipitate-matrix interfacial free energy, D and c_0 are the diffusivity and the equilibrium molar concentration at the given temperature, T , respectively, V_m is the molar volume of the precipitate, and R has its usual meaning. From the slope of the graphs in Figs. 2 and 4 the interfacial energy can be estimated using equation [1]. As a first approximation, the diffusion coefficient was taken as an average of the diffusivity of Si in Al and that of Ge in Al using the data from (8). The equilibrium concentration was roughly estimated as 0.2wt.% from (9), and the molar volume was calculated based on the values given in (1) for the diamond cubic structures of Si and Ge. As a first approximation, the calculated average value for the specific precipitate-matrix interfacial energy is 121 mJm^{-2} which seems to be of the right order of magnitude.

Figures 5 and 6 show the results of the microhardness measurements carried out at room temperature and at the temperature of the corresponding oil bath, respectively. As expected, the hardness measurements carried out at elevated

temperatures yield significantly lower values than those carried out at room temperature. The slope of the curves for the quaternary alloy is significantly higher than that for the ternary alloy at the same temperature. In all cases, the slope decreases with increasing time. These results correspond qualitatively to the observed coarsening behavior and also to the decrease in solute content with increasing temperature. However, in order to investigate the influence of Cu independently of other factors, samples of identical composition except for Cu have to be used.

Figure 7 shows the yield strength of the Al-1.1wt.%Si-1.55wt.%Ge-2.7wt.%Cu alloy as a function of aging time at 160°C. The maximum strength obtained was 45 ksi which is considerably below the 70-80 ksi requirement proposed by Boeing. Consequently, an alloy with a higher copper content (Al-1.0wt.%Si-1.0wt.%Ge-4.5wt.%Cu) was examined. Figure 8 compares the yield strength of this alloy with that of 2014 as a function of aging time at 315°F. Although the Ge content is less than optimum, the strength-aging curve does not appear to be any better than 2014. Other studies at Alcoa seem to indicate that we can not expect significant improvement with minor changes in Ge, Si, and Cu content. One should note, however, that the alloys studied thus far have not contained grain refining additions, nor have they been processed for optimum grain structure control.

Al-Si-Ge-Cu-Mg-Ag Alloy.

An Al-0.51wt.%Si-1.31wt.%Ge-3.25wt.%Cu-0.44wt.%Mg-0.37wt.%Ag was prepared in an attempt to replace the θ' , which coarsens fairly rapidly at 160°C, with Ω , which has been shown to have superior thermal stability when aged at that temperature. Figure 9 shows the age-hardening curves of the alloy at 160°C and 120°C. The highest peak hardness was obtained at the higher temperature; however, peak hardness was not obtained until after 800 hrs. aging at 120°C. Since that was the limit of our aging experiment, it is unclear whether or not the alloy would overage at 120°C. Limited

TEM examinations showed that θ' and S precipitates were present at all aging temperatures and times. No Si-Ge clusters or Ω precipitates were observed.

Summary

- Copper additions have a significant effect on the hardness and strength of Al-Si-Ge alloys. For alloys containing less than 2.7wt.% Cu the major affect is to aid the nucleation of the Si-Ge clusters. For alloys containing more than 2.7wt.% Cu, θ' precipitates in addition to the Si-Ge clusters.
- Neither the ternary Al-Si-Ge nor the quaternary Al-Si-Ge-Cu alloys show a decrease in hardness with aging up to 800 hours at 120°C; however, both overage at 160°C after approximately 50 hours.
- Although coarsening occurs during aging at 120°C, the changes are relatively small, at least up to 800 hours, and it does not appear to have a significant effect on the hardness of the alloy. The more rapid coarsening that occurs at 160°C does affect the hardness.
- In the alloys studied, copper appears to accelerate the coarsening of the Si-Ge precipitates. However, the Si and Ge contents of the two alloys were different and the absolute affect of Cu could not be determined in this study.
- The tensile properties of the Al-1.0Si-1.0Ge-4.5Cu after aging for various times at 315°F appear to be very similar to those of 2014.
- The results to date on the Al-Si-Ge-Cu-Mg-Ag were unsuccessful in replacing θ' with Ω . However, the hardness results at 120°C suggest that further investigation of this class of alloy is warranted.

References

1. E. Hornbogen, A.K. Mukhopadhyay, and E.A. Starke, Jr., "An Exploratory Study of Hardening in Al-(Si,Ge) Alloys," Z. Metallkd. **83**, 577-584 (1992).
2. E.E. Underwood and E.A. Starke, Jr., "Quantitative Stereological Methods for Analyzing Important Microstructural Features in Fatigue of Metals and Alloys," Fatigue Mechanisms, ASTM-STP 675, Philadelphia, PA, 633-682 (1979).
3. E.E. Underwood, "Quantitative Stereology," Addison-Wesley, 187-188 (1970).
4. W.A. Cassada III, M.S. Thesis, University of Virginia, 72-75 (1985).
5. I.M. Lifshitz and V.V. Slyozov, J. Phys. Chem. Solids **19**, 35-80 (1961).
6. C. Wagner, Z. Elektrochemie **65**, 581-591 (1961).
7. J.D. Boyd and R.B. Nicholson, Acta Met. **19**, 1379-1391 (1971).
8. M. Bishop and K.E. Fletcher, Int. Met. Rev. **17**, 203-225 (1972).
9. I.J. Polmear, "Light Alloys," Hodder & Stoughton, 18 (1989).

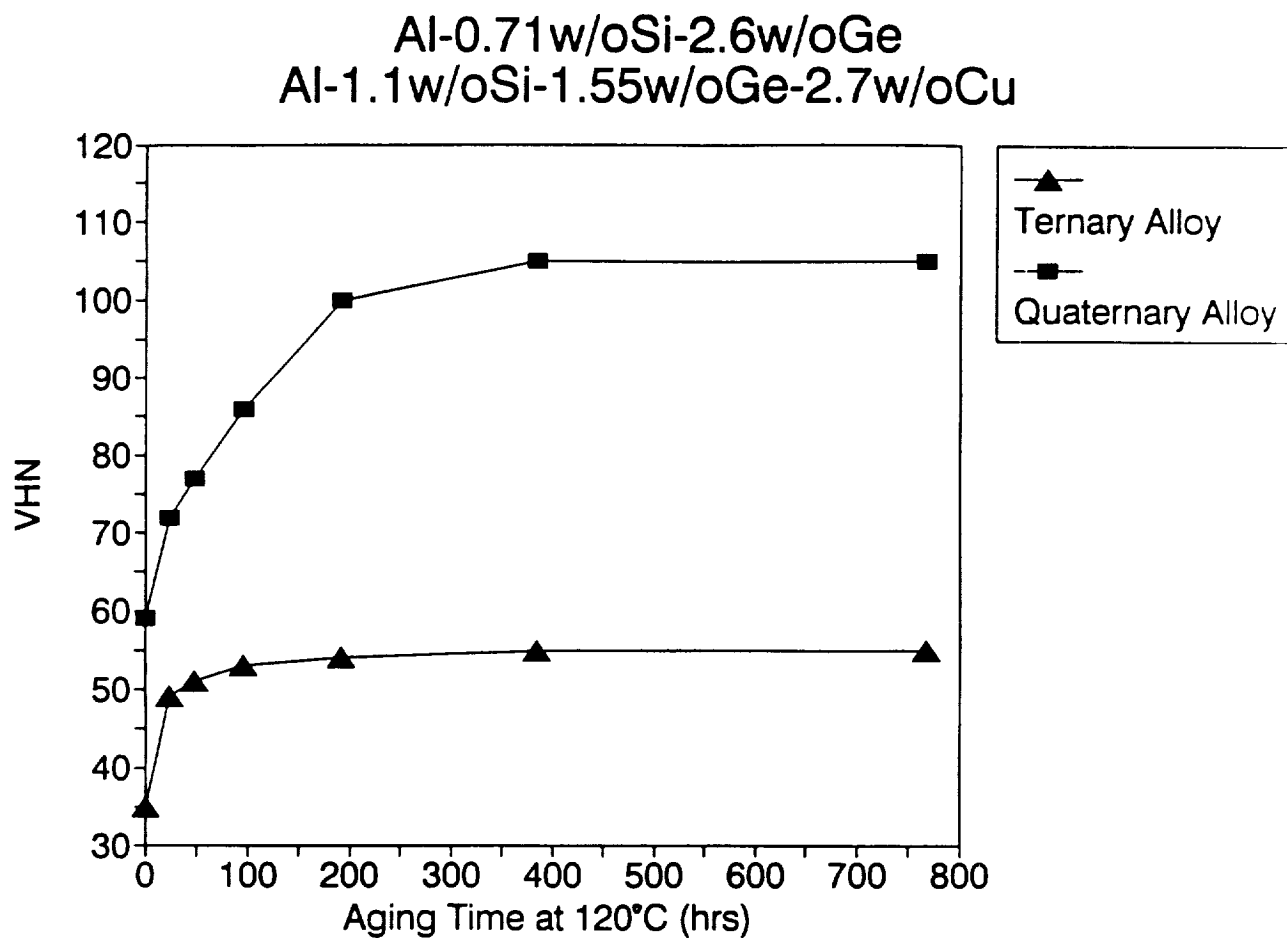


Figure 1. Hardness-time curves at 120°C for an Al-0.71wt.%Si-2.6wt.%Ge and an Al-1.1wt.%Si-1.55wt.%Ge-2.7wt.%Cu alloy.

Coarsening of Diamond Precipitates in Al-Si-Ge/Al-Si-Ge-Cu at 120°C

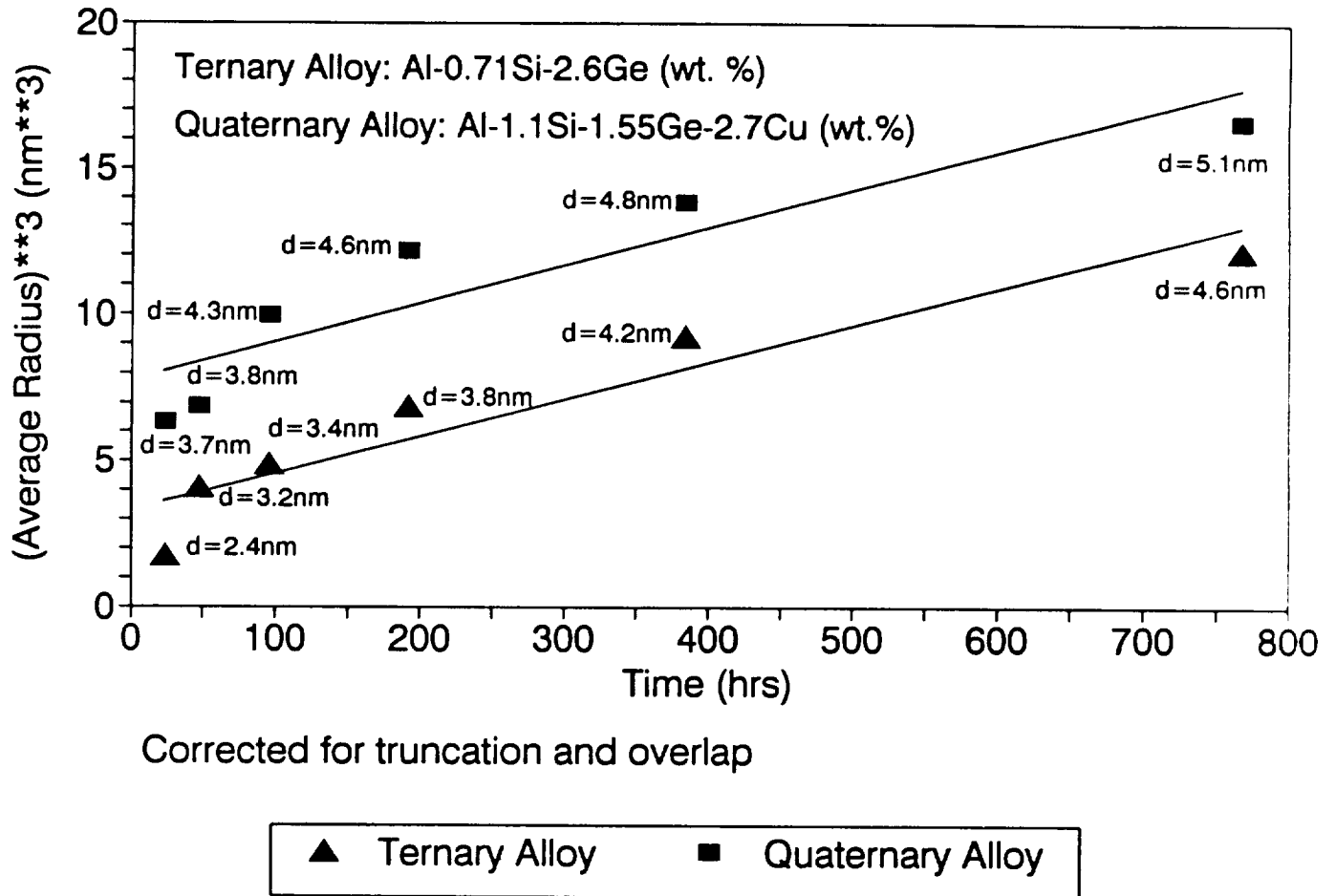


Figure 2. Coarsening behavior at 120°C of the diamond precipitates in an Al-Si-Ge and an Al-Si-Ge-Cu alloy.

Al-0.71w/oSi-2.6w/oGe
Al-1.1w/oSi-1.55w/oGe-2.7w/oCu

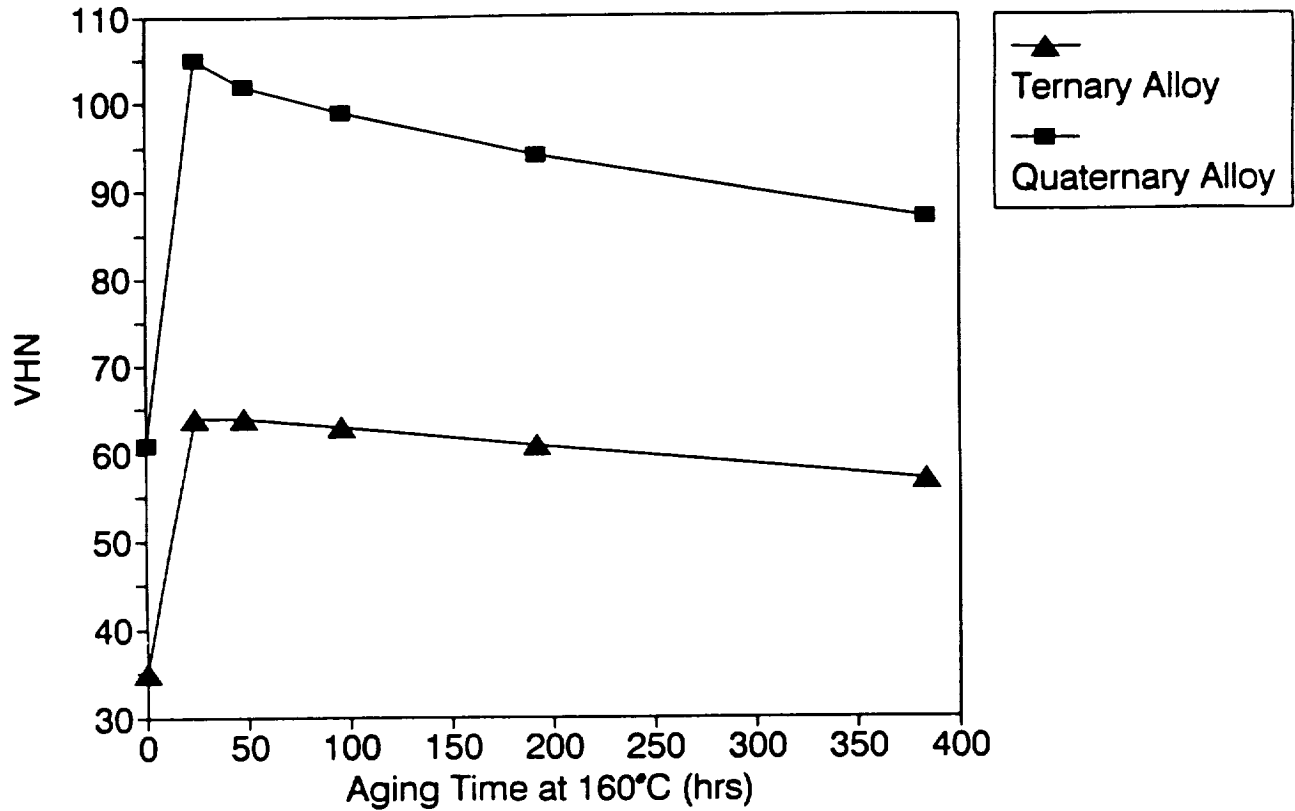


Figure 3. Hardness-time curves at 160°C for an Al-0.71wt.%Si-2.6wt.%Ge and an Al-1.1wt.%Si-1.55wt.%Ge-2.7wt.%Cu alloy.

Coarsening of Diamond Precipitates in Al-Si-Ge/Al-Si-Ge-Cu at 160°C

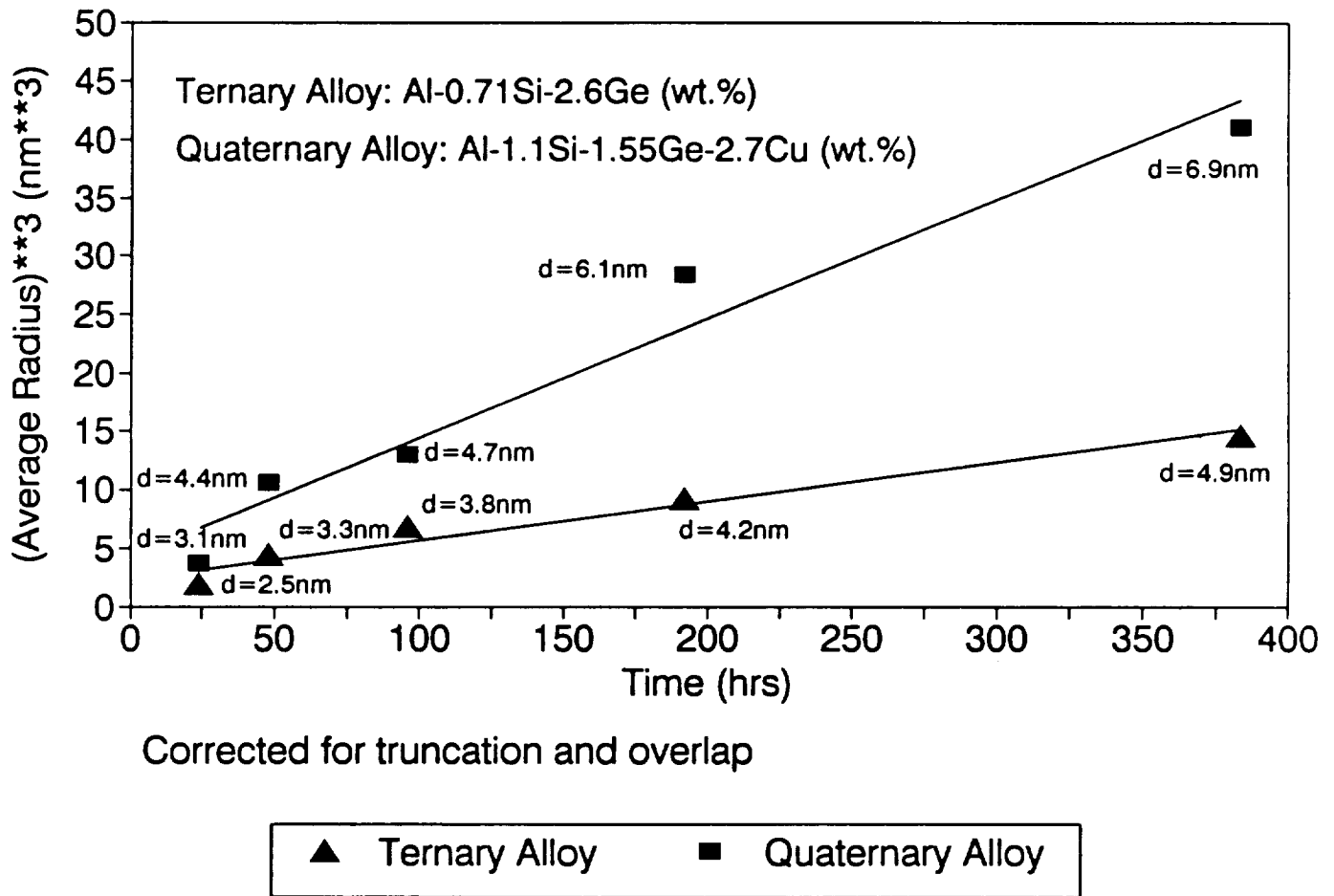


Figure 4. Coarsening behavior at 160°C of the diamond precipitates in an Al-Si-Ge and an Al-Si-Ge-Cu alloy.

RT Hardness Measurements Al-0.71Si-2.6Ge & Al-1.1Si-1.55Ge-2.7Cu

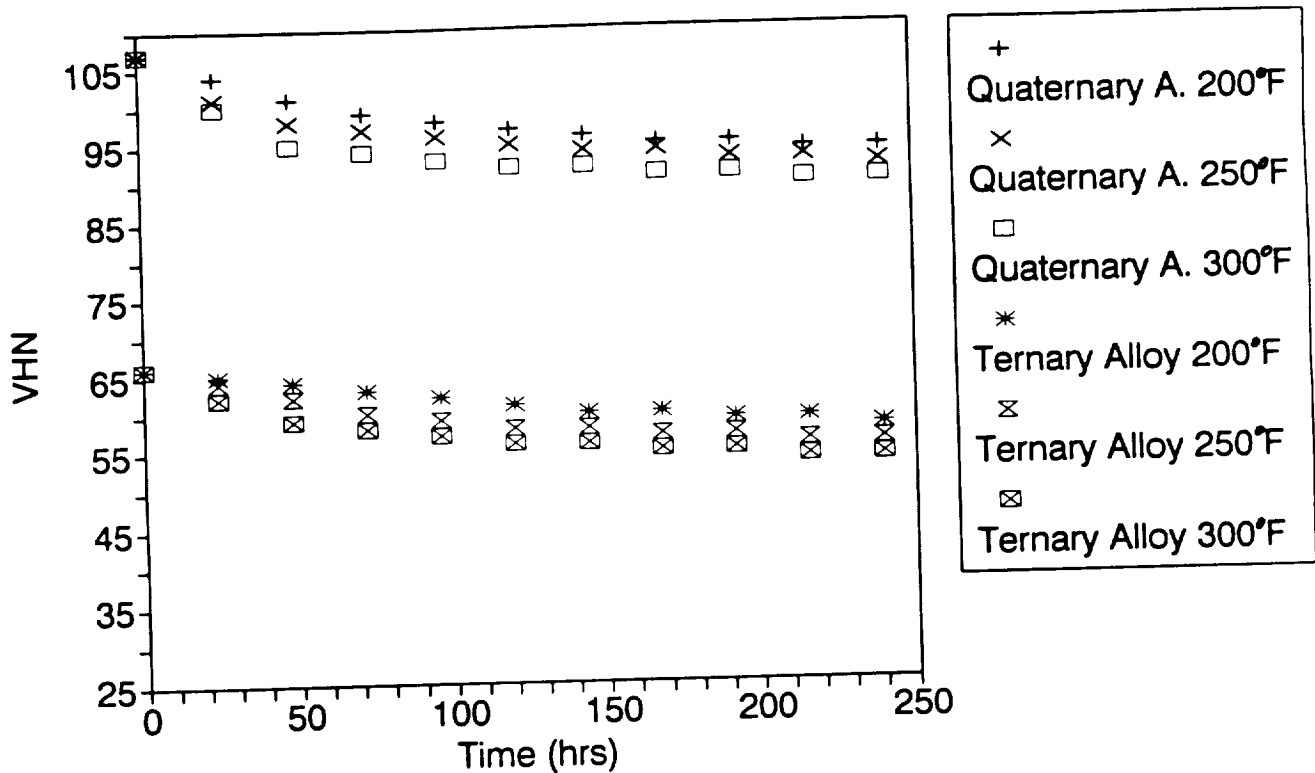


Figure 5. Room temperature hardness measurements of an Al-0.71wt.%Si-2.6wt.%Ge and an Al-1.1wt.%Si-1.55wt.%Ge-2.7wt.%Cu alloy after exposure for various times at various temperatures.

Hot Hardness Measurements Al-0.71Si-2.6Ge & Al-1.1Si-1.55Ge-2.7Cu

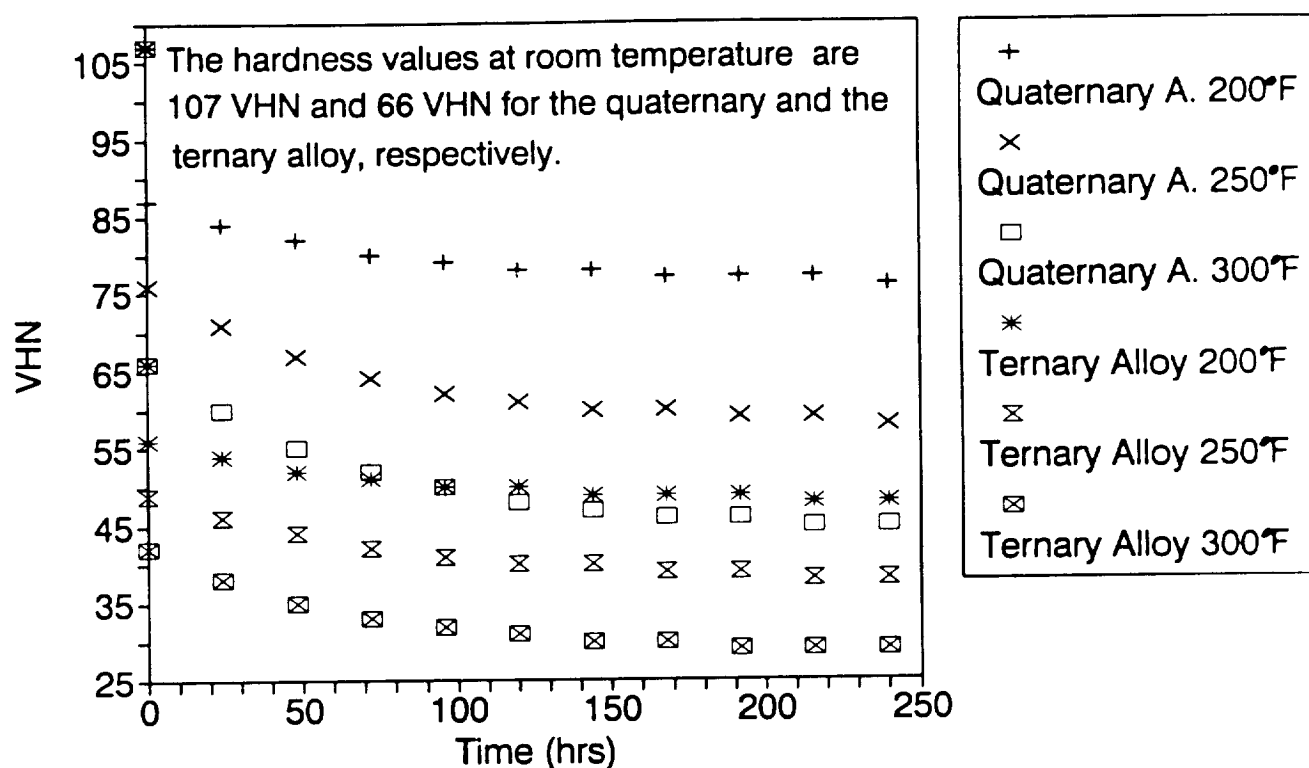


Figure 6. Hot hardness measurements as a function of time at various temperatures for an Al-0.71wt.%Si-2.6wt.%Ge and an Al-1.1wt.%Si-1.5wt.%Ge-2.7wt.%Cu alloy.

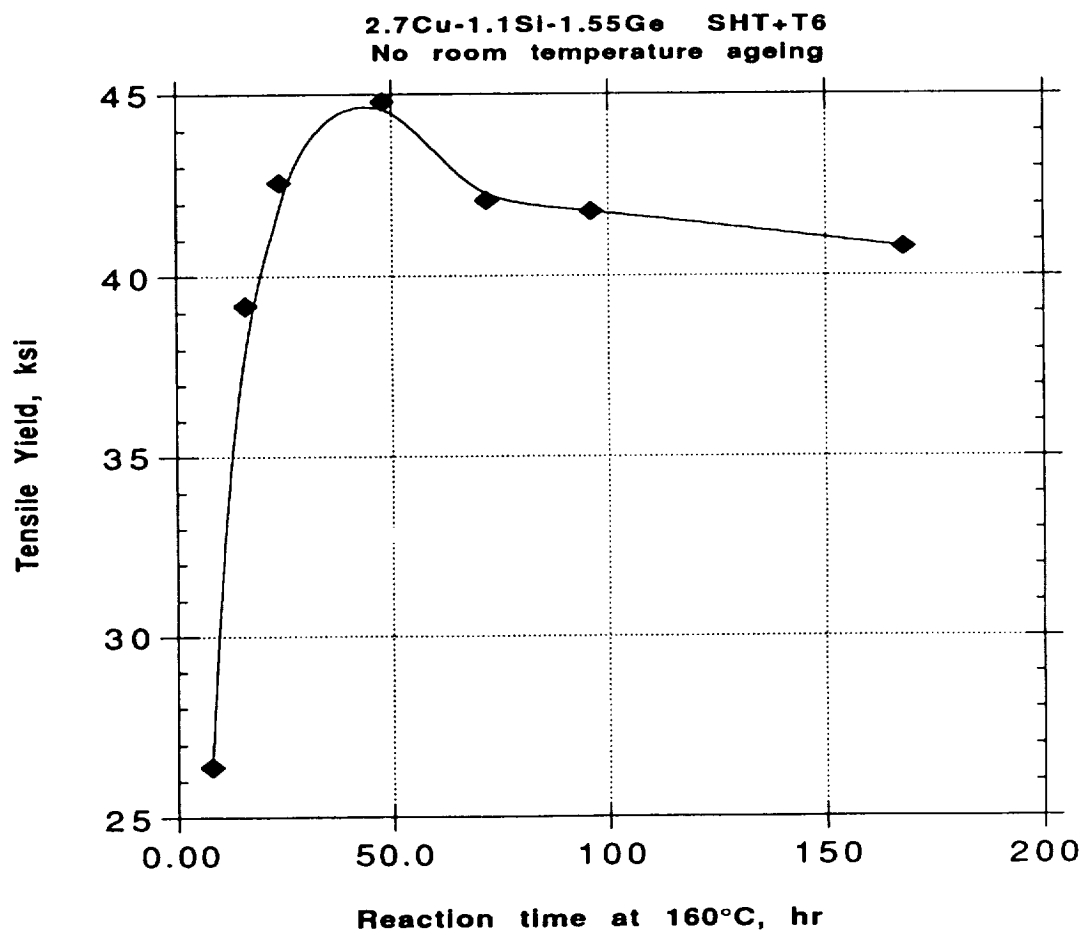


Figure 7. Tensile yield strength versus aging time at 160°C for an Al-1.1wt.%Si-1.55wt.%Ge-2.7wt.%Cu alloy.

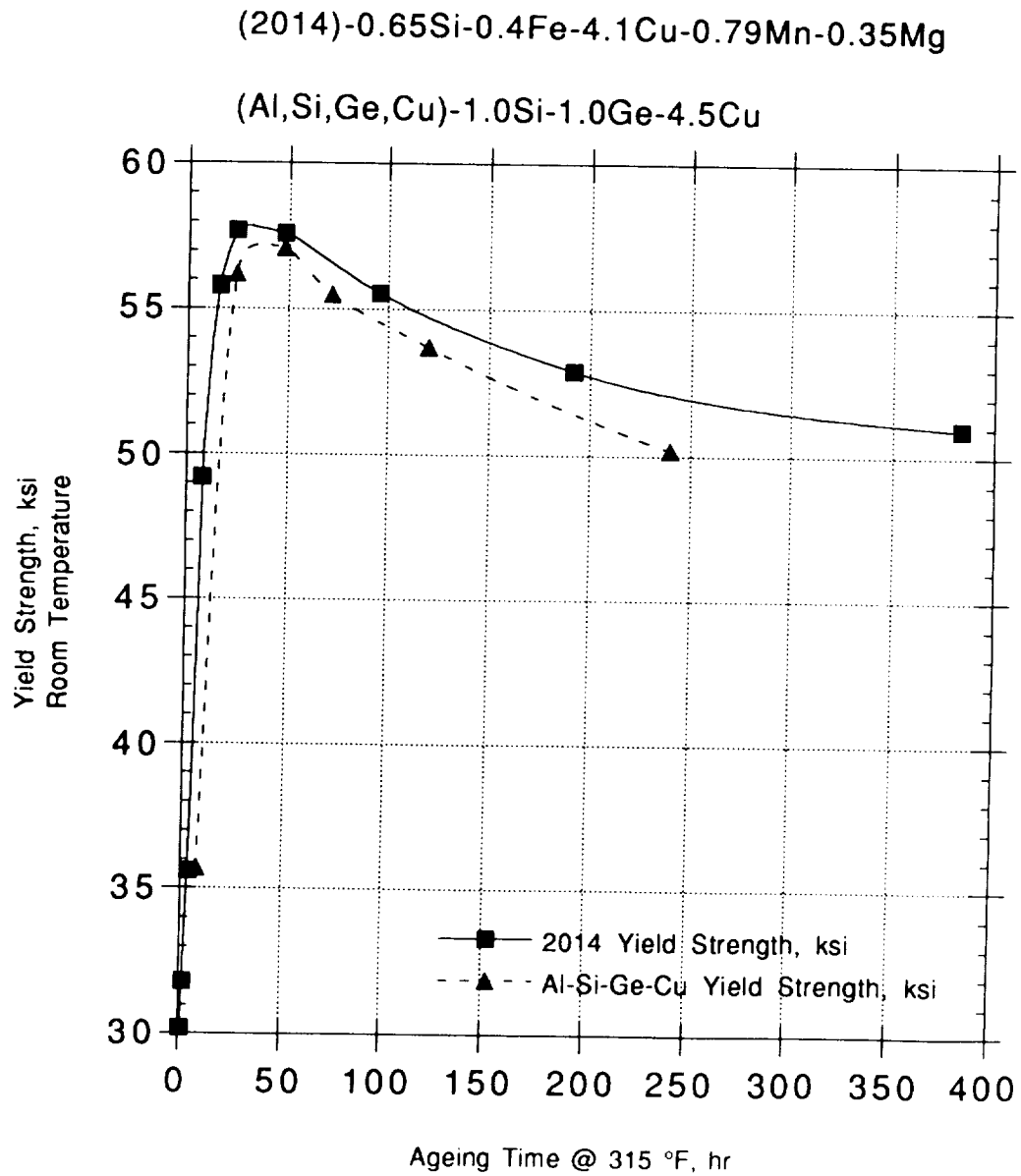
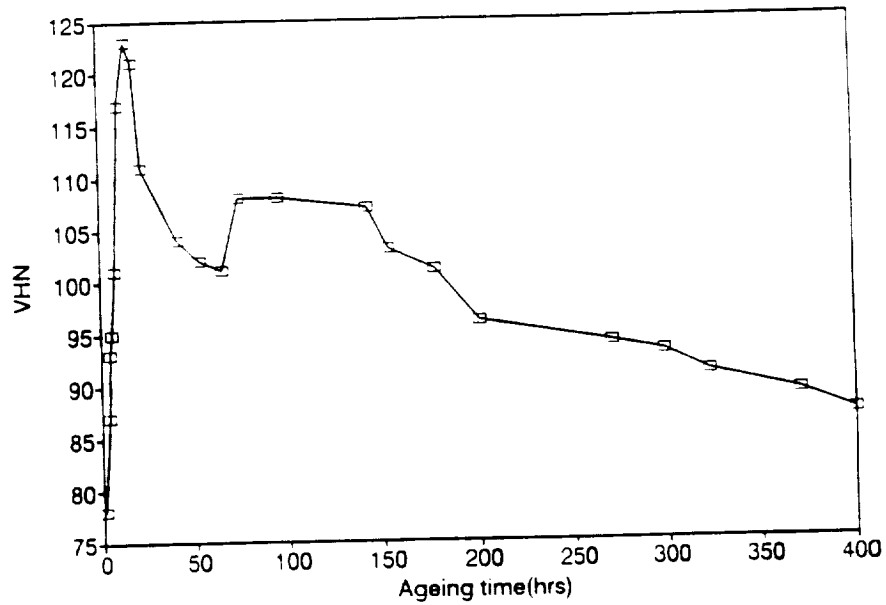
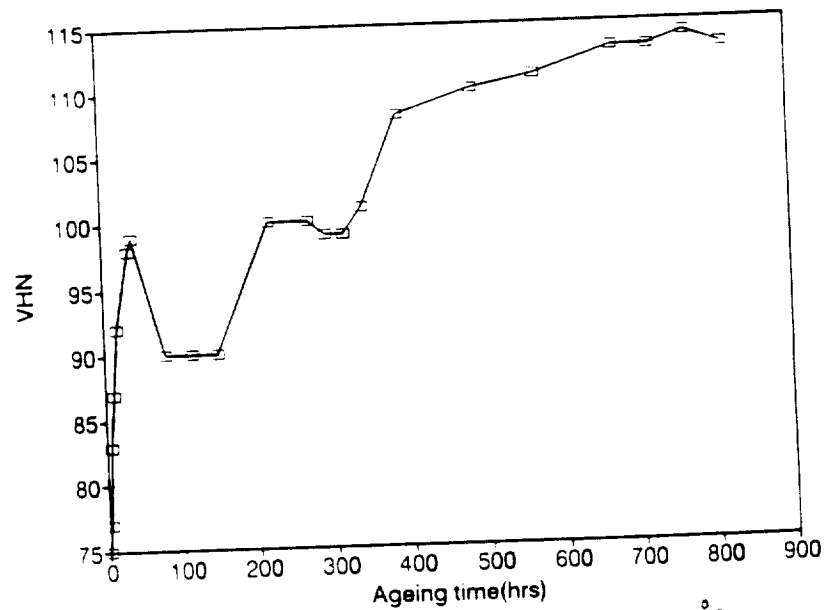


Figure 8. Tensile yield strength versus aging time at 315°F (157°C) for an Al-1.0wt.%Si-1.0wt.%Ge-4.5wt.%Cu alloy compared to 2014 (Al-0.65wt.%Si-0.4wt.%Fe-4.1wt.%Cu-0.79wt.%Mn-0.25wt.%Mg).



Al-0.5Si-1.3Ge-3.2Cu-0.45Mg-0.4Ag aged at 160°C

Fig. 1a



Al-0.5Si-1.3Ge-3.2Cu-0.5Mg-0.4Ag aged at 120°C

Fig. 1b

Figure 9. Hardness versus aging time at 160°C (a) and 120°C (b) for an Al-0.5wt.%Si-1.3wt.%Ge-3.2wt.%Cu-0.45wt.%Mg-0.4wt.%Ag.

TASK 5. TOUGHNESS STUDY OF P/M Al-Fe-X SYSTEM

Principal Investigator: Dr. L.M. Angers
Boeing Contact: Mr. P.G. Rimbo
Douglas Contact: Mr. R. Kahandal

Toughness & Ductility Minima in Al-Fe-Ce.

Objective

The objective of this task is to gain a greater understanding of the ductility and fracture toughness reductions that occur in the dispersion strengthened alloys as temperature is increased into the range of interest for HSCT. If the phenomena are understood, it may be possible to propose methods for reducing or eliminating the effect.

Background

Rapidly solidified Al-Fe-X alloys and mechanically alloyed materials exhibit a "ductility minima" at intermediate temperatures which have been attributed to dynamic strain aging by some researchers (1-3). Dynamic strain aging models assume that solute diffuses to tangles of immobile dislocations. When mobile dislocations encounter these obstacles, they are impeded to a greater extent than if the solute had not been there. The effect only occurs during deformation at intermediate temperatures. At lower temperatures, solute diffusion rates are too low to allow solute to diffuse to the tangles. At the higher temperatures, diffusion rates are high enough that the mobile dislocations can carry the solute along with them, i.e., the immobile dislocation tangles are no greater obstacles to mobile dislocations when solute atmospheres are present than when they are not. At these intermediate temperatures, the flow stress does not decrease as rapidly as expected and the strain rate sensitivity is decreased.

Not all researchers agree that the ductility minima are due to dynamic strain aging. Even though strain rate change tests performed on Al-Cr-Zr and Al-Fe-V-Si support the occurrence of

dynamic strain aging, i.e., combinations of strain rate and temperature which produce low ductilities are consistent with diffusion rates for the alloying additions, other experimental observations do not support it. No evidence of serrated yielding, which is generally accepted as a characteristic of dynamic strain aging, has been observed in stress strain curves for these materials. Furthermore, products of mechanically alloyed aluminum alloys, which should not contain excess solute, exhibit ductility minima.

W.C. Porr, Jr. (3) has done work on 8009 and proposed a model that does not involve dynamic strain aging. He suggests that dislocations climb around dispersoids during intermediate temperature deformation. When dislocations climb to avoid particle looping the result is intensified dislocation flow, plastic damage accumulation and void nucleation at oxides and dispersoid clusters. According to his model, reducing the amount of oxide in 8009 and/or improving the distributions of silicide dispersoids would eliminate void nucleation sites.

Much attention has been paid to the minima that occurs at elevated temperatures; however, very little work has been done to explore what effect the elevated temperature exposures have on microstructures and room temperature properties. There are some indications that there may also be a reduction in room temperature ductility (and possibly fracture toughness) after exposures of these materials to intermediate temperatures (4). Furthermore, there have been many questions raised about toughness data that are available. Alcoa data on F-temper material shows that the plane stress toughness of the Al-Fe-Ce alloy X8019 is excellent when compared to ingot metallurgy alloys although plane strain fracture toughness data show X8019 to be inferior. Unfortunately, little plane stress or plane strain toughness data are available for material exposed to elevated temperatures. Furthermore, any available plane stress toughness data are from Kahn tear tests, and, therefore, are not considered to be as reliable as wide panel

data.

Therefore, the primary goal of this portion of the investigation was to generate ductility and toughness data at room temperature before and after elevated temperature exposures and determine possible mechanisms for the observed behavior.

An experimental test plan was developed. Three different microstructures were to be produced in products using varying amounts of thermomechanical processing. Room temperature tensile and fracture toughness testing was to be conducted on all three products using the same sample geometries. In this way, the true effects of different amounts of thermomechanical processing could be studied and some of the questions regarding plane stress and plane strain behavior could be answered. One of the thicker product forms would also be tested using additional tensile and toughness sample geometries. Also, the effects of elevated temperature exposure would also be examined in one of the product forms.

All tensile and fracture toughness tests were to be performed at different strain rates. Since all tests would be carried out at room temperature, the effect of strain rate can be studied without the additional variable of solute diffusion being introduced, as is done when test temperatures are elevated.

A P/M Al-Fe-Ce alloy with Mg additions was selected for this task. The Mg-bearing alloys were selected for two reasons. Since Mg in solid solution affects dislocation/particle interactions and increases the work hardening behavior of aluminum, Al-Fe-Ce-Mg was considered a good system to examine the tensile and toughness behavior. Furthermore, Al-Fe-Ce powder with Mg additions was already available for use by the program. This allowed the timetable established for the program to be followed.

Al-8Fe-4Ce-0.4Mg (X8019) powders were cold isostatically pressed, hot pressed, and extruded to 2" x 4" bars. Some of the extruded material was rolled to 1" plate (8" wide) and some was rolled to 0.125" sheet (8" wide).

Procedure

The experimental details are summarized below: Three microstructures were produced: 2" extrusion, 1" plate, and 0.125" sheet. From each microstructure 0.125" thick compact tension fracture toughness samples (3.125" in width and 3" in height) were evaluated as well as sheet tensile samples. From the 1" plate, 0.6" compact tension fracture toughness samples (1.25" in width and 1.2" in height) and 1/4" round tensile samples were also taken. Tension tests and toughness tests were run at different crosshead speeds as indicated.

<u>Microstructures</u>	<u>Sample Geometry</u>	
	<u>Tensile</u>	<u>Toughness</u>
Extrusion, 2" thick	flat, 0.125" thick	0.125" thick compact tension
Plate, 1" thick	flat, 0.125" thick	0.125" thick compact tension
	round, 0.250" diameter	0.60" thick compact tension
Sheet, 0.125" thick	flat, 0.125" thick	0.125" thick compact tension

Cross Head Speeds (in./min)

<u>Tension</u>	<u>Toughness</u>
0.375	0.59
0.0375	0.059
0.00375	0.0059

Room temperature tensile and fracture toughness tests were performed on the three product forms in the as-fabricated conditions. In addition, the extrusion was exposed for 1000 hr at 300°F and tested at room temperature.

Results and Discussion

The results of tensile and fracture toughness testing are summarized in Table I. Tensile data include tensile yield

strength, tensile ultimate strength, and % elongation. Toughness data include K_{R25} values and/or K at maximum load. K_{R25} is a value for K on the R-curve based upon the 25% secant intercept of the load-displacement test record and the effective crack length at that point. K_{R25} is determined in general compliance with ASTM method E561 using a compact specimen. K_{R25} indicates a true property of the material.

The effects of thermomechanical processing, crosshead speed, specimen orientation, specimen geometry and location within the thickness have been examined.

For a given crosshead speed, the tensile yield strength of the P/M Al-Fe-Ce-Mg alloy increases as the amount of thermomechanical processing increases. As a result, sheet has the highest yield strength, followed by plate and extrusion. This is not unexpected since the same behavior has been observed in the P/M Al-Fe-Ce alloy with no Mg.

Mg increases the work hardening of the Al-Fe-Ce alloy. Tensile yield strength is plotted as a function of product thickness in Fig. 1 for the alloy of the present investigation and for the X8109 alloy, e.g., Al-8 Fe-4 Ce. The data for X8019 were collected on samples with similar thermal processing history (5). Note that the tensile yield strengths of both alloys were similar for all product forms; however, the ultimate tensile strengths of the alloys with Mg were much higher than those of the alloy having no Mg.

For all product forms and conditions, ultimate tensile strengths increased as crosshead speed increased. In general, no significant changes in elongation were noted as a function of crosshead speed for the different product forms, with one exception. In the case of the 1/8" sheet samples taken from 1" plate (t/4 plane), elongation increased as crosshead speed decreased.

For most of the conditions examined, tensile yield strength was relatively insensitive to crosshead speed. Here, the

exception was the 0.125" thick sheet, where the longitudinal tensile yield strength increased with decreasing strain rate and the transverse tensile yield strength was constant for fast and intermediate crosshead speeds but decreased at the slowest speed.

The effects of specimen location within the thickness and specimen geometry were examined in the 0.6" thick plate. For any given crosshead speed, tensile yield strength values were 1 to 2 ksi higher at $t/2$ than at $t/4$. The effects of specimen geometry are illustrated by comparing the data from 0.250" round specimens to data from 0.125" thick sheet specimens from the $t/2$ location. Differences in tensile yield and ultimate tensile strengths were insignificant at the slow and intermediate crosshead speeds. The difference in tensile yield strength of nearly 2 ksi which was observed between the two specimens tested at the fastest crosshead speed may be significant.

The effects of elevated temperature exposure, e.g., 1000 hr at 300°F, were studied in the 2" thick extrusion. While the tensile properties of the as-fabricated material were insensitive to crosshead speed, the tensile yield strengths of the exposed material exhibited a minima at the intermediate crosshead speed. For the high and low crosshead speeds, the tensile yield strengths of the exposed material were about 2 ksi higher than the tensile yield strengths of the as-fabricated material. Elongations were not affected by the elevated temperature exposure.

The best strength/fracture toughness combinations are achieved in product forms that see the highest degree of thermomechanical processing. Data in Table I for 0.125" thick specimens from as-fabricated sheet, plate and extrusions show that tensile yield strengths and K_{R25} values for the as-fabricated sheet are higher than those of plate and the tensile yield strengths and K_{R25} values for plate are higher than those of extrusions for all crosshead speeds studied.

Figures 2, 3 and 4 display crack growth resistance curves for 0.125" thick specimens from as-fabricated sheet, plate and

extrusions, respectively. For the as-fabricated sheet and plate, the slowest crosshead speed produces the greatest crack growth resistance and the most stable crack extension. In the extrusion, the greatest crack resistance and the most stable crack extension are obtained in the specimens tested at the slowest and fastest crosshead speeds. Regardless of crosshead speed, all of the 0.125" thick specimens from the sheet, plate and extrusion had fracture surfaces with a combination of slanted and flat regions.

Crack growth resistance curves for the 0.6" thick compact tension specimens taken from 1" plate are presented in Fig. 5. Duplicate samples were tested at each crosshead speed. For all crosshead speeds, values for toughness were low and very little stable crack growth was obtained. Failed test samples had flat fracture surfaces, indicative of plane strain conditions. The differences in the crack growth resistance curves of duplicate samples suggest that these data are not reproducible.

Figure 6 is a plot of crack growth resistance as a function of effective crack extension for 0.125" thick samples taken from the as-fabricated extrusion and the extrusion exposed for 1000 hr at 300°F. Specimens from the exposed extrusion exhibited the greatest crack growth resistance and the most stable crack extension when tested at the slowest crosshead speed. Specimens tested at the fastest crosshead speed exhibited the least crack growth resistance and the least stable crack growth. This behavior is somewhat different than the behavior of the as-fabricated extrusion, where specimens tested at the slowest and fastest crosshead speeds were similar in terms of crack growth resistance and the extent of stable crack growth. In general, the effect of the elevated temperature exposure was to increase crack growth resistance.

Many of the 0.125" thick fracture toughness specimens had fracture surfaces suggesting a mixed mode of failure, e.g., some plane stress and some plane strain character. These observations are summarized for the specimens from the extrusion in Table II.

In theory, brittle fracture is usually associated with a flat featureless surface without any shear lips whereas a slanted fracture surface has shear lips and is typically associated with an increase in the energy necessary for fracture and a more ductile type of fracture. A flat fracture is representative of plane strain conditions while a slanted fracture is representative of plane stress conditions. As-fabricated samples which were tested at intermediate crosshead speeds have a flat fracture surface while those samples tested at the slowest and fastest speeds have a combination of slanted and flat (mixed mode) fracture. Samples of the extrusion exposed to elevated temperatures exhibited slanted and flat (mixed mode) fracture surfaces when tested at the intermediate and slowest speeds and flat fracture when tested at the fastest speed. Values for K at maximum load correlate with the observed fracture morphology (see Table II), i.e., mixed mode fractures produce higher values for K than flat fractures. Regardless of crosshead speed, failed samples from the as-fabricated extrusion and the exposed extrusion had markings on the fracture surfaces that were correlated with rapid load drops on the load-displacement curves. The rapid load drops are due to regions of unstable crack propagation. These regions on the load-displacement curves were avoided when drawing secant intercepts.

Strength/toughness data generated for P/M Al-Fe-Ce-Mg alloy are compared with data on X8019 (6) in Fig. 7. The Al-Fe-Ce-Mg alloy has lower strengths and lower toughness values than X8019.

Summary

- Mg increases the work hardenability of P/M Al-Fe-Ce. Tensile yield strengths for X8019 and Al-8 Fe-4 Ce-0.4 Mg are similar, but ultimate tensile strengths are greater for Al-8 Fe-4 Ce-0.4 Mg.
- The highest tensile yield strengths are achieved in product

- forms receiving the most hot working during thermomechanical processing. Tensile yield strength increases in the following order: extrusion, plate and sheet. Similarly, the best strength/plane stress fracture toughness combinations are achieved in product forms receiving the most hot working.
- Except in sheet, crosshead speed had no significant effect on tensile yield strength or elongation to failure. In sheet, the tensile yield strength decreased slightly when crosshead speed was increased.
 - The effects of specimen geometry and location were small. When tested at the highest crosshead speed, the tensile yield strength measured in a round specimen was about 2 ksi higher than the tensile yield strength measured in the flat specimen. Also at the highest crosshead speed, the tensile yield strength measured in a flat specimen located at $t/2$ was 3 ksi higher than the tensile yield strength measured in a flat specimen located at $t/4$.
 - After exposure of the extrusion for 1000 hr at 300°F, tensile yield strengths measured at the slowest and fastest crosshead speeds were increased slightly while the tensile yield strength measured at the intermediate crosshead speed was decreased. Elongations to failure were not affected by the exposure. For all crosshead speeds, the exposure resulted in greater crack growth resistance and more stable crack growth.
 - In general, the greatest crack growth resistance and most stable crack growth was measured in specimens tested at the slowest crosshead speed. The effects at the fastest and intermediate crosshead speed varied for the different products, specimen geometries and locations.
 - For some toughness tests, transients of unstable crack growth resulted in discontinuities in the load-displacements curves.
 - When compared to X8019, Al-8 F-4 Ce-0.4 Mg alloy has a reduced strength/toughness relationship.

References

1. E. Bouchard, L. Kubin and H. Octor, Met. Trans. A, 22A, p. 1021-1028 (1990).
2. D.J. Skinner, M.S. Zedalis and P. Gilman, Mat. Sci. and Eng., A119, p. 81-86 (1989).
3. W.C. Porr, "Elevated Temperature Fracture of Advanced Powder Metallurgy Aluminum Alloy 8009," Ph.D. Dissertation, University of Virginia, 1992.
4. First Biannual Report.
5. L.M. Angers, unpublished research, Alcoa Technical Center, 1991.
6. D.K. Denzer, unpublished research, Alcoa Technical Center, 1988.

TABLE I. Results of tensile and fracture toughness testing of extrusions, plate and sheet from P/M Al-8 Fe-4 Ce-0.4 Mg alloy at various crosshead speeds.

Product Form	Temper	Orientation	Specimen Type	Crosshead Speed in./min	Tensile Yield Strength, ksi	Ultimate Tensile Strength, ksi	% Elongation	Orientation	Specimen Thickness in.	Crosshead Speed, in/min	K _{R25} ksi $\sqrt{\text{in.}}$	K @ P _{max} ksi $\sqrt{\text{in.}}$
2" Extrusion	F	L	0.125" Sheet	0.375	50.5	80.1	10	L-T	0.125"	0.59	35.2	36.2
				0.0375	50.2	79.1	10			0.059	(c)	28.3
				0.00375	50.1	76.4	9.5			0.0059	30.4	30.4
1" Plate	F + 1000 hr @ 300°F	L	0.125" Sheet	0.375	52.6	82.6	9	L-T	0.125"	0.59	(b)	25.3
				0.0375	46.9	80.4	9.5			0.059	39.73	41.1
				0.00375	52.2	77.7	9.5			0.0059	(c)	53.0
	F	L	1/4" round ^a	0.375	55.9	72.2	10.4	L-T	0.6"	0.59	(c)	19.2
				0.0375	54.7	69.2	10.3			0.059	(c)	20.6
				0.00375	54.3	66.9	10.5			0.0059	(c)	23.9
1/8" Sheet	L, 1/2	L, 1/2	1/8" Sheet	0.375	53.1	72.1	10.2	L-T	0.125"	0.59	42.5	49.0
				0.0375	54.6	70.4	11.1			0.059	53.9	60.7
				0.00375	53.9	68.1	11.6			0.0059	56.8	81.5
	L, 1/4	L, 1/4	1/8" Sheet	0.375	50.5	71.4	10	L-T	0.125"	0.59	37.5	39.6
				0.0375	52.7	69.8	13			0.059	(c)	27.6
				0.00375	52.6	67.0	15			0.0059	(c)	29.5
1/8" Sheet	F	L	1/8" Sheet	0.375	65.3	79.8	10	L-T	0.125"	0.59	51.0	61.2
				0.0375	67.5	77.8	9			0.059	58.7	73.2
				0.00375	68.4	75.2	10			0.0059	57.9	78.8
	F	T	1/8" Sheet	0.375	66.7	80.5	10	T-L	0.125"	0.59	42.4	45.6
				0.0375	67.1	78.2	9			0.059	47.8	56.2
				0.00375	62.5	74.9	10			0.0059	(c)	33.2

^a Duplicate tensile, duplicate toughness.

^b K_{R25} is not reported if it occurs after P_{max}.

^c Insufficient crack extension to obtain a K_{R25} value.

TABLE II. Fracture surface appearances as a function of crosshead speed for as-fabricated extrusions and exposed extrusions.

Crosshead Speed (in./min)	As-fabricated Extrusion		After 1000 hr at 300°F	
	K at P_{max} ksi $\sqrt{\text{in.}}$	Fracture Appearance	K at P_{max} ksi $\sqrt{\text{in.}}$	Fracture Appearance
0.59	36.2	mixed mode	25.3	flat
0.059	28.3	flat	41.1	mixed mode
0.0059	30.4	mixed mode	53.0	mixed mode

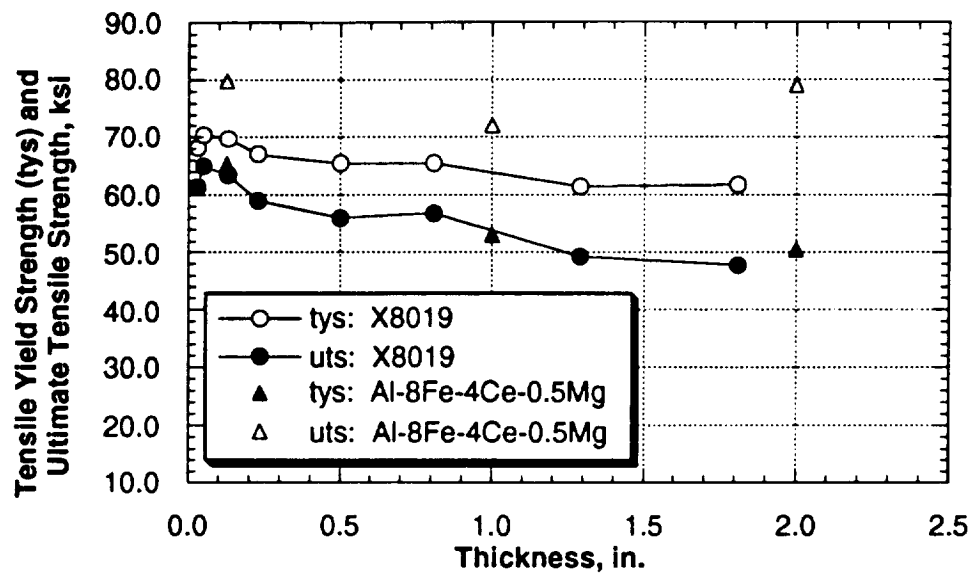


Figure 1. Tensile yield strength and ultimate tensile strength as a function of thickness for the P/M Al-8Fe-4Ce-0.5Mg alloy and X8019.

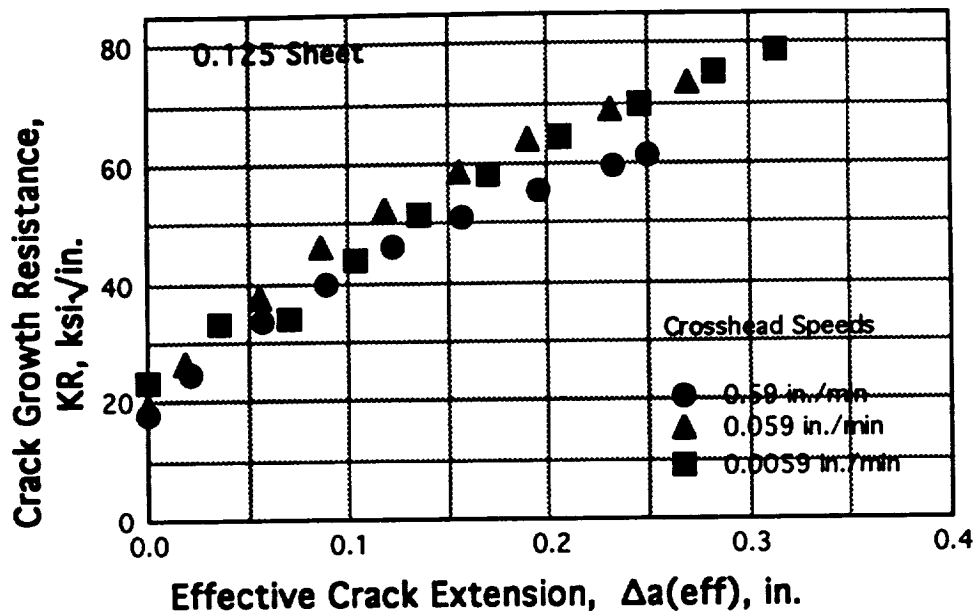


Figure 2. Crack growth resistance, K_R , as a function of effective crack extension for specimens from 0.125" thick sheet tested at various crosshead speeds. Compact tension fracture toughness specimens were 3.125" wide x 3" high x 0.125" thick.

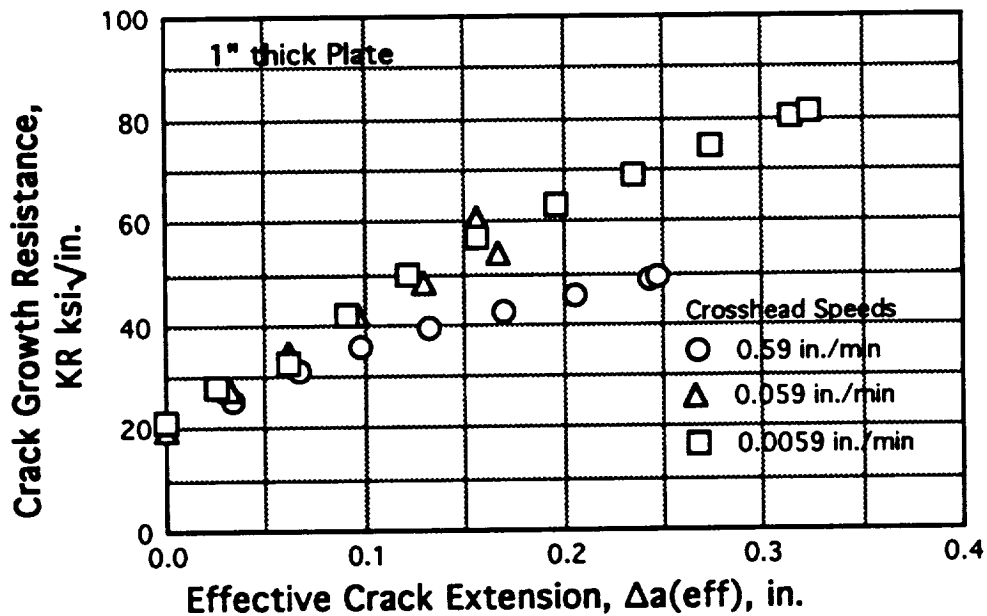


Figure 3. Crack growth resistance, K_R , as a function of effective crack extension for specimens from 1" plate tested at various crosshead speeds. Compact tension fracture toughness specimens were 3.125" wide x 3" high x 0.125" thick.

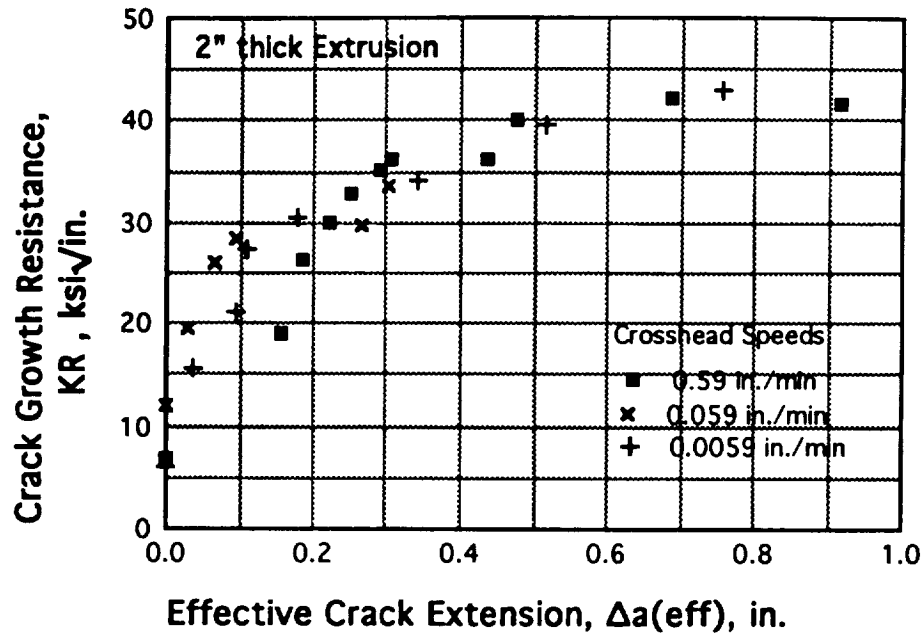


Figure 4. Crack growth resistance, K_R , as a function of effective crack extension for specimens from the 2" thick extrusion tested at various crosshead speeds. Compact tension fracture toughness specimens were 3.125" wide x 3" high x 0.125" thick.

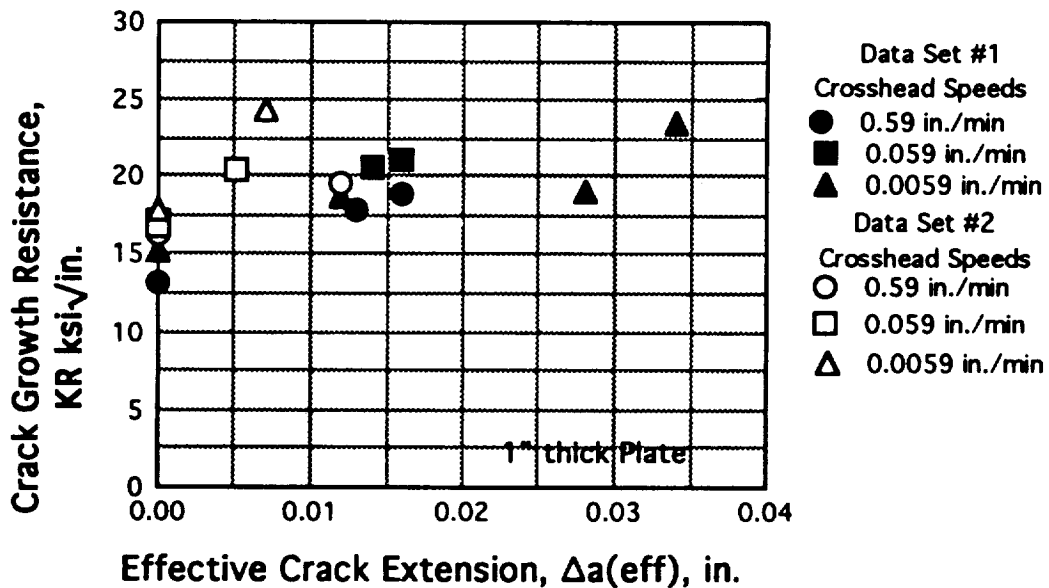


Figure 5. Crack growth resistance, K_R , as a function of effective crack extension for specimens from the 1" thick plate tested at various crosshead speeds. Compact tension fracture toughness specimens were 1.25" wide x 1.2" high x 0.60" thick.

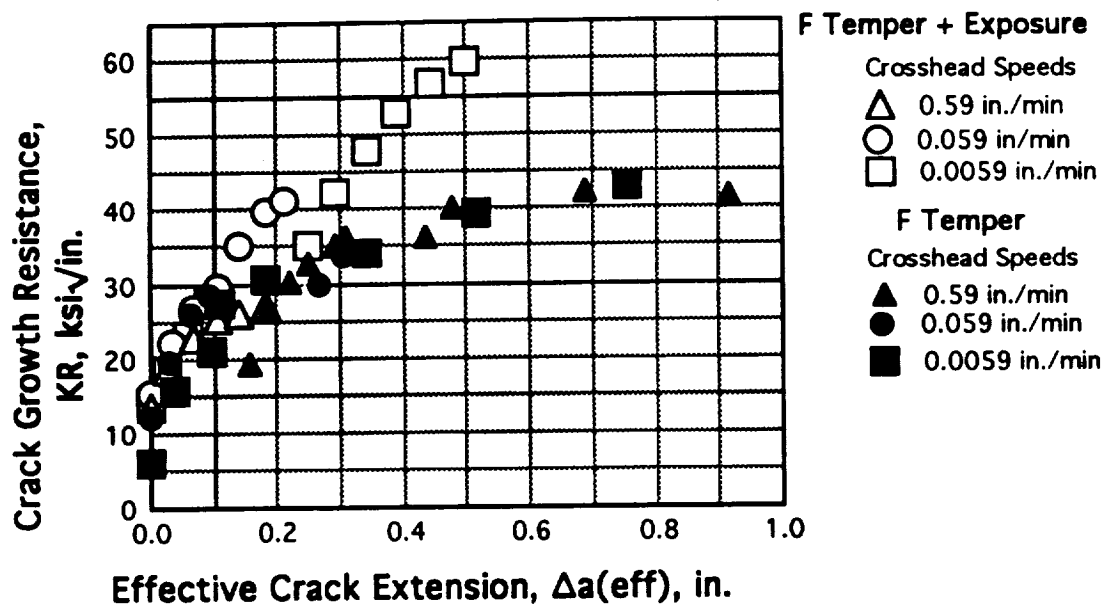


Figure 6. Crack growth resistance, K_R , as a function of effective crack extension for specimens from the 2" thick extrusion in the as fabricated condition and after exposure of 1000 h at 300°F, tested at various crosshead speeds. Compact tension fracture toughness specimens were 3.125" wide x 3" high x 0.125" thick.

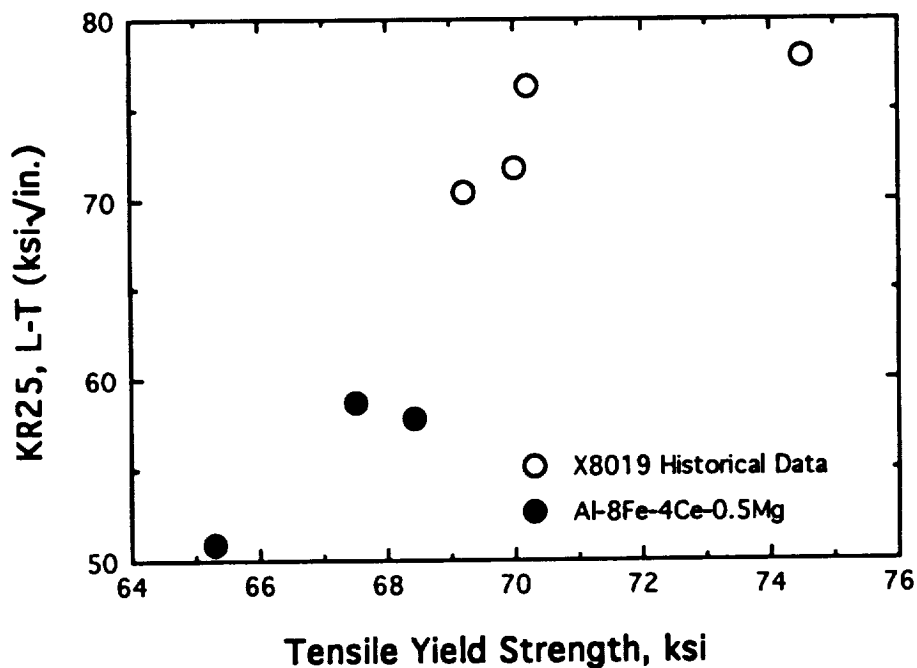


Figure 7. KR25 Fracture toughness as a function of tensile yield strength for Al-8Fe-4Ce-0.5Mg and X8019.

TASK 6. PROCESSING-BASED IMPROVEMENTS IN THE MECHANICAL ISOTROPY AND INTERMEDIATE TEMPERATURE DAMAGE TOLERANCE OF Al-Fe-V-Si ALLOY 8009 (Allied Signal/UVa)

Principal Investigator, UVa:	Prof. R.P. Gangloff
Research Associate, UVa:	Dr. Sang-Shik Kim
Principal Investigator, Allied Signal:	Dr. M.S. Zedalis

Objective

The objectives of this task are to: (a) reduce the extent of fracture toughness anisotropy and dynamic strain aging (DSA) by optimizing the processing of the 8009 alloy composition for high speed airframe applications, (b) improve intermediate temperature and prolonged-time fracture resistance of 8009 by microstructural modifications through processing, (c) establish micromechanical mechanisms for time-temperature dependent deformation and fracture of 8009-type alloys, and (d) provide initial characterization of the long-term damage tolerant properties of an optimized microstructure of HTA 8009.

The first three objectives have been emphasized to date and are being accomplished by attempting to: (a) reduce the oxide content at prior particle boundaries, (b) improve metallurgical bonding between powder particles, (c) reduce the concentration of Fe and V in the Al-solid solution matrix, (d) alter the density of mobile dislocations and (e) conduct mechanistic experiments and analyses at UVa. Task 6A at Allied Signal involves modifications to planar flow casting, powder degassing and consolidation practices conventionally employed to manufacture HTA 8009. Consolidated billets, from two modified ribbon casting procedures, are subjected to various hot and cold rolling schedules. The fracture toughnesses of these process-dependent microstructures are characterized in Task 6B by a J-integral fracture mechanics R-curve method, and as a function of elevated temperature and loading rate. Task 6B work is performed at the University of Virginia and by J.K. Donald at Fracture Technology Associates.

Subtask 6A. HTA 8009 Processing
(Allied-Signal)

Principal Investigator: Dr. M.S. Zedalis

Background

Commercially available high temperature Al-Fe-V-Si (HTA) alloy 8009 has emerged as a leading candidate Al-base material for aerospace applications with service temperatures approaching 600K (1-4). HTA 8009 (formerly designated FVS0812) is processed utilizing rapid solidification/powder metallurgy technologies and combines the room temperature strength, ductility and fracture toughness of conventional 2000 and 7000 series aerospace aluminum alloys with greatly improved elevated temperature strength and stability. HTA 8009 derives its excellent mechanical and physical properties from a uniform dispersion of $\text{Al}_{13}(\text{Fe},\text{V})_3\text{Si}$ particles dispersed in an aluminum solid solution matrix. The silicide dispersoids typically range from 50-80 nm in diameter after consolidation (e.g., extrusion, forging, and rolling) and are extremely resistant to particle coarsening at elevated temperatures. As a result, no measurable material degradation occurs even after exposure for 1000 hours to temperatures approaching 725K (5,6). HTA 8009 also exhibits approximately a 25% increase in Young's modulus over conventional Al-base alloy and, on a specific stiffness basis, is superior to Ti-6Al-4V and 17-4 PH steel to temperatures approaching 750K (7). This combination of properties makes HTA 8009 extremely attractive for applications which have been previously restricted to heavier titanium or steel alloys and superior to polymer composites at elevated temperatures. HTA 8009 is presently being evaluated for wing skins, aircraft landing wheels, missile bodies and fins as well as a variety of gas turbine engine components which operate at slightly elevated temperatures.

While the benefits of using HTA 8009 over titanium and steel

alloys for certain applications are clearly recognized, extensive mechanical characterization of the alloy has identified two (2) potential areas of concern to high speed aircraft and engine designers:

- i) mechanical anisotropy as a function of product form; and,
- ii) reduced plasticity in the 450-550K temperature range.

Anisotropy in the mechanical behavior of HTA 8009 is most apparent in the variation in toughness and ductility for samples tested in directions orthogonal to the rolling/extrusion directions. Porr et al. (8) has recently shown for HTA 8009 flat bar extrusions that values of plane strain fracture toughness, K_{IC} , could vary from as high as about 36.6 MPa \sqrt{m} for samples tested in the L-T orientation to as low as about 16.1 MPa \sqrt{m} for samples tested in the T-L orientation. Fractography performed by Chan (9,10) and later confirmed by Porr et al. (8), indicates that the variation in toughness is related to the extent of delamination occurring along oxide decorated prior particle boundaries. Based on these observations, Chan (9) concluded that K_{IC} values measured for samples tested in the L-T orientation are enhanced as a result of a loss in through-thickness constraint associated with delamination. The mechanism of "thin sheet toughening" is viewed as contributing substantially to L-T toughness, while leading to lower toughness in orthogonal orientations.

Reduced plasticity in the 450-550K temperature range in HTA 8009, on the other hand, has been attributed to the phenomenon of dynamic strain aging (DSA) occurring in the alloy (11). DSA is not uncommon to conventional aluminum alloys, but typically occurs below ambient temperatures due to the higher diffusivity of the more traditional alloying constituents (e.g., Cu, Mg, Si). For HTA 8009, Skinner et al. (11) has observed that DSA occurs at intermediate temperatures due to the more sluggish diffusivity of Fe and V present in the matrix. Solute levels of these two (2) elements in the Al-base matrix have been measured to be greatly in

excess of equilibrium levels, and at present, do not appear to be affected by hot working or static thermal exposure. While DSA is known to reduce ductility and toughness in HTA 8009 (6,11), the effect becomes significantly more serious when it is combined with the mechanical anisotropy of the material. For example Porr et al. (8) measured that K_{IC} values for samples tested in the L-T orientation decreased to a minimum of about 15 MPa \sqrt{m} over this intermediate temperature range compared to a minimum of about 9.5 MPa \sqrt{m} for samples tested at similar temperatures in the T-L orientation.

Objectives and Approach

The objectives of this research are to improve the mechanical isotropy and elevated temperature damage tolerance of high temperature aluminum (HTA) alloy 8009 plate and sheet by modifying the current processing parameters and practice. Specifically, these objectives will be accomplished by:

- (i) improving the metallurgical bonding between prior powder particles by reducing the oxide layer thickness at the particle interfaces; and,
- (ii) reducing the concentration of solute Fe, V and Si in the Al matrix as well as modifying the alloy's grain/subgrain structure by thermo-mechanical processing. In practice, the oxide layer present at the prior powder particle boundaries will be reduced by casting and comminuting the planar flow cast 8009 ribbon in a protective atmosphere. Moreover, supersaturated solute atoms as well as grain/subgrain structure in 8009 plate and sheet will be affected by employing a thermo-mechanical process which involves modifications to current hot/cold rolling practices. Each of these process modifications will be performed on commercial-scale quantities of material, and hence, may be directly implemented into current manufacturing specifications.

Progress During Report Period

A. Tensile Testing of HTA 8009 Extrusions

Tensile testing of HTA 8009 rolling preforms extruded at Spectrulite Consortium Inc. in Madison, IL was performed to assess the effect of extrusion conditions (e.g., temperature, lubrication, speed, etc.) on mechanical properties. Tensile testing was performed at 25°C (77°F) and 232°C (450°F) on specimens machined from both the nose and tail of HTA extrusions 92A022 and 92A024. Specimens were machined from various locations in the cross-section of the extrusion, Fig. 1, and were oriented in both the longitudinal and transverse directions (i.e., with respect to the extrusion direction).

Tensile testing was performed at AlliedSignal using an Instron 1125 testing machine. Testing was performed using a modified ASTM E21 procedure. Here, tests were initially run at a strain rate corresponding to 0.5%/min as per specification. At this strain rate, tensile yield and an ultimate tensile strength were measured. After the ultimate tensile strength of the sample was achieved, the imposed strain rate was then increased ten-fold to a rate of 5%/min, Fig. 2. This testing practice in effect provided tensile data for HTA 8009 at two (2) strain rates on a single sample. Measured total plastic elongation therefore represents the sum of plasticities exhibited for a combination of strain rates. [Note: post UTS strain rates were calculated based on original gauge sections. Corrections for strain in the neck were not made.]

Tensile data as a function of location and test temperature for specimens machined from the nose and tail of extrusions 92A022 and 92A024 are summarized in Table 1. Variation as a function of position and test temperature is graphically presented in Figs. 3 and 4. In general, there is very little difference in tensile strengths between the two (2) extrusions, and variations as a

function of sample position (with respect to the cross-section of the extrusion) were comparable. Based on this data, a number of observations and hypotheses may be made:

- (i) Increasing the strain rate ten-fold from 0.5%/min to 5.0%/min on average increases the tensile strength by approximately 14-21 MPa (2-3 ksi) for tests conducted at 298K (77°F) and 505K (450°F).
- (ii) Tensile strength, irrespective of strain rate, increases by approximately 14-21 MPa (2-3 ksi) for specimens machined from the mid-planes of the extrusion in comparison to specimens machined from the outer perimeter. This behavior may be attributed to the fact that the outer surface of the preform tends to be much hotter than the bulk due to frictional heating during extrusion. Higher surface temperature promotes a slightly coarser microstructure, and, therefore, lower strength. This tendency is present for specimens machined from the nose as well as the tail of the extrusions.
- (iii) Tensile ductility decreases in the mid-plane of the extrusion and overall is less for specimens oriented transverse to the extrusion direction irrespective of position in the extrusion. Ductility in these extrusions is largely dependent on the interparticle bonding of the HTA powder particles, and variations in ductility reflect the extent of shear the particles experience during extrusion (i.e., particles located near the surface of the preform, extruded through a shear-faced die, exhibit greater amounts of shear than particles located at mid-plane in the preform).
- (iv) Tensile ductility, on average, is comparable for specimens machined from extrusions 92A022 and 92A024. While shrouding of the melt puddle during planar flow casting resulted in a reduction in total oxide content

(i.e., related to hydrate layer thickness present on the powder particle surfaces), improved bonding of powder particles apparently was not substantially affected.

Tensile Testing of HTA 8009 Plate and Sheet

Tensile testing of HTA 8009 plate and sheet rolled at Kaiser Aluminum's Center for Technology (CFT) in Pleasanton, CA was conducted to assess the effect of rolling schedule and parameters on mechanical properties. The rolling campaign was designed to evaluate the major objectives of the program, namely:

- (i) To evaluate the effects of rolling direction and total reduction in gauge on mechanical isotropy in HTA 8009 plate and sheet; and,
- ii) To evaluate the application of thermo-mechanical processing to improve elevated temperature ductility and toughness by modifying the grain/subgrain structure in HTA 8009 sheet as well as by reducing the solute content in the Al matrix.

The specific rolling schedules designed to meet the aforementioned objectives are illustrated in Fig. 5. To evaluate the effects of rolling direction and total reduction in gauge on mechanical isotropy in HTA 8009 plate and sheet, one-half of the preforms from each casting modification received only cross-rolling (i.e., rolled normal to the extrusion direction), while the balance received only straight-rolling (i.e., rolled parallel to the extrusion direction). An identical pass schedule (i.e., reduction per pass and the number of passes per rolling heat) was practiced for all lots of material. Plate and sheet having respective gauges of 0.64 cm (0.25"), 0.22 cm (0.090") and 0.10 cm (0.040") were produced during this phase of the program.

To evaluate the application of thermo-mechanical processing (TMP) to improve elevated temperature ductility and toughness, HTA 8009 sheet was initially hot rolled to approximately 0.22 cm

(0.090") gauge. Three (3) different rolling practices were then employed to fabricate 0.10 cm (0.040") gauge sheet. The first rolling practice involved only hot rolling to the final gauge. Here the sheet was soaked at approximately 673K (750°F) prior to being rolled to gauge. Sheet temperature was monitored during rolling to verify that the sheet temperature never fell below about 500K (450°F).

The second rolling practice involved only cold rolling from 0.22 cm (0.090") to a final gauge of about 0.10 cm (0.040" gauge). Here the sheet was allowed to cool to approximately 298K (77°F) prior to being cold rolled to its final gauge. Some work induced, adiabatic heating of the sheet was experienced during cold rolling; however, the sheet temperature never exceeded about 340K (150°F).

The third rolling practice also involved only cold rolling [298K (77°F)] to the final gauge; however, here the sheet was subjected to an annealing treatment of approximately 673K (750°F) for 0.5 hrs, after every 30% reduction in gauge. The premise behind this TMP was to further reduce the concentration of Fe, V and Si in the HTA 8009 matrix via heterogeneous nucleation of dispersoids as well as through the "sweeping" action of glissile dislocations.

In total, approximately 150 kg of sheet were rolled at Kaiser Aluminum - CFT for the program, Tables 2 and 3. Prior to being shipped back to AlliedSignal, all of the sheet was trimmed to remove minor edge cracks and sectioned into approximately 250 cm (100") lengths. Approximately two-thirds of the HTA 8009 plate and sheet were supplied to the University of Virginia for testing.

Tensile data for the plate and sheet samples identified in Tables 2 and 3 are summarized in the following sections for HTA sheet rolled from extrusions 92A022 and 92A024. Tensile testing was performed on an Instron 1125 testing machine at temperatures of 298, 422, 505 and 589K (77, 300, 450 and 600°F). Testing was also performed on selected samples after exposure for 100 hrs to

644K (700°F). Testing at all temperatures was performed using a modified ASTM E21 procedure. Here, tests were initially performed at a strain rate corresponding to 0.5%/min as per specification. At this strain rate, a 0.2% tensile yield and an ultimate tensile strength were measured. After an ultimate tensile strength was achieved, the imposed strain rate was then increased ten-fold to a rate of 5%/min, Fig. 2, and the test was run until failure. This testing practice, in effect, provided tensile strength data for HTA 8009 at two (2) strain rates using a single sample. Measured total plastic elongation, therefore, represents the sum of ductilities for a combination of strain rates. To further assess the strain rate sensitivity of HTA 8009 plate and sheet, samples were also tensile tested at a single strain rate of 50%/min. Here, 0.2% yield strength, ultimate tensile strength and total plastic elongation were measured for a single strain rate.

Tensile data for plate and sheet samples rolled from extrusions 92A022 and 92A024 are summarized in Tables 4-6 a&b and Tables 7-12 a&b, respectively. (Table numbers followed by the letter "a" are in SI units, while Table numbers followed by the letter "b" are in traditional British units.)

Effect of Rolling Direction & Reduction in Gauge on Mechanical Isotropy

To evaluate the effect of rolling direction and reduction in gauge on mechanical isotropy in HTA 8009 plate and sheet, one-half of the preforms from each casting modification received only cross-rolling (i.e., rolled normal to the extrusion direction), while the balance received only straight-rolling (i.e., rolled parallel to the extrusion direction). An identical pass schedule (i.e., reduction per pass and number of passes per rolling heat) was practiced for all lots of material. Tensile testing was performed on plate and sheet have respective gauges of approximately 0.64 cm (0.25"), 0.22 cm (0.090") and 0.10 cm

(0.040").

Mechanical anisotropy in HTA 8009 plate and sheet is most clearly reflected in values for total plastic elongation measured during tensile testing. Tensile strength is observed to be fairly similar for samples oriented longitudinally or transverse to the preform rolling direction at all of the strain rates evaluated. As may be seen in Figs. 6-20 and Figs. 21-35 for plate and sheet rolled from extrusions 92A022 and 92A024, respectively, cross-rolled 0.64 cm (0.25") gauge plate exhibits mechanical isotropy within the scatter band for the material tested. Total plastic elongation measured over all temperatures is basically constant at this gauge and remains equivalent for sheet cross-rolled to thinner gauges. Straight-rolled sheet, on the other hand, indicates similar isotropy only for the sheet rolled to approximately 0.10 cm (0.040").

This response clearly indicates that rolling direction has a greater impact on improving mechanical isotropy in HTA 8009 plate and sheet than does the total reduction in gauge achieved during rolling. From a microstructural point of view, this response may be attributed to the fact that cross rolling more effectively breaks-up and disperses the oxide/hydrate layer present at the prior particle boundaries than straight rolling alone. While comparable levels of shear are achieved in sheet that has been cross and straight rolled to a similar gauge, the oxide/hydrate layer in straight-rolled sheet remains in contiguous bands oriented to the extrusion and rolling directions. As a result, tensile specimens oriented transverse to the rolling direction fail at lower plastic strains along the original prior particle boundaries.

The reduction in the oxide/hydrate layer thickness for plate and sheet rolled from extrusion 92A024, comprised of planar flow cast ribbon which was shrouded in a dry inert gas environment during casting, in comparison to plate and sheet rolled from conventionally processed extrusion 92A022 did not result in any

measurable improvement in transverse tensile ductility. While shrouding the melt puddle and the down-stream planar flow cast ribbon with a dry inert gas did reduce the hydrate layer thickness from approximately 3.25 nm to 2.9 nm and the total oxygen content from 0.087% to 0.079%, a consistent improvement in transverse tensile ductility was not observed for the plate and sheet samples examined in the study.

Effect(s) of Thermomechanical Processing

Hot rolled 0.22 cm (0.090") gauge HTA 8009 sheet from both lots of material (i.e., 92A022 and 92A024) was rolled to a final gauge of approximately 0.10 cm (0.040") following three (3) different rolling practices to evaluate the effect of thermomechanical processing (TMP) on ambient and elevated temperature tensile properties. The first rolling practice involved only hot (cross- and straight-) rolling to the final gauge. A second rolling practice involved only cold (cross- and straight-) rolling to the final gauge. And the third rolling practice involved cold (cross- and straight-) rolling to gauge; wherein, an intermittent annealing treatment of 673K (750°F) for approximately 0.5 hrs was performed after every 30% reduction in total gauge. Here, the hope was to reduce the Fe, V and Si solute content in the (rapidly solidified) matrix by inducing heterogenous nucleation of dispersoids and/or through the scavenging of solute atoms by glissile dislocations.

Tensile data for sheet rolled following these three (3) schedules from extrusions 92A022 and 92A024 clearly indicates a sizable variation in properties. Hot cross- and straight-rolled sheet exhibits the highest tensile strengths over the range of test temperatures for any of the plate and sheet rolled in the present program. Room temperature tensile strength is typically in the 430-450 MPa (63-65 ksi) range for tests run at a strain rate of 0.5%/min. Overall, this material also exhibits the lowest levels of ductility for all TMP batches over the range of test

temperatures. Tensile ductility is observed to decrease from approximately 7-10% at room temperature to approximately 2.1-2.7% at a test temperature of 422K (300°F). As the test temperature is increased, tensile ductility is observed to increase to as high as 26%.

Cold rolled 0.10 cm (0.040") gauge HTA 8009 sheet exhibits a sizable increase in tensile ductility in comparison to the hot rolled sheet, with only a small decrease in tensile strength. Tensile strengths (at 0.5%/min strain rate) for cold rolled sheet ranges from about 400-425 MPa (58.5-61.6 ksi) at 298K (77°F) and a very attractive level of about 150-193 MPa (22.4-28.0 ksi) at 589K (600°F). Tensile ductility for this material is also observed to exhibit a drop in ductility at intermediate test temperatures. Here, ductility values of about 15-19% at room temperature decrease to levels of only about 6-9% at 422K (300°F). As the test temperature is further increased, tensile ductility in this sample is observed to increase to values often in excess of 25%.

Tensile data for 0.10 cm (0.040") sheet cold rolled which received intermediate annealing treatments indicate a response fairly comparable to the sheet samples which received cold rolling only. Tensile strengths for this material was generally approximately 20-30 MPa (3-4 ksi) lower than measured for the cold-rolled sheet over the test temperatures. Values of tensile ductility and its variation with test temperature was very nearly equivalent to levels measured for sheet samples which received only cold rolling.

While this data clearly indicates that TMP had an effect on the tensile properties of 0.10 cm (0.040") gauge HTA 8009 sheet, the TMP's practiced did not substantially improve the intermediate temperature plasticity (e.g., ductility) as originally hoped and intended. Cold rolling, with and without intermittent annealing treatments did, however, result in an overall improvement in the measured tensile ductility over the range of test temperatures in comparison to values measured for hot rolled sheet. Further

discussion on the effects of TMP on the microstructure of HTA 8009 sheet is presented in the subsequent section on Transmission Electron Microscopy.

Percent Reduction in Area as a Function of Test Temperature for HTA 8009 Plate and Sheet

Values of % reduction in cross-sectional area as a function of test temperature for plate and sheet samples cross-rolled from extrusions 92A022 and 92A024 are summarized in Tables 4-6 and 7-9 and shown graphically in Figs. 36-37 and 38-39, respectively. While tensile ductility for all of the HTA 8009 plate and sheet rolled in the present program displays the characteristic ductility "dip" over the temperature range of 422-505K (300-450°F), measured values of % reduction in cross-sectional area are found to primarily decrease with increasing test temperature. This response is similar to toughness data measured by S.S. Kim and R.P. Gangloff at the UVA for sheet having similar pedigree provided for testing in their phase of the present program. Irrespective of rolling temperature or TMP practice, % reduction in area drops from about 40-50% at 298K (77°F) to about 25-30% at 422K (300°F) and higher.

Effect of Strain Rate on Ambient Temperature Tensile Strength & Ductility

The effect of strain rate on HTA 8009 has been examined by D.J. Skinner et al. (19), but only for extrusions or hot rolled sheet. In the present program, the effect of strain rate on ambient temperature tensile strength and ductility was evaluated over two (2) decades of imposed strain rates for all variants of 92A024 cross- and straight-rolled plate and sheet, Figs. 40-44. Irrespective of sheet gauge or rolling direction, increasing the strain rate by a factor of ten (10) typically adds approximately

15-25 MPa (2-3 ksi) to the ultimate tensile strength as well as typically increasing the % plastic elongation by as much as 50% in some cases, Tables 10-12. Strain rate sensitivity values for the plate and sheet samples tested in the present program indicates an "m" value ranging from about 0.015 to 0.030, irrespective of the rolling practice employed, (e.g., temperature, direction, TMP). Here, "m" may be calculated using the following equation:

$$m = [\ln (\sigma_2/\sigma_1)] / [\ln(\epsilon'_2/\epsilon'_1)],$$

where σ_1 is the original stress level and σ_2 is the new stress value obtained after increasing the strain rate from ϵ'_1 to ϵ'_2 . The values for "m" measured in the present study overlap the ambient temperature "m" value of approximately 0.025 previously measured by Skinner et. al. (19).

It has been suggested that the high strain rate sensitivity measured for HTA 8009 reflects the strong interplay between glissile dislocations and solute atoms in the Al-solid solution matrix. At intermediate temperatures, 422-505K (300-450°F), the strain rate sensitivity for HTA 8009, like its ductility, has been shown to exhibit a minimum (i.e., nearly equal to zero) (19). This drop in both ductility and the strain rate sensitivity has been attributed to a dynamic strain aging phenomenon in HTA 8009, wherein the movement of dislocations through the matrix is strongly impeded by solute atoms (e.g., Fe, V, Si). Attempts to improve the intermediate temperature ductility in HTA 8009 in the present program by employing various TMP practices to further reduce the amount of solute present in the Al-solid solution, was unsuccessful. This response indicates that more exotic TMP processes might be necessary to improve the intermediate temperature ductility, or alternatively, that the level of solute present in the Al-solid solution matrix represents a near "equilibrium" concentration for rapidly solidified Al-Fe-base alloys.

Effect of Exposure on Ambient Temperature Tensile Properties

The family of high temperature Al-Fe-V-Si alloys is recognized as the most thermally stable of all Al-Fe-base alloys. HTA 8009 has been found to resist degradation of tensile properties even after exposure for 1000 hrs at 723K (842°F) (20). In the present program, a somewhat modest exposure for 100 hrs at 644K (700°F) was applied to assess any effects of TMP practice on the thermal stability of HTA 8009. Tensile data for plate and sheet rolled in the present study after 100 hrs/644K exposure is summarized in Tables 4-9.

Irrespective of extrusion number or rolling direction, 100 hrs exposure at 644K (700°F) was found to have no effect on the tensile properties of hot-rolled 0.64 cm (0.25") or 0.25 cm (0.090") gauge plate and sheet, Tables 4 and 7. In fact, a slight increase in tensile strength is observed after exposure for these samples. Hot-rolled 0.10 cm (0.040") gauge sheet after 100 hrs/644K (700°F) exposure also indicates no apparent degradation in tensile strength; however, a slight decrease (10-30%) in total plastic elongation was noted for many of the samples.

Cold-rolled 0.10 cm (0.040") gauge sheet, which did not receive intermittent annealing treatments, indicates the largest response to 100 hrs/644K (700°F) exposure, Tables 5 and 8. Measured values of tensile yield and ultimate strength are observed to increase by as much as 70 MPa (approximately 10 ksi) after exposure. More significant, however, is the very sizable decrease in total plastic elongation measured for this material after exposure. Ductility levels as high as approximately 18% measured for as-rolled samples were observed to decrease to levels in the 3.0 - 6.6% range.

The response of exposed, cold-rolled 0.10 cm (0.040") gauge sheet, which did receive intermittent annealing treatments, is fairly similar to the aforementioned cold-rolled variant, Tables 6

and 9. Tensile strength after 100 hrs/644K (700°F) exposure was observed to increase by as much as approximately 90 MPa (13 ksi); however, the decrease in ductility for sheet rolled from extrusion 92A022 does not appear to be as severely affected after exposure. For this material, total plastic elongation decreases from about 16-17.5% to about 4.8-8.8% after exposure. Sheet rolled from extrusion 92A024, on the other hand, does exhibit a severe decrease in ductility after exposure to values ranging from 2-3%. Possible reasons for the larger decrease in the total plastic elongation for this particular extrusion is discussed in a subsequent section detailing the results of microstructural analyses.

Microstructural Analyses of HTA 8009 Extrusion. Plate and Sheet Samples

Transmission electron microscopy (TEM) was performed on all variants of HTA 8009 extrusion, plate and sheet samples. TEM was performed using a Philips EM400T electron microscope equipped with STEM and EDS capabilities. TEM foils were mechanically thinned and electropolished in a 20% HNO₃ - 80% CH₃OH solution at 223K. As anticipated, the microstructure of the as-extruded rolling preform 92A022 is comprised of very fine, 50-80 nm Al₁₃(Fe,V)₃Si dispersoids present in an Al-solid solution matrix, Fig. 45. Grain (or subgrain) size for this material was measured to be about 0.5μm.

Extrusion 92A024 indicates a fairly comparable microstructure to that of extrusion 92A022; however, large regions of carbon (i.e., graphite) contamination were observed to be scattered throughout the material, Fig. 46. The possibility of carbon contamination in this material had been identified early in the program by X-ray photoelectron spectroscopy (XPS) performed on planar flow cast ribbon manufactured specifically for this batch of material (i.e., Process Modification B which involved shrouding

the melt puddle and downstream ribbon surface with a dry inert gas). Since this contamination was not observed on the planar flow cast ribbon or 92A022 extrusions, etc., its source may be directly attributed to the graphite device added to the casting machine to shroud the melt puddle and ribbon surface with a dry, protective atmosphere. Carbon flakes were also observed to be present in plate and sheet samples rolled from extrusion 92A024, and it is suggested that their presence may be a source for the anomalously low tensile ductilities and percent reduction in cross-sectional area measured for this material. Because of the presence of contamination in 92A024 plate and sheet samples, detailed TEM was only performed on material rolled from extrusion 92A022. The results of these analyses are summarized below.

TEM performed on hot-rolled 0.64 cm (0.25") gauge 92A022 plate indicates a microstructure very comparable to that of the parent extrusion, Fig. 47. As reflected by comparable tensile strengths for both product forms, the silicide particle size and the grain/subgrain size do not appear to have been affected by hot rolling. Similarly, little change in microstructure is observed for hot-rolled 0.22 cm (0.090") gauge 92A022 sheet, Fig 48. As indicated, silicide particles associated with grain/subgrain boundaries are slightly coarser than particles present within the grains. Obviously, pipe diffusion along grain/subgrain boundaries is assisting this coarsening, and one can further assume that diffusion is fed by solute atoms dumped at these boundaries by scavenging glissile dislocations during hot rolling.

The tendency to find coarser silicide particles present at grain/subgrain boundaries in the thinner gauge, hot-rolled 92A022 sheet is clearly evident in Fig. 49, which is a photomicrograph of the hot-rolled 0.10 cm (0.040") gauge sheet. Very coarse silicide particles (> 300 nm in diameter) may be observed associated with subgrain boundaries in the material. Moreover, dislocation tangles decorating these boundaries are clearly apparent in the micrograph. It is suggested that the lower ductilities measured

for the hot rolled 0.10 cm (0.040") gauge sheet are the result of these coarser particles present along the grain/subgrain boundaries.

The microstructure of 0.10 cm (0.040") gauge sheet cold-rolled from 0.22 cm (0.090") gauge hot rolled sheet does not exhibit the same extent of coarse silicide particles present at the boundaries as the hot-rolled 0.10 cm (0.040") gauge sheet. In general, a fairly uniform distribution of dispersoid was observed to be present in this material, Fig. 50. The major differences noted for the cold-rolled sheet in comparison to any of the hot-rolled variants examined in the present study are the highlighted grain/subgrain and particle boundaries in the cold rolled material. In many areas, the grain/subgrain boundaries appear wider in size (indicated by the arrows in Fig. 50) than typically observed for hot-rolled variants. Weak beam, dark field electron microscopy performed on these highlighted areas in cold-rolled sheet, Figs. 51 (brightfield) and 52 (weak-beam darkfield), clearly indicate dislocations associated with these boundaries. Moreover, dislocation tangles are notably absent from within the grains, which is fairly typical for this material. A possible reason for the lack of tangles may simply be due to the fact that this material does not exhibit a large volume fraction of silicide particles present within the grains; hence, there are fewer obstacles to impede dislocation motion through the grains during cold deformation.

TEM performed on cold-rolled 0.10 cm (0.040") gauge sheet which experienced intermittent annealing treatments during the rolling campaign tends to indicate a microstructure representative of both the hot- and cold-rolled 0.10 cm (0.040") gauge sheets presented above, Fig. 53. At lower magnifications, the presence of coarse silicide particles at the grain/subgrain boundaries may be observed, (i.e., typical of the hot-rolled variant). Moreover, bands of silicide particles were also apparent in this material (indicated by the arrows in Fig. 53) which might reflect the

effect of the intermittent annealing treatments applied to this material during rolling. Decorated grain/subgrain and particle boundaries, typical of cold-rolled sheet, are also apparent in this sheet variant, Fig. 54.

Energy Dispersive X-ray Spectroscopy of the Al-Solid Solution Matrix

Energy dispersive X-ray spectroscopy (EDX) was performed to assess the effect of TMP on the solute content present in the Al-solid solution matrix of hot- and cold-rolled plate and sheet samples. Data was acquired on a JEOL 2010 TEM equipped with a Noran 5500 analyzer and an ultrathin window EDX detector. The spot size used was approximately 30 nm and data was acquired at a count rate around 1000 counts per second for a total of 150 seconds. Spectra were measured for five different locations in the samples, in all cases being as near the edge of the TEM foil as possible. Computed k-factors (supplied by the manufacturer) were used in the analysis (i.e., internal standards were employed) and standard pure element spectra were used for the curve fitting of the experimental spectra.

The results of EDX performed on extrusion 92A022, hot-rolled 0.64 cm (0.25") plate and cold-rolled 0.10 cm (0.040") gauge sheet, which experienced intermittent annealing treatments, are presented in Table 13. In all cases, the count rates for Si, V and Fe in the Al-solid solution matrix were very low. Error values noted in the table represent only one standard deviation. In comparison to V and Fe levels measured in the Al-solid solution matrix of extruded and hot-rolled 0.64 cm (0.25") plate, the cold rolled/annealed 0.10 cm (0.040") gauge sheet does not indicate any reduction in solute content. Si levels of about 0.4 wt.% are also noted for this variant which was found to be completely absent from the spectra for the extrusion and plate samples. These data support the results of mechanical testing, and specifically, the

fact that cold rolling with intermittent annealing treatments does not result in any sizable increase in intermediate temperature plasticity due to a lessened dynamic strain aging response resulting from lower solute present in the Al-solid solution matrix. This data also supports the aforementioned hypothesis that the true "equilibrium" level of solute Si, V or Fe in rapidly solidified HTA 8009 is in actuality multiple orders of magnitude greater than the equilibrium solute levels reported in the literature for these elements in Al.

Summary

Two (2) potential areas of concern identified by aircraft and engine designers when contemplating the use of rapidly solidified, high temperature aluminum (HTA) alloy 8009 were examined in the present study, namely

- i) mechanical anisotropy as a function of product form; and,
- ii) reduced plasticity in the 450-550K temperature range.

To further examine these unique characteristics for HTA 8009, modifications to practice and processing parameters were performed to:

- (i) improve the metallurgical bonding between prior powder particles by reducing the oxide layer thickness at the particle interface; and,
- (ii) improve intermediate temperature embrittlement in plate and sheet products by employing thermomechanical processing (TMP) treatments to reduce the concentration of solute Fe, V and Si in the Al-solid solution matrix.

During the first half of this program (Jan. - July 1992), the oxide layer thickness on planar flow cast HTA 8009 ribbon was successfully reduced by casting under a dry inert gas shroud. Moreover, extrusions, plate and sheet samples were fabricated

during this period following modified rolling practices that were specifically designed to alter the solute concentration in the Al-solid solution. The processes employed and detailed results of this effort are summarized in the 1992 mid-year report to the University of Va and NASA.

This report details the results of tensile and microstructural testing performed on the extruded and rolled HTA 8009 plate and sheet samples. The major conclusions that may be drawn from this effort are summarized below:

- (i) Employing casting modifications to reduce the oxide/hydrate layer thickness on HTA 8009 planar flow cast ribbon, while successful, had little, if any, effect on the tensile properties of extrusions, plate or sheet samples fabricated from these two (2) casting variants.
- (ii) Tensile strength, irrespective of strain rate, increases by approximately 14-21 MPA (2-3 ksi) for specimens machined from the mid-planes of the extrusion in comparison to specimens machined from the outer perimeter. This behavior may be attributed to the fact that the outer surface of the preform tends to be much hotter than the bulk due to frictional heating during extrusion. Higher surface temperature promotes a slightly coarser microstructure, and, therefore, lower strength. This tendency is present for specimens machined from the nose as well as the tail of the extrusions.
- (iii) Tensile ductility decreases in the mid-plane of the extrusion and overall is less for specimens oriented transverse to the extrusion direction irrespective of position in the extrusion. Ductility in these extrusions is largely dependent on the interparticle bonding of the HTA powder particles and variations in ductility reflect the extent of shear the particles

- experience during extrusion (i.e., particles located near the surface of the preform, extruded through a shear-faced die, exhibit greater amounts of shear than particles located at mid-plane in the preform).
- (iv) Increasing the strain rate ten-fold from 0.5%/min to 5.0%/min on average increases the tensile strength by approximately 14-21 MPa (2-3 ksi) for tests conducted on extrusions at 298K (77°F) and 505K (450°F).
 - (v) Rolling direction has a greater impact on improving mechanical isotropy in HTA 8009 plate and sheet than does the total reduction in gauge achieved during rolling. This response may be attributed to the fact that cross-rolling more effectively breaks-up and disperses the oxide/hydrate layer present at the prior particle boundaries than straight-rolling alone.
 - (vi) The reduction in the oxide/hydrate layer thickness for plate and sheet rolled from extrusion 92A024, comprised of planar flow cast ribbon which was shrouded in a dry inert gas environment during casting, in comparison to plate and sheet rolled from conventionally processed extrusion, 92A022 did not result in any measurable improvement in transverse tensile ductility.
 - (vii) Tensile properties for hot-rolled 0.64 cm (0.25") gauge plate and hot-rolled 0.22 cm (0.090") gauge sheet are fairly comparable over all of the temperatures tested. Tensile ductility for these materials is observed to exhibit a drop in ductility at intermediate test temperatures.
 - (viii) TMP clearly had an effect on the tensile properties of 0.10 cm (0.040") gauge HTA 8009 sheet; however, they did not substantially improve the intermediate temperature plasticity (e.g., ductility) as originally hoped and intended.
 - (ix) Hot cross- and straight-rolled 0.10 cm (0.040") gauge

sheet exhibits the highest tensile strengths over the range of test temperatures for any of the plate and sheet rolled in the program. Overall, this material also exhibits the lowest levels of ductility for all TMP variants over the range of test temperatures. At intermediate temperatures, ductility values ranging from 3-5% were not uncommon.

- (x) Cold-rolled 0.10 cm (0.040") gauge HTA 8009 sheet exhibits a sizable increase in tensile ductility in comparison to the hot-rolled sheet, with only a small decrease in tensile strength. Tensile ductility for this material is also observed to exhibit a drop in ductility at intermediate test temperatures.
- (xi) Tensile data for 0.10 cm (0.040") cold-rolled sheet which received intermittent annealing treatments indicate a response fairly comparable to the sheet samples which received cold rolling only. Tensile strengths for this material were generally lower than measured for the cold-rolled sheet over the test temperatures. Values of tensile ductility and its variation with test temperature were very nearly equivalent to levels measured for sheet samples which received only cold rolling.
- (xii) Cold rolling, with and without intermittent annealing treatments, did result in an overall improvement in the measured tensile ductility over the range of test temperatures in comparison to values measured for hot rolled sheet.
- (xiii) While tensile ductility for all of the HTA 8009 plate and sheet rolled in the present program displays the characteristic ductility "dip" over the temperature range of 422-505K (300-450°F), measured values of percent reduction in cross-sectional area are found to primarily decrease with increasing test temperature.

- Irrespective of rolling temperature or TMP practice, percent reduction in area drops from about 40-50% at 298K (77°F) to about 25-30% at 422K (300°F) and higher.
- (xiv) Irrespective of sheet gauge or rolling direction, increasing the strain rate by a factor of ten (10) typically adds approximately 15-25 MPa (2-3 ksi) to the ultimate tensile strength as well as typically increases the % plastic elongation by as much as 50% in some cases. Strain rate sensitivity values for the plate and sheet samples tested in the present program indicate an "m" value ranging from about 0.015 to 0.030, irrespective of the rolling practice employed, (e.g., temperature, direction, TMP).
 - (xv) Irrespective of extrusion number or rolling direction, 100 hrs exposure at 644K (700°F) was found to have no effect on the tensile properties of hot-rolled 0.64 cm (0.25") or 0.25 cm (0.090") gauge plate and sheet. In fact, a slight increase in tensile strength is observed after exposure for these samples.
 - (xvi) Hot-rolled 0.10 cm (0.040") gauge sheet after 100 hrs/ 644K (700°F) exposure also indicates no apparent degradation in tensile strength; however, a slight decrease (10-30%) in total plastic elongation was noted for many of the samples.
 - (xvii) Cold-rolled 0.10 cm (0.040") gauge sheet, which did not receive intermittent annealing treatments, indicated the largest response to 100 hrs/644K (700°F) exposure. Measured values of tensile yield and ultimate strength are observed to increase by as much as 70 MPa (approximately 10 ksi) after exposure. More significant, however, is the very sizable decrease in total plastic elongation measured for this material after exposure.
 - (xviii) The response of exposed, cold-rolled 0.10 cm (0.040")

gauge sheet, which did receive intermittent annealing treatments, is fairly similar to the aforementioned cold rolled variant. Tensile strength after 100 hrs/644K (700°F) exposure was observed to increase by as much as approximately 90 MPa (13 ksi); however, the decrease in ductility for sheet rolled from extrusion 92A022 does not appear to be as severely affected after exposure.

- (xix) The microstructure of the as-extruded rolling preform 92A022 is comprised of very fine, 50-80 nm $\text{Al}_{13}(\text{Fe},\text{V})_3\text{Si}$ dispersoids present in an Al-solid solution matrix. Grain (or sub-grain) size for this material is approximately 0.5 μm .
- (xx) Extrusion 92A024 exhibits a fairly comparable microstructure to that of extrusion 92A022; however, large regions of carbon (i.e., graphite) contamination were observed to be scattered throughout the material. The source of carbon contamination may be directly attributed to the graphite device added to the casting machine to shroud the melt puddle and ribbon surface with a dry, protective atmosphere during casting. Carbon flakes were also observed to be present in plate and sheet samples rolled from extrusion 92A024, and it is suggested that their presence may be a source for anomalously low tensile ductilities and percent reduction in cross-sectional area measured for this material.
- (xxi) TEM performed on hot-rolled 0.64 cm (0.25") gauge 92A022 plate and 0.22 cm (0.090") gauge sheet indicates a microstructure very comparable to that of the parent extrusion. Silicide particles in the hot-rolled 0.22 cm (0.090") gauge sheet that are associated with grain/sub-grain boundaries are slightly coarser than particles present within the grains.
- (xxii) Lower tensile ductilities measured for 0.10 cm (0.040")

gauge hot-rolled sheet may be attributed to a greater tendency to find coarser silicide particles present at grain/sub-grain boundaries as well as dislocation tangles associated with this boundaries. Coarsened silicide particles at boundaries were not observed for cold-rolled 0.10 cm (0.040") gauge sheet.

- (xxiii) Weak beam, dark field electron microscopy performed on cold-rolled 0.10 cm (0.040") gauge sheet clearly indicates dislocations associated with grain/sub-grain and particle boundaries. Moreover, dislocation tangles are notably absent from within the grains which is fairly typical for this material. A possible reason for the lack of tangles may simply be due to the fact that this material does not exhibit a large volume fraction of silicide particles present within the grains; hence, there are fewer obstacles to impede dislocation motion through the grains during cold deformation.
- (xxiv) TEM performed on cold-rolled 0.10 cm (0.040") gauge sheet which experienced intermittent annealing treatments during the rolling campaign tends to indicate the presence of coarser silicide particles at the grain/subgrain boundaries as well as apparent bands of silicide particles associated with these boundaries.
- (xxv) Energy dispersive X-ray spectroscopy (EDX), performed to assess the effect of TMP on the solute content present in the Al-solid solution matrix of hot- and cold-rolled plate and sheet samples, indicate that V and Fe levels measured in the Al-solid solution of cold rolled/annealed 0.10 cm (0.040") gauge sheet are comparable to levels measured in the matrix of extruded and hot-rolled 0.64 cm (0.25") plate.
- (xxvi) EDX data supports the hypothesis that the true "equilibrium" level of solute Si, V or Fe in rapidly solidified HTA 8009 is in actuality, multiple orders of

magnitude greater than the equilibrium solute levels reported in the literature for these elements in Al.

(xxvii) Some of the ductility trends as a function of gauge have been shown to be related to specimen geometry (J.D. Bryant, private communication). Total elongation may be related to the square of an effective specimen diameter because elongation is highly localized.

References

1. U.S. Air Force Contract F33615-85-R-5160, "900°F Aluminum-Base Materials Research", Awarded to the University of Virginia, 1985.
2. U.S. Air Force Contract F33615-87-R-3206, "Elevated Temperature Aluminum Program", Awarded to Lockheed - California Company, 1987.
3. Naval Air Development Center Contract N62269-88-C-0255, "Elevated Temperature Aluminum Base Alloys for Applications in Advanced Turbofan Jet Engines", Awarded to Allied-Signal Inc., January 1989.
4. E.Y. Ting and J.R. Kennedy, NASA Report No 181849, "Superplastic Forming and Diffusion Bonding of Rapidly Solidified, Dispersion Strengthened Aluminum Alloys for Elevated Temperature Structural Applications", 181-198 (1989).
5. D.J. Skinner, "The Physical Metallurgy of Dispersion Strengthened Al-Fe-V-Si Alloys", in Dispersion Strengthened Aluminum Alloys, Y.W. Kim and W.M. Griffith, eds., TMS, (1988).
6. P.S. Gilman, M.S. Zedalis, J.M. Peltier and S.K. Das, "Rapidly Solidified Aluminum-Transition Metal Alloys for Aerospace Applications", AIAA/AHS/ASEE Aircraft Design, Systems and Operations Conference, Atlanta, GA, Sept. 1988.
7. M.S. Zedalis and D.J. Skinner, "Young's Moduli of Al-Fe-X-Si Alloys and Al-Fe-V-Si-Base Metal Matrix Composites", in

- Lightweight Alloys for Aerospace Applications, eds., E.W. Lee, E.H. Chia and N.J. Kim, TMS, 335-344 (1989).
8. W.C. Porr, Y. Leng and R.P. Gangloff, "Elevated Temperature Fracture Toughness of P/M Al-Fe-V-Si", in Low Density, High Temperature P/M Alloys, TMS-AIME, Warrendale, PA, submitted (1990).
 9. K.S. Chan, "Evidence of Thin Sheet Toughening Mechanism in Al-Fe-X Alloys", Met. Trans., **20A**, 155-164 (1989).
 10. K.S. Chan, "Confirmation of Thin Sheet Toughening Mechanism and Anisotropic Fracture in Al-Fe-X Alloys", Met. Trans., **20A**, 2337-2344 (1989).
 11. D.J. Skinner, M.S. Zedalis and J.M. Peltier, "Anomalous Ductility Variation at Intermediate Temperatures in Rapidly Solidified Al-Base Alloys", in Lightweight Alloys for Aerospace Applications, eds., E.W. Lee, E.H. Chia and N.J. Kim, TMS, 71-78 (1989).
 12. A.I. Litvintsev and L.A. Arbuzova, Sov. P/M Met. Cer., **1**, 1 (1967).
 13. W.M. Mullins and B.L. Averbach, "The Electronic Structure of Anodized and Etched Aluminum Alloy Surfaces", Surf. Sci., **206**, 52 (1988).
 14. B.R. Strohmeier, Surf. and Interface Anal., "An ESCA Method for Determining the Oxide Thickness on Aluminum Alloys", **15**, 51 (1990).
 15. D.J. Skinner, K. Okazaki and C.M. Adam, "Physical Metallurgy and Mechanical Properties of Aluminum Alloys Containing Eight to Twelve Percent Iron", in Rapidly Solidified Powder Al Alloys, eds., M.E. Fine and E.A. Starke, ASTM, 211-236 (1986).
 16. C.M. Adam, V.R.V. Ramanan and D.J. Skinner, in Undercooled Alloy Phases, eds., E.W. Collings and C.C. Koch, TMS, 59 (1987).
 17. D.J. Skinner, V.R.V. Ramanan, M.S. Zedalis and N.J. Kim, "Stability of Quasicrystalline Phases in Al-Fe-V Alloys",

- Mat. Sci. Eng., **99**, 407-411 (1988).
18. M.S. Zedalis, V.R.V. Ramanan and D.J. Skinner, "Thermal Analysis of Rapidly Solidified Al-Fe-V Alloys, and SiCp Reinforced Al-Li-Cu-Mg-Zr Composites" in Thermal Analysis in Metallurgy, eds., R.D. Shull and A. Joshi, TMS, 279-295 (1992).
 19. D.J. Skinner, M.S. Zedalis and P.S. Gilman, "Effect of Strain Rate on Tensile Ductility for a Series of Dispersion Strengthened Aluminum-Based Alloys", Mat. Sci. & Eng., **A119**, 81-86 (1990).
 20. M. Zedalis, 1987 Fall TMS-AIME Meeting in Cincinnati, OH

Acknowledgements

The authors (M.S.Z & S.K.D) would gratefully like to acknowledge the members of AlliedSignal's High Performance Alloy Products Group for Manufacturing of HTA 8009 for the present program, especially P. Chipko, J.M. Peltier, E. Rainal, and J.D. Bryant. The expert assistance of W. Moore, W. Duncan and D. Timmons of Spectrulite Consortium Inc. and Kaiser Aluminum-CFT during the extrusion and rolling of HTA 8009, respectively, is also acknowledged. Finally, the authors would like to personally thank M. Rodriguez, P. Jeges, A. Townsend and R. Toscano of the Metals Laboratory as well as especially J. Marti and E. Leone of AlliedSignal's Analytical Laboratory for performing TEM, light microscopy and chemical analyses (XPS, EDS) on HTA 8009 ribbon and sheet samples.

Table 1a

EXTRUSION: 92A022 NOSE Temperature - 298K

Nos.	Spec. ID	Orient.	.2% Y.S. 0.5%/min (MPa)	U.T.S. 0.5%/min (MPa)	U.T.S. 5%/min (MPa)	% Elong.
1	T1	L	340.4	396.9	415.5	16.2
2	T2	L	343.8	396.2	413.5	17.8
3	T3	L	345.9	396.2	414.8	18.9
4	T4	L	345.9	392.7	409.3	15.0
5	M1	L	343.8	402.4	421.0	10.7
6	M2	L	347.9	401.7	418.9	8.7
7	M3	L	342.4	401.0	420.3	10.0
8	M1	T	350.7	414.8	433.4	7.8
9	M2	T	347.5	408.6	428.6	8.5
10	B1	T	343.1	410.6	427.2	8.3
11	B2	T	348.6	408.6	426.5	8.4
12	B3	T	346.6	408.6	427.9	9.8
13	B4	T	345.2	408.6	427.9	7.4

EXTRUSION: 92A022 TAIL Temperature - 298K

Nos.	Spec. ID	Orient.	.2% Y.S. 0.5%/min (MPa)	U.T.S. 0.5%/min (MPa)	U.T.S. 5%/min (MPa)	% Elong.
1	T1	L	306.6	354.1	372.5	15.1
2	T2	L	323.8	376.2	395.5	15.4
3	T3	L	322.4	375.5	395.5	16.6
4	T4	L	325.2	376.9	395.5	16.3
5	M1	L	332.8	383.8	402.4	18.1
6	M2	L	341.7	391.4	410.6	17.3
7	M3	L	359.0	392.6	418.2	17.2
8	M1	T	350.0	401.0	425.1	9.0
9	M2	T	351.4	406.5	427.2	9.6
10	B1	T	355.5	397.6	417.5	8.0
11	B2	T	359.0	397.6	418.2	8.2
12	B3	T	336.9	396.9	418.2	8.4
13	B4	T	338.3	398.2	419.6	9.7

Table 1b

EXTRUSION: 92A022 NOSE Temperature - 77°F

Nos.	Spec. ID	Orient.	2% Y.S. 0.5% min (ksi)	U.T.S. 0.5%/min (ksi)	U.T.S. 5%/min (ksi)	% Elong.
1	T1	L	49.4	57.6	60.3	16.2
2	T2	L	49.9	57.5	60.0	17.8
3	T3	L	50.2	57.5	60.2	18.9
4	T4	L	50.2	57.0	59.4	15.0
5	M1	L	49.9	58.4	61.1	10.7
6	M2	L	50.5	58.3	60.8	8.7
7	M3	L	49.7	58.2	61.0	10.0
8	M1	T	50.9	60.2	62.9	7.8
9	M2	T	50.4	59.3	62.2	8.5
10	B1	T	49.8	59.6	62.0	8.3
11	B2	T	50.6	59.3	61.9	8.4
12	B3	T	50.3	59.3	62.4	9.8
13	B4	T	50.1	59.3	62.1	7.4

EXTRUSION: 92A022 TAIL Temperature - 77°F

Nos.	Spec. ID	Orient.	2% Y.S. 0.5% min (ksi)	U.T.S. 0.5%/min (ksi)	U.T.S. 5%/min (ksi)	% Elong.
1	T1	L	44.5	51.4	54.1	15.1
2	T2	L	47.0	54.6	57.4	15.4
3	T3	L	46.8	54.5	57.4	16.6
4	T4	L	47.2	54.7	57.4	16.3
5	M1	L	48.3	55.7	58.4	18.1
6	M2	L	49.6	56.8	59.6	17.3
7	M3	L	52.1	57.7	60.7	17.2
8	M1	T	50.8	58.2	61.7	9.0
9	M2	T	51.0	59.0	62.0	9.6
10	B1	T	48.7	57.7	60.6	8.0
11	B2	T	49.2	57.7	60.7	8.2
12	B3	T	48.9	57.6	60.7	8.4
13	B4	T	49.1	57.8	60.9	9.7

Table 1a (cont.)

EXTRUSION: 92A022 NOSE Temperature - 505K

Nos.	Spec. ID	Orient.	.2% Y.S. 0.5 %/min (MPa)	U.T.S. 0.5%/min (MPa)	U.T.S. 5%/min (MPa)	% Elong.
1	T5	L	249.4	262.5	283.9	13.5
2	T6	L	252.2	266.6	285.2	12.1
3	T7	L	256.3	270.1	291.4	10.3
4	T8	L	253.6	270.1	292.1	10.4
5	M4	L	251.5	268.7	290.8	13.6
6	M5	L	257.7	279.0	300.4	7.4
7	M6	L	257.0	274.2	295.0	7.2
8	M3	T	250.8	270.8	292.1	3.3
9	M4	T	251.5	270.8	292.1	4.0
10	B5	T	254.2	273.5	296.3	4.8
11	B6	T	250.1	271.5	293.5	6.1
12	B7	T	250.8	270.8	293.5	5.2
13	B8	T	250.8	274.2	296.3	5.8

EXTRUSION: 92A022 TAIL Temperature - 505K

Nos.	Spec. ID	Orient.	.2% Y.S. 0.5 %/min (MPa)	U.T.S. 0.5%/min (MPa)	U.T.S. 5%/min (MPa)	% Elong.
1	T5	L	233.0	246.0	266.6	11.3
2	T6	L	236.3	248.7	268.7	14.0
3	T7	L	232.2	245.3	266.0	14.6
4	T8	L	237.0	250.8	271.5	16.1
5	M4	L	261.8	272.2	293.5	9.0
6	M5	L	255.6	265.3	283.9	10.8
7	M6	L	256.13	268.7	289.4	14.0
8	M3	T	260.4	280.4	302.5	6.3
9	M4	T	NM	NM	NM	NM
10	B5	T	234.9	259.1	281.8	8.0
11	B6	T	242.5	262.5	284.6	6.9
12	B7	T	237.7	259.1	279.7	7.1
13	B8	T	241.8	261.1	283.2	9.3

Table 1b (cont.)

EXTRUSION: 92A022 NOSE Temperature - 450°F

Nos.	Spec. ID	Orient.	2% Y.S. 0.5 %/min (ksi)	U.T.S. 0.5%/min (ksi)	U.T.S. 5%/min (ksi)	% Elong.
1	T5	L	36.2	38.1	41.2	13.5
2	T6	L	36.6	38.7	41.4	12.1
3	T7	L	37.2	39.2	42.3	10.3
4	T8	L	36.8	39.2	42.4	10.4
5	M4	L	36.5	39.0	42.2	13.6
6	M5	L	37.4	40.5	43.6	7.4
7	M6	L	37.3	39.8	42.9	7.2
8	M3	T	36.4	39.3	42.4	3.3
9	M4	T	36.5	39.3	42.4	4.0
10	B5	T	36.9	39.7	43.0	4.8
11	B6	T	36.3	39.4	42.6	6.1
12	B7	T	36.4	39.3	42.6	5.2
13	B8	T	36.4	39.8	43.0	5.8

EXTRUSION: 92A022 TAIL Temperature - 450°F

Nos.	Spec. ID	Orient.	2% Y.S. 0.5 %/min (ksi)	U.T.S. 0.5%/min (ksi)	U.T.S. 5%/min (ksi)	% Elong.
1	T5	L	33.9	35.7	38.7	11.3
2	T6	L	34.3	36.1	39.0	14.0
3	T7	L	33.7	35.6	38.6	14.6
4	T8	L	34.4	36.4	39.4	16.1
5	M4	L	38.0	39.5	42.6	9.0
6	M5	L	37.1	38.5	41.2	10.8
7	M6	L	37.2	39.0	42.0	14.0
8	M3	T	37.8	40.7	43.9	6.3
9	M4	T	NM	NM	NM	NM
10	B5	T	34.1	37.6	40.9	8.0
11	B6	T	35.2	38.1	41.3	6.9
12	B7	T	34.5	37.6	40.6	7.1
13	B8	T	35.1	37.9	41.1	9.3

NM - Not Measured

Table 1a (cont.)

EXTRUSION: 92A024 NOSE Temperature - 298K

Nos.	Spec. ID	Orient.	.2% Y.S. 0.5%/min (MPa)	U.T.S. 0.5%/min (MPa)	U.T.S. 5%/min (MPa)	% Elong.
1	T1	L	336.9	385.8	403.8	13.7
2	T2	L	334.2	383.1	403.1	13.8
3	T3	L	331.4	382.4	402.4	14.3
4	T4	L	328.7	378.3	398.2	14.3
5	M1	L	335.5	388.6	407.9	14.7
6	M2	L	334.2	386.5	406.5	15.0
7	M3	L	331.4	381.0	401.0	14.4
8	M1	T	354.8	408.6	428.6	8.7
9	M2	T	352.1	405.8	427.2	7.1
10	B1	T	361.7	413.4	435.4	10.8
11	B2	T	367.2	416.2	434.8	14.5
12	B3	T	357.6	413.4	434.8	13.3
13	B4	T	362.4	413.4	434.8	12.2

EXTRUSION: 92A024 TAIL Temperature - 298K

Nos.	Spec. ID	Orient.	.2% Y.S. 5%/min (MPa)	U.T.S. 5%/min (MPa)	U.T.S. 5%/min (MPa)	% Elong.
1	T1	L	334.9	383.8	403.1	12.8
2	T2	L	332.1	382.1	403.8	21.2
3	T3	L	339.0	383.8	402.4	18.6
4	T4	L	332.1	380.3	399.6	20.7
5	M1	L	334.9	381.7	401.0	19.5
6	M2	L	339.7	392.7	411.3	16.8
7	M3	L	355.5	394.8	414.8	14.8
8	M1	T	350.0	406.5	427.9	9.0
9	M2	T	352.8	410.0	427.9	6.7
10	B1	T	332.8	395.5	414.1	8.2
11	B2	T	337.6	396.2	418.2	7.6
12	B3	T	332.8	392.7	414.1	8.0
13	B4	T	356.9	395.5	413.4	7.0

Table 1b (cont.)

EXTRUSION: 92A024 NOSE Temperature- 77°F

Nos.	Spec. ID	Orient.	2% Y.S. 0.5%/min (ksi)	U.T.S. 0.5%/min (ksi)	U.T.S. 5%/min (ksi)	% Elong.
1	T1	L	48.9	56.0	58.6	13.7
2	T2	L	48.5	55.6	58.5	13.8
3	T3	L	48.1	55.5	58.4	14.3
4	T4	L	47.7	54.9	57.8	14.3
5	M1	L	48.7	56.4	59.2	14.7
6	M2	L	48.5	56.1	59.0	15.0
7	M3	L	48.1	55.3	58.2	14.4
8	M1	T	51.5	59.3	62.2	8.7
9	M2	T	51.1	58.9	62.0	7.1
10	B1	T	52.5	60.0	63.2	10.8
11	B2	T	53.3	60.4	63.1	14.5
12	B3	T	51.9	60.0	63.1	13.3
13	B4	T	52.6	60.0	63.1	12.2

EXTRUSION: 92A024 TAIL Temperature - 77°F

Nos.	Spec. ID	Orient.	2% Y.S. 5%/min (ksi)	U.T.S. 5%/min (ksi)	U.T.S. 5%/min (ksi)	% Elong.
1	T1	L	48.6	55.7	58.5	12.8
2	T2	L	48.2	55.6	58.6	21.2
3	T3	L	49.2	55.7	58.4	18.6
4	T4	L	48.2	55.2	58.0	20.7
5	M1	L	48.6	55.4	58.2	19.5
6	M2	L	49.3	57.0	59.7	16.8
7	M3	L	51.6	57.3	60.2	14.8
8	M1	T	50.8	59.0	62.1	9.0
9	M2	T	51.2	59.5	62.1	6.7
10	B1	T	48.3	57.4	60.1	8.2
11	B2	T	49.0	57.5	60.7	7.6
12	B3	T	48.3	57.0	60.1	8.0
13	B4	T	48.9	57.4	60.0	7.0

Table 1a (cont.)

EXTRUSION: 92A024 NOSE Temperature - 505K

Nos.	Spec. ID	Orient.	.2% Y.S. 0.5 %/min (MPa)	U.T.S. 0.5%/min (MPa)	U.T.S. 5%/min (MPa)	% Elong.
1	T5	L	234.9	246.7	267.3	10.1
2	T6	L	233.6	245.3	266.6	14.2
3	T7	L	232.9	246.7	267.3	15.2
4	T8	L	234.3	249.4	270.8	13.9
5	M4	L	230.1	263.2	263.2	10.4
6	M5	L	236.3	250.1	267.3	7.7
7	M6	L	237.7	272.8	272.8	10.1
8	M3	T	249.4	266.6	288.0	4.0
9	M4	T	248.7	266.6	288.0	3.7
10	B5	T	252.9	267.3	289.4	9.1
11	B6	T	252.9	268.0	288.7	9.1
12	B7	T	253.6	268.0	290.2	6.0
13	B8	T	272.8	273.5	296.3	7.0

EXTRUSION: 92A024 TAIL Temperature - 505K

Nos.	Spec. ID	Orient.	.2% Y.S. 0.5%/min (MPa)	U.T.S. 0.5%/min (MPa)	U.T.S. 5%/min (MPa)	% Elong.
1	T5	L	237.0	252.2	272.8	14.5
2	T6	L	235.6	251.5	272.8	13.2
3	T7	L	237.7	250.8	271.5	14.2
4	T8	L	238.4	250.8	271.5	13.3
5	M4	L	261.1	271.5	293.5	10.4
6	M5	L	247.4	259.8	279.0	11.3
7	M6	L	239.8	252.9	272.8	14.2
8	M3	T	250.1	274.2	294.9	5.1
9	M4	T	254.2	275.6	298.3	6.5
10	B5	T	249.3	294.2	294.2	5.9
11	B6	T	245.3	267.3	286.6	8.1
12	B7	T	248.7	291.4	291.4	7.0
13	B7	T	246.7	266.0	289.4	9.0

Table 1b (cont.)

EXTRUSION: 92A024 NOSE **Temperature - 450°F**

Nos.	Spec. ID	Orient.	2% Y.S. 0.5 %/min (ksi)	U.T.S. 0.5%/min (ksi)	U.T.S. 5%/min (ksi)	% Elong.
1	T5	L	34.1	35.8	38.8	10.1
2	T6	L	33.9	35.6	38.7	14.2
3	T7	L	33.8	35.8	38.8	15.2
4	T8	L	34.0	36.2	39.3	13.9
5	M4	L	33.4	38.2	38.2	10.4
6	M5	L	34.3	36.3	38.8	7.7
7	M6	L	34.5	39.6	39.6	10.1
8	M3	T	36.2	38.7	41.8	4.0
9	M4	T	36.1	38.7	41.8	3.7
10	B5	T	36.7	38.8	42.0	9.1
11	B6	T	36.7	38.9	41.9	9.1
12	B7	T	36.8	38.9	42.1	6.0
13	B8	T	39.6	39.7	43.0	7.0

EXTRUSION: 92A024 TAIL **Temperature - 450°F**

Nos.	Spec. ID	Orient.	2% Y.S. 0.5%/min (ksi)	U.T.S. 0.5%/min (ksi)	U.T.S. 5%/min (ksi)	% Elong.
1	T5	L	34.4	36.6	39.6	14.5
2	T6	L	34.2	36.5	39.6	13.2
3	T7	L	34.5	36.4	39.4	14.2
4	T8	L	34.6	36.4	39.4	13.3
5	M4	L	37.9	39.4	42.6	10.4
6	M5	L	35.9	37.7	40.5	11.3
7	M6	L	34.8	36.7	39.6	14.2
8	M3	T	36.3	39.8	42.8	5.1
9	M4	T	36.9	40.0	43.3	6.5
10	B5	T	36.2	42.7	42.7	5.9
11	B6	T	35.6	38.8	41.6	8.1
12	B7	T	36.1	42.3	42.3	7.0
12	B7	T	35.8	38.6	42.0	9.0

Table 2

MATERIAL SUPPLIED TO THE UVA FOR TESTING

Casting Modification A

<u>ID</u>	<u>Dimensions (cm)</u>	<u>Comments</u>
92A022-1C	0.63 x 36.80 x 88.90	Hot, Cross Rolled
92A022-1A	0.63 x 22.90 x 139.70	Hot, Straight Rolled
92A022-2A	0.26 x 35.60 x 114.30	Hot, Cross Rolled
92A022-2A	0.25 x 35.60 x 162.60	Hot, Cross Rolled
92A022-2B	0.26 x 22.90 x 167.60	Hot, Straight Rolled
92A022-2B	0.26 x 21.60 x 241.30	Hot, Straight Rolled
92A022-2C1	0.07 x 21.60 x 198.10	Hot, Straight Rolled
92A022-2C1	0.07 x 21.60 x 223.50	Hot, Straight Rolled
92A022-1B1	0.10 x 35.60 x 203.20	Hot, Cross Rolled
92A022-2C2	0.10 x 10.20 x 245.10	Cold, Straight Rolled
92A022-1B2	0.10 x 34.30 x 207.00	Cold Cross Rolled
92A022-2C3	0.10 x 17.10 x 124.50	Cold/Anneal, Straight Roll
92A022-2C3	0.10 x 15.90 x 124.50	Cold/Anneal, Straight Roll
92A022-1B3	0.10 x 35.60 x 204.50	Cold/Anneal, Cross Roll

Table 4a

Sample ID#	Temp (K)	Orient.	0.2% Y.S. (MPa)	U.T.S. 0.5% /min. (Mpa)	U.T.S. 5% /min. (MPa)	Elong. (%)	% R.A.
92A022-1C HOT CROSS ROLLED							
0.64 cm	298	L	381.0	413.9	427.5	18.4	48.4
	298	T	376.9	407.5	426.1	19.6	**
	422	L	295.6	342.8	359.0	8.6	32.8
	422	T	271.1	335.2	352.1	7.8	**
	505	L	246.7	266.2	293.6	16.2	27.6
	505	T	241.1	280.4	292.9	11.6	**
	589	L	155.2	171.4	197.9	25.8	25.1
	589	T	129.8	167.8	193.8	25.2	**
	298E*	L	403.8	427.9	447.9	14.0	48.1
	298E*	T	380.3	412.0	432.0	14.1	**
92A022-1A HOT STRAIGHT ROLLED							
0.64 cm	298	L	421.0	431.7	445.8	13.0	**
	298	T	396.2	421.0	433.0	11.6	**
	422	L	347.9	350.7	362.1	7.8	**
	422	T	319.0	347.9	361.7	6.5	**
	505	L	163.2	292.0	305.4	14.3	**
	505	T	241.2	267.0	294.8	10.7	**
	589	L	162.6	174.4	201.9	28.7	**
	589	T	155.4	190.0	203.5	18.3	**
	298E*	L	411.3	449.9	460.9	11.5	**
	298E*	T	401.0	429.9	441.0	9.7	**
92A022-2A HOT CROSS ROLLED							
0.25 cm	298	L	378.3	431.3	448.5	9.7	38.0
	298	T	372.1	408.2	427.5	13.5	**
	422	L	289.7	346.9	366.5	6.9	31.3
	422	T	291.4	338.6	357.9	8.3	**
	505	L	208.8	274.4	302.9	13.2	34.3
	505	T	130.1	255.0	284.1	14.6	**
	589	L	157.6	172.3	201.2	25.8	26.7
	589	T	156.5	175.1	203.9	21.3	**
	298E*	L	396.9	436.1	457.5	11.3	53.5
	298E*	T	392.7	443.0	453.4	7.6	**
92A022-2B HOT STRAIGHT ROLLED							
0.25 cm	298	L	34.4	438.7	457.3	10.1	**
	298	T	81.9	425.3	435.2	9.6	**
	422	L	325.6	347.9	364.5	6.4	**
	422	T	330.0	346.9	363.8	5.3	**
	505	L	243.9	256.7	285.5	16.7	**
	505	T	206.4	275.4	289.5	9.6	**
	589	L	162.1	173.9	202.0	26.3	**
	589	T	157.5	174.5	203.5	16.0	**
	298E*	L	394.1	434.8	450.6	9.3	**
	298E*	T	382.4	428.6	449.2	7.7	**

* Samples tested at 298K after 644K for 100 hrs. exposure

** Not Measured

Table 3

MATERIAL SUPPLIED TO THE UVA FOR TESTING

Casting Modification B

<u>ID</u>	<u>Dimensions (cm)</u>	<u>Comments</u>
92A024-1C	0.64 x 29.20 x 78.70	Hot, Cross Rolled
92A024-1A	0.64 x 23.50 x 83.80	Hot, Straight Rolled
92A024-1B	0.27 x 23.50 x 108.00	Hot, Straight Rolled
92A024-1B	0.27 x 23.50 x 185.40	Hot, Straight Rolled
92A024-1D	0.22 x 27.90 x 121.30	Hot, Cross Rolled
92A024-1D	0.22 x 27.90 x 182.90	Hot, Cross Rolled
92A024-2A1	0.08 x 24.10 x 125.70	Hot, Straight Rolled
92A024-2A1	0.08 x 25.40 x 73.70	Hot, Straight Rolled
92A024-2B1	0.10 x 29.80 x 175.30	Hot, Cross Rolled
92A024-2A2	0.10 x 10.10 x 160.00	Cold, Straight Rolled
92A024-2A2	0.09 x 10.80 x 80.00	Cold, Straight Rolled
92A024-2B2	0.10 x 26.70 x 171.50	Cold, Cross Rolled
92A024-2A3	0.09 x 15.20 x 63.90	Cold/Anneal, Straight Rolled
92A024-2B3	0.10 x 27.30 x 40.60	Cold/Anneal, Cross Rolled
92A024-2B3	0.11 x 27.30 x 177.80	Cold/Anneal, Cross Rolled

Table 4b

Sample ID#	Temp (°F)	Orient.	0.2% Y.S. (ksi)	U.T.S. 0.5% /min. (ksi)	U.T.S. 5% /min. (ksi)	Elong. (%)	% R.A.
92A022-1C HOT CROSS ROLLED							
0.25" Gauge	77	L	55.3	60.1	62.1	18.4	48.4
		T	54.7	59.2	61.9	19.6	**
	300	L	42.9	49.8	52.1	8.6	32.8
		T	39.4	48.7	51.1	7.8	**
	450	L	35.8	38.6	42.6	16.2	27.6
		T	35.0	40.7	42.5	11.6	**
	600	L	22.5	24.9	28.7	25.8	25.1
		T	18.8	24.4	28.1	25.2	**
	77E*	L	58.6	62.1	65.0	14.0	48.1
	77E*	T	55.2	59.8	62.7	14.1	**
92A022-1A HOT STRAIGHT ROLLED							
0.25" Gauge		L	61.1	62.7	64.7	13.0	**
	77	T	57.5	61.1	62.9	11.6	**
		L	50.5	50.9	52.6	7.8	**
	300	T	46.3	50.5	52.5	6.5	**
		L	23.7	42.4	44.3	14.3	**
	450	T	35.0	38.8	42.8	10.7	**
		L	23.6	25.3	29.3	28.7	**
	600	T	22.6	27.6	29.5	18.3	**
		L	59.7	65.3	66.9	11.5	**
	77E*	T	58.2	62.4	64.0	9.7	**
92A022-2A HOT CROSS ROLLED							
0.10" Gauge	77	L	54.9	62.6	65.1	9.7	38.0
	77	T	54.0	59.3	62.1	13.5	**
	300	L	42.1	50.4	53.2	6.9	31.3
	300	T	42.3	49.2	52.0	8.3	**
	450	L	30.3	39.8	44.0	13.2	34.3
	450	T	18.9	37.0	41.2	14.6	**
	600	L	22.9	25.0	29.2	25.8	26.7
	600	T	22.7	25.4	29.6	21.3	**
	77E*	L	57.6	63.3	66.4	11.3	53.5
	77E*	T	57.0	64.3	65.8	7.6	**
92A022-2B HOT STRAIGHT ROLLED							
0.10" Gauge	77	L	59.7	63.7	66.4	10.1	**
	77	T	58.6	61.7	63.2	9.6	**
	300	L	47.3	50.5	52.9	6.4	**
	300	T	47.9	50.4	52.8	5.3	**
	450	L	35.4	37.3	41.4	16.7	**
	450	T	30.0	40.0	42.0	9.6	**
	600	L	23.5	25.2	29.3	26.3	**
	600	T	22.9	25.3	29.5	16.0	**
	77E*	L	57.2	63.1	65.4	9.3	**
	77E*	T	55.5	62.2	65.2	7.7	**

* Samples tested at 77 °F after 700 °F for 100 hrs. exposure

** Not Measured

Table 5a

Sample ID#	Temp (K)	Orient.	0.2% Y.S. (MPa)	U.T.S. 0.5% /min. (MPa)	U.T.S. 5% /min. (MPa)	Elong. (%)	% R.A.
92A022-1B1 HOT CROSS ROLLED							
0.10 cm	298	L	418.9	436.1	448.2	10.2	44.3
	298	T	397.2	434.8	459.2	7.0	**
	422	L	272.8	359.3	377.6	2.1	37.6
	422	T	306.9	361.7	379.6	2.7	**
	505	L	258.2	267.2	295.4	10.8	30.4
	505	T	259.9	271.1	301.9	9.4	**
	589	L	128.9	156.3	182.5	23.9	27.3
	589	T	129.5	159.2	185.3	13.1	**
	298E*	L	370.0	441.6	453.4	5.7	51.3
	298E*	T	401.0	438.9	461.6	5.6	**
92A022-2C1 HOT STRAIGHT ROLLED							
0.10 cm	298	L	395.1	438.9	460.3	7.3	**
	298	T	384.1	448.5	481.6	6.6	**
	422	L	311.1	354.1	369.6	2.7	**
	422	T	313.8	369.6	390.0	2.2	**
	505	L	143.0	257.1	284.3	12.0	**
	505	T	230.7	250.8	278.6	12.2	**
	589	L	79.2	189.2	205.6	20.6	**
	589	T	128.4	169.1	201.0	16.8	**
	298E*	L	360.3	449.9	460.9	7.9	**
	298E*	T	430.6	456.1	476.8	4.5	**
92A022-1B2 COLD CROSS ROLLED							
0.10 cm	298	L	381.4	408.2	435.4	18.9	28.8
	298	T	345.5	405.1	431.3	17.1	**
	422	L	263.9	345.2	370.3	9.2	26.5
	422	T	256.3	343.8	369.3	10.1	**
	505	L	204.8	253.8	287.3	15.7	21.2
	505	T	186.1	246.7	280.1	15.2	**
	589	L	111.1	189.6	189.6	25.1	22.5
	589	T	126.1	156.1	192.0	25.4	**
	298E*	L	414.8	449.2	476.8	3.0	27.4
	298E*	T	421.0	476.8	491.3	5.7	**
92A022-2C2 COLD STRAIGHT ROLLED							
0.10 cm	298	L	376.2	397.2	423.7	15.5	**
	298	T	354.1	396.5	423.7	15.9	**
	422	L	271.1	338.6	365.2	8.3	**
	422	T	251.1	341.1	365.9	7.3	**
	505	L	210.9	248.0	280.8	15.9	**
	505	T	183.5	251.8	286.3	12.6	**
	589	L	110.2	154.3	188.4	25.9	**
	589	T	108.0	166.9	183.1	19.9	**
	298E*	L	435.4	459.6	487.1	6.6	**
	298E*	T	425.1	483.7	497.5	5.1	**

* Samples tested at 298K after 644K for 100 hrs. exposure

** Not Measured

Table 5b

Sample ID#	Temp (F)	Orient.	0.2% Y.S. (ksi)	U.T.S. 0.5% /min. (ksi)	U.T.S. 5% /min. (ksi)	Elong. (%)	% R.A.
92A022-1B1 HOT CROSS ROLLED							
0.040" Gauge	77	L	60.8	63.3	65.1	10.2	44.3
	77	T	57.7	63.1	66.7	7.0	**
	300	L	39.6	52.2	54.8	2.1	37.6
	300	T	44.6	52.5	55.1	2.7	**
	450	L	37.5	38.8	42.9	10.8	30.4
	450	T	37.7	39.4	43.8	9.4	**
	600	L	18.7	22.7	26.5	23.9	27.3
	600	T	18.8	23.1	26.9	13.1	**
	77E*	L	53.7	64.1	65.8	5.7	51.3
	77E*	T	58.2	63.7	67.0	5.6	**
92A022-2C1 HOT STRAIGHT ROLLED							
0.030" Gauge	77	L	57.4	63.7	66.8	7.3	**
	77	T	55.8	65.1	69.9	6.6	**
	300	L	45.2	51.4	53.7	2.7	**
	300	T	45.6	53.7	56.6	2.2	**
	450	L	20.8	37.3	41.3	12.0	**
	450	T	33.5	36.4	40.4	12.2	**
	600	L	11.5	27.5	29.8	20.6	**
	600	T	18.6	24.6	29.2	16.8	**
	77E*	L	52.3	65.3	66.9	7.9	**
	77E*	T	62.5	66.2	69.2	4.5	**
92A022-1B2 COLD CROSS ROLLED							
0.040" Gauge	77	L	55.4	59.3	63.2	18.9	28.8
	77	T	50.2	58.8	62.6	17.1	**
	300	L	38.3	50.1	53.8	9.2	26.5
	300	T	37.2	49.9	53.6	10.1	**
	450	L	29.7	36.8	41.7	15.7	21.2
	450	T	27.0	35.8	40.7	15.2	**
	600	L	16.1	27.5	27.5	25.1	22.5
	600	T	18.3	22.7	27.9	25.4	**
	77E*	L	60.2	65.2	69.2	3.0	27.4
	77E*	T	61.1	69.2	71.3	5.7	**
92A022-2C2 COLD STRAIGHT ROLLED							
0.040" Gauge	77	L	54.6	57.7	61.5	15.5	**
	77	T	51.4	57.6	61.5	15.9	**
	300	L	39.4	49.2	53.0	8.3	**
	300	T	36.5	49.5	53.1	7.3	**
	450	L	30.6	36.0	40.8	15.9	**
	450	T	26.6	36.5	41.6	12.6	**
	600	L	16.0	22.4	27.3	25.9	**
	600	T	15.7	24.2	26.6	19.9	**
	77E*	L	63.2	66.7	70.7	6.6	**
	77E*	T	61.7	70.2	72.2	5.1	**

* Samples tested at 77° F after 700° F for 100 hrs. exposure

** Not Measured

Table 6a

Sample ID#	Temp (K)	Orient.	0.2% Y.S. (MPa)	U.T.S. 0.5% /min. (MPa)	U.T.S. 5% /min. (MPa)	Elong. (%)	% R.A.
92A022-1B3 COLD CROSS ROLLED/ANNEALED							
0.10 cm	298	L	362.1	393.8	419.6	15.9	48.1
	298	T	346.2	386.5	415.1	15.8	**
	422	L	284.6	325.2	349.3	7.9	31.8
	422	T	244.6	328.3	352.8	8.0	**
	505	L	197.1	226.3	259.1	16.9	26.1
	505	T	201.7	243.2	276.4	14.1	**
	589	L	117.8	171.1	188.6	21.2	26.2
	589	T	111.3	159.2	193.7	24.4	**
	298E*	L	394.8	482.3	501.6	8.2	41.8
	298E*	T	422.4	467.8	481.6	4.9	**
92A022-2C3 COLD STRAIGHT ROLLED/ANNEALED							
0.10 cm	298	L	374.8	387.9	412.0	17.4	**
	298	T	335.5	388.6	415.1	16.6	**
	422	L	298.2	340.1	365.3	5.9	**
	422	T	280.8	348.0	362.1	6.2	**
	505	L	210.8	250.0	281.6	15.3	**
	505	T	205.3	249.4	283.9	13.4	**
	589	L	107.6	149.7	183.8	25.1	**
	589	T	109.6	155.8	189.5	23.2	**
	298E*	L	384.5	459.6	482.3	8.8	**
	298E*	T	413.4	480.2	493.3	4.8	**

* Samples tested at 298K after 644K for 100 hrs. exposure

** Not Measured

Table 6b

Sample ID#	Temp (°F)	Orient.	0.2% Y.S. (ksi)	U.T.S. 0.5% /min. (ksi)	U.T.S. 5% /min. (ksi)	Elong. (%)	% R.A.
92A022-1B3 COLD CROSS ROLLED/ANNEALED							
0.040" Gauge	77	L	52.6	57.2	60.9	15.9	48.1
	77	T	50.3	56.1	60.3	15.8	**
	300	L	41.3	47.2	50.7	7.9	31.8
	300	T	35.5	47.7	51.2	8.0	**
	450	L	28.6	32.9	37.6	16.9	26.1
	450	T	29.3	35.3	40.1	14.1	**
	600	L	17.1	24.8	27.4	21.2	26.2
	600	T	16.2	23.1	28.1	24.4	**
	77E*	L	57.3	70.0	72.8	8.2	41.8
	77E*	T	61.3	67.9	69.9	4.9	**
92A022-2C3 COLD STRAIGHT ROLLED/ANNEALED							
0.040" Gauge	77	L	54.4	56.3	59.8	17.4	**
	77	T	48.7	56.4	60.3	16.6	**
	300	L	43.3	49.4	53.0	5.9	**
	300	T	40.8	50.5	52.6	6.2	**
	450	L	30.6	36.3	40.9	15.3	**
	450	T	29.8	36.2	41.2	13.4	**
	600	L	15.6	21.7	26.7	25.1	**
	600	T	15.9	22.6	27.5	23.2	**
	77E*	L	55.8	66.7	70.0	8.8	**
	77E*	T	60.0	69.7	71.6	4.8	**

* Samples tested at 77° F after 700° F for 100 hrs. exposure

** Not Measured

Table 7a

Sample ID#	Temp (K)	Orient.	0.2% Y.S. (MPa)	U.T.S. 0.5% /min. (MPa)	U.T.S. 5% /min. (MPa)	Elong. (%)	% R.A.
92A024-1C HOT CROSS ROLLED							
0.64 cm	298	L	411.3	437.2	449.6	13.2	49.5
		T	411.0	423.7	443.0	13.8	**
422		L	328.9	354.1	372.1	7.4	28.7
		T	330.7	344.5	362.4	6.0	**
505		L	280.4	301.6	301.6	13.4	30.4
		T	277.9	289.9	303.6	12.5	**
589		L	178.5	201.3	214.7	22.8	31.0
		T	169.8	184.0	210.1	21.7	**
298E*		L	404.9	437.5	457.5	16.4	49.6
		T	409.7	438.2	458.9	11.3	**
92A024-1A HOT STRAIGHT ROLLED							
0.64 cm	298	L	407.9	437.9	456.5	16.6	**
		T	396.2	434.1	453.0	11.0	**
422		L	312.7	360.3	376.9	6.5	**
		T	321.9	350.4	367.9	7.9	**
505		L	265.9	273.8	301.6	13.2	**
		T	290.1	312.7	312.7	10.1	**
589		L	113.8	186.2	196.6	23.6	**
		T	162.8	183.6	210.5	20.9	**
298E*		L	414.2	434.8	454.4	15.1	**
		T	428.8	449.0	469.2	10.3	**
92A024-1D HOT CROSS ROLLED							
0.23 cm	298	L	408.6	429.2	456.8	8.9	44.6
		T	421.0	432.7	461.6	9.4	**
422		L	335.3	354.8	371.2	7.7	34.3
		T	308.7	351.4	365.2	8.9	**
505		L	207.5	280.4	308.2	13.0	32.2
		T	189.1	271.3	298.7	8.5	**
589		L	114.9	188.3	215.5	19.9	36.9
		T	172.5	201.8	215.9	20.9	**
298E*		L	404.2	443.7	465.1	10.3	35.1
		T	396.9	450.6	473.3	8.3	**
92A024-1B HOT STRAIGHT ROLLED							
0.23 cm	298	L	414.8	437.5	457.2	10.1	**
		T	404.8	442.3	459.2	8.2	**
422		L	327.3	355.0	369.9	4.9	**
		T	322.2	352.1	367.2	3.3	**
505		L	240.5	278.0	292.8	16.2	**
		T	242.6	286.3	315.5	9.5	**
589		L	169.9	204.8	219.9	22.7	**
		T	113.2	209.0	223.9	17.4	**
298E*		L	442.3	445.8	468.5	11.5	**
		T	435.5	461.6	473.3	13.1	**

* Samples tested at 298K after 644K for 100 hrs. exposure

** Not Measured

Table 7b

Sample ID#	Temp (°F)	Orient.	0.2% Y.S. (ksi)	U.T.S. 0.5% /min. (ksi)	U.T.S. 5% /min. (ksi)	Elong. (%)	% R.A.
92A024-1C HOT CROSS ROLLED							
0.25" Gauge	77	L	59.7	63.5	65.3	13.2	49.5
	77	T	59.7	61.5	64.3	13.8	**
	300	L	47.7	51.4	54.0	7.4	28.7
	300	T	48.0	50.0	52.6	6.0	**
	450	L	40.7	43.8	43.8	13.4	30.4
	450	T	40.3	42.1	44.1	12.5	**
	600	L	25.9	29.2	31.2	22.8	31.0
	600	T	24.6	26.7	30.5	21.7	**
77E*	L	58.8	63.5	66.4	16.4	49.6	
	T	59.5	63.6	66.6	11.3	**	
92A024-1A HOT STRAIGHT ROLLED							
0.25" Gauge	77	L	59.2	63.6	66.3	16.6	**
		T	57.5	63.0	65.8	11.0	**
	300	L	45.4	52.3	54.7	6.5	**
		T	46.7	50.9	53.4	7.9	**
	450	L	38.6	39.7	43.8	13.2	**
		T	42.1	45.4	45.4	10.1	**
	600	L	16.5	27.0	28.5	23.6	**
		T	23.6	26.7	30.6	20.9	**
77E*	L	60.1	63.1	66.0	15.1	**	
	T	62.2	65.2	68.1	10.3	**	
92A024-1D HOT CROSS ROLLED							
0.09" Gauge	77	L	59.3	62.3	66.3	8.9	44.6
		T	61.1	62.8	67.0	9.4	**
	300	L	48.7	51.5	53.9	7.7	34.3
		T	44.8	51.0	53.0	8.9	**
	450	L	30.1	40.7	44.7	13.0	32.2
		T	27.4	39.4	43.4	8.5	**
	600	L	16.7	27.3	31.3	19.9	36.9
		T	25.0	29.3	31.3	20.9	**
77E*	L	58.7	64.4	67.5	10.3	35.1	
	T	57.6	65.4	68.7	8.3	**	
92A024-1B HOT STRAIGHT ROLLED							
0.09" Gauge	77	L	60.2	63.5	66.4	10.1	**
		T	58.8	64.2	66.7	8.2	**
	300	L	47.5	51.5	53.7	4.9	**
		T	46.8	51.1	53.3	3.3	**
	450	L	34.9	40.4	42.5	16.2	**
		T	35.2	41.6	45.8	9.5	**
	600	L	24.7	29.7	31.9	22.7	**
		T	16.4	30.3	32.5	17.4	**
77E*	L	64.2	64.7	68.0	11.5	**	
	T	63.2	67.0	68.7	13.1	**	

* Samples tested at 77° F after 700° F for 100 hrs. exposure

** Not Measured

Table 8a

Sample ID#	Temp (K)	Orient.	0.2% Y.S. (MPa)	U.T.S. 0.5% /min. (MPa)	U.T.S. 5% /min. (MPa)	Elong. (%)	% R.A.
92A024-2B1 HOT CROSS ROLLED							
0.076 cm	298	L	360.7	442.0	463.4	7.7	45.7
		T	381.0	442.0	464.4	7.0	**
	422	L	334.9	370.0	379.6	2.2	26.9
		T	323.1	363.8	381.0	2.7	**
	505	L	158.3	268.5	296.2	8.7	27.9
		T	247.4	264.5	293.9	9.3	**
	589	L	151.1	196.3	227.9	22.2	34.4
		T	141.9	187.4	218.6	17.0	**
	298E*	L	386.5	427.9	449.2	4.6	28.9
		T	387.9	429.9	453.4	5.1	**
92A024-2A1 HOT STRAIGHT ROLLED							
0.10 cm	298	L	323.1	430.6	451.3	4.1	**
		T	376.2	439.2	479.5	3.9	**
	422	L	312.1	350.0	359.0	8.3	**
		T	321.8	362.4	369.3	11.0	**
	505	L	199.3	251.2	266.2	13.7	**
		T	217.0	249.3	280.0	6.2	**
	589	L	145.7	182.8	213.7	21.4	**
		T	147.9	198.8	215.5	26.0	**
	298E*	L	458.2	469.9	479.5	3.2	**
		T	454.1	468.5	479.5	2.8	**
92A024-2B2 COLD CROSS ROLLED							
0.10 cm	298	L	366.5	407.5	434.8	17.9	44.8
		T	357.9	404.8	430.6	12.2	**
	422	L	277.7	344.8	369.2	4.8	31.9
		T	281.1	343.8	369.7	4.6	**
	505	L	240.7	283.0	317.9	17.3	36.0
		T	212.8	261.5	295.4	17.1	**
	589	L	124.6	167.8	203.0	27.2	24.4
		T	143.4	192.6	209.9	24.9	**
	298E*	L	424.4	476.8	489.9	5.1	29.1
		T	434.1	480.2	493.3	4.8	**
2A024-2A2 COLD STRAIGHT ROLLED							
0.10 cm	298	L	354.8	424.4	424.4	16.7	**
		T	331.4	419.9	433.7	16.8	**
	422	L	291.4	353.5	373.4	6.8	**
		T	304.5	352.1	371.4	5.4	**
	505	L	224.6	251.7	287.2	12.8	**
		T	206.7	250.8	286.8	11.7	**
	589	L	132.3	174.2	208.1	22.3	**
		T	141.2	183.1	199.9	20.9	**
	298E*	L	429.9	485.1	500.9	5.2	**
		T	434.1	483.0	496.8	5.0	**

* Samples tested at 298K after 644K for 100 hrs. exposure

** Not Measured

Table 8b

Sample ID#	Temp (F)	Orient.	0.2% Y.S. (ksi)	U.T.S. 0.5% /min. (ksi)	U.T.S. 5% /min. (ksi)	Elong. (%)	% R.A.
92A024-2B1 HOT CROSS ROLLED							
0.03" Gauge	77	L	52.4	64.2	67.3	7.7	45.7
		T	55.3	64.2	67.4	7.0	**
	300	L	48.6	53.7	55.1	2.2	26.9
		T	46.9	52.8	55.3	2.7	**
	450	L	23.0	39.0	43.0	8.7	27.9
		T	35.9	38.4	42.7	9.3	**
	600	L	21.9	28.5	33.1	22.2	34.4
		T	20.6	27.2	31.7	17.0	**
	77E*	L	56.1	62.1	65.2	4.6	28.9
		T	56.3	62.4	65.8	5.1	**
92A024-2A1 HOT STRAIGHT ROLLED							
0.04" Gauge	77	L	46.9	62.5	65.5	4.1	**
		T	54.6	63.8	69.6	3.9	**
	300	L	45.3	50.8	52.1	8.3	**
		T	46.7	52.6	53.6	11.0	**
	450	L	28.9	36.5	38.6	13.7	**
		T	31.5	36.2	40.6	6.2	**
	600	L	21.2	26.5	31.0	21.4	**
		T	21.5	28.9	31.3	26.0	**
	77E*	L	66.5	68.2	69.6	3.2	**
		T	65.9	68.0	69.6	2.8	**
92A024-2B2 COLD CROSS ROLLED							
0.04" Gauge	77	L	53.2	59.2	63.1	17.9	44.8
		T	52.0	58.8	62.5	12.2	**
	300	L	40.3	50.1	53.6	4.8	31.4
		T	40.8	49.9	53.7	4.6	**
	450	L	34.9	41.1	46.1	17.3	36.1
		T	30.9	38.0	42.9	17.1	**
	600	L	18.1	24.4	29.5	27.2	24.4
		T	20.8	28.0	30.5	24.9	**
	77E*	L	61.6	69.2	71.1	5.1	21.1
		T	63.0	69.7	71.6	4.8	**
2A024-2A2 COLD STRAIGHT ROLLED							
0.04" Gauge	77	L	51.5	61.6	61.6	16.7	**
		T	48.1	61.0	63.0	16.8	**
	300	L	42.3	51.3	54.2	6.8	**
		T	44.2	51.1	53.9	5.4	**
	450	L	32.6	36.5	41.7	12.8	**
		T	30.0	36.4	41.6	11.7	**
	600	L	19.2	25.3	30.2	22.3	**
		T	20.5	26.6	29.0	20.9	**
	77E*	L	62.4	70.4	72.7	5.2	**
		T	63.0	70.1	72.1	5.0	**

* Samples tested at 77°F after 700°F for 100 hrs. exposure

** Not Measured

Table 9a

Sample ID#	Temp (K)	Orient.	0.2% Y.S. (MPa)	U.T.S. 0.5% /min. (MPa)	U.T.S. 5% /min. (MPa)	Elong. (%)	% R.A.
92A024-2B3 COLD CROSS ROLLED/ANNEALED							
0.10 cm	298	L	328.0	382.7	406.9	16.3	42.3
		T	321.8	384.1	405.5	13.8	**
	422	L	296.3	338.6	362.9	4.4	32.8
		T	301.8	338.8	364.1	4.4	**
	505	L	199.1	246.2	281.9	17.6	29.9
		T	185.8	246.6	279.4	16.7	**
	589	L	121.3	170.5	206.5	21.9	19.5
		T	119.3	169.6	205.7	20.1	**
	298E*	L	381.7	467.8	480.9	2.0	36.6
		T	411.3	475.4	493.3	2.3	**
92A024-2A3 COLD STRAIGHT ROLLED/ANNEALED							
0.10 cm	298	L	355.5	385.5	411.7	16.8	**
		T	359.0	388.3	407.9	14.0	**
	422	L	283.2	328.2	352.3	5.78	**
		T	293.5	316.8	340.5	5.94	**
	505	L	222.5	257.0	289.0	16.4	**
		T	207.4	243.0	276.7	11.3	**
	589	L	114.4	183.8	200.2	22.8	**
		T	117.8	166.7	200.4	21.2	**
	298E*	L	462.3	479.5	492.6	2.0	**
		T	443.0	486.4	498.1	3.1	**

* Samples tested at 298K after 644K for 100 hrs. exposure

** Not Measured

Table 9b

Sample ID#	Temp (F)	Orient.	0.2% Y.S. (ksi)	U.T.S. 0.5% /min. (ksi)	U.T.S. 5% /min. (ksi)	Elong. (%)	% R.A.
92A024-2B3 COLD CROSS ROLLED/ANNEALED							
0.040" Gauge	77	L	47.6	55.6	59.1	16.3	42.3
		T	46.7	55.8	58.9	13.8	**
	300	L	43.0	49.2	52.7	4.4	32.8
		T	43.8	49.2	52.9	4.4	**
	450	L	28.9	35.7	40.9	17.6	29.9
		T	27.0	35.8	40.6	16.7	**
	600	L	17.6	24.8	30.0	21.9	19.5
		T	17.3	24.6	29.9	20.1	**
	77E*	L	55.4	67.9	69.8	2.0	36.6
		T	59.7	69.0	71.6	2.3	**
92A024-2A3 COLD STRAIGHT ROLLED/ANNEALED							
0.040" Gauge	77	L	51.6	56.0	59.8	16.8	**
		T	52.1	56.4	59.2	14.0	**
	300	L	41.1	47.6	51.1	5.78	**
		T	42.6	46.0	49.4	5.94	**
	450	L	32.3	37.3	41.9	16.4	**
		T	30.1	35.3	40.2	11.3	**
	600	L	16.6	26.7	29.1	22.8	**
		T	17.1	24.2	29.1	21.2	**
	77E*	L	67.1	69.6	71.5	2.0	**
		T	64.3	70.6	72.3	3.1	**

* Samples tested at 77° F after 700 F for 100 hrs. exposure

** Not Measured

Table 10a

Sample ID#	Temp (K)	Orient.	U.T.S. 0.5% /min. (MPa)	U.T.S. 5% /min. (MPa)	U.T.S. 50% /min. (MPa)	Elong. 5% /min (%)	Elong. 50% /min (%)
92A024-1C HOT CROSS ROLLED							
0.64 cm	298	L	437.2	449.6	456.8	13.2	17.6
		T	423.7	443.0	465.8	13.8	17.6
	422	L	354.1	372.1	**	7.4	**
		T	344.5	362.4	**	6.0	**
	505	L	301.6	301.6	**	13.4	**
		T	289.9	303.6	**	12.5	**
	589	L	201.3	214.7	**	22.8	**
		T	184.0	210.1	**	21.7	**
	298E*	L	437.5	457.5	**	16.4	**
		T	438.2	458.9	**	11.3	**
92A024-1A HOT STRAIGHT ROLLED							
0.64 cm	298	L	437.9	456.5	456.8	16.6	21.9
		T	434.1	453.0	478.2	11.0	19.0
	422	L	360.3	376.9	**	6.5	**
		T	350.4	367.9	**	7.9	**
	505	L	273.8	301.6	**	13.2	**
		T	312.7	312.7	**	10.1	**
	589	L	186.2	196.6	**	23.6	**
		T	183.6	210.5	**	20.9	**
	298E*	L	434.8	454.4	**	15.1	**
		T	449.0	469.2	**	10.3	**
92A024-1D HOT CROSS ROLLED							
0.23 cm	298	L	429.2	456.8	494.7	8.9	11.7
		T	432.7	461.6	498.8	9.4	8.6
	422	L	354.8	371.2	**	7.7	**
		T	351.4	365.2	**	8.9	**
	505	L	280.4	308.2	**	13.0	**
		T	271.3	298.7	**	8.5	**
	589	L	188.3	215.5	**	19.9	**
		T	201.8	215.9	**	20.9	**
	298E*	L	443.7	465.1	**	10.3	**
		T	450.6	473.3	**	8.3	**
92A024-1B HOT STRAIGHT ROLLED							
0.23 cm	298	L	437.5	457.2	487.1	10.1	11.8
		T	442.3	459.2	482.3	8.2	10.2
	422	L	355.0	369.9	**	4.9	**
		T	352.1	367.2	**	3.3	**
	505	L	278.0	292.8	**	16.2	**
		T	286.3	315.5	**	9.5	**
	589	L	204.8	219.9	**	22.7	**
		T	209.0	223.9	**	17.4	**
	298E*	L	445.8	468.5	**	11.5	**
		T	461.6	473.3	**	13.1	**

* Samples tested at 298K after 644K for 100 hrs. exposure

** Not Measured

Table 10b

Sample ID#	Temp (F)	Orient.	U.T.S. 0.5% /min. (ksi)	U.T.S. 5% /min. (ksi)	U.T.S. 50% /min (ksi)	Elong. 5% /min (%)	Elong. 50% /min (%)
92A024-1C HOT CROSS ROLLED							
0.25" Gauge	77	L	63.5	65.3	66.3	13.2	17.6
	77	T	61.5	64.3	67.6	13.8	17.6
	300	L	51.4	54.0	**	7.4	**
	300	T	50.0	52.6	**	6.0	**
	450	L	43.8	43.8	**	13.4	**
	450	T	42.1	44.1	**	12.5	**
	600	L	29.2	31.2	**	22.8	**
	600	T	26.7	30.5	**	21.7	**
	77E*	L	63.5	66.4	**	16.4	**
		T	63.6	66.6	**	11.3	**
92A024-1A HOT STRAIGHT ROLLED							
0.25" Gauge	77	L	63.6	66.3	66.3	16.6	21.9
		T	63.0	65.8	69.4	11.0	19.0
	300	L	52.3	54.7	**	6.5	**
		T	50.9	53.4	**	7.9	**
	450	L	39.7	43.8	**	13.2	**
		T	45.4	45.4	**	10.1	**
	600	L	27.0	28.5	**	23.6	**
		T	26.7	30.6	**	20.9	**
	77E*	L	63.1	66.0	**	15.1	**
		T	65.2	68.1	**	10.3	**
92A024-1D HOT CROSS ROLLED							
0.09" Gauge	77	L	62.3	66.3	71.8	8.9	11.7
		T	62.8	67.0	72.4	9.4	8.6
	300	L	51.5	53.9	**	7.7	**
		T	51.0	53.0	**	8.9	**
	450	L	40.7	44.7	**	13.0	**
		T	39.4	43.4	**	8.5	**
	600	L	27.3	31.3	**	19.9	**
		T	29.3	31.3	**	20.9	**
	77E*	L	64.4	67.5	**	10.3	**
		T	65.4	68.7	**	8.3	**
92A024-1B HOT STRAIGHT ROLLED							
0.09" Gauge	77	L	63.5	66.4	70.7	10.1	11.8
		T	64.2	66.7	70.0	8.2	10.2
	300	L	51.5	53.7	**	4.9	**
		T	51.1	53.3	**	3.3	**
	450	L	40.4	42.5	**	16.2	**
		T	41.6	45.8	**	9.5	**
	600	L	29.7	31.9	**	22.7	**
		T	30.3	32.5	**	17.4	**
	77E*	L	64.7	68.0	**	11.5	**
		T	67.0	68.7	**	13.1	**

* Samples tested at 77° F after 700° F for 100 hrs. exposure

** Not Measured

Table 11a

Sample ID#	Temp (K)	Orient.	U.T.S. 0.5% /min. (MPa)	U.T.S. 5% /min. (MPa)	U.T.S. 50% /min. (MPa)	Elong. 5% /min (%)	Elong. 50% /min (%)
92A024-2B1 HOT CROSS ROLLED							
0.076 cm	298	L	442.0	463.4	429.2	7.7	13.0
		T	442.0	464.4	464.4	7.0	9.0
	422	L	370.0	379.6	**	2.2	**
		T	363.8	381.0	**	2.7	**
	505	L	268.5	296.2	**	8.7	**
		T	264.5	293.9	**	9.3	**
	589	L	196.3	227.9	**	22.2	**
		T	187.4	218.6	**	17.0	**
	298E*	L	427.9	449.2	**	4.6	**
		T	429.9	453.4	**	5.1	**
92A024-2A1 HOT STRAIGHT ROLLED							
0.10 cm	298	L	430.6	451.3	456.1	4.1	19
		T	439.2	479.5	438.9	3.9	39
	422	L	350.0	359.0	**	8.3	**
		T	362.4	369.3	**	11.0	**
	505	L	251.2	266.2	**	13.7	**
		T	249.3	280.0	**	6.2	**
	589	L	182.8	213.7	**	21.4	**
		T	198.8	215.5	**	26.0	**
	298E*	L	469.9	479.5	**	3.2	**
		T	468.5	479.5	**	2.8	**
92A024-2B2 COLD CROSS ROLLED							
0.10 cm	298	L	407.5	434.8	436.1	17.9	16.9
		T	404.8	430.6	467.8	12.2	13.0
	422	L	344.8	369.2	**	4.8	**
		T	343.8	369.7	**	4.6	**
	505	L	283.0	317.9	**	17.3	**
		T	261.5	295.4	**	17.1	**
	589	L	167.8	203.0	**	27.2	**
		T	192.6	209.9	**	24.9	**
	298E*	L	476.8	489.9	**	5.1	**
		T	480.2	493.3	**	4.8	**
2A024-2A2 COLD STRAIGHT ROLLED							
0.10 cm	298	L	424.4	424.4	436.8	16.7	17.0
		T	419.9	433.7	468.5	16.8	17.2
	422	L	353.5	373.4	**	6.8	**
		T	352.1	371.4	**	5.4	**
	505	L	251.7	287.2	**	12.8	**
		T	250.8	286.8	**	11.7	**
	589	L	174.2	208.1	**	22.3	**
		T	183.1	199.9	**	20.9	**
	298E*	L	485.1	500.9	**	5.2	**
		T	483.0	496.8	**	5.0	**

* Samples tested at 298K after 644K for 100 hrs. exposure

** Not Measured

Table 11b

Sample ID#	Temp (°F)	Orient.	U.T.S. 0.5% /min. (ksi)	U.T.S. 5% /min. (ksi)	U.T.S. 50% /min (ksi)	Elong. 5% /min (%)	Elong. 50% /min (%)
92A024-2B1 HOT CROSS ROLLED							
0.03" Gauge	77	L	64.2	67.3	62.3	7.7	13.0
		T	64.2	67.4	67.4	7.0	9.0
	300	L	53.7	55.1	**	2.2	**
		T	52.8	55.3	**	2.7	**
	450	L	39.0	43.0	**	8.7	**
		T	38.4	42.7	**	9.3	**
	600	L	28.5	33.1	**	22.2	**
		T	27.2	31.7	**	17.0	**
	77E*	L	62.1	65.2	**	4.6	**
		T	62.4	65.8	**	5.1	**
92A024-2A1 HOT STRAIGHT ROLLED							
0.04" Gauge	77	L	62.5	65.5	66.2	4.1	1.9
		T	63.8	69.6	63.7	3.9	3.9
	300	L	50.8	52.1	**	8.3	**
		T	52.6	53.6	**	11.0	**
	450	L	36.5	38.6	**	13.7	**
		T	36.2	40.6	**	6.2	**
	600	L	26.5	31.0	**	21.4	**
		T	28.9	31.3	**	26.0	**
	77E*	L	68.2	69.6	**	3.2	**
		T	68.0	69.6	**	2.8	**
92A024-2B2 COLD CROSS ROLLED							
0.04" Gauge	77	L	59.2	63.1	63.3	17.9	16.9
		T	58.8	62.5	67.9	12.2	13.0
	300	L	50.1	53.6	**	4.8	**
		T	49.9	53.7	**	4.6	**
	450	L	41.1	46.1	**	17.3	**
		T	38.0	42.9	**	17.1	**
	600	L	24.4	29.5	**	27.2	**
		T	28.0	30.5	**	24.9	**
	77E*	L	69.2	71.1	**	5.1	**
		T	69.7	71.6	**	4.8	**
2A024-2A2 COLD STRAIGHT ROLLED							
0.04" Gauge	77	L	61.6	61.6	63.4	16.7	17.0
		T	61.0	63.0	68.0	16.8	17.2
	300	L	51.3	54.2	**	6.8	**
		T	51.1	53.9	**	5.4	**
	450	L	36.5	41.7	**	12.8	**
		T	36.4	41.6	**	11.7	**
	600	L	25.3	30.2	**	22.3	**
		T	26.6	29.0	**	20.9	**
	77E*	L	70.4	72.7	**	5.2	**
		T	70.1	72.1	**	5.0	**

* Samples tested at 77 F after 700° F for 100 hrs. exposure

** Not Measured

Table 12a

Sample ID#	Temp (K)	Orient.	U.T.S. 0.5% /min. (MPa)	U.T.S. 5% /min. (MPa)	U.T.S. 50% /min (MPa)	Elong. 5%/min (%)	Elong. 50% /min (%)
92A024-2B3 COLD CROSS ROLLED/ANNEALED							
0.10 cm	298	L	382.7	406.9	405.1	16.3	20.0
		T	384.1	405.5	403.8	13.8	19.1
	422	L	338.6	362.9	**	4.4	**
		T	338.8	364.1	**	4.4	**
	505	L	246.2	281.9	**	17.6	**
		T	246.6	279.4	**	16.7	**
	589	L	170.5	206.5	**	21.9	**
		T	169.6	205.7	**	20.1	**
	298E*	L	467.8	480.9	**	2.0	**
		T	475.4	493.3	**	2.3	**
92A024-2A3 COLD STRAIGHT ROLLED/ANNEALED							
0.10 cm	298	L	385.5	411.7	434.8	16.8	16.4
		T	388.3	407.9	438.9	14.0	17.6
	422	L	328.2	352.3	**	5.78	**
		T	316.8	340.5	**	5.94	**
	505	L	257.0	289.0	**	16.4	**
		T	243.0	276.7	**	11.3	**
	589	L	183.8	200.2	**	22.8	**
		T	166.7	200.4	**	21.2	**
	298E*	L	479.5	492.6	**	2.0	**
		T	486.4	498.1	**	3.1	**

* Samples tested at 298K after 644K for 100 hrs. exposure

** Not Measured

Table 12b

Sample ID#	Temp (°F)	Orient.	U.T.S. 0.5% /min. (ksi)	U.T.S. 5% /min. (ksi)	U.T.S. 50% /min (ksi)	Elong. 5% /min (%)	Elong. 50% /min (%)
92A024-2B3 COLD CROSS ROLLED/ANNEALED							
0.040" Gauge	77	L	55.6	59.1	58.8	16.3	20.0
		T	55.8	58.9	58.6	13.8	19.1
	300	L	49.2	52.7	**	4.4	**
		T	49.2	52.9	**	4.4	**
	450	L	35.7	40.9	**	17.6	**
		T	35.8	40.6	**	16.7	**
	600	L	24.8	30.0	**	21.9	**
		T	24.6	29.9	**	20.1	**
	77E*	L	67.9	69.8	**	2.0	**
		T	69.0	71.6	**	2.3	**
92A024-2A3 COLD STRAIGHT ROLLED/ANNEALED							
0.040" Gauge	77	L	56.0	59.8	63.1	16.8	16.4
		T	56.4	59.2	63.7	14.0	17.6
	300	L	47.6	51.1	**	5.78	**
		T	46.0	49.4	**	5.94	**
	450	L	37.3	41.9	**	16.4	**
		T	35.3	40.2	**	11.3	**
	600	L	26.7	29.1	**	22.8	**
		T	24.2	29.1	**	21.2	**
	77E*	L	69.6	71.5	**	2.0	**
		T	70.6	72.3	**	3.1	**

* Samples tested at 77 °F after 700 °F for 100 hrs. exposure

** Not Measured

Table 13. Average Concentration of Si, Fe, and V Measured by Energy Dispersive X-ray Spectroscopy in HTA 8009

Sample ID	Al	Si	V	Fe
Extruded	99.8 + 0.05	ND	0.1 + 0.04	0.1 + 0.02
Hot Rolled 0.64 cm (0.25") Plate	99.7 + 0.05	ND	0.18 + 0.04	0.13 + 0.02
Cold Rolled / Annealed 0.10 cm (0.040") Gauge Sheet	99.3 + 0.2	0.4 + 0.2	0.16 + 0.02	0.12 + 0.02

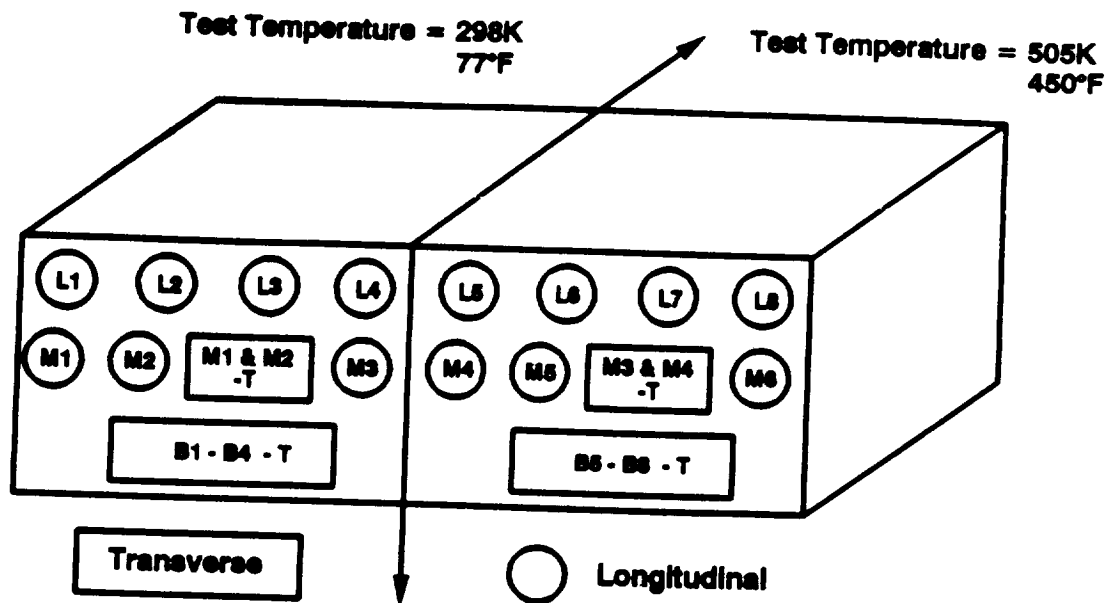


Fig. 1. Cut plan for specimens machined from the nose and tail of HTA 8009 extrusions 92A022 and 92A024.

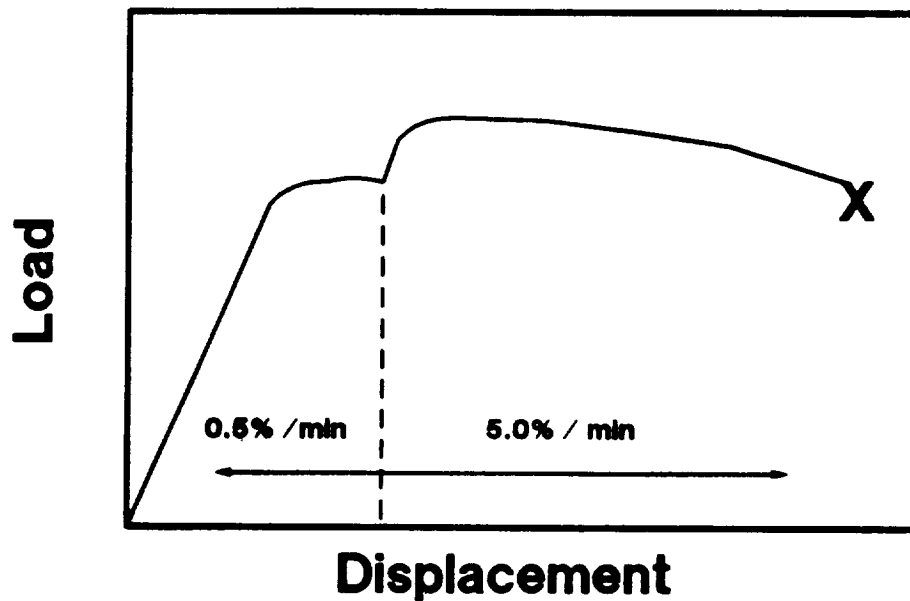


Fig. 2. Typical load-displacement curve for a tensile specimen tested in the present study. After the specimen experienced a maximum tensile stress, the strain rate was increased ten-fold from 0.5%/min to 5.0%/min and tested to failure.

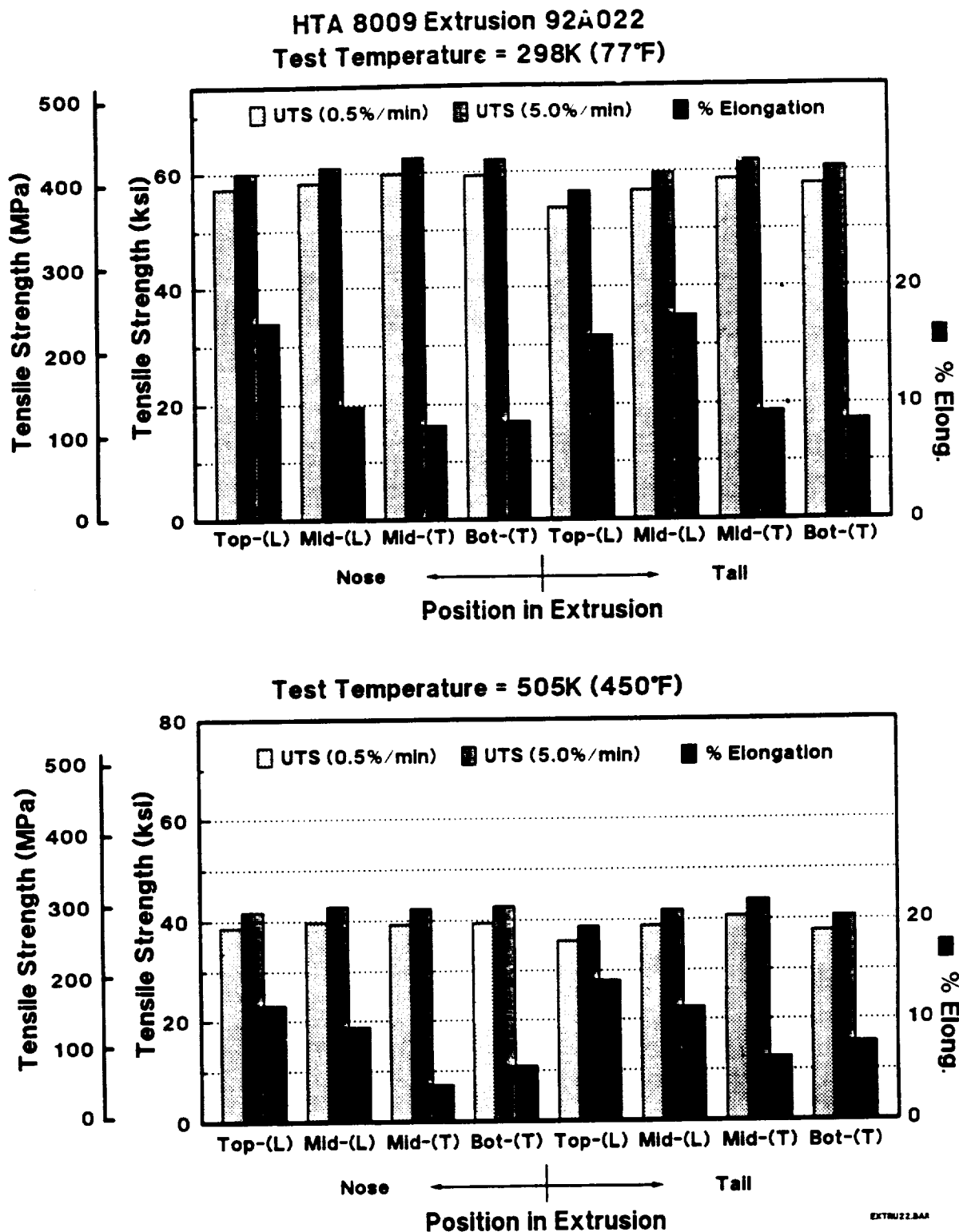


Fig. 3. Tensile strength and ductility as a function of position in HTA 8009 extrusion 92A022 at 298K (77°F) and 505K (450°F) for specimens machined from the nose and tail of the preforms.

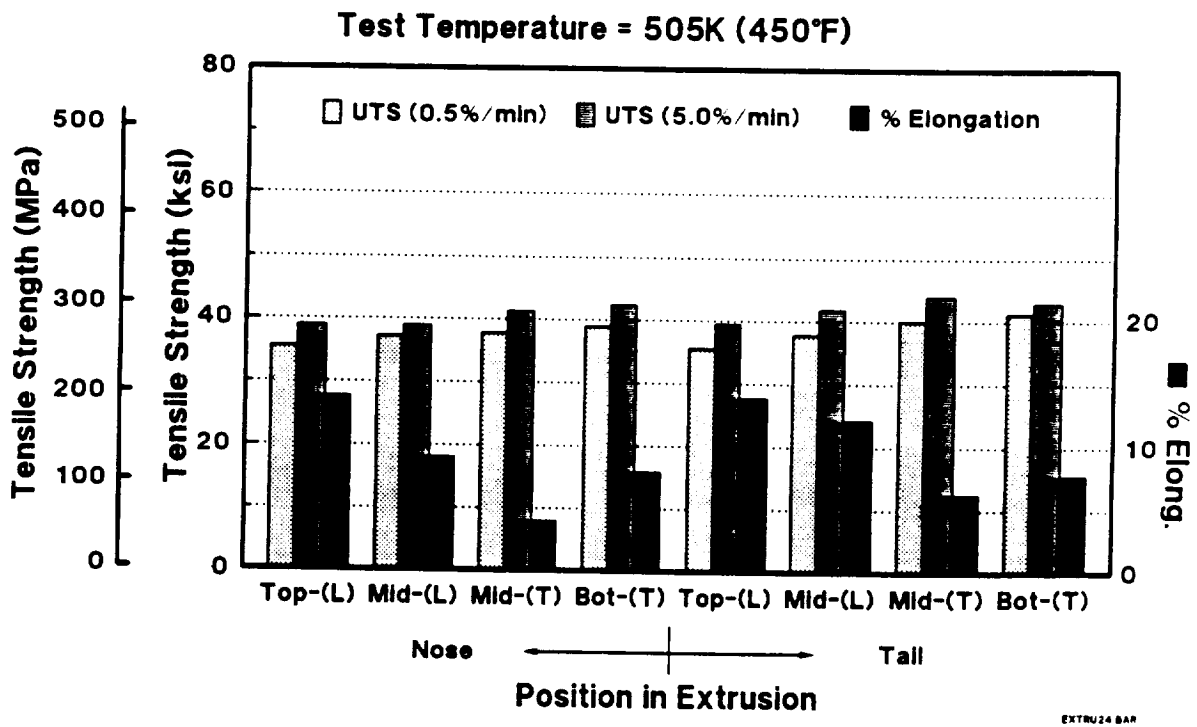
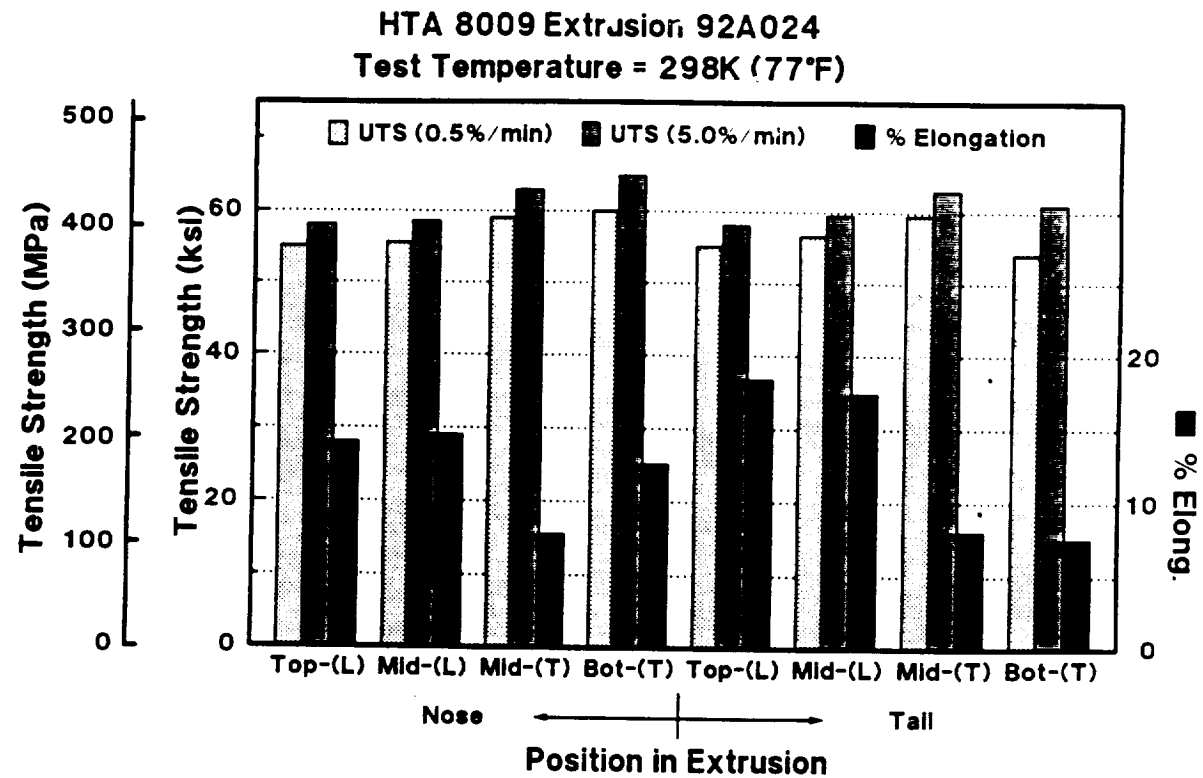
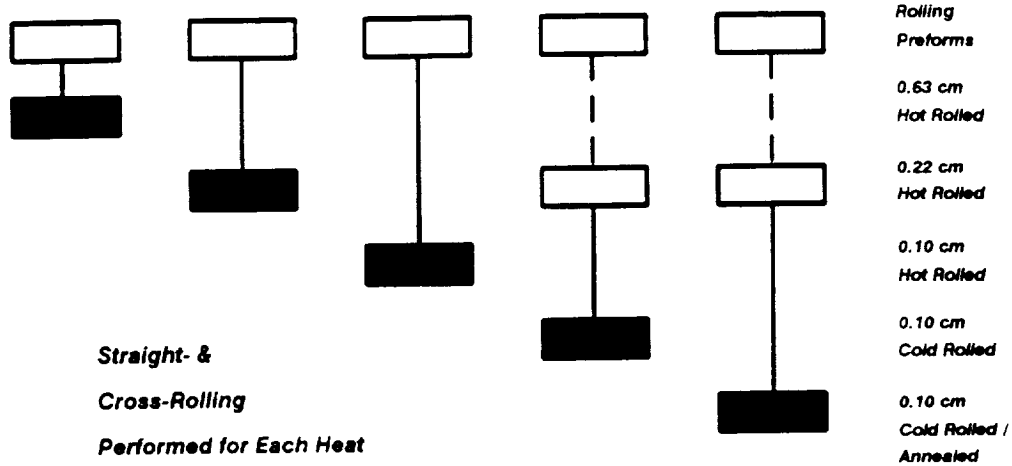


Fig. 4. Tensile strength and ductility as a function of position in HTA 8009 extrusion 92A024 at 298K (77°F) and 505K (450°F) for specimens machined from the nose and tail of the preforms.

Rolling Schedules Practiced at Kaiser CFT

Casting Modification A



Casting Modification B

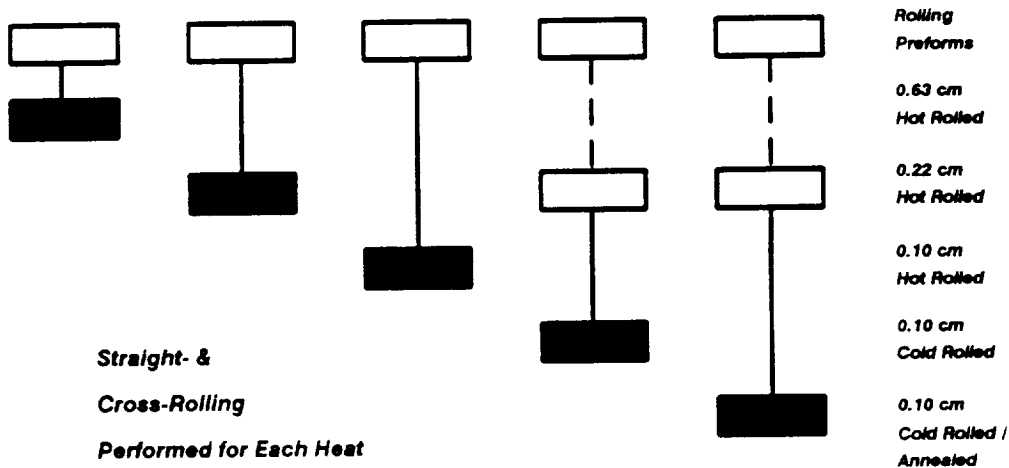


Figure 5. Pass schedules were designed to evaluate the effects of rolling direction and thermo-mechanical processing on ambient and elevated temperature mechanical properties of HTA 8009 plate and sheet.

Fig. 6

Tensile Properties vs. Test Temperature

92A022-1C Hot Cross Rolled 0.64 cm (0.25") Sheet

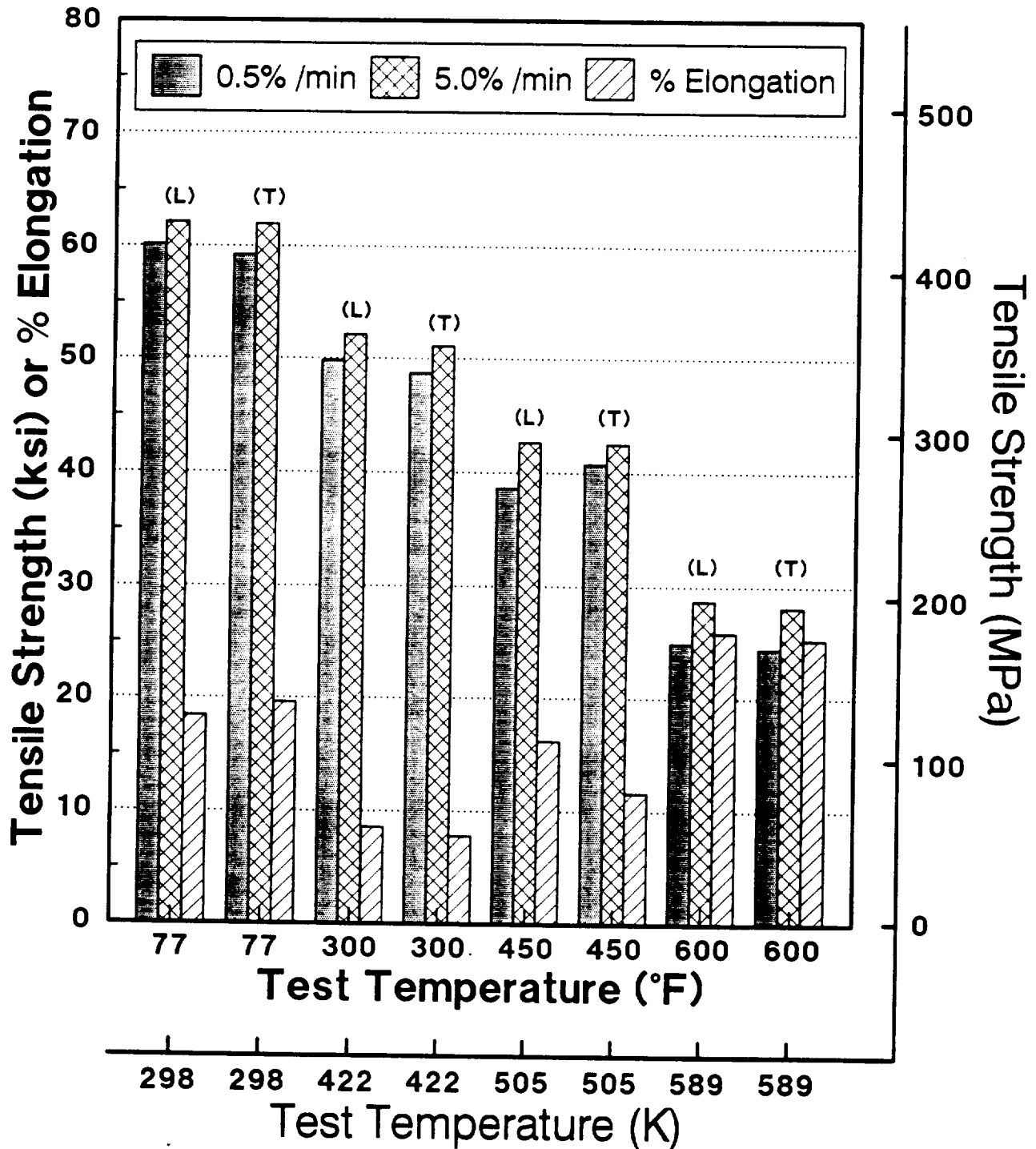


Fig. 7

Tensile Properties vs. Test Temperature

92A022-1A Hot Straight Rolled 0.64 cm (0.25") Sheet

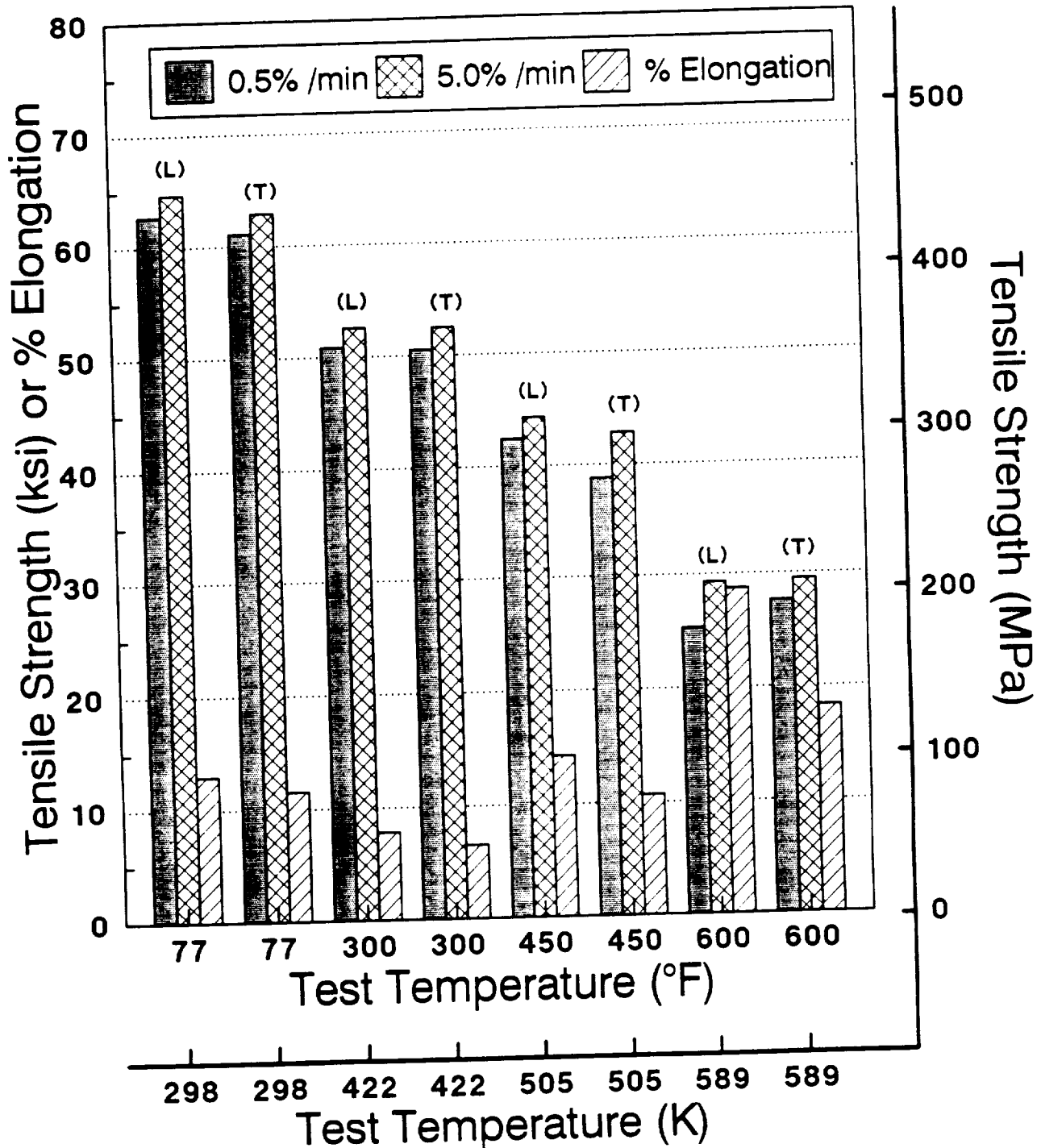


Fig. 8

Tensile Properties vs. Test Temperature

0.64 cm (0.25") Hot Cross vs. Hot Straight Rolled Sheet

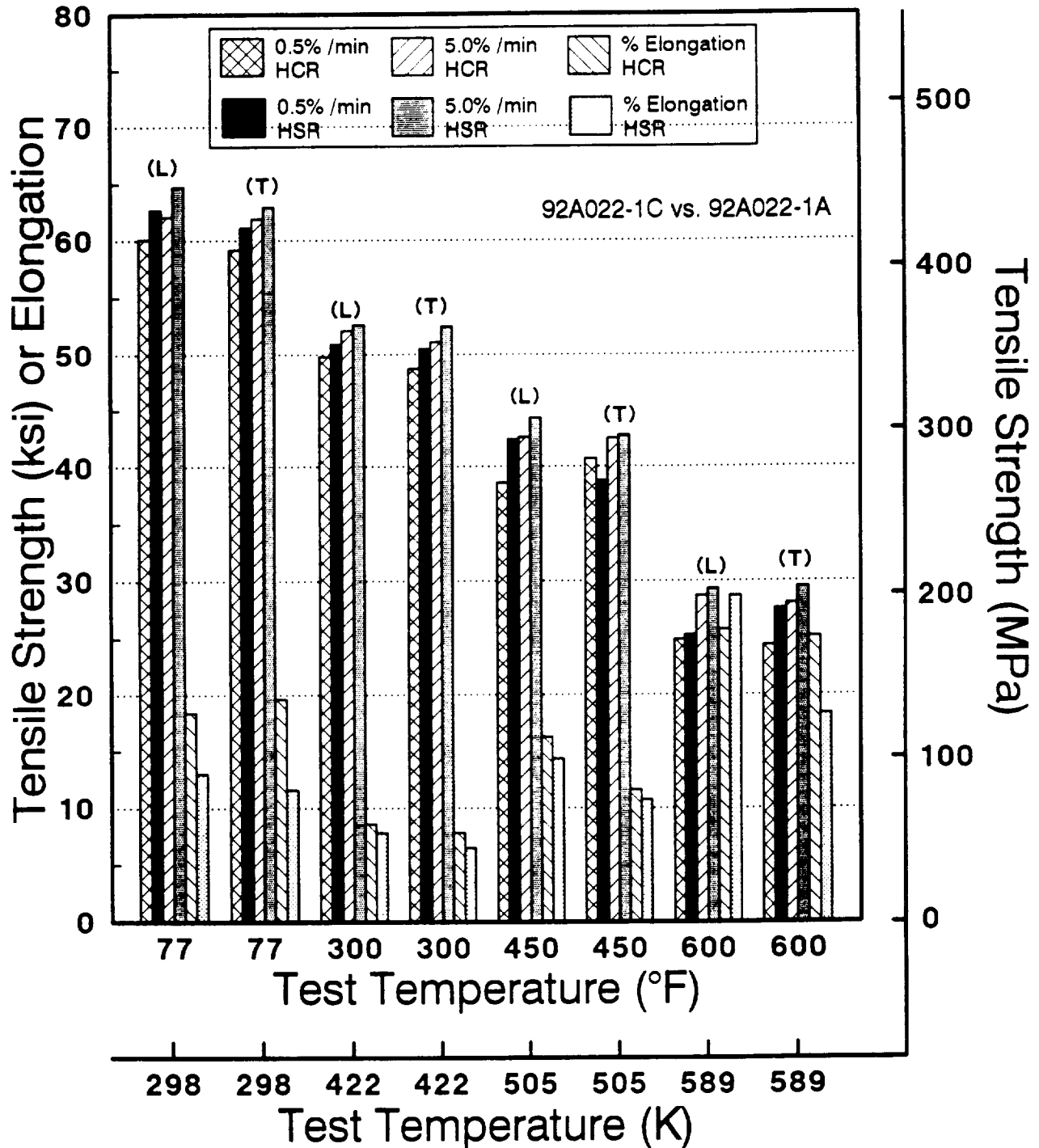


Fig. 9

Tensile Properties vs. Test Temperature

92A022-2A Hot Cross Rolled 0.25 cm (0.10") Sheet

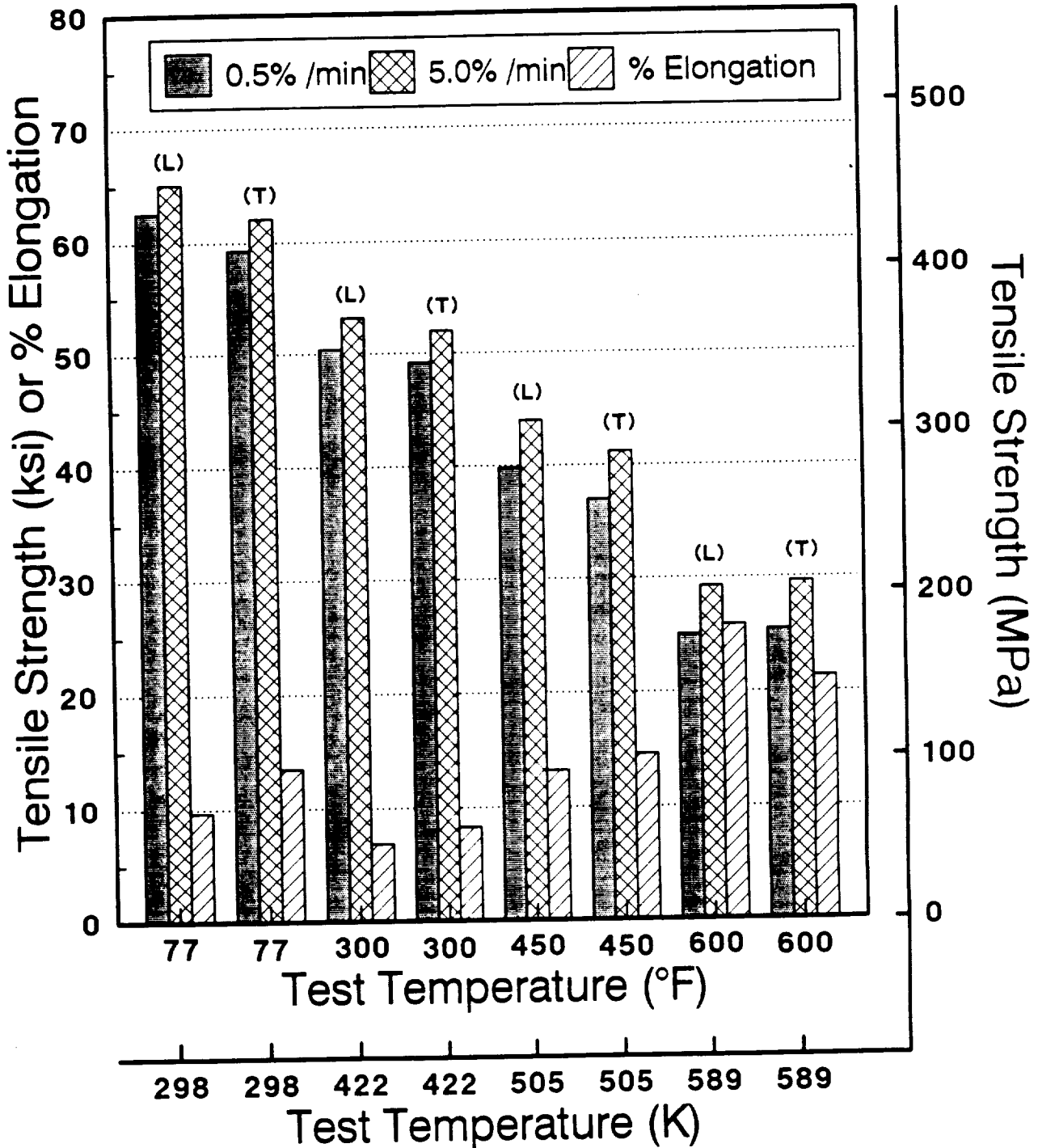


Fig. 10

Tensile Properties vs. Test Temperature

92A022-2B Hot Straight Rolled 0.25 cm (0.1") Sheet

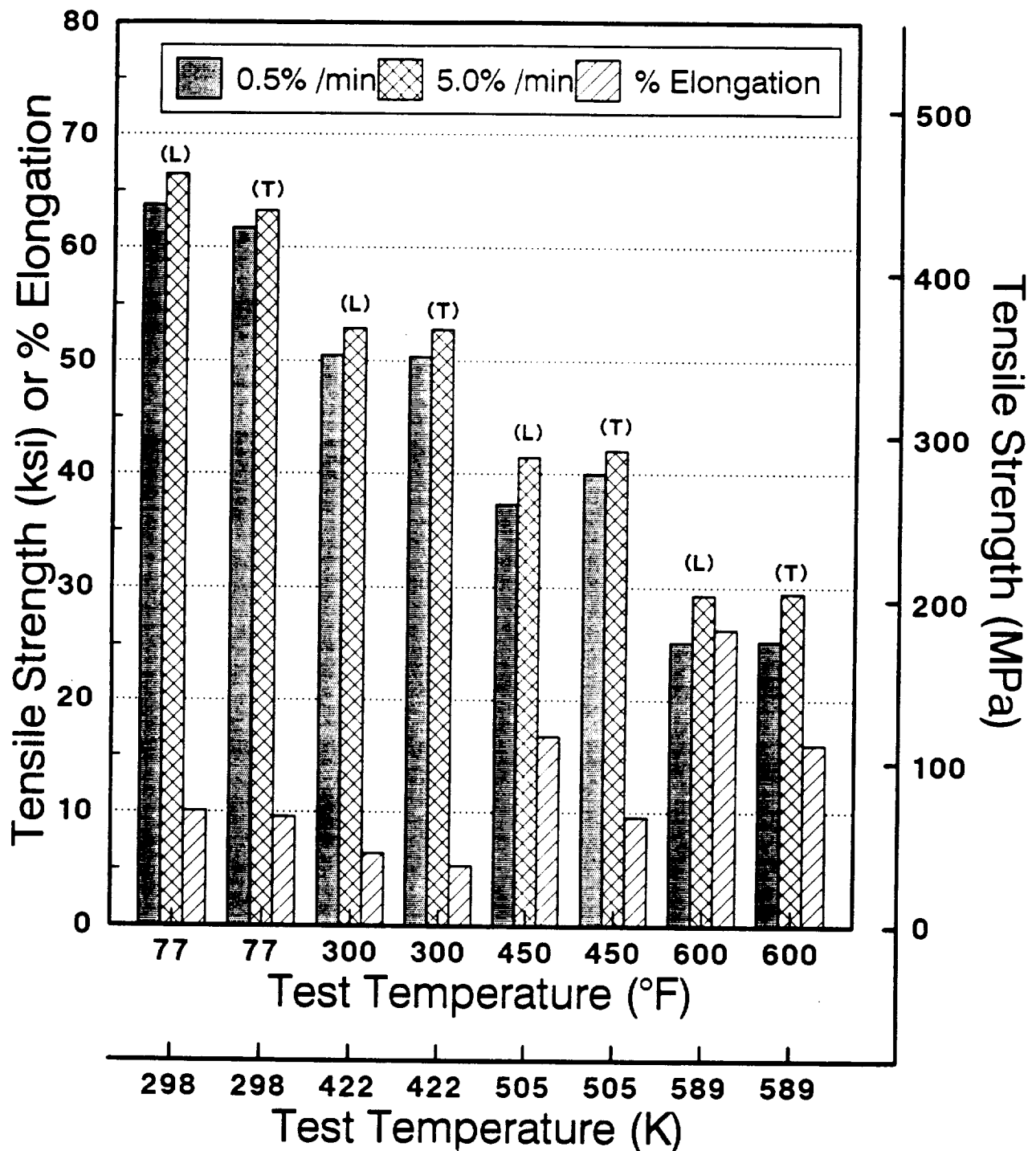


Fig. 11

Tensile Properties vs. Test Temperature 0.25 cm (0.1") Hot Cross vs. Hot Straight Rolled Sheet

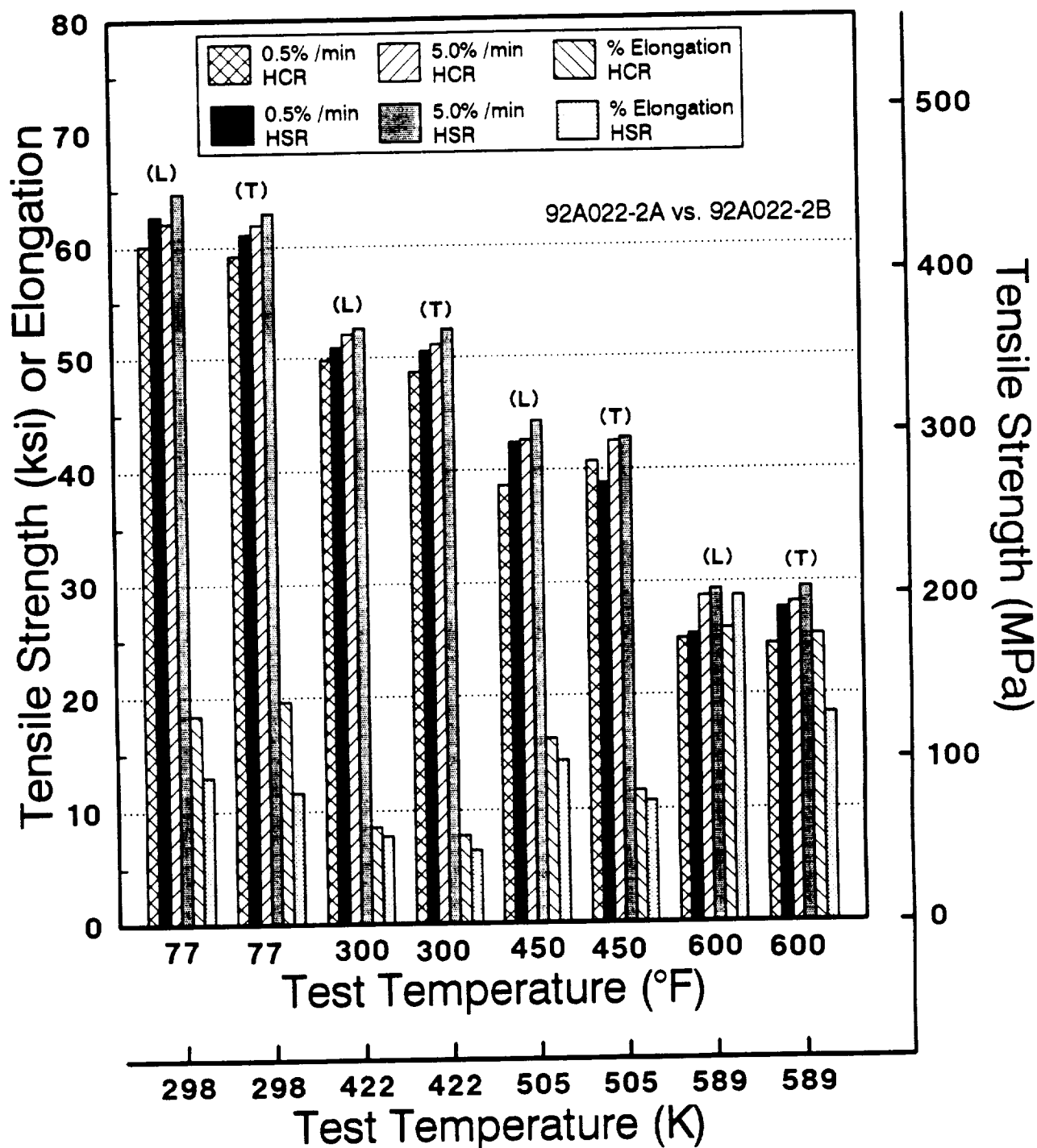


Fig. 12

Tensile Properties vs. Test Temperature

92A022-1B1 Hot Cross Rolled 0.10 cm (0.04") Sheet

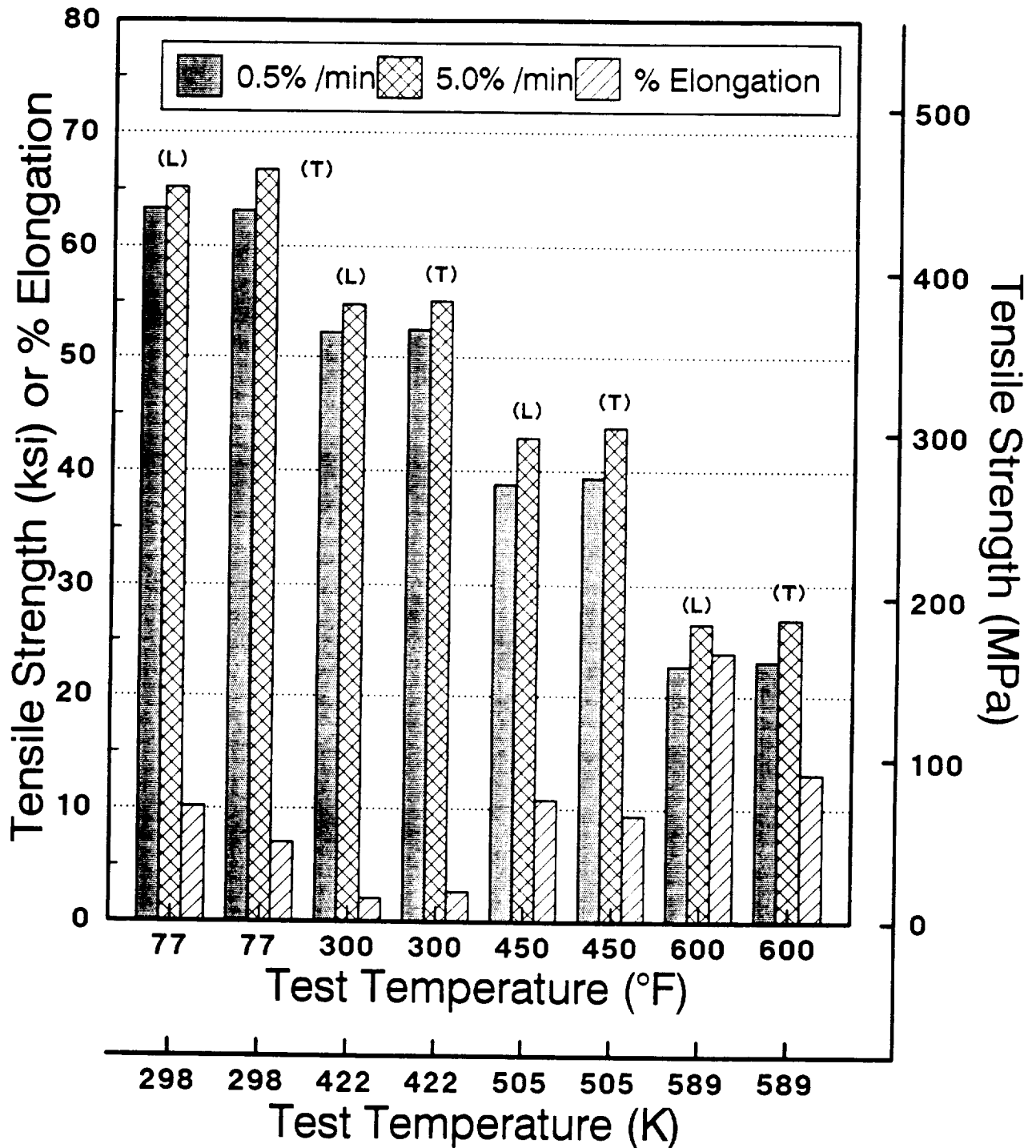


Fig. 13

Tensile Properties vs. Test Temperature

92A022-2C1 Hot Straight Rolled 0.08 cm (0.03") Sheet

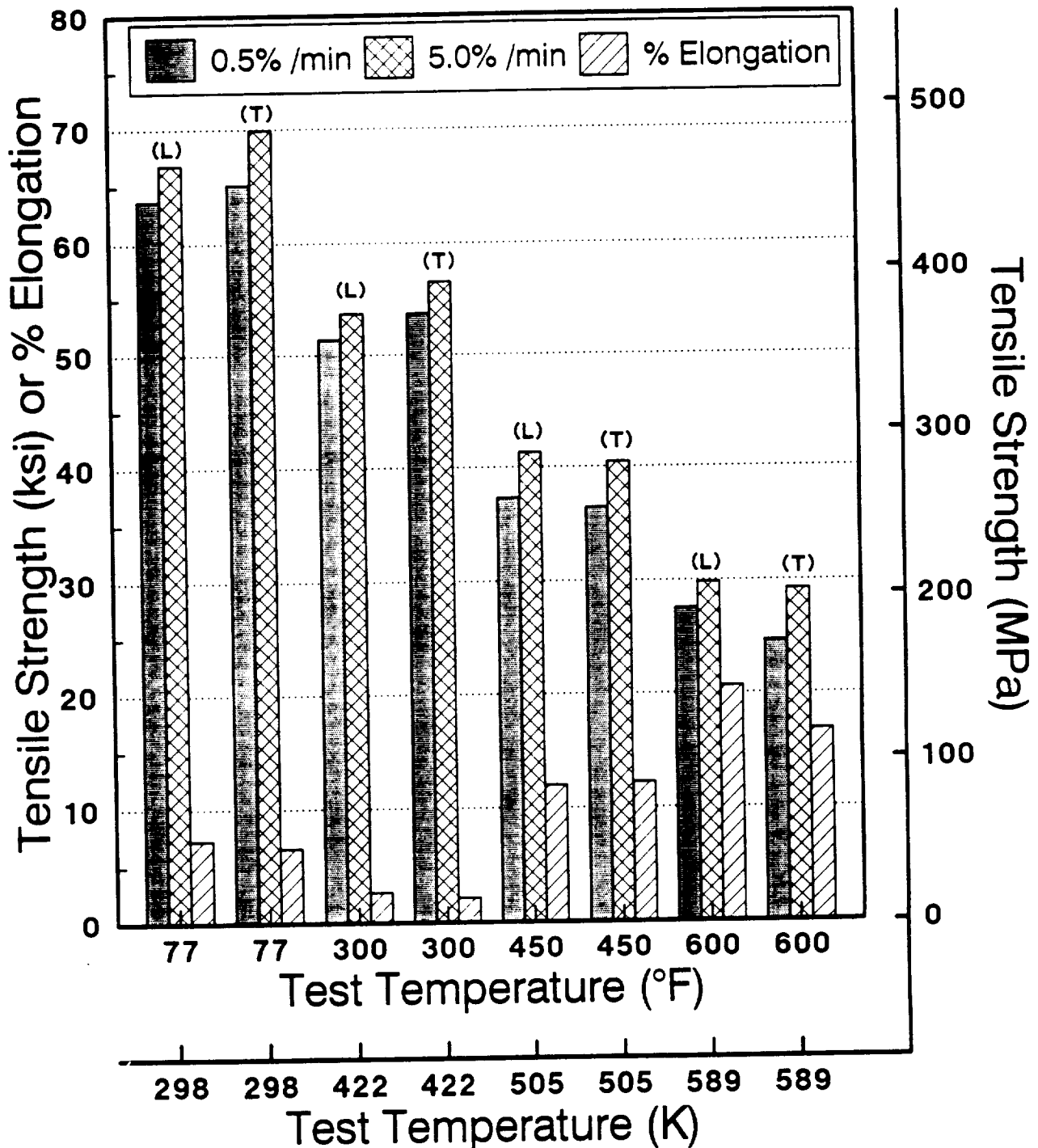


Fig. 14

Tensile Properties vs. Test Temperature

0.1 cm (0.04") Hot Cross vs. Hot Straight Rolled Sheet

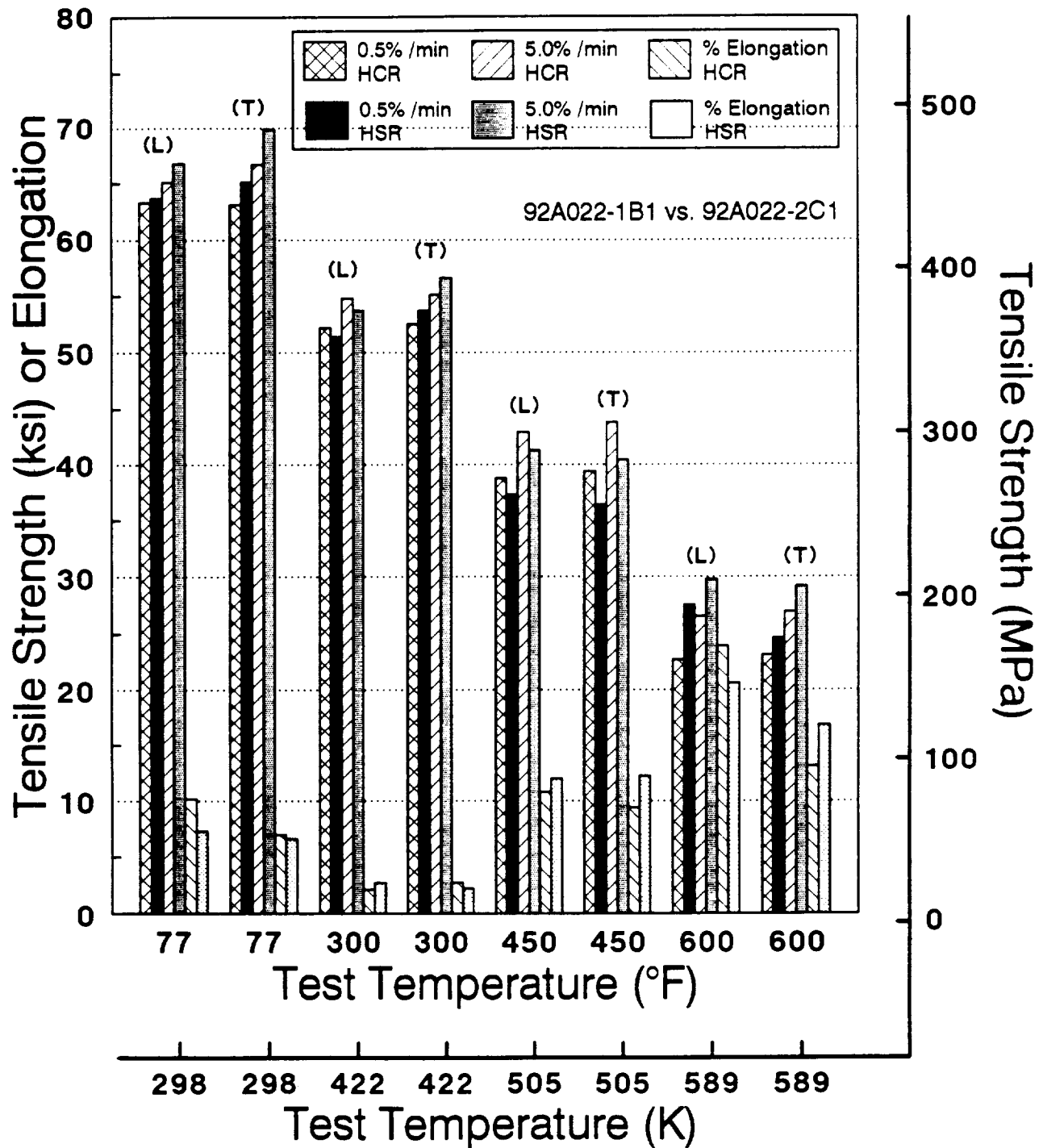


Fig. 15

Tensile Properties vs. Test Temperature

92A022-1 B2 Cold Cross Rolled 0.10 cm (0.04") Sheet

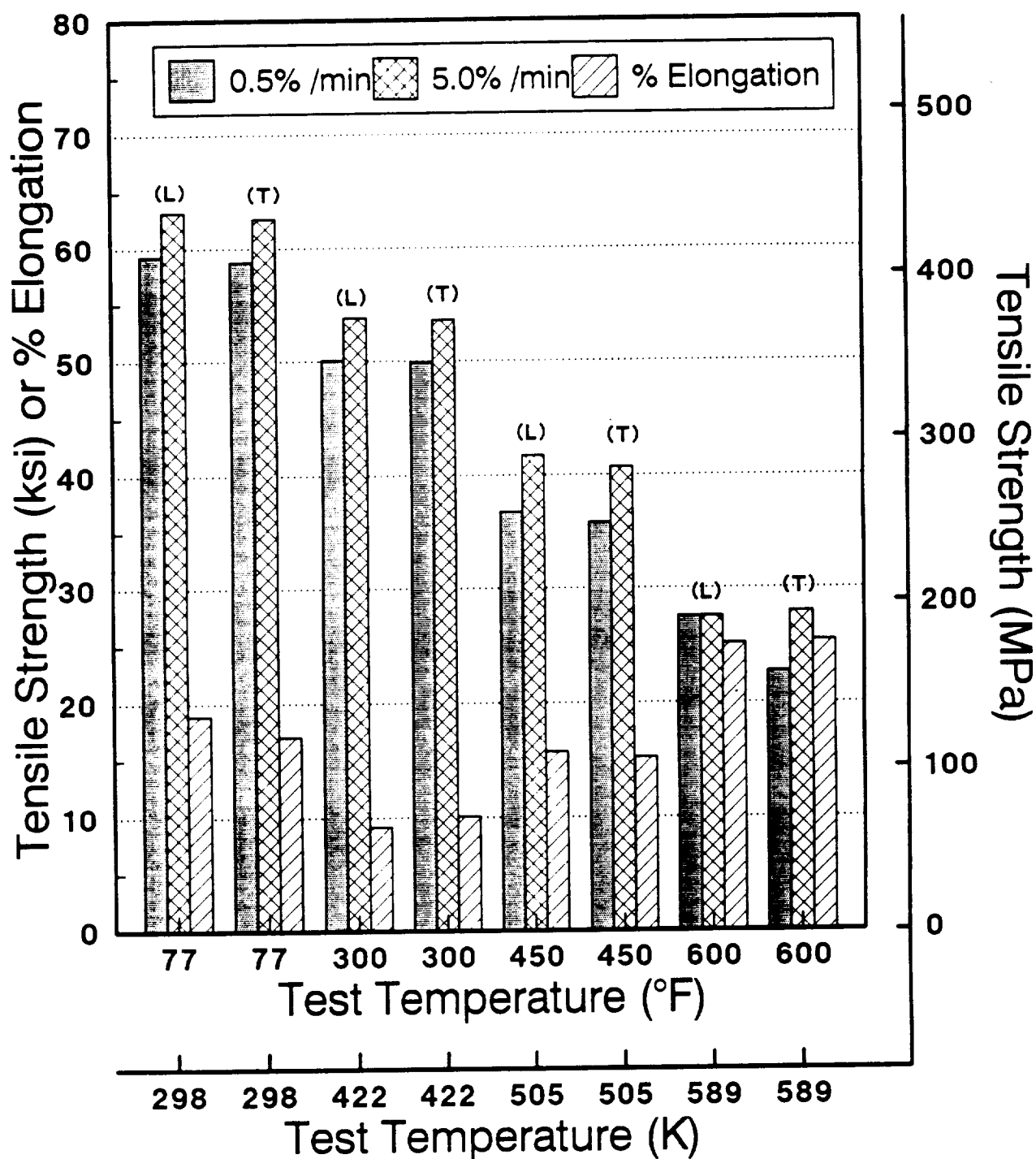


Fig. 16

Tensile Properties vs. Test Temperature

92A022-2C2 Cold Straight Rolled 0.10 cm (0.04") Sheet

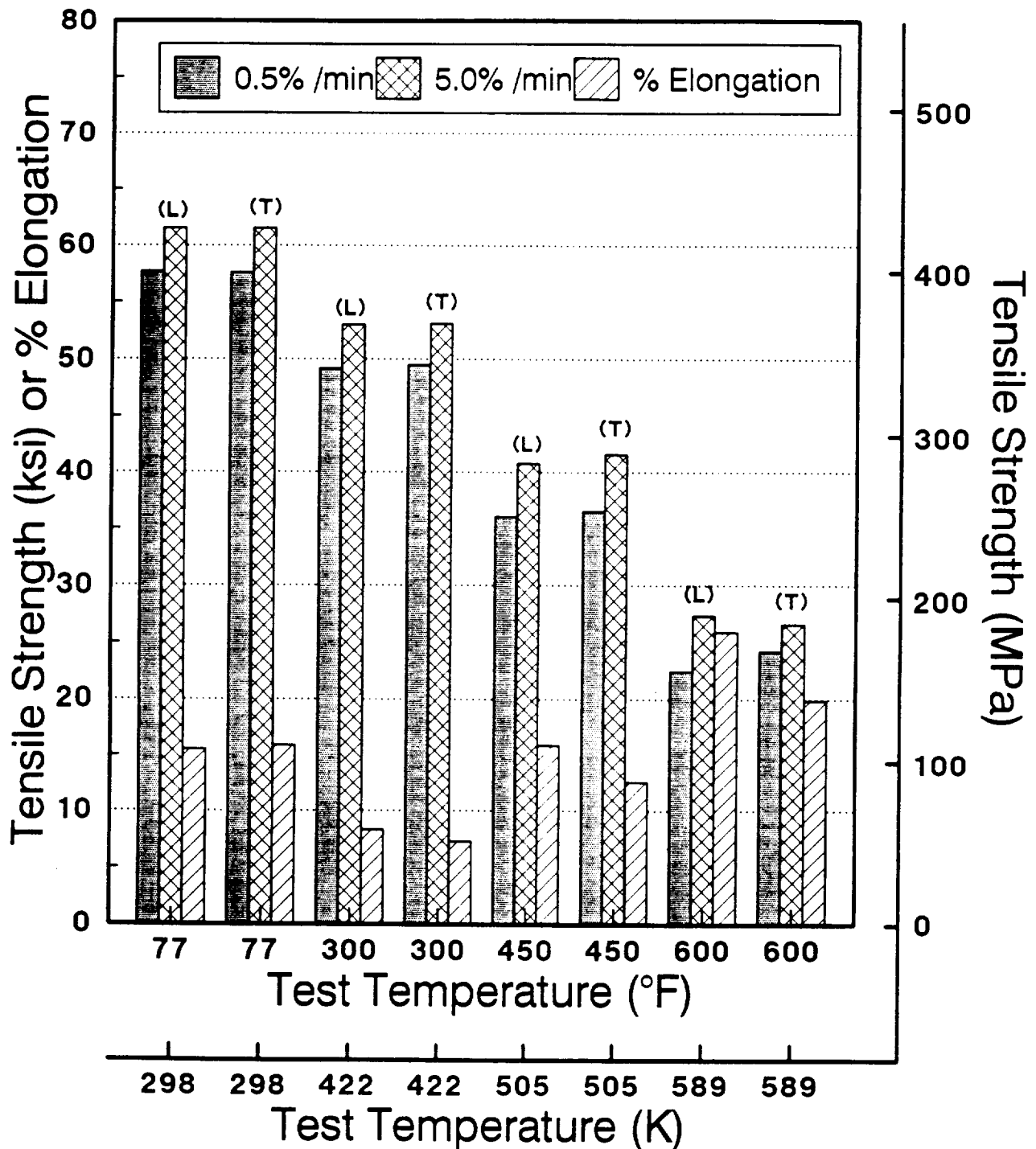


Fig. 17

Tensile Properties vs. Test Temperature

0.1 cm (0.04") Cold Cross vs. Cold Straight Rolled Sheet

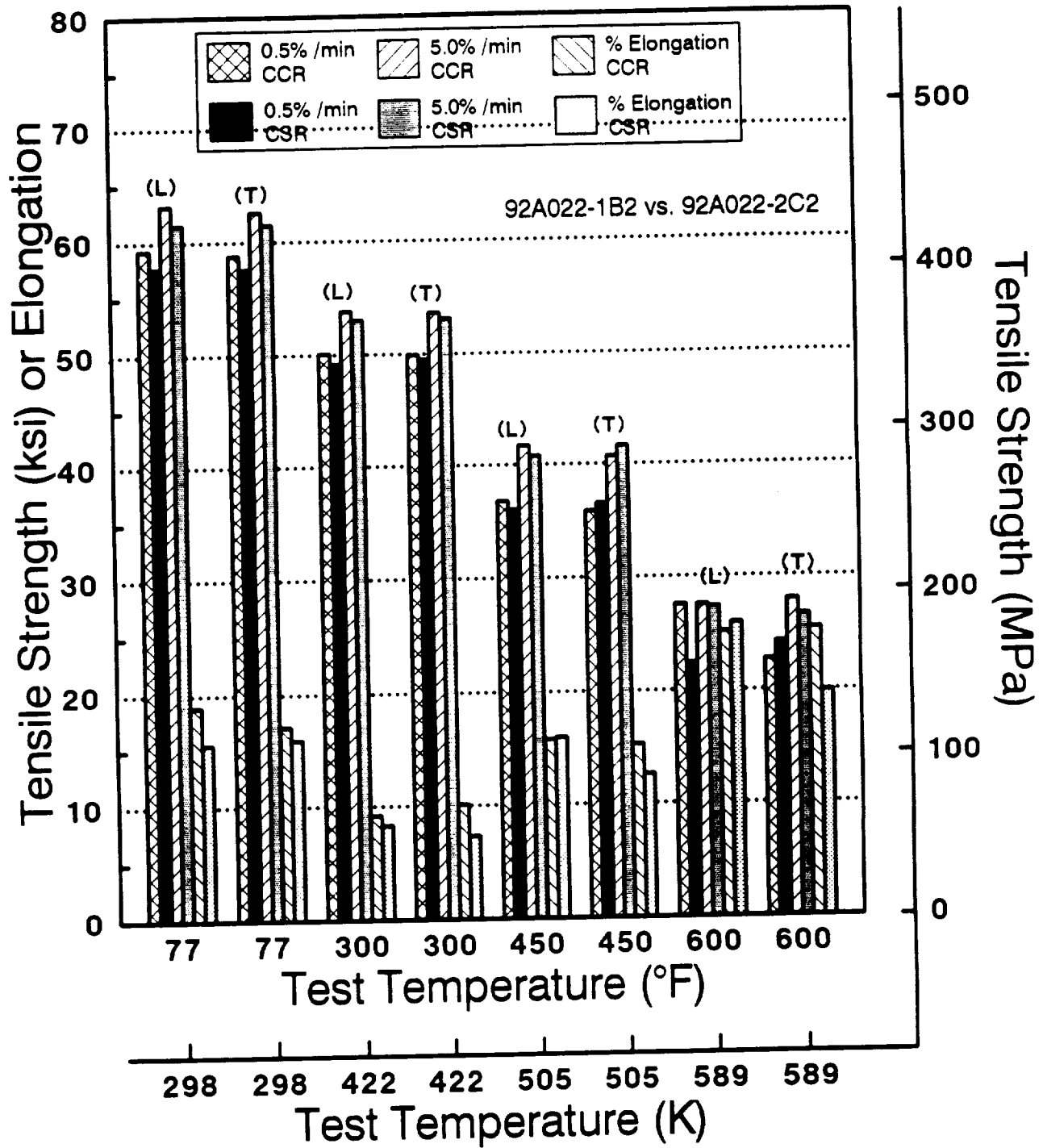


Fig. 18

Tensile Properties vs. Test Temperature

92A022-1B3 Cold Cross Rolled w/ Anneals 0.1 cm (0.04") Sheet

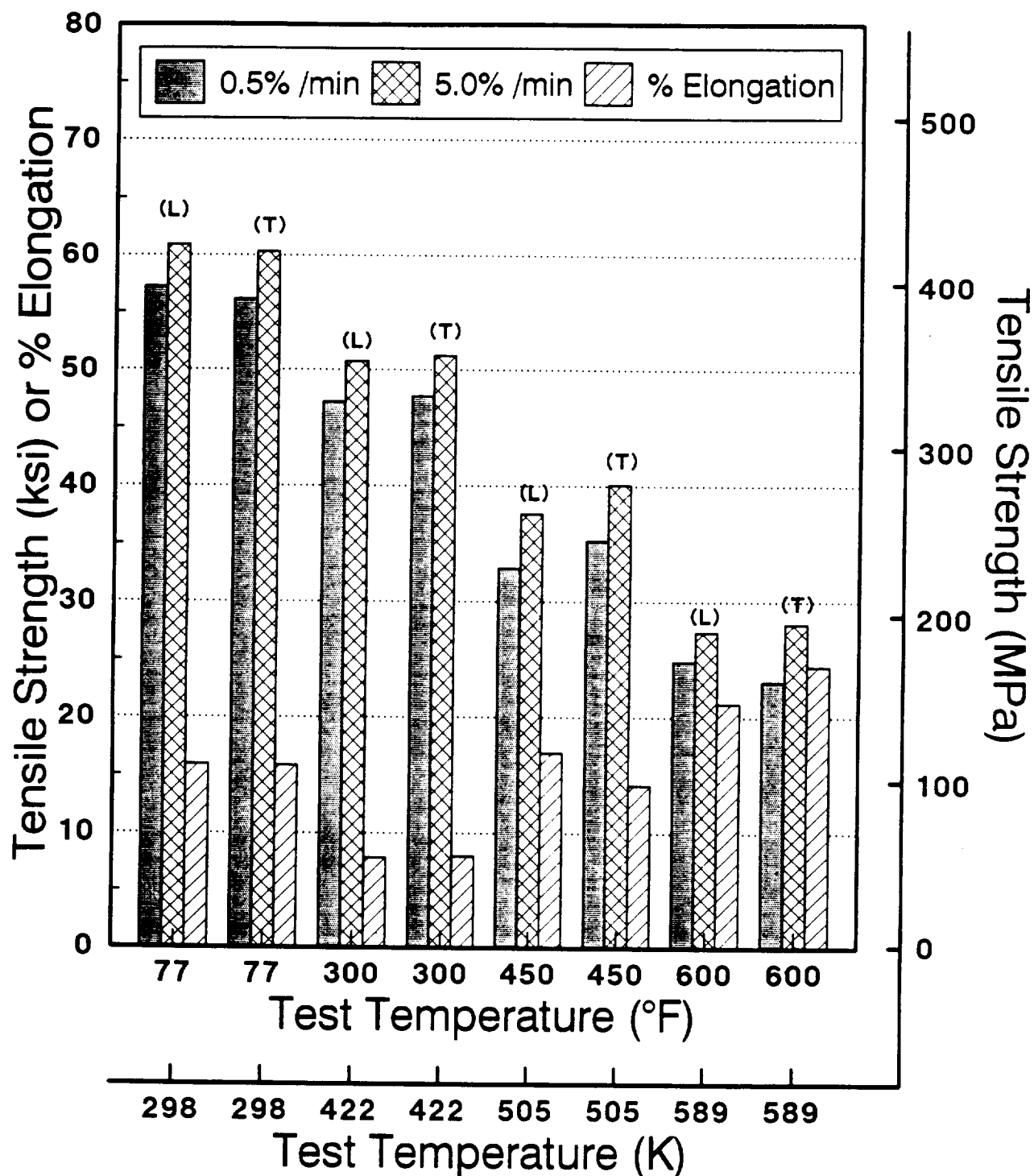


Fig. 19

Tensile Properties vs. Test Temperature

92A022-2C3 Cold Straight Rolled w/ Anneals 0.1 cm (0.04") Sheet

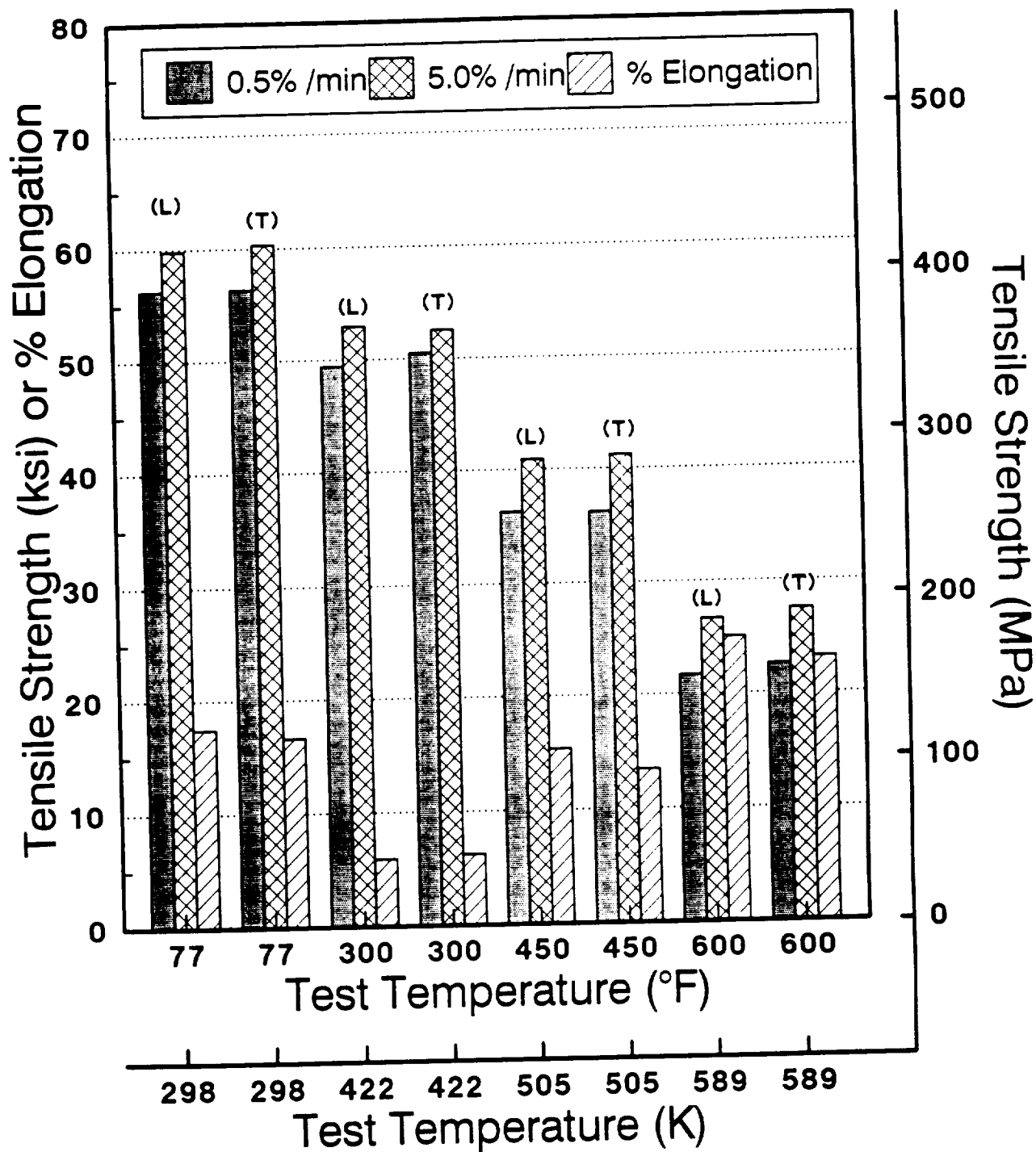


Fig. 20

Tensile Properties vs. Test Temperature

0.1 cm (0.40") Cold Cross vs. Cold Straight Rolled Sheet w/ Anneals

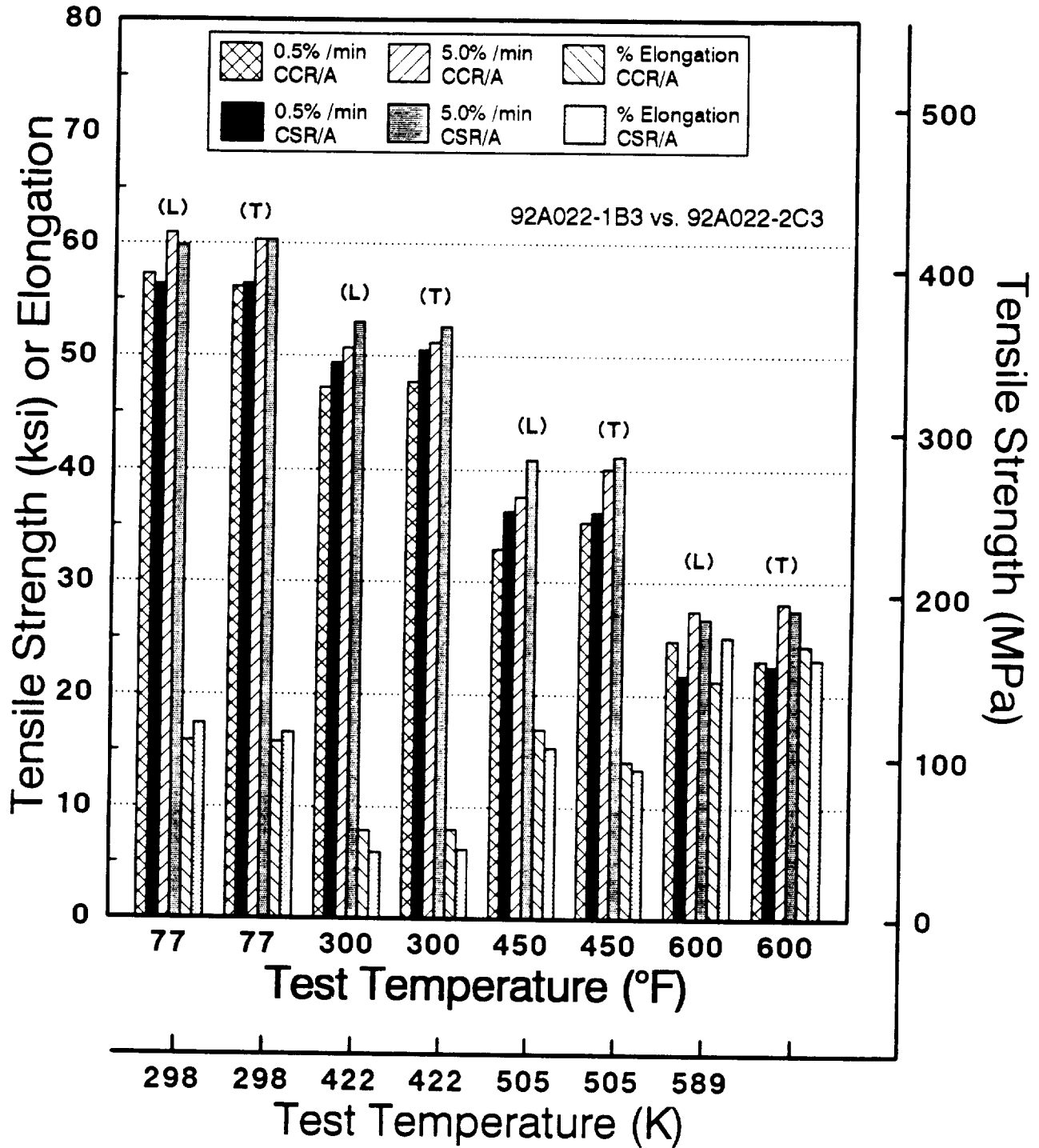


Fig. 21

Tensile Properties vs. Test Temperature

92A024- 1C Hot Cross Rolled 0.64 cm (0.25") Sheet

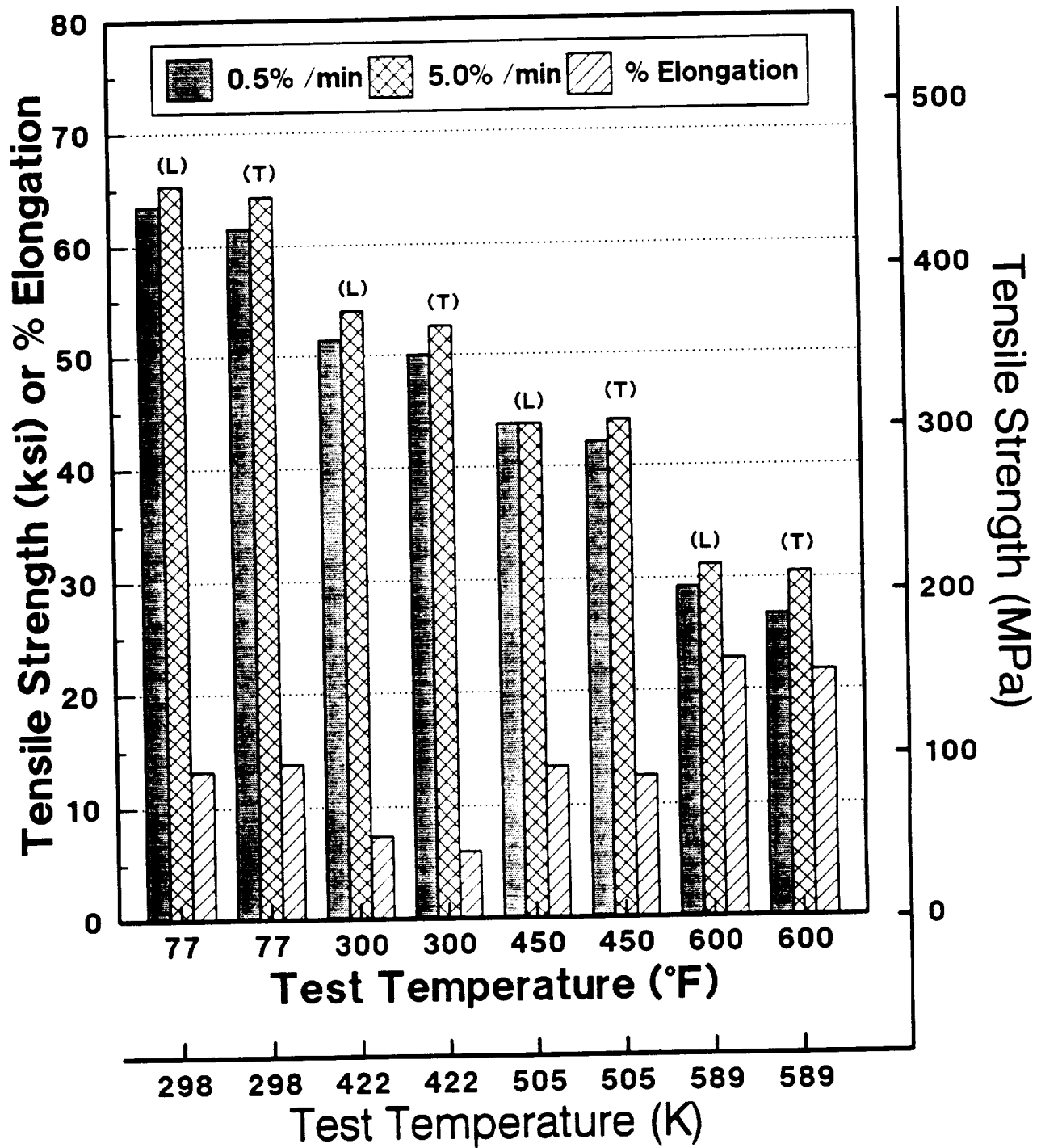


Fig. 22

Tensile Properties vs. Test Temperature

92A024- 1A Hot Straight Rolled 0.64 cm (0.25") Sheet

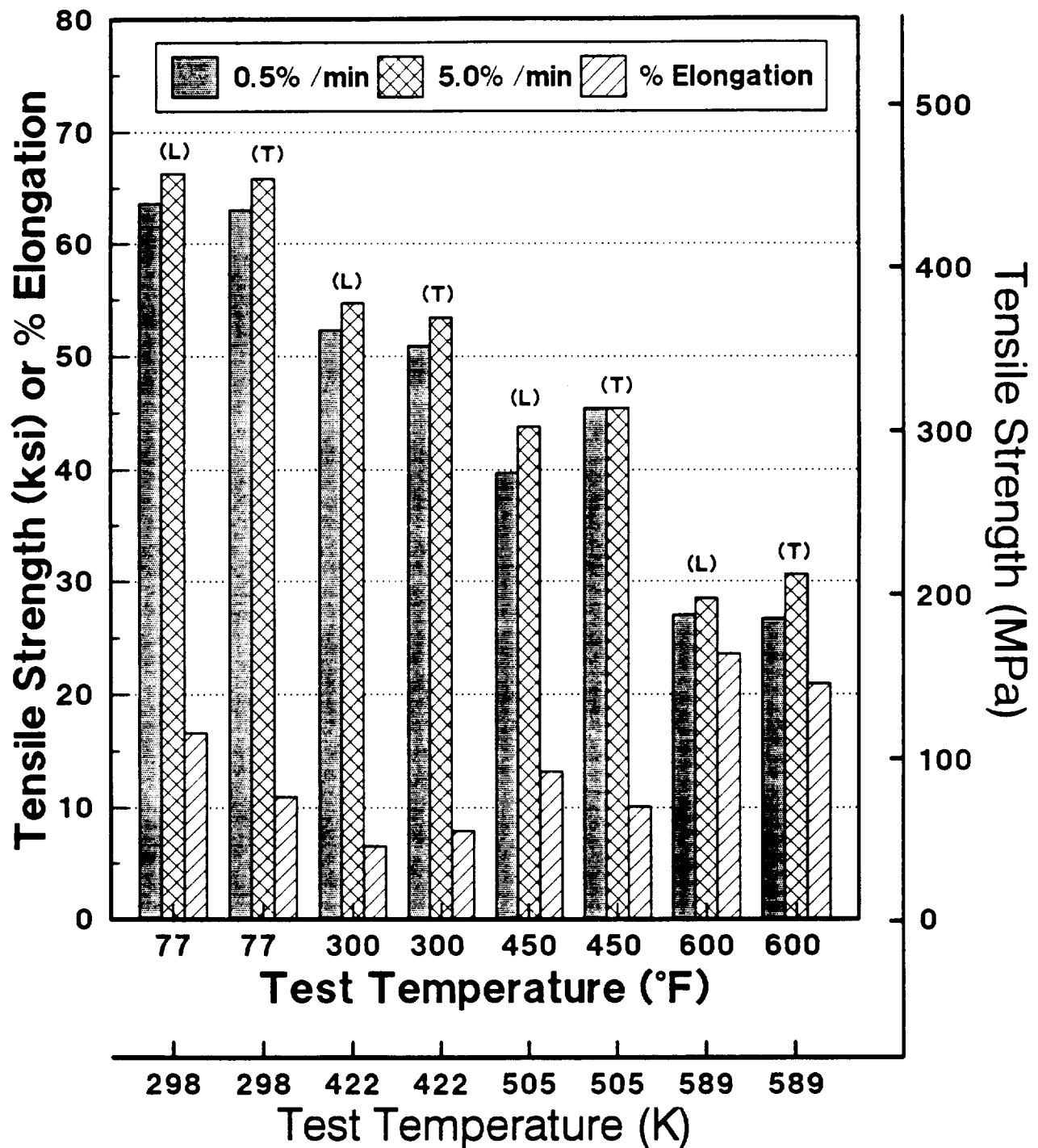


Fig. 23

Tensile Properties vs. Test Temperature

Hot Cross Rolled vs Hot Straight Rolled 0.64 cm (0.25") Sheet

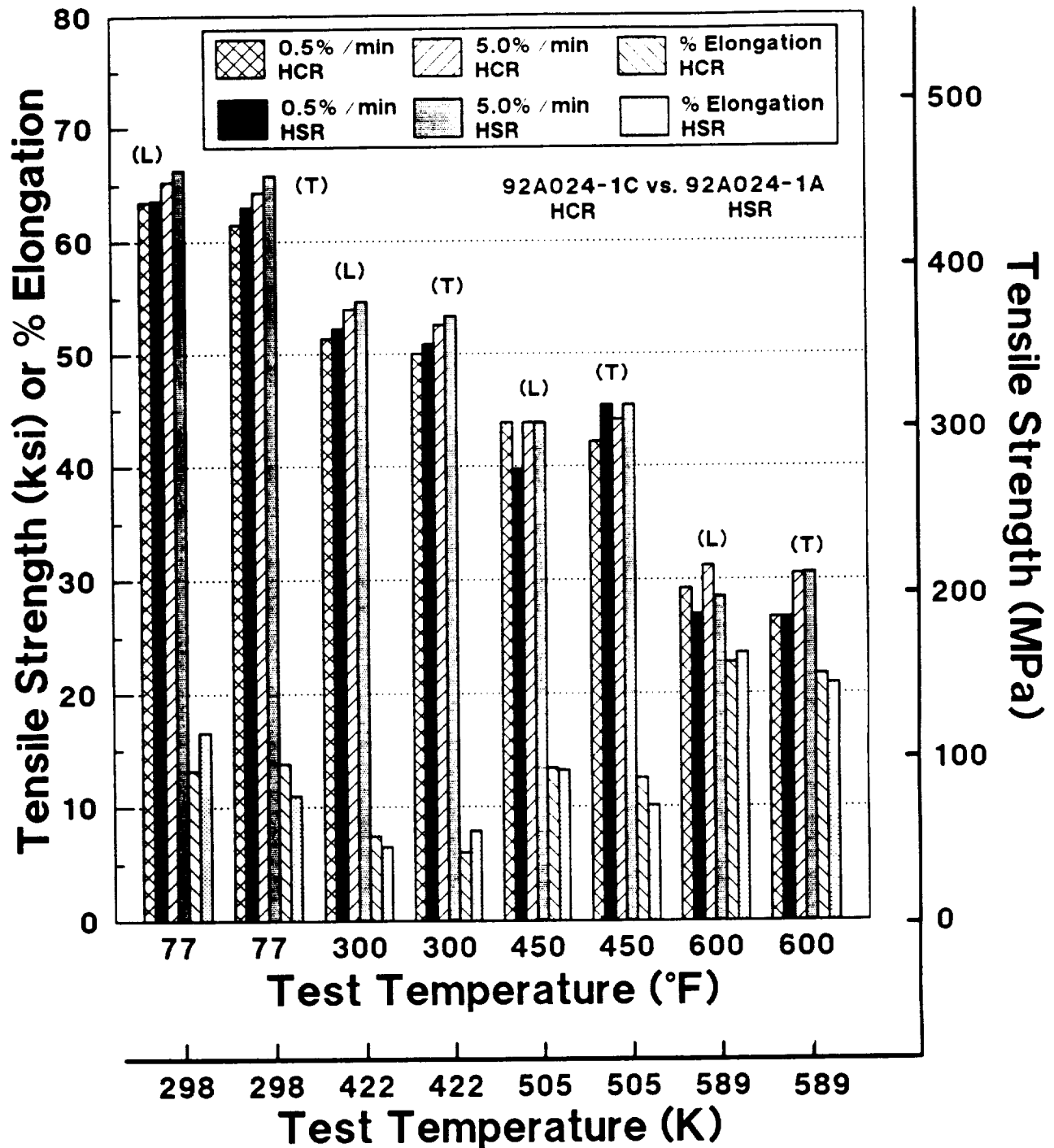


Fig. 24

Tensile Properties vs. Test Temperature

92A024-1D Hot Cross Rolled 0.23 cm (0.09") Sheet

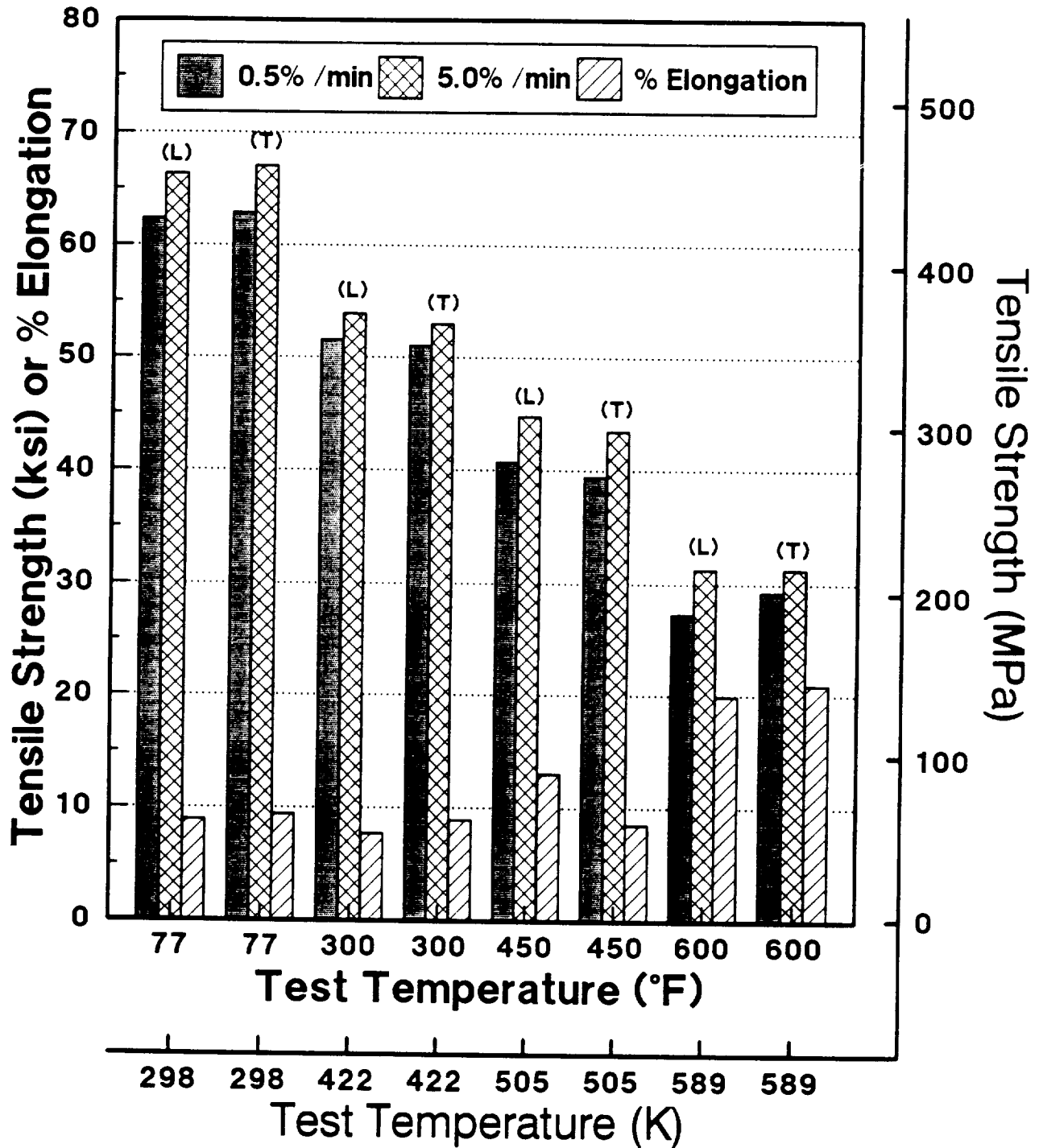


Fig. 25

Tensile Properties vs. Test Temperature

92A024- 1B Hot Straight Rolled 0.23 cm (0.09") Sheet

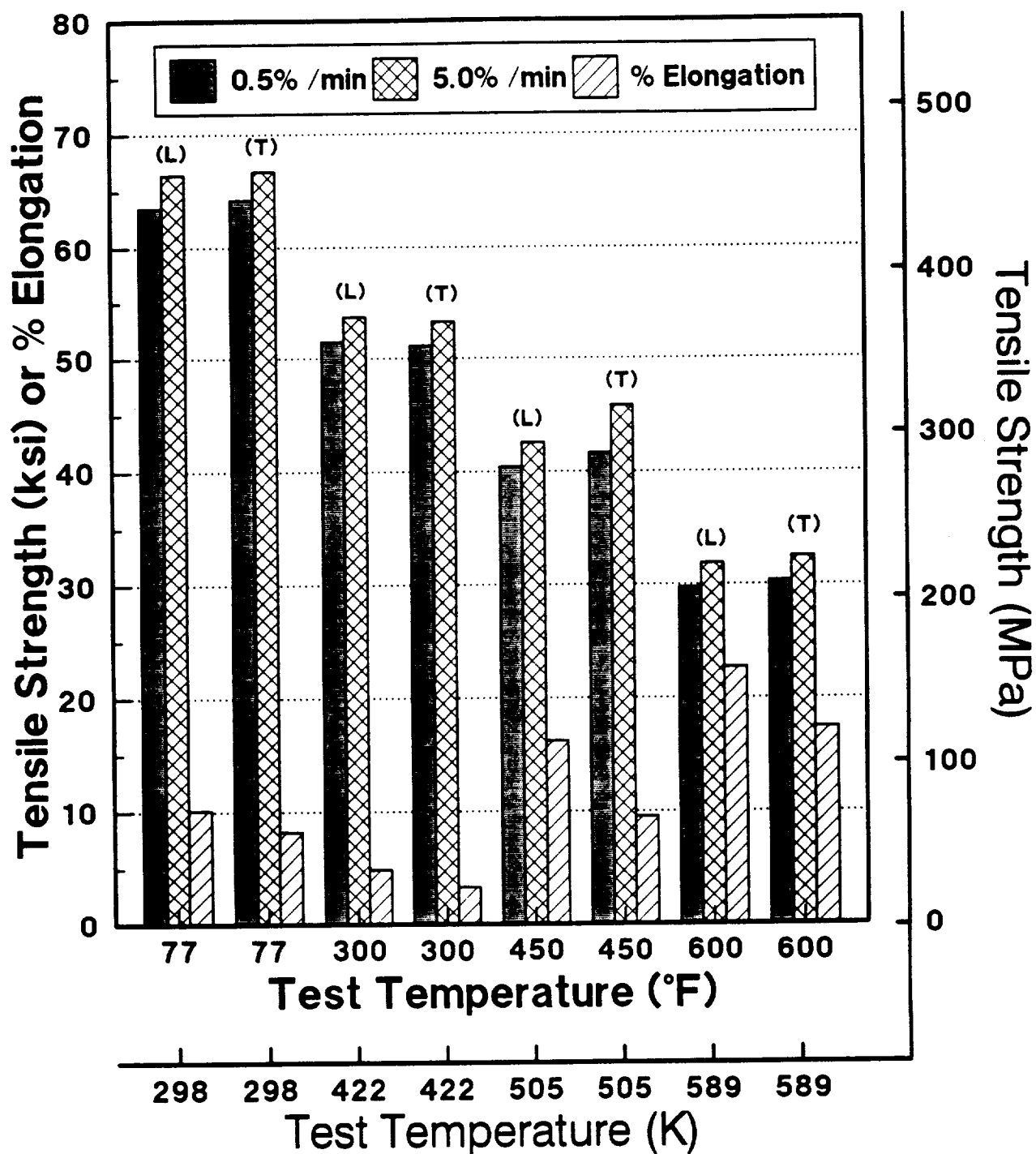


Fig. 26

Tensile Properties vs. Test Temperature

Hot Cross Rolled vs Hot Straight Rolled 0.26 cm (0.1") Sheet

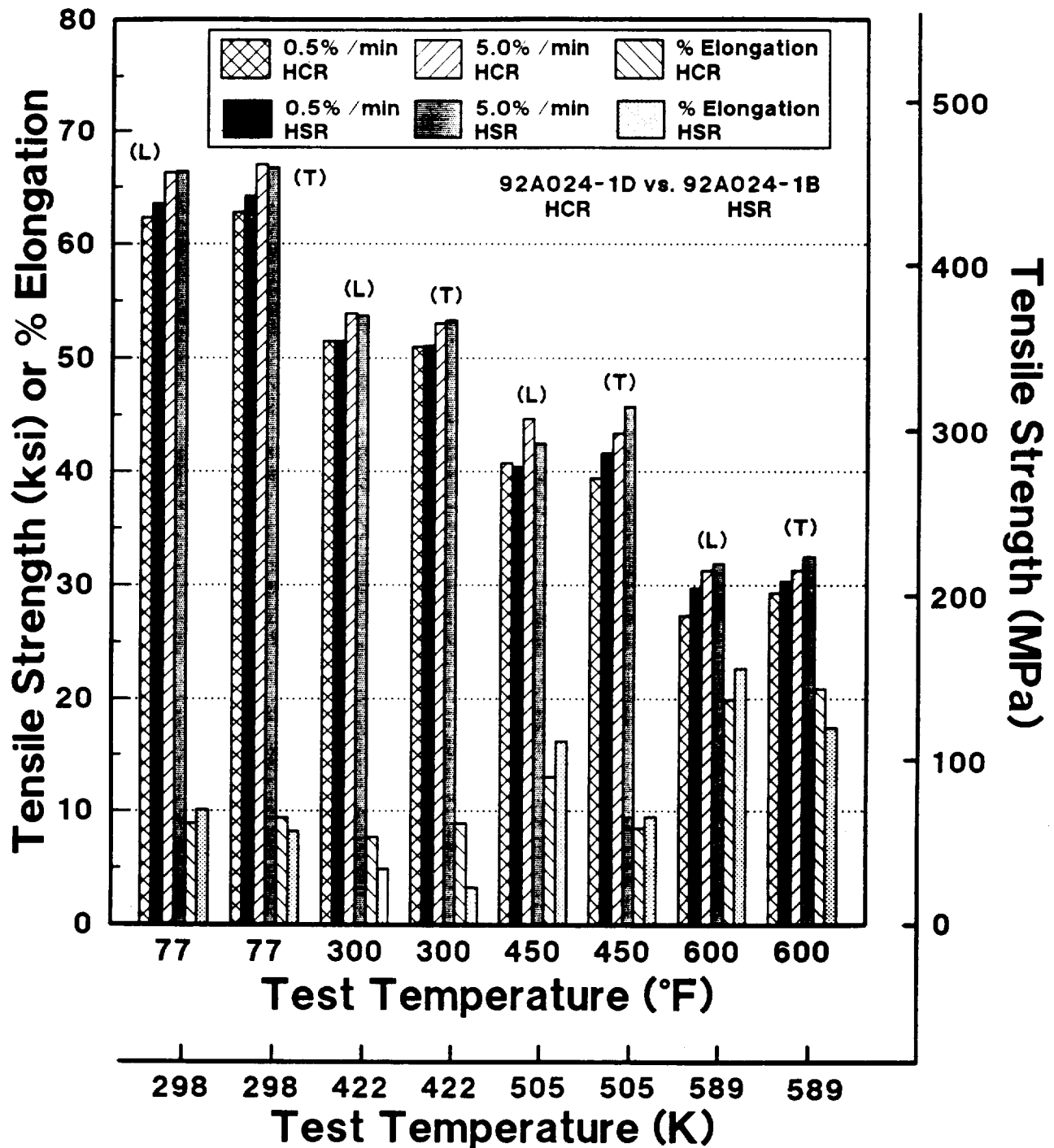


Fig. 27

Tensile Properties vs. Test Temperature

92A024-2B 1 Hot Cross Rolled 0.08 cm (0.03") Sheet

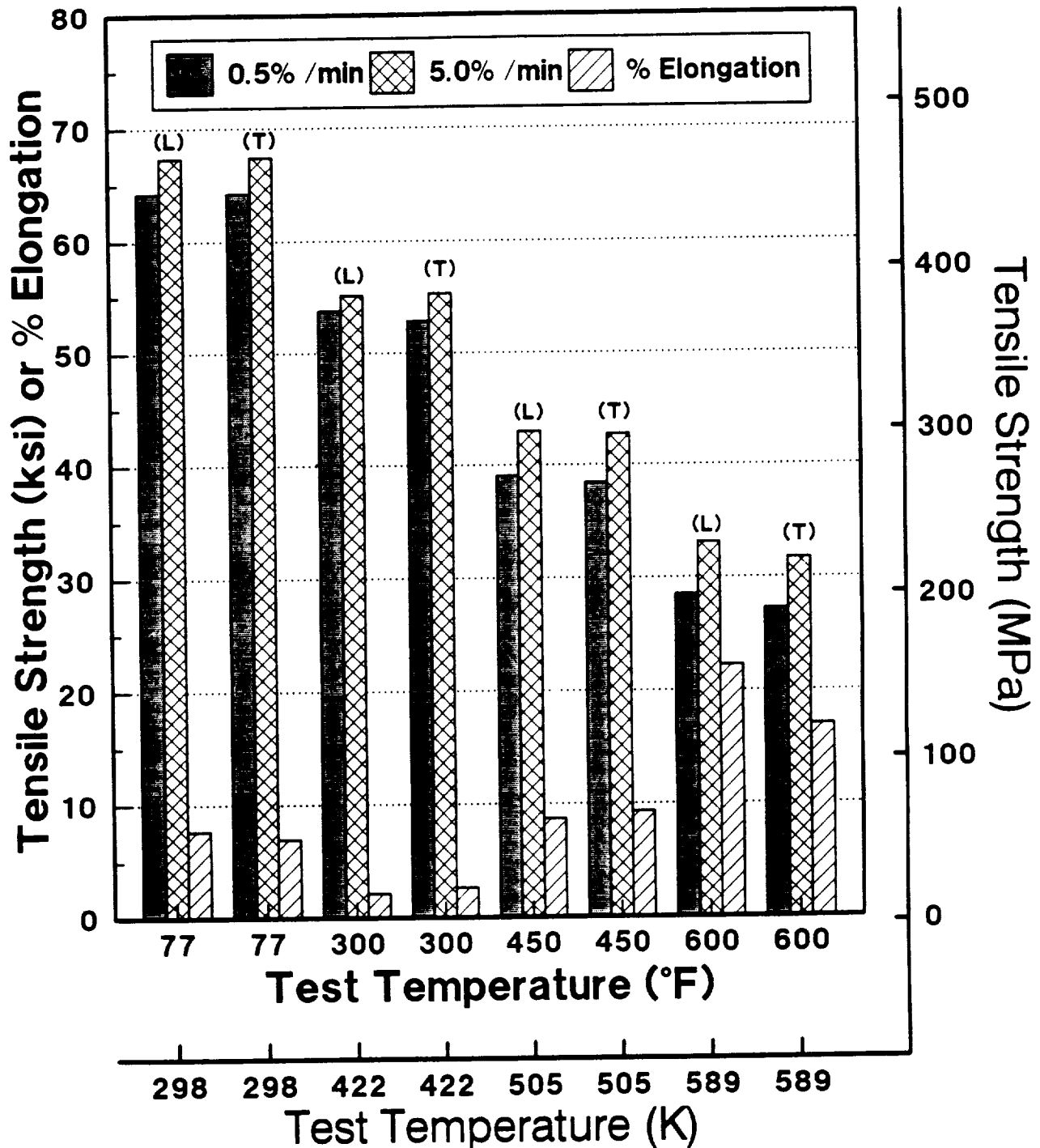


Fig. 28

Tensile Properties vs. Test Temperature

92A024-2A 1 Hot Straight Rolled 0.1 cm (0.04") Sheet

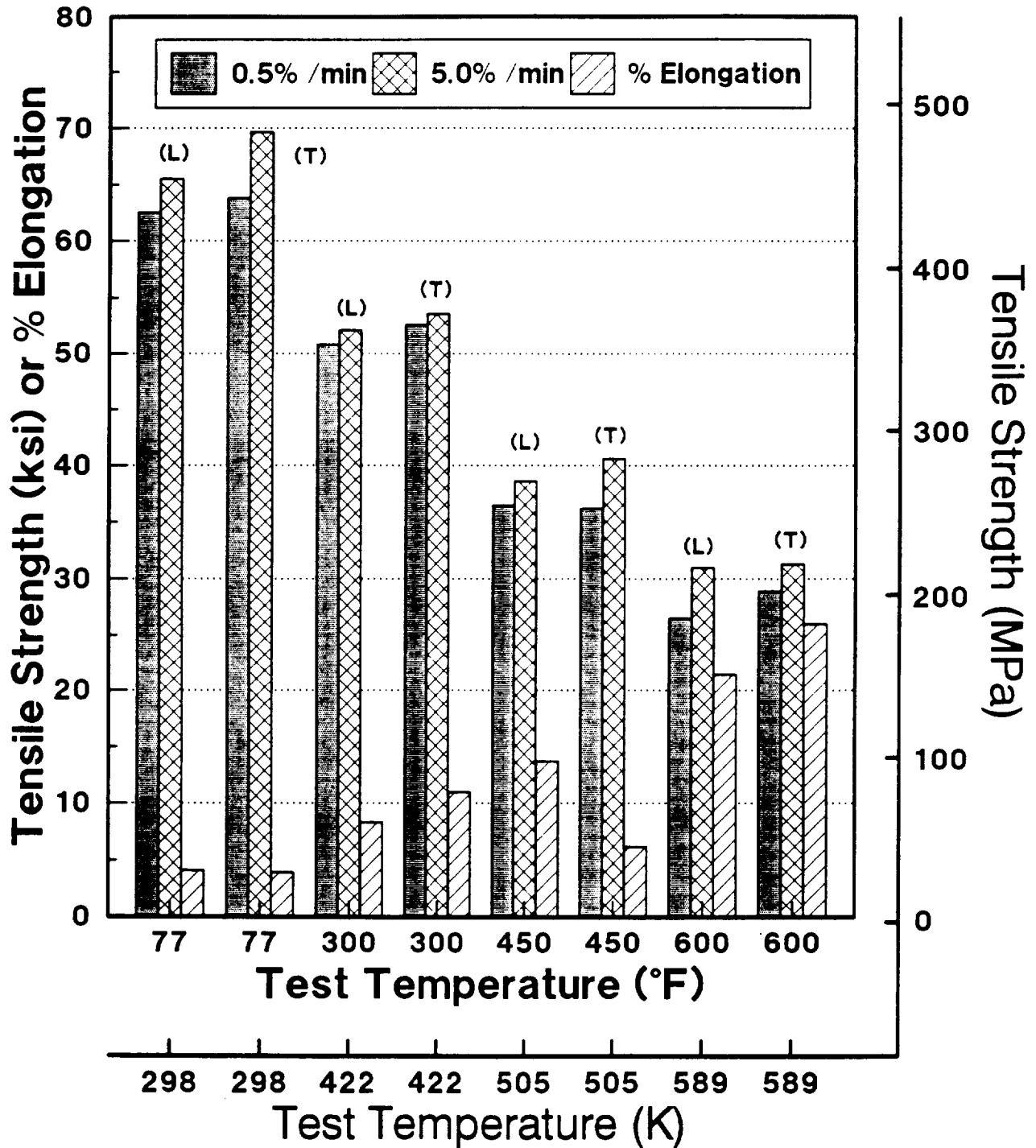


Fig. 29

Tensile Properties vs. Test Temperature

Hot Cross Rolled vs Hot Straight Rolled 0.10 cm (0.04") Sheet

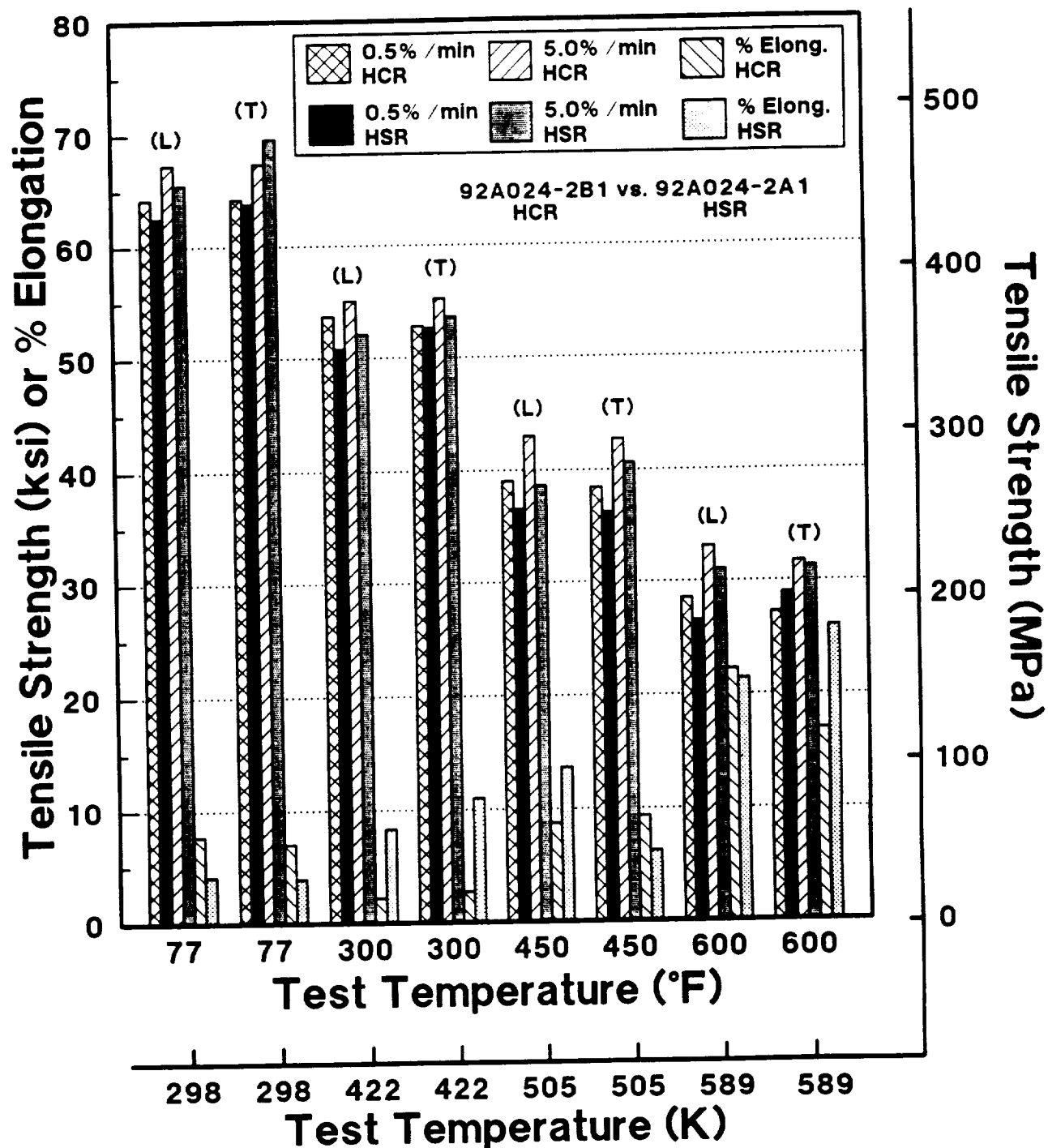


Fig. 30

Tensile Properties vs. Test Temperature

92A024-2B2 Cold Cross Rolled 0.1 cm (0.04") Sheet

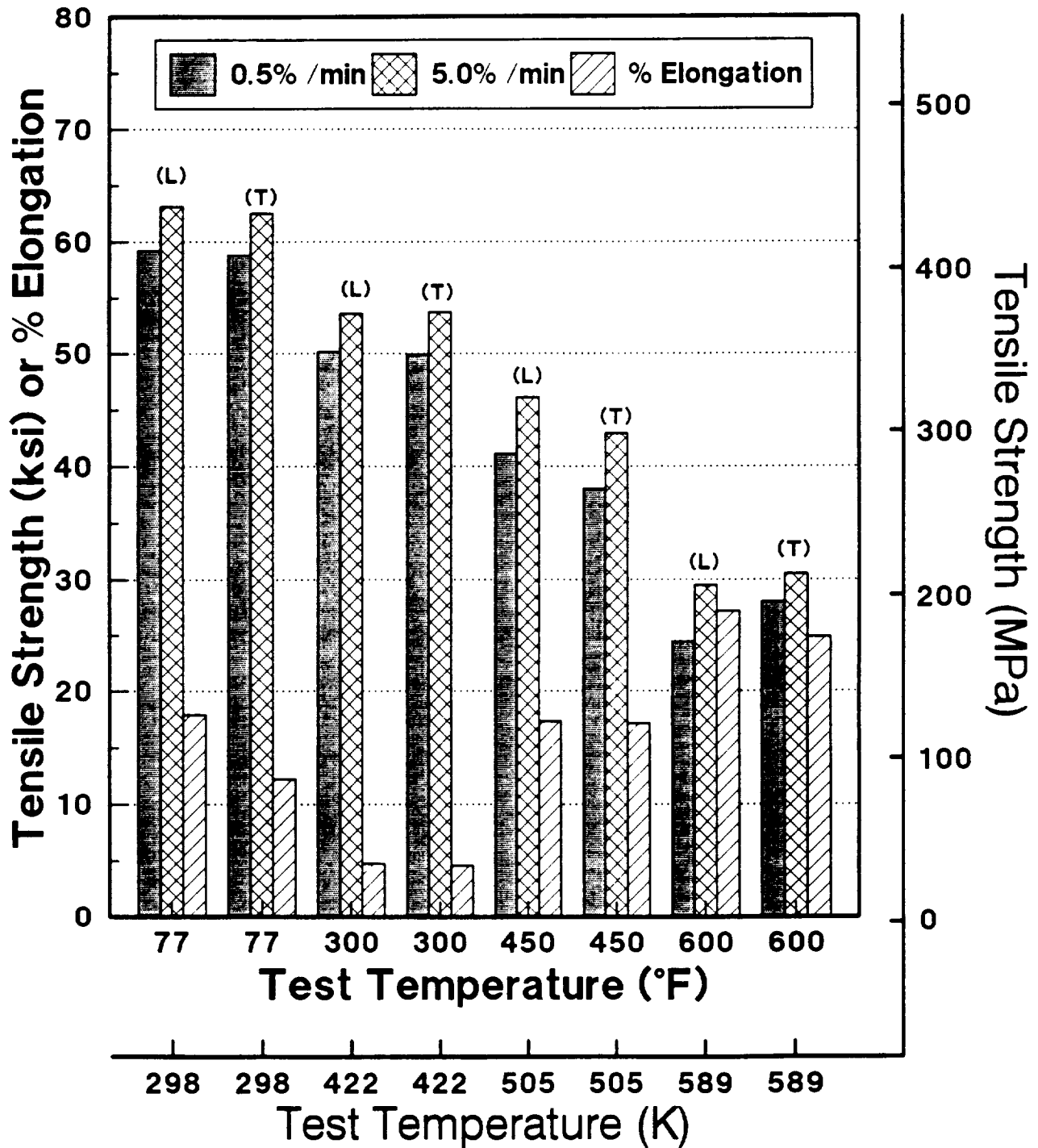


Fig. 31

Tensile Properties vs. Test Temperature

92A024-2A2 Cold Straight Rolled 0.1 cm (0.04") Sheet

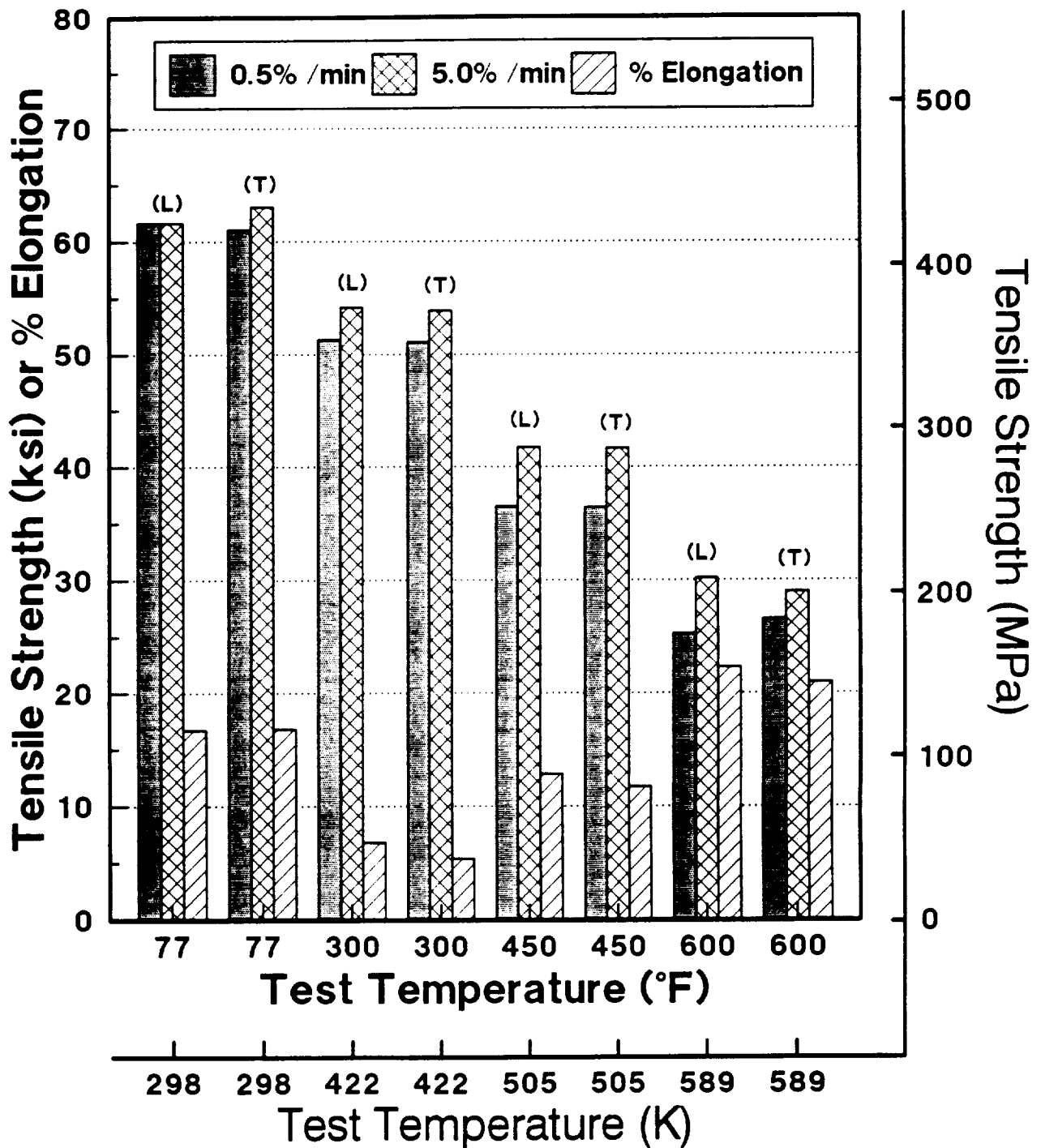


Fig. 32

Tensile Properties vs. Test Temperature

Cold Cross Rolled vs. Cold Straight Rolled 0.1 cm (0.04") Sheet

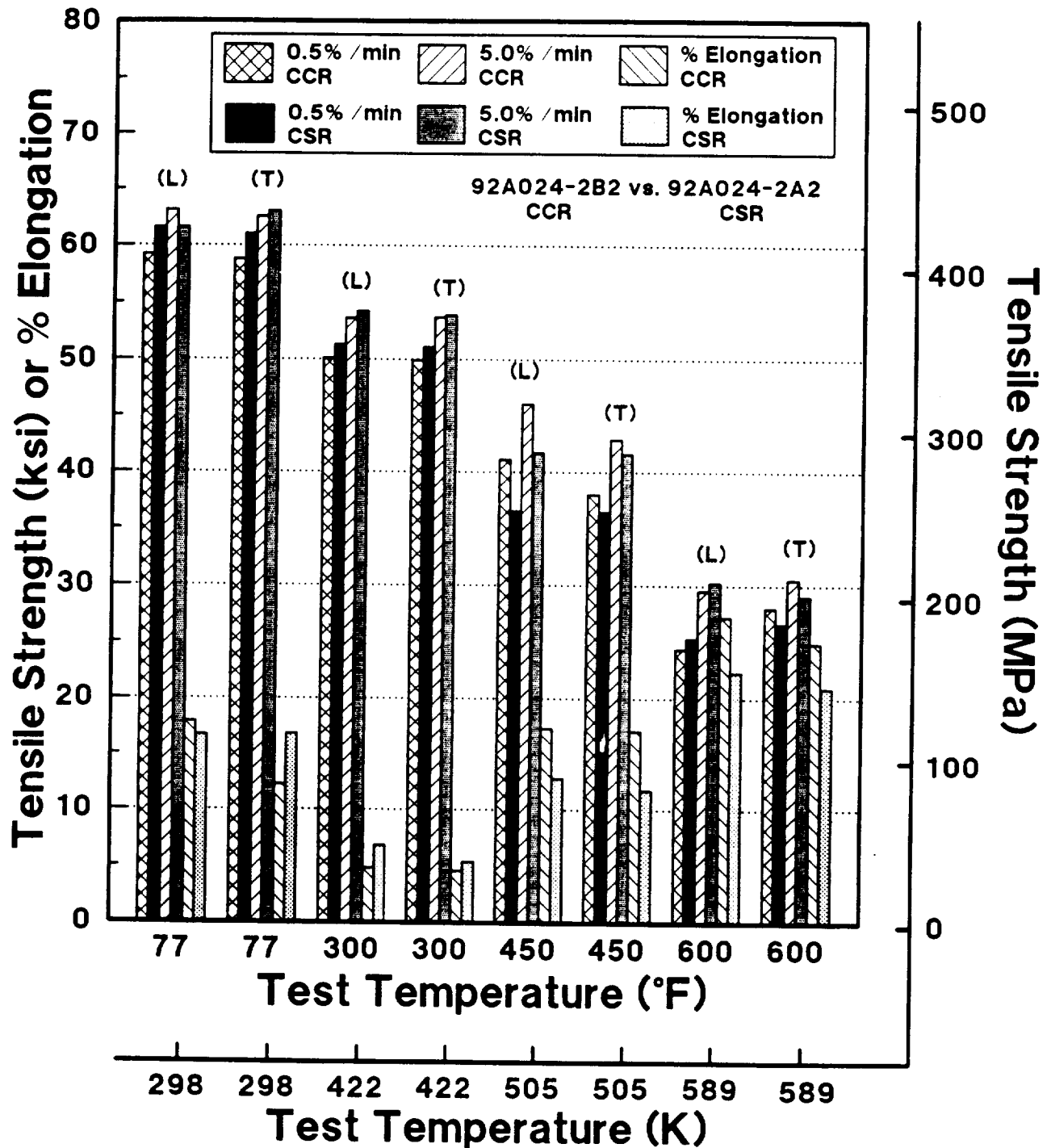


Fig. 33

Tensile Properties vs. Test Temperature

92A024-2B3 Cold Cross Rolled w/ Anneals 0.1 cm (0.04") Sheet

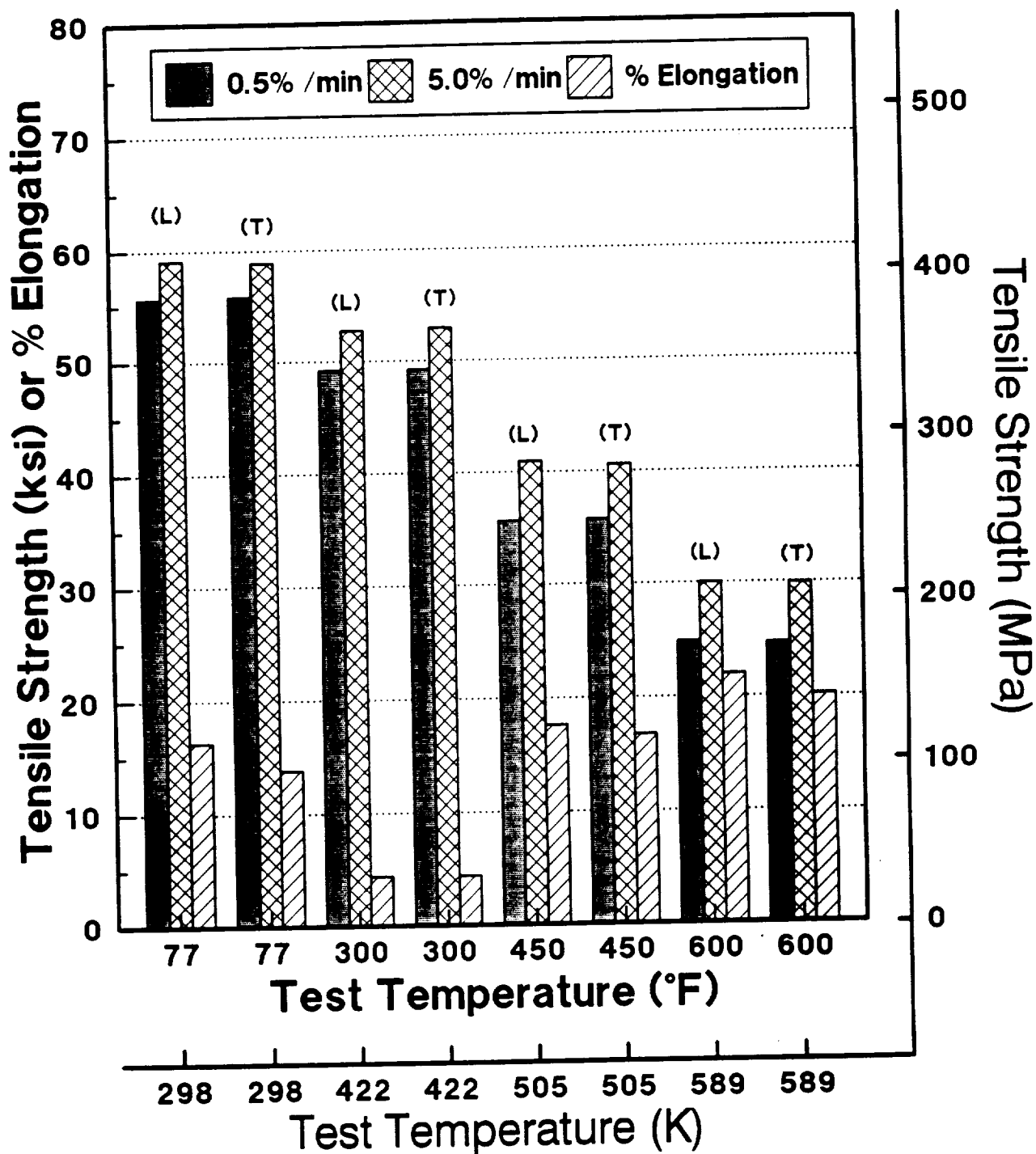


Fig. 34

Tensile Properties vs. Test Temperature

92A024-2A3 Cold Straight Rolled w/ Anneals 0.1 cm (0.04") Sheet

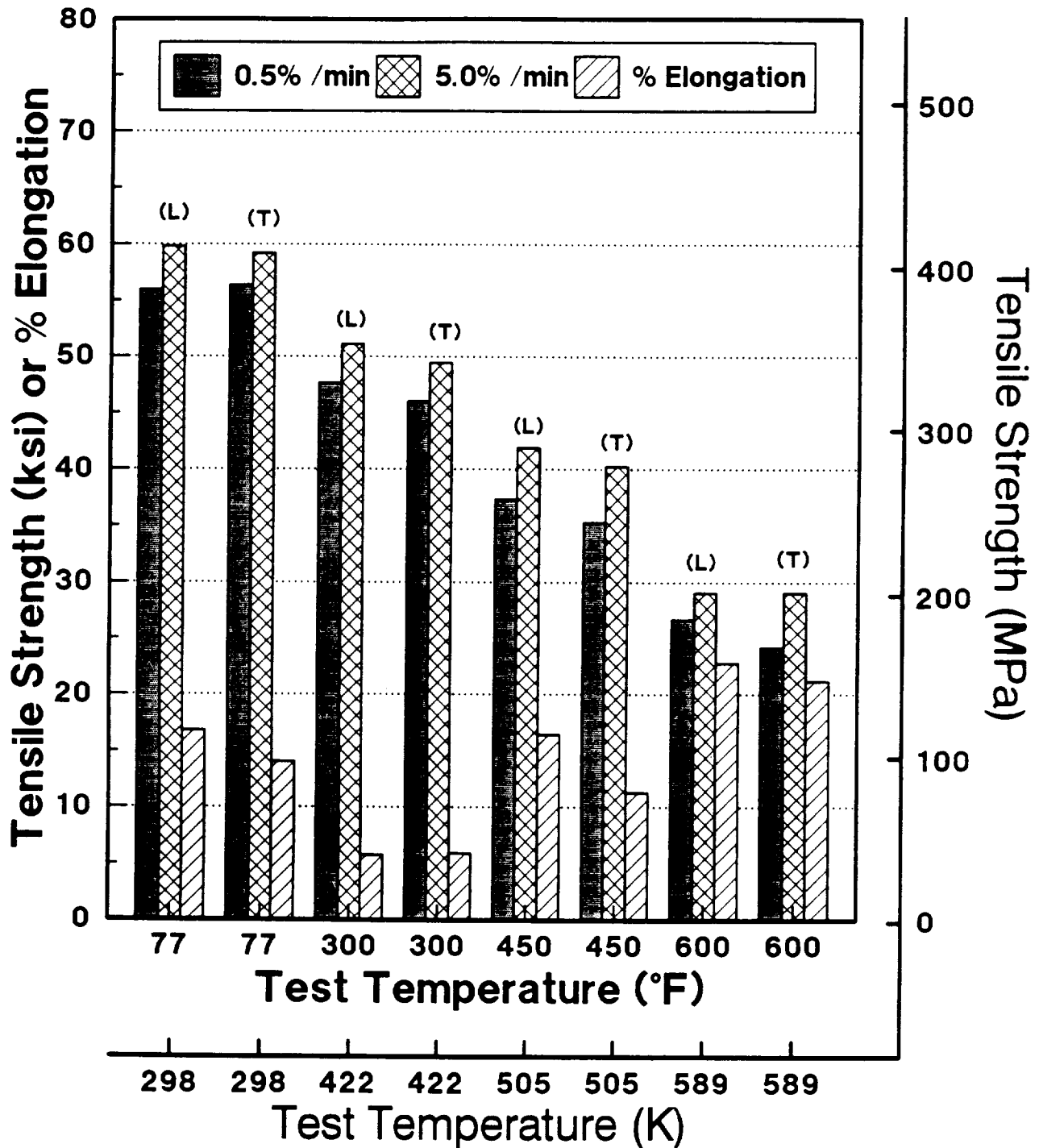


Fig. 35

Tensile Properties vs. Test Temperature

Cold Cross Rolled vs. Cold Straight Rolled 0.1 cm (0.04") Sheet w/ Anneals

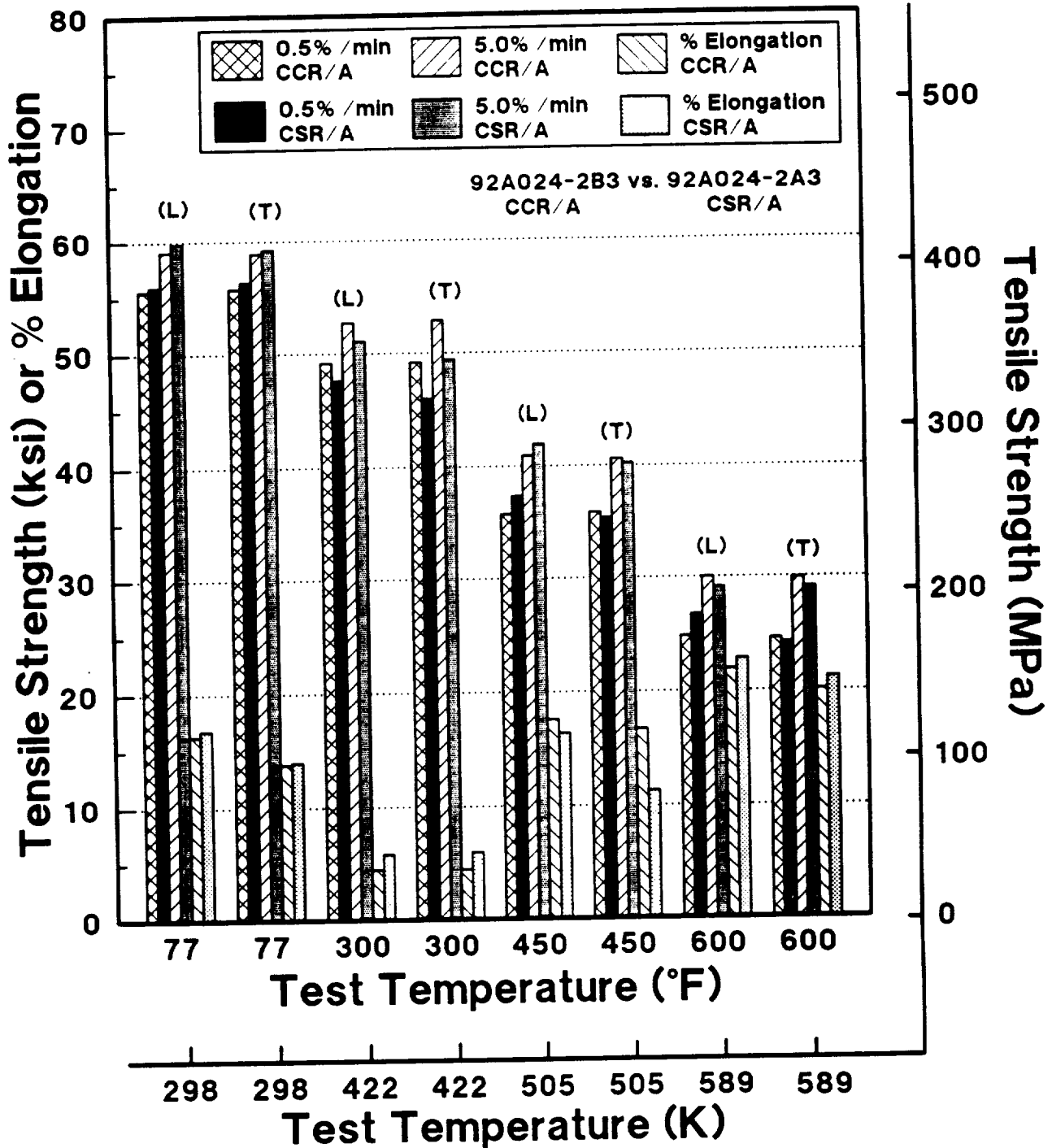


Fig. 36

Tensile Properties vs. Test Temperature Hot Rolled 92A022 Sheet

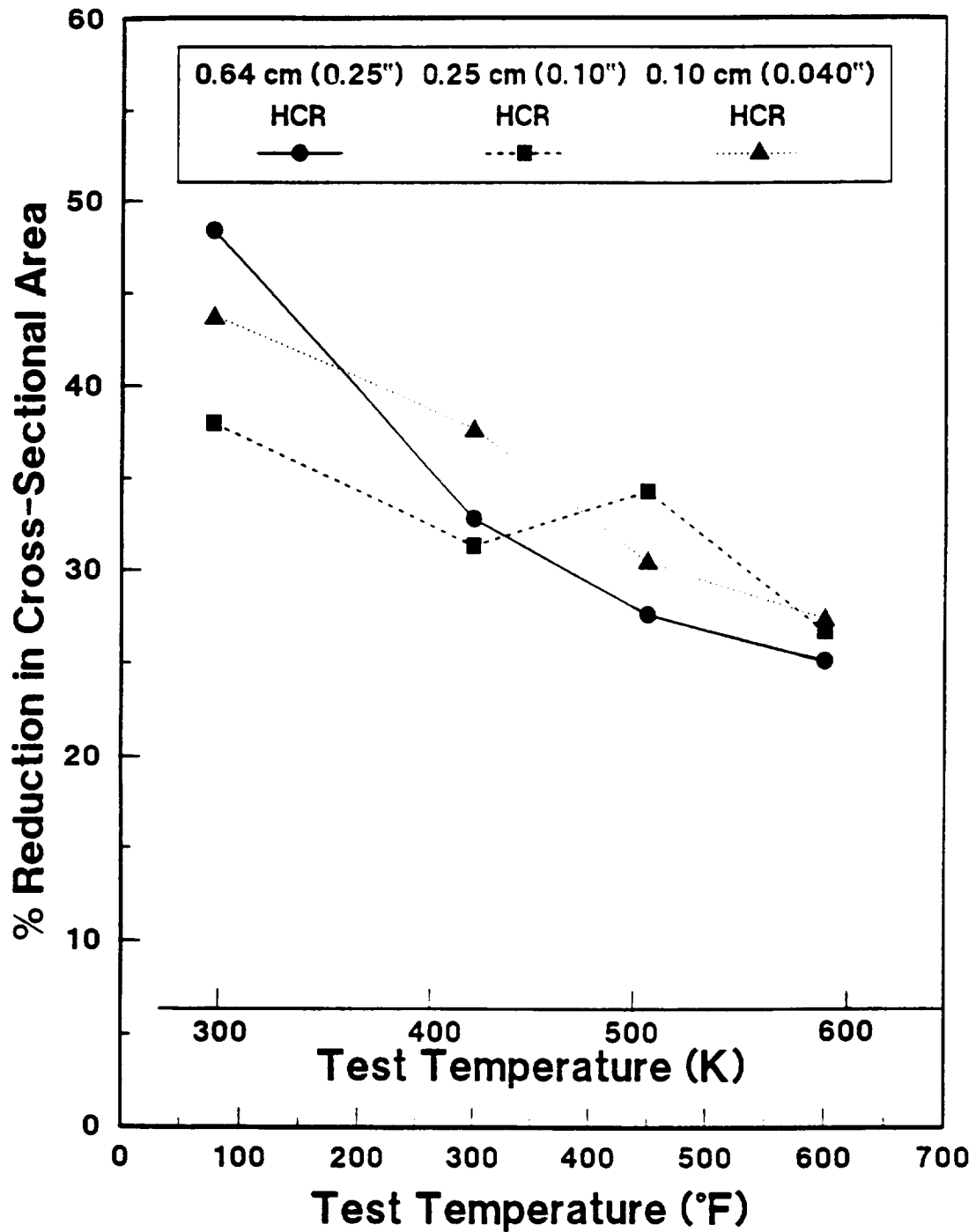


Fig. 37

Tensile Properties vs. Test Temperature **Cold Rolled 92A022 Sheet with & without Anneals**

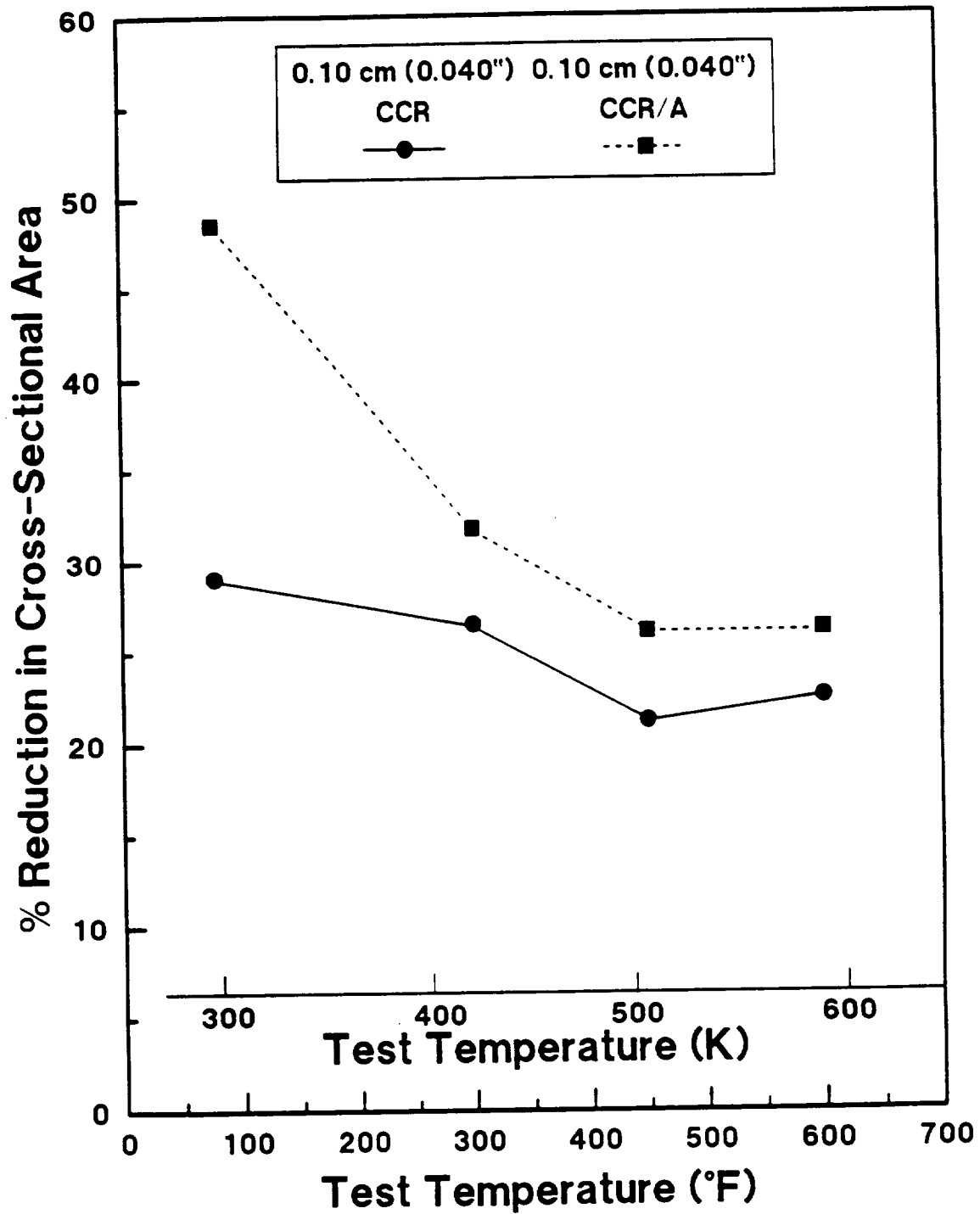


Fig. 38

Tensile Properties vs. Test Temperature Hot Rolled 92A024 Sheet

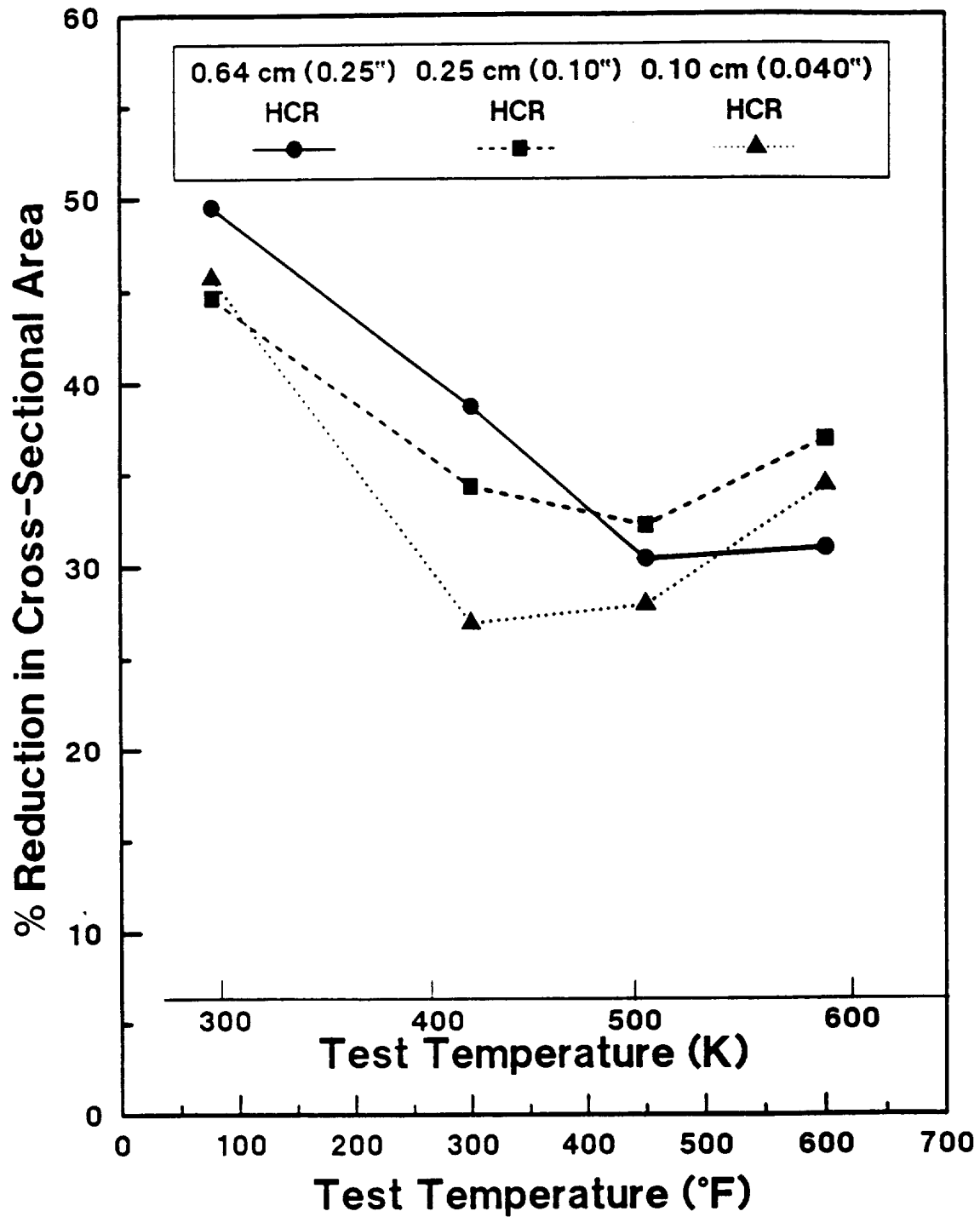


Fig. 39

Tensile Properties vs. Test Temperature **Cold Rolled 92A024 Sheet with & without Anneals**

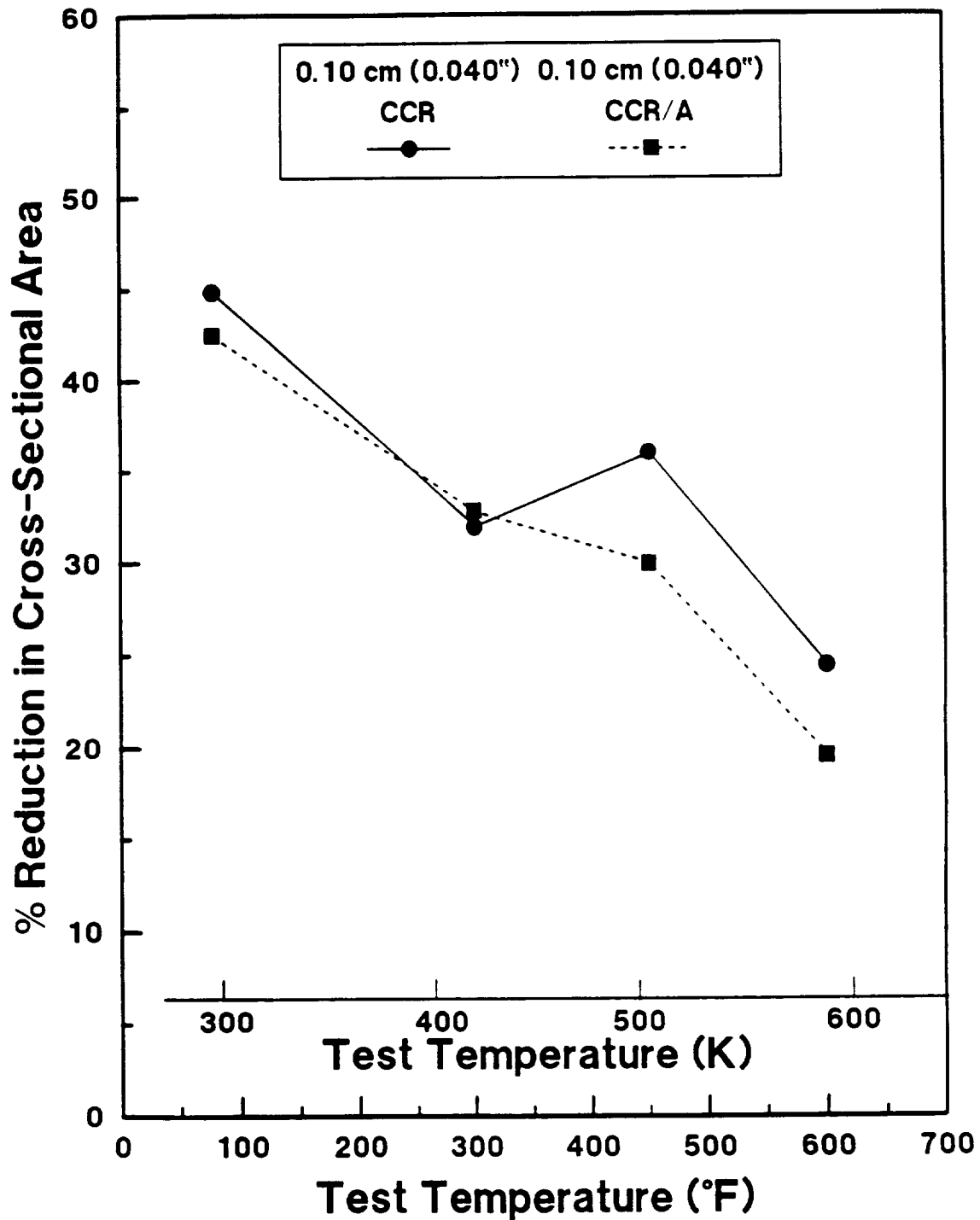


Fig. 40

Effect of Strain Rate on Tensile Properties

92A024- 1C&1A Hot Cross & Straight Rolled Sheet

0.64 cm (0.25") Gauge

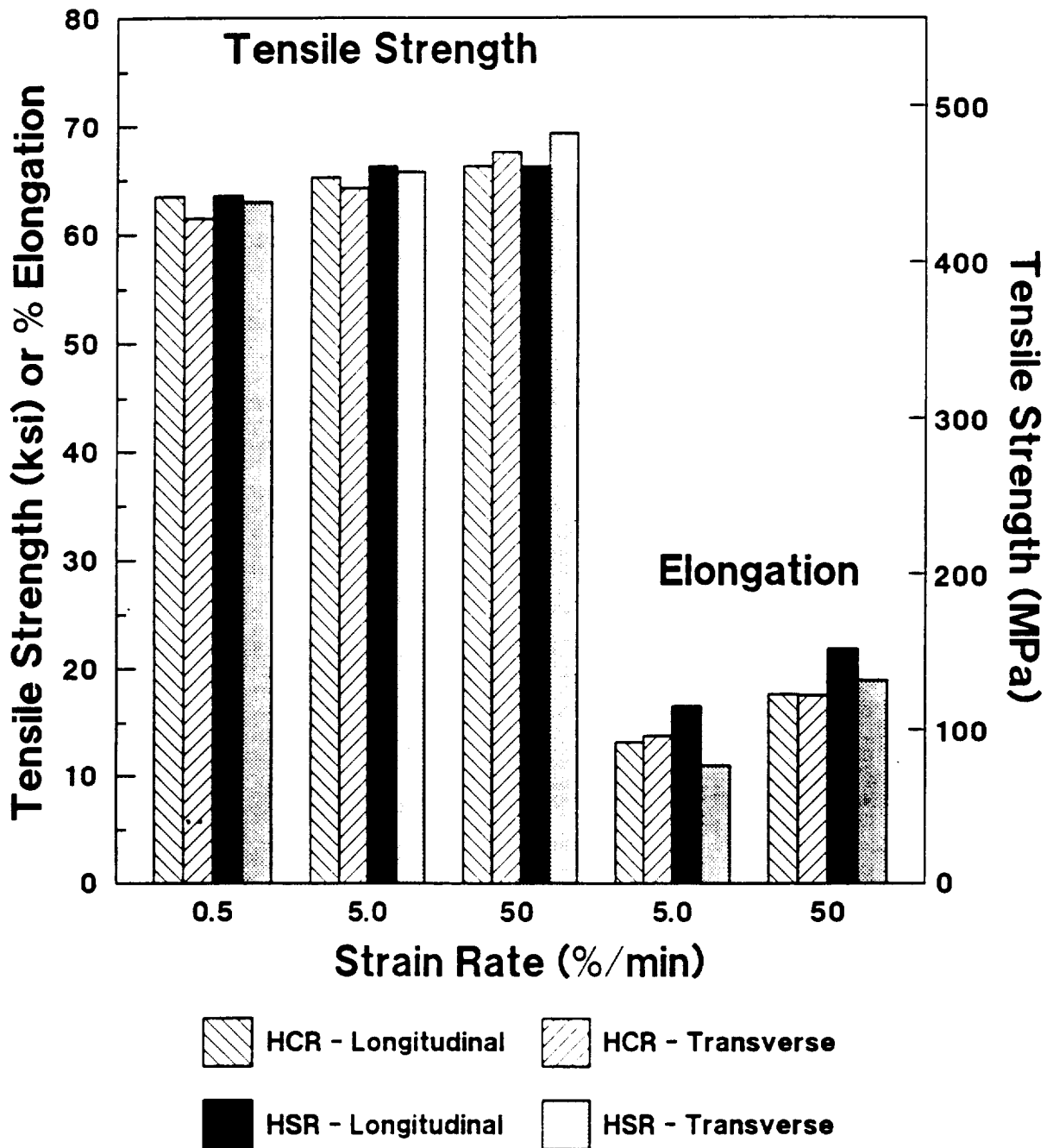


Fig. 41

Effect of Strain Rate on Tensile Properties

92A024- 1D& 1B Hot Cross & Straight Rolled Sheet

0.25 cm (0.90") Gauge

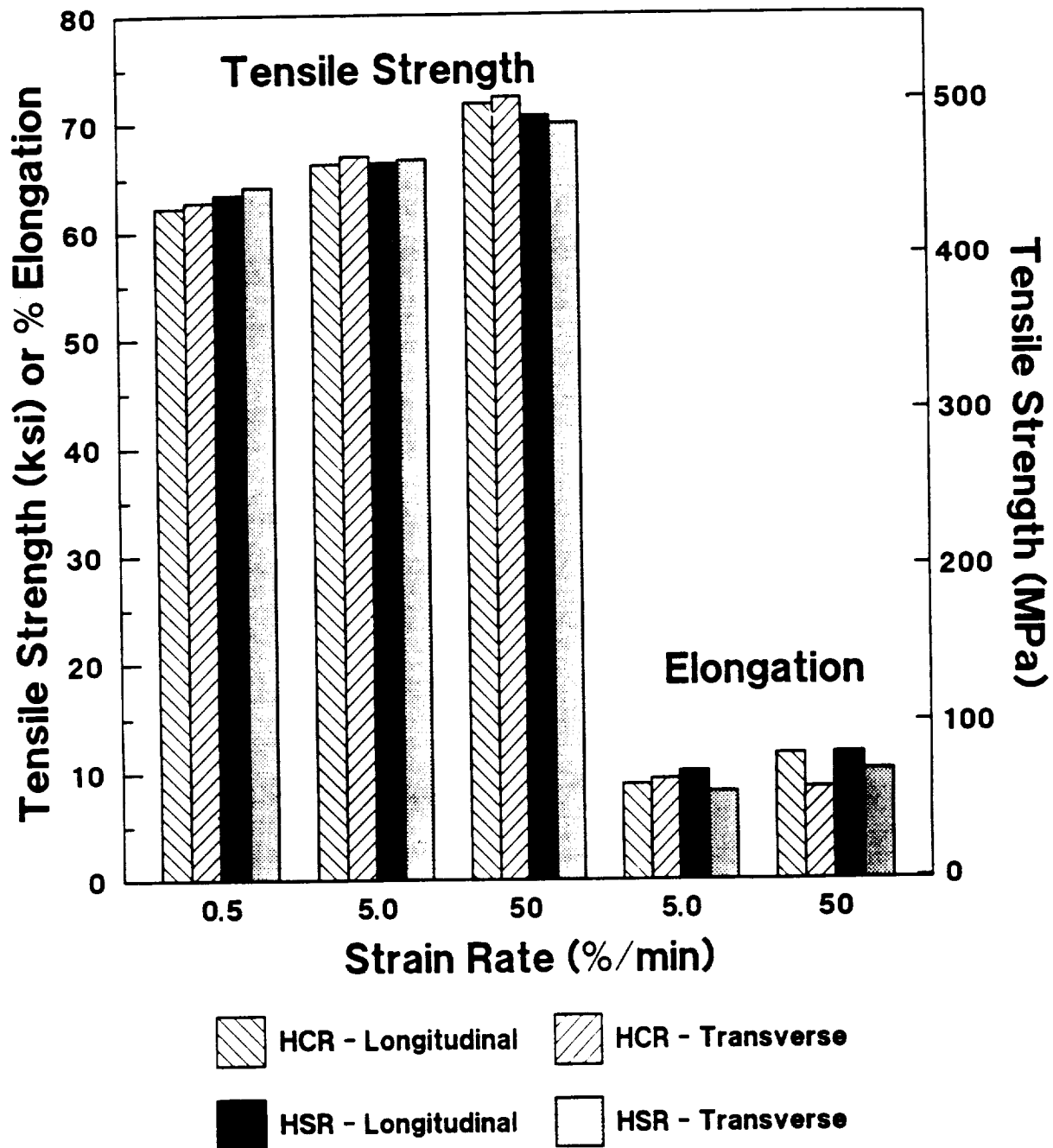


Fig. 42

Effect of Strain Rate on Tensile Properties

92A024- 2B 1&2A 1 Hot Cross & Straight Rolled Sheet

0.10 cm (0.04") Gauge

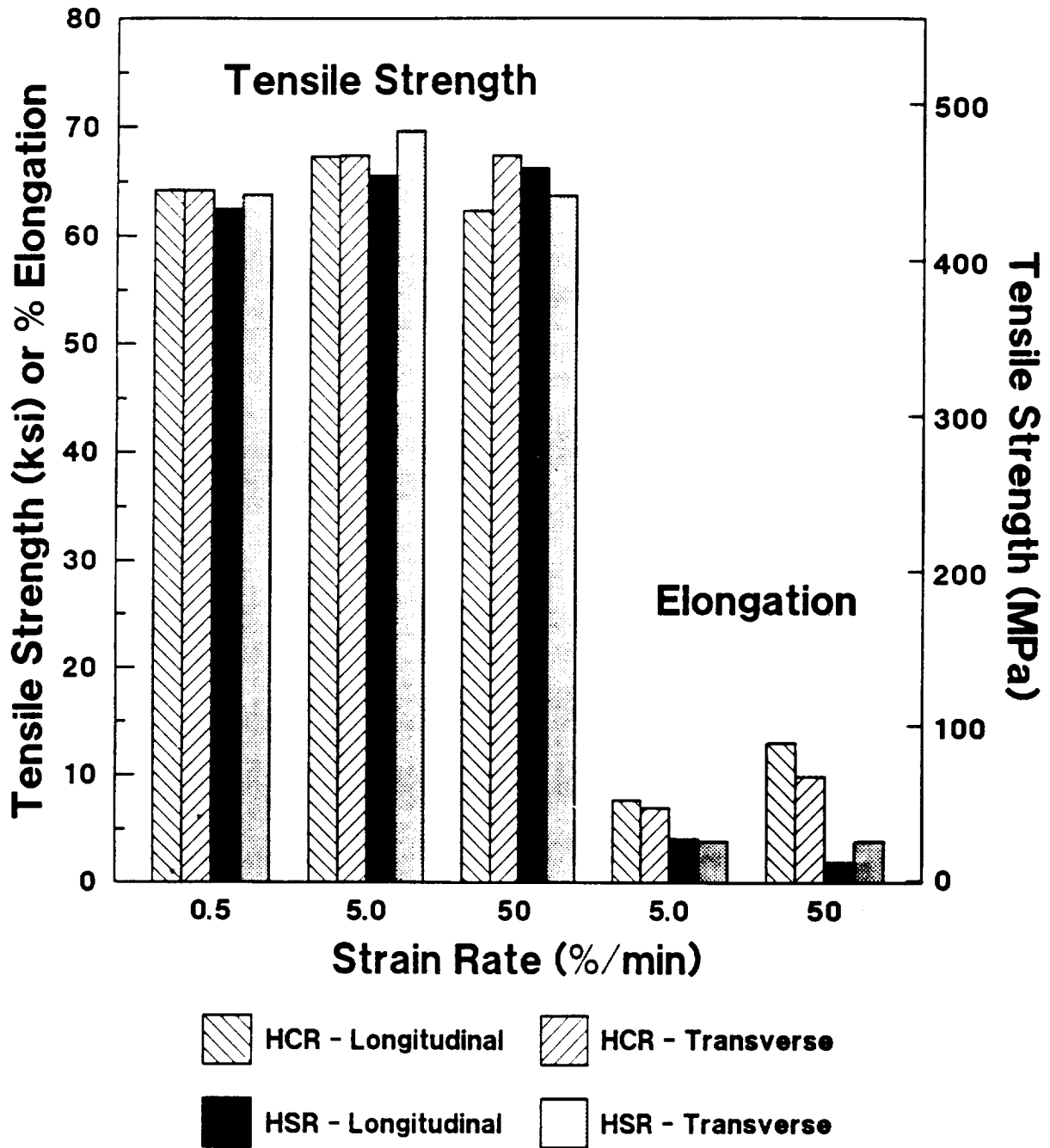


Fig. 43

Effect of Strain Rate on Tensile Properties

92A024- 2B2&2A2 Cold Cross & Straight Rolled Sheet

0.10 cm (0.04") Gauge

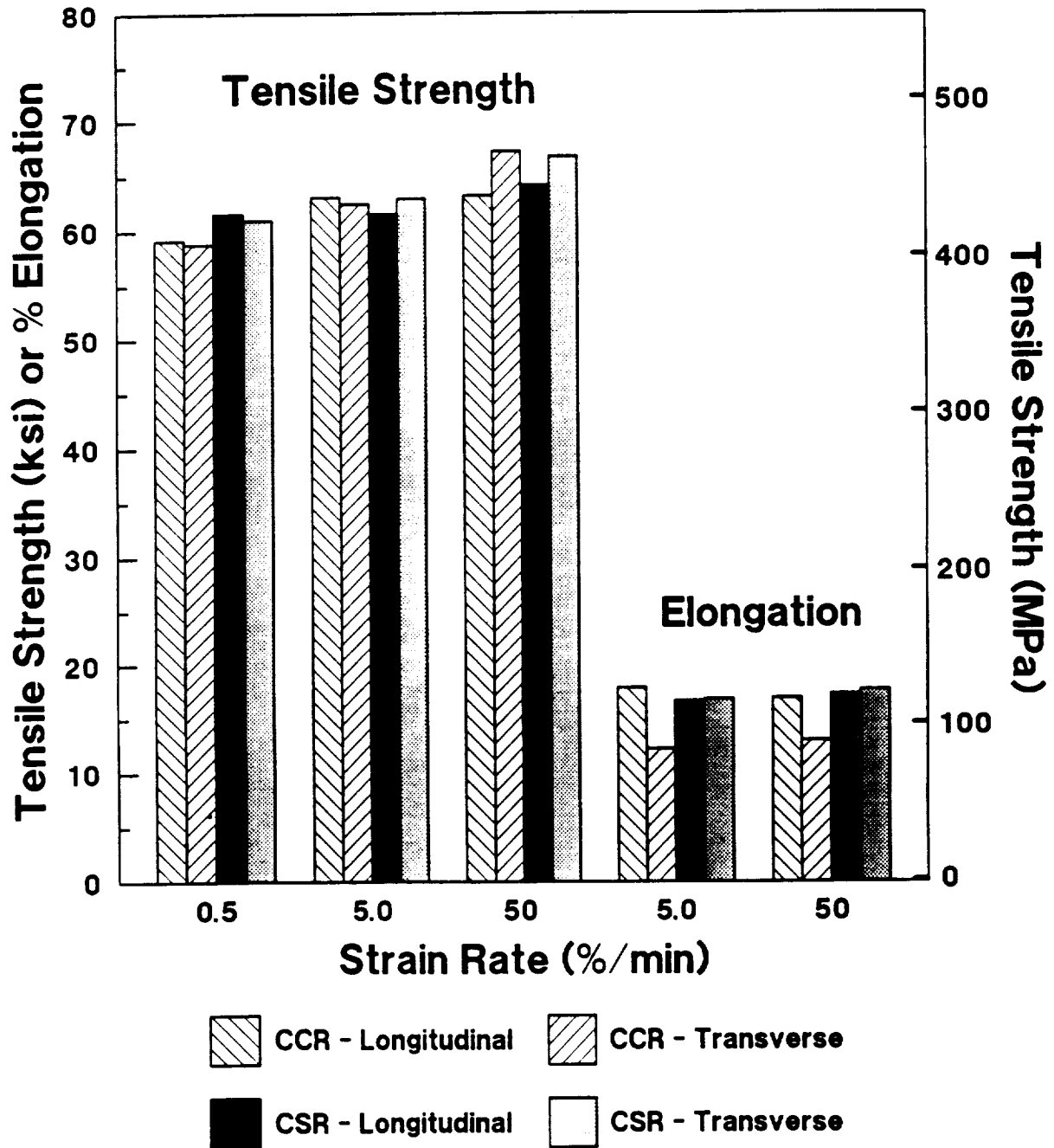
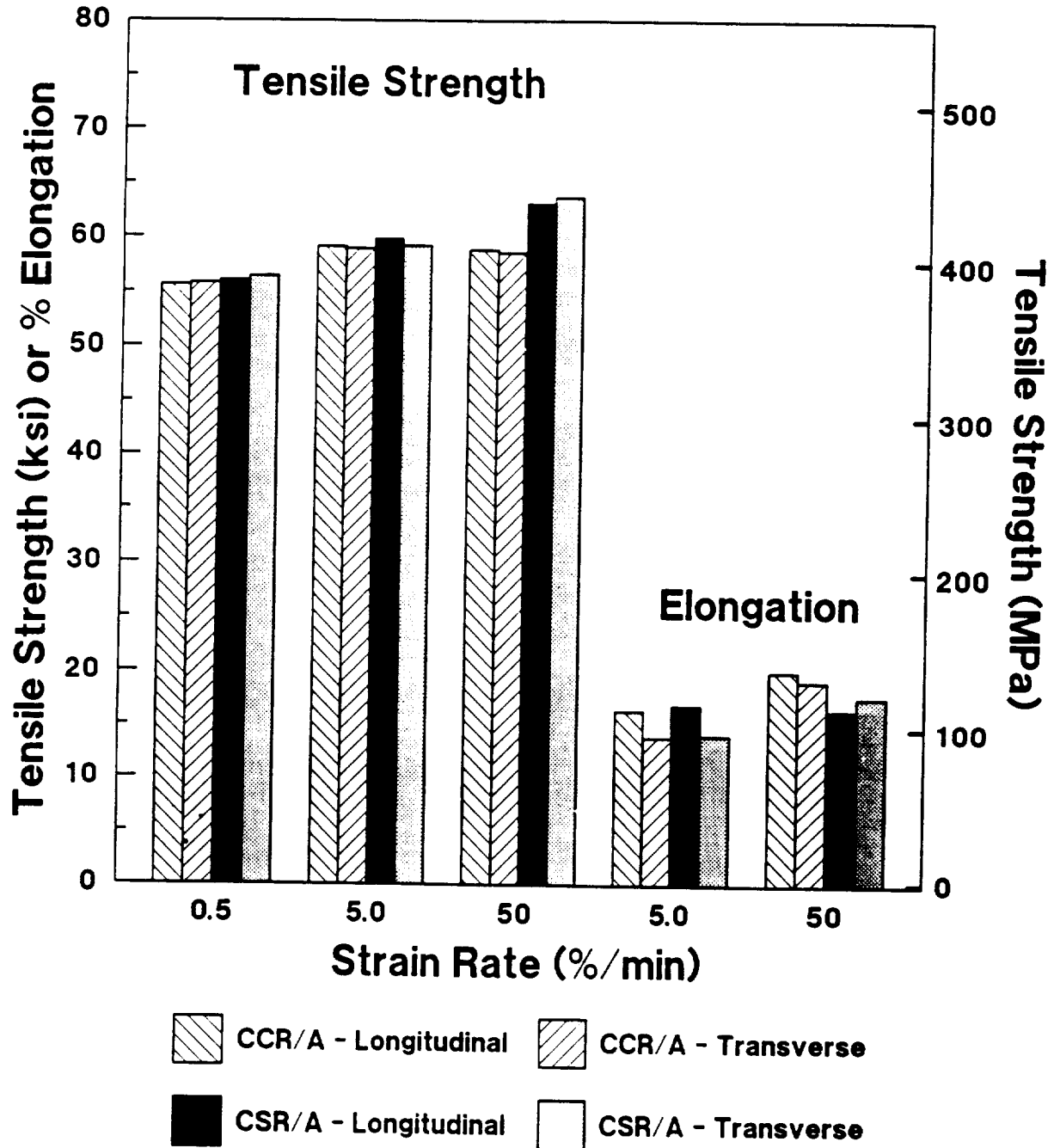


Fig. 44

Effect of Strain Rate on Tensile Properties

92A024- 2B3&2A3 Cold Cross & Straight Rolled Sheet w/ Anneals

0.10 cm (0.04") Gauge



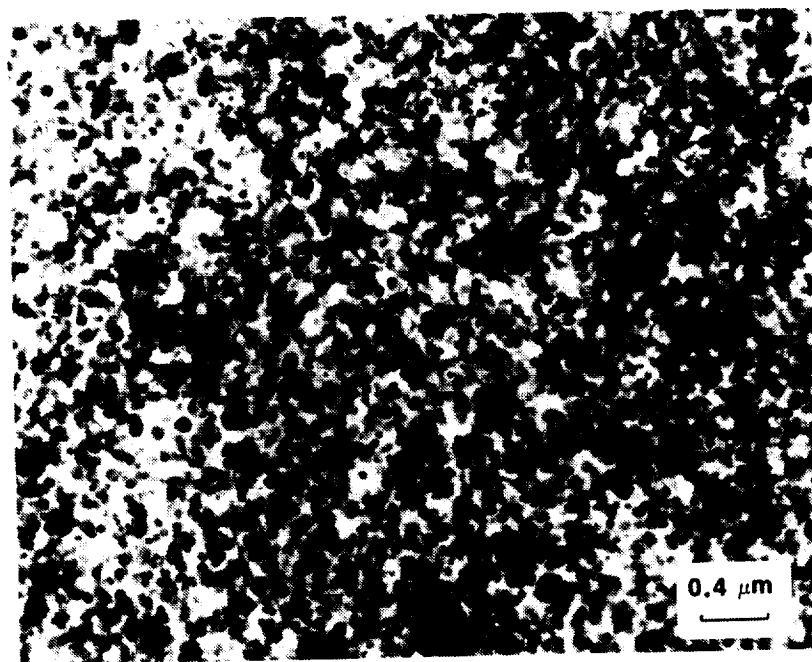


Fig. 45. The microstructure of the as-extruded rolling preform 92A022 is comprised of very fine, 50-80 nm $\text{Al}_{13}(\text{Fe},\text{V})_3\text{Si}$ dispersoids present in an Al-solid solution matrix.

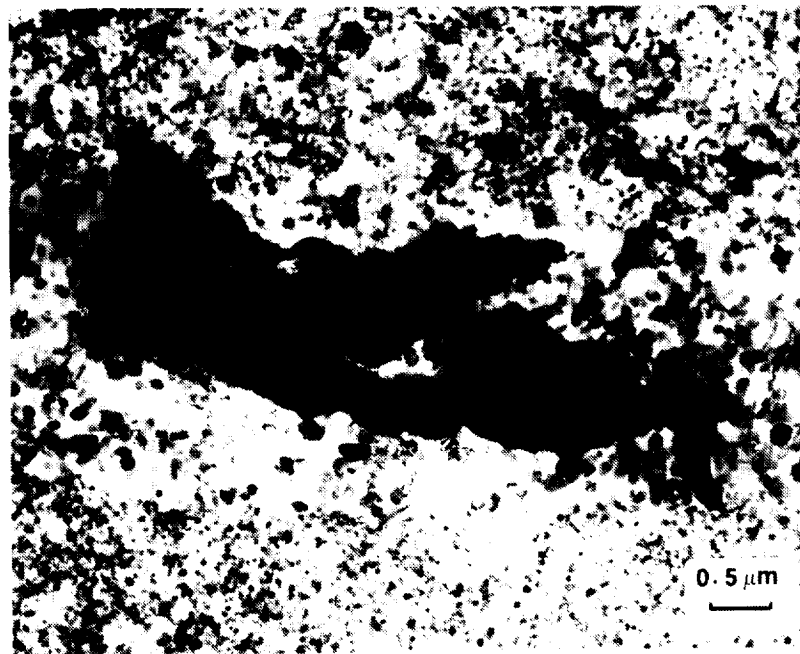


Fig. 46. Extrusion 92A024 indicates a fairly comparable microstructure to that of extrusion 92A022; however, large regions of carbon (i.e., graphite) contamination were observed to be scattered throughout the material.

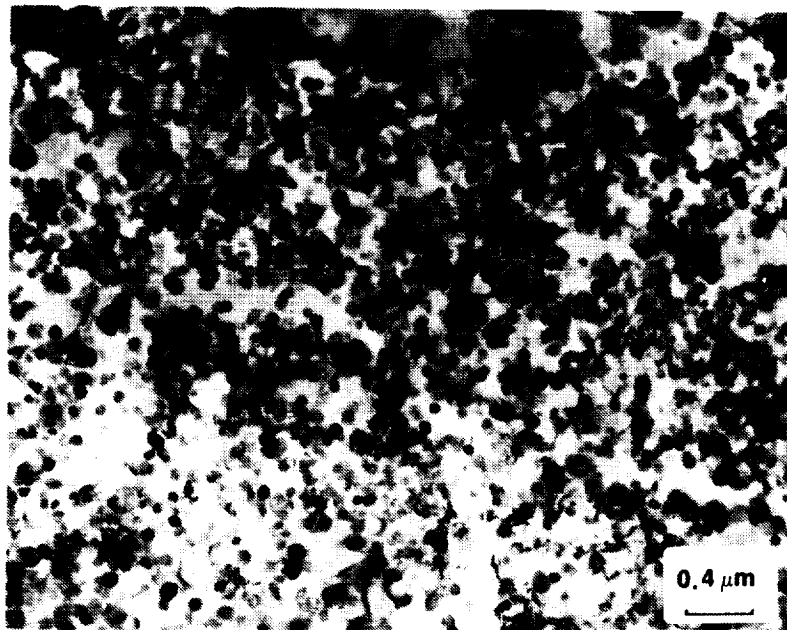


Fig. 47. TEM performed on hot-rolled 0.64 cm (0.25") gauge 92A022 plate indicates a microstructure very comparable to that of the parent extrusion.

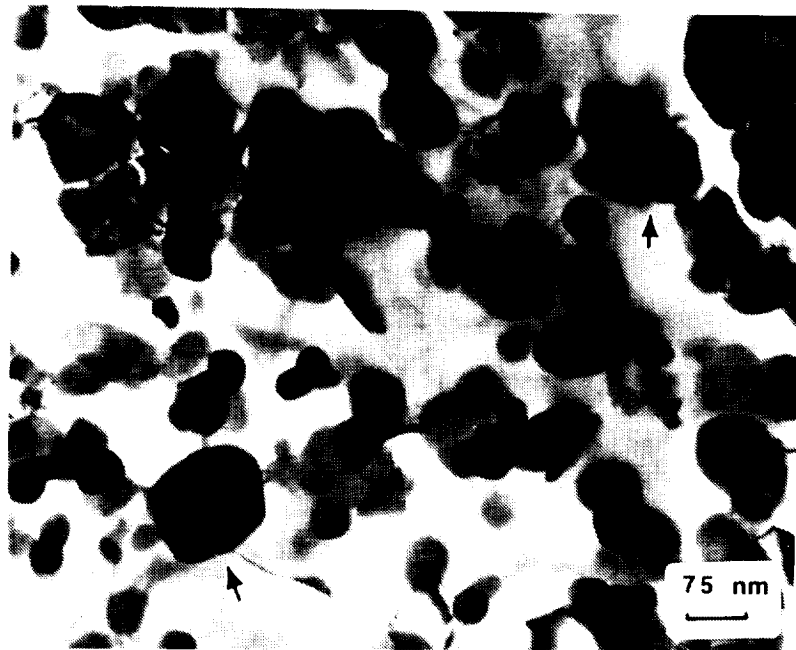


Fig. 48. Similarly, little change in microstructure is observed for hot-rolled 0.22 cm (0.090") gauge 92A022 sheet.

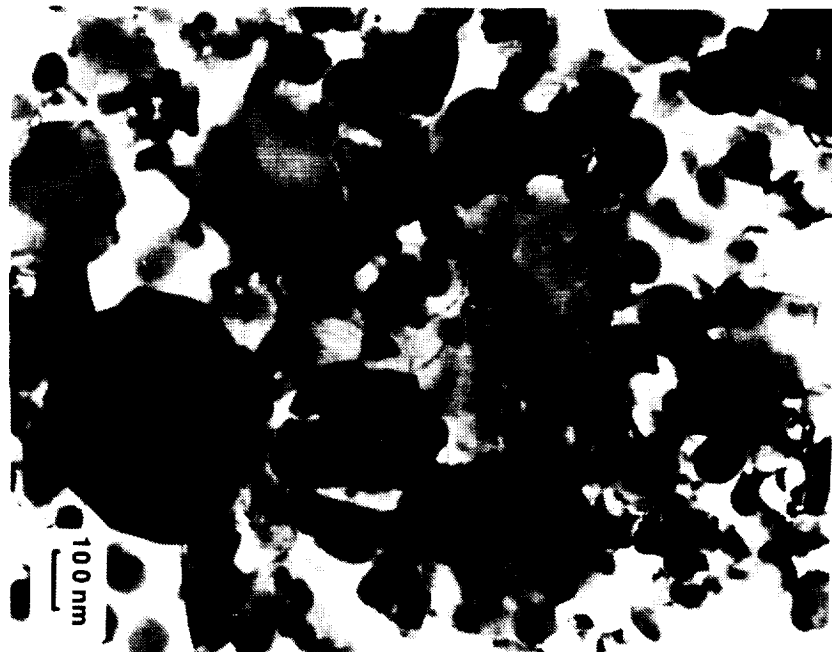


Fig. 49. The tendency to find coarser silicide particles present at grain/subgrain boundaries in the thinner gauge, hot-rolled 92A022 0.10 cm (0.040") gauge sheet is evident.

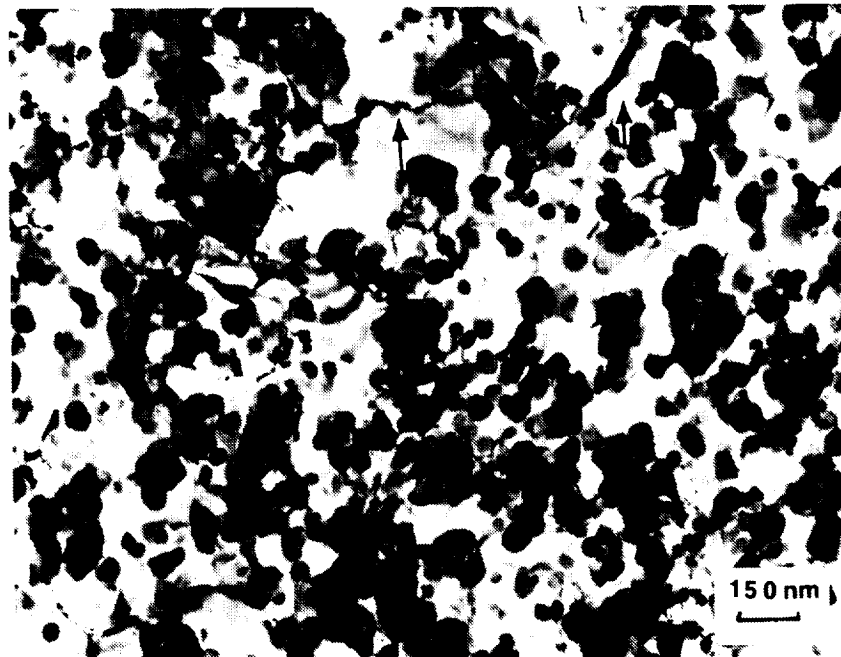


Fig. 50. The microstructure of 0.10 cm (0.040") gauge sheet cold-rolled from 0.22 cm (0.090") gauge hot rolled sheet does not exhibit the same extent of coarse silicide particles present at the boundaries as the hot-rolled 0.10 cm (0.040") gauge sheet.

Fig. 51



Fig. 51. Weak beam, dark field electron microscopy performed on these highlighted areas in cold-rolled sheet (brightfield), and Fig. 52 (weak-beam darkfield) clearly indicates dislocations associated with these boundaries.

Fig. 52

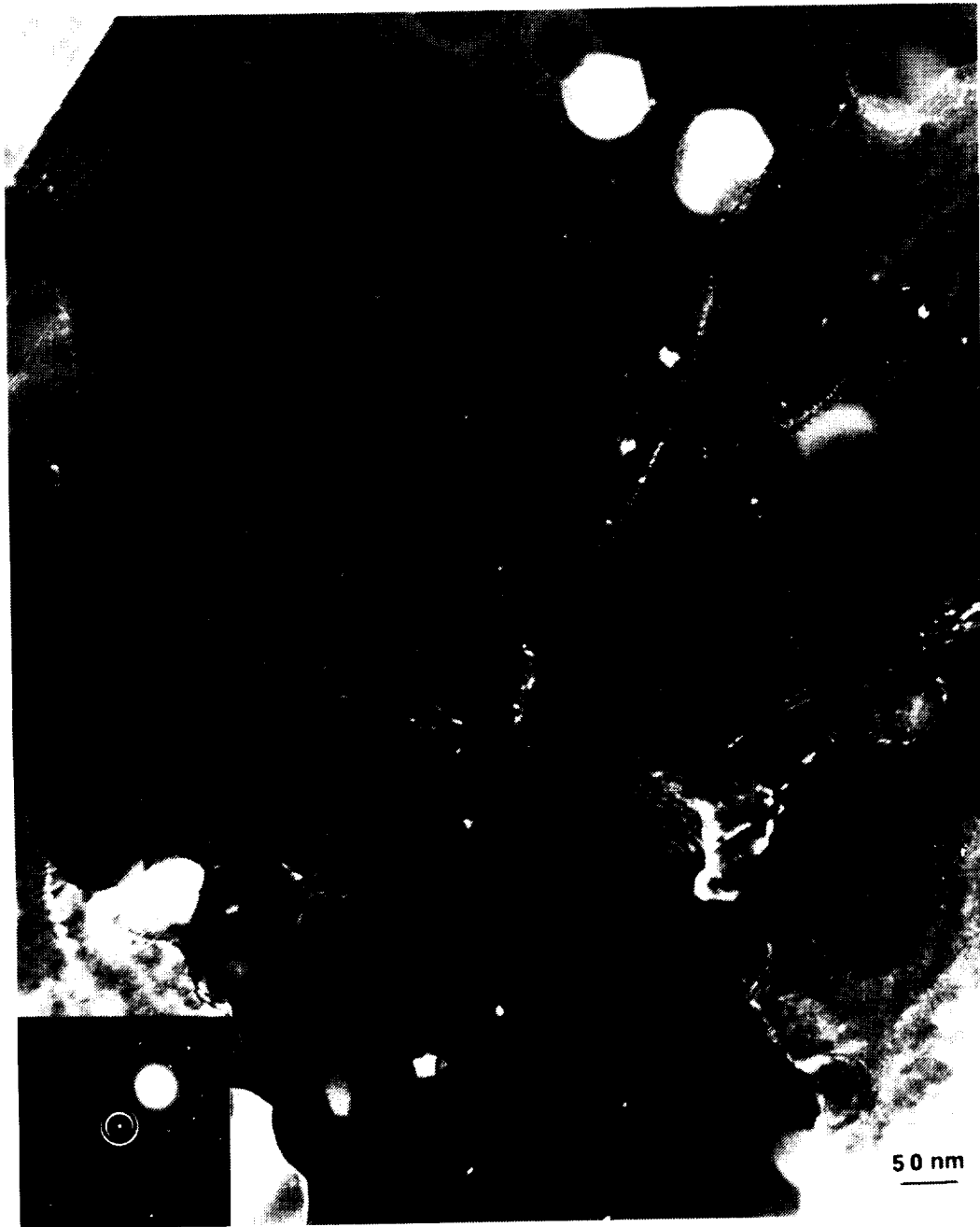


Fig. 52. Fig. 51 shows weak beam, dark field electron microscopy performed on these highlighted areas in cold-rolled sheet (brightfield), and Fig. 52 (weak-beam darkfield) clearly indicates dislocations associated with these boundaries.

Fig. 53

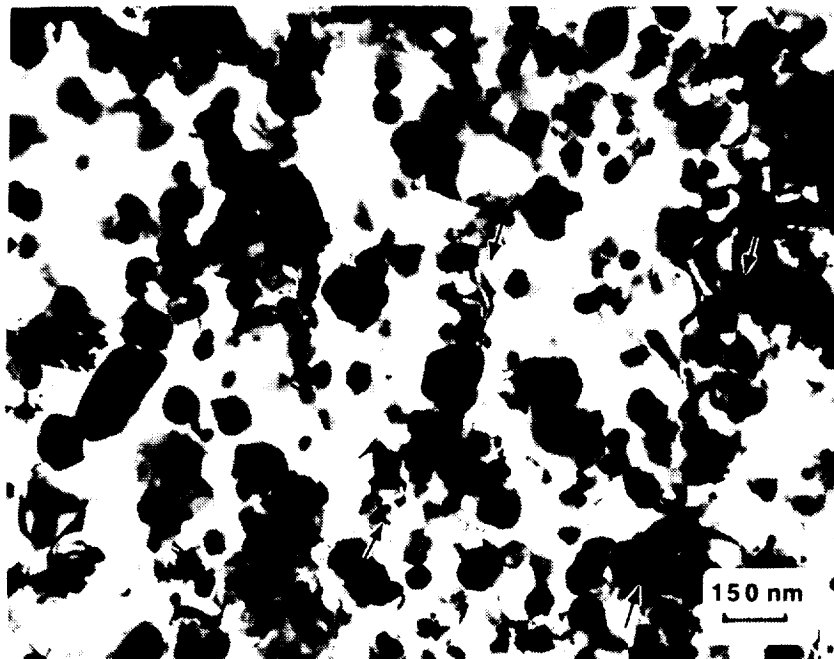


Fig. 53. Coarse silicide particles at the grain/subgrain boundaries may be observed (i.e., typical of the hot-rolled variant), while bands of silicide particles were also apparent (arrows) which might reflect the effect of the intermittent annealing treatments.

Fig. 54

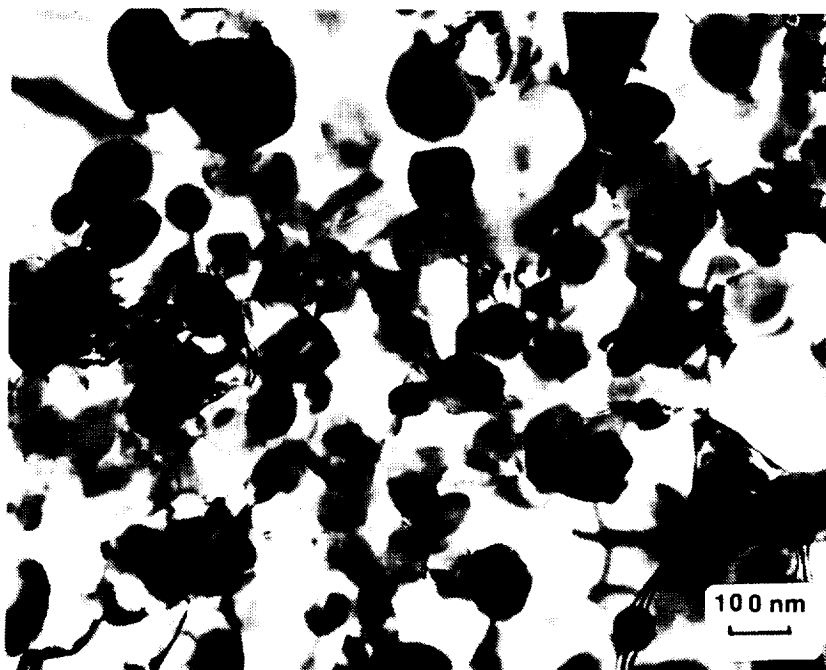


Fig. 54. Decorated grain/subgrain and particle boundaries, typical of cold-rolled sheet, are also apparent in this sheet variant.

Subtask 6B. Fracture Toughness Evaluations (UVa)

Principal Investigator: Professor R.P. Gangloff

Research Associate: Dr. Sang-Shik Kim

Progress During Report Period

During the reporting period, initiation and growth fracture toughness experiments were conducted within a temperature range between -60°C to 175°C on various product forms of 8009 sheet and plate, Modifications A and B, including:

- Modification A 8009; ribbon was melt spun in a dry inert gas atmosphere, then compacted to different gauge thicknesses with a variety of rolling schedules.
 - 92A022-1C: Hot cross-rolled; thickness of 6.4 mm
 - 92A022-2B: Hot straight-rolled; thickness of 2.5 mm
 - 92A022-2A: Hot cross-rolled; thickness of 2.6 mm
 - 92A022-1B1: Hot cross-rolled; thickness of 1.0 mm
 - 9A022-1B2: Cold cross-rolled; thickness of 1.0 mm
 - 92A022-1B3: Cold cross-roll/intermediate anneal; thickness of 1.0 mm
- Modification B 8009; ribbon was melt spun in a dry inert gas atmosphere, with an obstructed surface boundary gas layer, then compacted to different gauge thicknesses with a variety of rolling schedules.
 - 92A024-1C: Hot cross-rolled; thickness of 6.4 mm
 - 92A024-1B: Hot straight-rolled; thickness of 2.7 mm
 - 92A024-1D: Hot cross-rolled; thickness of 2.3 mm

The relevance and reproducibility of the small compact tension (C(T)) specimen characterization of K versus Δa were critically assessed at FTA and UVa. The source of interlaboratory differences in absolute toughness value was examined. UVa initiated critical experiments necessary to probe the mechanism for the time-temperature dependent cracking behavior of HTA 8009.

Fracture Toughness Characterization Methods

Conclusion FTA (compliance) and UVa (potential) fracture toughness measurements generally agree, and equivalently demonstrate the deleterious effect of increasing test temperature for each product form of 8009.

Figure 1 shows the effect of increasing test temperature on several measures of the plane strain crack initiation fracture toughness for 2.3 mm thick 8009 sheet (Preprogram Vintage, Allied Lot 90A677-1S). These data were obtained at FTA and UVa; each set of experiments with the C(T) specimen unequivocally demonstrate that increasing temperature reduces the fracture toughness of 8009 sheet and plate. The deleterious effect of increasing temperature was evidenced, without exception, based on experiments at UVa and FTA and for all 8009 processing conditions. Specific results are presented in the following sections.

Conclusion Intra- and interlaboratory variations in absolute values of fracture toughness (K_{IC} and tearing modulus) are significant, while the overall J or $K-\Delta a$ R-curve is less sensitive to experimental and analysis errors. Test method development and an interlaboratory round robin testing program are required.

The data in Fig. 1 demonstrate that significant interlaboratory variability was encountered when comparing fracture toughness results from UVa and FTA. Substantially less variability was observed for replicate experiments at either laboratory. Experiments and analyses were conducted to investigate the sources of this variability.

Several J-integral versus crack extension (Δa) R-curves are presented in Fig. 2 for three of the experiments represented in Fig. 1; LT 8009 (2.3 mm thick Preprogram Vintage, Allied Lot 90A677-1S) tested at 25°C. These R-curves are broadly similar; however, significant differences exist, consistent with the variability shown in Fig. 1. Consider the individual toughness values that are extracted from an R-curve. K_{IC} (UVa) is the stress intensity level corresponding to the value of the J-integral (J_i)

where crack extension is first resolved by high precision electrical potential measurements at the University of Virginia. K_{JIC} (UVa) is the initiation toughness corresponding to the J-integral value (J_{IC}) at the intersection between the 0.2 mm offset blunting line ($J = 2\sigma_{ys}\Delta a$) shown in Fig. 2, and a power law fit to the J- Δa data, over a specified range and as determined by electrical potential measurements without unloading. K_{JIC} (FTA) is the initiation toughness given by the J-integral value (J_{IC}) at the intersection of the 0.2 mm offset blunting line and a power-law fit to J- Δa data, as determined by the unloading compliance method at FTA. The slope of the R-curve is defined by the so-called tearing modulus, T_R ($T_R = (dJ/d\Delta a) (E/\sigma_o^2)$).

J_{IC} and K_{IC} values from the offset blunting line should be equal for both the electrical potential and unloading compliance methods, and should provide an operationally-defined method-insensitive indication of initiation toughness as defined in ASTM standard E813-89. Differences between J_i and J_{IC} , and hence between K_{IC} and K_{JIC} are expected, and will increase as T_R increases. Interlaboratory variability between K_{JIC} , and physical reasons for differences between K_{IC} and K_{JIC} are discussed.

Inter and Intralaboratory Variability

Intra- and interlaboratory differences in initiation toughness may be caused by several factors that are not addressed by ASTM Standards E813-89 and E1152-87. The J calculation procedures at UVa and FTA differ in detail, but were confirmed to give similar results for a common set of load, load-line displacement and crack length data. Recent calculations indicate a possible difference in the method for calculating the so-called plastic area from the load versus load-line displacement data. This issue will be pursued.

Initiation toughness variations are traced to differences in the initial stage of the J- Δa relationship, with the FTA results

indicating unexpectedly large amounts of crack growth at low J and compared to the blunting line shown in Fig. 2. At this point it is difficult to rationalize the extremely shallow slope of the beginning stage of the R-curve observed for 2.3 mm and 6.3 mm thick specimens. The origin of this behavior (possibilities include specimen location in the plate, loading pin friction, load cell error, and interpretation of electrical potential measurements) are not understood and must be examined.

Loading pin-clevice and loading pin-specimen friction effects were suspected to be important. During the reporting period, FTA performed a fracture toughness experiment on 2.3 mm thick 8009 sheet (Preprogram Vintage, Allied Lot 90A677-1S) at 25°C and with tightly-fitting pins to load the compact tension specimen. (Normal FTA procedure is to employ a ball bearing bushing inserted between the specimen hole and loading pin to reduce friction.) A 5% secant estimate of initiation toughness was 18.1 MPa \sqrt{m} with the ball bearing bushing and 25.4 MPa \sqrt{m} without the bushing.

The effect of loading pin friction was further examined at UVa. Figure 3 shows J -integral versus Δa R-curves for 2.3 mm thick 8009 (Allied Lot 90A677-1S) tested at 25°C with and without ball bearing bushings. Three test conditions give generally similar R-curves that indicate substantial fracture toughness, but different K_{JIC} values that varying by from 50 to 100%. These differences in K_{JIC} , and to a lesser extent K_{IC} , are due to the substantial differences in the initial portion of the R-curve. The two replicate experiments with the ball bearing bushings suggest pronounced amounts of crack growth at relatively low J compared to the simple pinned experiment. The reproducibility of the ball bearing results is poor. It is not clear if, for example at a J value of 20 kJ/m², the crack growth is actually 0.06, 0.16 and 0.3 mm for the three experiments in Fig. 3. The alternative explanation is that the electrical potential measurements and analyses may have been affected by an artifact that produced the shallow J - Δa relationship in Fig. 3. It appears that the

frictional interaction between the loading pin and C(T) specimen holes affects compliance and the crack tip stress intensity. For example, the shape of the ball-bearing R-curves in Fig. 3 is similar to the results reported by FTA (Fig. 2). Additional work is required to assess this aspect of the test method. The remainder of the results presented here were generally obtained without ball bearings, but with a 0.1 mm to 0.2 mm clearance between the pin and gripping holes.

While additional method development is required, it is clear that the complete $K-\Delta a$ R-curve should be reported and compared in alloy development studies. Single measurements of toughness (e.g., K_{IC} , K_{JIC} , T_R , or any of the K_C values from wide plate experiments) may significantly vary for replicate conditions, while the overall R-curve may be much less sensitive to experimental and analysis errors. A corollary to this argument is that single test values of a fracture toughness parameter should not be employed to rank alloys. Replicate R-curves should be determined for a given temperature, loading rate and metallurgical condition.

Differences Between K_{IC} and K_{JIC}

It was demonstrated that the absolute value of J_i determined by the first rising point in direct current electrical potential versus load-line displacement data significantly differs from J_{IC} , particularly for conditions that favor high T_R . A sectioned specimen from an interrupted fracture toughness test with 8009 exhibited a considerable amount of crack growth between J_i and J_{IC} . These, and similar data determined in parallel research at UVa, indicate that J_i is a true indication of the initial stage of crack tip process zone damage. In this report, we present both K_{IC} (from J_i) and K_{JIC} (from J_{IC}) to bracket the range of initiation toughnesses.

Conclusion *The small specimen compact tension J-integral characterization of K versus crack extension (Δa) is*

quantitatively relatable to results provided by a centrally fatigue precracked panel at fixed thickness of 8009 and any temperature.

Figure 4 shows applied K versus Δa data, measured at FTA, for 2.3 mm thick HTA 8009 sheet (Preprogram Vintage, Allied Lot 90A677-1S) at 25 and 175°C. Both the unloading compliance and potential difference methods were simultaneously employed to measure Δa in compact tension (C(T)) and middle crack tension (M(T)) specimens. Stress intensity was calculated from the J-integral ($K = (JE)^{1/2}$), including the elastic and plastic components of J , for each geometry.

For either temperature, K - Δa results are generally equivalent for the 5.1 cm wide C(T) specimen with an uncracked ligament of 2.2 cm, and the 12.2 cm wide M(T) specimen with an uncracked ligament of 3.9 cm. J-controlled crack extension to instability is over a wider Δa range in the M(T) geometry because the uncracked ligament is larger than that of the C(T) specimen. Yet wider M(T) specimens would yield a larger portion of the in-plane geometry independent R-curve for this thickness.

The notable point is that the small C(T) specimen provides an excellent characterization of crack initiation and growth resistance. Such results should be extendable by an analytical model to predict the fracture behavior of wider M(T) specimens, while retaining economy of material for alloy development studies and test machine load capacity. This result will be further evaluated in the pending NASA-sponsored round robin test program. Data to date clearly demonstrate that the C(T) method, coupled with precision crack growth monitoring, provides both an accurate plane strain crack initiation toughness (K_{IC} or K_{JIC}), that is likely to be comparable to thick specimen results from ASTM E399, and a quantitative measure of the mixed plane strain-plane stress K - Δa R-curve.

Effect of Processing on Fracture Toughness

Conclusion The initiation fracture toughness for Modifications A and B decreases with increasing temperature, independent of processing method and analogous to conventionally melt spun 8009.

Regardless of processing route and product form, fracture toughnesses for Modification A 8009 plate and sheet are significantly reduced at 175°C compared to 25°C. Figures 5, 6, and 7 show the initiation toughness values, K_{IC} and K_{JIC} determined at UVA, for Modification A HTA 8009 sheet and plate with different gauge thicknesses of 6.4, 2.6 and 1.0 mm, respectively, as a function of temperature. Due to the limited data, each point is connected with straight line. A detailed temperature dependence of toughness for extruded 8009 was previously determined by Porr at UVA (1). The initiation toughness for 6.3 mm thick 8009 (Modification B) plate similarly decreases with increasing temperature, as shown in Fig. 8.

Figure 9 shows the effect of temperature on tearing modulus, T_R , for 2.6 mm thick Modification A 8009 sheet (92A022-2A). Tearing modulus for other gauges of Modification A 8009 follow a similar trend. Regardless of product form, T_R decreases with increasing temperature from 25°C to 175°C, which is analogous to the behavior of Preprogram Vintage Material and extruded 8009 (1).

Conclusion K_{IC} for Modification A HTA 8009 decreases at -60°C compared to ambient temperature; absolute values of the low temperature toughness are slightly higher than those at 175°C.

During the reporting period, UVA initiated a study of the low temperature fracture toughness behavior of Modification A HTA 8009. Only limited work has been reported on the low temperature deformation mechanisms and fracture behavior of ultrafine grain size aluminum alloys. Low temperature toughness studies will provide important data necessary to understand the fracture mechanisms of HTA 8009.

Figures 5, 6 and 7 show that the toughness of Modification A

HTA 8009 decreases at -60°C compared to 25°C , regardless of processing route and gauge thicknesses. Absolute values of initiation toughness at -60°C range from 14 to $24 \text{ MPa}\sqrt{\text{m}}$, which is up to two-fold higher than those at 175°C . Tearing modulus decreases with decreasing temperature, Figure 9, and is generally zero for each form of 8009 at -60°C . At this temperature, Modification A 8009 plate and sheet exhibit unstable crack growth after initiation, T_R equals zero and K_{IC} equals K_{JIC} .

Conclusion *Modifications A and B are ineffective in generally improving the fracture toughness of HTA 8009 at both 25°C and 175°C .*

In order to understand the effect of each process modification on the toughness of HTA 8009, ambient and elevated temperature K_{IC} values are plotted in Fig. 10 for three different 6.3 mm thick hot cross-rolled plates of HTA 8009, including Preprogram Vintage 8009 (90A677-1S), Modification A (92A022-1C) and Modification B (92A024-1C). For comparison, LT orientation fracture toughnesses for extruded 8009 are included in the plot. The toughness data for Preprogram and Modification B HTA 8009 are for the LT orientation, while the results for Modification A represent the TL initiation toughness. Individual toughness values are indicated and averages are plotted in Fig. 10.

The initiation toughness changes from $33 \text{ MPa}\sqrt{\text{m}}$ for Preprogram Vintage to 22 and $29 \text{ MPa}\sqrt{\text{m}}$ for Modifications A and B, respectively, at 25°C , while the toughnesses at 175°C vary from $15 \text{ MPa}\sqrt{\text{m}}$ for extruded 8009 to $10 \text{ MPa}\sqrt{\text{m}}$ for 8009 plates, including Preprogram Vintage and Modifications A and B. Delamination, and possible associated toughening, was only observed for LT oriented fatigue precracked specimens from the extrusion, and then only for fracture at 25° (1).

At this point, it is not well understood why Modified processes give lower toughness compared to standard processed 8009; despite the refined oxide layer, improved microstructural homogeneity and reduced hydrogen content from the modified

processes. Modification B has a high carbon content, induced by the device to obstruct the surface boundary gas layer, which could reduce the fracture toughness. The reduced toughness values for Modification A 8009 may reflect the effect of ball bearing bushings, since all toughnesses for Modification A 8009 were measured with this refined gripping, while the toughnesses for Preprogram Vintage and Modification B were measured with regular fitting loading pins without bushings. This possibility will be examined in the next reporting period.

Conclusion *Changes in thermomechanical processing (rolling reduction, temperature and direction) affect initiation toughness for Modification A 8009. Further studies are required.*

Figure 11 shows the initiation fracture toughness values, K_{IC} , for three gauges of Preprogram Vintage HTA 8009 LT orientation at 25 and 175°C and a displacement rate of 2.5×10^{-3} mm/sec. 6.3 mm thick 8009 plate was hot cross-rolled, while 2.3 and 1.1 mm sheet were prepared with cold cross-rolling. The initiation fracture toughnesses decrease with thermomechanical processing from plate to sheet and at each temperature. It remains to be proven that such a decrease in toughness is independent of reduced specimen thickness. As shown in the previous semi-annual report, K_{IC} either slightly increases or is unchanged with decreasing C(T) specimen thickness when prepared by machining from the same plate of HTA 8009. In principle the J-integral method should give similar initiation toughnesses, regardless of specimen thickness above a critical value, as long as plane strain thickness requirements are satisfied. Such requirements are satisfied for each experiment represented in Fig. 11.

Figures 12 and 13 show the tensile properties and fracture toughness values, respectively, for Modification A hot cross-rolled sheet and plate with three different thicknesses of 6.3, 2.6 and 1.1 mm. At this point, low temperature tensile data are not available. Mechanical processing to reduced thicknesses at elevated temperatures slightly enhances yield strength, but

significantly reduces elongation for each test temperature. Elongation does not necessarily parallel tensile ductility and fracture toughness because of necking at relatively low strains.

The fracture toughness results in Fig. 13 for the three thicknesses of hot cross-rolled Modification A 8009 exhibit complex trends depending on the test temperature. The initiation fracture toughness at 175°C reflects the trend in tensile properties; toughness decreases with increasing rolling reduction. At -60°C, however, the trend is reversed such that the toughness increases from 14 MPa√m for 6.3 mm thick sheet to 24 MPa√m for 1.0 mm thick sheet. At 25°C, plane strain initiation toughness increases for an intermediate thickness of 2.6 mm, while it decreases for 1.0 mm thick sheet. The initiation toughness differences at 25°C and 175°C appear to be significant, but are approaching the order of magnitude of the expected variability in toughness from replicate experiments. Studies on the effect of thermomechanical processing on the deformation and fracture behavior of ultra-fine grain sized aluminum alloys are limited (2).

Transmission electron microscopy was employed to characterize the effect of processing route on the microstructure of 8009. TEM micrographs are presented in Fig. 14 for Preprogram Vintage 8009 with gauge thicknesses of: (a) 6.3 mm (hot cross-rolled), (b) 2.3 mm (cold cross-rolled) and (c) 1.1 mm (cold cross-rolled), respectively. It appears that cold rolling deformation tends to induce dislocation substructures within the existing subgrains, as evidenced in Fig. 14b for 2.3 mm thick 8009 sheet. Dislocation substructures from cold rolling deformation can develop into well defined subgrains. Consequently, 1.1 mm thick 8009 sheet may have a finer subgrain structure compared to thicker plate and sheet. Indeed, Fig. 14c shows very fine subgrain structure with an average size of 100 nm for 1.1 mm thick 8009 sheet, compared to 6.3 mm thick 8009 plate where the average grain size is approximately 300 nm.

Figures 15a, 15b and 16 show the effects of rolling temperature and intermediate annealing on yield strength, tensile elongation and initiation toughness, respectively, for 1.0 mm thick (Modification A) 8009 sheet. For comparison, tensile properties of 6.4 mm thick Modification A hot cross-rolled 8009 plate are included in Figs. 15a and b. It is shown that 1.0 mm thick hot cross-rolled sheet has lower elongation and higher yield strength than the cold and cold/anneal cross-rolled counterparts. Fracture toughness data for different rolling conditions (Fig. 16) demonstrate a complex trend depending on test temperature. Toughness at 175°C is unaffected by processing, or slightly decreases with hot cross-rolling or intermediated annealing, while toughness significantly increases with hot cross-rolling at -60°C. At ambient temperature, the effects are insignificant.

Westingen (2) conducted a detailed tensile study of fine grain sized ($\sim 1 \mu\text{m}$) aluminum alloys (Al-0.8Mn-2.0Fe in wt% and produced by strip casting) as a function of temperature and strain rate. Below a critical grain size, intragranular dislocation substructure does not develop during deformation and work hardening is minimal. He suggested that plastic instability during tensile deformation of such fine grained aluminum alloys is initiated by an abrupt increase in mobile dislocation density from grain boundary sources, causing a drop in the flow stress and the formation of Lüders bands. This instability can be suppressed if the specimens are slightly predeformed by rolling to activate dislocation sources throughout the grains. Such dislocation sources within the small grains were neither specified nor evidenced.

Improved tensile elongation with cold cross-rolling for 8009 sheet compared to the hot cross-rolled counterpart may be due to the dislocation substructures developed during cold rolling within the matrix. Dislocation substructure could promote yielding at lower stresses compared to conventional dislocation free grains in 8009, and could interrupt avalanches of localized slip to

homogenize deformation and increase strain hardening rate. Such homogenized deformation would lead to an increase in tensile elongation, effectively equalling the uniform strain to necking. This is schematically illustrated by Cases a and b in Fig. 17.

During hot rolling, dynamic recovery of the dislocation substructure (because of annihilation and combination of the dislocations) tends to be more active compared to cold rolling (3). The resulting structure is illustrated by Case c in Fig. 17. Plastic instability may then be increased with increasing hot rolling deformation, accompanied by decreased strain hardening rate and decreased tensile elongation (to necking), as shown in Fig. 12. Figs. 15a and b indicate that 6.3 mm thick hot cross-rolled Modification A 8009 plate has slightly better tensile properties compared to 1.0 mm thick cold cross-rolled 8009 sheet. One hypothesis is that a slight hot rolling for 6.3 mm thick plate (compared to 1.0 mm thick sheet) may activate subgrain interior dislocation sources without forming dislocation substructure (4). The activated dislocation sources can reduce the plastic instability by the mechanism originally suggested by Westingen. TEM characterization of hot cross-rolled Modification A 8009 sheet will be conducted in the next reporting period to understand the effect of rolling temperature on tensile properties as related to the microstructural changes.

The complex temperature dependence of fracture toughness with thermomechanical processing suggests that several factors affect the toughness behavior of 8009, other than the plastic instability as related to the dislocation substructures. It is unclear how necking instability in a uniaxial tensile bar, characterized by elongation to failure, relates to fracture toughness governed by damage within an elastically constrained, high stress/strain gradient plastic zone at a crack tip. Additionally, rolling reduction would refine the size and spacing of oxide particles along prior ribbon particle boundaries, and reduce the spacing between those boundaries. Microvoid nucleation at oxide-matrix

interfaces followed by ligament shear will be influenced by thermomechanical processing and eventually affect fracture toughness. Such effects on toughness have not been systematically studied.

Micromechanical modelling incorporating intrinsic tensile behavior can be used to predict the temperature dependencies of K_{IC} . A critical strain to fracture model, assuming microvoid nucleation dependent on a critical accumulation of plastic damage or strain at microstructural features over a critical distance ahead of a crack tip, expresses K_{IC} as follows (5):

$$K_{IC} = [(1/C_1 \alpha) \cdot E \cdot \sigma_{YS} \cdot \epsilon_f^* \cdot l^*]^{1/2}$$

ϵ_f^* = Critical fracture strain for the material and stress

state representative of the crack tip process zone,

l^* = Critical distance ahead of the crack tip and over which ϵ_f^* must be exceeded,

E = Elastic modulus,

σ_{YS} = Tensile yield strength,

C_1 and α = constants that depend on work hardening.

The critical fracture strain is an intrinsic material property and is not related to the elongation to fracture in a necking uniaxial tensile specimen. This model indicates that fracture toughness depends on changes in intrinsic tensile properties which are influenced by temperature and microstructure. Fracture toughness changes with thermomechanical processing at 175°C generally agree with the trend in tensile properties, as shown in Figures 12 and 13. At 25°C, however, the toughness trend does not necessarily follow the trend in tensile properties. Detailed discussion on cryogenic temperature fracture toughness behavior is not feasible at this point, given the lack of tensile properties, deformation mode characterization and quantitative fractography at this temperature.

Effect of Orientation on Fracture Toughness

Conclusion 8009 plate and sheet exhibit reasonably isotropic (in-plane) fracture toughness in contrast to the extruded alloy.

Previous studies conducted by Porr^[1] indicated that extruded 8009 has a considerable fracture toughness anisotropy. For example, at 25°C LT oriented 8009 extrusion shows approximately 50% higher initiation toughness than that for the TL orientation. The TL orientation is intrinsically less tough because of prior ribbon boundary cracking. Delamination does not occur because K_{IC} is low for TL orientation. Delamination for the LT extrusion case magnifies the difference in toughnesses. The degree of toughness anisotropy on extruded HTA 8009 decreases with increasing testing temperature.

Thermomechanical processing has been proven to effectively reduce the fracture toughness anisotropy in HTA 8009. Figure 18 presents the initiation toughness of 6.3 mm thick hot cross-rolled Preprogram Vintage HTA 8009 at a variety of temperatures. The effect of crack orientation on toughness is not observed in this 8009 plate. Figure 19 shows the blunting line offset fracture toughness values, K_{JIC} , obtained by FTA for 2.6 mm thick Modification A 8009 sheet (92A022-2A) at 25°C and 175°C for the LT and TL orientations. It appears that the TL orientation has higher toughness than LT. The final rolling direction for cross rolling is always perpendicular to the initial extrusion direction. Accordingly, if an orientation is expected to be lower toughness, it would be the LT case in cross-rolled plate, as controlled by fracture along the original extrusion-aligned prior ribbon boundaries. Compared to the 8009 extrusion, however, toughness anisotropy is significantly reduced (compare Figs. 18 and 19).

The increase in toughness anisotropy for 2.6 mm thick Modification A 8009 sheet compared to plate can be attributable to the formation of dislocation substructures which may possess a certain directionality. If this hypothesis is correct, tensile

anisotropy should increase with thermomechanical processing. Indeed, 6.3 mm thick hot, cross-rolled plate (92A022-1C) shows a 6% elongation difference between the L and T orientations, while the difference increases to 28% for 2.6 mm thick sheet (92A022-2A).

Fracture Mechanisms

During the reporting period, experiments were initiated to understand the unique time-temperature fracture and deformation behavior for HTA 8009, and several conclusions are drawn. Such investigations will be emphasized in 1993.

Conclusion *Long time heat treatment at 370°C, without stress, has no effect on the initiation fracture toughness of cold rolled Modification A 8009 sheet.*

Selected specimens from cold rolled Modification A 8009 sheet were heat treated at 370°C for 100 hrs without stress, and the toughness data are compared with as-received HTA 8009 in Fig. 20. High temperature exposure has no effect on toughness for HTA 8009 regardless of testing temperature, analogous to previous studies of high temperature exposure on the toughness of 8009 extrusion (1).

The present study indicates that temperature alone is not sufficient enough to induce damaging microstructural changes in HTA 8009. This result is notable because uniaxial tensile experiments at Allied Signal Inc. demonstrated that the 370°C annealing treatment substantially reduced the elongation to fracture (necking) of cold rolled 8009 sheet.

Conclusion *Fracture toughness decreases with decreasing displacement rate and therefore crack tip strain rate for 8009 at 25°C and 175°C. The lower bounding strain rate for reduced toughness decreases with decreasing temperature; the shift can be used to test models for time-temperature dependent cracking of 8009.*

It was demonstrated that the fracture toughness of HTA 8009,

both extrusion and plate, decreases with decreasing actuator displacement rate at 175°C (1). During the reporting period, fracture toughness experiments were conducted on 6.3 mm thick Preprogram Vintage 8009 (90A677-1S) at 25°C with a variety of displacement rates ranging from 6.1×10^{-6} mm/sec to 2.5×10^{-2} mm/sec. The results are represented in Fig. 21. Fracture toughness decreases with decreasing displacement rate at 25°C. These data demonstrate that the fracture toughness of HTA 8009 depends on temperature and time; low toughness fracture can be produced at 25°C provided that sufficient time is provided. Parallel studies at UVA on 2618 indicate that this behavior is not observed for conventional ingot metallurgy aluminum alloys.

Previously, Porr suggested that reductions in the intrinsic ductility and fracture toughness of 8009 are related to the change from dislocation-particle interaction to dislocation bypassing by thermally activated dislocation climb. This proposition is based on a model by Humphreys and Kalu which considers that the rate of dislocation accumulation at spherical particles is balanced by the rate of dislocation climb and/or diffusional relaxation around the particles at sufficiently high temperature and low strain rate (6). Even though a climb mechanism was not decisively evidenced with the preliminary TEM studies on tensile deformed 8009 at intermediate temperatures, dynamic recovery process during deformation may involve climb. The Humphrey and Kalu model predicts that the critical strain rate ($\dot{\epsilon}_c$), above which dislocations accumulate at particles, is approximately 4×10^{-6} sec⁻¹ at 25°C and 2×10^{-1} sec⁻¹ at 175°C for 8009 with an average silicide particle size of 80 nm. Essentially, a four to five order of magnitude increase in the critical strain rate is predicted for increasing temperature from 25°C to 175°C. Figure 21 indicates that K_{IC} for 6.3 mm 8009 plate is reduced by a factor of 2 (from 40 MPa√m to 20 MPa√m) at a loading rate of about 10^{-4} mm/sec for fracture at 25°C. Data from Porr for a similar 8009 plate and extrusion show that such a toughness decrease occurs at

a "critical" loading rate of about 10^{-2} mm/sec for fracture at 175°C. Accordingly, the toughness experiments indicate that the critical strain rate is increased by two orders of magnitude for increasing temperature from 25°C to 175°C. It is necessary to compare actuator displacement rates in this analysis because of uncertainties associated with calculating crack tip strain rate.

There is a substantial discrepancy between the predictions of the climb-based model for dislocation bypassing of silicides and localization in the surrounding aluminum (1), and the time dependence of K_{IC} measured at 25°C compared to 175°C. This result suggests that either the climb notion is incorrect, the diffusion and geometric parameters in the Humphries-Kalu model are incorrectly estimated, or the crack tip strain rates that actually govern time-dependent fracture are not directly proportional to actuator displacement rate. Alternately, the data in Fig. 21 may not be representative of the plate and extrusion of 8009 examined by Porr. In fact limited loading rate experiments by Porr at 25°C showed similar high toughnesses at room temperature loading rates of 2.5×10^{-3} mm/sec and 2.5×10^{-5} mm/sec for extruded 8009 (1). Room temperature toughness was reduced for plate 8009 at 5×10^{-6} mm/sec compared to 3×10^{-3} mm/sec from Fig. 21 (1). Comparing this latter value to 10^{-2} mm/sec yields a "strain rate shift" of four orders of magnitude, similar to the predictions of the dislocation climb model. These possibilities will be examined.

Conclusion *Regardless of process route and fracture temperature, 8009 fails by microvoid coalescence. The size and distribution of voids depend on temperature, strain rate and rolling reduction.*

Figure 22 shows SEM fractographs for 6.3 mm thick Preprogram Vintage HTA 8009 plate (90A677-1S) fractured at: (a) 25°C, 2.5×10^{-3} mm/sec, (b) 175°C, 2.5×10^{-3} mm/sec, (c) 25°C, 6.1×10^{-6} mm/sec, and (d) 25°C, 2.5×10^{-2} mm/sec, respectively. Regardless of testing temperature and displacement rate, Preprogram Vintage HTA 8009 fails by microvoid coalescence. At 25°C and an

intermediate displacement rate, the dimples are deeper than those at 175°C with the same displacement rate. More local plasticity around dimples is evidenced at 25°C than 175°C, indicating enhanced dislocation-particle interaction at ambient temperature. A similar fracture morphology with shallow dimples is observed at 25°C with an extremely slow displacement rate. A fracture morphology with deep dimples, and evidence of substantial matrix plasticity, is observed for the case of rapid loading at 175°C. Generally, high K_{IC} correlates with the locally rough fracture morphology and low K_{IC} (from slow loading rates or elevated temperatures) correlates with the shallow dimple morphology. These findings are consistent with extensive fractographic results by Porr for extrusion and plate 8009 (1).

Figure 23 shows high magnification SEM fractographs for 2.6 mm thick Modification A 8009 sheet (92A022-2A) fractured at: (a) 25°C, (b) 175°C and (c) -60°C, respectively. The general features of the fracture surfaces for Modification A are similar to those for Preprogram Vintage HTA 8009. At -60°C, the fracture surface is composed of extremely fine dimples, however, this morphology has not been studied in detail.

Conclusion *Unlike extruded 8009, which delaminates significantly at 25 and 300°C, 8009 plate and sheet do not exhibit significant delamination. Delamination toughening is not a primary factor in the fracture of plate and sheet 8009.*

At the early stage of 8009 development, delamination toughening was considered as a likely mechanism for reduced toughness at intermediate temperature, since extruded 8009 delaminates significantly at 25°C and 300°C, but not at 175°C. Once delamination occurs, it increases the initiation and growth toughness, as documented for Al-Li alloys (7).

Fracture toughness experiments with plate and sheet forms of 8009, however, demonstrate that the delamination mechanism is not a central factor to the time-temperature dependence of K_{IC} , and does not contribute to the excellent ambient temperature fracture

toughness. Figure 24 shows low magnification SEM fractographs for 1.0 mm thick modification A 8009 sheet (91A693-1A) fractured at (a) 25°C and (b) 175°C, respectively. Unlike extruded 8009, plate and sheet HTA 8009 do not exhibit any delamination, regardless of the testing temperature. Therefore, delamination toughening is an unlikely mechanism for the time-temperature dependent fracture of thermomechanically processed HTA 8009. Porr reached a similar conclusion (1).

Conclusion *Total process-dissolved hydrogen content has no effect on the fracture toughness of HTA 8009. Hydrogen embrittlement does not offer a simple mechanism for the time and temperature dependence of toughness.*

During rapid solidification, hydrogen is trapped within the ribbon surface oxide film, in the form of $\text{Al}_2\text{O}_3 \cdot x\text{H}_2\text{O}$, and is liberated by chemical decomposition of the hydrated oxide during subsequent processing at temperatures above about 350°C (8). The liberated atomic hydrogen could embrittle the aluminum matrix and interfaces. The present study, however, indicates no effect of total process-dissolved hydrogen content on the fracture toughness of HTA 8009. As demonstrated in Fig. 10, regardless of hydrogen content varying from 3.5 ppm to 1.5 ppm depending on the processing route, fracture toughness decreases with increasing temperature. Furthermore, absolute values of initiation toughness do not show any dependence on hydrogen content at 175°C. It is likely that hydrogen in 8009 is similarly and strongly bonded (or trapped) in each product form and at both 25°C and 175°C. Very high temperatures, perhaps 400°C, are required to chemically produce atomic hydrogen in the 8009 microstructure.

Conclusion *The fracture toughness of Exxon DS Aluminum decreases with increasing temperature; DSA is not a likely mechanism.*

It was suggested that dynamic strain aging occurs in HTA 8009 at intermediate temperatures due to the sluggish diffusion of substitutional Fe and V present in the matrix and causes loss of

tensile ductility (9). Figure 25 shows the initiation and growth fracture toughness values for high purity, ultra-fine grain size, dispersoid strengthened Exxon DS Aluminum. Despite the low solute content in the matrix, toughness significantly decreases with increasing temperature. Previous study also demonstrates that the toughness of Exxon DS Aluminum decreases with decreasing displacement rate at 25°C. This study suggests that DSA does not play an important role in the fracture of HTA 8009.

Conclusion *Time-temperature dependent dislocation interactions with silicides may govern damage accumulation and explain "intermediate temperature embrittlement" of 8009.*

Preliminary TEM studies indicate that the time-temperature dependent fracture behavior for HTA 8009 may be related to dislocation interactions with silicide and oxide particles. Figure 26 shows a dark field TEM micrograph of tensile deformed HTA 8009 at 25°C. Oxide and silicide particles are highly decorated with dislocations at 25°C. At 175°C, on the other hand, particles are free of dislocations and dislocation substructure is occasionally observed (Fig. 27). The evasion of dislocations from particles and dynamic recovery during deformation at elevated temperatures (or possibly with prolonged loading at lower temperatures) may reduce toughness due to enhanced localized deformation.

Summary

FTA (compliance) and UVA (potential) fracture toughness measurements demonstrate equivalently the deleterious effect of increasing test temperature for each product form of 8009. Intra- and interlaboratory variations in absolute values of K_{IC} and tearing modulus are significant, while the overall J or K- Δa R-curve is less sensitive to experimental and analysis errors. Test method development and an interlaboratory round robin testing program are required. The small specimen compact tension J-integral characterization of K versus crack extension (Δa)

provides an accurate indication of the wider-range results provided by a centrally-cracked panel for 8009.

The initiation fracture toughness for Modifications A and B decreases with increasing temperature, independent of processing method and analogous to conventionally melt spun 8009. Modifications A and B are ineffective in generally improving the fracture toughness of HTA 8009 at both 25°C and 175°C. K_{IC} for Modification A HTA 8009 decreases at -60°C compared to ambient temperature; absolute values of the low temperature toughness are slightly higher than those at 175°C. Changes in thermomechanical processing (rolling reduction, temperature and direction) affect initiation toughness for Modification A 8009. 8009 plate and sheet exhibit reasonably isotropic (in-plane) fracture toughness in contrast to the extruded alloy.

Regardless of process route and fracture temperature, 8009 fails by microvoid coalescence. The size and distribution of voids depend on temperature, strain rate and rolling reduction. Unlike extruded 8009, which delaminates significantly at 25 and 300°C, delamination toughening is not a primary factor in the fracture of plate and sheet 8009. Fracture toughness decreases with decreasing displacement rate and therefore crack tip strain rate for 8009 at 25° and 175°C. The lower bounding strain rate for reduced toughness decreases with decreasing temperature; the shift can be used to test models for time-temperature dependent cracking of 8009. Long-time heat treatment at 370°C, without stress, has no effect on the initiation fracture toughness of cold rolled Modification A 8009 sheet. The fracture toughness of Exxon DS Aluminum decreases with increasing temperature; DSA is not a likely mechanism. Time-temperature-dependent dislocation interactions with silicides may explain "intermediate temperature embrittlement" of 8009.

Current and Potential Problem Areas

None.

References

1. W.C. Porr, Jr., "Elevated Temperature Fracture of Advanced Powder Metallurgy Aluminum Alloy 8009", PhD dissertation, University of Virginia (1992).
2. H. Westingen, in Microstructural Control in Aluminum Alloys: Deformation, Recovery and Recrystallization, E.H. Chia and H.J. McQueen, eds., TMS-AIME, Warrendale, Pennsylvania (1985) pp. 109-122.
3. H.J. McQueen, H. Chia and E.A. Starke, in Microstructural Control in Aluminum Alloys: Deformation, Recovery and Recrystallization, E.H. Chia and H.J. McQueen, eds., TMS-AIME, Warrendale, Pennsylvania (1985) pp. 1-18.
4. T. Sheppard, M.A. Zaidi, P.A. Hollinshead and N. Raghunathan, in Microstructural Control in Aluminum Alloys: Deformation, Recovery and Recrystallization, E.H. Chia and H.J. McQueen, eds., TMS-AIME, Warrendale, Pennsylvania (1985) pp. 19-43.
5. R.O. Ritchie and A.W. Thompson, Met. Trans. A, Vol. 16A (1985) pp. 233-248.
6. F.J. Humphreys and P.N. Kalu, Acta Met., Vol. 35 (1987) pp. 2815-2829.
7. K.T. Venkateswara Rao, W. Yu and R.O. Ritchie, Met. Trans. A, Vol. 20A (1989) pp. 485-497.
8. Y.W. Kim, Progress in Powder Metallurgy, Vol. 43 (1987) pp. 13-31.
9. D.J. Skinner, M.S. Zedalis and P. Gilman, Mat. Sci. and Engr., Vol. A119 (1989) pp. 81-86.
10. D.P. Clausing, Intl. J. Frac. Mech., Vol. 6 (1970) pp. 71-89.

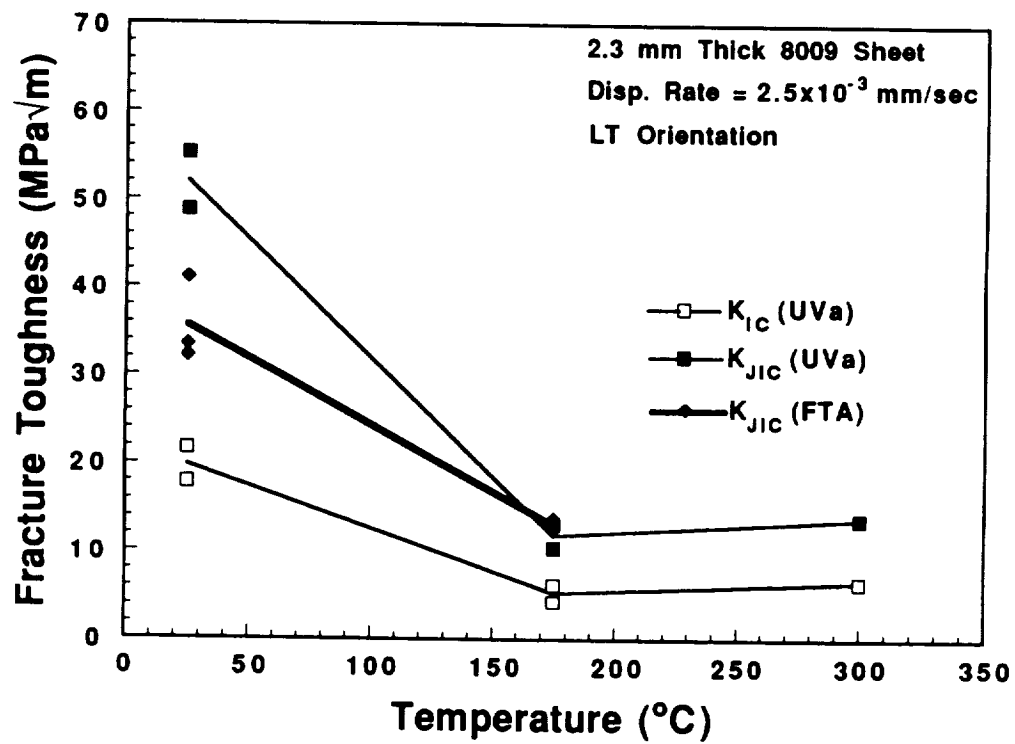


Figure 1 The effect of temperature on the initiation fracture toughness of 2.3 mm thick 8009 sheet (Allied Lot 90A677-1S).

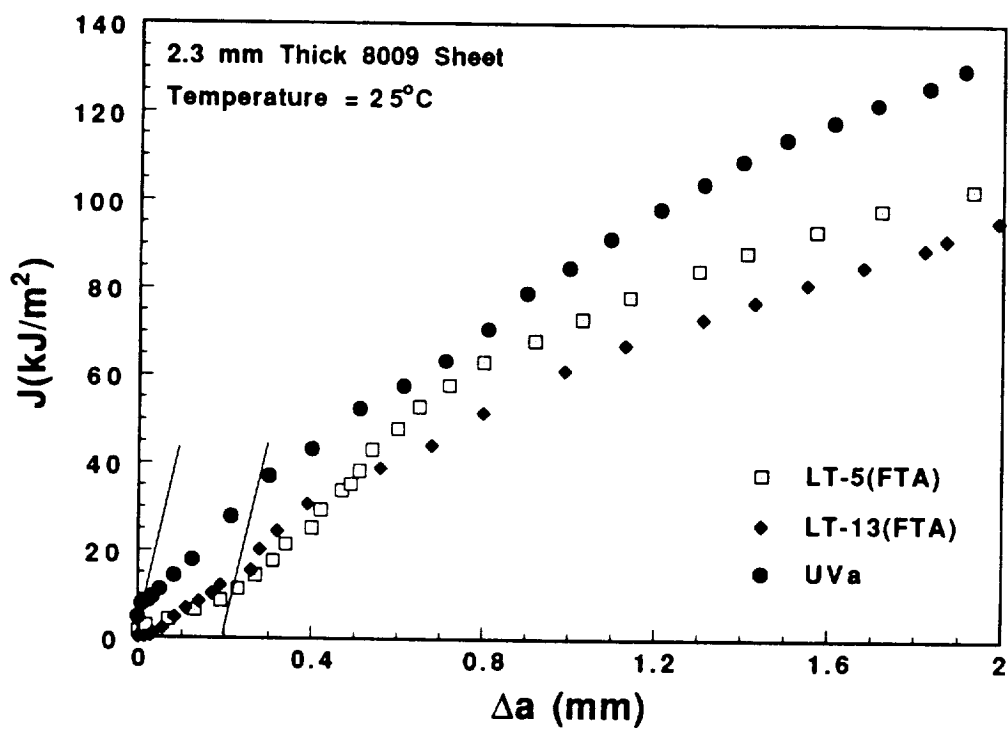


Figure 2 J-integral versus Δa R-curves for 2.3 mm thick 8009 sheet (Allied Lot 90A677-1S) at 25°C, obtained at FTA and UVa.

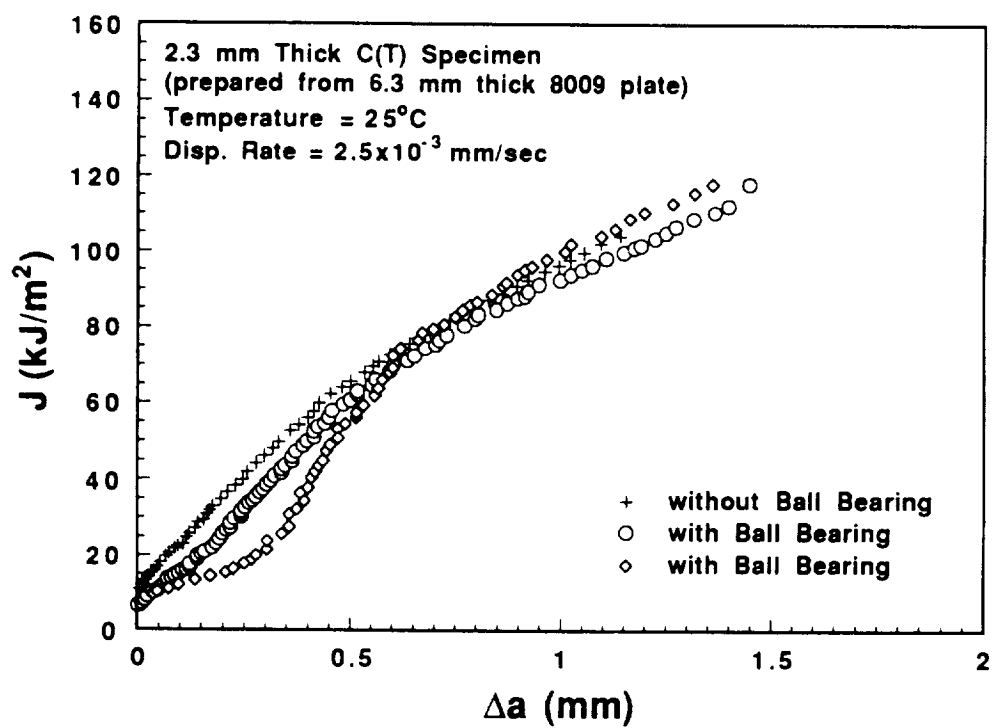


Figure 3 J-integral versus Δa R-curves for 2.3 mm thick 8009 sheet (Allied 90A677-1S) at 25°C with and without ball bearing bushings.

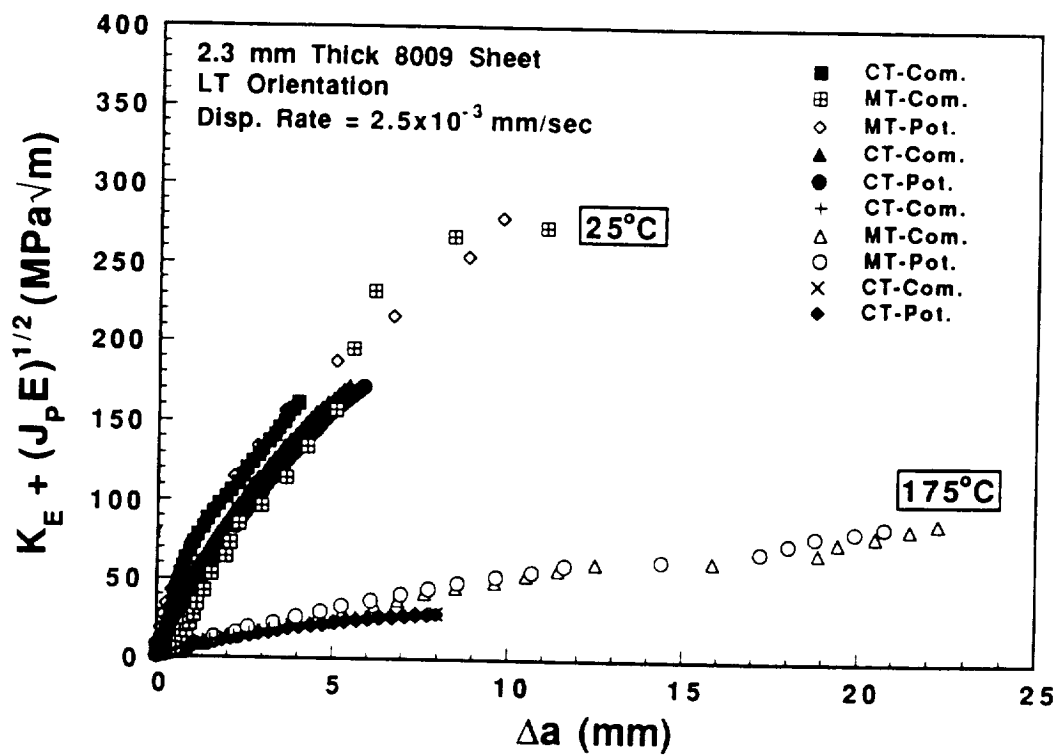


Figure 4 Stress intensity versus Δa R-curves for 2.3 mm thick 8009 sheet (Allied L. 90A677-1S) at 25 and 175°C, determined by C(T) and M(T) specimens with unloading compliance and electric potential.

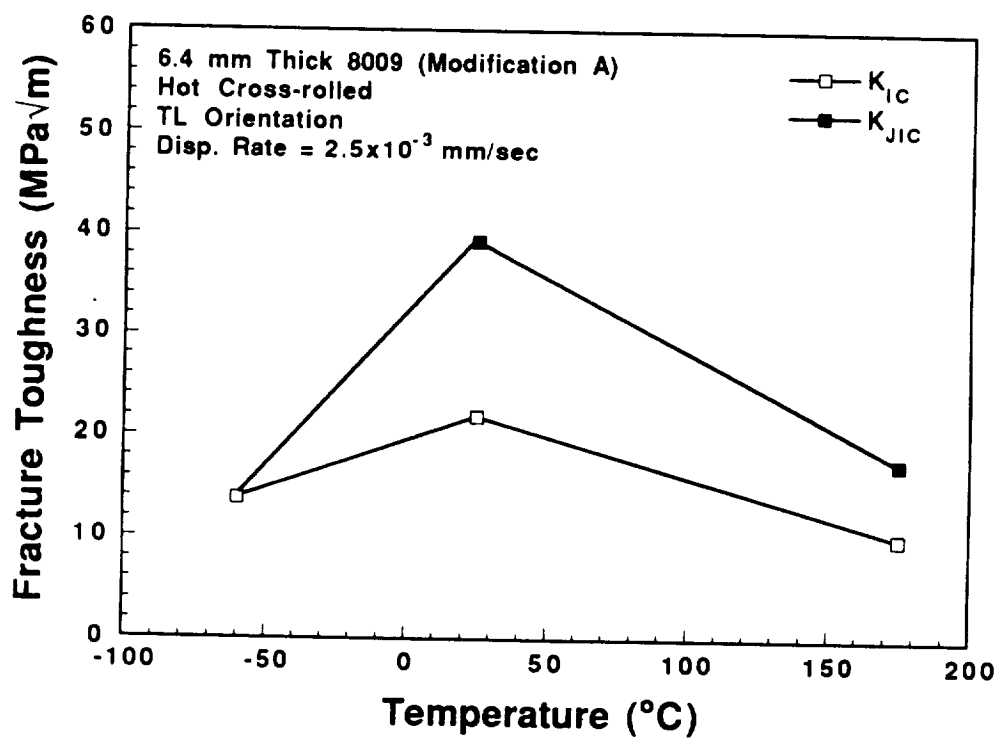


Figure 5 The effect of temperature on the fracture toughness of 6.4 mm thick Modification A 8009 plate (92A022-1C).

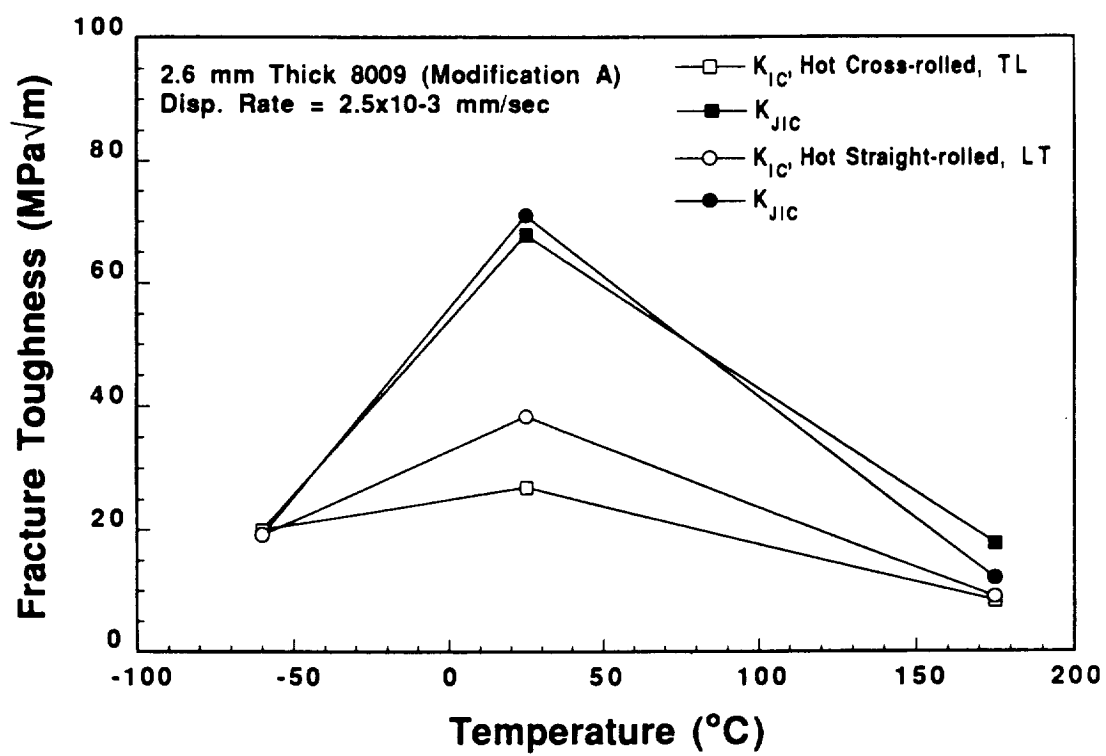


Figure 6 The effect of temperature on the fracture toughness of 2.6 mm thick Modification A 8009 sheet (92A022-2A and 92A022-2B).

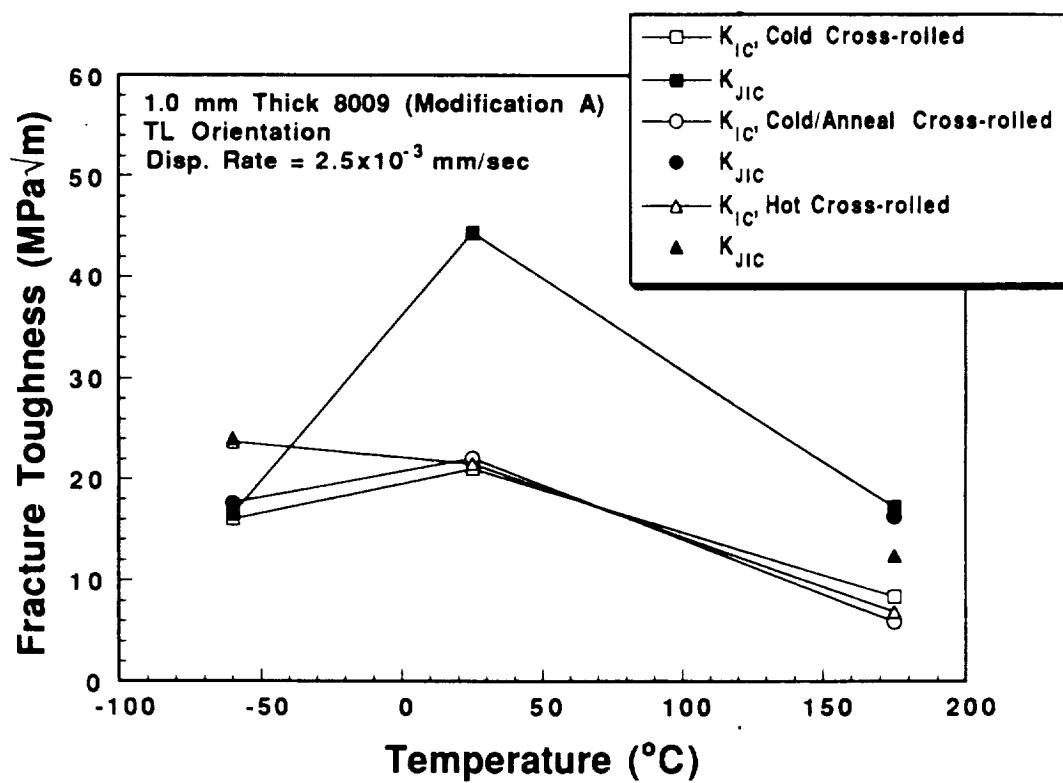


Figure 7 The effect of temperature on the fracture toughness of 1.0 mm thick Modification A 8009 sheets (92A022-1B1, 92A022-1B2 and 92A022-1B3).

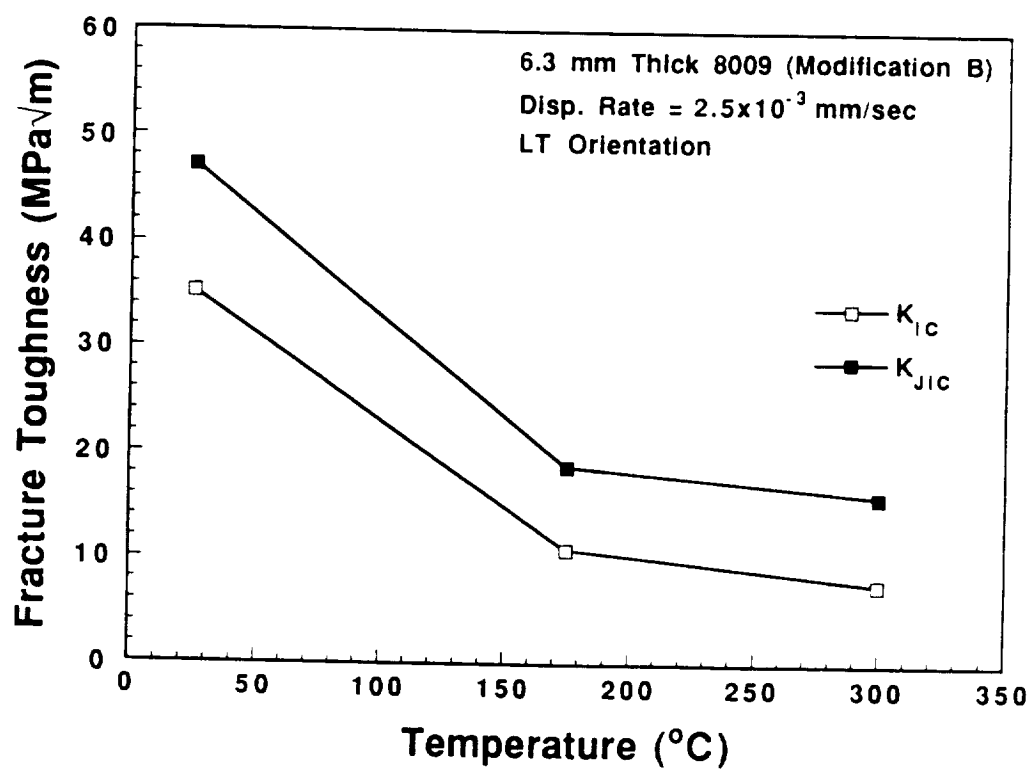


Figure 8 The effect of temperature on the fracture toughness of 6.4 mm thick Modification B 8009 plate (92A024-1C).

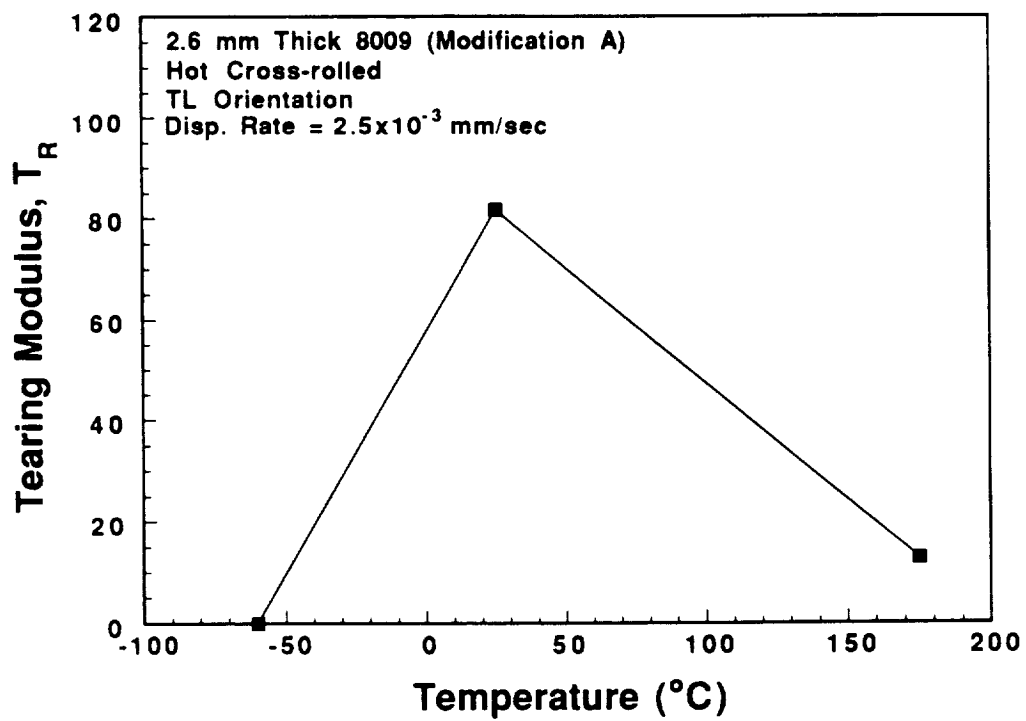


Figure 9 Tearing modulus as a function of temperature for 2.3 mm thick Modification A 8009 sheet (92022-2A).

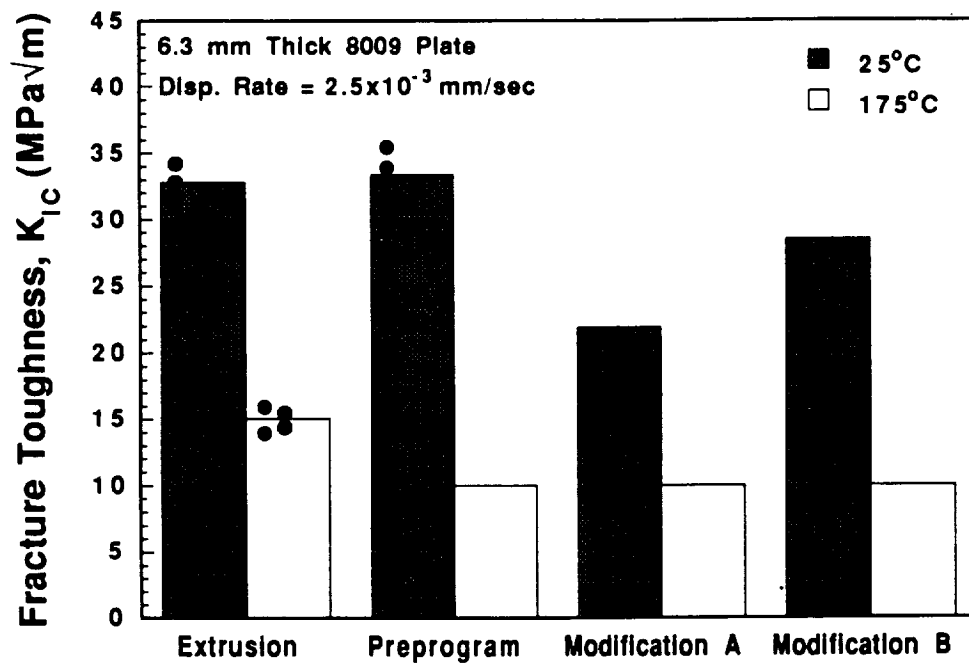


Figure 10 The effect of processing procedure on the fracture toughness of 6.3 mm thick 8009 plate (90A438-B, 92A022-1C and 92A024-1C).

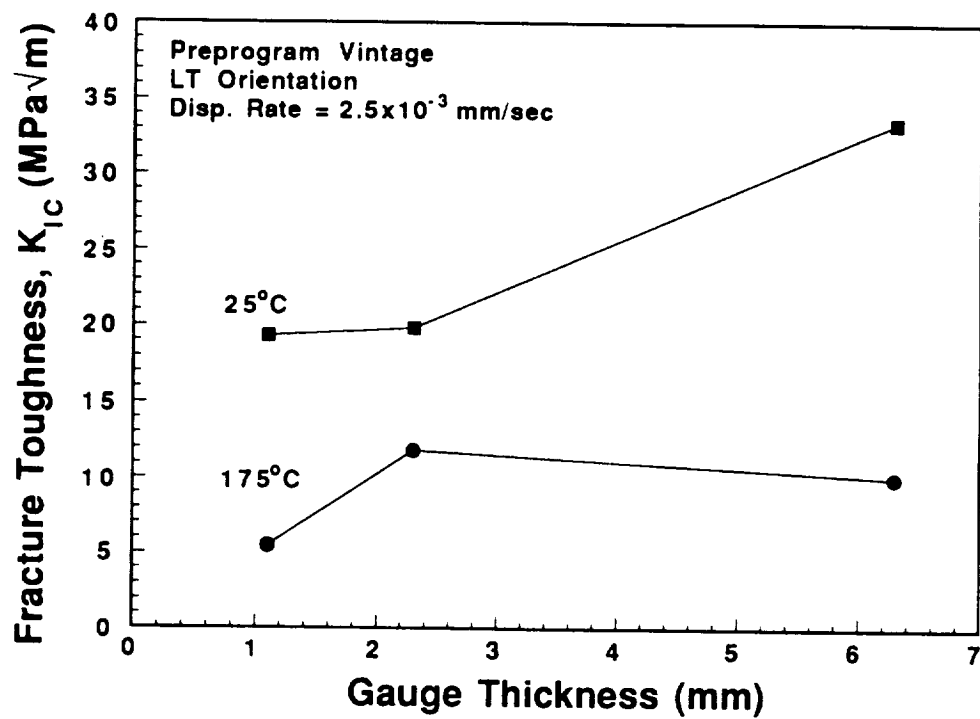


Figure 11 The effect of thermomechanical processing on the fracture toughness of Preprogram Vintage (90A438-B, 90A677-1S and 91A693-1A).

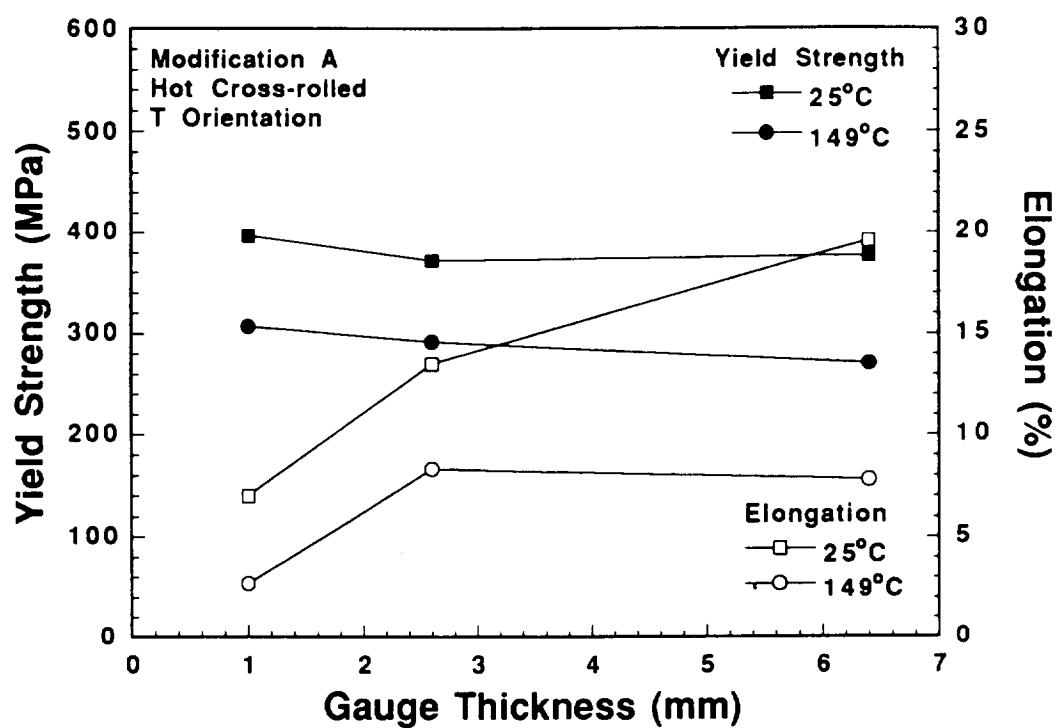


Figure 12 The effect of thermomechanical processing on the tensile properties of Modification A, hot cross-rolled 8009 plate and sheet (92A022-1C, 92A022-2A and 92A022-1B1). Data were obtained at Allied Signal Inc..

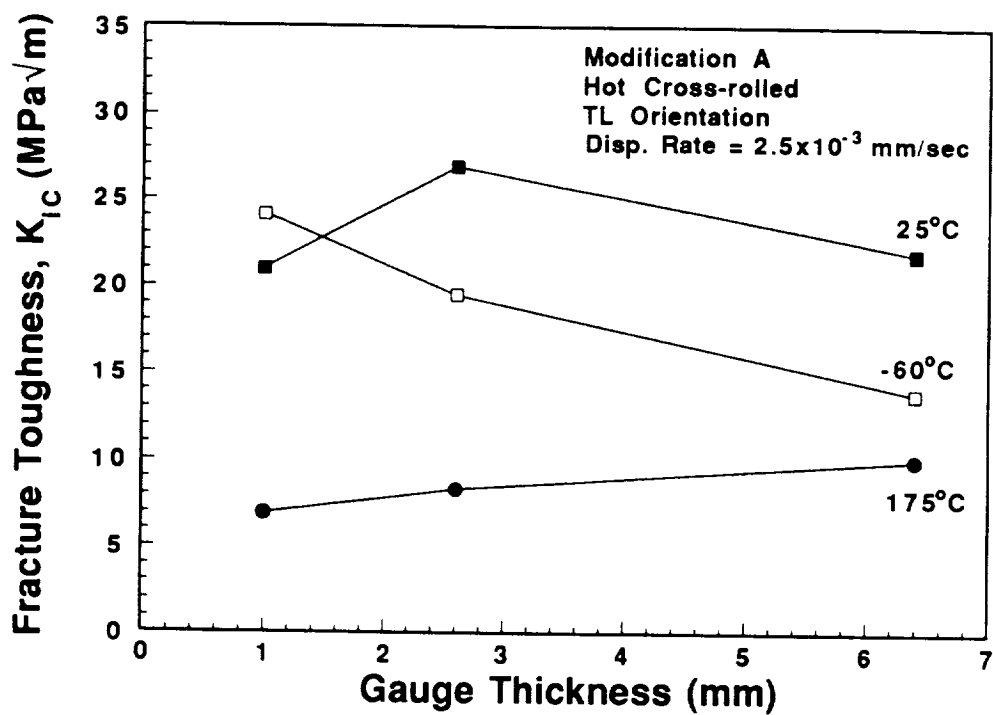
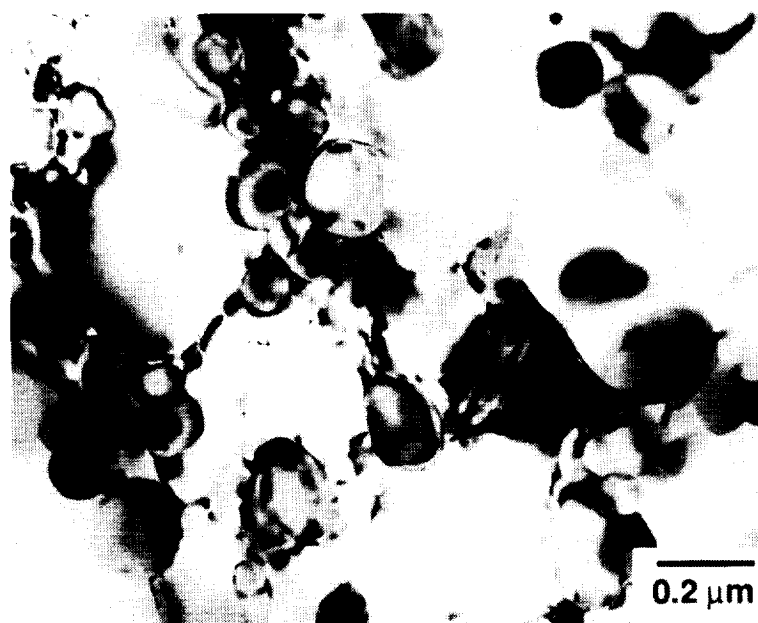
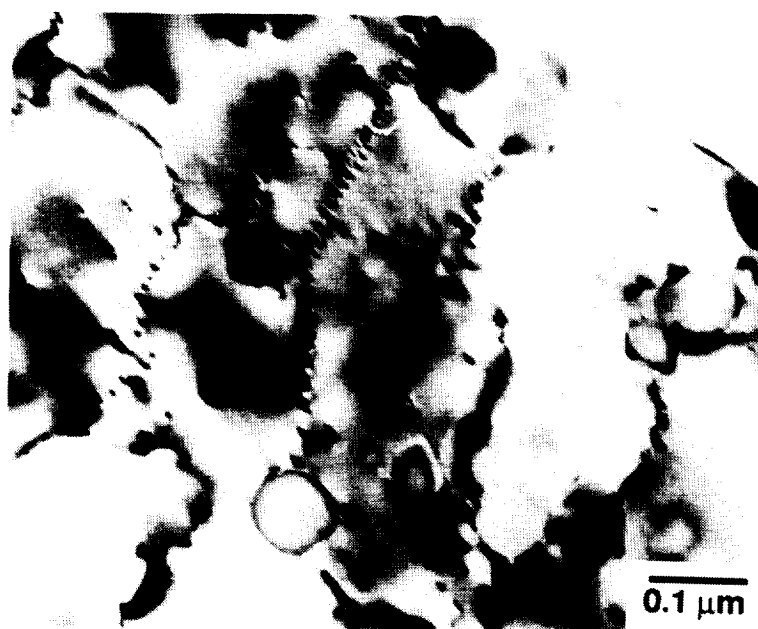


Figure 13 The effect of thermomechanical processing on the fracture toughness Modification A, hot cross-rolled 8009 plate and sheet (92A022-1C, 92A022-1B1, 92A022-1A and 92A022-1B1).

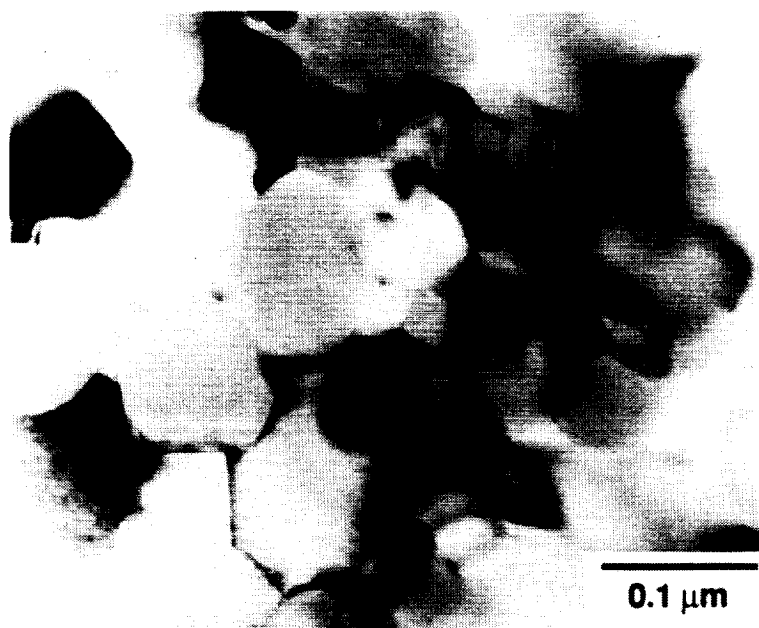


(a)

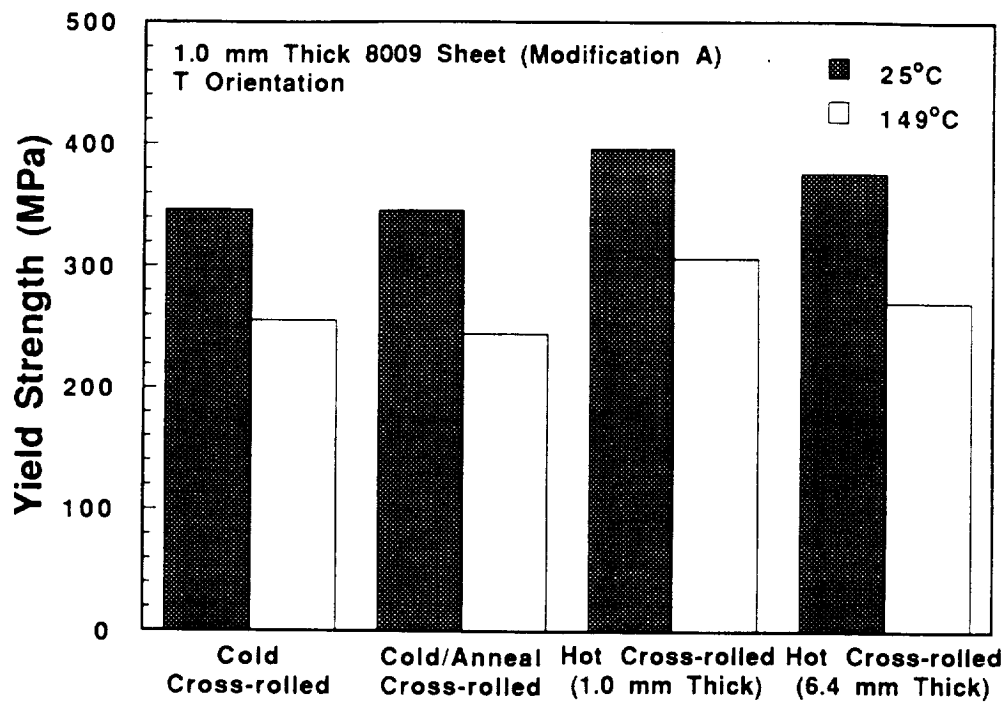


(b)

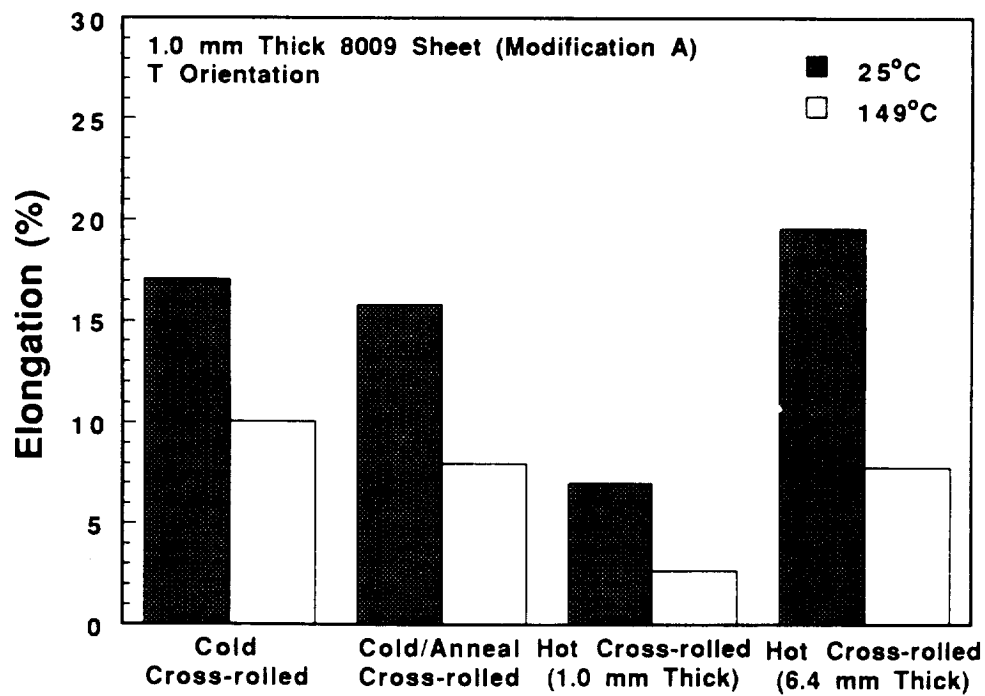
Figure 14 TEM micrographs of Preprogram Vintage 8009 with gauge thicknesses of (a) 6.3 mm, (b) 2.3 mm and (c) 1.1 mm.



(c)



(a)



(b)

Figure 15 The effects of rolling temperature and annealing on (a) yield strength and (b) tensile elongation of 1.0 mm thick Modification A 8009 sheet (92A022-1B1, 92A022-1B2 and 92A022-1B3). Data were obtained at Allied Signal Inc

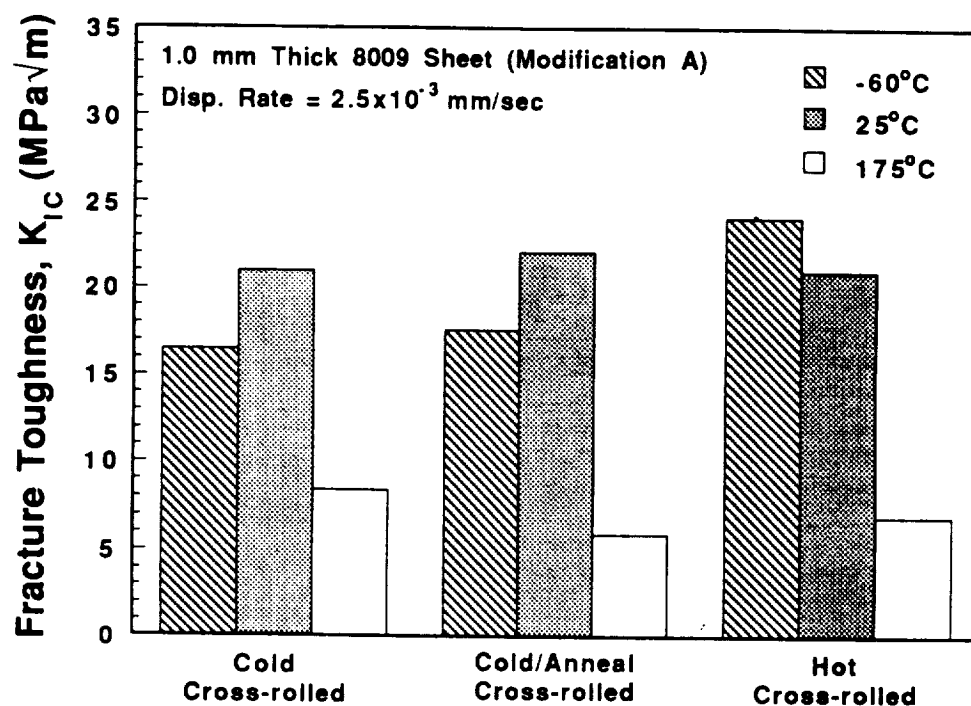


Figure 16 The effects of rolling temperature and annealing on the fracture toughness of 1.0 mm thick Modification A 8009 sheet (92A022-1B1, 92A022-1B2 and 92A022-1B3).

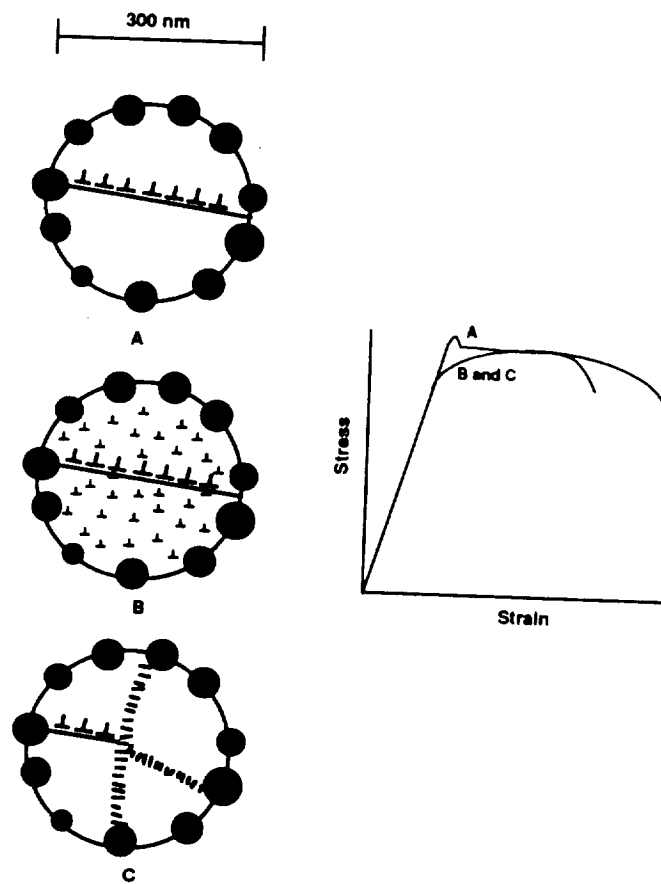


Figure 17 Schematic illustration of the tensile behavior of ultrafine grain steel material.

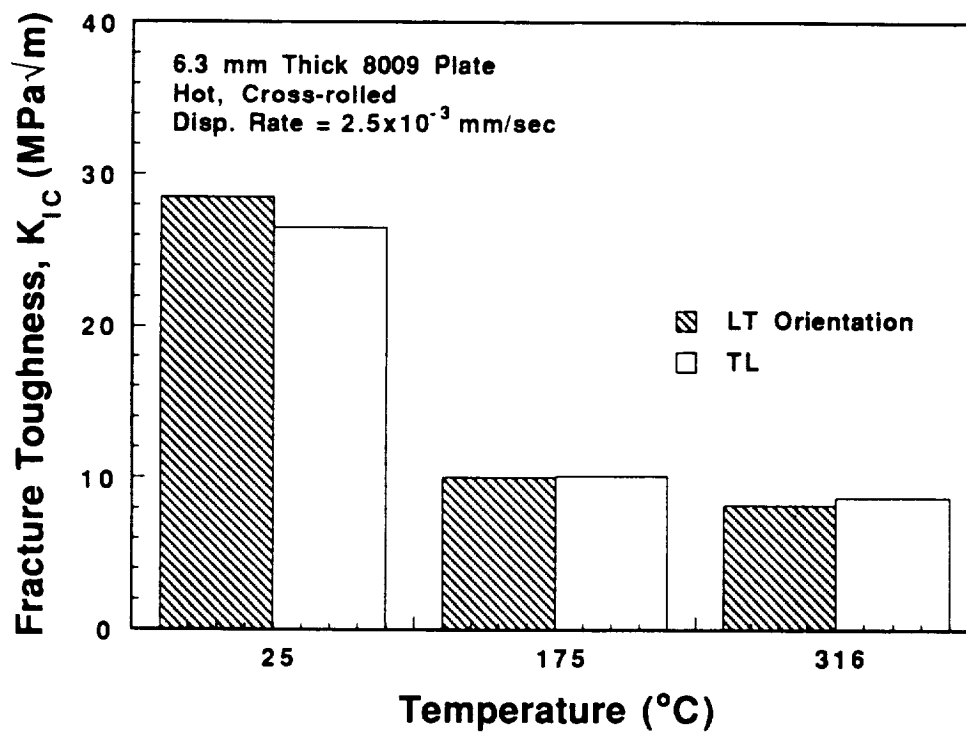


Figure 18 The effect of crack orientation on the fracture toughness of 6.3 mm thick Preprogram Vintage 8009 plate (1991 vintage).

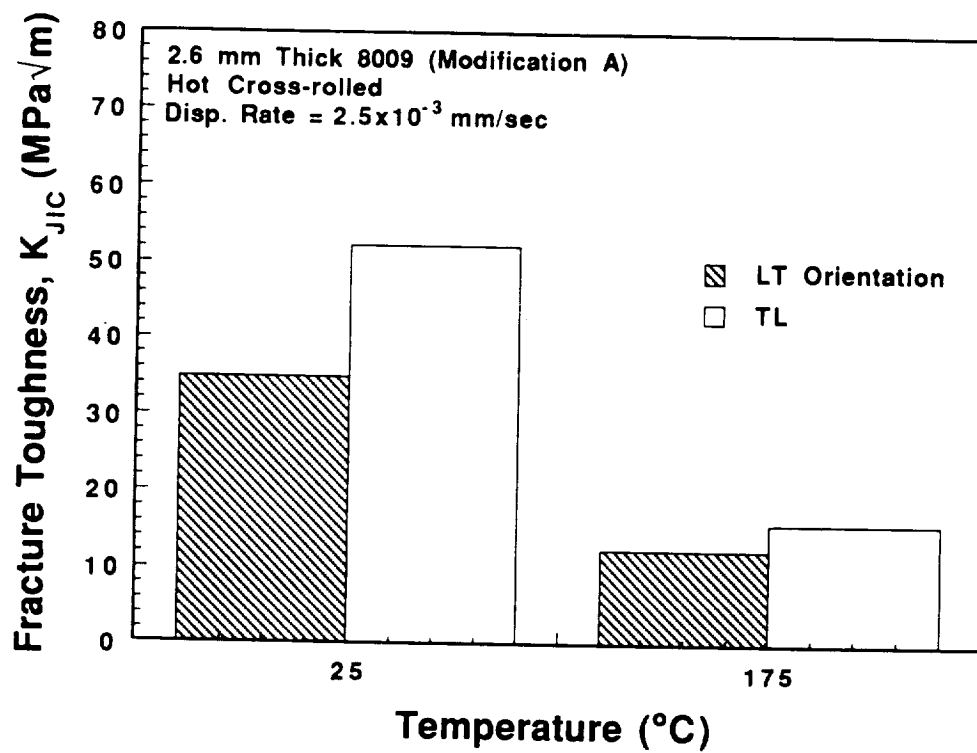


Figure 19 The effect of orientation on the fracture toughness of 2.6 mm thick Modification A 8009 sheet (92A022-2A).

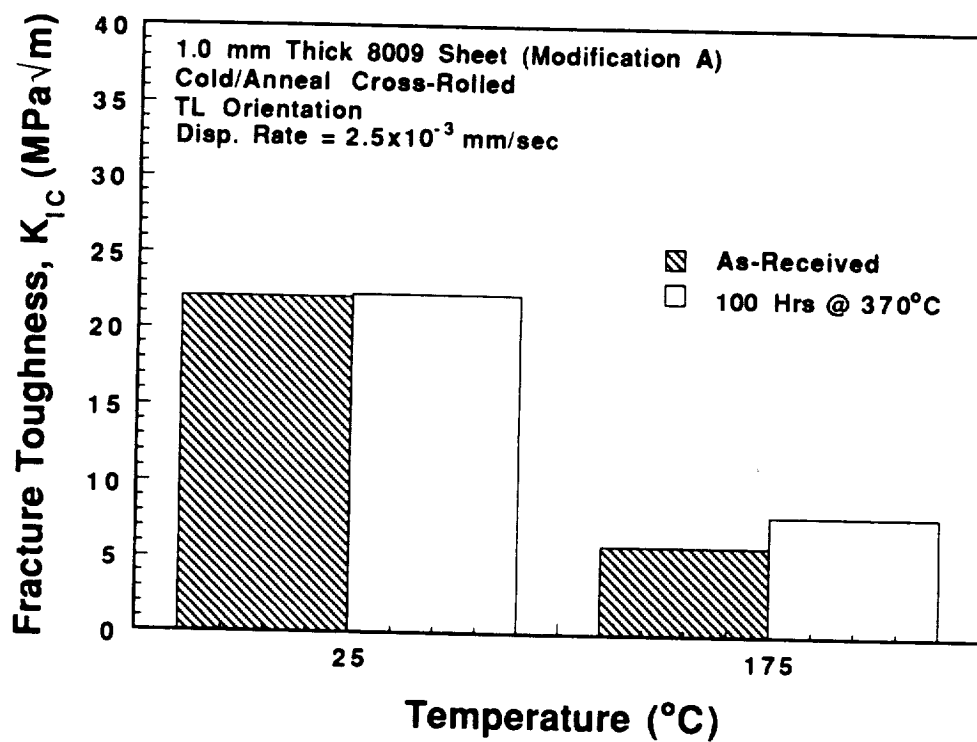


Figure 20 The effect of high temperature exposure on the fracture toughness of 1.0 mm thick Modification A 8009 sheet (92A022-1B3).

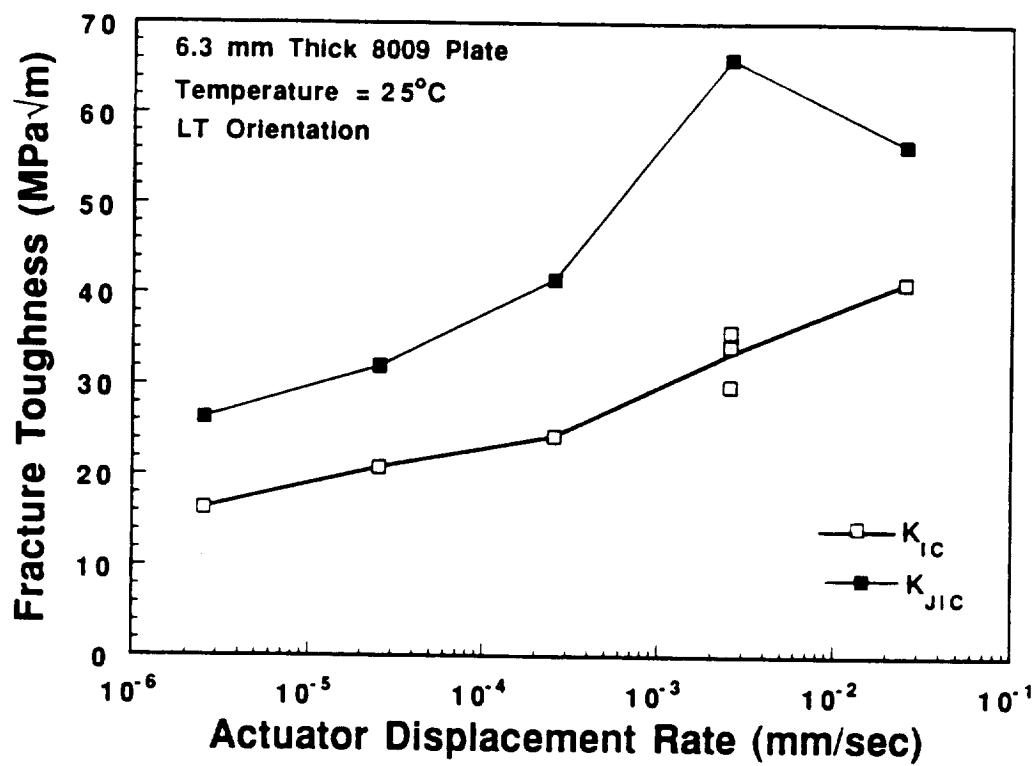


Figure 21 The effect of actuator displacement rate on the fracture toughness of 6.3 mm thick Preprogram Vintage 8009 plate (90A438-B) at 25°C.

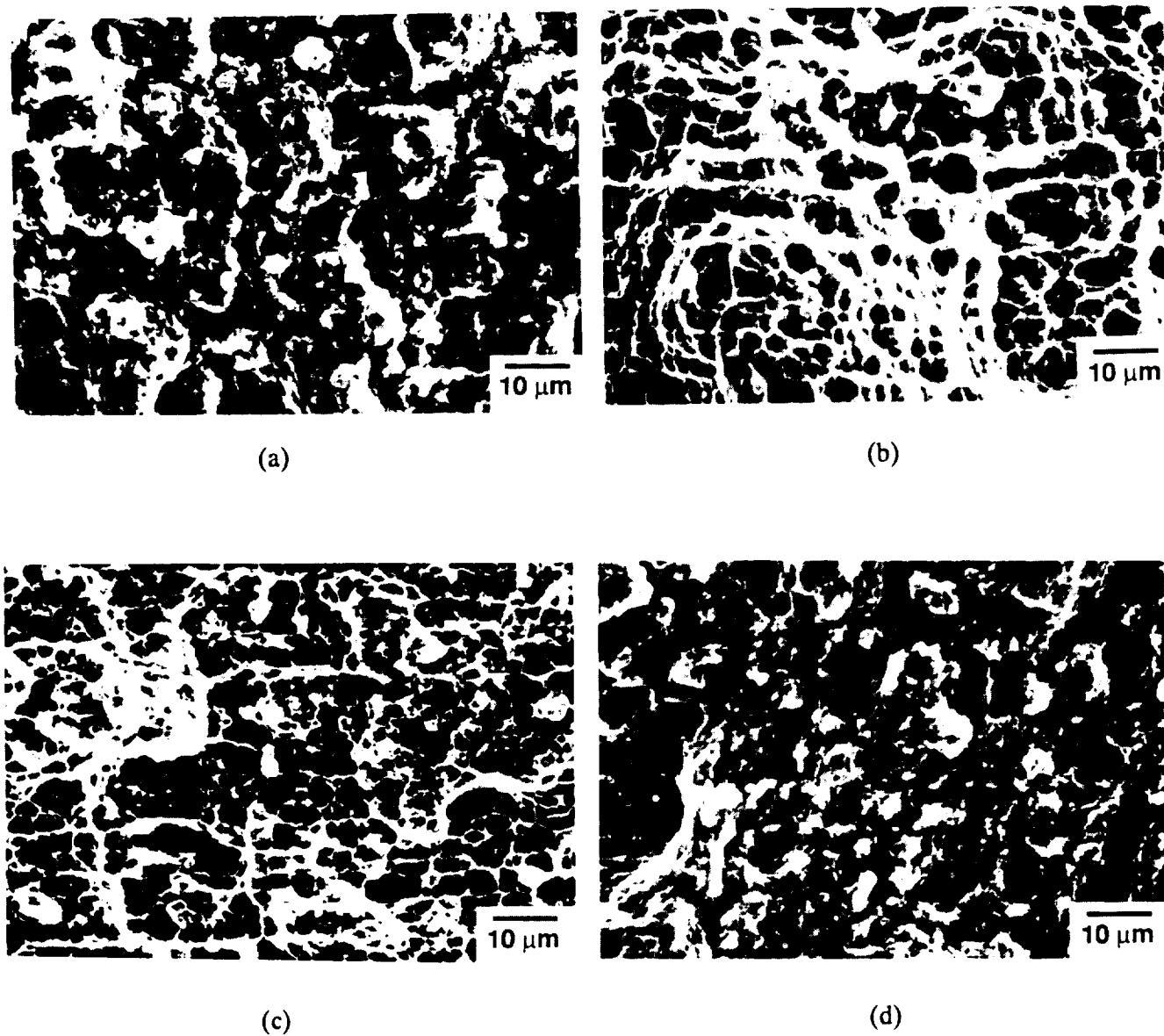
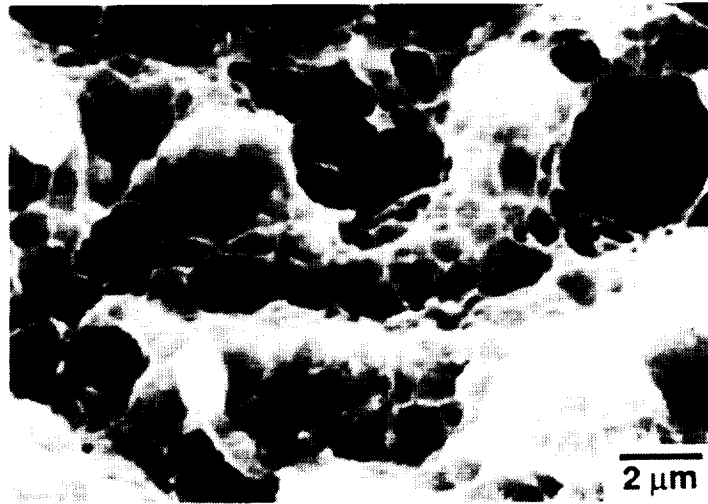
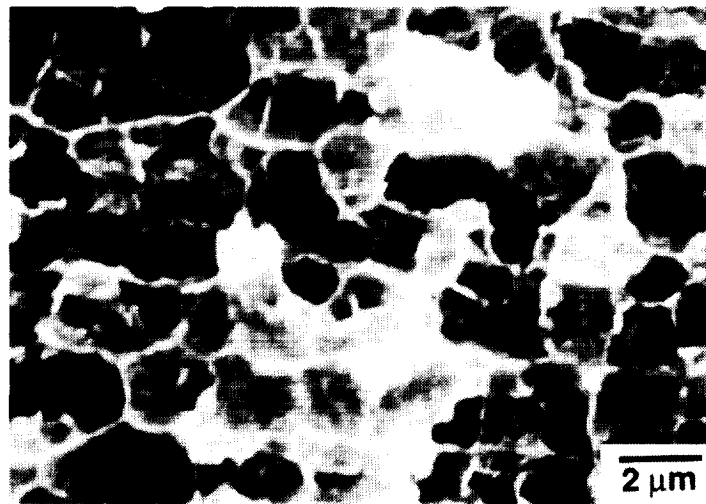


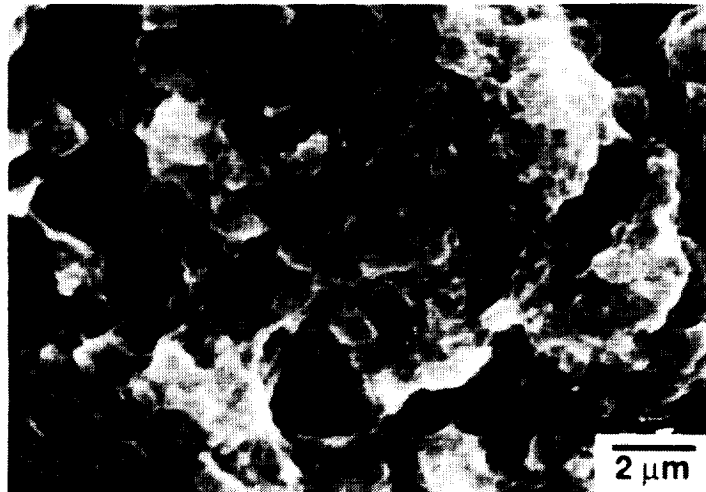
Figure 22 SEM fractography of 6.3 mm thick Preprogram Vintage HTA 8009 plate (90A438-B) tested at:(a) 25°C, 2.5×10^{-3} mm/sec, (b) 175°C, 2.5×10^{-3} mm/sec (c) 25°C, 6.1×10^{-6} mm/sec, and (d) 25°C, 2.5×10^{-2} mm/sec.



(a)

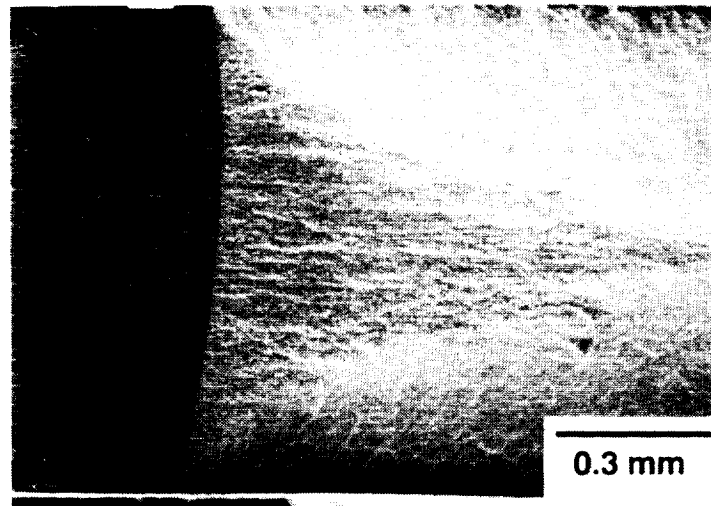


(b)

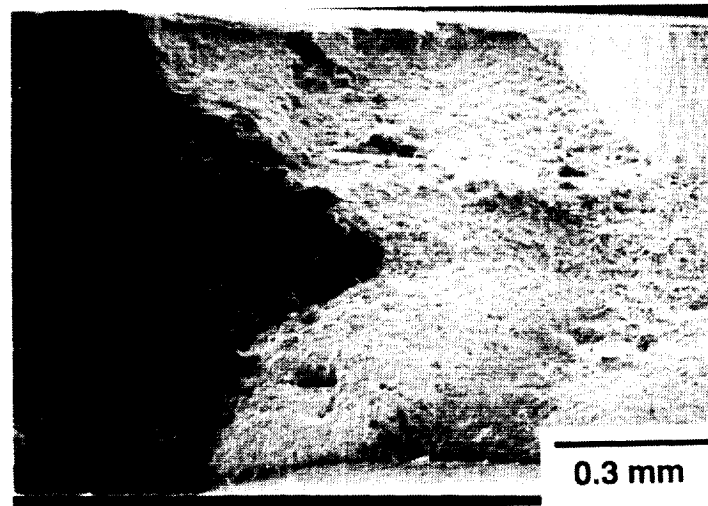


(c)

Figure 23 High magnification SEM fractography of 2.6 mm thick Modification A 8009 sheet (92A022-2A) tested at:(a) 25°C, (b) 175°C, and (c) -60°C.



(a)



(b)

Figure 24 Low magnification SEM fractographs of 1.1 mm thick Modification A 8009 sheet (91A693-1A) tested at (a) 25°C, and (b) 175°C.

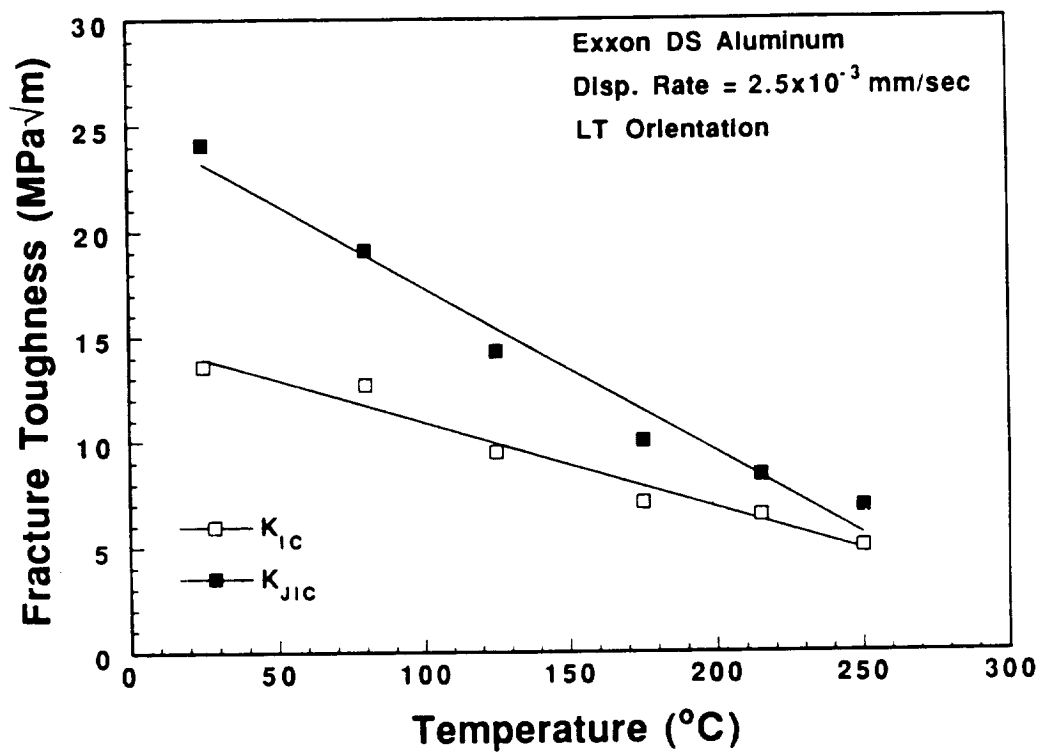


Figure 25 The effect of temperature on the fracture toughness of Exxon DS Aluminum.



Figure 26 TEM micrograph of tensile deformed 6.3 mm thick HTA 8009 plate at 25°C.



Figure 27 TEM micrograph of tensile deformed 6.3 mm thick HTA 8009 plate at 175°C.

TASK 7. STRENGTH/TOUGHNESS COMBINATION IN DMMCs

Principal Investigator:	Dr. L.M. Angers, Alcoa
Senior Engineer:	Dr. G. Dixon, Alcoa
Boeing Contact:	Mr. P.G. Rimbo
Douglas Contact:	Mr. R. Kahandal

Objective

The objective of this task is to characterize sheet produced from discontinuously reinforced metal matrix composites. Room temperature tensile and plane stress fracture toughness tests will be conducted on materials aged to peak strengths.

Background

Three materials were identified for evaluation: 2080/SiC/20_p, MB85/SiC/20_p, and 6113/SiC/20_p. The notation indicates that these materials contain 20 vol% SiC. The SiC particles used in this study were faceted, with a nominal size of 9 microns and an aspect ratio of up to 2. 2080/SiC/20_p and MB85/SiC/20_p are similar in composition, i.e., 3.8% Cu-1.8% Mg except 2080/SiC/20_p has 0.25% Zr and MB85/SiC/20_p has 0.35% Zr. By examining different rolling practices and two levels of Zr, it was intended that significantly different grain structures would be produced. As a result, different strength/toughness combinations might be expected.

The 2080/SiC/20_p and MB85/SiC/20_p were fabricated using two different rolling practices. The different rolling practices were used in an attempt to produce material with two different grain structures: a large grain size material, i.e., ASTM grain size of 2, and a fine grain size material, i.e., ASTM grain size of 8.

Procedure

Atomized powders of 2080, MB85, and 6113 and SiC reinforcement powders were donated to the University of Virginia

Subcontract No. 5-28406 so that fabrication, consolidation and characterization could proceed without delay.

The aluminum powders were blended with SiC reinforcement, cold isostatically pressed, hot pressed, extruded and rolled. Two 2" x 4" extruded bars at least 30" in length were fabricated for 6113/SiC/20_p and four 2" x 4" extruded bars at least 30" in length were fabricated for 2080/SiC/20_p and MB85/SiC/20_p.

For 2080/SiC/20_p and MB85/SiC/20_p, the rolling practice intended to produce fine grain material (Process A) required a reheat every other pass whereas the rolling practice intended to produce the coarse grain material (Process B) required a reheat every pass. In theory, a fine grain size can be produced by increasing the amount of deformation during processing. Ideally, cold rolling would be the most feasible way to produce the fine grain size but since edge cracking becomes a problem when cold rolling, hot rolling is required. 2080/SiC/20_p and MB85/SiC/20_p samples were heated to 850°F prior to rolling.

6113/SiC/20_p was heated to 900°F prior to rolling and reheated when the temperature dropped between 800°F and 700°F .

Each composite was rolled to 1/8" thickness and to 6 1/2" to 7" in width.

MB85/SiC/20_p and 2080/SiC/20_p were both solution heat treated at 930°F for 4 hr followed by a cold water quench and then aged at 350°F for 24 hr to produce the T6 temper. 6113/SiC/20_p was solution heat treated at 1047°F for 1 hr followed by a room temperature water quench and 24 hr of artificial aging at 325°F to produce the T6 temper.

Tensile and toughness data were generated for each DMMC. Tensile tests in L and LT directions were performed on 1/8" thick and 4" long sheet type tensile specimens with a 1/4" reduced section width. Toughness tests were performed on 1/8" thick, 6.3" x 20" center cracked panels.

Results and Discussion

Micrographs taken from the MB85/SiC/20_p and 2080/SiC/20_p material produced using the two rolling practices, Process A and Process B, are shown in Figs. 1 and 2. It was difficult to determine the grain sizes for both 2080/SiC/20_p and MB85/SiC/20_p due to the large volume of SiC (20%) present.

Table I lists the strength data generated for MB85/SiC/20_p and 2080/SiC/20_p as a function of fabrication history. No significant differences are observed between the 2080/SiC/20_p and MB85/SiC/20_p materials fabricated using Process B. The MB85/SiC/20_p material fabricated using Process A, however, has higher strengths than the 2080/SiC/20_p material fabricated using Process A for L and T orientations. For Process A, MB85/SiC/20_p is believed to have more unrecrystallized grains than 2080/SiC/20_p due to its higher Zr level.

Figure 3 is a plot of fracture toughness as a function of tensile yield strength for MB85/SiC/20_p (Process A and Process B), 2080/SiC/20_p (Process A and Process B) and 6113/SiC/20_p. The 6013/SiC/20_p exhibits greater toughness but at a yield strength lower than either MB85 or 2080 composites. The 2080/SiC/20_p and MB85/SiC/20_p materials show comparable toughness levels. Data from a 2080/SiC/20_p composite tested at a thinner gage, i.e., 0.063", using a wider panel, i.e., 16" wide, is included for comparison in Fig. 3. In addition, data for the I/M 2XXX alloy, S. No. 689248-T8, is also included. The toughness values for the composites are seen to be very low in comparison to the monolithic alloy.

Some limited amounts of metal are available for additional evaluations. Material was lost due to edge cracking and warpage, so the original experimental plans were altered.

Summary

- MB85/SiC/20_p and 2080/SiC/20_p made by process A and process B show comparable toughness values.
- MB85/SiC/20_p made by process A had higher tensile yield and ultimate strengths in both L and T directions than 2080/SiC/20_p.
- 6113/SiC/20_p exhibited higher toughness values than MB85/SiC.20_p or 2080/SiC/20_p but at lower yield strengths.

TABLE I. Results of tensile and fracture toughness testing of the discontinuously reinforced metal matrix composites.

Identification	Fabrication History	Orientation	Tensile Yield Strength	Ultimate Tensile Strength, ksi	Elongation, %	Orientation	K _c , ksi $\sqrt{\text{in.}}$	K _{app.} , ksi $\sqrt{\text{in.}}$
MB85/SiC/20p	Process A	L	76.2	82.4	4.0	L-T	24 ^a	22 ^a
		T	72.0	80.7	4.3			
	Process B	L	70.2	80.6	5.5	L-T	28 ^b	24.9 ^b
		T	68.1	78.6	5.3			
2080/SiC/20p	Process A	L	71.7	80.0	4.6	L-T	23 ^a	21.5 ^a
		T	69.2	78.6	4.8			
	Process B	L	70.9	79.2	4.0	L-T	22 ^b	20.7 ^b
		T	68.6	78.9	4.0			

^a Average of 3 L-T specimens.

^b Single specimen.

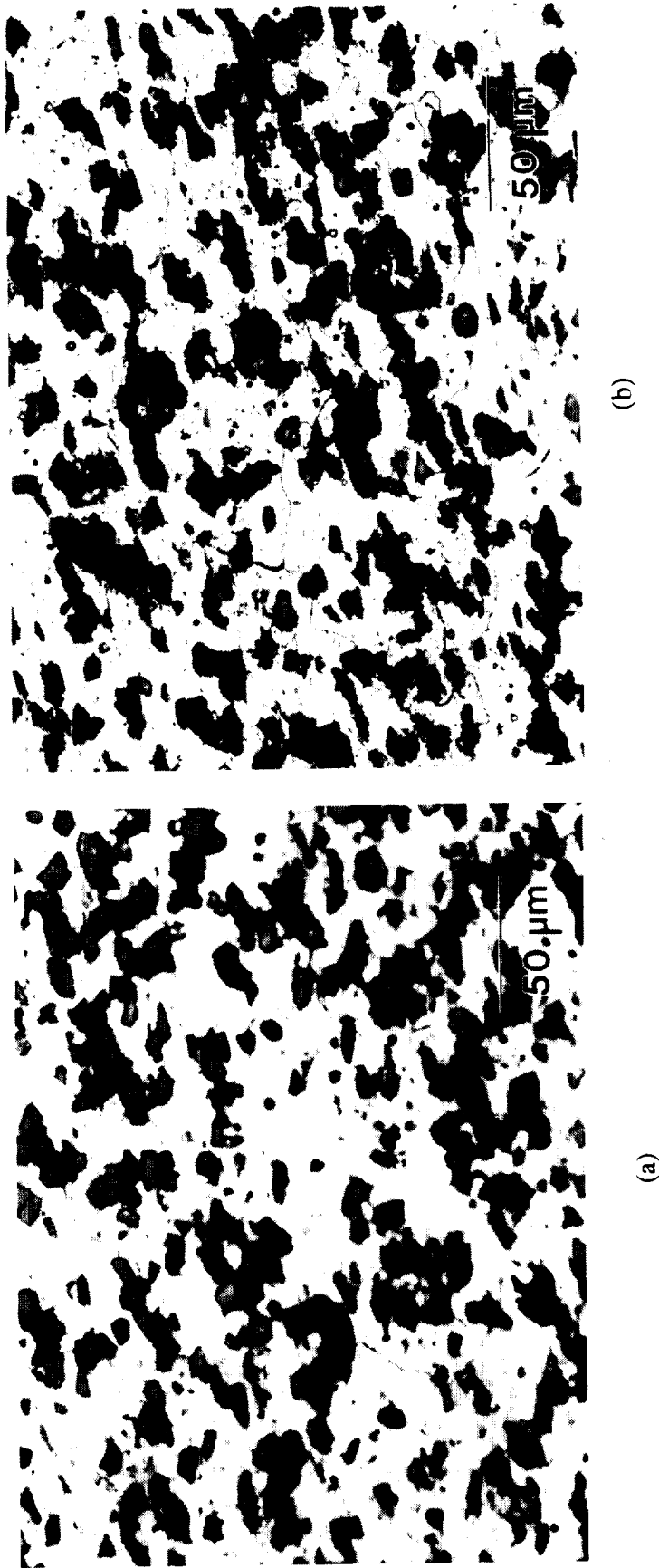
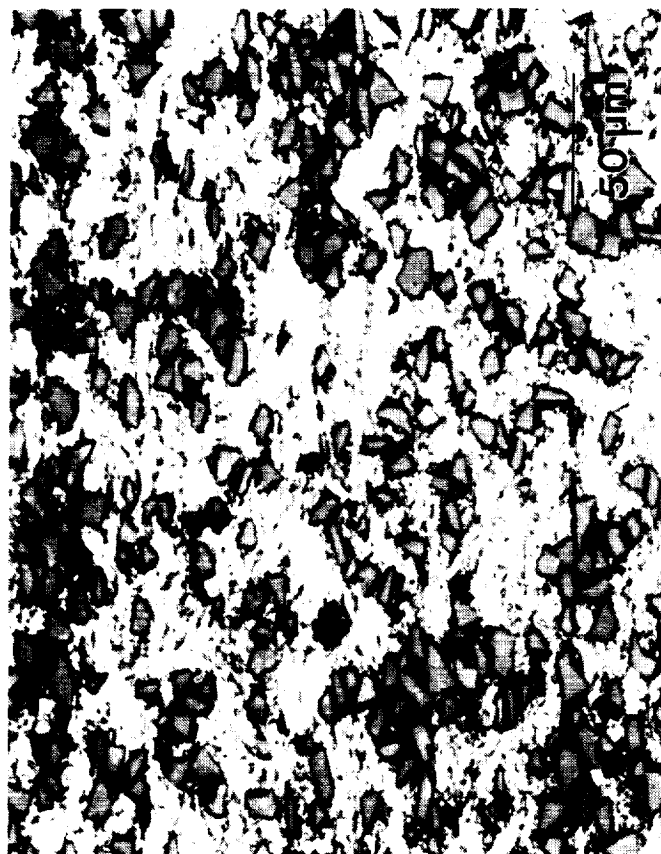


Figure 1. Optical micrographs of MB85/SiC/20p-T6 rolled to 0.125" thick sheet, using: (a) Process A and (b) Process B.



(a)



(b)

Figure 2. Optical micrographs of 2080/SiC/20p-T6 rolled to 0.125" thick sheet, using: (a) Process A and (b) Process B.

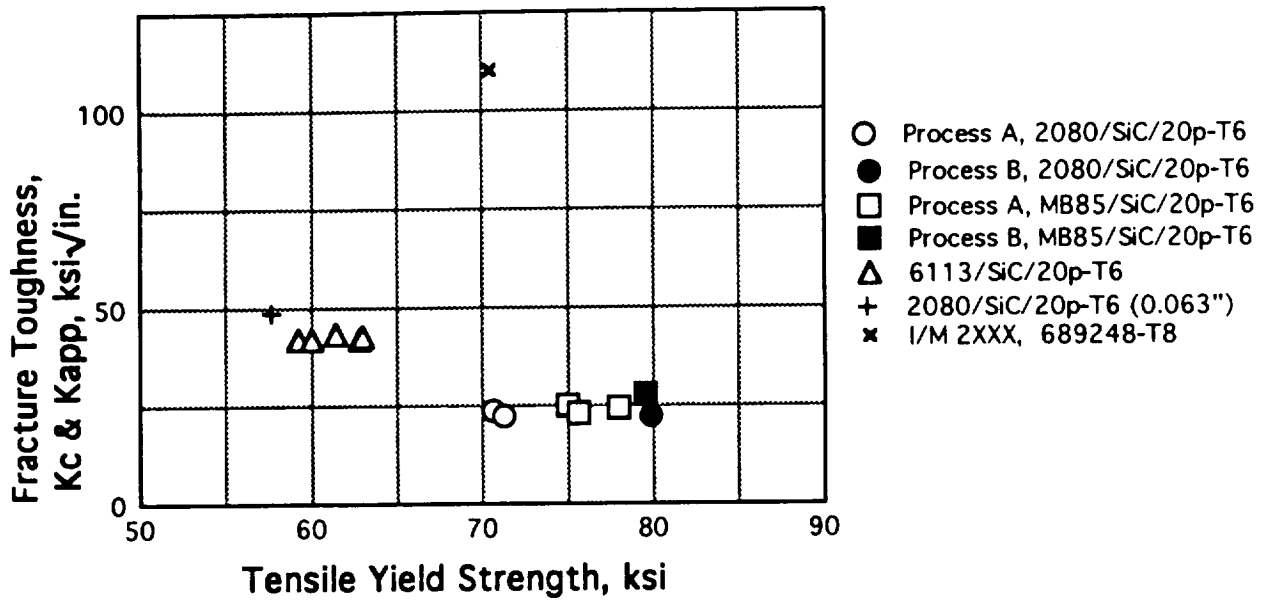


Figure 3. Fracture toughness, K_c and K_{app} , as a function of tensile yield strength for the DMMC sheet. Included for comparison is a datum for an I/M 2XXX alloy: 689248-T8.

TASK 8. INVESTIGATION OF THE FORMATION OF THE Ω PHASE IN MODIFIED 2009 AND CHARACTERIZATION OF THE MODIFIED ALLOYS' THERMOMECHANICAL PROPERTIES

Principal Investigator:
Graduate Student:

Dr. F.E. Wawner
Mr. Qiong Li

Introduction

Work reported on in the first semi-annual report (UVA report under Grant No. NAG-1-745, for the period 1/1/92-6/30/92) demonstrated that the Ω phase was readily achieved in several cast matrix alloy compositions. In addition, a coherent-coplanar precipitate was obtained in the alloys which was recognized as the previously identified σ phase (1). Characterization was initiated on the alloys microstructure, heat treatment response, thermal stability, and mechanical properties. The present report presents results obtained during the period 7/1/92-12/31/92.

Objective and Technical Approach

The objective of this investigation is to modify 2009 (a product of Advanced Composite Materials Corporation) with Ag to enhance the formation of the Ω phase in the SiC particulate reinforced Al-Cu-Mg matrix composite in order to increase the composite's elevated temperature stability.

The technical approach initially taken is to fabricate potential matrix alloys at UVA to determine optimum Cu/Mg ratio and optimum amount of Ag in order to generate a maximum volume fraction of the coherent Ω phase. Initial composite samples will be produced by compocasting at UVA, incorporating SiC into the alloy composition determined to be best for achieving the Ω phase. Microstructural studies of these composites will be made to ascertain if the Ω phase is retained after introduction of the ceramic particles. If it is not, other iterations of matrix composition will be made to achieve maximum Ω in the composite. After establishing the optimum composition ACMC will produce a P/M

sample for evaluation of the material's thermomechanical properties and stability at UVA.

Experimental

Initial experimental alloys are being produced using an induction heater to melt the metal charge in a glove box containing an argon atmosphere. The composition of the alloys investigated thus far are listed in Table 1.

TABLE 1

<u>Sample</u>	<u>Cu wt%</u>	<u>Mg wt%</u>	<u>Ag wt%</u>	<u>Al wt%</u>
A11M	3.2	0.45	0.4	bal
A11MM	3.2	0.45	0.5	bal
A12M	4.0	0.45	0.4	bal
A13M	2.6	0.45	0.4	bal

After casting, all alloys were first hot rolled and then homogenized for 24 hours at 495°C, solutionized for 19 hours at 525°C, quenched in ice water, and artificially aged at different times and temperatures. Hardness tests were made on an Indentron Rockwell hardness tester to establish peak aging conditions. A Perkin Elmer DSC7 differential scanning calorimeter was used to investigate the precipitation process and melting temperature in the alloys. For the microstructural investigations a Philips EM 400T with EDS and a JEOL 4000EX high resolution transmission electron microscope were utilized. Determination of shear strength was made using the blanking shear test technique, since sufficient material was not available for tensile testing.

Composite Fabrication.

Since the objective of this study is to modify 2009 (a Al-Cu-Mg/SiC particulate material) it is necessary to evaluate composite

samples to determine if the introduction of ceramic particles alters the type of phases that precipitate in the matrix. To expedite determination of the optimum matrix composition for maximum Ω phase, composite samples are being produced at UVA by compocasting. A compo-cast Al1M/SiC composite was fabricated successfully. The approach was to melt an Al alloy and add the appropriate amount of Al, Cu, Ag and some of ACMC 2009 material (with SiC particles already incorporated) to give a matrix with composition of Al1M, agitate the melt, then cast. This approach yields a composite with a lower volume fraction of particulate (about 8%). The lower volume fraction of reinforcement may lead to a lower dislocation density. This could influence the amount of s' or θ' (since these phases will nucleate on dislocations) formed. This should not, however, alter the objective of the experiment, to verify that the Ω phase can be formed in the composite. Examining this casting showed that there is reasonable uniform particle distribution for casting composites.

Results

Alloys

The experimental alloys' compositions are shown in Table 1. The Al3M alloy has been dropped from consideration as a candidate for the matrix alloy because of its low hardness data. All of the other alloys contain Ω and s phases.

The Ω phase (Al_7Cu) forms on the $\{111\}$ Al matrix planes as a uniform dispersion of large but very thin hexagonal-shaped plates (2). TEM micrograph Fig. 1. shows the hexagonal-shaped plates along $\langle 111 \rangle_{\text{Al}}$; other orientations show the inclined Ω plates. The angles between these plates are either 120° or 60° . The small hexagonal-shaped particles are σ ($\text{Al}_5\text{Cu}_6\text{Mg}_2$) phase which is coherent-coplanar with Al (1). The σ phase was recently found in Al alloys (1,6). The misfit between σ and matrix is 3.1%, which is small compared to the Ω phase. Because of the small misfit, a strain field pattern can be seen near the interface region.

Figure 2 shows the strain field pattern caused by misfit dislocations and the periodic lobes in the matrix near interface, the period is about 6.7 nm. The periodic lobes are not observed in a large misfit interface. Accurate strain data can be measured by convergent beam electron diffraction. Moire fringes also are visible in the micrograph since the Ω phases are embedded in the matrix. Figure 3 shows the microstructure of four phases formed in the alloys. The precipitate phases are Ω (Al_2Cu on $\{111\}$ plane), θ' (Al_2Cu), σ ($\text{Al}_5\text{Cu}_6\text{Mg}_2$) and s' (Al_2CuMg). These precipitates have certain non-uniformity in the alloys. The θ' and s' phases tend to form at grain boundaries, subgrain boundaries, and dislocations; the Ω and σ phases have more uniformity in the matrix than the θ' and s' phases do but they tend to form in regions with one phase dominating. Figures 4a, b, which were taken from a region with rich σ or Ω phase, shows the σ and Ω phase electron diffraction patterns with $\langle 001 \rangle_{\text{Al}}$, $\langle 011 \rangle_{\text{Al}}$, $\langle 112 \rangle_{\text{Al}}$, and $\langle 111 \rangle_{\text{Al}}$ orientations respectively. The large spots are from aluminum matrix; the small spots from either σ or Ω phases. The strong reflections of Ω and σ phases imply a large amount of the precipitates, and weak θ' and s' reflections imply a small amount of these precipitates.

Thermal stability

Figure 5 is a plot of shear strength of the alloys as function of thermal exposure at 150°C and 200°C. The results show the alloys with Ω and σ phase have better thermal stability than 2124P/M alloy. The alloys with the Ω and σ phases aged at 150°C have no substantial drop in shear strength but the shear strength of 2124P/M alloy decreased almost 12%. For the alloys exposed at 200°C, all of the shear strengths have a substantial decrease but the 2124 P/M has the largest drop. The reason for the large drop in the shear strength for Al2M is unclear. Table 2 shows the strength drop by percentage after long time thermal exposure.

Table 2. Shear Strength Drop after Thermal Exposure

<u>Conditions</u>	<u>A11M</u>	<u>A11MM</u>	<u>A12M</u>	<u>2124 P/M</u>
150°C 643 hrs	5.3%	4.5%	3.4%	11.7%
200°C 405 hrs	16.2%	15.5%	34.6%	36.8%

The reason is that in 2124 the dominant precipitates are s' and θ' which coarsen rapidly at elevated temperature. In these experiments, the shear test load-elongation curve implies that the alloys with Ω and σ phase also have better ductility and toughness than 2124P/M.

TEM samples were taken from each shear test sample (A11MM and A11M since they only have a slight difference in Ag content and shear strengths) for a coarsening study. The TEM micrographs in Fig. 6 show that there is no size change in the σ phase. After exposure for more than 400 hrs at 200°C, the σ phase still remains in a high density in the alloy, and the diffraction pattern shows strong σ phase reflections. The TEM micrograph in Fig. 7 shows that the Ω phase is larger than σ and slightly coarsens after long time aging. The Ω phase appears as the highlighted lines. The size of each phase was determined by measuring more than 200 precipitates for each aging condition, then plotting the mean value of the size as function of time. The σ phase was measured at the cube edges. The Ω phase was measured in length of the plate. Figure 8a is the plot of precipitate size versus time. The graph indicates that Ω' phase has a higher coarsening rate and larger initial size than does the σ phase. After initial growth, the coarsening rate of the σ phase is essentially zero. An empirical equation is given that can predicate the precipitate size as function of time. The θ' precipitate coarsening data (3), Fig. 8b, shows that the θ' phase has a much larger size than Ω or σ and a higher coarsening rate.

The coarsening behavior of the Ω phase and σ phase is due to

the difference of their misfit, interfacial energy and their growth ledge morphology. The misfit of Ω phase and Al is 8.3% (4,5), for the σ phase the value is 3.1% (6). On the other hand, the σ phase is coherent-coplanar phase, but the Ω phase is not. This is why the Ω phase developed a plate shape precipitate and the σ phase developed a cubic shape. TEM studies indicate that the σ phase has a smaller size and fewer growth ledges than the other phases. The micrographs in Figs. 9a, b, show the growth ledges on the Ω and σ phases. They both show a low number of ledges. The micrograph Fig. 9c shows growth ledges on the θ' phase in a Al1M/SiC_p composite aged 2 hrs at 250°C. The micrograph shows the growth ledges with some non-facet steps in the θ' phase. Figure 9d shows antiphase domain boundaries in ordered θ' . The number of APB per particle increases linearly with aging time. This is due to the precipitate coalescence during growth and precipitate-dislocation interactions (7). The lower coarsening rate of the Ω and σ phases indicate that both have lower interfacial energy, consequently smaller and fewer growth ledges.

Effect of deformation (hot rolling) on Ω and σ phase

When an alloy with Ω and σ phases is deformed from a slab to a thin foil by hot rolling, the amount of Ω and σ phases is reduced. This happened after hot rolling a 3mm thick Al1M alloy down to a 0.13 mm. The micrographs in Fig. 10 show the predominant θ' phase with smaller amounts of the Ω and σ phases. The cause of this could be due to a surface effect. An element like Mg with high diffusivity could migrate to the surface, which would reduce Mg content in the sample.

Composite Microstructure

In Al1M/SiC composites with 8% SiC volume fraction fabricated by compo-casting, no Ω and σ phases were observed. Figures 11a, b shows the precipitates in the matrix of the Al1M/SiC_p composite. Electron diffraction indicates they are mainly θ' and s' phases. A

chemical analysis, Table 3 from Alcoa shows that there is a 0.5% Si dissolved in the matrix which is probably due to the molten Al reacting with SiC particles. This change in matrix composition (i.e., added Si) could have an effect on nucleation of the Ω and σ phase.

Table 3. Materials Actual Composition

<u>Sample</u>	<u>Cu wt%</u>	<u>Mg wt%</u>	<u>Ag wt%</u>	<u>Si wt%</u>
A11M	3.3	0.47	0.39	<0.1
A11M/SiC _p	3.1	0.5	0.31	0.52

Thus far compo-casting techniques have not been successful in producing Al/SiC_p composites with Ω and σ phases. If this results from dissolved Si, it may be possible to compo-cast composites using other types of particles that will not react (Al₂O₃, spinel particles etc.) or use other processing techniques (such as P/M) to get an Al/SiC_p composite with Ω and σ phases.

For comparison with the compo-cast composite, a 2009/SiC_p(P/M) sample was analyzed with TEM. The micrograph in Fig. 12a shows the Ω and σ phase in A11M alloy, the beam direction is $\langle 001 \rangle_{Al}$, the arrows point out the hexagonal-shaped Ω phase. In Fig. 12b, the beam direction is in same orientation as in Fig. 12a. Here an Ω phase with the hexagonal-shape was observed (indicated by an arrow) in 2009/SiC_p. Both diffraction patterns show the same pattern from the Ω phase reflections but with different intensity which represents the density of the phase. Other observations indicate that there is a trace of Ω and σ phases (Fig. 13a) in the matrix which is very encouraging for future work.

The precipitates in the matrix of 2009/SiC_p consisted primarily of s' phase. The electron diffraction pattern shows that s' phase is predominate (because of its greater intensity). A

nonuniform distribution of the precipitates is observed in the sample. The micrograph in Fig. 13a shows that this grain contains only a few precipitates whereas the grain in Fig. 13b has considerably more precipitates. The reason for this is probably due to s' preferring to form at subgrain boundaries, grain boundaries or dislocations. Because of the residual stresses due to CTE differences in the composite, many subgrain boundaries form in the matrix. Figure 14 shows a subgrain boundary formed by the dislocation network and precipitation in the subgrain boundary. In the composite, some small grains could become precipitate free grains because the s' phase formed at surrounding subgrain boundaries, grain boundaries, dislocations and the interface of SiC/Al at elevated temperature.

Interfacial Region in the Composite

Observation of the interfacial region in the composite shows many interfacial precipitates. Fig. 15 shows typical precipitation at the interface. Energy dispersive X-ray spectrum indicates the composition of the phase, which implies the precipitates mainly are θ at the interface in the Al1M/SiC. This precipitation could deplete the matrix of the Cu necessary to form Ω (or σ). Figure 16 shows strain contrast in an SiC particle edge near the interface. The residual stress is caused by the differential CTE.

SiC particles structure

The SiC particles microstructure also varies from particle to particle, Fig. 17. Some particles are nearly perfectly crystalline, while some particles have many stacking faults. Observations also show some precracks or microcracks in the SiC particles which could result from powder fabrication or during composite's manufacture.

Conclusions

- The strengths of the alloys do not drop dramatically after aging more than 600 hrs at 150°C. There is an apparent strength drop after aging at 200°C.
- Higher Cu/Mg ratio gives higher strength as shown in Al2M. Lower Cu/Mg ratio gives more thermal stability as shown in Al1M and Al1MM.
- The σ phase has a small size and uniform size distribution and its coarsening rate is almost zero after exposure to 200°C for 405 hrs.
- The Ω phase has a higher coarsening rate than the coherent-coplanar σ phase.
- The θ' phase has a larger size and a higher coarsening rate than Ω and σ phase
- Hot rolling may reduce Ω phase and σ phase formation in the foil, due to the high dislocation density which favors formation of s' and θ' .
- Small amounts of silicon (0.5%) in the Al matrix introduced by the reaction of molten Al with SiC particles during the compo-casting may alter the precipitation kinetics of the Ω and σ phases.

References.

1. R. Schueller, A. Sackdev, and F. Wawner, "Identification of a Cubic Precipitate observed in an Al-4.3Cu-2Mg/SiC Castcomposite," Scripta Met. et Mat. **27** (1992), 617.
2. K. Knowles and W. Stobbs, "The Structure of {111} Age-Hardening Precipitates in Al-Cu-Mg-Ag Alloys," Acta Cryst. **B44** (1988), 207.
3. J.D. Boyd and R.B. Nicholson, "The Coarsening Behavior of θ'' and θ' Precipitates in Two Al-Cu Alloys," Acta Met. **19** (1971), 1379.
4. A. Garg and J. Howe, "Nucleation and Growth of Ω Phase in Al-

- 4.0Cu-0.5Mg-0.5Ag Alloy - An in situ Hot-stage TEM Study," Acta Met. 39 (1991), 1925.
5. A. Garg and J. Howe, "Convergent-Beam Electron Diffraction Analysis of Ω Phase in Al-4.0Cu-0.5Mg-0.5Ag Alloy," Acta Met. 39 (1991), 1939.
 6. R. Schueller, "Identification and Analysis of a Unique 'Cubic Phase' in an Al-Cu-Mg/SiC Composite," Ph.D Dissertation, University of Virginia (1992).
 7. G.C. Weatherly, "Antiphase Domain Boundaries in Ordered θ' (CuAl₂) Precipitates in an Al-4% Cu Alloy," Acta Met. 18 (1970), 15.



Figure 1. The precipitates in Al1M aged 200°C, 19 hrs, $B=\langle 111 \rangle$, the micrograph shows the hexagonal-shaped Ω phase and other variances on $\{111\}$ planes and σ phase and θ' phase.



Figure 2. The micrograph shows the strain lobes near interface in the matrix which is due to the misfit between σ phase and Al, the period is about 6.7 nm.

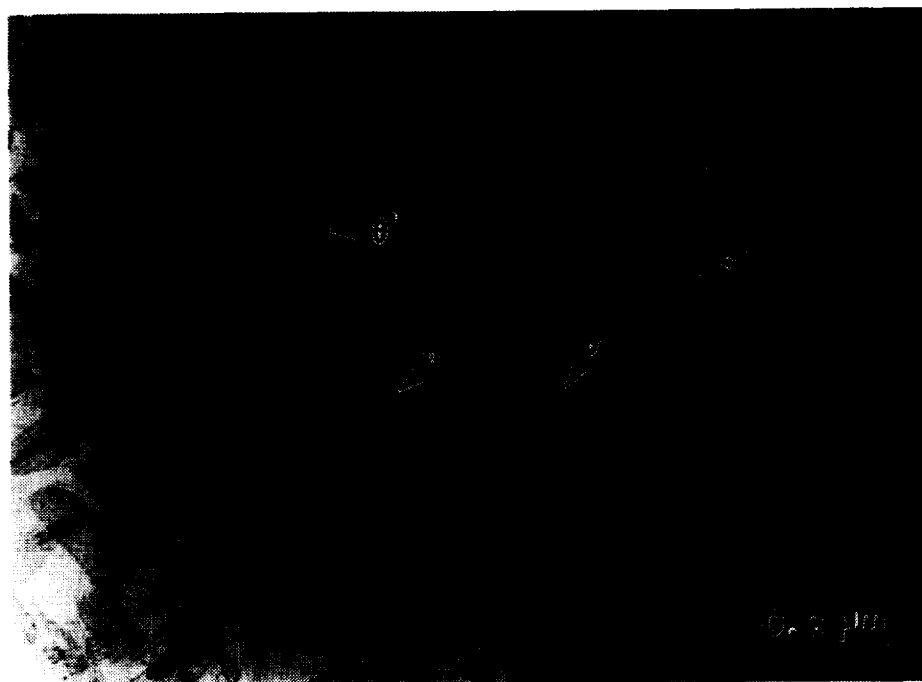


Figure 3. TEM micrograph shows all four precipitate phases in the Al1M alloy aged 3 hrs at 200°C.

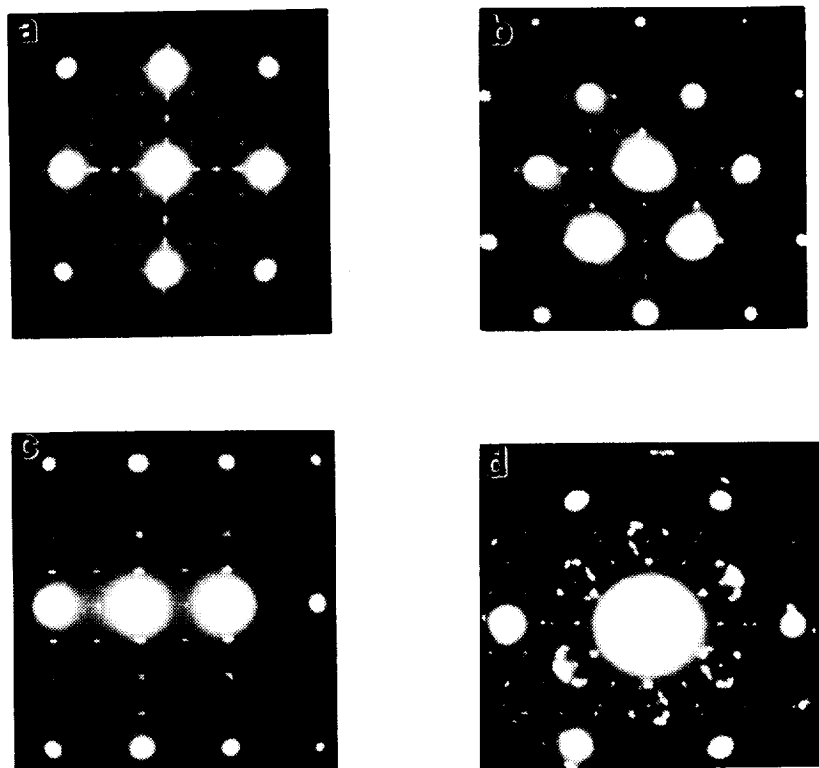


Figure 4a. Electron diffraction patterns of σ phase. (a) σ phase along $B=\langle 011 \rangle_{Al}$, (b) σ phase along $B=\langle 111 \rangle_{Al}$, (c) σ phase along $B=\langle 112 \rangle_{Al}$, (d) σ phase along $B=\langle 111 \rangle_{Al}$.

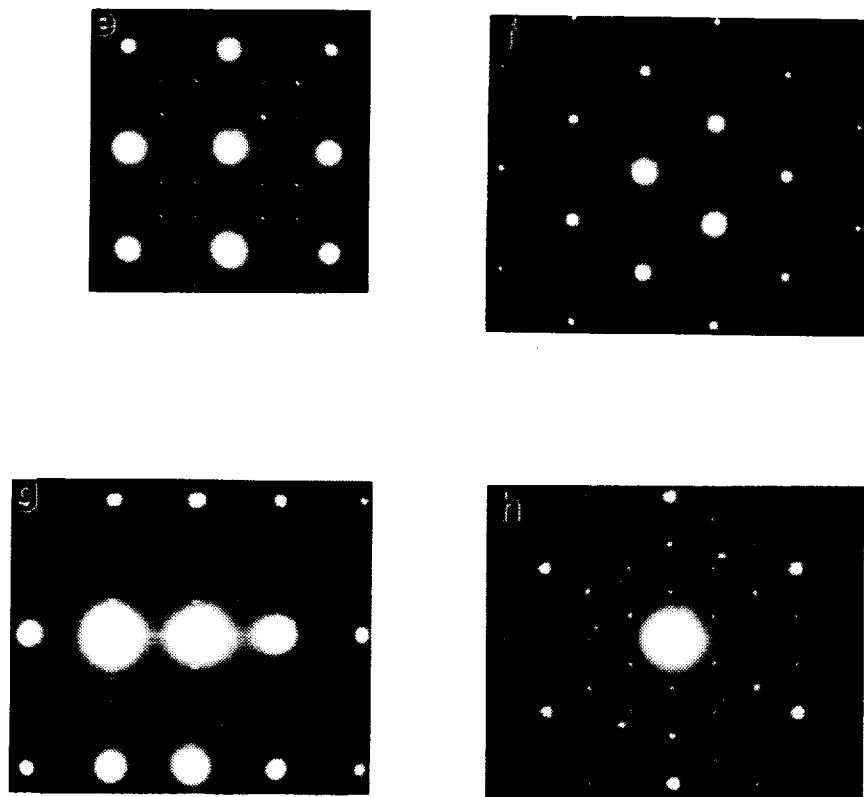
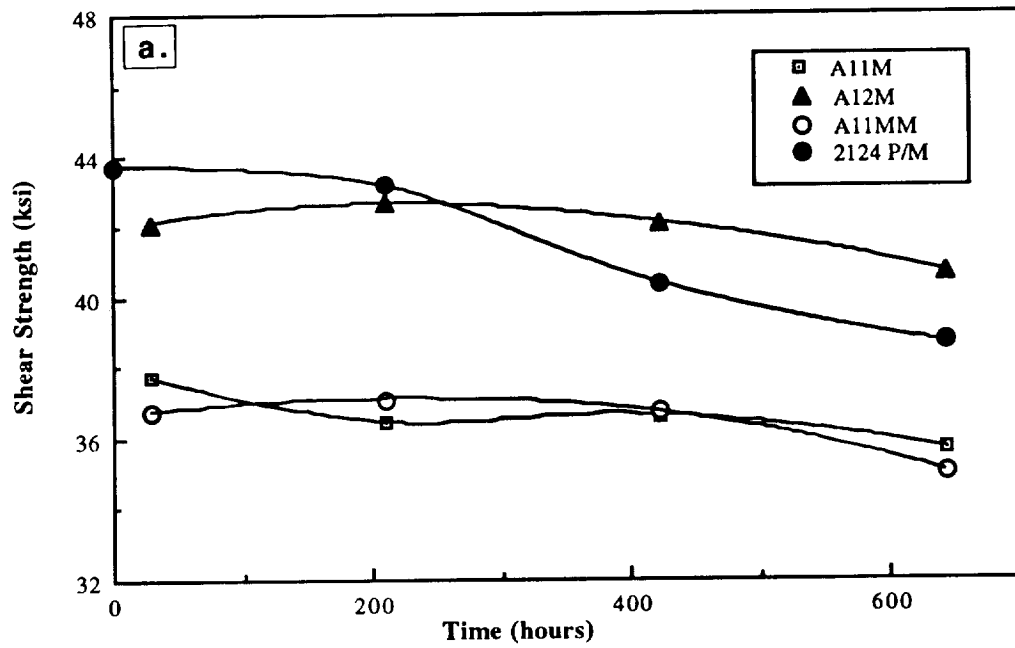
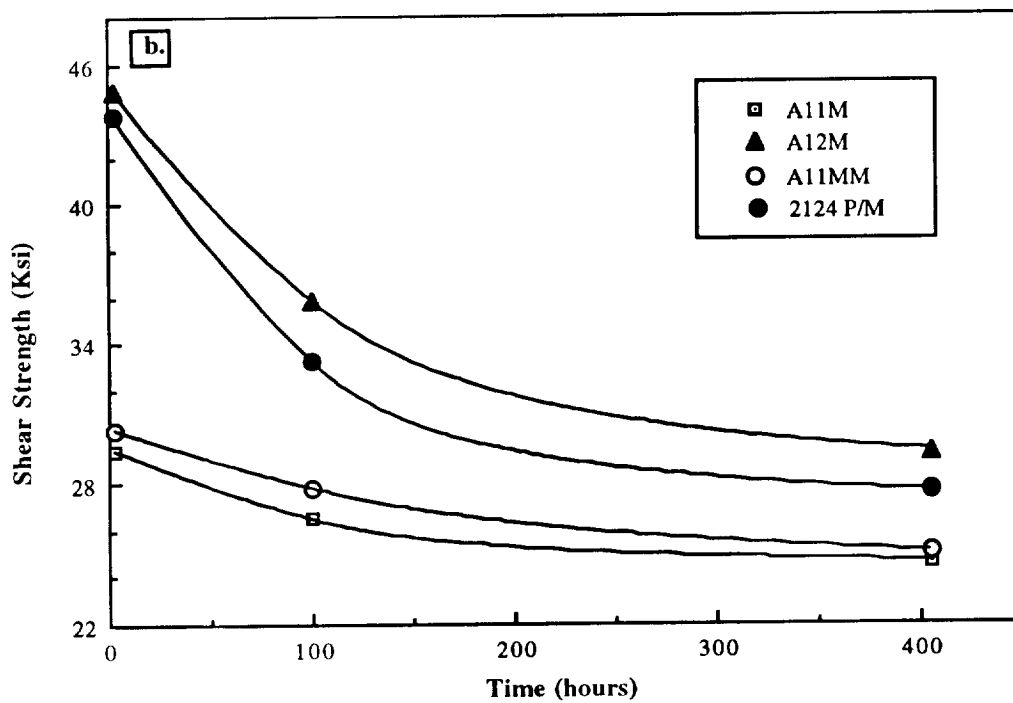


Figure 4b. Electron diffraction patterns of Ω phase. (e) Ω phase along $B=\langle 001 \rangle_{Al}$, (f) Ω phase along $B=\langle 111 \rangle_{Al}$, (g) Ω phase along $B=\langle 112 \rangle_{Al}$, (h) Ω phase along $B=\langle 111 \rangle_{Al}$.



Shear strength after thermal exposure at 150C



Shear strength after thermal exposure at 200C

Figure 5. Shear strengths of the alloys as function of thermal exposure.

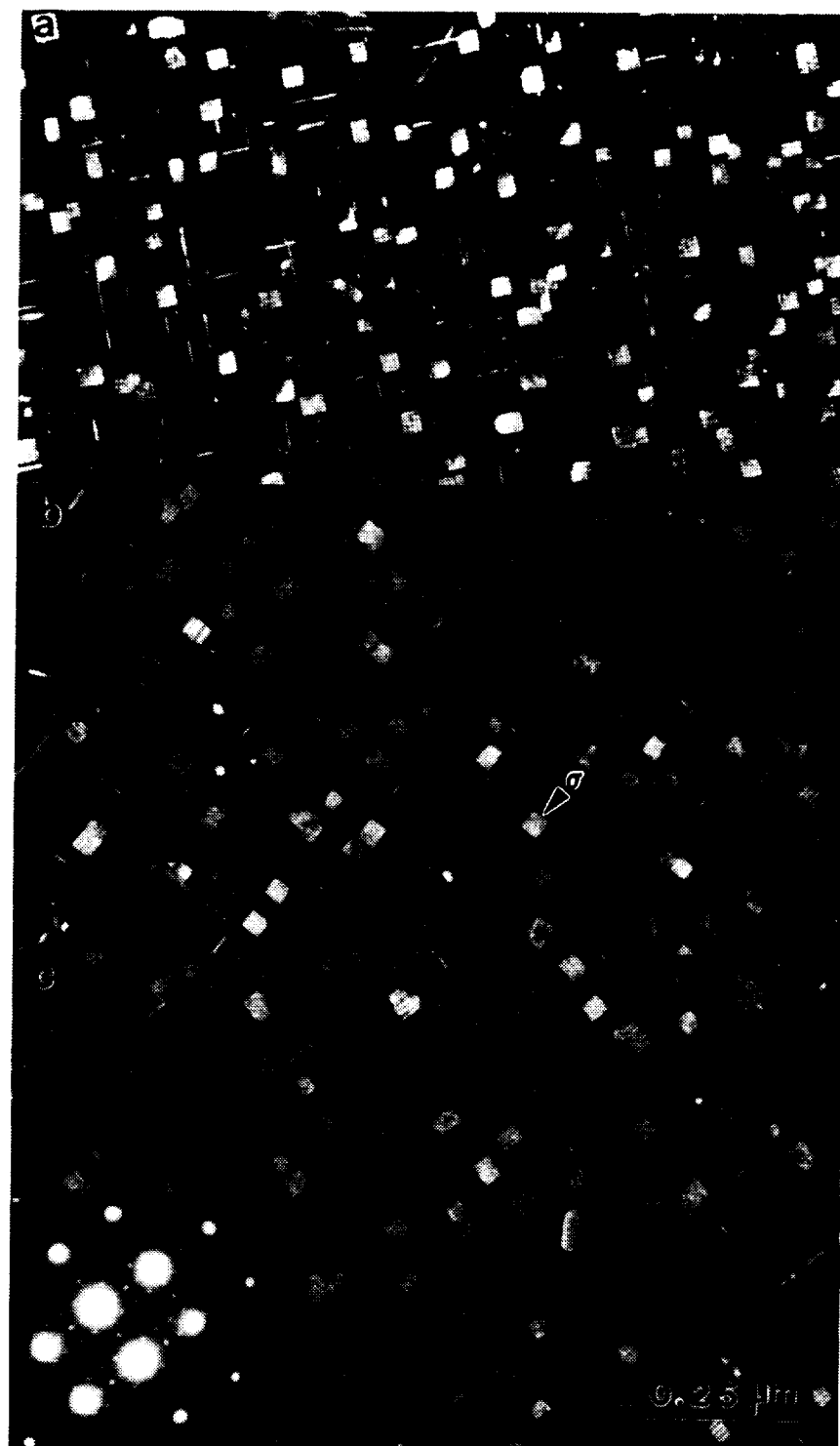


Figure 6. σ phase size change as function of time, the sample is aged 200°C. a). 26.2 hours, b). 100 hours, c). 405 hours.

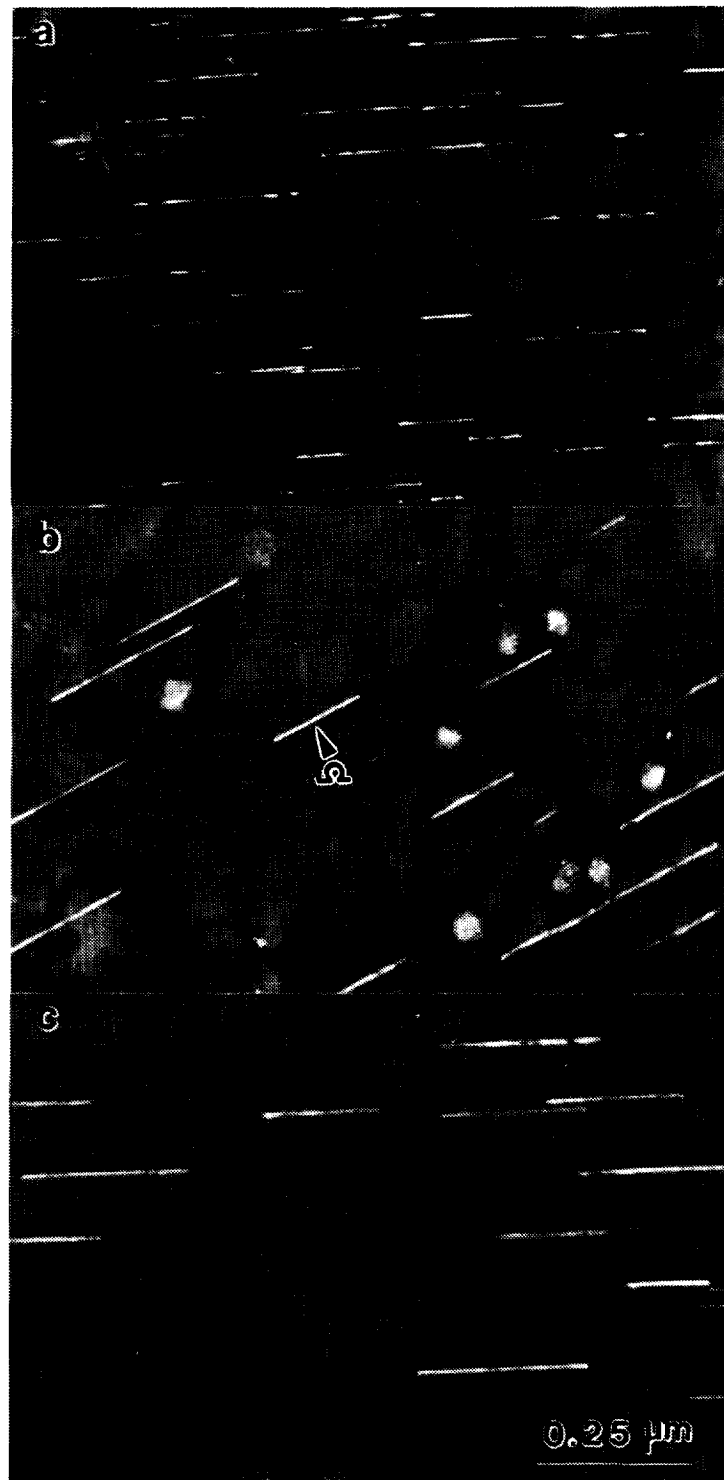


Figure 7. Ω phase size change as function of time, the sample is aged at 200°C. a). 26.2 hours, b). 100 hours, c). 405 hours.

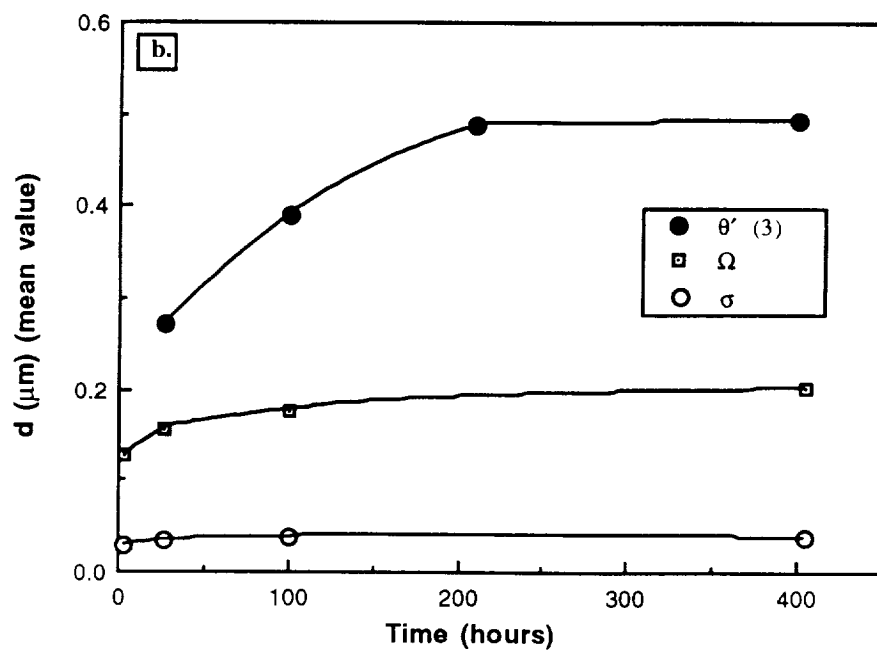
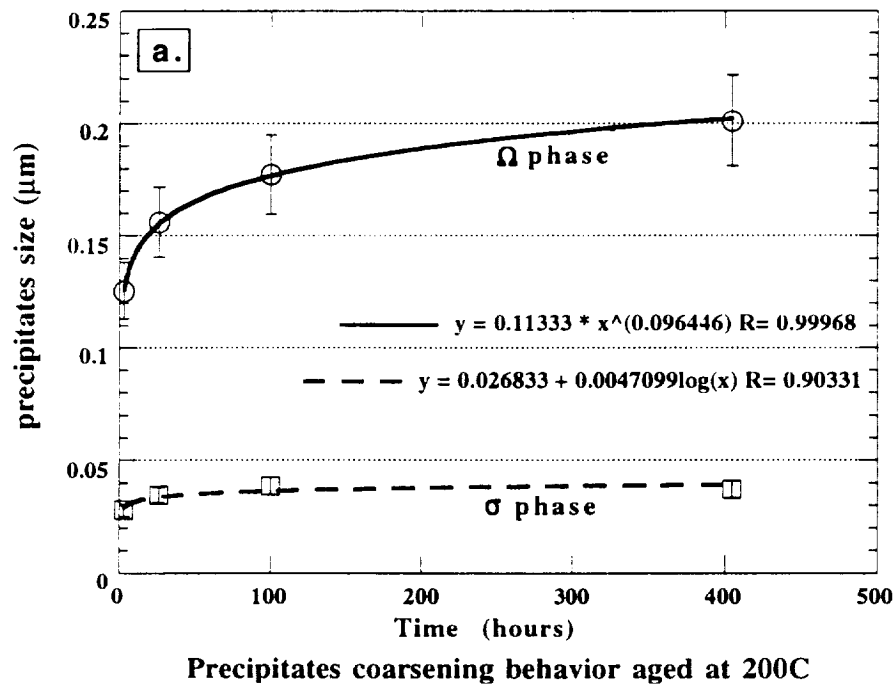


Figure 8. Precipitates coarsening behavior at 200 C.

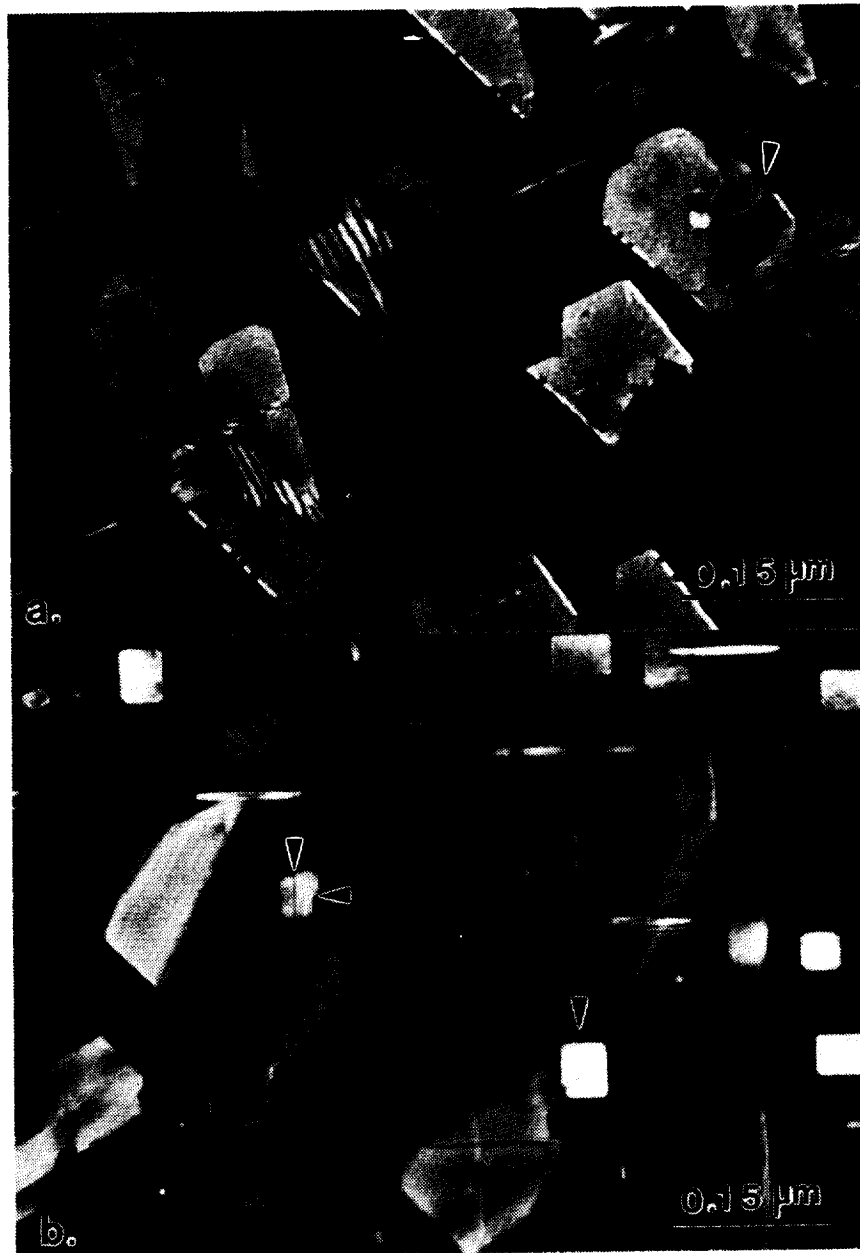


Figure 9. Growth ledges on the different phases a). several layers of facet ledges in Ω phase can be seen, b). short and straight single ledges in σ phase.



Figure 9. c) Growth ledges on α' phase, layered rounded ledges in β' phase, d) antiphase domain boundary in α' .

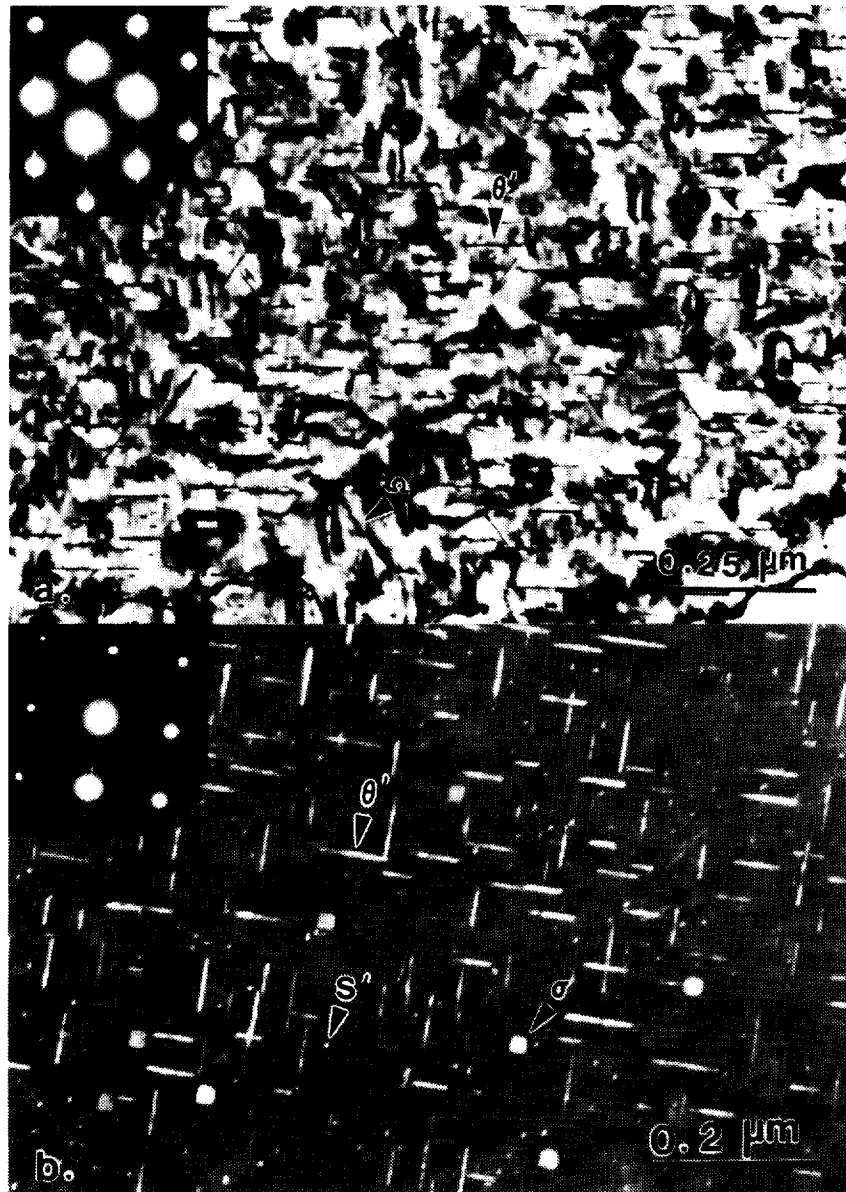


Figure 10. The TEM micrographs show that less Ω phase and σ phase formed after hot rolling (i.e. deformation) A11M from 3 mm to 0.13 mm. a) along [011] direction showing Ω phase and b) along [001] direction showing σ phase.



Figure 11. Precipitates in Al1M/SiC_p, a) sample aged at 250C 2 hours, b) sample aged at 200C, 3 hours, diffraction pattern shows the reflections of s' and θ' phase.

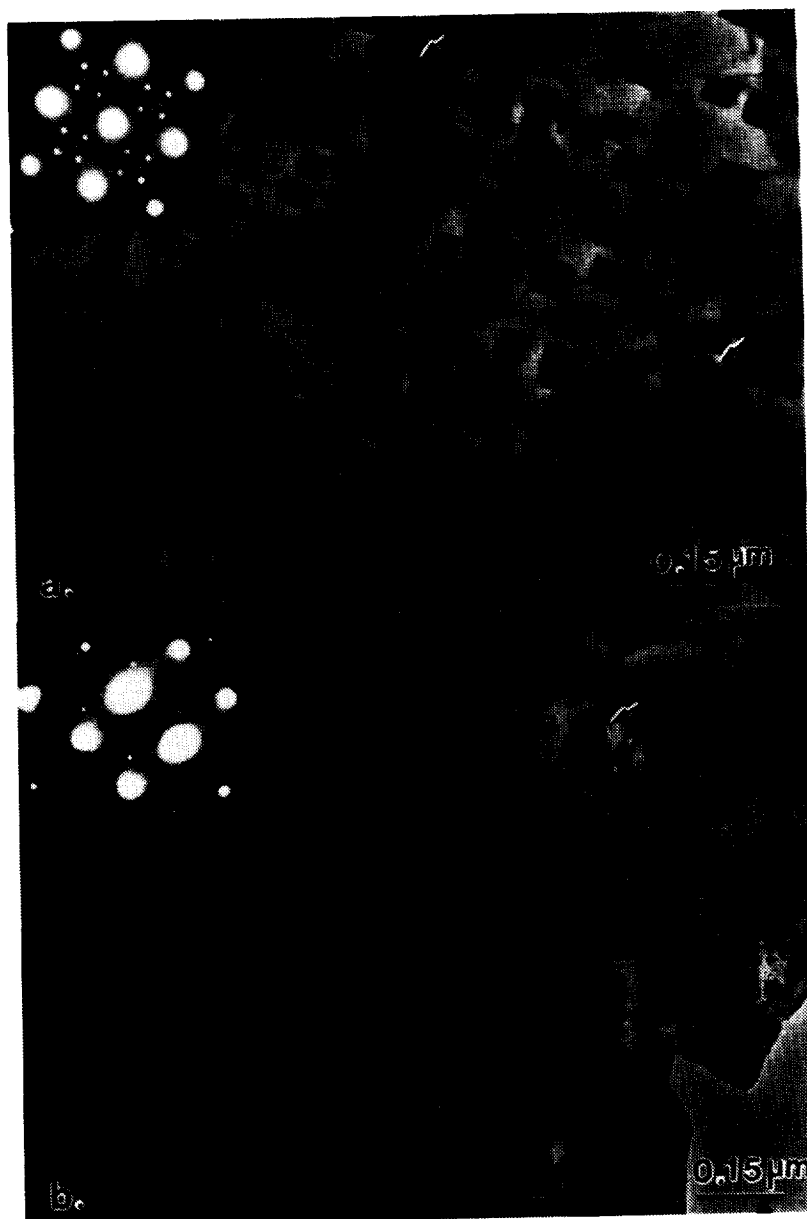


Figure 12 a) Ω and σ phase in Al1M, $B=\langle 001 \rangle$, arrows points out the hexagonal-shaped Ω phase. b) a Ω precipitate with the hexagonal-shape is shown by an arrow in 2009/SiCp, $B=\langle 001 \rangle$. Both diffraction patterns show the same Ω phase reflections but with different intensity.



Figure 13. A non-uniform precipitate distribution in the 2009/SiCp. a) shows a grain with very few precipitates; b) shows s' precipitates in another grain (diffraction pattern in upper left taken from the grain) and large s' precipitation in a grain boundary (diffraction pattern in upper right from grain boundary). Both grains oriented in $\langle 001 \rangle$ direction.



Figure 14. Subgrain boundary in 2009/SiC_p, the micrograph shows the dislocation network and the formation of s' in subgrain boundary.

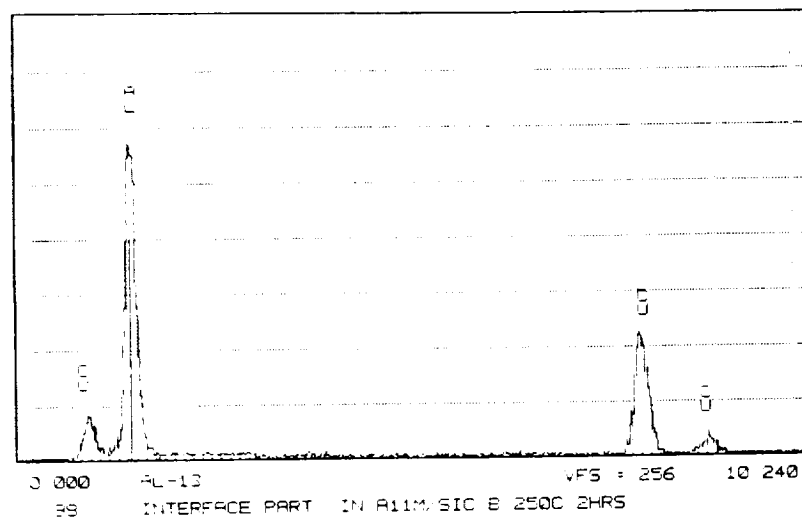
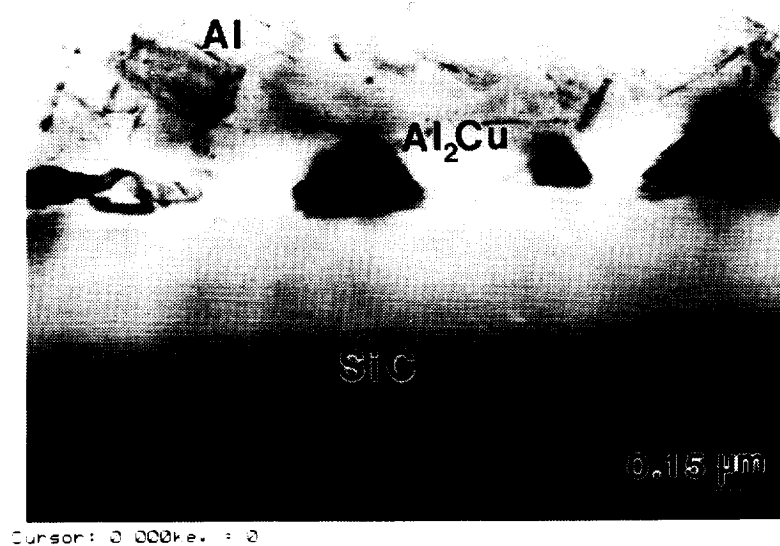


Figure 15. Interface precipitation in compo-cast Al1M/SiC_p composite, the EDS indicates the composition of the precipitates.

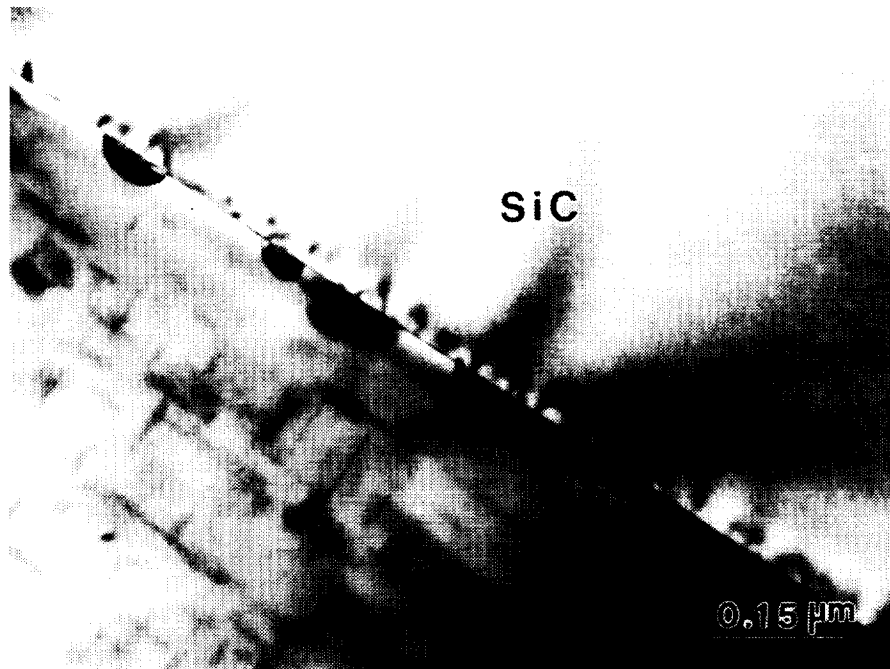


Figure 16. A strain field can be seen in a SiC particle edge; precipitation is obvious on the particle surface.



Figure 17. SiC particles demonstrate nonuniformity. (a) shows a SiC particle with a near perfect crystalline structure, very light stacking fault streaks appear in the diffraction pattern; (b) a SiC particle showing many stacking faults and microcracks.

TASK 9. ACCELERATED EXPOSURE STUDY (ALCOA)

Principal Investigator:	Dr. L.M. Angers
Senior Engineer:	Dr. G. Dixon

Objective

There are two objectives to this task. The first objective requires development of fixtures for simultaneously exposing samples to constant stress and elevated temperature. The second objective involves using the fixtures to obtain data needed to develop accelerated test methods for HSCT applications. Once the fixtures are developed and shown to function properly, representative samples from three classes of HSCT candidate materials will be exposed and tested for residual tensile properties.

Background

A spring fixture was developed for creep aging materials for the HSCT program and initial tests to verify the suitability were performed (1). A spring, loaded in compression, imparts a tensile load to the specimen located in the center of the spring. This fixture has been designed to load 1/8" diameter tensile specimens. After aging the specimen under load, the specimen can be removed from the fixture and tested to determine the residual tensile strength of the material.

The current fixture can be used at temperatures up to 400°F and will load specimens to stresses of up to 20 ksi. Stiffer springs can be obtained which will permit loading specimens to 60 ksi. The fixture is quite compact, e.g., 2" in diameter and approximately 7" long, permitting a large number of specimens to be aged in a single oven.

Three materials were identified for accelerated exposures in the constant-stress aging fixtures: 2080/SiC/20_p-T6, 2519-T87 and 6013-T6. These materials were chosen since they represent three

different candidates for a Mach 2.0 aircraft: a discontinuously reinforced metal matrix composite for use on the upper wing and two different precipitation strengthened monolithic alloys for use in the fuselage and lower wing. Exposure temperatures of 300°F and 215°F were to be used. The temperature of 300°F was considered a reasonable temperature for accelerated tests intended to simulate Mach 2.0 service. To simulate 120,000 hr at 215°F, exposures of 600 to 1000 hr at 300°F were to be considered. Tensile specimens were to be taken out at various time intervals and tested at room temperature for residual strength and elongation. Both stressed (18 ksi) and unstressed samples were placed in aging ovens. The original test matrix is included as Table I.

Results and Discussion

Table II summarizes residual tensile data at room temperature for specimens exposed at both 215°F and 300°F. Values are averages from two tests. After exposure at 215°F, no significant differences were observed between the stressed and unstressed samples for all alloys tested. The data generated after exposure at 300°F for each material have been plotted and are shown in Figs. 1 through 3. Original room temperature tensile yield strengths and ultimate tensile strengths are included on each plot for comparison. No effect of stress is observed for the 2519-T87 and 2080/SiC/20_p. Degradation in tensile yield strength after 2000 hr at 300°F is roughly 12% for 2519-T87, 22% for 2080/SiC/20_p-T6 and 6% for 6013-T6. While the 6013-T6 appears more stable than the 2519-T87 and the 2080/SiC/20_p-T6, it should be pointed out that the original strength of the 6013-T6 was much lower than the strengths of the others. Stressed samples may exhibit greater stability and higher strengths than unstressed samples for 6013-T6, although the effect is small. No clear effect of stress on residual tensile elongation was noted for any of these materials.

Data generated thus far goes up to exposures of 2000 hr.

Samples undergoing 3000 hr of exposure have been taken out of the ovens but will not be tested because the program has been discontinued. Samples to be exposed for times greater than 3000 hr will remain in the ovens and will be taken out at the designated times and also will not be tested.

Summary

- The tensile yield strength for 2519-T87 decreases by 12%, by 22% for 2080/SiC/20_p and by 6% for 6013-T6 after 2000 hr at 300°F.
- No significant effect of stress is observed for 2519-T87 and 2080/SiC/20_p exposures. A small stress effect may exist for 6013-T6 after 1,000 hr and 2,000 hr at 300°F.

Reference

1. E.A. Starke, Jr., "NASA UVa Light Aerospace Alloy and Structure Technology Program Supplement: Aluminum-Based Materials for High Speed Aircraft," NASA Contractor Report 4517, June 1993.

TABLE I. Accelerated exposure. Test matrix of accelerated exposures for:
2519-T87, 2080/SiC/20p and 6013-T6

300°F Stressed: 18 ksi		300°F Unstressed	
No. of Specimens	Time (hr)	No. of Specimens	Time (hr)
2	1000	2	1000
2	2000	2	2000
2	3000	2	3000
2	5000	2	5000

215°F Stressed: 18 ksi		215°F Unstressed	
No. of Specimens	Time (hr)	No. of Specimens	Time (hr)
2	1000	2	1000
2	3000	2	3000
2	5000	2	5000
2	7000	2	7000
2	9000	2	9000

TABLE II. Residual tensile properties of 2519-T87, 2080/SiC/20p-T6 and 6013-T6 at room temperature.

Alloy	Exposure Temp., (°F)	Time (hr)	Stress (ksi)	Tensile Yield Strength, ksi	Ultimate Tensile Strength, ksi	Elongation, %
2519-T87	-	-	-	61.0	67.0	12
	215	1000	0	62.4	68.1	13
	215	1000	18	62.4	68.2	12
	-	-	-	61.0	67.0	12
	300	250	0	59.8	67.1	10
	300	250	18	61.0	68.4	12
	300	500	0	58.2	66.0	10
	300	500	18	59.3	67.4	10
	300	1000	0	56.9	65.4	12
	300	1000	18	55.4	63.8	12
	300	2000	0	54.3	63.6	8
	300	2000	18	53.8	63.1	10
	-	-	-	66.0	78.0	4
	215	1000	0	63.2	77.0	6
2080/SiC/20p-T6	215	1000	18	64.0	78.3	5
	-	-	-	66.0	78.0	4
	300	1000	0	54.2	65.4	6
	300	1000	18	52.8	68.2	6
	300	2000	0	51.3	65.8	4
	300	2000	18	51.1	65.4	6

TABLE II. (cont'd). Residual tensile properties of 2519-T87, 2080/SiC/20p-T6 and 6113-T6 at room temperature.

Alloy	Exposure Temp., (°F)	Time (hr)	Stress (ksi)	Tensile Yield Strength, ksi	Ultimate Tensile Strength, ksi	Elongation, %
6013-T6	-	-	-	53.0	58.0	15
	215	1000	0	51.6	55.2	16
	215	1000	18	51.2	55.2	14
	-	-	-	53.0	58.0	15
	300	1000	0	50.6	53.4	15
	300	1000	18	51.5	55.6	14
	300	2000	0	50.0	52.8	11
	300	2000	18	51.4	55.6	12
	-	-	-	53.0	58.0	15
	215	1000	0	51.6	55.2	16
	215	1000	18	51.2	55.2	14
	300	1000	0	50.6	53.4	15

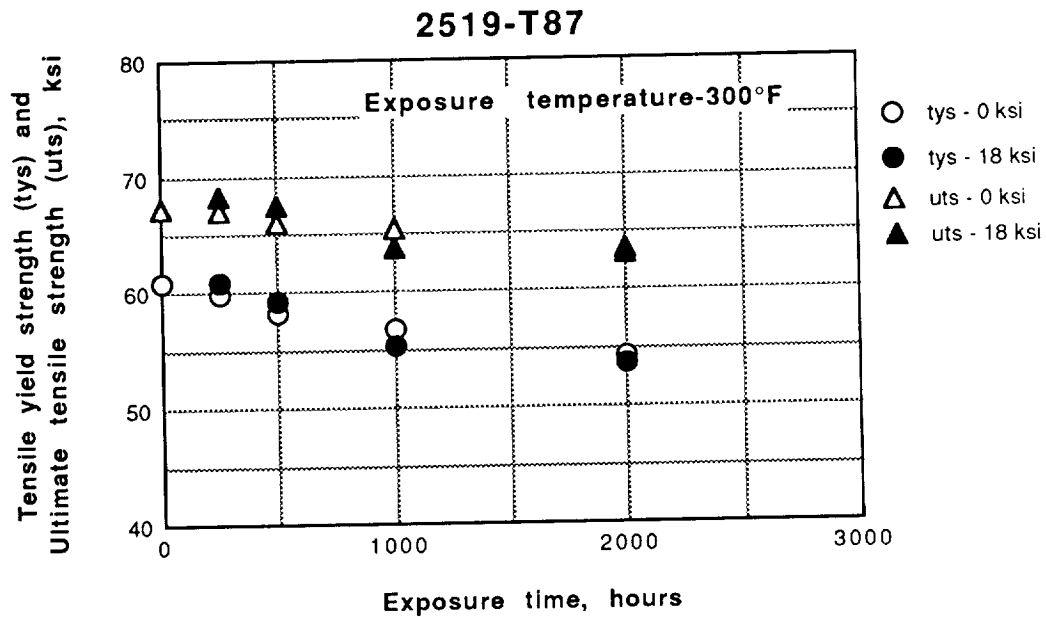


Figure 1. Tensile yield strength and ultimate tensile strength as a function of exposure time at 300°F for stressed and unstressed samples of 2519-T87.

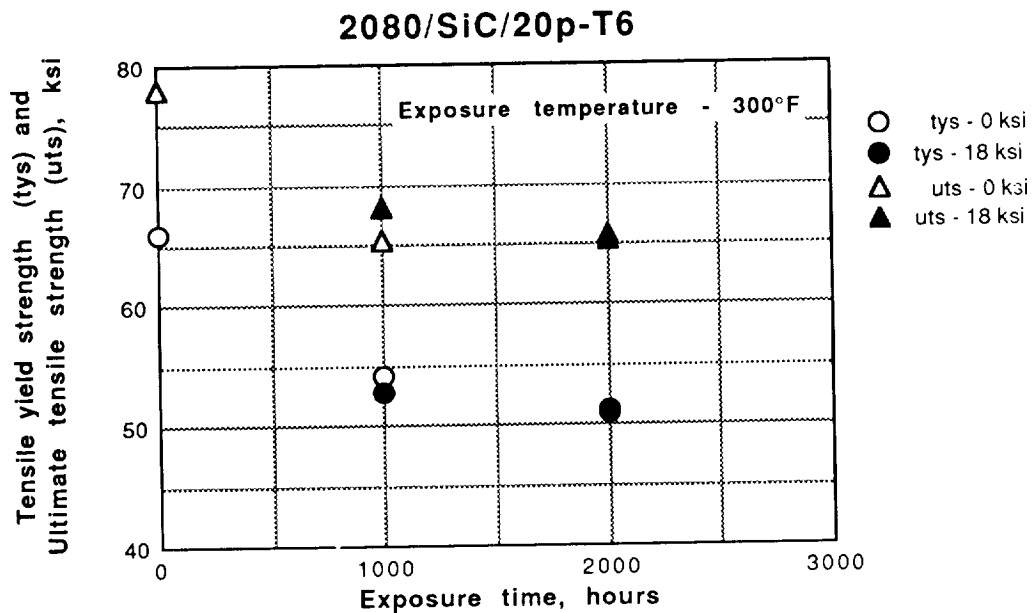


Figure 2. Tensile yield strength and ultimate tensile strength as a function of exposure time at 300°F for stressed and unstressed samples of 2080/SiC/20p-T6.

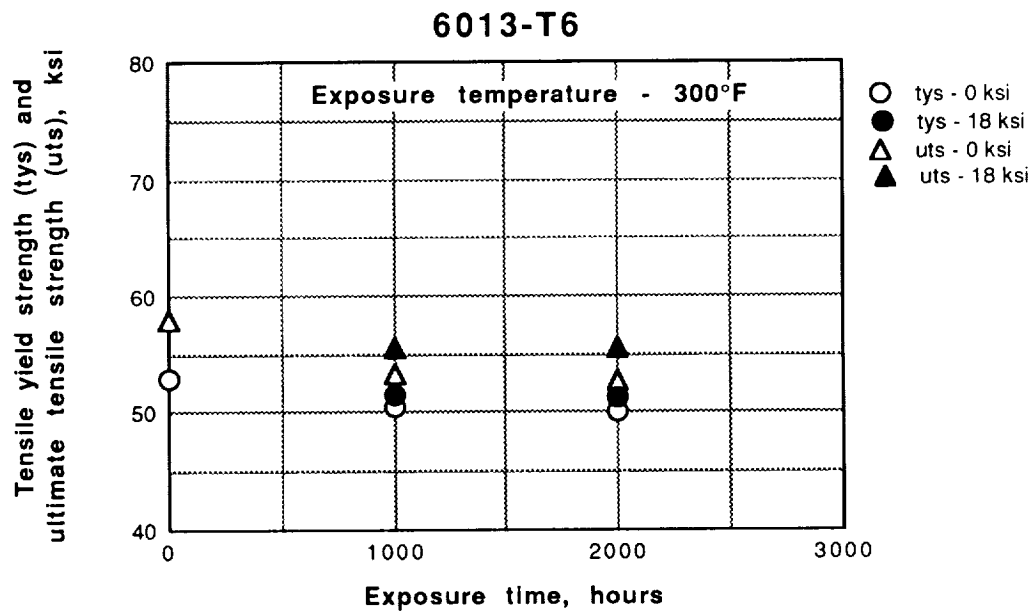


Figure 3. Tensile yield strength and ultimate tensile strength as a function of exposure time at 300°F for stressed and unstressed samples of 6013-T6.

**TASK 10A. MATERIALS TECHNOLOGY TRADE-OFF STUDIES FOR
THE AIRFRAME (Boeing)**

Principal Investigator: Dr. W.E. Quist

See Boeing Report on Materials Characterization

Item C. Task 10A: Trade Studies in Support of an
"Aluminum" HSCT

This task was subdivided into four Phases as shown in Fig. 1. As no materials properties were generated during the subject program that could be reduced to very preliminary property allowables for use in the design studies, it was not possible to initiate Phases I, III, and IV of the trade studies. However, substantial progress has been made in Phase II, particularly with respect to the development of structural/manufacturing concepts that would be particularly applicable to an "Aluminum" HSCT.

The aluminum structural/manufacturing design concepts for the wingbox, wing strake, and fuselage were developed with reference to projected materials properties from ongoing internal Boeing studies (Low-Cost Airplane Trade Study - LCATS). Aluminum material structural design concepts are summarized in the matrices shown in Figs. 2, 3 and 4. They are grouped into four major design families: (A) integrally stiffened, (B) sandwich, (C) hybrid concepts, and (D) conventional skin/stringer construction. The details are described below:

- A. Integrally Stiffened** Three arrangements are included: extruded stringers, orthogrid, and isogrid according to airplane location and type and magnitude of loading.
- B. Sandwich** Arrangements include two variations on sandwich edge treatments according to location and loading.
- C. Hybrids** (conventionally stiffened thin-sandwich skins)

Included to study effects of hybrids on structural performance and cost. In addition, hybrids could provide redundant load paths, fail safety, and better damage tolerance, among other benefits.

- D. Conventional skin/stringer** Included to provide a baseline from which to measure concept improvements in terms of both performance and cost. (these concepts are not shown in Figs. 2, 3, and 4).

To make the best use of materials, a tailored structural approach was used. Materials possessing desired properties, along with novel structural arrangements that matched design and manufacturing process requirements at different locations, were selected. In developing each of the concepts, care was taken to address low-cost producible structure, as well as low weight and high performance.

Structural sizing of each of the design concepts is in progress. We will continue this during the next phase of the study to quantitatively evaluate weight at the concept level. Sizing will focus on refining the most promising concepts and processes to provide design data for weight and later cost estimation. To understand the sensitivity to material and structural concept changes, performance first will be evaluated and compared at the concept level. For 1993, the plan and schedule for these activities have been revised as shown in Figs. 5 and 6. This allows us to directly use and complement parallel NASA-funded programs where concept-level data will be assembled into a full airplane structural configuration.

From this information, the most promising structural materials and desired property levels, along with structural design concepts and required product forms and manufacturing processes can be identified.

Objectives:

- (1) To evaluate aluminum-based materials and processes in terms HSCT airplane performance.

Approach:

Phase I - Material Property Projections

- (1) Review/update LCATS property projections
- (2) Develop property projections for non-LCATS alloys
- (3) Develop prel. "allowables" for non-LCATS alloys

Phase II - Concept Weight Evaluation

- (1) Select concepts
- (2) Conduct structural analysis on selected concepts
- (3) Develop weights data

Phase III - Airplane Performance Evaluation

- (1) Develop three (3) airplane concepts/materials
- (2) Develop point-design weights
- (3) "Fly" airplanes for equivalent mission sizing

Phase IV - Technology Recommendations

- (1) Prepare list critical technical needs
- (2) Prepare technology recommendations

Deliverables:

Phase I - Material Property Projections

- (1) Material property projections.

Phase II - Concept Weight Evaluation

- (1) Concept relative weights.

Phase III - Airplane Performance Evaluation

- (1) Airplane concepts/materials
- (2) Mission-sized relative MTOWs

Phase IV - Technology Recommendations

- (1) List of technical needs
- (2) Technology recommendations

Figure 1. 1992 Material Technology Trade Studies for the Airframe

LCATS/UVA ALUMINUM CONCEPTS SUMMARY

Aluminum Concept Package Summary

WING CONCEPTS

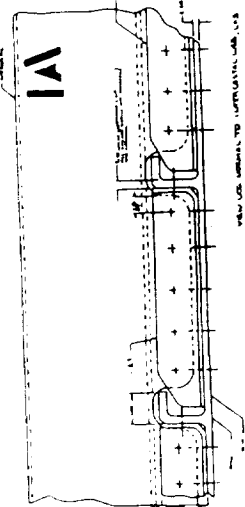
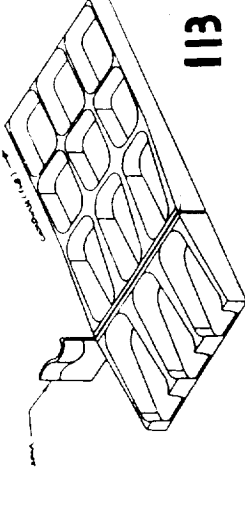
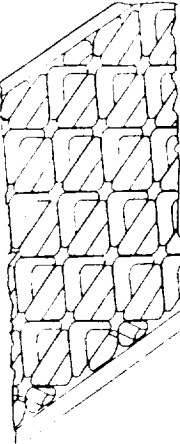
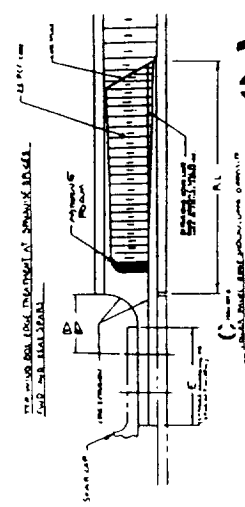
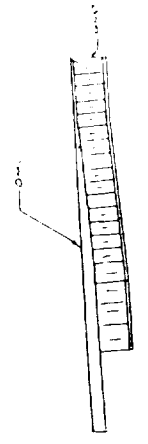
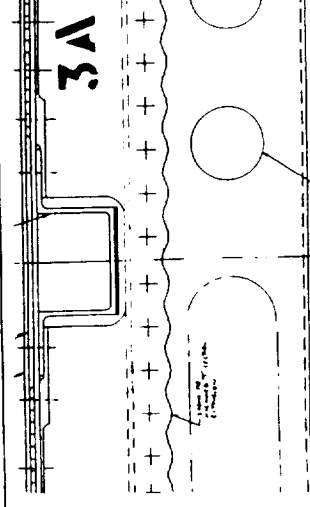
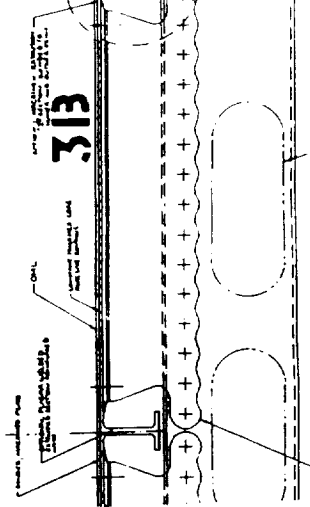
CONCEPT TYPE	WING BOX UPPER PANELS	WING BOX LOWER PANELS	STRAKE WING LWR/UPPR
INTEGRALLY STIFFENED	1A	1B	1C
SANDWICH PANELS	2A	2A	2B
THIN SANDWICH STIFFENED	3A	3B	3A & 3B
SKIN/STRINGER CONVENTIONAL	N/A	N/A	N/A

FUSELAGE CONCEPTS

CONCEPT TYPE	WING BOX UPPER PANELS	WING BOX LOWER PANELS	STRAKE WING LWR/UPPR
INTEGRALLY STIFFENED	7A	7B	7A OR 7B
SANDWICH PANELS	8A	8B	8C
THIN SANDWICH STIFFENED	9A	9A	9B
SKIN/STRINGER CONVENTIONAL	N/A	N/A	N/A

N/A: Pictorial representation of this concept family is not available at this moment. However extensive amount of information is available for this conventional type of structural arrangement.

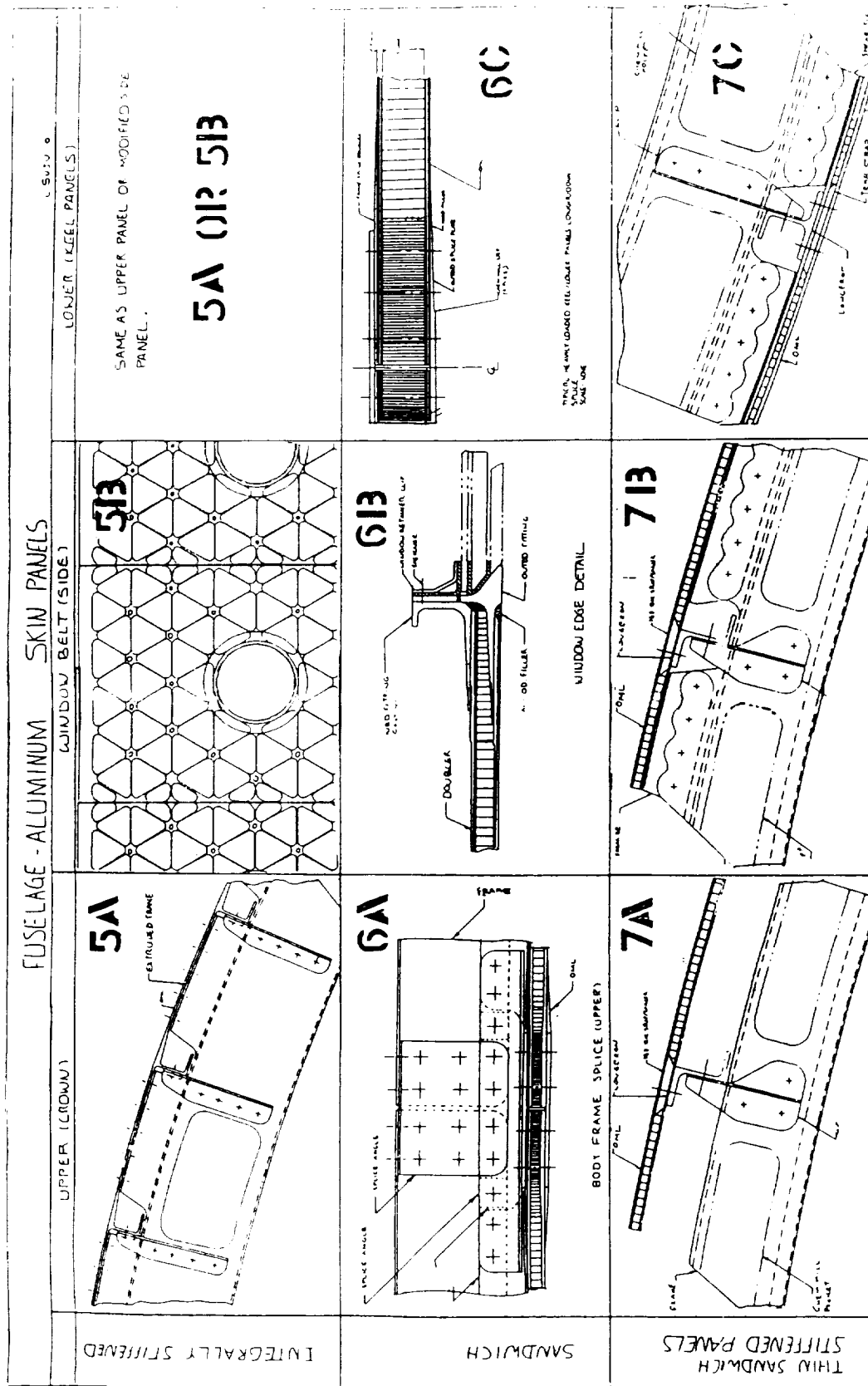
Figure 2. LCTAS/UVA Aluminum Concepts Summary

WING - ALUMINUM SKIN PANELS			
WING BOX - UPPER		WING BOX - LOWER	
TYPE	WING BOX - UPPER	WING BOX - LOWER	STRAKE WING/UPPER
INTEGRALLY STIFFENED			
SANDWICH		<p>SAME AS WING-BOX - UPPER EXCEPT AS NOTED</p>	
THIN SANDWICH STIFFENED PANELS			<p>SAME AS UPPER AND LOWER WING BOX</p>

NOTE

Distribution Limited to Participants in the NASA/UVA
"Aluminum-Based Materials For High-Speed Aircraft" Program

Figure 3. HSCT Wing - Aluminum Skin Panel Concepts



NOTE
 Distribution Limited to Participants in the NASA/UVA
 "Aluminum-Based Materials For High-Speed Aircraft" Program

Figure 4. HSCT Fuselage - Aluminum Skin Panel Concepts

Objectives:

- (1) To evaluate aluminum-based materials and processes in terms HSCT airplane performance.

Approach:

Phase I - Material Property Projections

- (1) Review/update LCATS property projections
- (2) Review supplier updates

Phase II - Concept Weight Evaluation

- (1) Develop/update/select design concepts
- (2) Conduct structural analysis on selected concepts
- (3) Develop concept-level weights data

Phase III - Technology Recommendations

- (1) Prepare list critical technical needs
- (2) Prepare technology recommendations

Deliverables:

Phase I - Material Property Projections

- (1) Material property projections

Phase II - Concept Weight Evaluation

- (1) Concept-level relative weights

Phase III - Technology Recommendations

- (1) List of technical needs
- (2) Technology recommendations

Figure 5. 1993 Material Technology Trade Studies for the Airframe

Phase	Title	1 9 9 3											
		JAN	FEB	MAR	APR	MAY	JUN	JUL	AUG	SEP	OCT	NOV	DEC
I	<i>Material Property Projections</i>	Preliminary "Allowables" ▽ []			Supplier Updates ▽ []			Supplier Updates ▽ []					
II	<i>Concept Weight Evaluation</i>	Concept Selection ▽ []			Concept Refinement ▽ []			Concept Weights ▽ []					
III	<i>Technology Development Recommendations</i>							Structural Analysis △ []			Technology Recommendations ▽ []		
											Critical Tech Needs △ []		

Figure 6. Material Technology Trade Studies for the Airframe

**TASK 10B. MATERIALS TECHNOLOGY TRADE-OFF STUDIES FOR
 THE AIRFRAME (Douglas)**

See McDonnell Douglas Report on Materials Characterization

BOEING REPORT ON MATERIALS CHARACTERIZATION

Principal Investigator: Dr. W.E. Quist

Progress for Report Period

There was little activity by Boeing in support of the subject contract in the first half of the contract period (January through June). The primary reason for this situation was that no alloys were received for evaluation by Boeing, either from the materials suppliers or the University of Virginia, during the January through June time period. The evaluation of new or improved alloys developed during the contract period was anticipated to be a major Boeing contribution to this effort. Tests were to be performed on alloys from subtasks 1A, 1B, 2C, 3A, 5A, and 7A. The goal of the Boeing tests was to provide a consistent reference for several important engineering properties, including strength, fracture toughness, fatigue, and thermal stability. The test matrix was basic, but referee tests of this type have been found to uncover many inconsistencies, discrepancies and property shortfalls. The 1992 Boeing test plan for each down selected material is shown in Table 1. One goal of this test program was to help generate very preliminary property allowables to aid in the design studies.

It was also anticipated that substantive interaction between Boeing, NASA, UVA and the materials suppliers would take place concerning the specifics of the alloy systems to be developed and evaluated. This would include details of alloy design, heat treatments and relevant processing issues. This did not happen to the degree anticipated during the first half of the contract period.

In the second half of the contract year, Boeing activity increased and there was substantial progress in three areas. They were as follows;

- A. Discussions with NASA, UVA, and suppliers on the properties, metallurgy, and processes for the new or improved materials, both through meetings and by teleconference.
- B. The development of fracture toughness criteria and test methods for the evaluation of new or improved alloys.
- C. Trade studies for the evaluation of new or improved aluminum alloys in support of an "Aluminum" HSCT. See Task 10A.

Again, however, no new or improved alloys were received for evaluation by Boeing during the second half of the contract year.

Discussions with NASA, UVA, and Suppliers of New or Improved Materials

Based on engineering property data generated to date by the suppliers and UVA, two materials systems are emerging as front runners for HSCT use, two or three others require further evaluation, and one appears not suitable, considering its present state of development. At present, the Weldalite type alloys (RX 818 and modifications), and alloys based on the 2519 system appear the most promising based on their strength-toughness blend and thermal stability. The limited data developed to date for alloys based on the 6013 system, P/M 2XXX alloys, and metal matrix composites (MMCs) with 2XXX matrices dictated that additional development and evaluation is required before any decision on the viability of these materials for HSCT use can be made. The high temperature aluminum alloys, based on the Al-Fe-X composition, demonstrate extreme strain rate and temperature sensitivity with respect to their fracture toughness. Furthermore, data generated during this program has shown that there is not an easy remedy for this problem. Therefore, at this time, these types of materials do not appear suitable for primary structure on the HSCT, and will not be pursued further under the present contract.

Fracture Toughness Test Methods

A concern had arisen during the early part of the contract period concerning the proper method to evaluate the fracture toughness of the new or improved alloys developed during the present program. Therefore, a round-robin testing program was developed that would utilize various test methods requiring only small amounts of material, with the purpose of determining which of these methods would give the closest correlation to valid, wide center-cracked fracture specimens.

Obtaining valid plane stress fracture information (K_{Ic} and K_{Iap}) on 2024-T3 was a necessary first step to the process. Fortunately, the needed valid fracture toughness data could be, and was, made available to the subject NASA program from an ongoing Boeing IR&D fracture toughness evaluation program on sheet 2024-T3. Both technical and timing requirements were able to be met.

The Boeing plane stress fracture tests of interest to the subject program are completed. The test procedures and results of two 60 inch wide by 96 inch long 2024-T3 L-T center cracked fracture toughness test panels have been forwarded to NASA. These panels were 0.063 and 0.125 inches thick, respectively, and come from stock that was normally slated for aircraft fuselage applications. The remnants of the two fracture toughness panels were cut into eight 14" by about 34" long L-T panels (for each thickness). An additional four L-T panels of similar size (from each thickness) were cut from untested stock from which the 60" by 96" fracture panels were taken. Finally, three 14" by about 30" T-L panels were also taken from the subject 0.063" untested stock and two 14" by about 28" T-L panels were taken from the 0.125" thickness untested stock. The layout diagrams for these panels are shown in Figs. 1 through 4. Boeing retained one L-T panel from both the tested and untested material (from each thickness) and one T-L panel from the 0.063" thickness untested material and

sent the remaining 10 L-T and 2 T-L panels (from each thickness) to NASA for distribution to the participating laboratories.

Acknowledgments

The valuable contributions of Ludwig Suju (Design), Ken Barlow (Durability), Don Rudee (Fracture Test Laboratory) and John Lee (Materials) are gratefully acknowledged.

Table I. Test Matrix For The NASA/Boeing/UVA Program For Al Alloy Development-1992

Test Type	Subtask	Subtasks with Boeing Participation					
		Subtask 1A (page 20) 2XXX Ingot (Alcoa)	Subtask 1B (page 27) 6XXX Ingot (Alcoa)	Subtask 2C (page 36) Weldalite Type (Reynolds)	Subtask 3A (page 41) 2xxx P/M (Alcoa)	Subtask 5A (page 54) Al-Fe-X (Alcoa)	Subtask 7A (page 74) DMMC-2009 (Alcoa)
Tensile Strength R.T., L, LT -65 F, L. 215 F, L		4	4	4	4	4	4
		2	2	2	2	2	2
		2	2	2 at 275 F	2	2 at 350 F	2
Thermal Stability (tensile-L) Room Temp. 275 F/2500hrs		From TS above	From TS above	From TS above	From TS above	From TS above	From TS above
		2	2	2	2	2	2
Microstructure Room Temp. 275 F/100hr 275 F/1000 275 F/2500		1	1	1	1	1	1
		1	1	1	1	1	1
		1	1	1	1	1	1
		1	1	1	1	1	1
Kahn Toughness No Exposure L-T T-L 275 F/2500hr L-T		2		2	2	2	2
		2		2	2	2	2
		2		2	2	2	2
da/dn, CCP 2 Hz 60 Hz						2	
						2	

Boeing/NASA/UVA TP-92, WEQ

**Table II Fracture Toughness Activities in Support of the
NASA/UVA/Boeing Contract - 1992**

- **Fracture Toughness Test Results Were Reported To NASA For
Two Large 2024-T3 Center Cracked Panels.**
 - **60" wide by 96" long by 0.063" thick**
 - **60" wide by 96" long by 0.125" thick**
- **Supplied NASA with Material from the Above Test Panels
For Round Robin Fracture Tests by the Program Participants.**
 - **Twelve 0.063" thick by 14" wide by ~34" long L-T panels***
 - **Two 0.063" thick by 14" wide by ~34" long T-L panels**
 - **Twelve 0.125" thick by 14" wide by ~34" long L-T panels***
 - **Two 0.125" thick by 14" wide by ~34" long T-L panels**
- *** Eight panels were cut from the tested panel (1 through 8) and 4 from the untested
stock from which the panel was taken. Boeing retained one panel of each type for
in-house testing.**

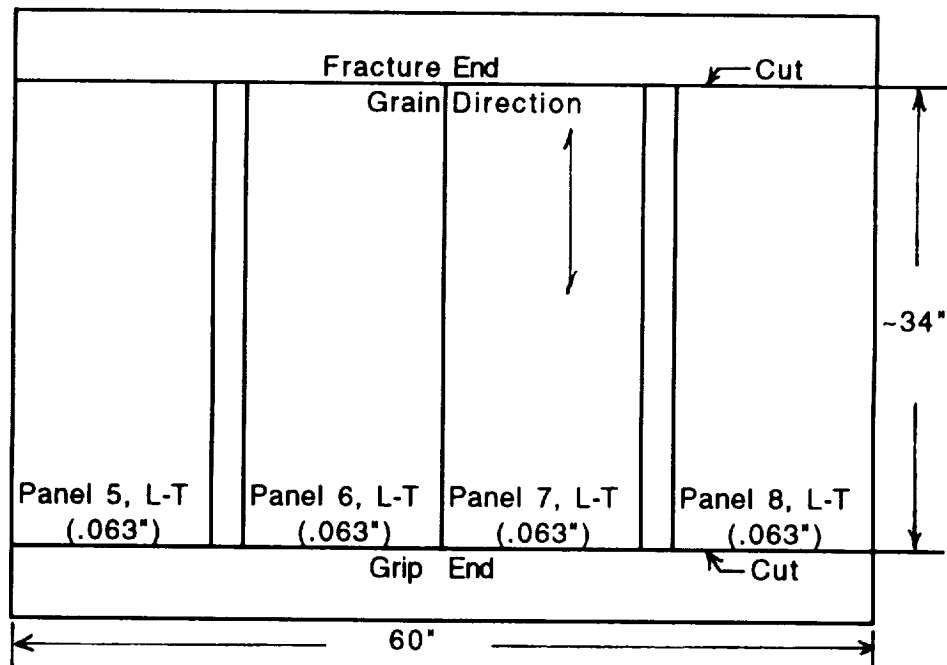
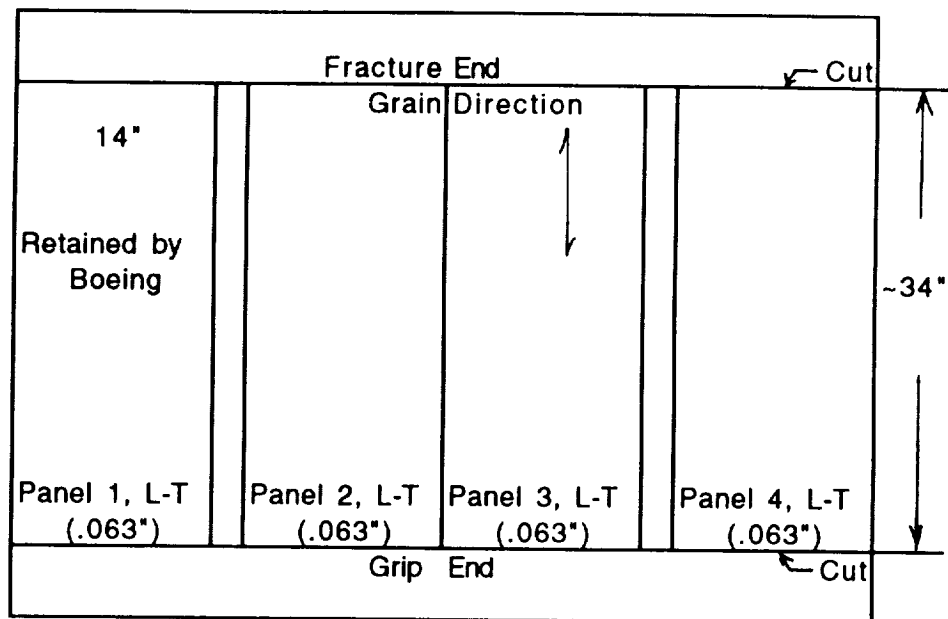


**Figure 1: 2024-T3 Fracture Panel, 60" x 96", 0.063" Thick
Boeing I.D. Number: AWD,**

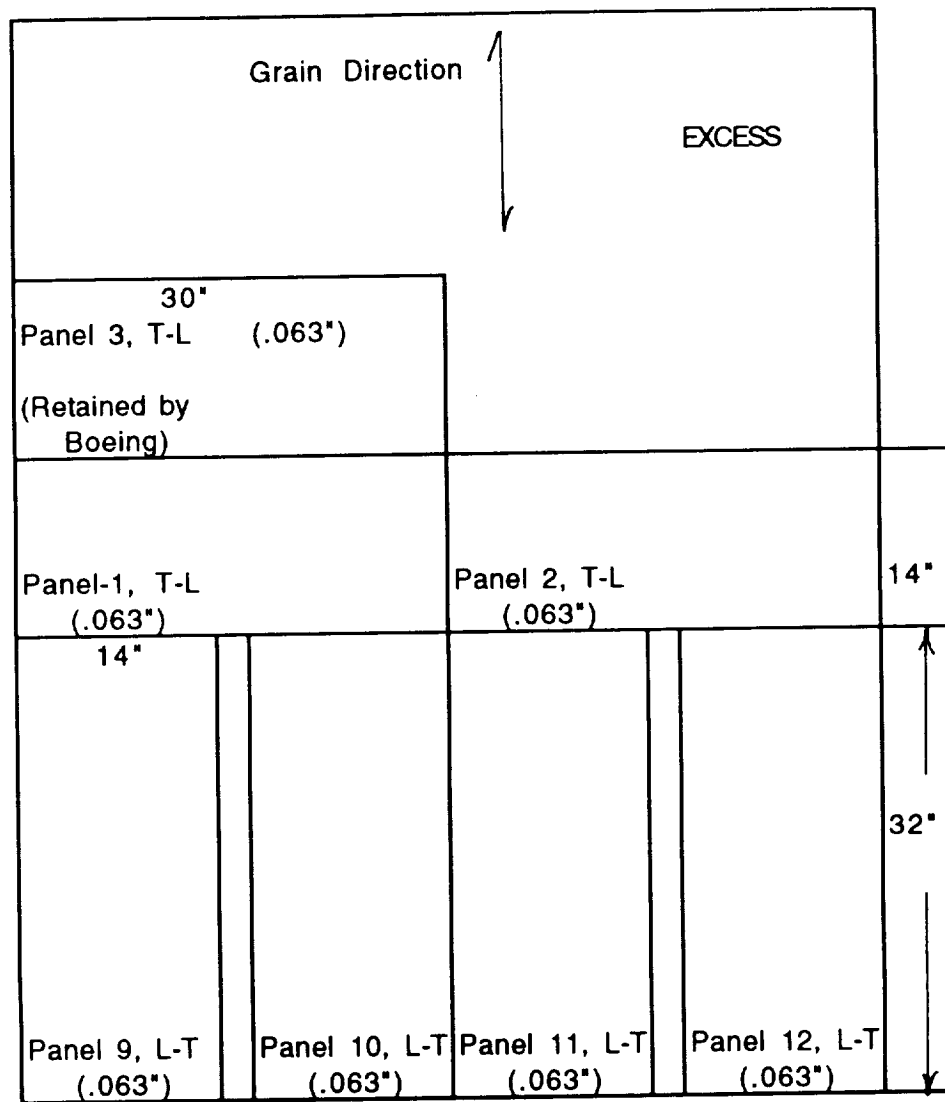


**Figure 2: 2024-T3 Stock From Which Panel Was Cut
(0.063" Thick)
Boeing I.D. Number: AWD, Size 60" x 79"**

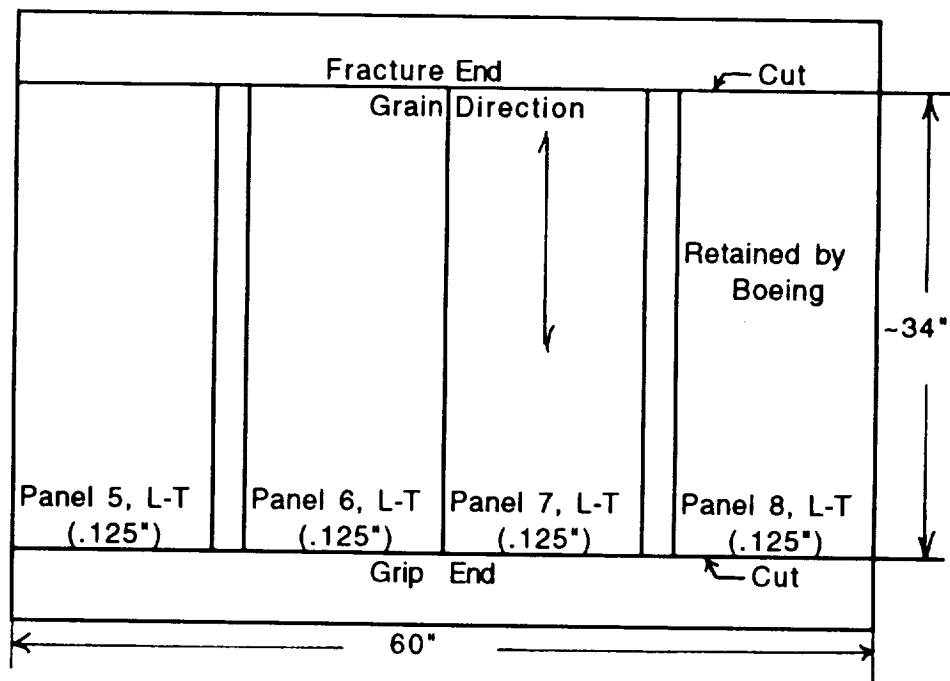
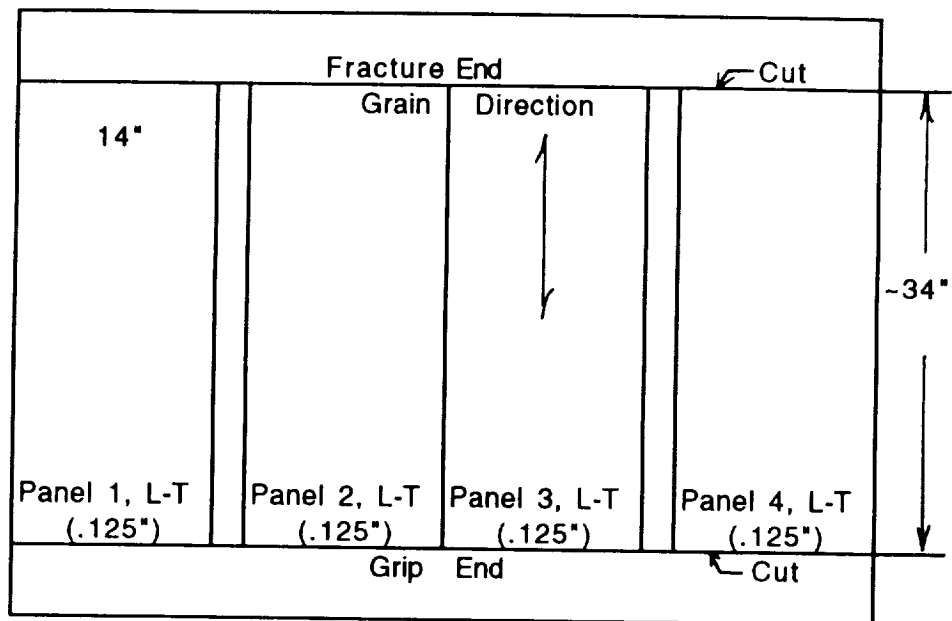


**Figure 3: 2024-T3 Fracture Panel, 60" x 96", 0.125" Thick
Boeing I.D. Number: AWF,**

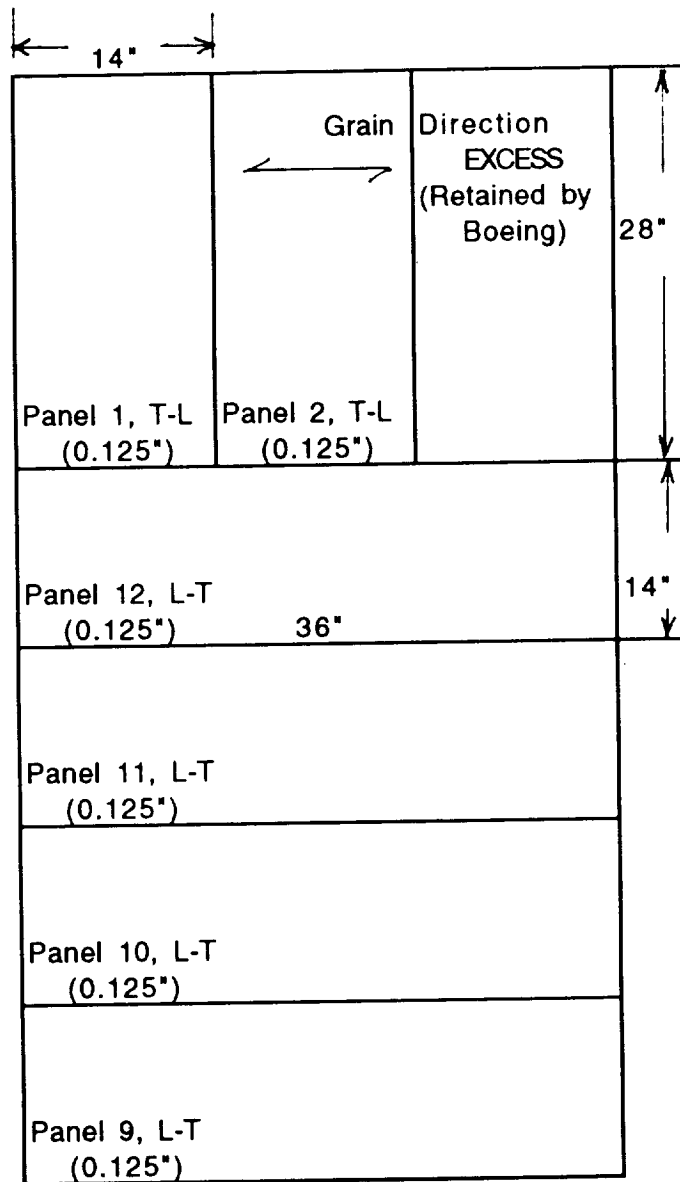


**Figure 4: Stock From Which Panel Was Cut
(0.125" Thick)
Boeing I.D. Number: AWF, Size 36" x 84"**

McDONNELL DOUGLAS REPORT ON MATERIALS CHARACTERIZATION

Principal Investigator: Dr. R. Kahandal

Objective

The economic viability of the next generation of supersonic transport depends upon the timely development of materials and structures which can perform efficiently for extended periods in an elevated temperature environment. The University of Virginia as directed by NASA-LaRC has assembled a team of material suppliers experienced in alloy development in a program to address this challenge. The overall objective of this program is to investigate and develop improved aluminum alloys and metal-matrix composites (MMCs) as candidates for application on a high speed civil transport (HSCT). These materials will be developed to meet target properties supplied by HSCT airframers McDonnell Douglas Aerospace-Transport Aircraft Unit (MDA-TA) and Boeing. The most promising candidates will be evaluated in baseline designs to obtain optimized material and structural vehicle concepts.

In addition to guiding the material development efforts by supplying target properties, MDA-TA will evaluate several developmental alloys to measure their ability to achieve these goals. MDA-TA will then use improved material properties to conduct HSCT structural sizing studies, vehicle optimization, and calculate aircraft configuration weight.

Approach

The approach for this program includes a six-month material development effort followed by six months of evaluation and structural/vehicle studies. MDA-TA will perform material evaluation in Tasks 1A, 1B, 2D, 3B and 7B according to the test matrix shown in Table 1. In addition, MDA-TA trade studies will be performed in Task 10B.

Results/Discussion

Material development efforts continued throughout the twelve-month contract period. As a result, no material was delivered to MDA-TA for evaluation. NASA-LaRC has extended the period of performance for twelve additional months. All contracts have been received and accepted for MDA-TA's participation in the extension.

On August 4, 1992, Ravi Kahandal attended the first semi-annual program review for this program held at Hampton, Virginia. Mr. Kahandal presented MDA-TA's plans for participation to NASA, UVa, material suppliers, and airframer personnel in attendance.

Jin Yu represented MDA-TA at the NASA-LaRC HSR Fracture Mechanics Technology Workshop held on September 10, 1992, at Langley, Virginia. This meeting was held to establish a standardized method for determining the toughness of emerging light alloys for the HSCT. A round-robin test program was established for validating plane-stress fracture toughness test methods using small, inexpensive specimens.

The second semi-annual program review was held January 19-20, 1993, at Hampton, Virginia. Mr. Kahandal represented MDA-TA. He detailed our plans for involvement and our recently revised tests matrix. We are currently awaiting material delivery from the suppliers.

TABLE 1. Test Matrix for Evaluating Candidate Materials

TEST	ORIENTATION	TESTS
FRACTURE TOUGHNESS (ASTM E399) [2]	L-T, T-L	4
SALT-FOG CORROSION (ASTM B117) [2]		
BLANK COUPONS	NA	4
INTERFERENCE-FIT FASTENERS [3]	NA	4
STRESS CORROSION CRACKING (ASTM G49) [2,4]	LT	18
MACHINING TRIALS		
CUTTING	NA	6
DRILLING/REAMING	NA	6
FORMING TRIALS		
BRAKE FORMING [5]	L, 30, 45, 60, LT	50
HYDROFORMING	NA	5
JOINING STUDY		
WELDING [6]	NA	6
ADHESIVE BONDING	NA	6
CHEMICAL PROCESSING		
CHEM MILLING	NA	2
ANODIZING	NA	2
TOTAL TESTS/ALLOY		113

[1] MATERIAL REQUIRED: 1000 SQUARE INCHES/LOT; MULTIPLE LOTS ACCEPTABLE; 12-INCH MINIMUM SHEET WIDTH

[2] TESTING BEFORE AND AFTER THERMAL EXPOSURE

[3] SIX EACH TI FASTENERS INSTALLED WET AND DRY AT STANDARD INTERFERENCE PER SPECIMEN

[4] SPRING-LOADED FLAT TENSILE SPECIMENS TESTED BY ALTERNATE IMMERSION

[5] MINIMUM BEND RADIUS: 2 SPECIMENS/RADII FOR 5 RADII

[6] TIG, LASER, CAPACITOR DISCHARGE, AND FLASH WELDING TECHNIQUES USED SUCCESSIVELY UNTIL ACCEPTABLE WELDS PRODUCED

